Transactions of the ASME®

Journal of Fluids Engineering

Published Quarterly by The American Society of Mechanical Engineers

VOLUME 124 • NUMBER 2 • JUNE 2002

FLUIDS ENGINEERING DIVISION
Editor
JOSEPH KATZ (2005)
Editorial Assistant
LAUREL MURPHY (2005)

Associate Editors
J. BRIDGES (2002)
S. CECCIO (2004)
I. CELIK (2003)
W. COPENHAVER (2004)
T. GATSKI (2003)
E. GRAF (2003)
G. KARNIADAKIS (2002)
J. MARSHALL (2003)
Y. MATSUMOTO (2002)
L. MONDY (2002)
M. ÖTÜGEN (2004)
M. PLESNIAK (2004)
A. PRASAD (2003)
B. SCHIAVELLO (2002)
Y. TSUJIMOTO (2002)

BOARD ON COMMUNICATIONS
Chair and Vice-President
OZDEN OCHOA

OFFICERS OF THE ASME
President, **W. A. WEIBLEN**
Exec. Director
D. L. BELDEN
Treasurer
R. E. NICKELL

PUBLISHING STAFF
Managing Director, Engineering
THOMAS G. LOUGHLIN
Director, Technical Publishing
PHILIP DI VIETRO
Managing Editor, Technical Publishing
CYNTHIA B. CLARK
Managing Editor, Transactions
CORNELIA MONAHAN
Production Assistant
MARISOL ANDINO

Transactions of the ASME, Journal of Fluids Engineering (ISSN 0098-2202) is published quarterly (Mar., June, Sept., Dec.) by The American Society of Mechanical Engineers, Three Park Avenue, New York, NY 10016. Periodicals postage paid at New York, NY and additional mailing offices.
POSTMASTER: Send address changes to Transactions of the ASME, Journal of Fluids Engineering, c/o THE AMERICAN SOCIETY OF MECHANICAL ENGINEERS, 22 Law Drive, Box 2300, Fairfield, NJ 07007-2300.
CHANGES OF ADDRESS must be received at Society headquarters seven weeks before they are to be effective. Please send old label and new address.

STATEMENT from By-Laws. The Society shall not be responsible for statements or opinions advanced in papers or ... printed in its publications (B7.1, Par. 3).
COPYRIGHT © 2002 by the American Society of Mechanical Engineers. Authorization to photocopy material for internal or personal use under those circumstances not falling within the fair use provisions of the Copyright Act, contact the Copyright Clearance Center (CCC), 222 Rosewood Drive, Danvers, MA 01923, tel: 978-750-8400, www.copyright.com. Request for special permission or bulk copying should be addressed to Reprints/Permission Department.

INDEXED by Applied Mechanics Reviews and Engineering Information, Inc. Canadian Goods & Services Tax Registration #126148048.

Special Section on Pump Analysis and Design

TECHNICAL PAPERS

ADDITIONAL TECHNICAL PAPERS

(Contents continued on inside back cover)

This journal is printed on acid-free paper, which exceeds the ANSI Z39.48-1992 specification for permanence of paper and library materials. ∞™
♲ 85% recycled content, including 10% post-consumer fibers.

Downloaded 03 Jun 2010 to 171.66.16.159. Redistribution subject to ASME license or copyright; see http://www.asme.org/terms/Terms_Use.cfm

(**Contents continued**)

Journal of Fluids Engineering **Volume 124, Number 2** **JUNE 2002**

TECHNICAL BRIEFS

ANNOUNCEMENTS

Journal of Fluids Engineering

Guest Editorial

Seven of the papers in this issue's special section were presented at the 4th International Symposium on Pumping Machinery in 2001. An additional four related papers are also included here. Together these papers summarize the progress that has been made in pump analysis and design since the earlier pumping machinery symposia in 1989, 1993 and 1997. There are still new and ongoing developments in many areas of the pump field, and this collection, which is representative of the advances in CFD and experimental applications. In these papers, it is evident that CFD is becoming commonplace in the analysis of both single- and two-phase flows in all types of pump geometry. This is in addition to experimental measurements via LDA and other techniques. Fundamental to the progress that has been made during this period is the extensive research and development that has been done by contributors from universities, pump manufacturers, and pump users.

Some of these papers deal with aspects of overall pump design and performance. Design systems with embedded CAD and CFD elements now utilize inverse methods of blade shape generation. CFD is now used routinely for performance prediction, as considerable progress in predicting the head curve shapes from shutoff to runout, has been made. In particular, there is progress made in the prediction of performance as influenced by cavitation. In this connection, progress is reported in the simulation of the impeller-volute interaction. Further, flow visualization is still used to aid the pump design process.

Experimental and analytical studies of the flow in pump components are treated in the papers on rotating cavitation in impellers, new discoveries relating to stall in vaned diffusers, and the rather obscure but profound influence of impeller ring leakage flows on hydrodynamic axial thrust. Additionally, the fluid induced rotordynamic forces and instabilities associated with unshrouded impellers have been addressed. New concepts for pumps and pump components are introduced, including a MEMS micropump.

What is clearly evident in all of the papers in this collection is the continuing creative application of fluids engineering expertise that is required to produce viable new concepts in both design and performance improvement.

Thanks go not only to reviewers of these papers, but also to their respective organizations for recognizing and supporting the continuous improvement of pumping machinery through application of the latest analytical and experimental methods, as well as the continual exercise of creative fluid dynamical insights that fuel the technology of these machines for the benefit of pump researchers, designers, and users. Finally, the authors themselves must be acknowledged for their major contribution to this collection of papers.

Dr. Adiel Guinzburg
The Boeing Company

Dr. Paul Cooper
Fluid Machinery Research, Inc.

Use of Surface Flow Visualization Methods in Centrifugal Pump Design

Christopher P. Hamkins

Stephan Bross

KSB Aktiengesellschaft, Frankenthal, Germany

Surface flow patterns generated with oils or oil paint have been used in centrifugal pump design for many years. Here it is shown how modern image analysis methods allow quantitative predictions of the corresponding pressure distribution by analyzing surface flow patterns. Further, the surface flow patterns can be used to confirm computational fluid dynamics (CFD) results, improve their boundary conditions and determine their limits of validity. The authors see the need for a new type of boundary condition for CFD packages, in which a measured flow pattern could be used as "input." [DOI: 10.1115/1.1470477]

Introduction

The use of oil mixtures for surface flow visualization in hydraulic machinery has a long history. In 1931 Busmann [1] used the method to do flow visualization in axial flow pumps. In preparation, he studied the flow pattern on rotating disks, even performing angle measurements to confirm von Kármán's 1921 [2] theoretical treatment. In recent years, however, the potential of these methods has been increased greatly through the use of automatic image analysis and computational fluid dynamics (CFD). Whereas oil surface flow patterns were used only quantitatively in the past, it will be shown here how quantitative information can be derived from them today.

One expects the surface flow pattern to be influenced by the pressure and flow distribution in the main flow. The authors have investigated what sort of quantitative conclusions are possible about the main flow by analyzing the surface flow angles.

Experimental Method

For the flow visualization, the operating point of the pump is adjusted while pumping normal test facility water and then the pump is turned off. Without changing the valve settings in the test loop, the pump is disassembled and a slow-drying oil paint (Leinos "Naturharz-Weißblack," article no. 820) is brushed on to the impeller, diffuser or casing. The thickness of the paint layer should be as for normal painting. Some knowledge of the expected flow pattern is helpful, since the paint need only be applied to the "upstream" regions and will flow naturally to those downstream, keeping in mind that the boundary layer flow direction can deviate substantially from the main throughflow. When the flow could result in a conglomeration of paint (paint from many starting points flows into a single ending region), then the paint should be applied very sparingly, and only at the starting points.

The pump is then assembled, the loop filled again with water, and the pump run for 1 or 2 minutes. The best length of time depends on the flow velocities and must be determined by trial and error. To start and stop the pump without disturbing the flow pattern, the speed of rotation is slowly increased with a frequency converter and after the test slowly decreased again; this should lead to approximately similar flow during the entire test. The development of the streaklines could be observed through a plexiglas cover plate in some of the rigs, which also confirmed that the beginning and ending transients had no visible influence on the developed flow pattern. Further details of the method are given by Hamkins [3].

A typical result for a flow pattern on the pump casing wall opposite the impeller is shown in Fig. 1. Although this pattern in the impeller side gap was taken at the best efficiency point of the pump, substantial asymmetries can be seen because the casing did not match the operating point of the impeller. Pressure was measured at 40 pressure taps distributed over the surface. Isobars estimated by interpolating between these taps are shown overlaid in Fig. 1. A definite correlation between pressure distribution and flow pattern can be seen.

Image Processing

The flow patterns were photographed with conventional photographic equipment under diffuse lighting (digital cameras currently have insufficient resolution). The photographs were analyzed at the Institute for Machine Design of the Technical University of Berlin, Department for Hydraulic Turbomachines and Fluid Dynamics, using custom-developed image processing software. The parts of each photo relevant to the flow were grayscale digitized (scanned). Each image was then divided into small square regions. In each region a Fourier-transformation was performed and the strongest frequencies present were determined. These frequencies give information about the flow direction.

The analysis uses methods that were originally developed to do particle image velocimetry (see [4] and [5]). One method of processing the particle images involves analyzing the so-called "Young's fringes." Essentially the same technique is used to determine the direction of the oil film pattern here. By analyzing the peaks in the Fourier transformation using a calculated center of gravity and assuming a Gaussian distribution, the location of the peak, and hence the flow angle, can be determined with a resolution better than a single pixel. Figure 2 shows the flow directions determined for the pattern shown in Fig. 1. The blank areas show where no analysis was possible.

This Fourier analysis of the flow angles was found to give much better results than attempting to identify the streaks as distinct features. Even with somewhat low-contrast images, satisfactory results could be obtained. The method fails in regions of paint conglomeration with no well-defined streakline direction, as one might argue that it should.[1] According to an analysis by Hamkins [3], an individual angle measurement by this method has an un-

---

Contributed by the Fluids Engineering Division for publication in the JOURNAL OF FLUIDS ENGINEERING. Manuscript received by the Fluids Engineering Division August 6, 2001; revised manuscript received December 17, 2001. Associate Editor: J. Katz.

[1] The method also often fails when applied to flow visualization photographs presented in printed journals because of aliasing. The photographs are usually rasterized to make them printable, which unfortunately introduces spurious frequencies which obscure the true flow direction.

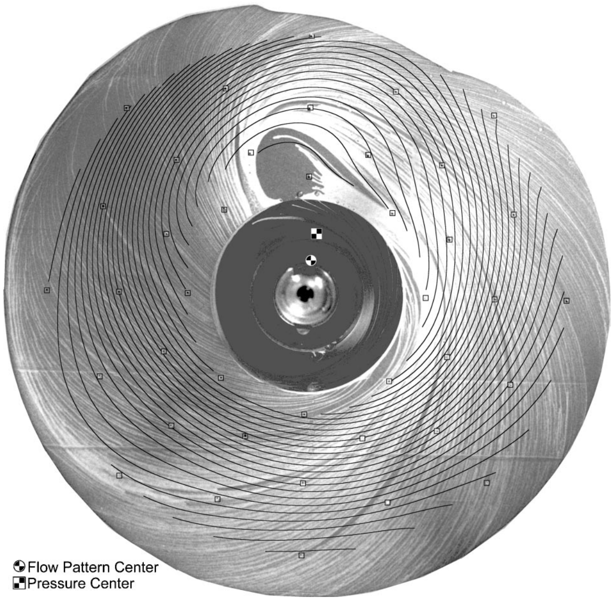

Fig. 1 Flow pattern on the back casing wall opposite the impeller, overlaid with isobars

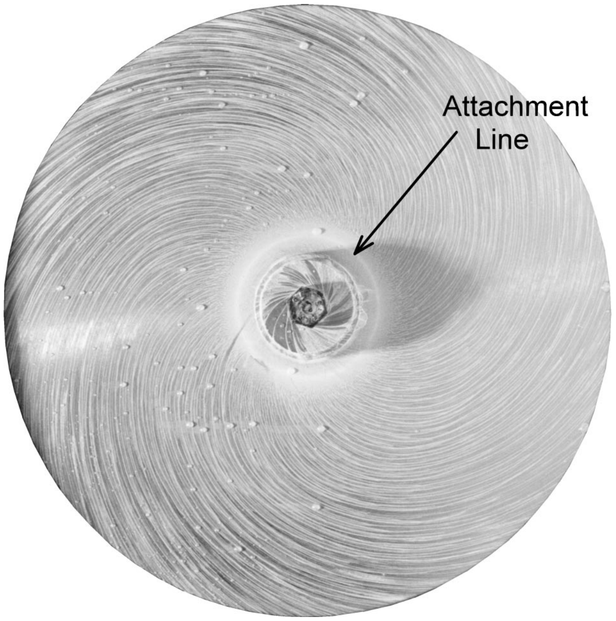

Fig. 3 Flow pattern on an impeller shroud for Re=$1.66\cdot10^{6}$ with radial inflow QL=−0.00008

certainty of about 5 deg, partly due to angle measurement errors but also due to deviations of the paint streakline from the ''true'' limiting flow angle. By making many angle measurements and averaging them (curve fits), uncertainties of under 0.5 deg are possible, which was confirmed by doing repeated measurements under the same conditions.

Application to Rotating Flows

Figure 3 shows the type of pattern which occurs on a rotating disk or as in this case, an impeller. Figure 4 shows the results of the angle determination using the automatic image analysis. The flow angle is defined relative to the tangential direction. Points further than 3 standard deviations from the fitted curve were removed, and the curve recalculated. The trend shown is typical in that the surface flow angle increases toward the inner radii.

Many boundary layer analyses of the rotating disk are present in the literature, most of them variations on von Kármán's original treatment [2]. Reference [3] contains a summary of the methods. The methods predict that the flow angle should be different for laminar and turbulent flow, but that it is otherwise independent of Reynolds' number. This prediction runs counter to many measurements in the literature and to the author's own measurements, both of which are shown in Fig. 5 (taken from [3]). The computed angles are very sensitive to the flow profiles assumed for the boundary layer analysis.

The values shown in Fig. 5 for the literature represent angle measurements reported by various authors ([6–9]) but also reanalysis of published photographs ([1,8,10,11]) using the current

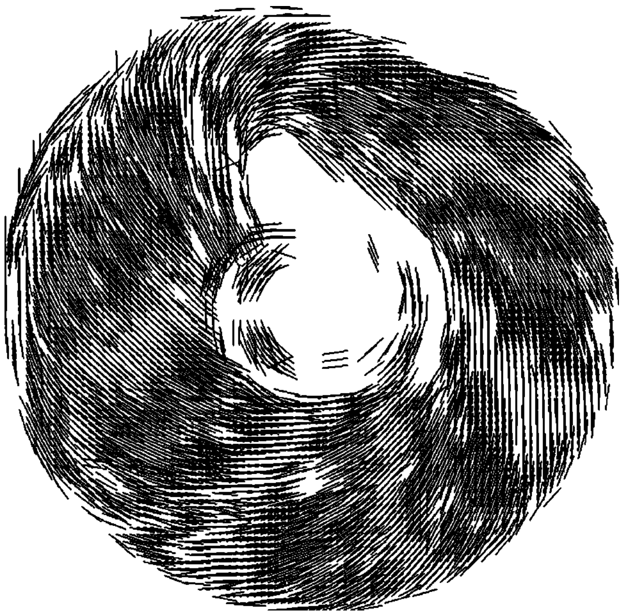

Fig. 2 Flow directions determined by imaging processing of Fig. 1

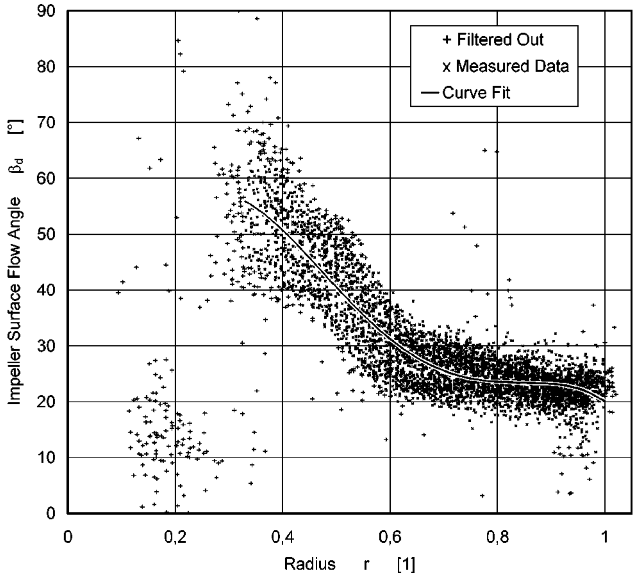

Fig. 4 Flow angles (individual points ±5 deg; curve fit ±0.5 deg) determined by image analysis of Fig. 3

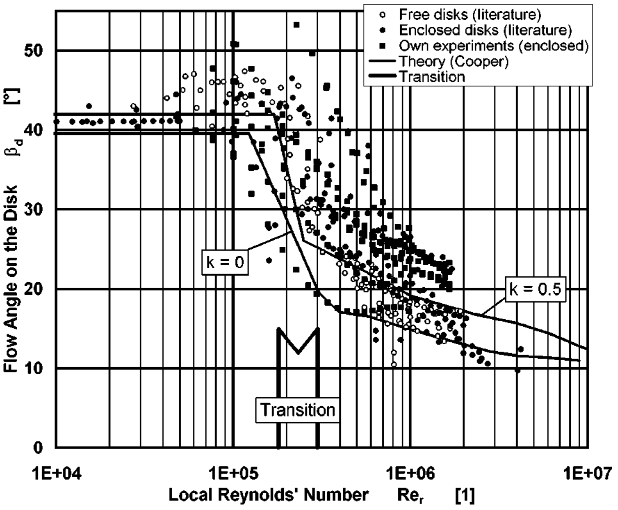

Fig. 5 Flow angles (±0.5 deg) dependent on local Reynolds number

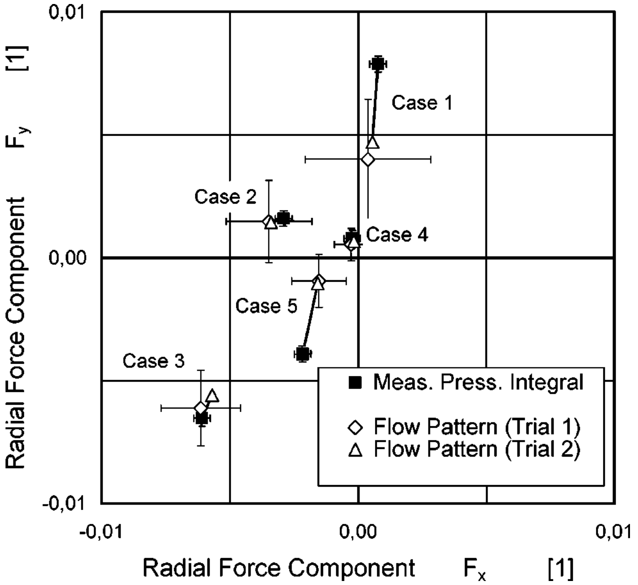

Fig. 6 Correlation of impeller radial force determined by integrating the measured pressures and by analyzing the flow pattern

methods. The author's own experiments are reported in detail in [3] as well as a list of published photographs which could not be analyzed due to the reasons in footnote 1.

A clear trend of decreasing flow angle for higher Reynolds' numbers can be seen, albeit with quite a bit of scatter. Hamkins [3] discovered that part of the scatter can be explained by differences in the rate of core fluid rotation in the impeller side gap. A faster core leads to larger limiting flow angles. A very gross empirical correlation was found as

$$\Delta \boldsymbol{\beta}_{\mathbf{d}} \approx 2\Delta \mathbf{k} \tag{1}$$

where the flow angle $\boldsymbol{\beta}_d$ is expressed in radians and $\mathbf{k}$ is the core rotation rate. The delta symbol designates the differences in flow angle and rotation rate, all else being constant.

The only theoretical treatment found in the literature which predicts both the Reynolds' number and core rotation effects was that of Cooper [12], shown as lines in Fig. 5. The classical (von Kármán) boundary layer methods do predict a core rotation effect, but underestimate its magnitude compared to the measurements.

The pressure gradient in the impeller side gap is related to the core rotation as

$$\partial \mathbf{p}/\partial \mathbf{r} = \mathbf{r}\mathbf{k}^2 \tag{2}$$

Using the correlation in Eq. (1), the core rotation can be estimated by analyzing the flow angles; the pressure distribution can then be obtained by integration of Eq. (2). Unfortunately, the uncertainty in the gross empirical correlation is so large that the predicted pressure distribution is hardly more accurate than those obtained using purely theoretical methods.

An improvement in accuracy can be obtained when an attachment line is present in the pattern. In Fig. 3, such an attachment line can be seen at the radius $\mathbf{r}=0.23$. The attachment line forms when the core fluid and the disk or impeller are rotating at the same speed. The core fluid rotates faster than the impeller at smaller radii and more slowly than the impeller at larger ones. In other words, the attachment line fixes the radius at which $\mathbf{k}=1$. This knowledge can result in a significant improvement in predicting the pressure distribution. Such large core rotation rates are only present with strong radial inflow in the impeller side gap, however.

When an asymmetric pressure distribution is present at the impeller periphery, as is the case for off-design operation in a volute casing, for example, the flow in the impeller side gap is also influenced. The asymmetries are clearly visible in the surface flow patterns, which can be quantitatively analyzed to determine a "flow pattern center" which correlates with the center of the pressure distribution. The correlation can be used to estimate the circumferential pressure distribution and impeller radial force.

In [3], it was discovered that in these cases a rotationally symmetric but eccentric core flow in the impeller side gap is a good model to explain the measured pressure distributions there. In other words, the core flow rotates smoothly about some point, but that point does not coincide with the axis of rotation of the impeller. Using this model, the circumferential pressure distribution can be estimated by assuming that the "flow pattern center" correlates with the center of core flow rotation. The details are given in [3].

Figure 6 shows the results of the correlation. The radial forces were calculated by integrating the measured pressure distribution and by analyzing the flow pattern. The correlation is good, but is limited by the uncertainties involved in finding the flow pattern center.

Comparison of Patterns and CFD Results

By using numerical codes, the proper setting of boundary conditions is necessary to achieve a physically correct solution. In case of hydrodynamic turbomachines, the well known boundary conditions *velocity inlet* and *pressure outlet* are in use. Especially for the outlet condition one has to make sure that the real outlet flow is not influenced by distortions appearing downstream of the outlet plane. In case of pump stages with impeller and diffuser, it is state of the art to treat each element separately, reducing the complexity and computational efforts of the problem. This is valid as long as the interaction of both elements can be neglected and therefore the pressure outlet condition can be used.

In Figs. 7(*a*) and 7(*b*) a comparison of experimentally and numerically evaluated oil flow pictures on the pressure side of a vane of a radial impeller operating at its best efficiency point is presented. Looking from the impeller outlet into the blade channel, the hub and shroud as well as two vane trailing edges can be identified. The impeller inlet is located on the bottom. The observed shear stress lines (streaklines) are slightly curved passing from the hub to the impeller shroud. Looking at the computed streamlines, a good agreement of both flow patterns can be stated. These calculations were performed for the isolated impeller using the normal pressure outlet conditions. Here, the influence of the diffuser vanes vanishes and the assumptions included in the outlet conditions are valid.

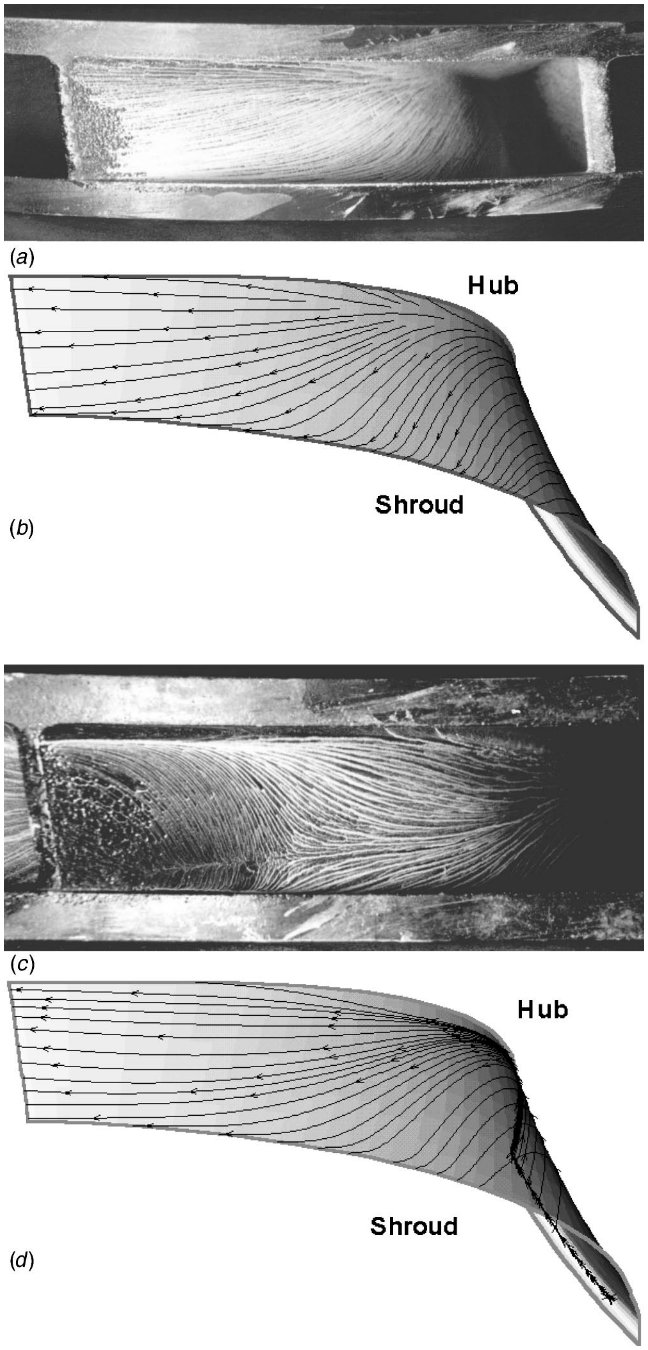

Fig. 7 Comparison of experimental and numerical impeller oil flow pictures. (*a*) **Experimental, 100% BEP,** (*b*) **computational, 100% BEP,** (*c*) **experimental 57% BEP,** (*d*) **computational 57% BEP.**

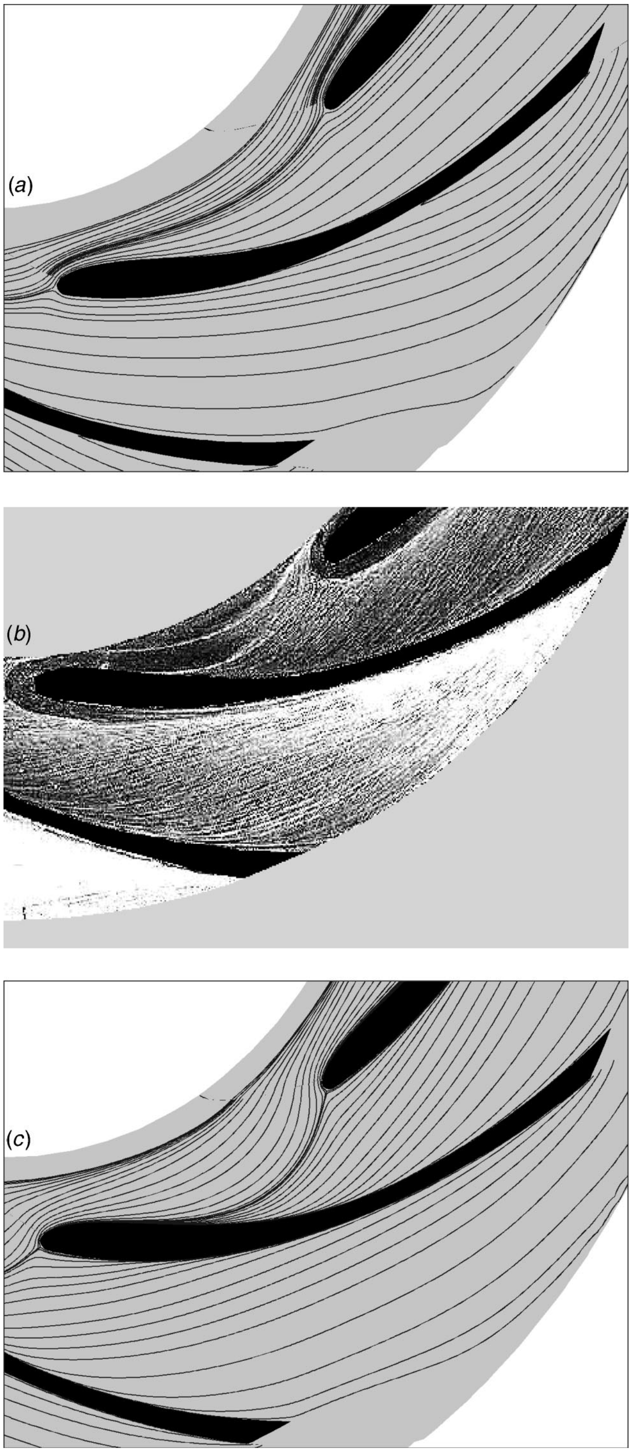

Fig. 8 Flow patterns in a vaned diffuser. (*a*) **Computational result with uniform inlet velocity profile boundary condition,** (*b*) **experimental oil flow pattern,** (*c*) **computational result with distorted inlet velocity profile boundary condition.**

Reducing the flow rate to 57% of best efficiency flow rate, only a part of the calculated flow pattern can be identified in the experiment (Fig. 7(c)). Here, the flow at the impeller outlet is mainly influenced by a strong interaction, creating a reverse flow from the diffuser back into the impeller. Of course this behavior cannot be simulated using the normal outlet condition, so that a complete stage simulation has to be performed, or a better outlet condition has to be defined using the oil flow pictures as a reference. The limits of applicability of the flow field computation have been determined by performing the flow visualizations.

Similar results occur if the diffuser of a radial pump stage is treated separately using velocity inlet and pressure outlet boundary conditions. In this case, the pressure outlet represents the physical reality quite well, especially if a volute or a large ring casing is used downstream. Here, it is the unknown inlet condition e.g., the inlet velocity profile (impeller outlet velocity profile) that mainly influences the numerical solution.

In Fig. 8, the oil flow pattern occurring in a radial pump stage diffuser running at 80% of BEP is presented. On the measured oil flow picture (Fig. 8(*b*)) a distinct curved streamline can be identified, connecting the blade pressure (concave) side of one blade with the leading edge stagnation point of the next. Moreover, rather than being parallel to the blades, the surface streamlines in the blade channel are inclined from the blade pressure (concave side) to the blade suction (convex) side. By using a uniform velocity profile as the inlet flow condition (Fig. 8(*a*)), the agreement between numerical and experimental results is weak. By using a distorted inlet velocity profile (Fig. 8(*c*)), good agreement between both results was reached. The shape of the inlet profile was evaluated by trial and error. During the adjustment, the tangential velocity was left constant, but the radial velocity profile was changed from a uniform profile to a linear distribution between hub and shroud (keeping the flow rate constant). Three or four tries were necessary to achieve the agreement shown. In this case, the experimental oil flow pictures were used as an additional boundary condition to get some information about the expected impeller outlet flows.

Conclusion

Surface oil flow patterns can be analyzed to directly obtain quantitative information about a flow field. They can also be used to adjust boundary conditions for computational fluid dynamics (CFD) simulations by trial and error until a good match with the measured pattern is found. The resulting computation should be a better representation of the flow than that with a simple boundary condition.

As proposed by Hellmann [13], the authors see the need for an additional type of boundary condition for CFD packages, namely the measured angles of the surface flow pattern itself. They see the development of such an ''inverse'' calculation method as a problem that is likely to be tractable, albeit challenging, but which will have many advantages. Eventually it could be possible for a CFD package to perform an image analysis on a flow pattern to produce the input boundary condition for a calculation. The results of such a calculation ought to have a high degree of reliability since they are based on a measured pattern.

Acknowledgments

The authors would like to thank Prof. R. D. Flack, Mr. D. Baun, and Mr. J. Kuss of the University of Virginia for providing the flow visualization and pressure measurements shown in Fig. 1.

Nomenclature

F = force
$\mathbf{F}$ = dimensionless force $\mathbf{F}=F/2\pi\rho {r_0}^4\omega^2$
$\mathbf{k}$ = core rotation $\mathbf{k}=u_\theta/\omega r$
p = pressure
$\mathbf{p}$ = dimensionless pressure $\mathbf{p}=(p-p_0)/\rho {r_0}^2\omega^2$
$\mathbf{Q}_L$ = dimensionless radial flow in side gap $\mathbf{Q}_L=Q_L/2\pi {r_0}^3\omega$
r = radius
r_0 = outer radius of disk or impeller
$\mathbf{r}$ = dimensionless radius $\mathbf{r}=r/r_0$
$\mathbf{Re}$ = disk Reynolds' number $\mathbf{Re}=\omega {r_0}^2/\nu$
$\mathbf{Re}_r$ = local Reynolds' number $\mathbf{Re}_r=\omega r^2/\nu$
u = velocity of fluid
ν = viscosity
ρ = fluid density
ω = angular speed of disk or pump rotation

References

[1] Busmann, F., 1931, ''Versuche über die Grenzschicht-Bewegung auf rotierenden Scheiben,'' Forschung auf dem Gebiet der ingenieur Wesen, Forschung, 2. Band, **9**, pp. 335–339.
[2] Von Kármán, T., 1921, ''Über laminare und turbulente Reibung,'' Zeitschrift für angewandte Mathematik und Mechanik, **1**(4), pp. 233–252.
[3] Hamkins, C. P., 2000, ''The Surface Flow Angle in Rotating Flow: Application to the Centrifugal Pump Impeller Side Gap,'' Shaker Verlag, Aachen, dissertation of the University of Kaiserslautern.
[4] Scheffler, T., 1998, ''Particle-Image-Velocimetry zur Untersuchung Hydraulischer Strömungsmaschinen,'' dissertation, Technische Universität Berlin.
[5] Ulbrich, C., 1997, ''Experimentelle Untersuchung der Pumpencharakteristiken und Geschwindigkeitsfelder einer Einschaufel-Kreiselpump,'' dissertation, Technische Universität Berlin.
[6] Arakawa, C., and Tagori, T., 1980, ''Fundamental Experiments of Oil Films on a Rotating Disk,'' Flow Visualization II: Proceedings of the 2nd Internat. Symp. on Flow Visualization, Sept. 9–12, Bochum, West Germany, Hemisphere Publishing, Washington, DC, 1982, ISBN 0-89116-232-1.
[7] Itoh, M. et al., 1992, ''Experiments on Turbulent Flow Due to an Enclosed Rotating Disk,'' Exp. Therm. Fluid Sci., **5**, pp. 359–368.
[8] Kato, H., Watanabe, K., and Naya, K., 1978, ''Visualization of Fluid Flow Near a Rotating Disk in Dilute Polymer Solutions,'' Bull. JSME, **21**(161), pp. 1618–1622.
[9] Kurokawa, J., and Sakuma, M., 1998, ''Flow in a Narrow Gap Along an Enclosed Rotating Disk with Throughflow,'' JSME Int. J., Ser. II, **31**(2), pp. 243–251.
[10] Bilgen, E., 1971, ''On the Stability of Viscoelastic Flow Due to a Rotating Disk,'' Chem. Eng. Prog., Symp. Ser., **67**(11), pp. 74–84.
[11] Jaksic, M., and Tobias, C. W., ''Hydrodynamic Flow Visualization by an Electrochemical Method,'' Flow Visualization II: Proc. of the 2nd Internat. Symp. on Flow Visualization, op cit.
[12] Cooper, P., 1972, ''Turbulent Fluid Friction of Rotating Disks,'' PhD dissertation, Case Western Reserve Univ.
[13] Hellmann, D.-H., Private correspondence, Universität Kaiserslautern.

Hydrodynamic Design of Pump Diffuser Using Inverse Design Method and CFD

Akira Goto
Ebara Research Co., Ltd.,
Fujisawa-shi, Japan

Mehrdad Zangeneh
Department of Mechanical Engineering,
University College London,
London, UK

A new approach to optimizing a pump diffuser is presented, based on a three-dimensional inverse design method and a Computational Fluid Dynamics (CFD) technique. The blade shape of the diffuser was designed for a specified distribution of circulation and a given meridional geometry at a low specific speed of 0.109 (non-dimensional) or 280 (m^3/min, m, rpm). To optimize the three-dimensional pressure fields and the secondary flow behavior inside the flow passage, the diffuser blade was more fore-loaded at the hub side as compared with the casing side. Numerical calculations, using a stage version of Dawes three-dimensional Navier-Stokes code, showed that such a loading distribution can suppress flow separation at the corner region between the hub and the blade suction surface, which was commonly observed with conventional designs having a compact bowl size (small outer diameter). The improvements in stage efficiency were confirmed experimentally over the corresponding conventional pump stage. The application of multi-color oil-film flow visualization confirmed that the large area of the corner separation was completely eliminated in the inverse design diffuser. [DOI: 10.1115/1.1467599]

Introduction

Computational Fluid Dynamics (CFD) has become one of the most essential tools for optimizing the hydrodynamic and aerodynamic design of various turbomachines. CFD can predict the occurrence of unfavorable flow phenomena, such as flow separation, as a result of complex interactions between various types of secondary flow motion and the development of viscous layer under the influence of an adverse pressure gradient, at least qualitatively. However, CFD does not directly state what modification of the blade shape should be made to improve such unfavorable flow phenomena. Consequently, in spite of the significant advancement of CFD and enormous amount of information on the flow fields, the design method of the blade geometry itself still remains very conventional and relies greatly on empiricism. The conventional design approach faces difficulty in optimizing blade geometry under the complex three-dimensional (3-D) effects of the flow fields.

Two approaches are possible for optimizing turbomachinery blade geometry: one based on the iterative use of a CFD code for different geometry (so-called direct method), and the other based on an inverse method whereby the required flow field features are specified as input and the corresponding blade geometry is calculated theoretically. A two-dimensional theory of the inverse method for turbomachinery has found industrial applications for designing new two-dimensional blade profiles suitable for a cascade [1]. However, the two-dimensional theory has not been truly useful for designing turbomachinery blades, since even in axial-flow machines, 3-D effects cannot be ignored.

Hawthorne and his co-workers proposed a practical 3-D theory for turbomachinery blade design. Hawthorne et al. [2] and Tan et al. [3] developed an inverse design method based on the use of Clebsch formulation. Then Borges [4] extended the theory to 3-D theory for designing incompressible radial-inflow turbines, and finally Zangeneh [5] extended the theory further for designing mixed and radial flow turbomachines in a compressible flow. The inverse design method, however, assumes an inviscid flow, while the viscous effects dominate the flow fields in the actual machine. Also, it is not clear what type of flow field feature, specified for the inverse design, is optimum for a given design specification.

The problems were solved with advances in CFD and computer hardware. Now, it is easy to numerically simulate 3-D viscous flow fields to validate and optimize the input for the inverse design method. Once such optimum input data, having a solid physical background, is found, then it can be applied to similar designs of turbomachinery blades. The inverse design method has good control of 3-D pressure fields and makes it possible to achieve an innovative design of turbomachinery blades such as to obtain a high efficiency design, a high suction performance design, and a very compact design. Zangeneh et al. [6] and Goto et al. [7] applied the method to a mixed-flow pump impeller to suppress the meridional component of secondary flows. A complete description of the methodology to design centrifugal and mixed-flow impellers (both for pumps and compressors) with suppressed secondary flows was given by Zangeneh et al. [8].

In the present paper, a design method, featuring a blade design based on the 3-D inverse design method and the assessment of hydrodynamic design based on the 3-D viscous flow calculation method, was applied to re-design a diffuser pump stage. Figure 1 presents a computational grid used for CFD of a stage flow. The specific speed of the target pump was 0.109 (nondimensional) or 280 (m^3/min, m, rpm). Although both the impeller and the diffuser

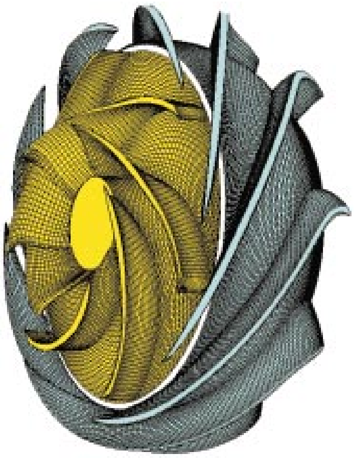

Fig. 1 Computational grid (Case G)

Contributed by the Fluids Engineering Division for publication in the JOURNAL OF FLUIDS ENGINEERING. Manuscript received by the Fluids Engineering Division August 6, 2001; revised manuscript received January 18, 2002. Associate Editor: B. Schiavello.

were re-designed by the inverse method, the design methodology was validated mainly for the vaned bowl diffuser in this paper. For details on the application of the 3-D inverse design method for impellers, see Zangeneh et al. [8].

Firstly, the flow fields in a conventional design pump stage were investigated by a CFD prediction using Dawes 3-D Navier-Stokes code (Walker and Dawes, [9]), focusing the flow mechanism leading to the occurrence of a large-scale corner separation on the hub surface. Then the 3-D inverse design method proposed by Zangeneh [10] was applied to redesign the diffuser blade and the validity of the design methodology was confirmed numerically using the Dawes code. Finally, the performance and the flow fields of the inverse design pump stage were compared with the conventional design experimentally to confirm the advantages of this new design methodology.

Numerical Method

Inverse Design Method. The 3-D inverse design method proposed by Zangeneh [5] was used in the present work. In this potential based method, the flow is assumed to be irrotational and steady. The blade mean camber surface is represented by a sheet of vorticity, whose strength is determined by a specified distribution of bound circulation $2\pi r V_\theta$. Here, V_θ is a circumferentially averaged swirl velocity. The effects of the blade thickness are simply considered as blockage effects in the continuity equation of the mean flow. The method has been extended by Zangeneh [10] to include the effects of inlet shear flow, which is important for the design of diffuser blades receiving non-uniform flow from the upstream impeller.

The blade shape is determined by integration of a first order hyperbolic partial differential equation along the meridional projections of streamlines on the blade surface. An initial value of a blade shape (a rake angle) along a quasi-orthogonal at the trailing edge was specified as input in this paper, which is called the stacking condition.

The input of this design method are (i) blade loading (distribution of bound circulation $2\pi r V_\theta$), (ii) meridional geometry, (iii) axial and radial velocity distribution at inlet, (iv) rotational speed ω which is zero for a diffuser design, (v) blade thickness distribution, (vi) blade number, and (vii) stacking condition. Among these, the loading distribution is the most important design parameter to control 3-D flow fields. The inlet velocity distribution can be specified on the basis of the CFD prediction for the upstream impeller. The blade thickness is determined based on the consideration for structural strength. The meridional geometry and the blade number are specified based on existing knowledge, but they may be optimized by a systematic survey for the same loading distribution if necessary. In the conventional design method, the modification of meridional geometry will also affect the loading distribution at the same time, even if the blade angle distribution is kept the same. However, in the inverse design, it is possible to investigate the effects of the changes in meridional geometry while keeping the blade loading pattern the same.

In the present design system, the blade loading is specified by giving the distribution of $\partial(rV_\theta)/\partial m$, which is the derivative of angular momentum (rV_θ) along the meridional distance m. Figure 2 shows the blade loading parameter $\partial(rV_\theta)/\partial m$ for the diffuser Case G (the optimized diffuser case discussed in the following chapters). The $\partial(rV_\theta)/\partial m$ distribution is specified for each of the casing and the hub surfaces, then the rV_θ distribution is derived by the integration of $\partial(rV_\theta)/\partial m$ along the meridional distance m on hub and casing surfaces. The distribution is defined by a "three-segment" method, which employs a combination of two parabolic curves and an intermediate linear line. Three design parameters (connection point locations NC and ND, slope of the linear line) are used to define the distribution curve. The rV_θ distributions in the intermediate part of the blade are obtained by a linear interpolation for rV_θ between the hub and the casing.

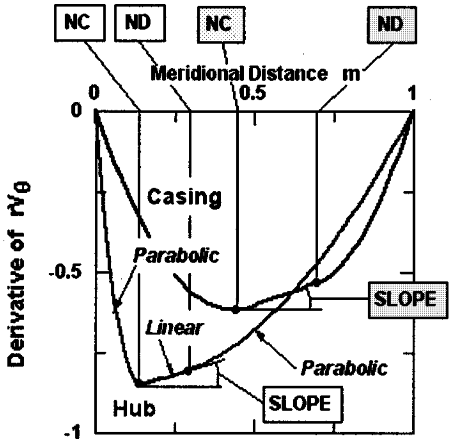

Fig. 2 Definition of blade loading parameter (Case G)

The design parameter is directly related to the pressure loading ($p^+ - p^-$: the pressure difference across the blade) through the following equation for incompressible potential flows, see Zangeneh [5] for detail.

$$p^+ - p^- = (2\pi/B)\rho W_{\mathrm{mbl}} \partial(rV_\theta)/\partial m. \qquad (1)$$

where B is the blade number, ρ is density, W_{mbl} is the meridional component of a relative velocity on the blade. The zero values of $\partial(rV_\theta)/\partial m$ at $m=0$ (LE: leading edge) and $m=1.0$ (TE: trailing edge) automatically specify the zero flow incidence and the Kutta condition, respectively. The fore-loaded and aft-loaded designs are easily achieved by arranging the peak location of $\partial(rV_\theta)/\partial m$ in the forepart and in the aft part of the blade, respectively. Controlling values of NC, ND and SLOPE can do this very easily.

CFD Method. The CFD code used in the present paper is a Dawes code for incompressible flow (Walker and Dawes, [9]) and its extension to a stage version (Goto, [11]), which solve Reynolds averaged Navier-Stokes equations using the Baldwin-Lomax turbulence model and Chorin's method of artificial compressibility. An inter-row mixing plane model (Denton, [12]) was incorporated into the stage version between adjacent blade rows to simulate steady flows within a pump stage having a rotating impeller and a stationary vaned bowl diffuser. The boundary conditions at the mixing plane were extrapolated from variations of fluxes at upstream and downstream cells, allowing the circumferential variations of fluxes on both sides of the mixing plane while maintaining the overall conservation of the fluxes across the mixing plane. For details about the mixing plane model, see Denton [12].

In order to validate the design for a variety of the blade loading distribution, the computational grid size for CFD needs to be minimized to reduce CPU time per design case. A relatively coarse grid was used in the present paper: the number of the grid points was typically 58,121 per blade pitch: (pitchwise, streamwise, spanwise)=(19, 161, 19). Additional calculations were carried out using 130,625 grid points for grid dependency tests, and it was confirmed that the differences in overall performance and the flow fields were very small. The predicted stage efficiency difference between these two grid cases was 0.1 points for Case G. The grid points were clustered near endwalls and blade surfaces to resolve viscous layer, and the log law was employed to estimate the wall shear stress. Figure 3 compares the flow pattern on wall surfaces in the conventional pump diffuser (Case C) between CFD and experiments, which will be discussed later in detail. It can be confirmed that the current grid is suitable for capturing the corner separation in the bowl diffuser that is the most important flow feature for the present study.

In the performance prediction, the mixing losses downstream from the diffuser due to the exit swirl and the flow nonuniformity

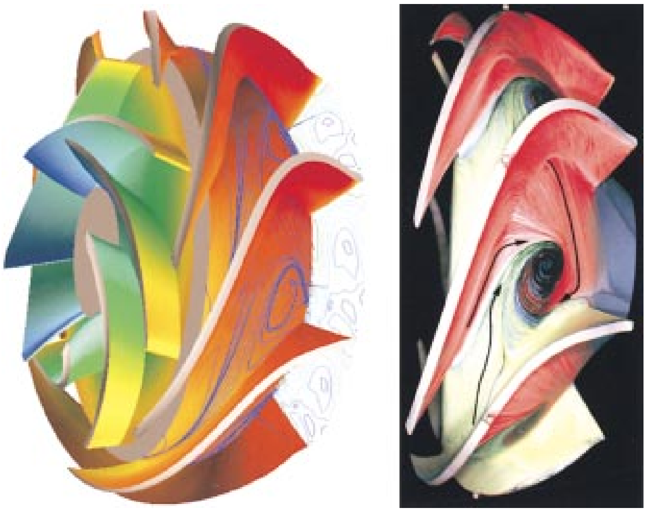

Fig. 3 Conventional design stage Case C (design point). (*a*) CFD prediction; (*b*) oil-film flow pattern

were taken into account. For details, see Goto [13]. However, the effects of leakage flows through wearing rings and balance holes and the disk friction action on the impeller hub and shroud back surfaces were neglected, since all these effects are identical for all design cases and do not affect the relative comparison of pump performance. The Dawes code has been validated extensively by Goto [14] for pump impellers, and Goto [11], Takemura and Goto [15], and Goto [13] for diffuser pump stages.

Conventional Design and Discussion

Pump Specification. The model pump is a low-specific-speed diffuser pump stage with a centrifugal impeller and a vaned bowl diffuser, see Fig. 3(*a*). The conventional diffuser had seven blades and is designated as ‘‘Case C’’ diffuser. The design specification was flow rate of 3.3 m^3/min and pump head of 8.77 m at a rotational speed of 800 rev/min, giving a specific speed of 0.109 (nondimensional) or 280 (m^3/min, m, rpm). The midspan impeller outer diameter was $D_{2m}=0.328$ m, and the design head coefficient was $\Psi=H/(U_{2m}^2/g)=0.46$. Here, $U_{2m}=\omega D_{2m}/2$ is the peripheral speed of the impeller. The diffuser was designed to be compact and the maximum outer diameter of the diffuser was 1.28 times the outer diameter of the impeller. The reduction of the outer diameter of the diffuser inevitably increases blade loading and careful control of the flow fields is required to achieve high performance.

Conventional Diffuser Design. Conventionally, the 3-D geometry of a vaned bowl diffuser is designed by specifying blade angle distribution in the meridional direction, together with meridional geometry of the flow passage. The inlet angle of the blade is arranged so that the incoming flow from the upstream impeller matches the diffuser blade. On the other hand, the outlet blade angle of the blade is arranged at around 90 degrees (in the axial direction) aiming to reduce the swirl velocity at the diffuser exit. The blade angle distribution connecting the inlet and the outlet is designed based on various criteria. Some designer uses a monotonous and smooth curve based on the experience, while another designer may decide the blade shape based on cascade flow consideration. However, there is no established method to design the blade shape considering the 3-D pressure fields and related viscous flow phenomena in the bowl diffuser, although the flow is highly three-dimensional and dominated by complex secondary flows as will be discussed in the following section. The blade angle distribution for the conventional diffuser Case C is presented in Fig. 11.

Experiments and CFD Prediction. The conventional design pump Case C was manufactured from a block of aluminum alloy by a five-axis numerically controlled milling machine. The manufacturing error was confirmed to be less than 0.2 mm. Then, the Case C model pump was placed in a closed flow loop consisting of a 200-mm-dia suction pipe, a 350-mm-dia delivery pipe, a 10.3-m^3 reservoir tank, and a return line with a 200-mm-dia magnetic flow meter and throttle valves. The rotational speed of the impeller was 800 rpm, giving a Reynolds number of Re $=U_{2m}D_{2m}/\nu=4.5\times10^6$. Performance tests were carried out according to ISO standards. The uncertainty in performance tests was evaluated as ±0.8% for flow rate, ±0.3% for total pressure rise, and ±0.5% for shaft power at the design point. Measured performance curves are presented in Fig. 16.

To visualize wall surface streamlines, a multi-color oil-film method, proposed by Goto [11], was applied. Fluorescent powder, having three different colors (red, blue, and yellow), was used as pigment with oleic acid, turbine oil, grease oil, and kerosene. The viscosity of the oil-film was adjusted to get a clear picture of the flow pattern by changing the mixture ratio, depending on local flow velocity. In the present study, the hub and the casing (shroud) surfaces were painted with blue oil-film, while the blade suction and pressure surfaces were painted with yellow and red oil-films respectively. The flow pattern obtained with the three colors and the mixed colors is very useful for determining the interaction between secondary flows, as well as the source of secondary flows.

Figure 3 compares the results of the multi-color flow visualization of diffuser wall surface streamlines with particle path lines predicted by CFD. Although the flow rate was that for the design point, a large separation vortex was observed on the hub surface. In this conventional diffuser, such extensive corner separation was observed even at 130% of the design flow rate. Figure 4 presents the velocity vectors predicted by CFD, which shows the detail secondary flow pattern. The strong cross flow at the diffuser inlet region, moving from the blade suction surface towards the blade pressure surface along the hub, was clearly identified as yellow streamlines on the hub in Fig. 3(*b*). The yellow oil-film was originally painted only on the blade suction surface, and so it is clear that the cross flow was originated as strong spanwise secondary flows on the blade suction surface, also see Fig. 4(*a*). Conversely, at the after part of the diffuser, a strong cross flow in the opposite direction, i.e., from the blade pressure surface towards the blade suction surface, was observed experimentally (red streamlines on the hub in Fig. 3(*b*)), as well as numerically (Fig. 3(*a*) and Fig. 4(*c*)).

Figure 5 shows the static pressure contours on the blade suction surface and the total pressure contours on the annular cross-section at 25%-chord location of the diffuser. Here, the local value of the static and the total pressure coefficients were defined as follows:

$$\text{Pressure coefficient: } \Psi=(\text{pressure rise})/(\rho U_{2m}^2) \qquad (2)$$

$$\text{Static pressure rise coefficient: } \Delta\Psi_{\mathrm{s}}=\Psi_{\mathrm{s}}-\Psi_{\mathrm{s,TE}} \qquad (3)$$

$$\text{Total pressure loss coeficient: } \Delta\Psi_{\mathrm{t}}=\Psi_{\mathrm{t}}-\Psi_{\mathrm{t,TE}}. \qquad (4)$$

Where $\Psi_{\mathrm{s,TE}}$ and $\Psi_{\mathrm{t,TE}}$ are the mass-averaged value of the static and total pressure at the impeller trailing edge respectively. Low total pressure fluids, generated in the fore part of the blade suction surface (Region A in Fig. 5(*a*)), were brought into the hub due to the meridional secondary flows (Fig. 4(*a*)). The total pressure loss became very high in the corner region (Region C in Fig. 5(*b*)). Downstream from this region, the adverse pressure gradient became high in Region B in Fig. 5(*a*). The thick viscous layer, generated by the accumulation of low total pressure fluids in Region C, is less resistant against the adverse pressure gradient, and the flow is separated at this corner region.

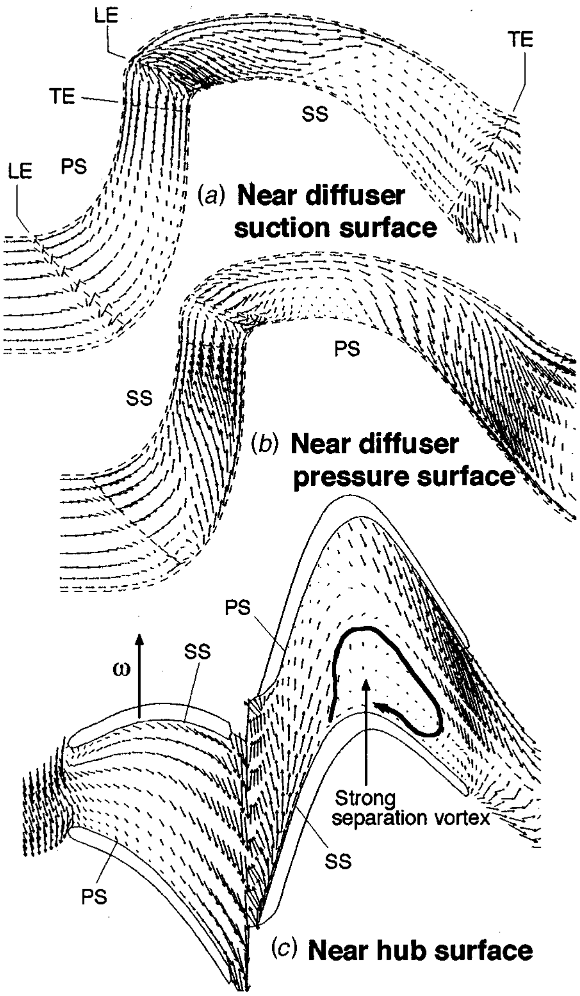

Fig. 4 Velocity vectors near blade and hub surfaces of conventional stage Case C at design point

Note here that the static pressure contours are not very smooth at the inlet part of the diffuser blade, see Fig. 5(*a*). This was caused by the mismatched flow incidence, which must be improved in the redesign of the diffuser blades.

Preliminary Design and Discussion

Effects of Meridional Geometry and Blade Number. As was described in the previous section, both CFD and experiments showed the occurrence of major flow separation in the conventional diffuser, which was believed to cause significant reduction in efficiency. In addition to the redesign of blade shape by the application of the 3-D inverse design method, two possible measures were examined. One is the change of meridional configuration, since the diffuser flow passage area of Case C seems to be expanding too rapidly between the mid-chord and the trailing edge location, which may cause excessive diffusion of the flow and flow separation. The other is the increase of the blade number to reduce the loading per each diffuser blade. Through the detail investigation using CFD in the following sections, however, it was clarified that it is not very straightforward to improve the diffuser flow by these design modifications.

Preliminary Design. The meridional configuration along the hub surface was modified to reduce the passage area towards the diffuser exit and also the diffuser blade number was increased from seven to eight. Then, three diffusers with different blade shapes were designed to have relatively simple/conventional blade angle distributions: Cases A, F, and N. Case A represents the aft-loaded diffuser blade, where the blade-to-blade passage changes its direction at the after part of the diffuser. The blade angle increases steeply after about 70%-chord location, as shown by square symbols in Fig. 6. Conversely, Case F represents the fore-loaded diffuser blade, where the blade angle started increasing rapidly at around 30%-chord as shown by circles in Fig. 6. Case N represents the intermediate loading between Cases A and F, and the blade angle increases rapidly after 50%-chord location. When the blade angle increases rapidly, the flow turns its direction from the tangential towards the axial direction. The blade-to-blade streamline curvature becomes large, which generates a large pressure gradient in the pitchwise direction and the blade loading across the blade becomes large.

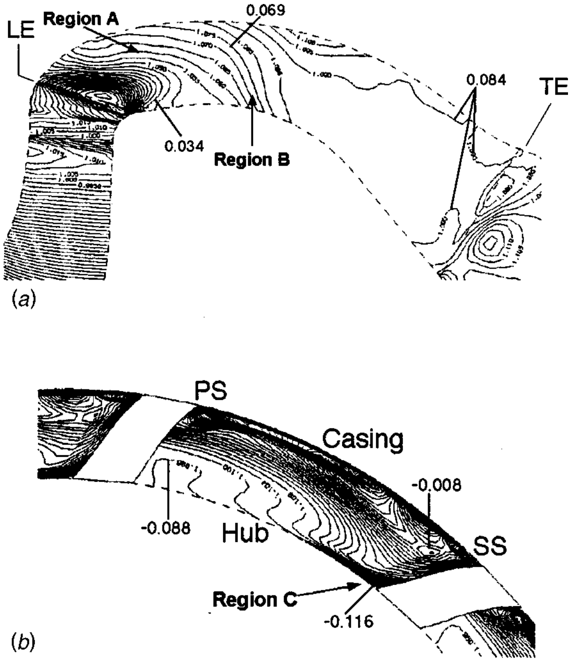

Fig. 5 Static and total pressure fields in conventional diffuser Case C at design point. (*a*) Static pressure $\Delta\Psi_s$ on diffuser suction surface; (*b*) total pressure $\Delta\Psi_t$ on quasi-orthogonal plane at 25%-chord location

In all cases, the inlet and the outlet blade angles were fixed to be identical, and the blade thickness distribution was the same. Based on these blade angle distributions, the 3-D diffuser blade shapes were generated. The flow fields of these conventional diffusers were then calculated using the stage version of Dawes

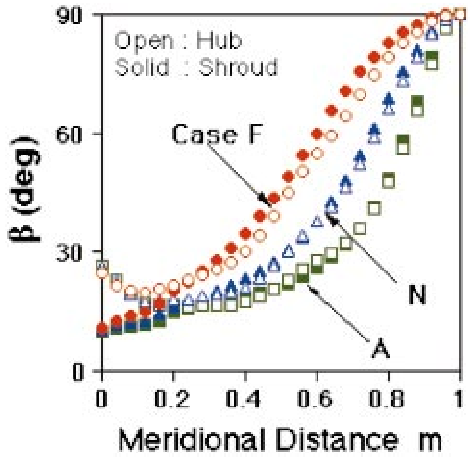

Fig. 6 Blade angle distribution of preliminary design cases having conventional blade angle features

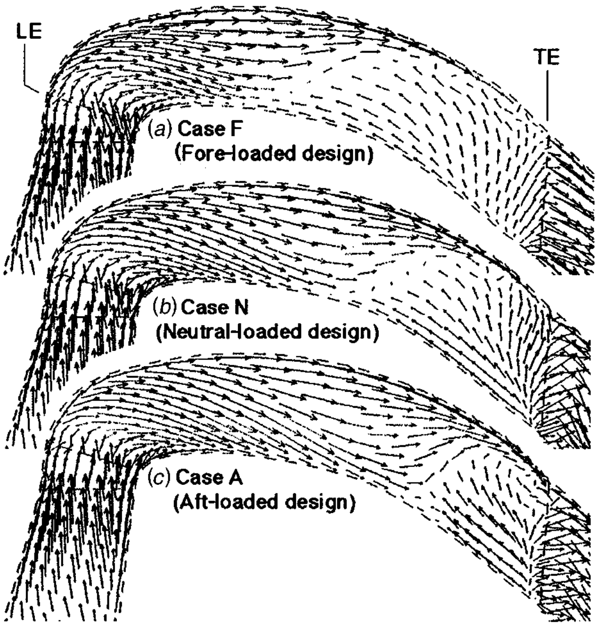

Fig. 7 Velocity vectors near suction surfaces of conventional diffusers at design point

Navier-Stokes code. Note here that the same impeller, which was redesigned by the 3-D inverse design method, was used for all three cases.

Figures 7 and 8 show the numerically predicted velocity vectors close to the blade suction surface of the diffuser and close to the hub surface, respectively. In each case, a wide area of reverse flow was observed on the blade suction surface (Fig. 7). A huge separation vortex was observed in Case F, occupying the whole blade-to-blade passage in the hub region. As the blade loading was shifted downstream, the core location of the separation vortex also moved downstream, and the pitchwise extent of separation was also reduced. In Case N and Case A, the area of flow separation was narrower than that in Case F, but it still occupied significant areas of the flow passages. Although the location and the magnitude of the separation vortex were different between Case A, N, and F, the basic flow structure featuring 3-D flow separation at hub-suction surface corner was identical.

Figure 9 shows the static pressure contours on the blade suction surface and the total pressure contours on the annular flow passage at 59%-chord location for Case N. Basic flow structure is identical to Case C, see Fig. 5. In all cases presented here, the corner flow separation in the diffuser passage was caused by the similar flow mechanism as Case C. Namely, the low momentum fluid, generated by the high friction at the diffuser inlet, was accumulated along the corner between the hub and the blade suction surface (ex. Region C, Fig. 9(*b*)) due to the secondary flow action. The thick viscous layer thus formed along the corner separated when it was exposed to the severe adverse pressure gradient where the blade started turning more rapidly (ex. Region B, Fig. 9(*a*)).

Figure 10 summarizes the numerically predicted overall loss $\Delta\Psi$ generated between a streamwise location and the pump inlet, together with the hydraulic efficiency η of the pump stage and the pressure recovery coefficient Cp for the diffuser in each design case.

$$\Delta\Psi=\Psi_e-\Psi_{\text{ave,t}} \tag{5}$$

$$\eta=\Psi_{\text{t,OA}}/\Psi_e \tag{6}$$

$$Cp=(\Psi_{\text{s,OA}}-\Psi_{\text{s,TE}})/(\rho V_{\text{TE}}^2) \tag{7}$$

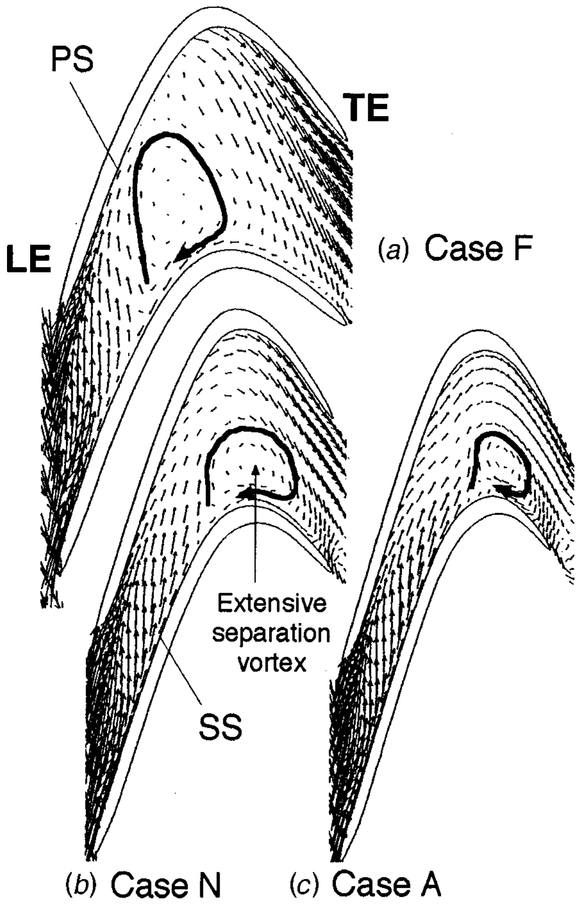

Fig. 8 Velocity vectors near hub surface of conventional diffusers at design point

Here, Ψ_e is the Euler head generated by the impeller, $\Psi_{\text{ave,t}}$ is the mass-averaged total pressure rise at a streamwise location, $\Psi_{\text{t,OA}}$ is the mass-averaged total pressure rise at diffuser exit including downstream mixing losses, $\Psi_{\text{s,OA}}$ is the mass-averaged static pressure rise at diffuser exit, and V_{TE} is the area-averaged absolute velocity at impeller TE.

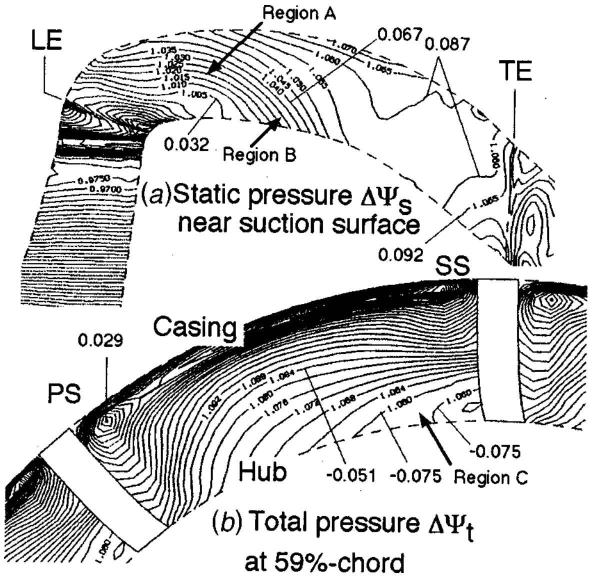

Fig. 9 Static and total pressure fields in conventional diffuser Case N at design point

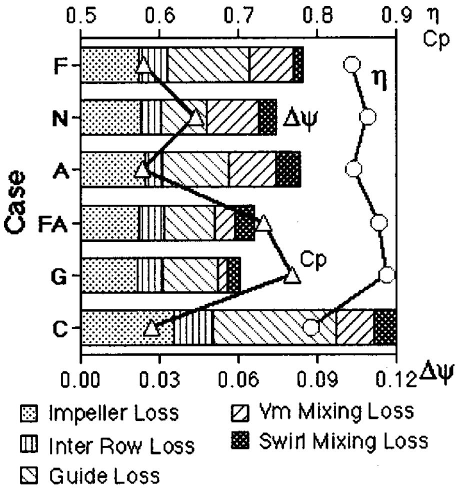

Fig. 10 Comparison of predicted overall performance and hydraulic loss analysis at design point

The bar graphs of flow losses show the overall loss and its components. Here, the losses generated in the flow passage are classified into the following five components.

- "Impeller Loss"-Inlet boundary to impeller TE
- "Inter Row Loss"-Impeller TE to diffuser LE
- "Guide Loss"-Diffuser LE to diffuser TE
- "Vm Mixing Loss"-Downstream of diffuser TE (Mixing loss due to the flow non-uniformity)
- "Swirl Mixing Loss"-Downstream of diffuse TE (Mixing loss of exit swirl velocity)

In Case F, the majority of the loss was generated inside the diffuser flow passage, while in Case N the mixing loss downstream from the diffuser was highest. The predicted stage efficiency was 84.5% for Case F, 86.4% for Case N, and 84.6% for Case A. The pressure recovery was highest for Case N, which was 0.647.

It is easily understood that it will be difficult to avoid this type of flow separation without controlling the pressure gradient and the secondary flow phenomena. Because of this, the use of an inverse design methodology considering the 3-D flow phenomena in the bowl diffuser is worth to be examined. Note here, similar corner separation is commonly observed in diffuser pumps with compact machine size or under part-load operating conditions.

Inverse Design Approach and Discussion Based on CFD

Inverse Design Diffuser Case G. It is well acknowledged that a thick boundary layer is easy to separate when it is exposed to a high adverse pressure gradient, while a thin boundary layer is more resistant to the adverse pressure gradient. Under such circumstances, it is necessary to decelerate the flow as quickly as possible in the fore part of the flow passage. Such a consideration is especially important when designing low specific speed diffusers, because the flow coming into the diffuser has a very high swirl velocity and most of the friction losses are generated in the fore part of the diffusers. However, careful control of the flow fields is required to avoid flow separation due to excessive deceleration. At the same time, it is important to consider the effects of the migration of low momentum fluids in the corner region which is another cause of the corner separation as shown in Case C and Case N.

A series of diffuser blades was designed using the 3-D inverse design method with different combinations of loading distributions between the hub and the casing. Here, the meridional geometry, blade number, and blade thickness distribution for this design are the same as Cases F, N, and A. The flow was then calculated using the 3-D Dawes Navier-Stokes code, and overall performance and the flow fields were evaluated. The most desirable loading distribution was found to be a fore loading at the hub, see Fig. 2. From Eq. (1), it is clear that the hub is more fore-loaded as compared to the casing.

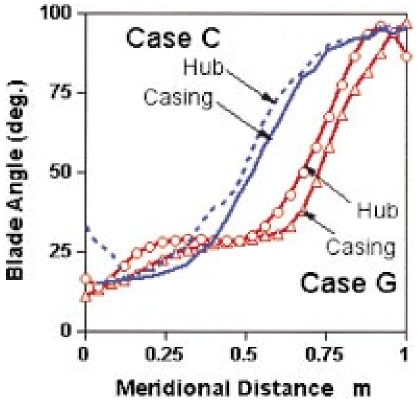

Fig. 11 Comparison of blade angle distribution between conventional Case C and inverse design Case G

The use of the optimized blade loading significantly reduced the extent of the corner separation. So, the key design aspect is apparently the optimization of the blade loading parameter. However, a very small region of corner separation was still observed.

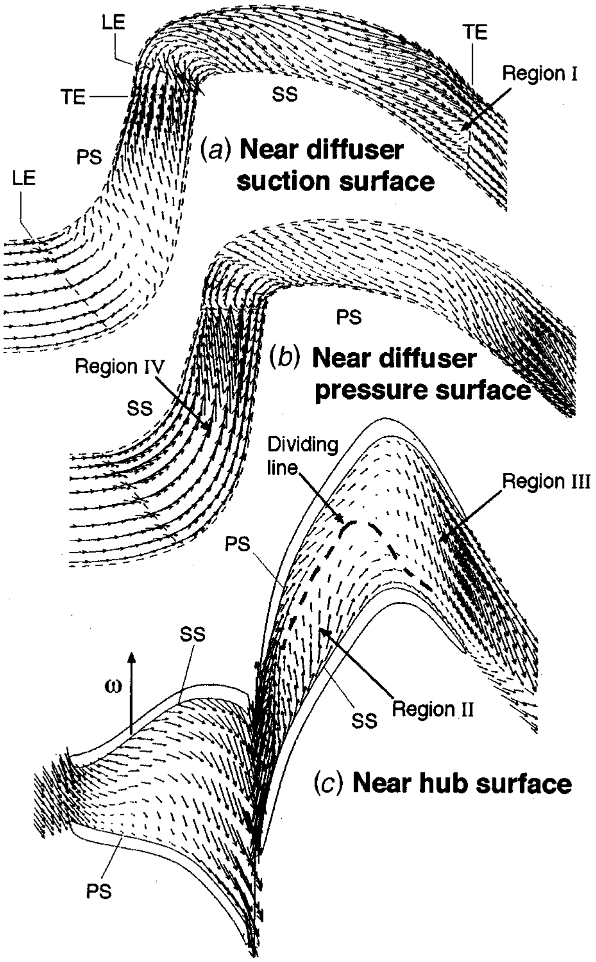

Fig. 12 Velocity vectors near blade and hub surfaces of inverse design stage Case G at design point

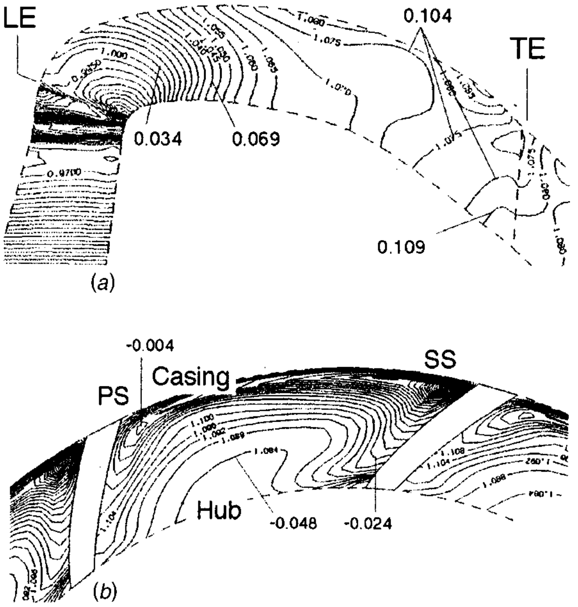

Fig. 13 Static and total pressure fields in inverse design diffuser Case G at design point; (*a*) Static pressure $\Delta\Psi_s$ on diffuser suction surface; (*b*) total pressure $\Delta\Psi_t$ on quasi-orthogonal plane at 25%-chord location

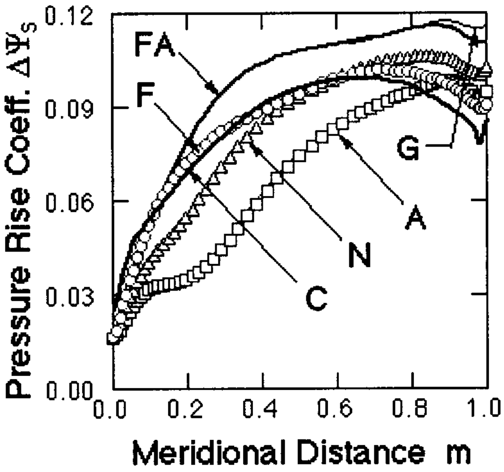

Fig. 14 Streamwise change in mass averaged static pressure rise coefficient at design point

So, the effects of other design parameters in the 3-D inverse design were investigated further, and it was found that the small corner separation could be eliminated by the introduction of a stacking of 0.15 radians (rake angle) at the trailing edge plane. Namely, the angular co-ordinate of the trailing edge at the hub preceded that at the casing by 0.15 radians in the direction of impeller revolution. This design is designated as "Case G." The effects of rake angles are discussed in detail in Appendix.

The blade angle distribution of Case G is compared with that of Case C in Fig. 11. The blade angle at the hub is greater than that at the casing in the region of $m<0.4$, which reflects the higher loading in the front part of the blade at the hub side as compared to the loading at the casing side.

In the following sections, the flow mechanism in Case G, leading to avoid the corner separation, will be discussed in detail based on the CFD predictions by Dawes 3-D Navier-Stokes code.

Suppression of Corner Separation. The flow fields in the inverse design stage are presented in Figs. 12 and 13. The corner flow separation observed in the conventional stage Case C (and other conventional diffusers Cases F, N, and A) was completely eliminated in the inverse design diffuser Case G. Due to the fore loading at the hub surface, the static pressure contour lines are more perpendicular to the flow passage (compare Fig. 13(*a*) with Fig. 5(*a*)). Because of this change in 3-D pressure fields, the secondary flows, flowing towards the hub surface on the diffuser blade suction surface, became much stronger than those for Case C, compare Fig. 4(*a*) and Fig. 12(*a*). The stronger spanwise secondary flows swept the low momentum fluids away from the corner region, and the low momentum fluids were accumulated in the midpitch location (Fig. 13(*b*)). The momentum exchange between the low momentum fluids and the surrounding main flows is more active in the midpitch location than the same in the corner region, which contributed to prevent the onset of flow separation. At the same time, the adverse pressure gradient around the mid-chord location was reduced (see Fig. 13(*a*)) by the fore loading at the hub. Those flow patterns are more resistant to the onset of corner flow separation.

Pressure Recovery. Figure 14 compares the mass-averaged pressure rise coefficients $\Delta\Psi_s$ of the different designs. The Case G diffuser, designed by the 3-D inverse method, shows good pressure recovery with a slight reduction after the 90%-chord location. The fore-loaded diffuser (Case F) shows a rapid increase of static pressure in the fore part of the passage, but the rate of pressure recovery was reduced after 25%-chord due to the occurrence of the extensive corner separation. No recovery occurred after 70%-chord. In Case G (and Case FA), the pressure recovery was significantly improved between 20% and 40%-chord due to the suppressed corner flow separation. The aft-loaded diffuser (Case A) shows very poor pressure recovery in the fore part of the passage due to the lower blade loading (and the smaller velocity deceleration). The pressure recovery of Case C was similar to Case F, which shows the peak value of 0.1 at 69%-chord and then decreases toward the diffuser exit. The predicted pressure recovery coefficient Cp for the conventional design Case C was 0.58 while it was 0.77 for the inverse design Case G, see Fig. 10.

Overall Efficiency and Loss Components. In Fig. 10, the predicted overall stage efficiency and the loss components of Case G are compared to those of other design cases. The loss at each streamwise location for Case G was significantly reduced from the same for Case C. Because of this, the predicted stage efficiency of Case G is 89.0% and was higher than that of Case C by 9.8 points. The loss inside the diffuser passage (between the leading and trailing edges) for Case G is higher than Case N. However, the mixing loss due to the flow non-uniformity in meridional velocities was reduced from Case N. The improvements in stage efficiency from Case N were 1.7 points for Case G.

Exit Flow Uniformity. Figure 15 compares the velocity ratio VR defined as $\mathrm{VR}=V_{m,m\text{-ave}}/V_{m,a\text{-ave}}$, here $V_{m,m\text{-ave}}$ represents circumferentially mass-averaged meridional velocity and $V_{m,a\text{-ave}}$ circumferentially area-averaged meridional velocity. Velocity ratio VR becomes 1.0 when the flow is perfectly uniform, and it increases as the meridional velocity becomes less uniform. In Cases A and N, VR is much higher at the hub side region as the separated flow region stayed at the hub side, and so the high mixing loss observed in Fig. 10 was generated mainly in this region. However, in Case F, the corner separation occurred at a location much farther upstream, and the separated flow region rolled up away from the hub surface and finally moved to the casing region at the diffuser exit. This is why the flow non-uniformity is high at the casing region in Case F. The flow in Case G is more uniform throughout the span by the optimized blade loading and the introduction of the stacking effects. The flow in Case C is extremely non-uniform and VR was as large as 4.5 at the hub side and larger than 2.5 up to 80%-span location (not plotted in Fig. 15).

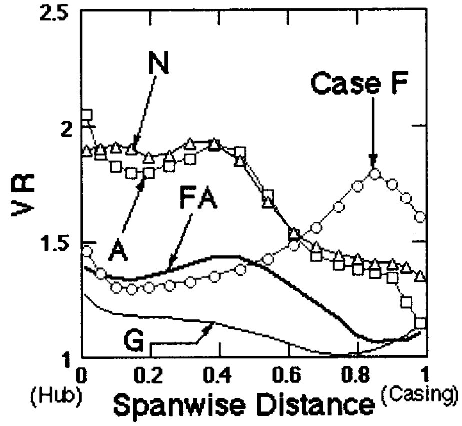

Fig. 15 Exit flow nonuniformity at diffuser trailing edge at design point

Improvements for Impeller. The impeller for Case G stage was also re-designed by the 3-D inverse design method. The gain from the redesign of the impeller by 3-D inverse method is one third of the overall loss reduction obtained by Case G compared to Case C, see Fig. 10. The impeller for Case G was designed following the design criteria proposed by Zangeneh et al. [8] to suppress meridional component of secondary flow. The results of this design can be confirmed in Fig. 12(*b*) which shows suppressed secondary flows in Case G on the blade suction surface (Region IV) compared to the same in Case C presented in Fig. 4(*b*). Careful control of the impeller flow and the more uniform flow at impeller exit reduced the impeller loss (including inter-row mixing loss) by about 40%. Note here, the same re-designed impeller, with suppressed secondary flows, was used for all numerical calculations for Cases F, N, A, and G.

Experimental Validation

Overall Performance. The inverse design pump Case G was manufactured in the same manner as conventional Case C, and its overall performance was measured using the same test loop as Case C pump testing. Figure 16 compares the measured overall performance for Case C (Symbols) and Case G (lines). All data were normalized by the value at the best efficiency point of Case C. Significant improvements were obtained in the inverse designed Case G for the flow range below 125% of the design flow rate. The peak efficiency was improved by 5.3 points. The Case G impeller was designed by the 3-D inverse design method for the same Euler head specification as Case C impeller. Because of this, the shaft power characteristics are identical between Case G and Case C, except very close to the shut-off condition. So, most of the improvement in pump efficiency was obtained by the reduction of the flow losses. Also Case G impeller had limit load characteristics, as was the case for Case C impeller.

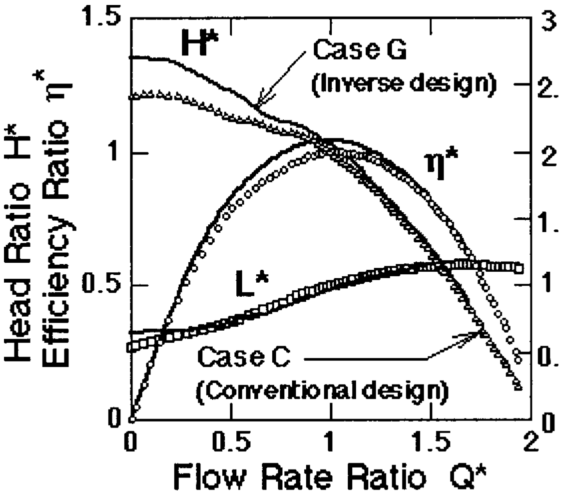

Fig. 16 Comparison of overall performance between conventional design Case C and inverse design Case G

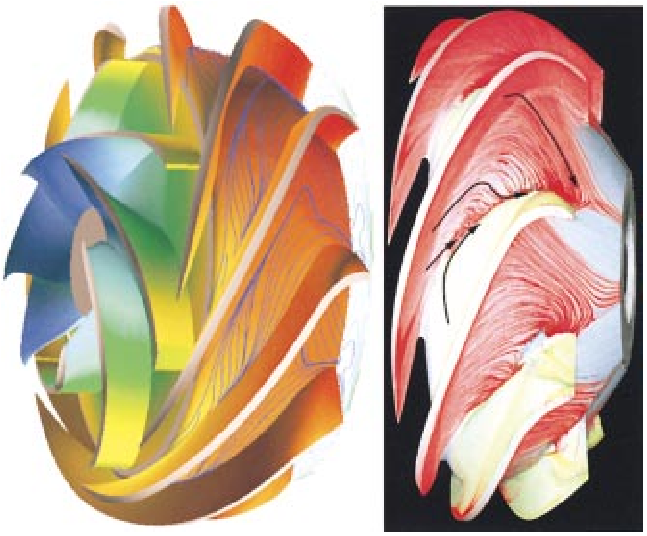

Fig. 17 Inverse design stage Case G (design point). (*a*) CFD prediction; (*b*) oil-film flow pattern

Diffuser Matching. The Case G pump achieved peak efficiency exactly at the design point. In the inverse design of Case G diffuser, the blade loading parameter was specified as zero at the leading edge as shown in Fig. 2, aiming to impose zero incidence at the design point. The experimental results show that a zero value of $\partial(rV_\theta)/\partial m$ at the leading edge gives the correct matching condition between the impeller and the diffuser. So, the specification of the impeller-diffuser matching is more straightforward compared to the conventional method such as adjustment of the diffuser throat area.

Conventionally, the inflow velocity triangle is assumed and then the inlet blade angle is decided. However, because of the circulation around the diffuser blade and the induced tangential velocity, the flow changes its direction as it comes close to the blade leading edge and zero incidences cannot be guaranteed. Conversely, if we specify $\partial(rV_\theta)/\partial m = 0.0$ at the blade leading edge, then the inverse design will provide exact matching between the inflow and the diffuser inlet.

Flow Visualization. Figure 17 compares the 3-D representation of the flow fields for Case G predicted by CFD with the result of the multi-color oil-film flow visualization of diffuser wall surface streamlines at the design point. The corner separation, observed in conventional design Case C (Fig. 3) was eliminated completely in the inverse design diffuser Case G. The strong cross-flow from the blade suction surface towards the blade pressure surface along the hub at the inlet region was clearly identified as yellow streamlines on the hub in Fig. 17(*b*). The cross-flow was caused by strong spanwise secondary flows on the blade suction surface, which brought yellow oil-film originally painted only on the blade suction surface. At the after part of the diffuser, a strong cross flow in the opposite direction, i.e., from the blade pressure surface toward the blade suction surface, was observed experimentally, as well as numerically. These two different secondary flows interacted with each other from the inlet of the diffuser, and a dividing line was formed along the interaction zone. The location of the dividing line was close to the pressure surface at the inlet and moved towards the blade suction surface at the outlet. This flow pattern was also well predicted by the numerical calculations, see thick broken line in Fig. 12(*c*). Close to the trailing edge on the suction surface, the numerical calculation predicted a slightly unstable flow pattern (Region I in Fig. 12(*a*)). This phenomenon was also observed experimentally in the form of a weak vortical motion on the blade suction surface very close to the trailing edge. In overall, the flow fields in the inverse design diffuser Case G showed significant improvements over the conventional design diffuser Case C.

Concluding Remarks

The predicted flow fields by CFD gives a lot of potentially very useful information for improving the fluid dynamic design of turbomachines. However, in many cases, it is not very clear what kind of modification will most effectively improve the flow fields due to the strong 3-D effects inducing a variety of secondary flows. Therefore, the design of a flow passage shape or the modification of an existing one still remains very conventional, depending heavily on the designer's intuition, empiricism, background data with a trial and error method. This paper presents a new design methodology based on the application of a 3-D inverse design and its validation by CFD. The effectiveness of this new approach was proven with the redesign of a pump diffuser, having a low specific speed of 0.109 (non-dimensional) or 280 (m^3/min, m, rpm). The main conclusions are as follows.

- In conventional design diffusers, extensive flow separation appeared at the corner between the hub and the blade suction surfaces, which induced a high flow loss inside the diffuser, as well as a high mixing loss at downstream from the diffuser trailing edge.
- Such corner separation was suppressed by applying the 3-D inverse design method using fore loading at the hub as compared to the casing. The accumulation of high loss fluid in the corner region was suppressed by the alteration in the static pressure fields and the resulting change of secondary flows, especially on the blade suction surface.
- The introduction of the blade lean (by specifying nonzero stacking at the trailing edge) induced favorable flow pattern, which brings high total pressure fluids towards the corner region.
- The numerically predicted flow losses and the pressure recovery of inverse design diffuser Case G showed significant improvements over those of conventional diffusers. The improvements of overall performance and flow fields (suppressed corner flow separation) were confirmed experimentally.
- No blade loading, i.e., $\partial(rV_\theta)/\partial m = 0$, at the diffuser leading edge ensures the best match between impellers and diffusers.

The validity of this new design methodology, which directly controls 3-D pressure fields and secondary flows, has already been confirmed for a wide range of diffuser pump specific speeds. Appreciable improvements in hydraulic performance have been confirmed experimentally over conventional designs by using CFD based state-of-the-art approach.

Appendix

A diffuser blade, having no rake angle at the trailing edge but with the optimized blade loading (used for Case G design), was designed by the 3-D inverse design method. This inverse design diffuser is designated as "Case FA." The only difference between Case FA and Case G is the stacking condition (or rake angle) specified at the trailing edge plane.

Figure 18 shows the velocity vectors near the blade suction surface and the hub surface. Because of the blade design by 3-D inverse design method with optimized blade loading, the major corner separation was eliminated. So, the inverse design Case FA showed a substantial improvement in the pressure recovery coefficient of 0.732 and the stage efficiency of 87.9% compared to the Cases F, N, and A, as shown in Fig. 10. However, a small region of reverse flows is still observed on the suction surface close to the exit, see Fig. 18.

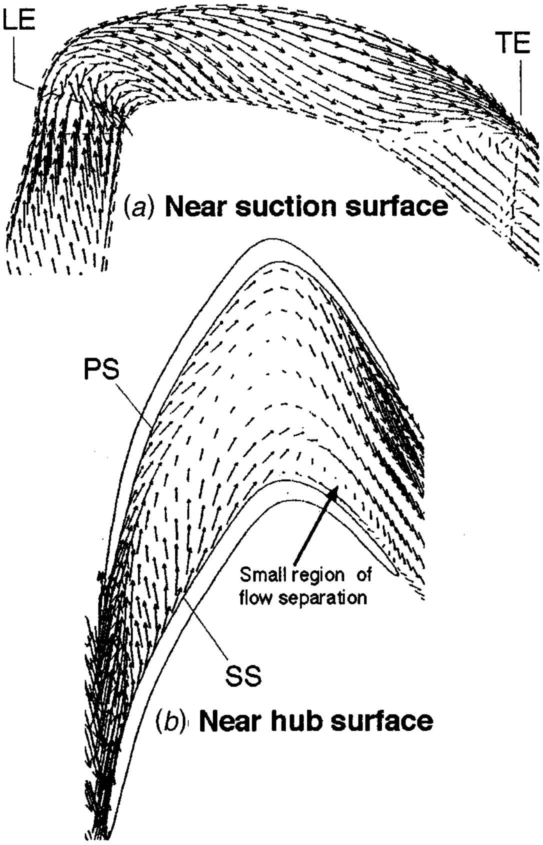

Fig. 18 Velocity vectors of inverse design diffuser Case FA at design point

As has been described in the present paper, by the introduction of the staking condition (rake angle) at the trailing edge location, Case G managed to eliminate the small region of corner flow separation as shown in Fig. 12. To clarify the effects of the stacking, the total pressure contours on quasi-orthogonal planes are compared for Case FA and Case G at two different streamwise locations of 75% and 90% of the meridional chord length in Fig. 19. In Case FA, the major low total pressure fluids were swept away from the corner due to the spanwise secondary flow from the casing to the hub in the fore part of the passage (Fig. 19(*a*)), and two regions of low total pressure fluids were formed sepa-

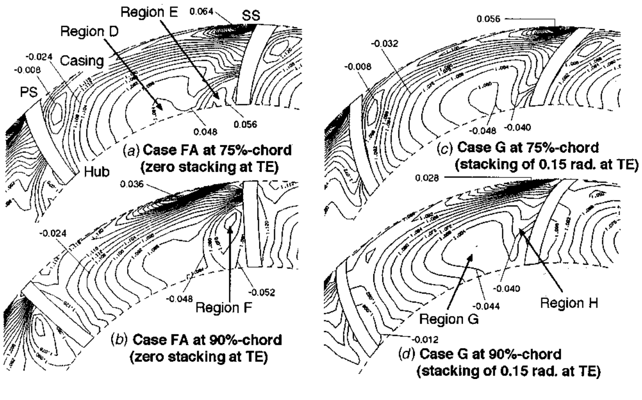

(*a*) Case FA at 75%-chord (zero stacking at TE)

(*b*) Case FA at 90%-chord (zero stacking at TE)

(*c*) Case G at 75%-chord (stacking of 0.15 rad. at TE)

(*d*) Case G at 90%-chord (stacking of 0.15 rad. at TE)

Fig. 19 Effects of stacking condition on total pressure distribution $\Delta \psi_t$ at design point

rately: one in the corner between the hub surface and the blade suction surface (Region E), and the other around the 35%-pitch location from the blade suction surface at the hub (Region D). At the downstream location, these two regions merged into a single region of low total pressure in the corner region (Region F in Fig. 19(*b*)), which forms a small scale corner separation.

The introduction of stacking of 0.15 radians at the trailing edge affected the blade shape only after the 50%-chord location. Figures 19(*c*) and (*d*) show circumferentially inclined blade sections for Case G. The introduction of the stacking mostly affected the flow fields close to the blade suction surface. In Case G, the high total pressure fluids were brought into the corner region as can be observed in Fig. 19(*d*), Region H. Because of this flow phenomena, accumulation of high loss fluids and resulting corner separation were completely avoided in Case G, while small corner separation existed in Case FA.

Although the corner separation in Case FA appeared in a very limited region close to the blade suction surface at the exit, it had noticeable effects of inducing the mixing loss downstream from the diffuser trailing edge. As shown in Fig. 10, the loss generated inside the Case FA diffuser flow passage was identical to the same in Case G. However, the downstream mixing loss, generated by the non-uniformity of the meridional velocity and the swirl velocity, was twice as much as those for Case G diffuser. Figure 15 clearly shows that the flow non-uniformity is much higher in Case FA than in Case G.

In Fig. 14, the pressure recovery shows a slight reduction after the 85%-chord location for Case FA diffuser, where the two regions of low total pressure (Fig. 19(*a*)) merged into a single region of low total pressure at the corner (19(*b*)). The introduction of stacking for Case G improved the flow fields and the pressure recovery in this region.

The pressure recovery coefficient and the stage efficiency in Case FA were 0.732 and 87.9%, and the same in Case G were 0.77 and 89.0%, respectively. So, the introduction of the stacking gave increase in the pressure recovery coefficient of the diffuser by 3.9 points and the stage efficiency by 1.1 points. Here, the effects of the stacking were investigated numerically, and experimental validation is necessary to clarify the actual flow phenomena.

References

[1] Hobbs, D. E., and Weingold, H. D., 1984, ''Development of controlled diffusion aerofoils for multistage compressor applications,'' ASME J. Eng. Gas Turbines Power, **106**, pp. 271–278.

[2] Hawthorne, W. R., Tan, C. S., Wang, C., and McCune, J. E., 1984, ''Theory of Blade Design for Large Deflections: Part I-Two Dimensional Cascades,'' ASME J. Eng. Gas Turbines Power, **106**, pp. 346–353.

[3] Tan, C. S., Hawthorne, W. R., Wang, C., and McCune, J. E., 1984, ''Theory of Blade Design for Large Deflections: Part II-Annular Cascades,'' ASME J. Eng. Gas Turbines Power, **106**, pp. 354–365.

[4] Borges, J. E., 1990, ''A Three-Dimensional Inverse Design Method in Turbomachinery: Part I-Theory,'' ASME J. Turbomach., **112**, pp. 346–354.

[5] Zangeneh, M., 1991, ''A Compressible Three Dimensional Blade Design Method for Radial and Mixed Flow Turbomachinery Blades,'' Int. J. Numer. Methods Fluids, **13**, pp. 599–624.

[6] Zangeneh, M., Goto, A., and Takemura, T., 1996b, ''Suppression of Secondary Flows in a Mixed Flow Pump Impeller by Application of 3-D Inverse Design Method: Part I-Design and Numerical Validation,'' ASME J. Turbomach., **118**, pp. 536–543.

[7] Goto, A., Zangeneh, M., and Takemura, T., 1996, ''Suppression of Secondary Flows in a Mixed Flow Pump Impeller by Application of 3-D Inverse Design Method: Part 2-Experimental Validation,'' ASME J. Turbomach., **118**, pp. 544–551.

[8] Zangeneh, M., Goto, A., and Harada, H., 1998, ''On the Design Criteria for Suppression of Secondary Flows in Centrifugal and Mixed Flow Impellers,'' ASME J. Turbomach., **120**, pp. 723–735.

[9] Walker, P. J., and Dawes, W. N., 1990, ''The Extension and Application of Three-Dimensional Time-Marching Analysis to Incompressible Turbomachinery Flows,'' ASME J. Turbomach., **112**, pp. 385–390.

[10] Zangeneh, M., 1996a, ''Inverse Design of Centrifugal Compressor Vaned Diffusers in Inlet Shear Flows,'' ASME J. Turbomach., **118**, pp. 385–393.

[11] Goto, A., 1995, ''Numerical and Experimental Study of 3-D Flow Fields within a Diffuser Pump Stage at Off-Design Condition,'' FED-**227**, pp. 1–9, ASME-JSME Fluids Engineering Joint Conference.

[12] Denton, J. D., 1990, ''The Calculation of Three Dimensional Viscous Flow Through Multistage Turbomachines,'' ASME Paper No. 90-GT-19.

[13] Goto, A., 1997, ''Prediction of Diffuser Performance using a 3-D Viscous Stage Calculation,'' FEDSM97-3340, ASME Fluids Engineering Division, Summer Meeting.

[14] Goto, A., 1992, ''Study of Internal Flow in a Mixed Flow Pump Impeller at Various Tip Clearances Using 3-D Viscous Flow Calculations,'' ASME J. Turbomach., **114**, pp. 373–382.

[15] Takemura, T., and Goto, A., 1996, ''Experimental and Numerical Study of Three-Dimensional Flows in a Mixed-Flow Pump Stage,'' ASME J. Turbomach., **118**, pp. 552–561.

Hydrodynamic Design System for Pumps Based on 3-D CAD, CFD, and Inverse Design Method

Akira Goto
Ebara Research Co., Ltd.,
Fujisawa-shi, Japan
e-mail: goto05296@erc.ebara.co.jp

Motohiko Nohmi
e-mail: nohmi@ebara.co.jp

Takaki Sakurai
e-mail: sakurai02@ebara.co.jp

Yoshiyasu Sogawa
e-mail: sogawa@ebara.co.jp

EBARA Corporation,
Tokyo, Japan

A computer-aided design system has been developed for hydraulic parts of pumps including impellers, bowl diffusers, volutes, and vaned return channels. The key technologies include three-dimensional (3-D) CAD modeling, automatic grid generation, CFD analysis, and a 3-D inverse design method. The design system is directly connected to a rapid prototyping production system and a flexible manufacturing system composed of a group of DNC machines. The use of this novel design system leads to a drastic reduction of the development time of pumps having high performance, high reliability, and innovative design concepts. The system structure and the design process of "Blade Design System" and "Channel Design System" are presented. Then the design examples are presented briefly based on the previous publications, which included a centrifugal impeller with suppressed secondary flows, a bowl diffuser with suppressed corner separation, a vaned return channel of a multistage pump, and a volute casing. The results of experimental validation, including flow fields measurements, were also presented and discussed briefly. [DOI: 10.1115/1.1471362]

Introduction

Tremendous development of numerical methods and computer technology has made Computational Fluid Dynamic technique (CFD) one of the most essential tools for hydrodynamic design of pumps. A pump designer can evaluate his design numerically by CFD in advance of experimental model tests and obtain a significant amount of information on 3-D flow fields, which is potentially very valuable to improve the design. The designer tries to improve his design by changing the blade/passage configuration based on such information. However, the redesign process for most of the cases is not very straightforward due to the complex nature of 3-D internal flow fields. The partial modification of blade/passage configuration affects the entire flow field.

The 3-D geometry modeling tools using a CAD system, such as Favre [1], accelerate the design process to some extent. However, the fundamental problem for such approaches is the fact that the way to define the blade/passage shape, such as blade angle distribution between the leading and the trailing edges, relies greatly on empiricism and the experience/intuition of a talented designer. Such conventional design approaches face difficulties in improving pump performance, which is already at high level, or in optimizing the pump configuration for a critical design specification beyond previous experience. In addition to this, the demands for supplying a custom pump for minimum cost and minimum time of delivery are increasing, and the design cycle is required to be more and more efficient.

In the present paper, a novel design system is proposed to overcome the above difficulties based on a 3-D inverse design method, CFD, 3-D CAD modeling, and an automatic grid generation method. Design examples are given for an impeller blade with suppressed secondary flows, a diffuser blade with suppressed corner separation, and a vaned return channel of a multistage pump, together with some results of experimental and numerical validations.

Overview of Design System

The new design system consists of two subsystems as shown in Fig. 1. One is the ''Blade Design System'' for designing blades or vanes of impellers/diffusers, and the other is the ''Channel Design System'' for designing complex 3-D flow passage such as a volute casing and a vaned return channel.

The Blade Design System consists of a 3-D inverse design system, a 3-D Navier-Stokes flow analysis system, and a 3-D CAD modeling system. The system starts from the design of meridional shape of impellers/diffusers using a database. Then the blades are designed subject to a specified circulation distribution using the 3-D inverse design method proposed by Zangeneh [2]. The computational grids for CFD are generated in a semi-automatic manner employing H-type grids. Finally, the 3-D flow fields within the impellers/diffusers are analyzed and evaluated by solving Reynolds Averaged Navier-Stokes equations by a Dawes N-S solver (Walker and Dawes [3]). For diffuser blades, a stage version of Dawes code (Goto [4]) is used. In addition to the Dawes post-processor, the commercial visualization software EnSight is used and macro commands were prepared to evaluate 3-D flow fields efficiently in daily design work. The use of this system is suitable

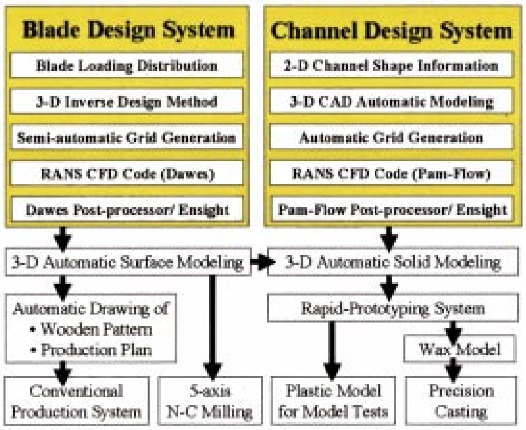

Fig. 1 Pump design system

Contributed by the Fluids Engineering Division for publication in the JOURNAL OF FLUIDS ENGINEERING. Manuscript received by the Fluids Engineering Division August 6, 2001; revised manuscript received January 18, 2002. Associate Editor: J. Katz.

for the systematic design of impeller/diffuser blades with different meridional shapes and the blade loading distributions, which enables a very rapid optimization of the design parameters. The 3-D surface modeling of the impeller/diffuser blades was made full automatic by writing macro commands in the 3-D CAD system.

On the other hand, the Channel Design System consists of a 3-D CAD surface modeling system, an automatic grid generation system and a 3-D Navier-Stokes flow analysis system. The system starts from the specification of major design parameters such as volute cross sections in 2-D form. Next, the 3-D surface model of the flow channel is fully automatically generated using the customized 3-D CAD system, where the CAD surface patches are systematically pre-arranged to guarantee high grid quality in the following automatic grid generation process. Then the grids for CFD calculations are generated fully automatically based on the Advancing Front Method (Lohner [5]). The 3-D N-S solver used in this process employs the solution adaptive technique (Lohner [6]), which automatically reduces or increases computational grids depending on the flow solution during the computation, to minimize the CPU time required for analyzing the flows in complex 3-D flow channels. The Channel Design System has achieved a drastic reduction in design time, which had been required for the modeling and the flow analysis of complex 3-D flow channels.

The 3-D blade/channel configuration, generated either by the inverse design system or the 3-D CAD system, is directly fed into the solid modeling process using a 3-D CAD system and then manufactured by Rapid Prototyping (RP) using Laser Stereo Lithography (LSL) or Selective Laser Sintering (SLS). The LSL is suitable for creating a wax model for precision casting or for direct manufacturing of stationary parts such as diffusers. The SLS production system is more commonly used for manufacturing a model impeller, which can be used directly for water model tests. Impeller/diffuser models can also be manufactured by using 5-axis numerically controlled milling machine from the 3-D surface models if necessary. When the impeller/diffuser blade products are to be manufactured by a conventional production system, the drawings of a wooden pattern and a production plan can be automatically generated from the 3-D surface model by using the 3-D CAD system.

Blade Design System

Inverse Design Method. The 3-D inverse design method proposed by Zangeneh [2] is adopted in the present system. Using this method, the blades are represented by sheets of vorticity, whose strength is determined by a specified distribution of bound circulation $2\pi rV_\theta$. Here, V_θ is a circumferentially averaged swirl velocity. The CPU time required to obtain a converged blade shape is very short, typically a few minutes on a Work Station. Zangeneh [7] has extended the method to include the effects of inlet shear flow, which is important for the design of a blade row receiving a non-uniform inflow. The stability of the inverse design method has been improved and pre- and post-processors were developed and integrated into the system.

The inputs of this design method are as follows:

- meridional shape
- loading distribution (distribution of bound circulation $2\pi rV_\theta$)
- rotational speed ω, which is zero for a stationary blade
- blade thickness distribution
- blade number
- stacking condition

In the present design system, the blade loading is specified by giving the distribution of $\partial(rV_\theta)/\partial m$, which is the derivative of angular momentum (rV_θ) along the meridional distance m. Figure 2 shows the schematic distribution of the blade loading parameter for an impeller. In the present design system, the distribution of the blade loading parameter $\partial(rV_\theta)/\partial m$ is defined by a ''three-segment'' method which employs a combination of two parabolic curves and an intermediate linear line. Four design parameters (connection point locations NC and ND, slope of the linear line, and LE) are used to define the distribution curve. The $\partial(rV_\theta)/\partial m$ distribution is specified for each of the shroud and the hub surfaces, then the rV_θ distribution is derived by the integration of $\partial(rV_\theta)/\partial m$ along the meridional distance m on hub and shroud surfaces. The rV_θ distributions in the intermediate part of the blade are obtained by a linear interpolation for rV_θ between the hub and the shroud. This ''three-segment'' method is very useful as we can define the entire 3-D blade surface with only eight design parameters. A smooth distribution of hydrodynamic design parameter rV_θ guarantees a favorable flow pattern.

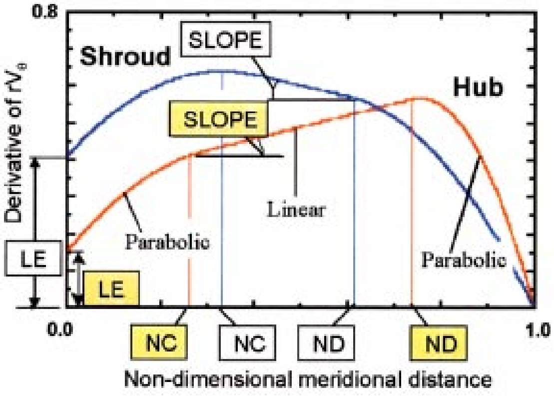

Fig. 2 Definition of blade loading parameter

The design parameter is directly related to the pressure loading ($p^+ - p^-$: the pressure difference across the blade) through the following equation for incompressible potential flows.

$$p^+ - p^- = (2\pi/B)\rho W_{\mathrm{mbl}} \partial(rV_\theta)/\partial m$$

where B is the blade number, ρ is density, W_{mbl} is the blade-to-blade average of the meridional component of the relative velocity on the blade. Zero values of $\partial(rV_\theta)/\partial m$ at $m=0$ (LE$=0$ at the leading edge) and $m=1.0$ (at the trailing edge) automatically specify the zero flow incidence and the Kutta condition respectively. Fore-loaded and aft-loaded designs are easily achieved by arranging the peak location of $\partial(rV_\theta)/\partial m$ in the forepart and in the aft part of the blade respectively.

It should also be emphasized that a design procedure based on 3-D theory is essential for optimizing the blade shape further beyond our current state-of-the-art design. This is true even for axial flow pumps since the spanwise blade force has large effects on the 3-D pressure fields.

Optimization of Meridional Shape. It can be seen from the foregoing descriptions that the blade design method is truly inverse only in the sense that the final shapes emerge from the specification of the circulation or blade loading distributions. Other inputs, including the meridional shapes, are not determined in an inverse manner; rather, they are supplied from a database of hydrodynamic design experience for several families of pumps.

However, the important design inputs such as meridional shapes may be optimized further through a systematic application of inverse designs and CFD evaluations as follows.

Step A: assumption of the initial meridional shape based on a database
Step B: a series of inverse designs and CFD calculations to optimize the blade loading for the assumed initial meridional shape
Step C: inverse designs and CFD calculations for a series of modified meridional shapes with the fixed blade loading distribution obtained in Step B
Step D: final tuning of the blade loading for the best meridional shape obtained in Step C

CFD Code. The inverse design method, used in the present design system, assumes a potential flow. So, the important viscous flow features, such as secondary flows and flow separation, must be evaluated by the application of CFD codes. The inverse design method has become a very practical and powerful tool only because of the recent significant advancement of 3-D viscous CFD codes.

The CFD code used in the blade design system is a Dawes code for incompressible flow (Walker and Dawes [3]), and its stage version developed by one of the authors (Goto [4]), which solve Reynolds Averaged Navier-Stokes equations using the Baldwin-Lomax turbulence model and the Chorin's method of artificial compressibility. In the stage version, an inter-row mixing plane following Denton's model [8] was incorporated between adjacent blade rows to simulate steady stage flows having a rotating impeller and a stationary vaned diffuser. The Dawes code has been validated extensively by Goto [9] for pump impellers and by Goto [4], Takemura and Goto [10], and Goto [11] for diffuser pump stages.

Based on the CFD prediction of impeller/stage flows, the following items are evaluated.

- Euler head (work input)
- impeller and stage efficiency
- suction performance (minimum pressure in impeller)
- impeller stall characteristics (onset of inlet recirculation)
- diffuser stall characteristics (onset of corner flow separation)
- velocity distortion at impeller/diffuser outlet
- secondary flows and other internal flow fields

Here, the stage efficiency is calculated including the mixing losses downstream from the stage exit due to exit swirl and flow non-uniformity. For details, see Goto [11].

Blade Design Examples

Impeller Design With Suppressed Secondary Flows. It is well acknowledged that the secondary flow phenomena in an impeller have important effects on the efficiency and stability of the impeller. In addition to this, the secondary flow has dominating influence on the generation of the exit flow non-uniformity (so-called "jet-wake" flow pattern) and affects the performance and stability of the downstream diffuser. The secondary flows on blade suction surfaces are important, since the boundary layers are thicker on the suction surfaces than on the pressure surfaces. However, the design procedure to control secondary flows has not been established until very recently due to the complex three-dimensionality of the pressure fields. Zangeneh et al. [12] presented a logical method based on 3-D inverse design to suppress meridional secondary flows within centrifugal and mixed-flow impellers, which is briefly described here.

Figure 3(*a*) shows the flow pattern in a conventional impeller having a typical blade angle distribution which connects the inlet and exit blade angles by smooth monotonous curves. Strong spanwise secondary flows were clearly observed, which were generated by the reduced static pressure gradient between the hub and the shroud. Because of this, the exit flow nonuniformity became very high as shown in Fig. 4(*a*).

The secondary flow control by the 3-D inverse design method is rather straightforward as we can easily control the pressure fields by controlling the blade loading parameter $\partial(rV_\theta)/\partial m$. Namely, the shroud was fore-loaded while the hub was aft-loaded to reduce the spanwise pressure gradient between the shroud and the hub in the aft part of the impeller suction surface. Figures 3(*b*) and 4(*b*) present the flow fields in the inverse design impeller, where well suppressed secondary flows and the more uniform exit flow pattern are confirmed. The blade angle distribution between these two designs is very different, and it can be confirmed that the conventional design practice of using smooth blade angle distributions does not necessarily guarantee good flow fields. This fact clearly demonstrates the importance of carrying out the blade design based on the hydrodynamic design parameter and not the geometric design parameter.

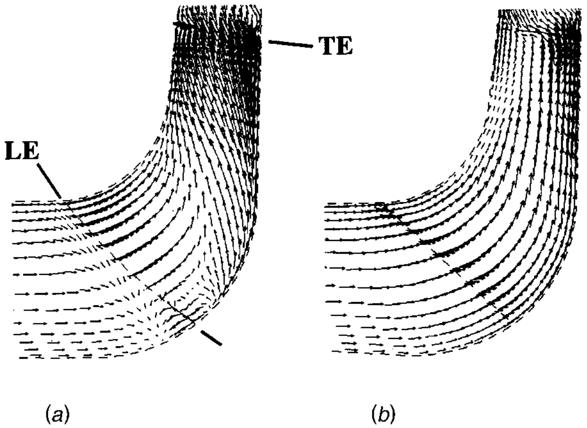

Fig. 3 Velocity vectors on blade suction surface. (*a*) Conventional design; (*b*) inverse design

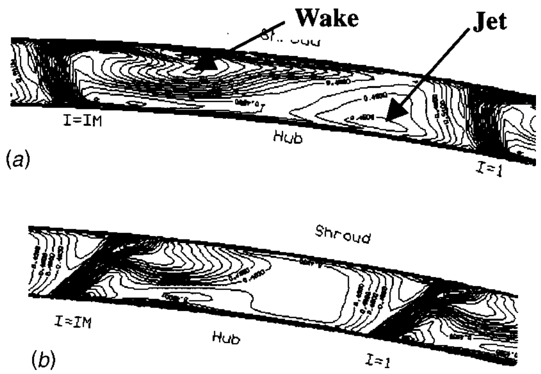

Fig. 4 Velocity contours at impeller trailing edge. (*a*) Conventional design; (*b*) inverse design

Diffuser Design With Suppressed Corner Stall. The hub surface of a vaned bowl diffuser can be highly loaded when the outer diameter of the diffuser is made compact. Under such situation, the optimization of blade shape is extremely important to avoid a large-scale flow separation along the corner region between the diffuser blade suction surface and the hub surface. Goto and Zangeneh [13] presented a design procedure for diffuser blades using the 3-D inverse design method, which is briefly described here.

Figure 5 presents the results of CFD prediction of stage flows for a conventional diffuser pump stage with low specific speed (280 [m, rpm, m^3/min]) and the multi-color oil-film flow pattern within the vaned bowl diffuser part. Due to the spanwise pressure gradient on the diffuser blade suction surface at inlet, the spanwise secondary flows were generated towards the hub surface. At the same time, on the hub surface, the secondary flows towards the blade suction surface were generated due to the blade-to-blade pressure gradient. Because of these two types of secondary flows, the low momentum fluids were accumulated in the hub/suction surface corner region. The adverse pressure gradient is also high in this region and a large-scale corner flow separation occurred around the middle part of the hub surface.

In the inverse design case, the hub surface was fore-loaded while the shroud surface was aft-loaded. The spanwise secondary flows were enhanced at the inlet part of the diffuser blade suction surface, and the accumulation of low momentum fluids in the corner region was prevented and also the adverse pressure gradi-

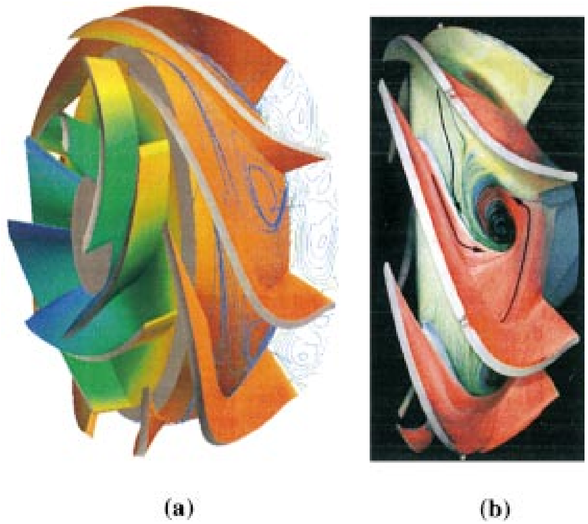

Fig. 5 Conventional design stage. (*a*) CFD prediction; (*b*) oil-film flow pattern

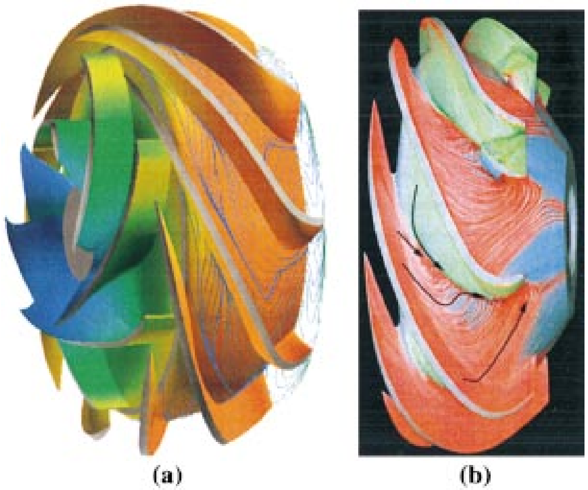

Fig. 6 Inverse design stage. (*a*) CFD prediction; (*b*) oil-film flow pattern

ent around the middle part of the hub surface was reduced. Because of the optimized 3-D pressure fields, the corner flow separation had been completely eliminated as shown in Fig. 6.

Inverse Design Process and Its Application to Series Development. The above described design guidelines for controlling impeller secondary flows and suppressing diffuser corner stall can be widely applied to improve the performance of mixed-flow diffuser pumps. They are also very effective to make more compact machine size with high efficiency. The wide applicability of the design guidelines is because the principal design parameter of the Blade Design System is a hydrodynamic parameter (blade loading) and not a geometrical parameter. The design process will proceed as follows:

Step 1: calculation of design specific speed for a given design specification (flow rate, pump head and rotation speed)

Step 2: selection of meridional shape for the design specific speed using a database of hydrodynamic design experience

Step 3: calculation of required Euler head based on design pump head and estimated hydraulic efficiency

Step 4: inverse design of impeller blades using fore loading at the shroud and aft loading at the hub for the specified inlet swirl (typically zero) and the required Euler head

Step 5: CFD of the impeller and its evaluation (such as flow fields, impeller efficiency, minimum pressure etc.), and go back to Step 4 or Step 2 if necessary

Step 6: modeling of impeller exit flows for using it as an inlet boundary condition in the diffuser design

Step 7: inverse design of diffuser blades using fore loading at the hub and aft loading at the casing for the specified inlet boundary condition and the exit swirl (typically zero)

Step 8: CFD of the stage flow and its evaluation (diffuser flow fields, stage efficiency, etc.), and go back to Step 7 or Step 2 if necessary

Using the Blade Design System, several pump series have been developed for different applications such as diffuser pumps, non-clogging impellers, and multistage pumps. For the series development, all of the design parameters such as meridional shape and the blade loading parameters are defined as functions of a design specific speed of the pump. So, once such a pump series is established, a high performance pump can be designed very quickly for an intermediate design specific speed, see Sakurai et al. [14] for detail. Figure 7 shows an example of a diffuser pump series with medium compactness. If we have three different pump series having different characteristics, for example, then we can cover a wide range of customers' requirements. The new concept of series development based on the inverse design method enables the ''mass customized'' design of pumps.

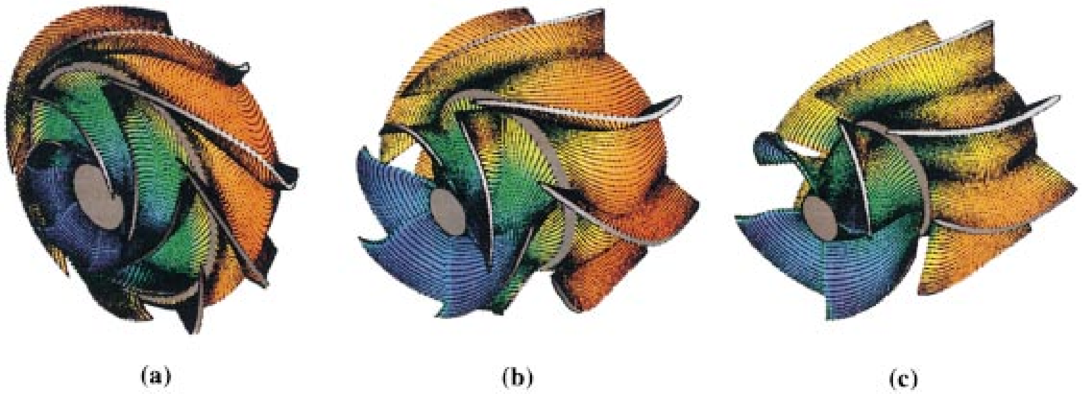

Fig. 7 Diffuser pump series (Ns800:specific speed of 800 [m, rpm, m^3/min]). (*a*) Ns280; (*b*) Ns800; (*c*) Ns1350

Channel Design System

Geometry Modeling Process. The geometry of an ordinary blade to blade passage can be defined precisely enough using a combination of 2-D curves such as meridional lines and blade-to-blade lines on several stream surfaces. They are easily defined by the inverse design process and are fed to CFD process almost automatically. However it is difficult to define some complicated passage geometry in pumps such as a volute casing and a vaned return channel by only using 2-D curves. Conventionally, hydraulic designers define such geometry using 2-D drawings, which consist of axial projection, meridional figure and a few principal cross section figures. In these 2-D drawings, the precise 3-D surface of the channel cannot be defined perfectly. Because of this, some geometrical patchwork or even some geometrical modification is necessary in the following manufacturing process. On the other hand, if we use modern 3-D CAD software, any complicated geometry can be defined manually by using surface modeling functions or solid modeling functions. However, it still takes a few hours or days of designers' time.

In the present Channel Design System, complicated geometry is defined using 3-D CAD surface modeling function. The 3-D surface of the objective geometry consists of many surface patches. The patch topology is well arranged to guarantee the easy automatic grid generation for CFD and the easy manufacturing in the following process. This patchwork process is standardized and imported to a commercial 3-D CAD system as a user's function. Designers specify major design parameters only as seen in the 2-D drawing. These data are input to the 3-D CAD system, then the surface model of objective geometry is generated automatically by the 3-D CAD system in less than 10 minutes. This automatic patchwork process has been developed for vaned return channels of multi-stage pumps and volute casings.

Here, the design example is presented briefly for a vaned return channel of a multi-stage pump. The objective vaned return channel consists of a vaned diffuser section, a U-bend section and a deswirl vane section. The U-bend section connects the diffuser vane section and the deswirl vane section, forming a continuous return channel passage as shown in Fig. 8. A designer defines 4 corner lines for the diffuser vane section and also 4 corner lines for the deswirl vane section. These lines are defined as the coordinates of point series over corner lines as shown in Fig. 9. It is also possible to generate the vane geometry by the application of the Blade Design System using the 3-D inverse design method. Some additional 2-D information for the U-bend section, which defines the channel configuration viewed from the radial direction, is also required. These data are input to the 3-D CAD system, then the surface model is generated fully automatically as shown in Fig. 10.

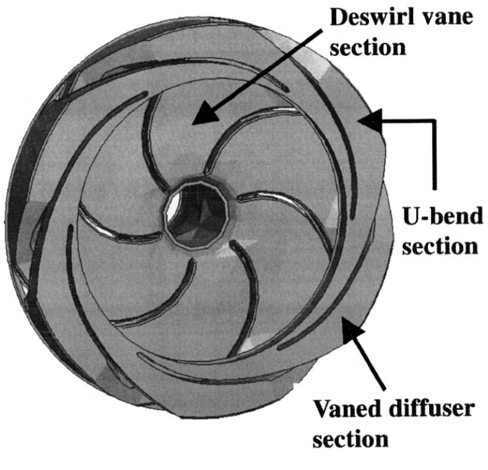

Fig. 8 Vaned return channel of multi-stage pump

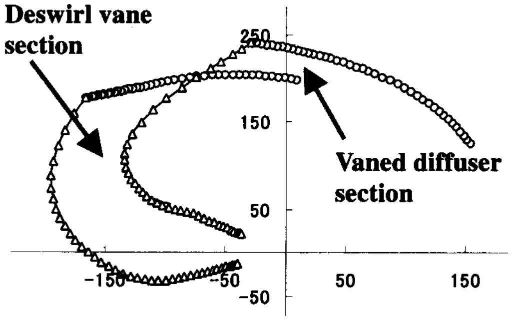

Fig. 9 2-D information of vaned return channel

A similar system has been developed for the volute casing design. Here, a designer as shown in Fig. 11(*a*) defines the plan view and some cross sections. Then the surface model is generated fully automatically as shown in Fig. 11(*b*). It should be noted here that the fillet around a root of the volute tongue is modeled exactly.

CFD Process. In CFD analyses, a commercial code, PAM-FLOW is applied. PAM-FLOW is based on Lohner's research and is a finite element method solver for 3-D turbulent flows with tetrahedral grids and H-refinement (Lohner [6]). The PAM-FLOW preprocessor has an automatic grid generation function based on the advancing front method (Lohner [5]).

The surface model of the objective channel is output in PAM-FLOW native format. After some manual cleaning of geometry data by using the PAM-FLOW preprocessor, tetrahedral grids are generated automatically within about 10 minutes. It is necessary to survey surface grids by an operator, because highly skewed grids are generated in some cases. In that case the operator has to modify patch topology manually and also control parameters for grid generation to achieve high quality grids in the whole compu-

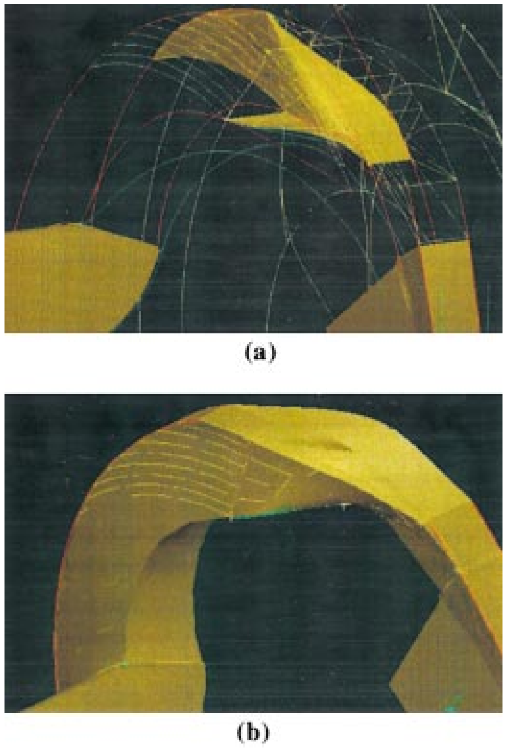

Fig. 10 3-D surface model on vaned return channel. (*a*) Generating surface patch; (*b*) final surface patch

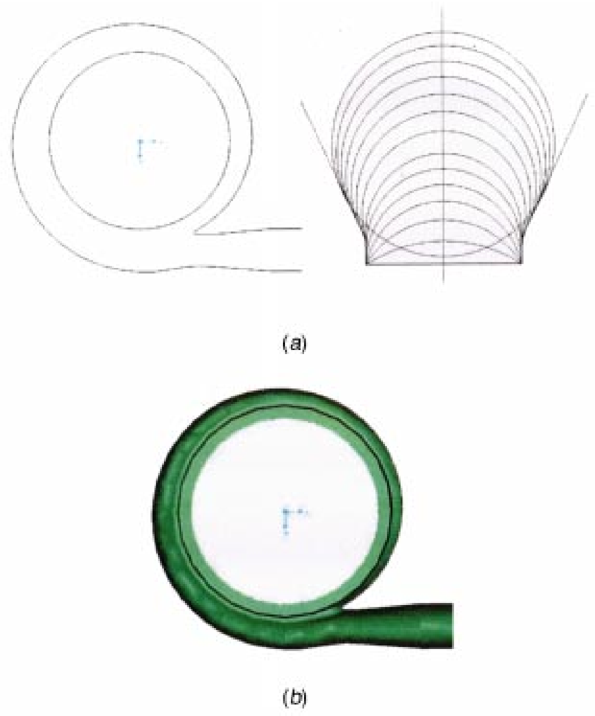

Fig. 11 3-D CAD modeling of volute casing. (*a*) 2-D information; (*b*) 3-D surface model

tation domain. It takes 3 to 4 hours for all of these cleaning and grid generation processes. It is much less than the time that is consumed in fully manual grid generation.

After the grid generation, CFD computation is carried out. Inlet boundary conditions are derived from the exit flow of impeller CFD results. PAM-FLOW has an H-refinement function for solution adaptation. Computational grids are refined or coarsened depending on the computed results. Even if the initial grids are coarse, accuracy can be increased by grid refinement without much increase in CPU time. Coarse grids after refinement are shown in Fig. 12. In some cases, refined results with initially coarse grids slightly differ from the results with initially fine grids without refinement. If the designer has time, refined computation with an initially fine grid is recommended. Typical CFD calculations take 5 to 15 hours of CPU time on FUJITSU VXE super computer. Computed results are evaluated by using the PAM-FLOW post-processor and commercial visualization software EnSight.

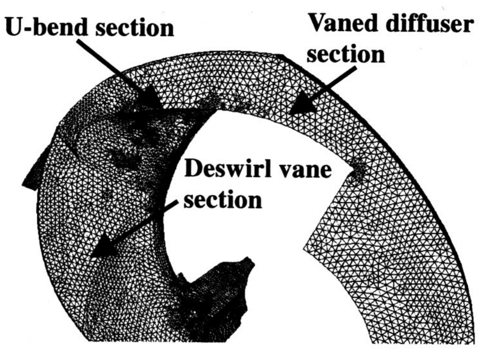

Fig. 12 Automatic grid generation (after refinement)

By summing the time for geometry modeling and CFD, it can be said that the channel design process can be accomplished in one day.

Channel Design Examples

Experimental validation for a vaned return channel of a multistage pump is discussed briefly. For the precise measurements, a model pump test rig was constructed. Flow field measurements such as total pressure, wall static pressure and channel outlet velocity measurements were carried out. Some flow visualization techniques were also applied. For evaluation of the computed flow fields some cross sections were set in the computation domain and mass-averaged total pressure was calculated. The location of total pressure probes and cross sections for total pressure averaging are shown in Fig. 13. From the flow visualization using tracer particles (ion exchange resin particles), the flow separation is observed at the diffuser section as shown in Fig. 14(*a*). This separation was also predicted by CFD as shown in Fig. 14(*b*), and it is extended to the suction side of the deswirl vane. Total pressure results are shown in Fig. 15. Both experimental and computed results and also mass-averaged total pressure at each cross section are plotted. A discrepancy between measured and computed total

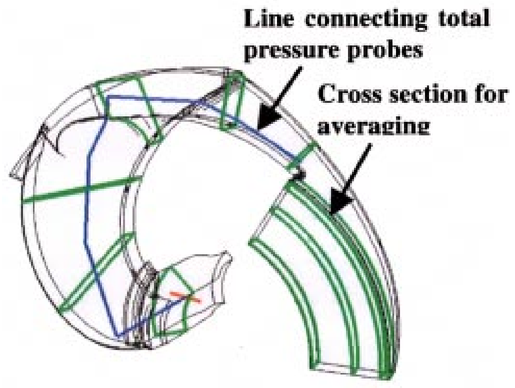

Fig. 13 Vaned return channel and measurement locations

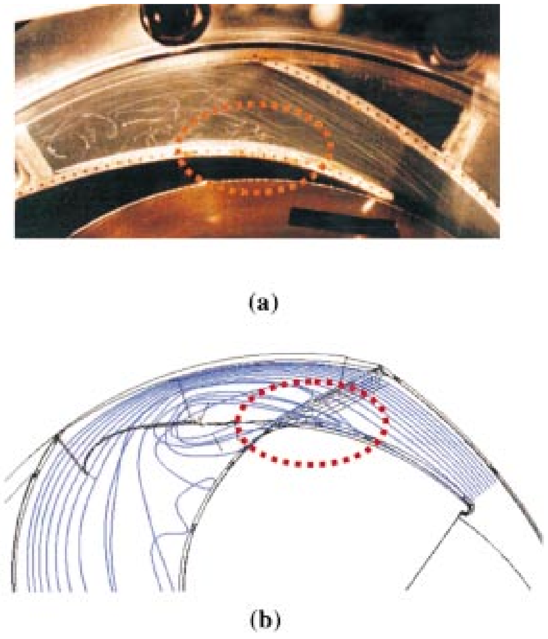

Fig. 14 Flow pattern in diffuser part. (*a*) 3-D flow visualization; (*b*) particle path lines by CFD

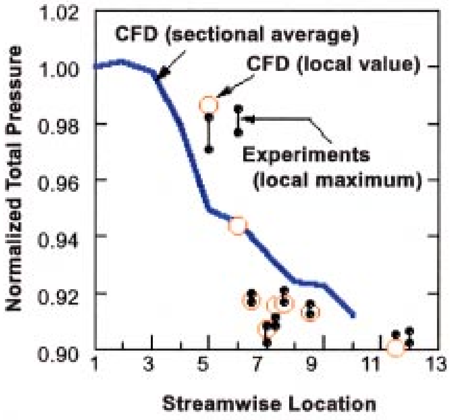

Fig. 15 Total pressure change in vaned return channel

pressures can be seen at the diffuser section. This discrepancy may be caused by insufficient accuracy to predict the extent of the separated region in the computation. At other channel sections, measured and computed results of total pressure show good agreement. From the averaged total pressure a designer can find the region where a large amount of flow loss is generated. This information is very useful for design improvements. For more detailed information about this validation work see Nohmi and Goto [15].

Concluding Remarks

A computer-aided design system for pumps has been developed on the basis of the 3-D inverse design method, the automatic grid generation method, 3-D CFD analysis, and 3-D CAD modeling. The design system is directly connected to a rapid prototyping production system and a flexible manufacturing system composed of a group of DNC machines and has been operated for actual daily design work. The use of this novel design system leads to a drastic reduction of the development time of hydrodynamic design of pumps having high performance, high reliability and innovative design concepts.

The key aspect of this new design system is the efficient and systematic optimization of the principal design parameters. In Blade Design System, for example, the inverse design method enables the evaluation of twenty design cases per day, which can bring a drastic change in the design work. It is true that we still need a lot of experience to find the optimum meridional shape, the optimum loading distribution etc. However, the strength of using the 3-D inverse design method is the fact that it is easy to apply established design strategy, such as secondary flow control, to other similar designs and to construct more systematic and universal design know-how. This has become possible because the principal design parameter (blade loading) is a hydrodynamic parameter having a more universal nature. It is useful to pay serious attention to the design know-how of our predecessors since we can integrate it into the present new design system in a more logical way, which in turn reduces development costs and accelerates further improvements of the design.

References

[1] Favre, J-N., 1995, ''Development of a Tool to Reduce the Design Time and to Improve the Radial or Mixed-Flow Pump Impeller Performance,'' ASME Fluids 95, FED-Vol. 222, pp. 1–9.

[2] Zangeneh, M., 1991, ''A Compressible Three Dimensional Blade Design Method for Radial and Mixed Flow Turbomachinery Blades,'' Int. J. Numer. Methods Fluids, **13**, pp. 599–624.

[3] Walker, P. J., and Dawes, W. N., 1990, ''The Extension and Application of Three-Dimensional Time-Marching Analysis to Incompressible Turbomachinery Flows,'' ASME J. Turbomach., **112**, pp. 385–390.

[4] Goto, A., 1995, ''Numerical and Experimental Study of 3-D Flow Fields within a Diffuser Pump Stage at Off-Design Condition,'' ASME Fluids 95, FED-Vol. 227, pp. 1–9.

[5] Lohner, R., 1987, ''Three-Dimensional Grid Generation by the Advancing Front Method,'' *Numerical Methods in Laminar and Turbulent Flow V*, Pineridge Press, Swansea, pp. 1092–1105.

[6] Lohner, R., 1987, ''The Efficient Simulation of Strongly Unsteady Flows by the Finite Element Method,'' AIAA Paper, AIAA-87-0555.

[7] Zangeneh, M., 1996, ''Inverse Design of Centrifugal Compressor Vaned Diffusers in Inlet Shear Flows,'' ASME J. Turbomach., **118**, pp. 385–393.

[8] Denton, J. D., 1990, ''The Calculation of Three Dimensional Viscous Flow Through Multistage Turbomachines,'' ASME Paper No. 90-GT-19.

[9] Goto, A., 1992, ''Study of Internal Flow in a Mixed Flow Pump Impeller at Various Tip Clearances Using 3-D Viscous Flow Calculations,'' ASME J. Turbomach., **114**, pp. 373–382.

[10] Takemura, T., and Goto, A., 1996, ''Experimental and Numerical Study of Three-Dimensional Flows in a Mixed-Flow Pump Stage,'' ASME J. Turbomach., **118**, pp. 552–561.

[11] Goto, A., 1997, ''Prediction of Diffuser Pump Performance Using a 3-D Viscous Stage Calculation,'' ASME Fluids 97, FEDSM97-3340.

[12] Zangeneh, M., Goto, A., and Harada, H., 1998, ''On the Design Criteria for Suppression of Secondary Flows in Centrifugal and Mixed Flow Impellers,'' ASME J. Turbomach., **120**, pp. 723–735.

[13] Goto, A., and Zangeneh, M., 2002, ''Hydrodynamic Design of Pump Diffuser using Inverse Design Method and CFD,'' ASME J. Fluids Engineering, **124**, published in this issue, pp. 319–328.

[14] Sakurai, T., Saito, S., Goto, A., and Ashihara, K., 1999, ''Pump Design System based on Inverse Method and its Application to the Development of Diffuser Pump Series,'' ASME Fluids 99, FEDSM99-6845.

[15] Nohmi, M., and Goto, A., 1998, ''Experimental and Computational Study of the Flow in a Vaned Return Channel of a Low Specific Speed Pump,'' ASME Fluids 98, FEDSM98-4857.

Hydraulic Axial Thrust in Multistage Pumps—Origins and Solutions

Marjan Gantar
Turboinstitut,
Rovsnikova 7,
1210 Ljubljana,
Slovenia
e-mail: marjan.gantar@turboinstitut.si

Dusan Florjancic

Brane Sirok

University of Ljubljana,
Faculty for Mechanical Engineering,
Askerceva c. 6,
1000 Ljubljana,
Slovenia

In this paper, axial thrust problems of multistage pumps are presented. The entire investigation has been focused on the pump design concept having all impellers in series (facing in one direction) and is valid for barrel casing type as well as for segmental type. The major part of the investigation has been experimental on one stage testing arrangement, using also Laser Doppler Anemometry (LDA) for determination of fluid rotation in the impeller side chamber. Numerical flow analysis (NFA) has been applied for some flow variants in order to verify whether a numerical approach could simulate the test results. The phenomenon of fluid rotation in side chambers and its effect on impeller hydraulic axial thrust have been determined for different leakage flow regimes. The influence of increased wear ring radial clearance on axial thrust has been analyzed together with the solutions for pump hydraulic axial thrust reduction. [DOI: 10.1115/1.1454110]

Keywords: Multistage Pump, Axial Thrust, Impeller Side Chamber, Fluid Rotation, Static Pressure Distribution

Introduction

High head multistage pumps play an important role in systems where the need for high reliability is vital. For the proper and economical design of axial thrust bearings, together with the hydraulic balancing devices, extensive knowledge of the origin of hydraulic axial thrust is essential. The problems become even more demanding when increased pump power concentration and frequent off-design operation are required.

A typical multistage pump design with barrel casing is shown in Fig. 1. Hydraulic axial thrust on the impellers is primarily balanced by the balancing piston, with the rest of the thrust loaded on the axial bearing. The other possibility for balancing axial thrust when all impellers are in series is with a balancing disk or a combination piston/disk.

Many authors [1–4] have given a lot of thought to this subject in the past. It is already known that the flow in the gaps between impeller and casing wall influences the pressure distribution on the impeller front and back shroud to a great extent. Flow in the impeller side chambers is turbulent with separate boundary layers. Within the flow in the peripheral direction, the core layer is formed between the impeller shroud boundary layer and casing wall boundary layer. This fluid rotates in the same direction as the impeller but with reduced angular speed. Within the flow in the radial direction, the impeller shroud boundary layer flow is radially outwards, in the casing wall boundary layer it is radially inwards, and in the core layer there is no radial flow.

For the type of multistage pump under consideration, the flow regimes in side chambers of normal impeller stages are different from that in the last impeller stage (Fig. 1). At all of the impeller front shrouds, the direction of flow in the side chamber is radially inwards. At the impeller back shrouds in normal stages, the flow direction is radially outwards, while in the last stage it is inwards, up to the piston gap entry. The leakage quantity is also increased compared with normal stages. The quantity of flow in the impeller side chambers changes with the pump operation regime, and grows even more over time due to increased radial clearances in wear rings and piston labyrinths.

The investigation has been focused on the following:

- to clarify in greater detail the flow field in the impeller side chambers,
- to investigate the possibilities for hydraulic axial thrust reduction without essential changes in the pump design and efficiency,
- to reduce the sensitivity of hydraulic axial thrust to increased wear ring radial clearance.

The major part of the investigation has been experimental, carried out on a test pump arrangement. Parallel with testing, a numerical flow analysis for impeller side chambers has been worked out as well. The main contribution of the paper is to show the possibility that with simple measures the fluid rotation in the impeller side chambers can be affected and consequently the hydraulic axial thrust can be reduced.

Experimental Investigation and Test Results

Description of Testing Arrangement. A series of tests was carried out on the testing arrangement, which consisted of one separate stage of a multistage pump. The bearing bracket was designed to enable hydraulic axial thrust measurements using calibrated strain gauges. The dimensions of the impeller side chamber can be altered and the flow in the side chamber can be changed in direction and magnitude as well (Fig. 2). The leakage fluid injection was performed by an auxiliary system, which consisted of a circulating pump, valve combination, and flowmeter.

Tests were performed in the pump test rig in a closed system. Pump flow rate was measured by a calibrated orifice plate, and all pressures by absolute or differential pressure transducers. The casing wall of the impeller side chamber was built of a transparent material in order to enable measurements of velocity distribution by the LDA method (Laser Doppler Anemometry). The device has an argon-ion laser with an exit power of 4W and Bragg's cells with carrier frequency of 40 MHz. A separate lens system connected by a fiber optic cable was used in order to ensure simple and accurate positioning of laser beam cross-sections in the axial and radial directions. The measuring volume was 0.1 mm in diameter and 1.0 mm in length.

The basic geometrical parameters of the tested pump can be

Contributed by the Fluids Engineering Division for publication in the JOURNAL OF FLUIDS ENGINEERING. Manuscript received by the Fluids Engineering Division April 12, 2001; revised manuscript received September 12, 2001. Associate Editor: Y. Tsujimoto.

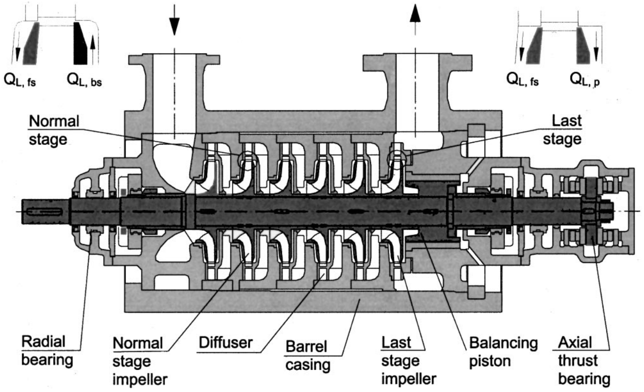

Fig. 1 Multistage pump with barrel casing

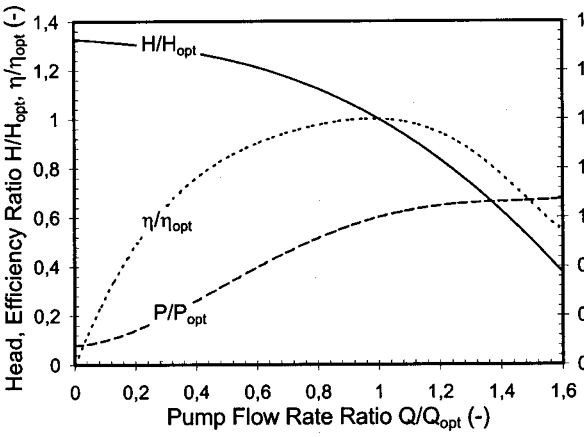

Fig. 4 Dimensionless pump characteristics

seen in Fig. 3. Radial clearances *A* and *B* between impeller and diffuser and overlapping U_e have been designed according to EPRI recommendations [5].

The rotational speed of the tested pump was on a level which assures turbulent flow with separate boundary layers in the impeller side chamber ($Re=3.8.10^6$). The definition of Re number is, due to possible comparison, the same as that used by Daily and Nece [1] and Senoo and Hayami [6].

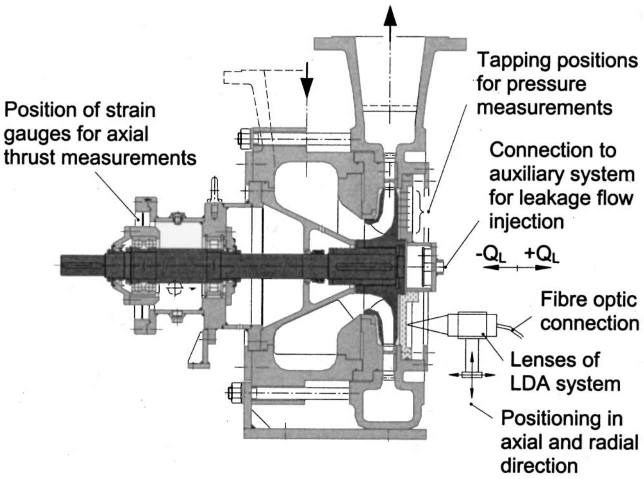

Fig. 2 Testing arrangement, pump specific speed nq 22 (ns_{USA} 1135)

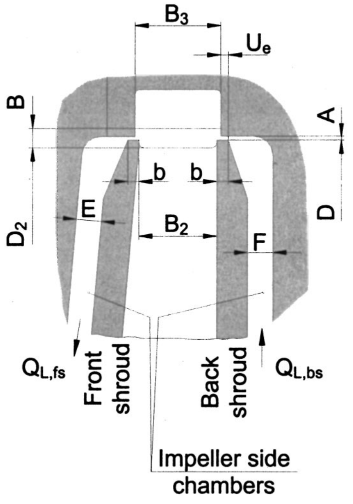

	(mm)
b	3
A	1
B	3.5
B_2	20
B_3	22
D	319
D_2	315
E	6.5
F	6.5
U_e	2

Fig. 3 Geometry of tested pump

The specific speed of the tested pump is nq 22 (ns_{USA} 1135), and the dimensionless characteristics are shown in Fig. 4. Measuring inaccuracies of experimental work were the following: pump flow rate ±0.5%, leakage flow rate ±0.6%, pump head and static pressures ±0.3%, pump efficiency ±0.7%, velocities in side chamber ±2%, hydraulic axial thrust ±4%.

Test Results—Static Pressure Distributions. Static pressures were measured on the casing wall at 6 different radial positions. This gives a sufficient amount of data for the correct determination of the pressure distribution in the entire impeller side chamber. The most important parameter, which affects the static pressure distribution, is the flow in the impeller side chamber. In Fig. 5 the pressure distributions are shown for the pump flow rate Q_{opt} and impeller central position relative to the diffuser. It can be seen that the pressure distribution is greatly influenced by the quantity and direction of flow in the side chamber through the complete impeller periphery. The influence of q_L is the lowest at the outer impeller side chamber perimeter and increases in the radial direction toward the impeller wear ring. Measured pressure distributions, especially at leakage flow regimes $+q_L$, differ greatly from the pressure distribution, presented by Stepanoff [7], which has been taken in the past as the basis for hydraulic axial thrust determination.

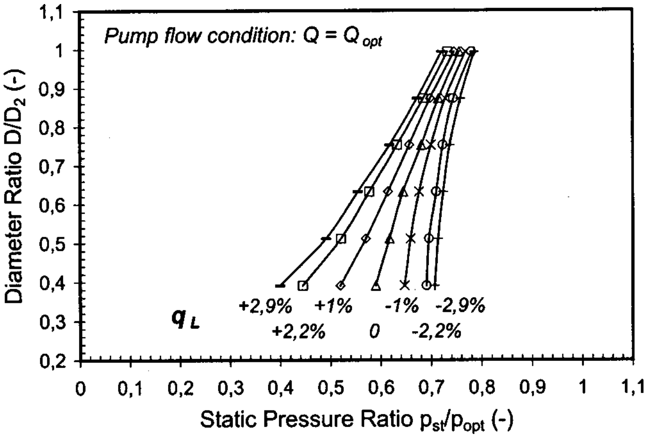

Fig. 5 Static pressure distributions for different leakage flow conditions

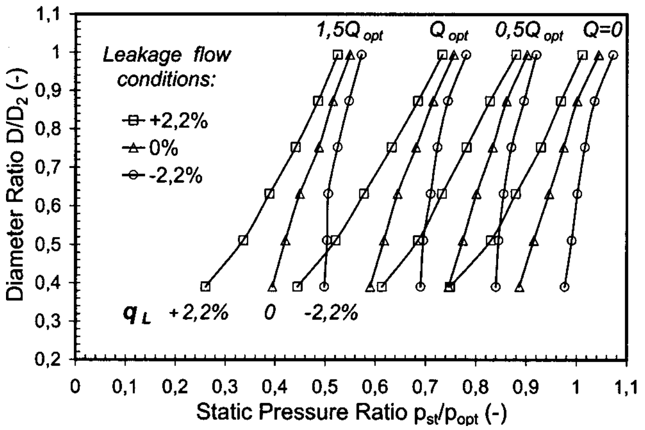

Fig. 6 Static pressure distributions for different pump flow conditions

As the static pressure at the impeller exit is changed, according to the pump operating regime, pressure levels and internal flows in the impeller side chambers (Fig. 6) are also influenced. An impact from eventual flow recirculation in the area of the impeller exit/diffuser inlet was not observed in the impeller side chamber. This can be explained by the fact that the main impeller passages and side chambers are sufficiently separated by throttling via small radial clearance A and overlapping U_e. This also accounts for the fact that at part flows, no significant instability can be observed in the measured hydraulic axial thrust. Similar conclusions can also be found in Makay and Barrett [8]. Additional test results about the influence of gap A and overlapping U_e on pump characteristics are presented in Gantar et al. [9].

Test Results—Velocity Distributions. The velocity distribution in the impeller side chamber has been measured by a two-component LDA measuring system. The method used is contact free and does not disturb the flow field in the measured area. Peripheral and radial velocity components were measured in the impeller side chamber at six radial positions. At each radial position, 10–15 measuring points have been taken through the side chamber width. The main goal of this measurement is to determine the peripheral velocity component of the core layer in the impeller side chamber and its distribution in the radial direction. In Fig. 7 the peripheral velocity component is shown for different relative leakage flows q_L. When the leakage flow direction is radially outwards, the rotation of the core layer is lower and opposite to that of the inward leakage flow direction. This result matches logically with static pressure test results (Fig. 5). Although at the outer impeller side chamber perimeter the peripheral velocity component is dependent on the direction and quantity of relative leakage flow q_L, the difference increases radially toward the impeller wear ring. We can summarize that the fluid rotation in the core layer is dominant for the pressure distribution on the impeller front and back shrouds, and consequently, for pump hydraulic axial thrust.

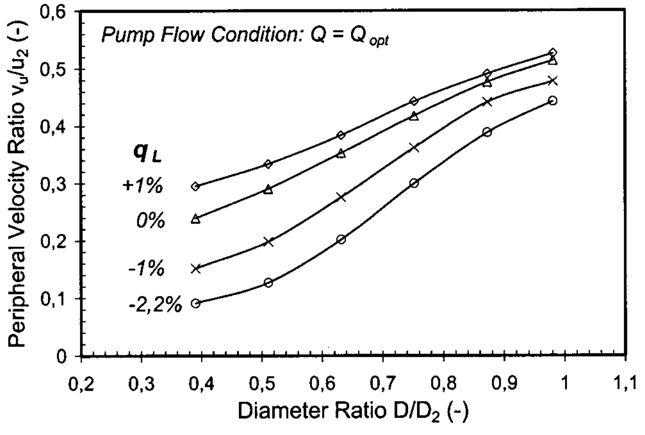

Fig. 7 Measured peripheral velocity component in the middle of impeller side chamber width

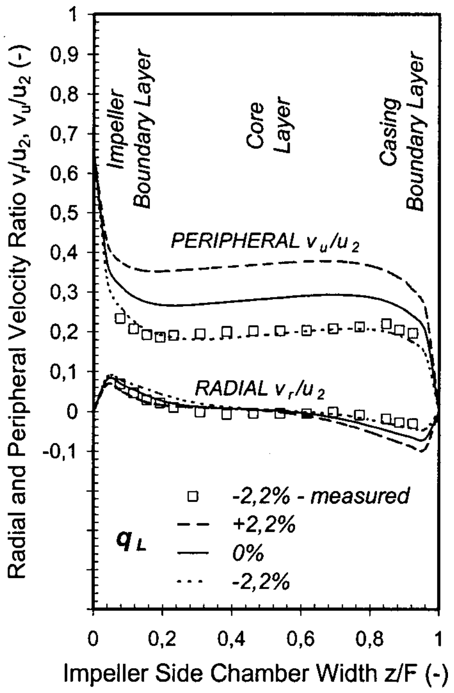

Fig. 8 Calculated velocity distributions by NFA at diameter ratio $D/D_2=0{,}63$

Numerical Flow Analysis

Varied software for numerical flow analysis is available and its application in the field of hydraulic machinery is almost a standard tool. In this investigation a three-dimensional k-ε turbulent code named Tasc-flow has been used, which is second-order accurate in space. The main goal of the NFA was to determine whether the numerical approach could satisfactorily simulate the test results. Due to simplification the flow analysis has been done for impeller side chamber flow separately, uncoupled from the main impeller flow.

Several flow conditions were analyzed and the results give a clear and detailed picture of the velocity and pressure distributions in the impeller side chamber. In Fig. 8 the velocity profiles are shown in the peripheral and radial directions. Two separate boundary layers with a central core layer can be observed. The calculated velocity distribution of the core layer matches well with LDA test results. An example is shown in Fig. 8 for the regime $-q_L$.

The static pressure distribution in the side chamber is an important factor when judging the usefulness of NFA for hydraulic axial thrust prediction. In Fig. 9 the comparison of measured and calculated static pressure distributions are shown. Matching is satisfactory and confirms the usefulness of NFA for pressure distribution calculation of different geometries of impeller side chambers in order to optimize the pump elements in conjunction with axial thrust balancing system.

It has to be stated that the important factor for realistic NFA results is the introduction of proper boundary conditions at the outer impeller periphery. This means application of the circumfer-

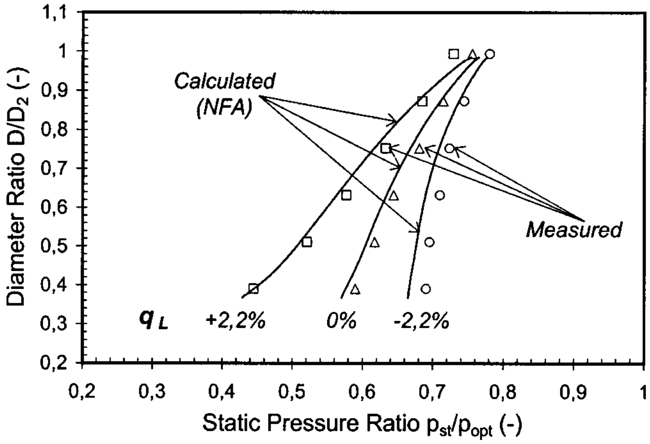

Fig. 9 Comparison of calculated and measured static pressure distributions

ential velocity component as well as the basic static pressure in gap *A* for both directions of Q_L. The following boundary conditions were applied at gap *A*:

- velocity direction: ratio between axial and peripheral velocity component-1:20, radial velocity component-zero,
- flow rate: calculated from relative leakage flow rate for three conditions ($q_L = +2{,}2\%, 0\%, -2{,}2\%$), and
- average static pressure: measured values from the tapping in the vicinity of gap *A*.

Impeller shroud and casing wall roughness have to be taken into account when defining wall function in the NFA (logarithmic wall function, roughness: equivalent sand grain 2.10^{-5}). The numerical model used was axisymmetric with approximately 25,000 nodes. Computational time for one leakage flow variant on a PC computer with a 450 MHz processor and 512 MB RAM was about 60 minutes. Criteria for maximum residual level were ERTIME$=10^{-3}$.

Fluid Rotation in Impeller Side Chamber

Velocity profiles measured via LDA in the core layer of the impeller side chamber (shown in Fig. 7) were recalculated into the form of relative fluid rotation *k*. Relative fluid rotation in the core layer is the ratio between the angular velocity of fluid and the angular velocity of the impeller: $k = \beta/\omega$. In Fig. 10, relative fluid rotation is presented, based on measurements in the core layer for different leakage flow quantities and directions. It can be noticed clearly that at constant relative leakage flow q_L, the relative fluid rotation *k* changes with the radial position in the side chamber. At the outer impeller side chamber perimeter the influence of leakage flow on fluid rotation is smaller, and increases radially inwards. Inward leakage flow increases fluid rotation; the opposite is valid for outward leakage flow.

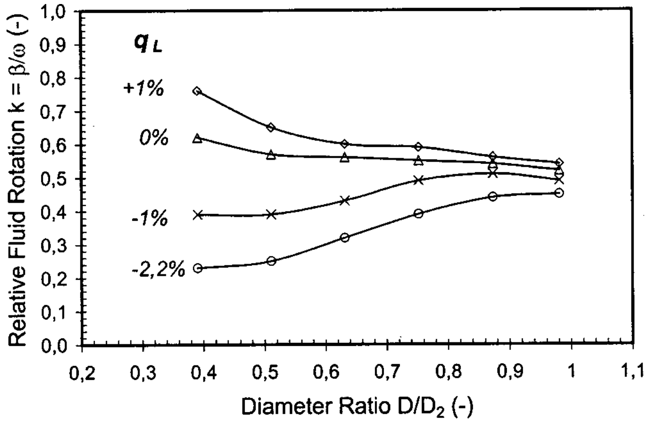

Fig. 10 Relative fluid rotation in the impeller side chamber

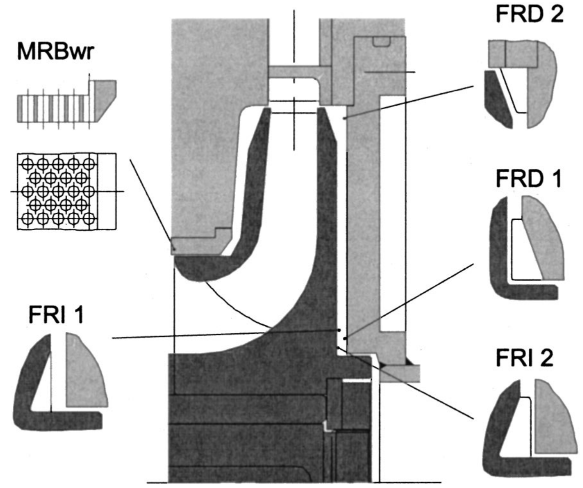

Fig. 11 Execution of FRI, FRD and MRBwr on one stage test arrangement

When the distribution in the radial direction of relative fluid rotation in the impeller side chamber is compared to static pressure distribution (Fig. 5), it is then obvious that the pressure changes at different leakage flows resulted from differences of fluid rotation in the core layer. Another important conclusion can be derived from the above stated results as well. In order to alter the pressure distribution and accordingly the hydraulic axial thrust on the impeller, the fluid rotation of the core layers in the side chambers (gaps *E* and *F* in Fig. 3) has to be changed artificially.

Measures for Hydraulic Axial Thrust Reduction

The main part of the total hydraulic axial thrust in a multistage pump is generated in the normal stages, where the leakages in the impeller front and back shroud side chambers flow in opposite directions (Fig. 1). The idea of axial thrust reduction is to increase fluid rotation on the back shroud side chamber and to decrease it on the front shroud side chamber. Efforts to alter fluid rotation should be achieved by means that do not have a significant negative effect on pump characteristics, especially on the pump efficiency.

Series of tests were carried out on the testing arrangement, Fig. 2. The Fluid Rotation Increaser (FRI) and the Fluid Rotation Decreaser (FRD) were built into the impeller side chamber, Fig. 11. The FRI is effective for outward leakage flows and the FRD for inward flows. Results are shown in Figs. 12 and 13. The FRI consists of numerous radial ribs, located at the outer side of the impeller back shroud (at inner side chamber perimeter) and rotates together with the impeller. As expected, the FRI produces the highest additional fluid rotation at the wear ring area, and the effect decreases toward outer impeller side chamber perimeter (see effect on static pressure in Fig. 12). No effect on pump efficiency has been observed due to the introduction of the FRI. This can be explained by the following facts:

- for the leakage flow direction radial outwards the FRI represents a simplified small impeller, acting in the same direction as the main impeller, and
- disk friction losses are smaller at higher fluid rotation, according Senoo and Hayami [6].

An effective FRD is type 2, which causes a considerable pressure increase in the impeller side chamber at the inner area and a

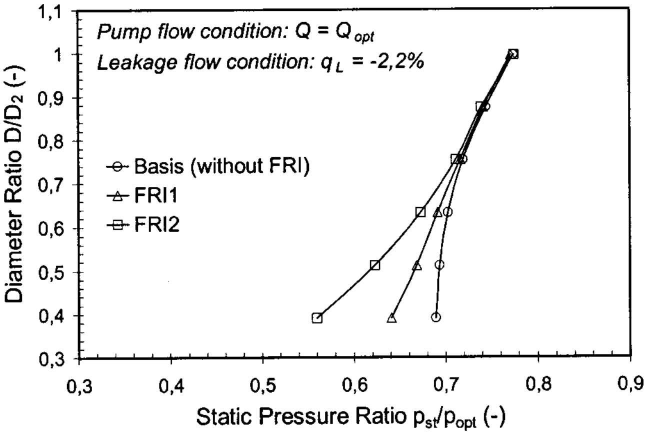

Fig. 12 Effect of FRI on static pressure distribution

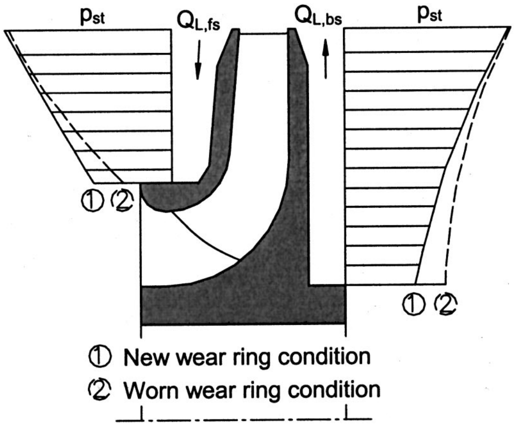

Fig. 14 Schematic pressure distributions on back and front shroud-normal stage impeller

corresponding impeller axial thrust reduction (see effect on static pressure in Fig. 13). The FRD2 consists of numerous stationary radial ribs, located at the outer corner of the impeller side chamber. The negative aspect of the FRD2 is an efficiency reduction of about 1% at Q_{opt} due to additional mixing losses in the FRD area.

The FRI and FRD have to be installed on all stages of a multistage pump. They can be cast together with impeller (FRI) or inter-stage casing (FRD). In order to obtain the maximal effectiveness on fluid rotation in the impeller side chambers, the design and execution of FRI and FRD should be studied in greater detail.

Effect of Increased Wear Ring Radial Clearance

During pump operation the radial clearances on impeller wear rings can increase. How rapidly the clearances increase depends on modes of operation, fluid properties, solid contents, material of rings, speed of rotation, etc. According to API 610/8 the pump elements (balancing device with thrust bearing) should be sized for continuous operation, when all loads should be defined at design internal clearances and at two times as much design internal clearances.

With wear of the radial wear rings, the volumetric losses and consequently leakage flows Q_L in both impeller side chambers increase. The pressure distribution on both impeller sides is changed, as schematically shown in Fig. 14 for a normal stage impeller. The increased radial clearance causes hydraulic axial thrust on the front shroud to decrease, while on the back shroud it increases; consequently, axial thrust on the impeller increases.

We were looking for a solution to this problem of wear rings, which would result in lower changes of leakage flow with increased wear. This would have a positive effect on axial thrust as well as on pump efficiency. The main efforts have been focused on a design variation, which has a high pressure loss factor also at increased radial clearances. A solution applied is called Multi Radial Bore wear ring (MRBwr), shown in Fig. 11. The outer wear ring dimensions are the same as a classical plain ring, but additional radial openings (cavities) were machined. The principle is similar to honeycomb wear rings; however, the number and shape of radial cavities is different. On the basis of the results from Childs et al. [10] it can be concluded that an additional positive effect of the MRBwr is improved pump rotordynamic behavior due to changed stiffness and damping coefficient.

Modified Multistage Pump Design

Based on the results of the above described investigation a modified pump design was worked out and tested. This design includes the installation of FRI2 on all impeller front side chambers and the installation of MRBwr on all impeller front and back wear rings. The positive effect of FRI is reduced hydraulic axial thrust, and of MRBwr lower sensitivity of axial thrust and efficiency on increased wear ring radial clearance. The effectiveness of FRI and MRBwr was verified on a three-stage pump constructed with the same impeller/diffuser elements as shown in Figs. 2 and 3. Results are presented in Fig. 15 and are summarized in Table 1 as a comparison between the modified design and the classic multistage pump design.

There are several advantages of the modified design:

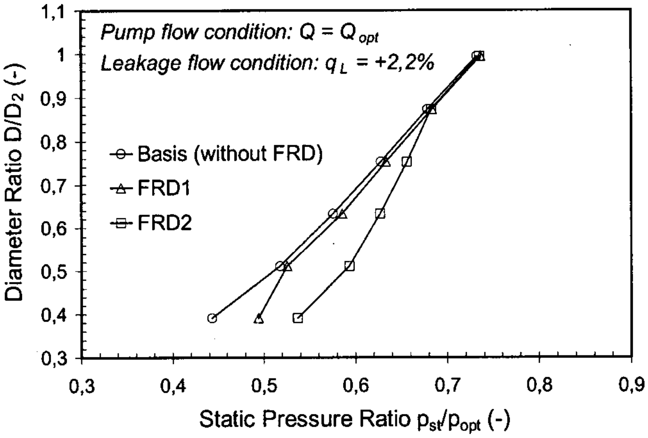

Fig. 13 Effect of FRD on static pressure distribution

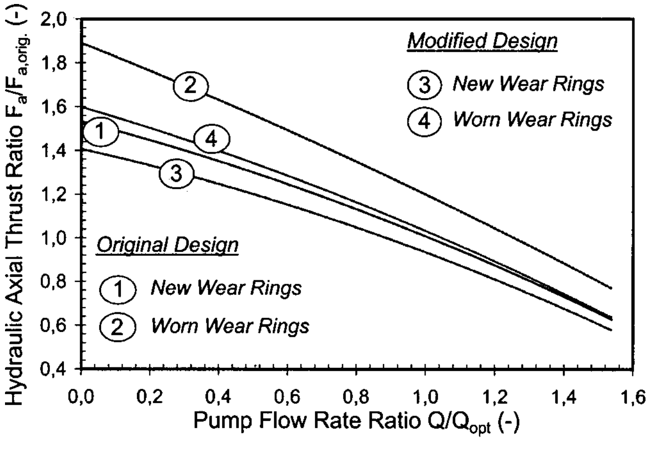

Fig. 15 Effect of modified pump design on hydraulic axial thrust of three-stage pump

Table 1 Comparison between original and modified design of three-stage pump of specific speed nq22 (ns_{USA} 1135). Pump flow condition: $Q=Q_{opt}$

	New Wear Rings $S_R/R_2 = 0{,}0015$		Worn Wear Rings $S_R/R_2 = 0{,}0030$	
	Original Design	Modified Design	Original Design	Modified Design
Relative Axial Thrust $F_a/F_{a,orig}$	1,00	0,94	1,20	1,03
Relative Pump Efficiency η/η_{orig}	1,000	1,003	0,952	0,975

Original design: plain wear rings
Modified design: MRB wear rings with FRI2

- lower hydraulic axial thrust,
- smaller increase of axial thrust at twice the normal wear ring clearances,
- smaller efficiency drop at twice the normal wear ring clearance,
- improved rotordynamic behavior due to changed stiffness and damping effects of MRBwr.

A disadvantage of the modified design are the additional machining costs for MRBwr. The pump construction containing FRI and FRD is the subject of patent application.

Conclusions

From the presented investigation the following main conclusions can be made:

1. The pressure distribution on the impeller front and back shrouds can be influenced by introduction of Fluid Rotation Increasers (FRI) and Fluid Rotation Decreasers (FRD), which results in axial thrust reduction. The final consequence is a smaller piston diameter and a smaller axial bearing.

2. Sensitivity of hydraulic axial thrust to radial labyrinth wear is considerably reduced by the introduction of Multi Radial Bore wear rings (MRBwr).

3. With proper execution of radial clearance A and overlapping U_e, flow in the side chamber can be effectively separated from the influence of main flow at impeller exit. This is also important to avoid axial thrust instability at part load operation of the pump.

4. Numerical flow analysis is an effective tool for axial thrust prediction at the design stage.

Nomenclature

A = radial clearance
B = radial clearance (vane passage)
B_2, B_3 = impeller, diffuser channel width
D = diameter
Re = $\omega \cdot R_2^2/\nu$-Reynolds number
E = axial width of impeller front shroud side chamber
F = axial width of impeller back shroud side chamber
F_a = axial thrust
H = head
P = power
Q = flow rate
Q_L = leakage flow
R = radius
S_R = radial clearance
U_e = impeller/diffuser wall overlapping
b = impeller shroud thickness
n = speed of rotation
nq = $n(min^{-1}) \cdot Q(m^3/s)^{0.5}/H(m)^{0.75}$-specific speed
ns_{USA} = $n(rpm) \cdot Q(GPM)^{0.5}/H(ft)^{0.75}$-specific speed
p = pressure
p_{opt} = $\rho \cdot g \cdot H_{opt}$-pump total pressure at Q_{opt}
q_L = Q_L/Q_{opt}-relative leakage flow
u = peripheral velocity
v = velocity
z = axial coordinate, impeller side chamber width
β = fluid angular velocity
η = efficiency
ν = kinematic viscosity
ρ = fluid density
ω = impeller angular velocity

Indices

bs = back shroud
fs = front shroud
opt = optimal, best efficiency point
orig = original
p = piston
r = radial
st = static
u = peripheral
wr = wear ring
2 = impeller outlet
3 = diffuser inlet

References

[1] Daily, J. W., and Nece, R. E., 1960, "Chamber Dimension Effects on Induced Flow and Frictional Resistance of Enclosed Rotating Disks," J. Basic Eng., **83**, pp. 217–232.
[2] Kurokawa, J., and Toyokura, T., 1972, "Study on Axial Thrust of Radial Flow Turbomachinery," Proceedings, The Second International JSME Symposium-Fluid Machinery and Fluidics, Tokyo, Japan, pp. 31–40.
[3] Iino, T., Sato, H., and Miyashiro, H., 1980, "Hydraulic Axial Thrust in Multistage Centrifugal Pumps," ASME J. Fluids Eng., **102**, pp. 64–69.
[4] Thomae, H., and Stucki, R., 1970, "Axial Thrust Occurring in Multistage Radial Pumps," Sulzer Technical Review, .
[5] EPRI Report TR-102102, 1993, "Feedpump Operation and Design Guidelines," Electric Power Research Institute, Palo Alto, CA, pp. 1/35–1/46.
[6] Senoo, Y., and Hayami, H., 1976, "An Analysis on the Flow in a Casing Induced by a Rotating Disk Using a Four-Layer Flow Model," ASME J. Fluids Eng., **99**, pp. 192–198.
[7] Stepanoff, A. J., 1966, *Centrifugal and Axial Flow Pumps*, Wiley, New York.
[8] Makay, E., and Barrett, J. A., 1984, "Changes in Hydraulic Component Geometries Greatly Increased Power Plant Availability and Reduced Maintenance Cost: Case Histories," Proceedings, The First International Pump Symposium, Texas A&M University, College Station, Texas, pp. 85–97.
[9] Gantar, M., Florjancic, D., and Sirok, B., 2001, "Changes in Hydraulic Component Geometries and its Influence on Axial Thrust in Multistage Pumps" (in German), Industriepumpen+Kompressoren, Vulkan Verlag, Essen, Germany.
[10] Childs, D. W., Elrod, D., and Hale, K., 1988, Annular Honeycomb Seal Test Results for Leakage on Rotordynamic Coefficients; Comparison to Labyrinth and Smooth Configurations, ASME Paper 88-Trib-35, ASME/STLE (1988), Tribology Conference.

Theoretical Analysis of Fluid Forces on an Open-Type Centrifugal Impeller in Whirling Motion

Akira Hiwata
Matsushita Electric Industries Co., Ltd,
Air-Conditioning Research Laboratory,
2-3-1-1 Noji-Higashi, Kusatsu, Japan,
525-8520
e-mail: PAN77672@pas.mei.co.jp

Yoshinobu Tsujimoto
Osaka University,
Graduate School of Engineering Science,
1-3 Machikaneyama, Toyonaka, Japan,
560-8531
e-mail: tujimoto@me.es.osaka-u.ac.jp

For turbomachines operating at supercritical shaft speed, it is important to understand the characteristics of unsteady fluid forces on the impeller that occur due to shaft vibration. The present paper treats the forces on an open-type centrifugal impeller in whirling motion using unsteady potential flow theory. The whirling forces obtained agree reasonably with experimental results and show a destabilizing region at small positive whirl. It was found that the destabilizing force is due to the forces on the hub caused by temporal change in the thickness of the flow channel, with minor contribution of tip leakage on the destabilization. [DOI: 10.1115/1.1458582]

Introduction

For turbomachines operating at supercritical shaft speed, it is important to understand the characteristics of unsteady fluid forces on the impeller that occur due to shaft vibration. They are called ‘‘rotordynamic forces’’ [1]. Shaft vibration has two modes: whirling motion and precessing motion (Fig. 1), and considerable knowledge has been obtained for whirling closed-type centrifugal impellers. Although the impeller whirling forces are basically stabilizing the rotor [2], they become destabilizing under the following conditions: (i) at reduced flow rate [2,3], (ii) when there is interaction with volute or vaned diffuser [4–7], or (iii) when the clearance between front shroud and casing of 3-D impeller is small [4,8–11].

For axial flow turbines, it was found independently by Thomas [12] and Alford [13] that tip leakage plays an important role in the mechanism of producing rotordynamic forces. Detailed flow measurements were carried out [14] and an actuator disk model with tip leakage effect was proposed [15,16]. For axial flow compressors, it was clarified recently [17] that the rotordynamic forces are mostly in the direction to promote backward whirl caused by reduced blade loading at wider tip clearance. Several flow models are examined [18] to simulate the whirling forces. Thus, the tip leakage is the key factor in producing rotordynamic forces on axial flow turbines and compressors. Axial flow pump inducers are more complicated with inherent backflow but rotordynamic forces promoting forward whirl have been reported [19].

On the other hand, little has been known about the rotordynamic forces on open-type centrifugal impellers although they are widely used for gas compressors. In certain applications such as for reinjection, the density of the gas can be of the same order as that of the liquids. In such cases, the rotordynamic forces on compressor impeller can be as large as for pumps. Recent experiments [20] on an open-type centrifugal impeller show that forward whirl is promoted even at the design point and without interaction with the volute or the guidevanes.

The purpose of the present study is to propose an analytical method to predict rotordynamic forces on open-type centrifugal impellers and to explain the mechanisms of destabilizing rotordynamic forces observed in experiments. Major differences from the treatment of closed-type impeller are: (i) effects of the temporal changes in tip clearance and the distance between hub and casing should be taken into account, (ii) pressure forces on hub should be taken into account. These requirements are the same as for open-type axial flow-machines, but the effects of the change in hub/casing distance and the pressure force on the hub will be less important for axial flow machines with smaller hub/tip ratios and larger specific speed. We focus on centrifugal/mixed flow impellers with smaller specific speed for which two-dimensional treatment of flow is possible as a first-order approximation. We assume that the flow is two-dimensional, inviscid, and incompressible.

Fundamental Equations and Mapping

As stated in the Introduction, we assume that the distance between the hub and the casing, b, is so small compared to the outlet radius, r_2, that the flow in the impeller can be represented by a two-dimensional flow in a representative flow surface as shown in Fig. 2(a). We use radial (r), circumferential (θ), and meridional (m) coordinates in the physical plane fixed to the impeller. The shape of the flow surface in the meridional section $r=r(m)$ is assumed to be given. The flow thickness b can change in meridional direction (m) and also in time (t) due to the whirling motion of the impeller. The impeller rotates around the x_3-axis with an angular velocity Ω. The center of the impeller (x_3-axis) whirls around an axis parallel to x_3-axis with a constant eccentricity ε and an angular velocity ω (not illustrated in Fig. 2(a), see Fig. 1(a)). The flow surface (m,θ) is mapped to a flat plane (R,Θ) using the mapping relations:

$$\frac{d\Theta}{d\theta}=\frac{\Theta}{\theta}=1,\quad \frac{1}{r}\frac{dm}{d\theta}=\frac{1}{R}\frac{dR}{d\Theta} \tag{1}$$

Fundamental Equations. The continuity equation in representative flow surface is:

$$\frac{\partial}{\partial t}(\rho b)+\frac{\partial}{r\partial m}(\rho r w_m b)+\frac{\partial}{r\partial \theta}(\rho w_\theta b)=0 \tag{2}$$

where b is the thickness of the flow defined as the distance between hub and casing. (w_m, w_θ) are relative velocity components in m and θ directions. Since the absolute flow can be assumed to be irrotational, the absolute velocity (v_m, v_θ) can be represented by using a velocity potential Φ.

$$v_m=\frac{\partial\Phi}{\partial m}=w_m,\quad v_\theta=\frac{\partial\Phi}{r\partial\theta}=w_\theta+r\Omega \tag{3}$$

Contributed by the Fluids Engineering Division for publication in the JOURNAL OF FLUIDS ENGINEERING. Manuscript received by the Fluids Engineering Division August 1, 2001; revised manuscript received September 6, 2001. Associate Editor: J. Katz.

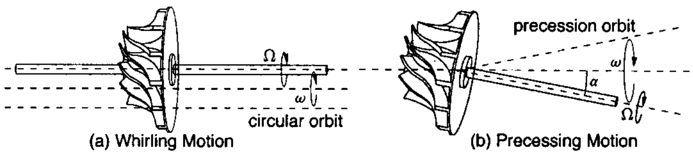

Fig. 1 Two fundamental vibration modes of an impeller

If we put Eq. (3) into Eq. (2) and use the mapping relations (1), we obtain:

$$\nabla^2\Phi=\frac{\partial}{R\partial R}\left(R\frac{\partial\Phi}{\partial R}\right)+\frac{1}{R^2}\frac{\partial^2\Phi}{\partial\theta^2}$$

$$=-\frac{1}{b}\left\{\left(\frac{r}{R}\right)^2\left(\frac{\partial b}{\partial t}-\Omega\frac{\partial b}{\partial\Theta}\right)+\frac{\partial b}{\partial R}V_R+\frac{\partial b}{R\partial\Theta}V_\Theta\right\} \tag{4}$$

where

$$V_R=\frac{\partial\Phi}{\partial R}=\frac{r}{R}\frac{\partial\Phi}{\partial m}=\frac{r}{R}v_m$$

$$V_\Theta=\frac{\partial\Phi}{R\partial\Theta}=\left(\frac{r}{R}\right)\frac{\partial\Phi}{r\partial\theta}=\frac{r}{R}v_\theta \tag{5}$$

On the other hand, irrotational flow with a source distribution q^m satisfies:

$$\nabla^2\Phi=q^m \tag{6}$$

Hence, the flow in the representative flow surface can be represented by using an irrotational flow in the mapping plane with the source distribution.

$$q^m=-\frac{1}{b}\left\{\left(\frac{r}{R}\right)^2\left(\frac{\partial b}{\partial t}-\Omega\frac{\partial b}{\partial\Theta}\right)+\frac{\partial b}{\partial R}V_R+\frac{\partial b}{R\partial\Theta}V_\Theta\right\} \tag{7}$$

This method has been used by Tsujimoto et al. [21] for the analysis of unsteady torque on mixed flow impellers.

Complex Velocity. The absolute irrotational velocity in the mapped plane can be expressed as:

$$U-iV=(V_R-iV_\Theta)e^{-i\Theta}$$

$$=\frac{Q}{2\pi Z^m}+\frac{1}{2\pi}\int\int_F\frac{q^m(Z_F^m,t)}{Z^m-Z_F^m}dF$$

$$+\frac{1}{2\pi i}\sum^N\int_{s_1^m}^{s_2^m}\frac{\gamma_b^m(s^m,t)}{Z^m-Z^m(s^m)}ds^m$$

$$+\frac{1}{2\pi i}\sum^N\int_{s_2'^m}^{\infty}\frac{\gamma_v^m(s'^m,t)}{Z^m-Z^m(s'^m)}ds'^m \tag{8}$$

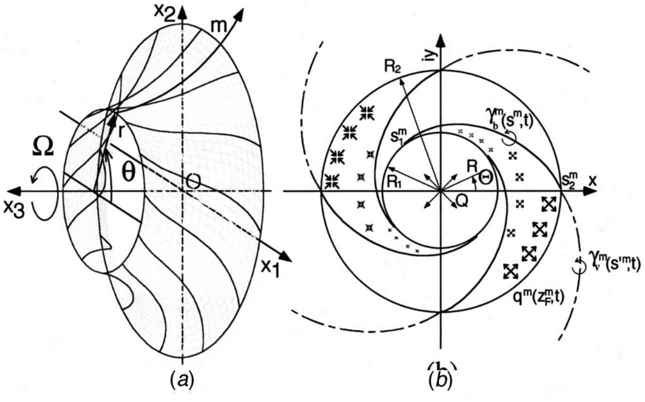

Fig. 2 (*a*) Representative flow surface, (*b*) mapped plane

where Q is a source at the center of the impeller, $q^m(Z_F^m,t)$ is the source distribution given by Eq. (7), $\gamma_b^m(S^m,t)$ is a vortex distribution which represents the effect of blades, and $\gamma_v^m(s'^m,t)$ represents the free vortex wake shed from the blades.

Velocity Due to Rotational and Whirling Motion. The velocity due to rotational and whirling motion observed at a point fixed to the impeller is:

$$v_m^\varepsilon=\mathrm{Re}^{(i)}[e^{i\theta}(i\varepsilon\omega-j\varepsilon\omega)]e^{j(\omega-\Omega)t}$$

$$v_\theta^\varepsilon=r\Omega-\mathrm{Im}^{(i)}[e^{i\theta}(i\varepsilon\omega-j\varepsilon\omega)]e^{j(\omega-\Omega)t}\sin\eta(s) \tag{9}$$

where $\mathrm{Re}^{(i)}$, $\mathrm{Im}^{(i)}$ are real and imaginary part with respect to i. $\eta(s)=\cos^{-1}(dm/dr)$ is the angle between x_3-axis and the representative flow surface.

Tip Clearance Leakage. Since we focus on the open-type centrifugal impeller, we need to evaluate the effect of the change in tip clearance although we cannot simulate three-dimensional tip leakage in the present two-dimensional flow method. The effect of leakage is simulated by assuming the normal velocity on the blade surface given by:

$$w_n=\frac{t_c}{b}\sqrt{\frac{2\Delta p}{\rho\zeta}} \tag{10}$$

where Δp is the pressure difference across the blade, t_c is the tip clearance, and ζ is the loss coefficient. In this paper, ζ is set to be 1. Effects of the change in tip clearance t_c and in pressure difference Δp are both considered. An iterative method was used to determine w_n and Δp. Chen et al. [22] have shown that the tip leakage can be simulated reasonably by the pressure difference.

Boundary Conditions on the Blades. The relative flow velocity on the blade is given by subtracting the blade velocity $(v_m^\varepsilon,v_\theta^\varepsilon)$ due to rotation and whirling motion from the absolute flow velocity (v_m,v_θ) obtained from Eqs. (5) and (8) with $V_R-iV_\Theta=(U-iV)e^{i\Theta}$. Then we equate the normal component with the velocity of Eq. (10) representing the effect of tip leakage.

$$(v_m-v_m^\varepsilon)\cos\beta(s)+(v_\theta-v_\theta^\varepsilon)\sin\beta(s)=w_n \tag{11}$$

This provides the boundary condition on the blade.

Analytical Method

The whirling motion affects the flow through the source distribution of Eq. (7) representing the effect of the change in the thickness b of the flow, and the boundary condition of Eqs. (11) with (9). In a frame rotating and whirling with the impeller, it can be shown that the unsteady component of $q^m(Z_F^m,t)$ fluctuates as $e^{j(\omega-\Omega)t}$ if we describe it in a frame fixed to the impeller. Then we express:

$$q^m=\overline{q}^m+\tilde{q}^m e^{j(\omega-\Omega)t},\quad \gamma_b^m=\overline{\gamma}_b^m+\tilde{\gamma}_b^m e^{j(\omega-\Omega)t}$$

$$\gamma_v^m=\overline{\gamma}_v^m+\tilde{\gamma}_v^m e^{j(\omega-\Omega)t},\quad U=\overline{U}+\tilde{U}e^{j(\omega-\Omega)t} \tag{12}$$

$$V=\overline{V}+\tilde{V}e^{j(\omega-\Omega)t},\quad b=\overline{b}+\tilde{b}e^{j(\omega-\Omega)t}$$

and separate Eqs. (8), (10), and (11) into steady and unsteady components. First, steady components are used to determine the steady flow. The results of steady flow analysis are then used to determine the unsteady components. Finally the fluid forces are calculated using the results of the steady and unsteady flow analysis.

Analysis of Steady Flow Components. For steady flows, the unknowns are $\overline{q^m}$ and $\overline{\gamma_b^m}$ since $\overline{\gamma_v^m}=0$. Exactly speaking, $\overline{q^m}$ should be evaluated from Eq. (7) using local values of V_R and V_Θ. In this study, simplifications have been made by approximating the contributions of the first two terms of Eq. (8) by $V_R=Q/(2\pi Rb(R))$ and $V_\Theta=0$. Then the unknown is the vortex distribution on the blade $\overline{\gamma_b^m}$ and it was determined numerically using a singularity method. The blade surface was separated into M-1 segments and the values of $\overline{\gamma_b^m}$ at M segment boundaries are specified as unknowns. If we apply the boundary condition of Eq. (11) at the mid-point of each segment, we obtain M-1 linear equations in terms of the value of $\overline{\gamma_b^m}$ at M boundary points. In addition to these M-1 equations for M unknowns, we apply Kutta's condition $\overline{\gamma_b^m}=0$ at the trailing edge. For steady flow we can assume that $\overline{\gamma_b^m}$ distribution is the same as for all blades. Then we can determine the vortex distribution by solving the M linear equations. The integrals in Eq. (8) were evaluated by assuming linear distribution of $\overline{\gamma_b^m}$ over the segment. On the segment closest to the leading edge, it was assumed that $\overline{\gamma_b^m}=\overline{\gamma_{b0}^m}/\sqrt{s}$ ($\overline{\gamma_{b0}^m}$ is an unknown constant and s is the distance from the leading edge) taking account of the singularity at the leading edge.

Analysis of Unsteady Flow Components. For unsteady flows free vortices are shed from the trailing edge following Kelvin's vortex conservation law. We assume that the vortices are transported on a mean relative velocity in the physical plane, which is associated with: (i) concentrated source and total circulation of the blades at the center of the impeller, (ii) rotation of the impeller. Under these approximations, the strength of the free vortices is related with the blade circulation by:

$$\tilde{\gamma}_v^m=-\frac{1}{(R/r)^2\overline{W}(s'^m)}\frac{\partial}{\partial\tau}\left[\int_{s_1^m}^{s_2^m}\gamma_b^m ds^m\right]\tag{13}$$

where

$$\tau=t-\int_{s_2^m}^{s^m}\frac{ds^m}{(R/r)^2\overline{W}(s'^m)}$$

$\overline{W}(s'^m)$ is the mean relative velocity on the wake s'^m. The location of the free vortex wake in the mapped plane is represented by:

$$\Theta(R)=\frac{N\Gamma_s}{Q}\ln\frac{R}{R_2}-\frac{2\pi\Omega}{Q}\int_{R_2}^{R}\frac{r^2}{R}dR+\Theta_2\tag{14}$$

where (R_2,Θ_2) is the location of the trailing edge. From Eqs. (13) and (14), the strength of the free vortex on the wake is expressed as follows.

$$\tilde{\gamma}_v^m=-\frac{j(\omega-\Omega)\exp\left(-j(\omega-\Omega)\frac{2\pi}{Q}\int_{R_2}^{R_v}\frac{r^2}{R}dR\right)}{(R/r)^2\overline{W}(s'^m)}\int_{s_1^m}^{s_2^m}\tilde{\gamma}_b^m ds^m\tag{15}$$

The unsteady component of the source q^m is given by linearizing Eq. (7). Circumferentially averaged values are used for the steady components of $\overline{V_R}$ and $\overline{V_\Theta}$. Once the steady flow velocity of $\overline{V_R}$, $\overline{V_\Theta}$ and the thickness of the flow channel $b(t,R)$ are given, we can determine the values of all terms except for $\partial\overline{b}/\partial R\cdot\tilde{V}_R$. This term is evaluated by using an iterative method.

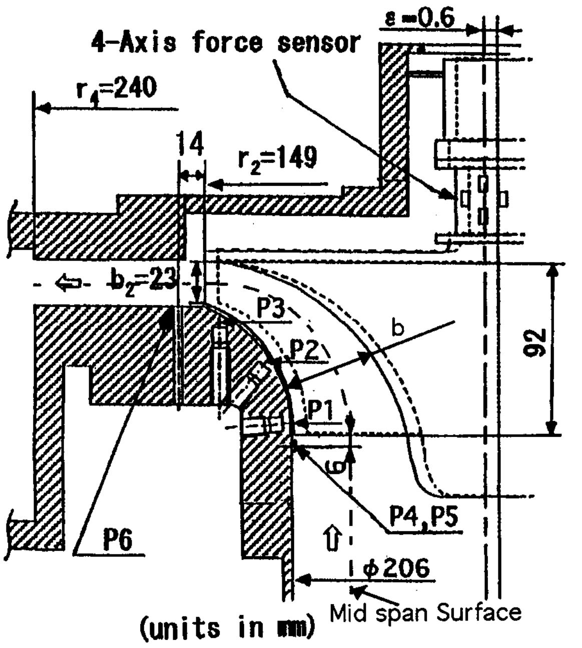

Fig. 3 Cross section of the test rig (impeller, casing and instrumented shaft)

The unknown for the unsteady components is the vortex distribution $\tilde{\gamma}_b^m$ on the blade and it was determined by using a singularity method in the same way as for the steady flow analysis. The unsteady Kutta's equation is given by Eq. (15) with $R=R_2$ and $\tilde{\gamma}_v^m(R_2)=\tilde{\gamma}_b^m(s_2^m)$, which has been used combined with the unsteady part of the boundary condition (11) on the blade surface. For the unsteady component we have to treat the vortex distribution $\tilde{\gamma}_b^m$ on each blade independently.

Modeling the Impeller Geometry. The present method is applied to an impeller shown in Figs. 3 and 4 for which experimental results are available [20]. The impeller is a model of a gas compressor with blade count 12, inlet and outlet blade angles 32 and 45 degrees, respectively, and specific speed $k=2\pi n\sqrt{Q}/(\Delta E)^{3/4}=1.3$, where n is the rotational speed, Q is the volumetric flow rate and ΔE is specific reversible work. The mid-span surface shown in Fig. 3 and Fig. 4(*a*) is used as the "representative flow surface."

It was found that the flow thickness b can be approximated by the following equation for a whirling motion with whirl radius ε and whirl angular velocity ω.

$$b=\overline{b}(R)+\varepsilon\left\{1-\left(\frac{R-R_1}{R_2-R_1}\right)^2\right\}\cos(\Theta-(\omega-\Omega)t)\tag{16}$$

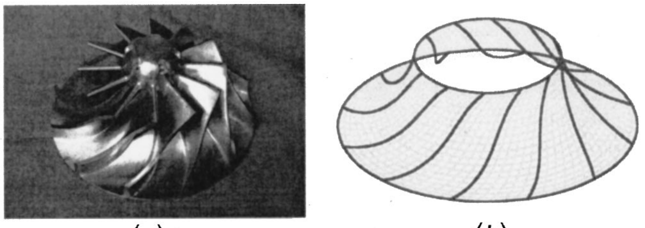

(*a*) (*b*)

Fig. 4 (*a*) Impeller, (*b*) mid-span surface

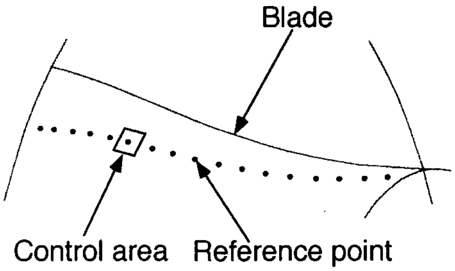

Fig. 5 Cell and reference point on representative flow surface

where $\overline{b}(R)$ is the mean thickness. The tip clearance t_c can be approximated by a similar equation.

Evaluation of Unsteady Pressure Field. In order to calculate the unsteady fluid forces, the unsteady pressure field on representative flow surface should be calculated. The unsteady pressure equation in the coordinate fixed to the impeller can be represented as:

$$\frac{p}{\rho}+\frac{1}{2}|w|^2+\frac{\partial\Phi}{\partial t}-\frac{1}{2}v_t^2=c(t) \tag{17}$$

where v_t is the moving velocity of the coordinate fixed to the impeller, $v_t^2=v_m^{\varepsilon^2}+v_\theta^{\varepsilon^2}$ and w is the fluid velocity relative to rotating and whirling impeller. The center of the impeller in the mapping plane is selected to be the reference point for pressure evaluation. The total pressure and velocity potential there are denoted by p_c and Φ_c respectively. Then Eq. (17) can be reduced to:

$$\left.\frac{p}{\rho}\right|_{Z=Z,t=t}=\frac{p_c}{\rho}-\frac{\partial}{\partial t}(\Phi-\Phi_c)-\frac{1}{2}|w|^2+\frac{1}{2}v_t^2 \tag{18}$$

The second term of Eq. (18) is evaluated as the sum of the contributions of the vortex distribution on the blades, the vortex distribution on the wakes and the source distribution between blades. Then Eq. (18) results in:

$$\begin{aligned}\left.\frac{p}{\rho}\right|_{Z^m=Z^m,t=t}&=\frac{p_c}{\rho}-\frac{1}{2}|w|^2+\frac{1}{2}v_2^t+\frac{1}{2\pi}\int\int_F\frac{\partial q^m(Z_F^m,t)}{\partial t}\ln|Z^m\\&\quad-Z_F^m|dF+\frac{1}{2\pi}\int_{s_1^m}^{s_2^m}\Delta\Theta(s^m)_{Z^m\to c}\frac{\partial\gamma_b^m(s^m,t)}{\partial t}ds^m\\&\quad+\frac{1}{2\pi}\int_{s_2^{\prime m}}^{\infty}\Delta\Theta(s'^m)_{Z^m\to c}\frac{\partial\gamma_v^m(s'^m,t)}{\partial t}ds'^m\end{aligned} \tag{19}$$

$\Delta\Theta(s^m)_{Z^m\to c}$ and $\Delta\Theta(s'^m)_{Z^m\to c}$ of Eq. (19) are expressed as follows.

$$\begin{aligned}\Delta\Theta(s^m)_{Z^m\to c}&=Arg(Z^m-Z(s^m))-Arg(Z_c^m-Z(s^m))\\\Delta\Theta(s'^m)_{Z^m\to c}&=Arg(Z^m-Z(s'^m))-Arg(Z_c^m-Z(s'^m))\end{aligned} \tag{20}$$

where $Z(s^m)$ is the location of vortex distribution and Z_c^m is the center of the impeller.

Fluid Forces on the Impeller. The unsteady fluid forces on the impeller are evaluated as the sum of the pressure forces on the hub and the blades.

The forces on the hub are evaluated by numerically integrating the pressure force components on the representative flow surface using the mesh as shown in Fig. 5.

The force on the blade is also evaluated by integrating the pressure distribution. In the present model assuming infinitely thin blades, leading edge suction forces are evaluated from the strength of the singularity of γ_b distribution at the leading edge.

The evaluated forces are normalized by using $F_0=\rho\pi r_2^2 b_2\varepsilon\Omega^2$, where r_2 and b_2 are impeller outlet radius and thickness, respectively.

Results and Discussions

Although the unsteady components observed at a point fixed to the whirling impeller fluctuates with the frequency $\omega-\Omega$, the total force on the impeller becomes steady when it is expressed in terms of components of normal (F_r, positive if outward) and tangential (F_t, positive if it is in the direction of impeller rotation) to the whirling orbit. This expression is extremely useful since we can determine the stability for whirl. If F_t is in the same direction as the assumed whirling motion, it promotes the whirl and if it is opposite, it dampens the whirl. So, the results are shown as plots of F_r and F_t as functions of assumed whirl speed ratio ω/Ω.

Comparison With the Experimental Results. The nondimensional whirling forces are shown in Figs. 6–8 for flow coefficients $\phi=Q/(2\pi r_2 b_2\cdot r_2\Omega)=0.330$, 0.424 and 0.508. The design flow coefficient is $\phi_d=0.424$. Experimental results from Ishii et al. [20] are also plotted. No significant effect of ϕ can be found and let us first focus on the case of the design flow coefficient $\phi_d=0.424$, Fig. 7. We observe a destabilizing region $F_t>0$ at small positive whirl speed ratio $0<\omega/\Omega<0.25$. This is simulated by the calculation. Although quantitative agreement cannot be obtained, the present results can predict a general trend with ω/Ω fairly well. In experiments, we can observe that $|F_r|$ and $|F_t|$ in

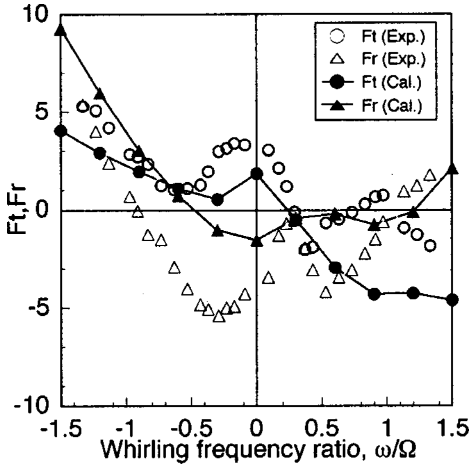

Fig. 6 Radial and tangential force components (ϕ=0.330)

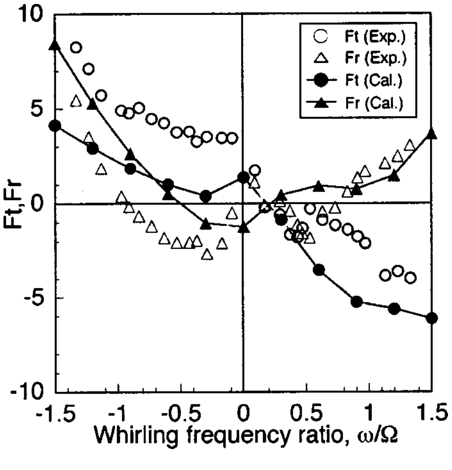

Fig. 7 Radial and tangential force components (ϕ=0.424)

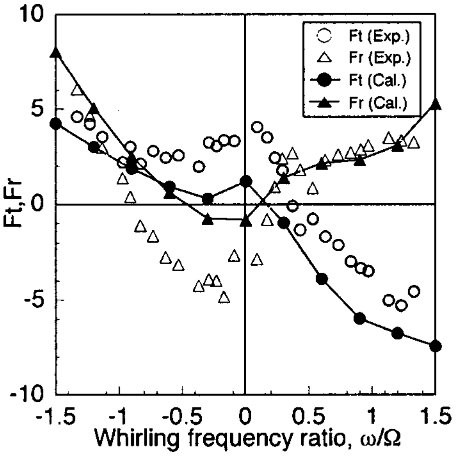

Fig. 8 Radial and tangential force components (ϕ=0.508)

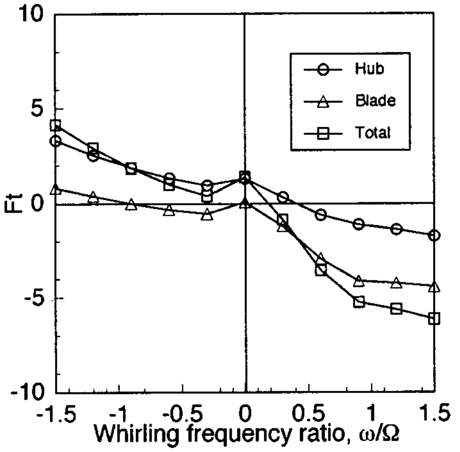

Fig. 9 Tangential force components of hub and blade

the region $0.8<\omega/\Omega<1.5$ increase as we increase the flow coefficient. This trend can be simulated by the present model. Figure 9 shows the decomposition of the tangential force F_t into the components due to the forces on the hub and the blades. We find that the force on the hub is predominant for negative whirl and the forces on the blades are important for positive whirl. We should note that the destabilizing force in $0<\omega/\Omega<0.25$ is caused by the force on the hub.

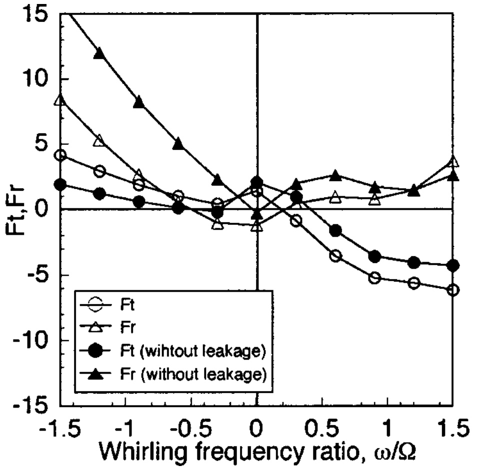

Fig. 10 The influence of the leakage flow (ϕ=0.424)

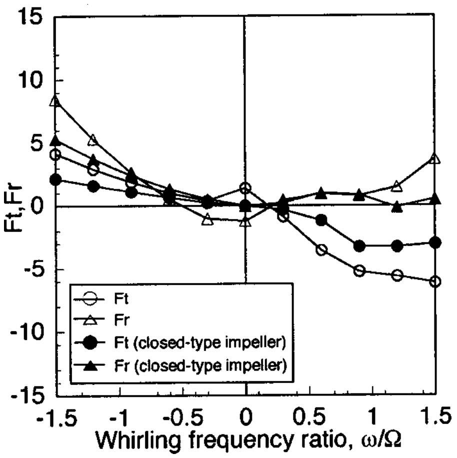

Fig. 11 The effect of front shroud (ϕ=0.424)

Effects of Tip Leakage. Figure 10 compares the results with and without tip leakage at the design flow rate. Tip leakage mainly affects the tangential force at negative whirl. Without the tip leakage, the destabilizing region at small positive whirl is increased. This shows that the tip leakage has a stabilizing effects on the forward whirl, which can be qualitatively explained by the load reduction on the blades at the location with larger tip clearance, as shown by Storace et al. [17] for an axial compressor.

Effects of the Front Casing. The effects of the front casing can be easily examined by comparing the results with and without the casing. The forces on the closed-type impeller with a front casing can be calculated by the present method by simply neglecting the effects of: (i) temporal change of flow thickness *b*, (ii) effects of tip leakage, (iii) forces on the hub (in this analysis the effects of the pressure difference on the hub and the casing have been neglected). The centrifugal force due to whirling motion will contribute to increasing the pressure difference and results in additional radial force Fr). Figure 11 compares the results for open- and closed-type impellers with the same blade geometry. Magnitudes of the forces are significantly smaller for closed-type impeller. Observe that no destabilizing region exists for the closed-type impeller without temporal change of impeller thickness.

Conclusions

An analytical method is proposed for the prediction of unsteady forces on whirling open-type centrifugal impeller. The validity is confirmed by comparisons with experiments on an impeller with specific speed 1.3. The results of the present study can be summarized as follows.

1 The predicted whirling forces agree qualitatively with experimental results and show a destabilizing region at small positive whirl speed ratio.

2 The destabilizing force at small positive whirl speed ratio is due to the forces on the hub.

3 Tip leakage has a stabilizing effect on forward whirl. This effect can be qualitatively explained by a smaller blade load at the locations where the tip clearance is larger.

4 Comparisons of the results for open- and closed-type impeller with the same geometry clearly show that the destabilizing forces on the open-type impeller are caused by the temporal change of the distance between the hub and the casing due to whirling motion.

Nomenclature

b = distance between hub and casing
F_r, F_t = force components, radial and tangential
i = complex unit (in space)

j = complex unit (in time)
m, θ = meridional and tangential coordinates in representative flow surface
N = blade number
p = static pressure
q = source distribution
Q = strength of source
$r = r(m)$ = radial location of representative flow surface
R, Θ = radial and circumferential coordinate in mapped plane
s = coordinate along blade
s' = coordinate along wake
t = time
U, V = absolute velocity components in x and y direction on mapped plane
w = relative velocity in representative flow surface
W = relative velocity in mapped plane
x_1, x_2, x_3 = Cartesian coordinate fixed to the impeller
β = blade angle
γ = vortex distribution
Γ = circulation
ε = radius of the whirling motion
η = angle between center line and representative flow surface
ϕ = pump flow coefficient
Φ = velocity potential
ω = angular velocity of whirling motion
Ω = angular velocity of impeller rotation

Superscript

m = quantities defined in mapped plane
$\bar{\ }$ = steady component
$\grave{\ }$ = unsteady component
$\tilde{\ }$ = complex amplitude of unsteady component

Subscript

1,2 = inlet and outlet of the impeller
b = blade
n, s = normal and tangential component
v = free vortex wake

References

[1] Brennen, C. E., 1994, *Hydrodynamics of Pumps*, Concepts ETI and Oxford University Press.
[2] Ohashi, H., and Shoji, H., 1987, ‘‘Lateral fluid forces on whirling centrifugal impeller (2nd report: Experiment in vaneless diffuser),’’ ASME J. Fluids Eng., **109**, pp. 94–99.
[3] Tsujimoto, Y., and Acosta, A. J., 1987, ‘‘Theoretical study of impeller and/or vaneless diffuser attributed rotating stalls and their effects on whirling instability of a centrifugal impeller,’’ Work group on the behavior of hydraulic machinery under steady oscillatory conditions, Lille, France.
[4] Jery, B., Acosta, A. J., Brennen, C. E., and Caughey, T. K., 1985, ‘‘Forces on centrifugal pump impellers,’’ Proc. Second Int. Pump Symp., Houston, Texas, 21–32.
[5] Adkins, D. R., and Brennen, C. E., 1988, ‘‘Analyses of hydrodynamic radial forces on centrifugal pump impellers,’’ ASME J. Fluids Eng., **110**, pp. 20–28.
[6] Tsujimoto, Y., Acosta, A. J., and Brennen, C. E., 1988, ‘‘Theoretical study of fluid forces on a centrifugal impeller rotating and whirling in a volute,’’ ASME J. Vib., Acoust., Stress, Reliab. Des., **110**, pp. 263–269.
[7] Tsujimoto, Y., Acosta, A. J., and Yoshida, Y., 1988, ‘‘A theoretical study of fluid forces on a centrifugal impeller rotating and whirling in a vaned diffuser,’’ NASA CP 3026, pp. 307–322.
[8] Ohashi, H., Sakurai, A., and Nishijima, J., 1988, ‘‘Influence of impeller and diffuser geometries on the lateral fluid forces of whirling centrifugal impeller,’’ NASA CP 3026, 285–306.
[9] Bolleter, U., Wyss, A., Welte, I., and Sturcher, R., 1987, ‘‘Measurement of hydrodynamic interaction matrices of boiler feed pump impellers,’’ ASME J. Vib., Acous., Stress, Reliab. Des., **109**, pp. 144–151.
[10] Guinzburg, A., Brennen, C. E., Acosta, A. J., and Caughey, T. K., 1994, ‘‘Experimental results for the rotordynamic characteristics of leakage flows in centrifugal pump,’’ ASME J. Fluids Eng., **116**, pp. 110–115.
[11] Childs, D. W., 1989, ‘‘Fluid structure interaction forces at pump-impeller-shroud surface for Rotordynamic calculations,’’ ASME J. Vib., Acoust., Stress, Reliab. Des., **111**, pp. 216–225.
[12] Thomas, H. J., 1958, ‘‘Instabile Eigenschwingungen von Turbinenlaufern Angefacht durch die Spaltstroemung in Stopfubuchsen und Bechauchflug (Unstable Natural Vibrations of Turbine Rotors Induced by the Clearance Flows in Glands and Blading),’’ Bull. De. L. A. I. M., **71**, pp. 1039–1063.
[13] Alford, J. S., 1985, ‘‘Protecting Turbomachinery from Self-Excited Rotor Whirl,’’ ASME J. Eng. Power, **87**, Oct., pp. 333,334.
[14] Martinez-Sanchez, M., Jaroux, B., Song, S. J., and Yoo, S., 1995, ‘‘Measurement of Turbine Blade-Tip Rotordynamic Excitation Forces,’’ ASME J. Turbomach., **117**, July, pp. 384–393.
[15] Song, S. J., and Martinez-Sanchez, M., 1997, ‘‘Rotordynamic Forces Due to Turbine Tip Leakage-Part I: Blade Scale Effects,’’ ASME J. Turbomach., **119**, Oct., pp. 695–703.
[16] Song, S. J., and Martinez-Sanchez, M., 1997, ‘‘Rotordynamic Forces Due to Turbine Tip Leakage-Part II: Radius Scale Effects and Experimental Verification,’’ ASME J. Turbomach., **119**, Oct., pp. 704–713.
[17] Storace, A. F., Wisler, D. C., Shin, H.-W., Beacher, B. F., Ehrich, F. F., Spakovszky, Z. S., Martinez-Sanchez, M., and Song, S. J., 2000, ‘‘Unsteady flow and whirl-inducing forces in axial-flow compressors. Part I—experiment,’’ Proceedings of ASME Turbo Expo 2000.
[18] Ehrich, F. F., Spakovszky, Z. S., Martinez-Sanchez, M., Song, S. J., Wisler, D. C., Storace, A. F., Shin, H.-W., and Beacher, B. F., 2000, ‘‘Unsteady flow and whirl-inducing forces in axial-flow compressors. Part II—analysis,’’ Proceedings of ASME Turbo Expo 2000.
[19] Bhattacharyya, A., Acosta, A. J., Brennen, C. E., and Caughey, T. K., 1997, ‘‘Rotordynamic Forces in Cavitating Inducers,’’ ASME J. Fluids Eng., **119**, Dec., pp. 768–774.
[20] Ishii, N., Yoshida, Y., Tsujimoto, Y., Ohashi, H., and Kano, F., 1999, ‘‘The Rotordynamic forces on an open-type centrifugal compressor impeller in whirling motion,’’ ASME J. Fluids Eng., **121**, No. 2, pp. 259–266.
[21] Tsujimoto, Y., Imaichi, K., Tomohiro, T., and Gotoo, M., 1986, ‘‘A Two-Dimensional Analysis of Unsteady Torque on Mixed Flow Impellers,’’ ASME J. Fluids Eng., **108**, pp. 26–33.
[22] Chen, G. T., Greitzer, E. M., Tan, C. S., and Marble, F. E., 1991, ‘‘Similarity Analysis of Compressor Tip Clearance Flow Structure,’’ ASME J. Turbomach., **113**, pp. 260–271.

Numerical Simulation of the Dynamic Effects Due to Impeller-Volute Interaction in a Centrifugal Pump

José González
Joaquín Fernández
Eduardo Blanco
Carlos Santolaria

Universidad de Oviedo,
Área de Mecánica de Fluidos,
Campus de Viesques,
33271 Gijón, Asturias, Spain
e-mail: aviados@correo.uniovi.es

This paper shows the capability of a numerical simulation in capturing the dynamic and unsteady flow effects inside a centrifugal pump due to the impeller-volute interaction. The object of the study is a commercial centrifugal water pump with backward curved blades, which is built within a vaneless single tongue volute. For the numerical simulation, the viscous Navier-Stokes equations are handled with an unsteady calculation and the sliding mesh technique is applied to take into account the impeller-volute interaction. In keeping the unsteady terms of the equations active it is possible to correctly simulate the effects of the blade passage in front of the tongue and both the flow and pressure fluctuations induced. Time averaged numerical results are compared with the experimental performance curve and good agreement is found. The numerical flow analysis allows the study of different variables which are always difficult to measure experimentally. The dynamic variables obtained with the proposed numerical model are compared with the experimental data. In particular, the amplitude of the fluctuating pressure field at the blade passing frequency is successfully captured by the model for a wide range of operating flow rates. Therefore, the main achievement of the work is in providing the modeling possibilities for the prediction of the dynamic interaction between the flow at the impeller exit and the volute tongue. Such effects at the blade passing frequency appear to follow a clear flow rate dependent spatial pattern around the volute. [DOI: 10.1115/1.1457452]

Introduction

Flow in centrifugal pumps produces a complex three-dimensional phenomenon involving turbulence, secondary flows, unsteadiness, etc. (Brennen [1]). Moreover, the geometry is complex and asymmetric due to the volute shape. The relative movement between impeller and volute generates an unsteady interaction which affects not only the overall pump performance (flow structure, losses), but is also responsible for pressure fluctuations. Pressure fluctuations interact with the volute casing or even with the circuit and give rise to dynamic effects (mainly unsteady forces) over the mechanical parts (Adkins et al. [2]), which are one of the most important sources of vibration and hydraulic noise (Dong et al. [3]). Both experimental and numerical approaches have been reported and have contributed to the understanding of the highly complex flow interactions that occur in a centrifugal pump.

Some authors (Kaupert et al. [4]) have measured the unsteady pressure field inside the impeller of a centrifugal pump using piezoresistive pressure transducers and a telemetry system. They found amplitudes particularly high at the trailing edge of the blades (pressure side) and relative values up to 35 percent of the pump head at off-design conditions. Another important contribution to the understanding of the relation between unsteady flow and mechanical problems was pinpointed by visualization (Chu et al. [5]). In that paper a PIV technique was used to observe the influence of the blade passing in front of the volute tongue and the unsteadiness generated.

For the present paper, the unsteady pressure fields at the blade passing frequency for different operating conditions were measured by means of fast response piezo-electric transducers. Those transducers, placed on the volute wall, were able to find a spatial pattern as a function of the flow rate at the blade passing frequency.

Although predictions on the unsteady flow field are always valuable, numerical simulation of centrifugal pumps is not easy due to the usual CFD difficulties: turbulence modeling, flow separation, boundary layer, etc. (Lakshminarayana [6]). Besides that, there are also specific problems, as:

—Extremely complex geometry: a great number of cells is needed and, due to skewness, usually unstructured grids give better convergence than structured ones.

—Energy transfer is generated mainly by the centrifugal force in the impeller. A cascade simulation is not valid and these force source terms must be included in the equations of the moving zone.

—The interaction between impeller and volute requires an unsteady solution process to calculate the time dependent terms in the equations. In addition, the blade position with respect to the volute tongue must be taken into account. This can be partially accomplished in a quasi-steady way: calculating the steady solution with different grid positions. Nonetheless, it is always much better if the code is able to perform an unsteady flow calculation at the same time that slides the impeller grid for each time step.

CFD has proven to be a very useful tool in the analysis of the flow inside pumps, both in design and performance prediction. Much research has been carried out in the last years: Croba et al. [7] give an updated list of general selected papers while Denus et al. [8] give a more extended and specific bibliography. However, due to the difficulties of the task, most of these studies have been carried out with strong simplifications of the problem either in the geometry or in the flow characteristics. Research is slowly tending toward more complete simulations (see for example Miner [9]) and the approach developed here follows this trend.

A numerical study of a centrifugal pump is used to capture the effects due to the dynamic interaction between the flow leaving the impeller and the volute tongue. Calculations have been performed with a commercial software package, FLUENT®. This

---

Contributed by the Fluids Engineering Division for publication in the JOURNAL OF FLUIDS ENGINEERING. Manuscript received by the Fluids Engineering Division July 1, 2001; revised manuscript received September 12, 2001. Associate Editor: Y. Tsujimoto.

code uses the finite volume method and the 3D Navier-Stokes equations are solved on an unstructured grid. The unsteady flow is solved using a sliding mesh technique, which has been applied to turbomachinery flows (Croba et al. [7]).

The unsteady pressure fields at the blade passing frequency obtained both experimentally and numerically are compared and a high level of concordance is found for a large range of the operating flow regimes.

Some flow patterns are often difficult to measure directly and cover a wide range of unsteady very important aspects, such as: pressure changes in the volute for different flow rates; incidence at the leading edge of the blades with different flow conditions and secondary flows generated in the volute due to the radial gap change between the impeller and the tongue. An example of these secondary flow patterns is also investigated.

Experimental Results

The unsteady pressure signals recorded and analyzed by a FFT procedure describe the dynamic behavior of the flow inside the volute. In this case, the instantaneous pressure on the volute was measured. First, the experimental routines and measurements chain are described and afterwards a summary of the results is presented in this section.

Pump Facility and Measurements Chain. The pump was tested in a hydraulic setup designed according to the international Standards [10]. In the circuit, water is pumped from and returned to a 100 m^3 reservoir. The flow rate is regulated by a set of butterfly valves located close to the reservoir discharge. The pump is a single axial suction and vaneless volute casing, Worthington EWP-65-200, with seven impeller blades.

The main dimensions of the pump tested and geometric arrangements are presented in Table 1. More details about this pumping facility and test apparatus for static measurements can be found in González [11]. Flow rate uncertainties were found to be always less than 2.5 percent (confidence level of 95 percent). The head and efficiency uncertainties were kept under 3 percent and 4 percent respectively, within the same confidence level. All uncertainty analysis were carried out following the procedures proposed in Kline [12].

On the volute of that pump (shroud side) 36 pressure taps were located (one each 10 deg) in a circumference with $R=107$ mm (see Fig. 1). Four Kistler-601 miniature fast-response piezoelectric pressure transducers were consecutively installed in the 36 possible taps in order to measure the unsteady pressure signals. Each transducer was connected to a charge amplifier, which produced a pressure measurement with an estimated combined uncertainty of less than ±1.5 percent. An optic device provides a triggering signal to start all the measurements in the same impeller position. The resulting pressure signals, as well as the signal from the tachometer could be digitalized and stored in a PC equipped with a multi-channel analog-to-digital conversion card. Afterwards, spectral analysis (FFT, with Hanning window) of the signals were performed. A detailed description of such arrangement was described in Parrondo et al. [13].

Table 1 Main characteristics of the tested pump

$D_2 = 200$ mm	Impeller outlet diameter.
$b_2 = 16.9$ mm	Impeller outlet width.
$R_T = 116.4$ mm	Radial position of the tongue.
$\beta_2 = 29°$	Outlet blade angle.
$\omega = 169.65$ rd/s	Rotational speed.
$Q_N = 0.015$ m^3/s	Nominal flow rate.
$H_N = 12.88$ m	Head at nominal flow rate.
$\omega_S = 0.52$	Specific head.

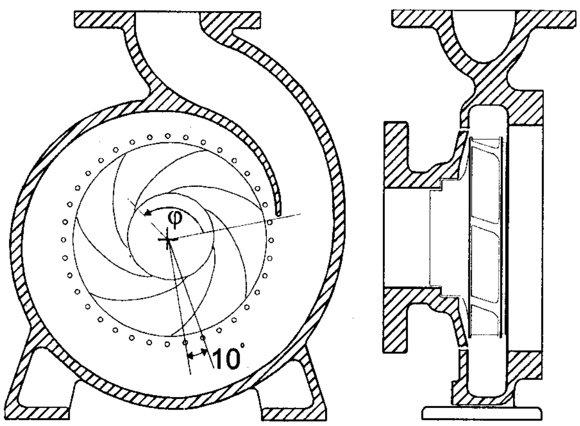

Fig. 1 Pressure taps and angular reference around the volute for unsteady measurements

Results at the Blade Passing Frequency. With the unsteady pressure signals measured as a function of the flow rate, different representations were made in order to draw conclusions. In particular, the study was centered on the fluctuation at the blade passing frequency. With the amplitude and angular phase of that fluctuation, a filtered signal was recovered (real signal filtered at the blade passing frequency). This signal produces a clear spatial pattern for each flow rate. Two representative distributions can be seen in Fig. 2, namely 20 percent of the nominal flow rate and the

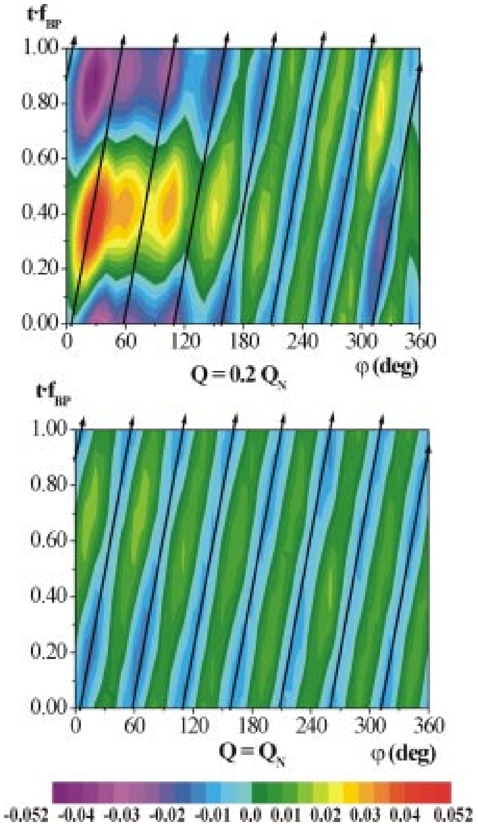

Fig. 2 Flow pattern at the blade passing frequency for two different flow rates (0.2 Q_N and Q_N) as function of the circumferential position (φ)

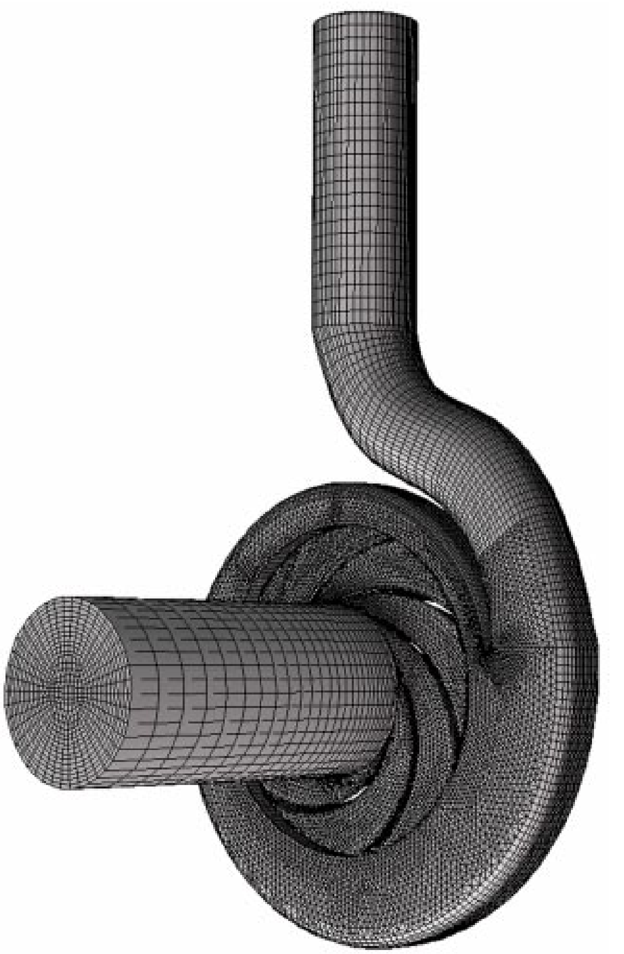

Fig. 3 Sketch of the pump unstructured mesh. (Inlet and outlet pipe portions are added.)

nominal flow rate (Q_N). In this figure, the nondimensional magnitude $p_A/(1/2\rho U_2^2)$ is mapped as a function of the angular position from the volute tongue (φ) and for a time equal to the passage of one blade channel. Bold arrows represent the angular position of the seven blades.

The resulting distributions, shown in Fig. 2 characterize the dynamic behavior of the impeller-tongue interactions for the different flow rates (Parrondo et al. [13]). For the nominal flow rate, a spatial periodic pattern is found for the pressure fluctuations (at any time). On the other hand, for off-design conditions a big disturbance downstream of the tongue location (φ=30 deg) can be seen. Therefore, it can be observed how the tongue has no dynamic effect for flow rates near the nominal one, whereas it affects quite severely the pressure fluctuations for off-design conditions. The relative blade to tongue effect for a blade passing period is also made visible.

Model Description and Computational Method

Geometry and Grid. A geometrical discretization of the centrifugal pump is made for the numeric treatment. Structured hexahedral cells are generated to define the inlet and outlet zones (34883 cells and 44684 cells, respectively) while unstructured tetrahedral cells are used to define the impeller and volute (162974 cells and 89712 cells, respectively). In the volute, a mesh refinement zone is defined near the tongue. Once the geometry is defined, the model is ready to be simulated. A view of the generated grid can be seen in Fig. 3, while a detail of the impeller grid is shown in Fig. 4.

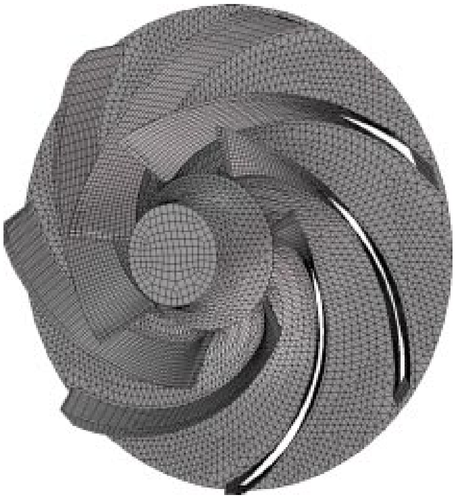

Fig. 4 Detail of the impeller mesh. (Only half of the mesh points are made visible.)

The size of the resulting cells is not enough for a full boundary layer simulation but it gives correct values for the pump performance and allows the analysis the details of the main phenomena involved.

Surfaces between inlet-impeller and impeller-volute define the grid interfaces needed for the relative rotation of the impeller. The sliding mesh technique provided by FLUENT allows that relative motion of the impeller grid with respect to the inlet and the volute during unsteady simulation. Grid faces do not need to be aligned on both sides as an interpolating routine is defined (a discussion about this technique was presented in González [11]).

Mathematical Model. The code solves the fully 3D incompressible Navier-Stokes equations, including the centrifugal force source in the impeller and the unsteady terms.

Turbulence is simulated with the standard k-ϵ model. Although grid size is not adequate to investigate local boundary layer variables, global ones are well captured. For such calculations, wall functions, based on the logarithmic law, have been used. The time dependent term scheme is second order, implicit. The pressure-velocity coupling are calculated through the SIMPLEC algorithm. Second order, upwind discretizations have been used for convection terms and central difference schemes for diffusion terms.

Boundary Conditions. The modeled boundary conditions are the ones considered with more physical meaning for turbomachinery flow simulations, that is, total pressure at the inlet and a variable static pressure proportional to the kinetic energy at the outlet. The flow rate is changed by modifying the static pressure to kinetic energy ratio at the outlet condition, which simulates different closing positions of a valve. Some tests were carried out using a fixed flow rate at the inlet. Although it provides a better stability and faster convergence, this condition was found to be less physically correct, because the pressure fluctuations obtained were quite different to the measured ones. Also, nonslip boundary conditions have been imposed over the impeller blades and walls, the volute casing and the inlet pipe wall.

Total pressure at the inlet and variable static pressure at the outlet conditions allow simultaneous unsteady pressure and velocity fluctuations at the domain boundaries. Again, a constant velocity or pressure boundary condition would not be able to capture both unsteady fluctuations at the same location. The influence of the pump circuit itself has not been included in this simulation. Studies about such interactions have been performed by Longatte et al. [14].

In the two grid interfaces between a stationary and moving mesh, inlet-impeller and impeller-volute, the overlapping faces in the interface zones are determined at each new time step. Fluxes across each grid interface are calculated proportionally to the areas of the superposed faces. The pressure and velocity fluctuations at the interface have been numerically tested and the sliding technique has proven its reliability, keeping the same accuracy levels observed in any other mesh position.

Numerical Solution Control. The code was run in a cluster of six Athlon-K7 (500 MHz) nodes. The time step used in the unsteady calculation has been set to $2.94\cdot 10^{-4}$ seconds in order to get enough time resolution for the dynamic analysis (Courant number was kept below 2, which assures very good time accuracy and numerical stability). The impeller grid movement is related with this time step and the rotational speed imposed ($\omega = 169.65$ rd/s), so a complete revolution is performed each 126 time steps.

The number of iterations has been adjusted to reduce the residual below an acceptable value in each time step. In particular, the ratio between the sum of the residuals and the sum of the fluxes for a given variable in all the cells is reduced to the value of 10^{-5} (five orders of magnitude). Initializing the unsteady calculation with the steady solution, over 5 impeller revolutions are necessary to achieve the periodic unsteady solution convergence.

Intensive grid size dependence tests were carried out with several grid spacing and the overall performance of the pump was the same even with less than a half of the cells finally used for the computations (the variations observed in flow rate, head and efficiency were kept under very reasonable values, 1 percent, 0.5 percent, and 1.2 percent, respectively). Although the static values change in that range, more detailed flow patterns, especially near the walls, could be observed with increasing cell numbers. The numerical accuracy for the pressure fluctuations was estimated to be 0.001 (nondimensional values, that is p_A divided by $1/2\rho U_2^2$).

Flow Study Using the Numerical Model

The possibilities of the numerical simulation in the study of the flow inside a pump are wider than the experimental ones. In particular, results corresponding to the pressure distributions inside the impeller and near-tongue region and the flow in the volute are presented. The latter is very interesting not only for the prediction of the losses during the pressure recovery (diffusion) process for which the volute is designed but also to characterize the secondary flow pattern inside a pump.

Figure 5 shows a three dimensional view of the static pressure (p) over the shroud, blades and part of the volute surface for the nominal flow rate obtained with the numerical simulation. It can be seen that pressure in the hub side is higher than in the shroud, due to the flow turning from the axial to the radial direction. Also the flow impact over the tongue varies from the center, where the flow comes directly from the impeller, to the sides.

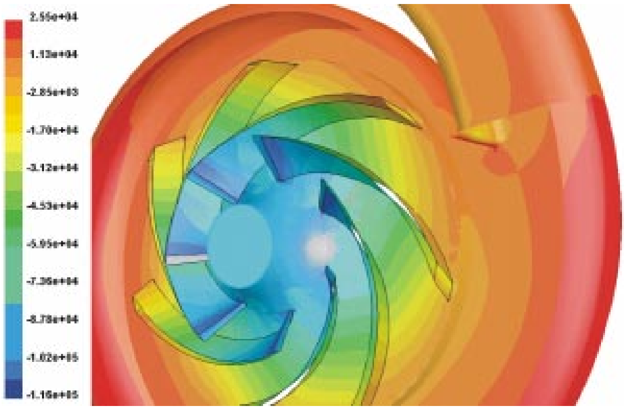

Fig. 5 **Static pressure contours (Pa) at nominal flow rate**

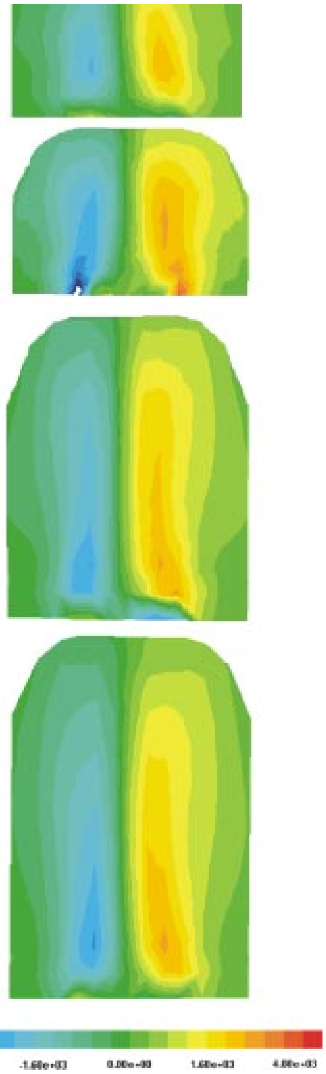

Fig. 6 **Helicity at various angular points around the volute in m/s^2. (From volute tongue, each 90° in the rotating sense.)**

In Fig. 6, the helicity inside the volute at various angular positions around the volute is mapped for a fixed time instant. Helicity is defined by the dot product of the vorticity and the velocity vectors, that is: $(\nabla \times \vec{u})\cdot \vec{u}$. It provides information on the vorticity aligned with the fluid stream. It has been plotted here looking for the secondary flows. The surfaces are radial planes and two counter-rotating vortices are captured. It can be seen that the vortex centers are kept more or less at the same distance from the impeller outlet all around the volute. Only small differences are found at both sides of the center plane (middle surface in the axis direction).

Prior to the unsteady calculations, a comparison for both the numerical and experimental performance curves for the tested pump was executed. The result can be observed in Fig. 7. Both data, experimental and numerical, are obtained after averaging the unsteady values. Concerning the efficiency curves, a direct comparison is not possible. The numerical efficiency is calculated with the torque values corresponding to the rotor inner surfaces, without considering the disk friction losses and mechanical losses at the bearings. On the other hand, the experiments use the shaft torque to calculate the efficiency.

Four different flow rates are compared in Fig. 7, the nominal

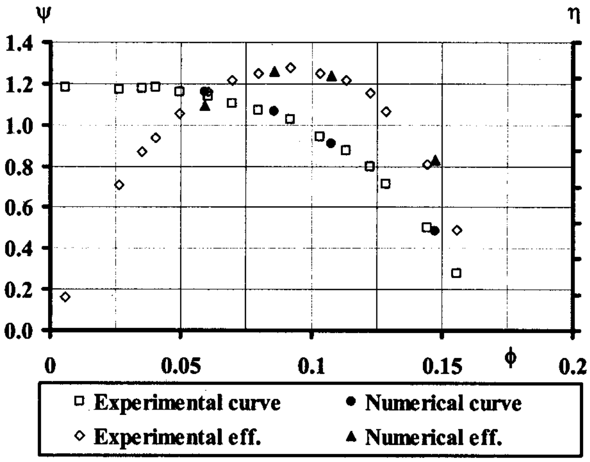

Fig. 7 Comparison of the performance curves. (Nondimensional head and efficiency.)

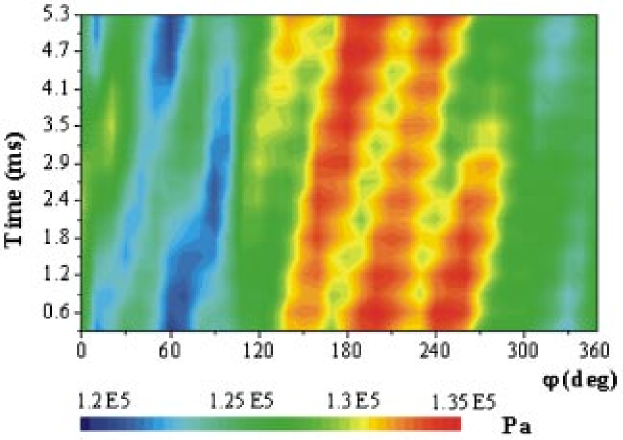

Fig. 9 Unsteady pressure distributions around the impeller. (Numerical results for the nominal flow rate.)

and three off-design ones (two higher and a lower one). The head obtained in these points matches very well with the experimental ones. The efficiency correspondence is also very good, if one considered the unavoidable simplifications that are behind the numerical simulation. More details on the flow structure analysis and static comparison between numerical results and experimental data were already presented in Blanco et al. [15].

Comparison of the Fluctuating Fields

The results of the numerical simulation were recorded for the same locations considered in the experiments. Pressure fluctuations with time are compared in Fig. 8 using both techniques (average value subtracted). This signal corresponds to a circumferential position opposite to the tongue. Agreement between the numerical and experimental data is fairly good, although the numerical result is obtained for a complete revolution of the impeller once the periodic state is achieved and the experimental signal is an instantaneous measurement. These experimental results have not been phase averaged and therefore include random fluctuations.

As an example of the numerical instantaneous results, the static pressure in the intersection between the center plane and a cylinder with $R=107$ mm, for different time steps with nominal flow rate, is shown in Fig. 9. The displacement of the wake at the outlet of the blades is clear in angular positions far from the tongue. Approaching the tongue, the circumferential pressure distortion partly smooths out the wake. This has been generated by taking from each time step the data around the volute some millimeters above the impeller near the frontal case of the volute. If a fixed abscissa (angular position) is selected, the ordinate represents the pressure change in time; if a fixed ordinate (time instant) is chosen, the abscissa shows the pressure around the volute at that instant. The time range represented is only a blade passage. In this figure it can be observed how the wakes advance around the volute. In such representation, the wave generated by the blades (shown in Fig. 2) is superimposed to the average pressure distribution around the volute. At the angular positions opposite to the tongue (φ around 180 deg), the blade passage in front of the tongue has little effect, while near the tongue, the blade wave is more or less smoothed depending on the blade position with respect to the tongue. This tendency depends strongly on the considered flow rate (Fig. 9 corresponds to nominal conditions and the pressure fluctuations are kept below 5 percent of the average value of the static pressure for this flow rate).

Pressure Fluctuations Inside the Volute. Pressure at different flow rates is obtained numerically in the 36 points at $R=107$ mm, on the shroud wall of the volute, corresponding to the same locations for which experimental data was available. After recording the pressure at that points, FFT was performed and relevant amplitudes and phases were obtained for the different frequencies and particularly for the blade passing frequency. The

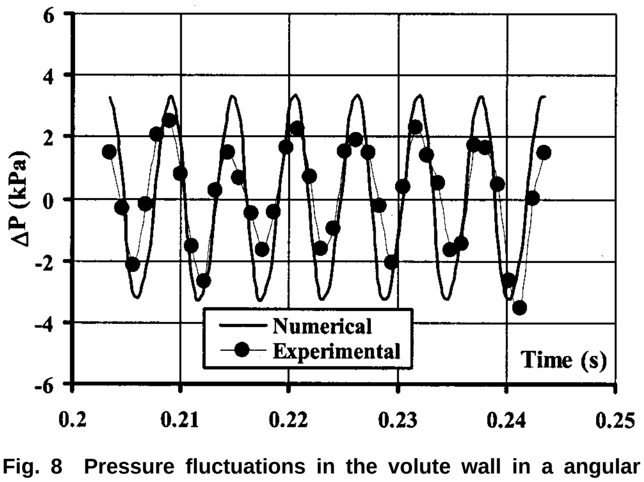

Fig. 8 Pressure fluctuations in the volute wall in a angular position opposite to the tongue at a radius R=107 mm

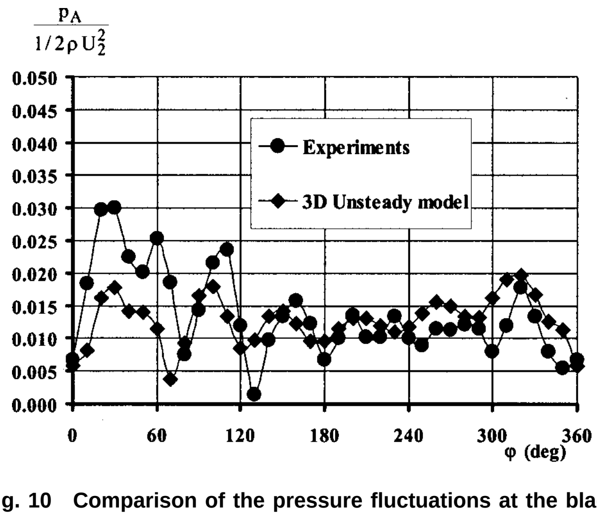

Fig. 10 Comparison of the pressure fluctuations at the blade passing frequency for $Q=0.5\ Q_N$. Tongue at $\varphi=0$ deg.

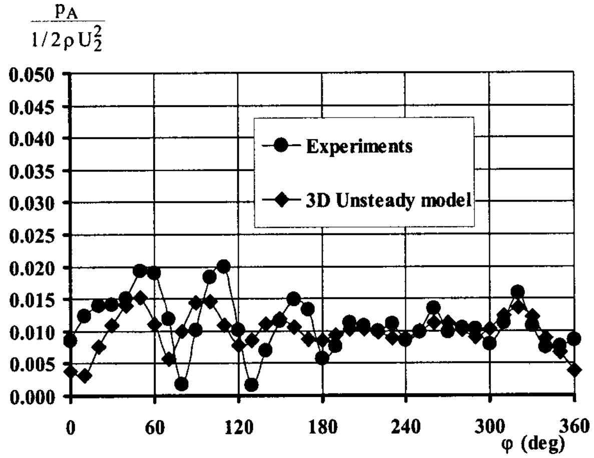

Fig. 11 Comparison of the pressure fluctuations at the blade passing frequency for $Q=0.7\ Q_N$. Tongue at $\varphi=0$ deg.

resulting pressure fluctuations at that frequency were properly nondimensionalized (using the dynamic head of the tangential outlet velocity: $1/2\rho U_2^2$). And therefore, a comparison between numerical and experimental results at the blade passing frequency is possible. As examples, Figs. 10–14 show that comparisons in function of the angular position for the flow rates corresponding to 0.5 Q_N, 0.7 Q_N, Q_N, 1.3 Q_N, and 1.5 Q_N. For these figures, the origin reference for the angles (φ) is placed in the tongue angular position (as shown in Fig. 1).

As it can be observed, the agreement for nominal and higher flow rates (Figs. 12–14) is really good and the spatial amplitudes pattern is well captured by the numerical model. The quadratic mean difference divided by the mean value of the fluctuations is around 20 percent (this is a very good result when compared with the average static pressure, which is around 100 times higher). For low flow rates (Figs. 10 and 11) more differences are found in the comparison, especially in the near tongue region (φ between 10 and 100 deg). This effect means a limit for the numerical approach in the prediction of the dynamic impeller-volute dynamic interaction, giving always lower amplitudes than the measured ones. There is also some discrepancy for high flow rates and positions opposite to the tongue. Both effect could be possibly due to the pump-piping circuit interaction, which is not considered in the simulation.

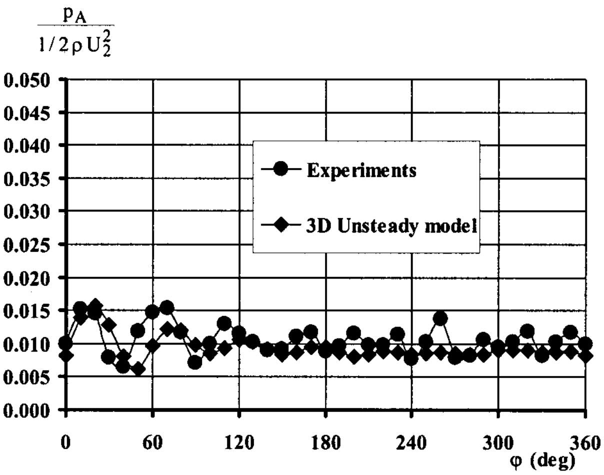

Fig. 12 Comparison of the pressure fluctuations at the blade passing frequency for $Q=Q_N$. Tongue at $\varphi=0$ deg.

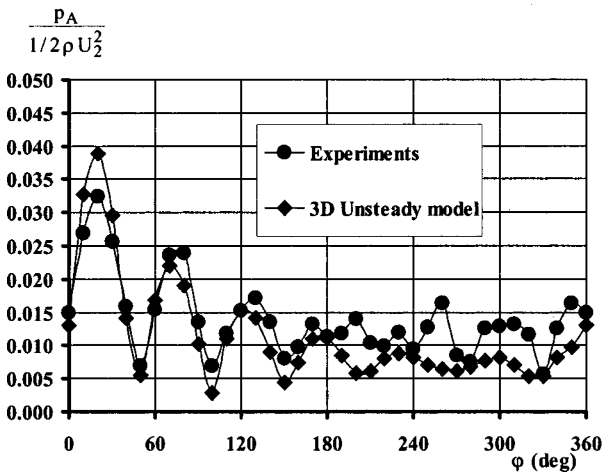

Fig. 13 Comparison of the pressure fluctuations at the blade passing frequency for $Q=1.3\ Q_N$. Tongue at $\varphi=0$ deg.

Some differences have arisen in the comparison between the numerical and experimental pressure fluctuations in the volute of the tested centrifugal pump at the blade passing frequency, especially in the near tongue region for low flow rates. Nevertheless, and generally speaking, it is clear (Figs. 10–14) that the numerical model developed would have been able to predict the main characteristics of the dynamic impeller-volute interactions for a wide flow rate range. On the other hand, those differences are not seen in the performance curve prediction (Fig. 7).

Resulting Forces. The fluctuating pressure field gives rise to dynamic forces which can cause fatigue failure of the pump axis (especially at off-design operating conditions). Once the pressure predictions have been proven to be quite accurate, the numerical model developed has shown its worth and can be used to calculate these forces. An example of such calculation can be seen in Fig. 15 where both magnitude and phase (relative to the horizontal direction) of the total force are plotted against time for a flow rate 130 percent of the nominal one. From this total force, the fluctuating terms can be obtained by subtracting the average value for a blade passing period. In Fig. 16, a polar representation is chosen for these terms, where the modulus and phase of the fluctuating force (with respect to the horizontal direction) can be obtained.

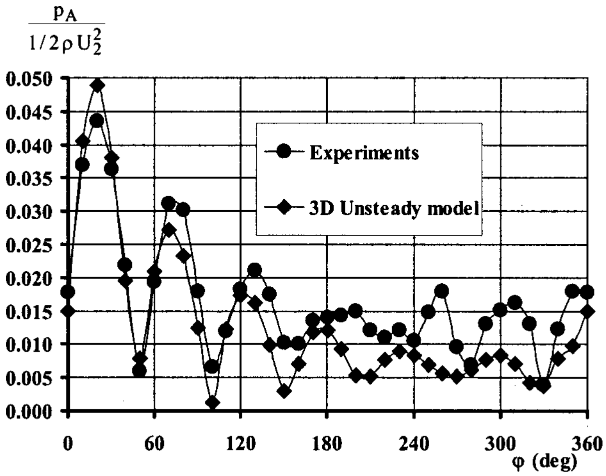

Fig. 14 Comparison of the pressure fluctuations at the blade passing frequency for $Q=1.5Q_N$. Tongue at $\varphi=0$ deg.

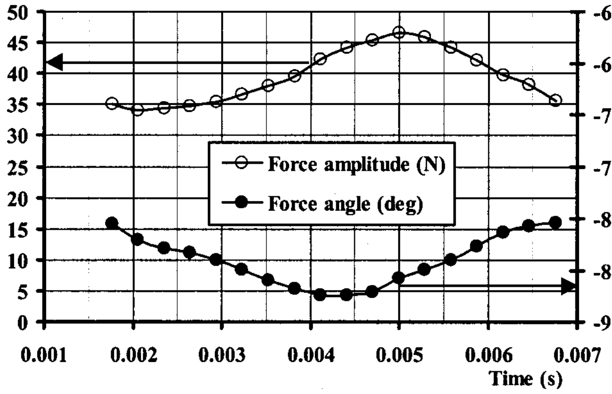

Fig. 15 Numerical calculation of the total force on the impeller for a blade passing period and $Q=1.3\ Q_N$.

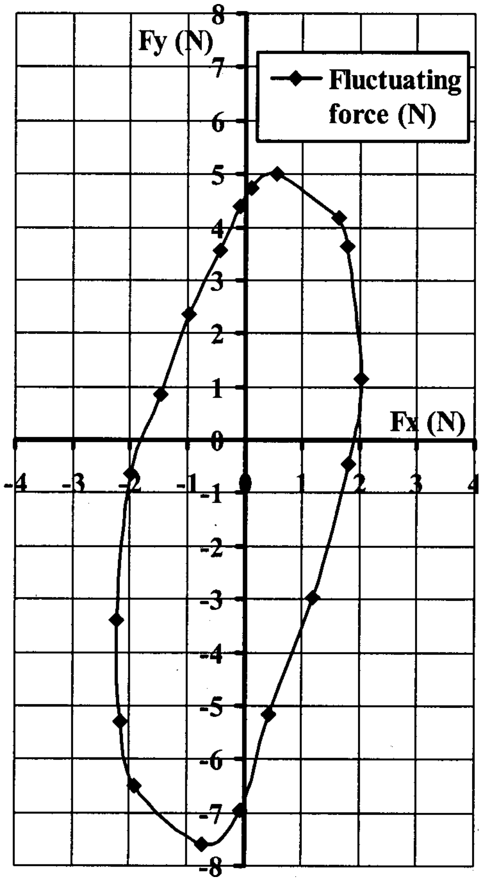

Fig. 16 Polar representation of the fluctuating force (numerical result), $Q=1.3\ Q_N$. Force at the blade passing frequency.

Conclusions

The impeller-volute interaction in a centrifugal pump is successfully predicted by a numerical model developed using a finite volume commercial code. Both experiments and numerical prediction show the presence of a spatial fluctuation pattern at the blade passing frequency as function of the flow rate. That frequency is predominant in what refers to the dynamic effects inside the pump and conditions the possible limitations in what refers to the use of the dynamic data for design purposes. Unsteady forces have been calculated using the numerical results.

Considering the model results obtained, secondary flow pattern in the volute was numerically analyzed through the helicity magnitude, showing that the stronger effects of such secondary flow are concentrated in radial positions close to the impeller exit.

The pressure fluctuations at the blade passing frequency reveal the blade tongue interaction with the flow at the impeller outlet plane. Such interaction clearly increases the fluctuation levels for off-design conditions, which produces other effects already studied in the bibliography (limiting operation ranges, increase of losses, etc.).

The unsteady calculation combined with the sliding mesh technique has proven to be a useful tool to investigate the flow field inside a centrifugal pump including the dynamic effects. Altogether, the main goal was to gain a deeper knowledge of the flow dynamic variables inside a centrifugal pump (pressure and forces), which could be used in a design process. This has been achieved.

Acknowledgments

The authors gratefully acknowledge the financial support of the Comisión Interministerial de Ciencia y Tecnología (CICYT) under Projects TAP99-0738-C02-02, entitled “Sistema de monitorización en tiempo real por control remoto para caracterización de la firma vibratoria de maquinaria industrial” and 1FD97-TAP1204-C02-01 entitled “Desarrollo de un prototipo de cuba de estaño para la fabricación de vidrio.”

Nomenclature

b_2 = impeller width at outlet
D_2 = impeller diameter at outlet
f_{BP} = blade passing frequency
H, H_N = pump head and pump head at best efficiency point (nominal)
p, p_A = pressure, pressure amplitude at the blade passing frequency
Q, Q_N = flow rate and flow rate at nominal point
R = radial coordinate
$\vec{u}$ = flow velocity
U_2 = peripheral velocity at impeller outlet
β_2 = impeller blade angle (outlet section)
ϕ = flow coefficient $\phi=Q/(\pi D_2 b_2 U_2)$
ρ = density of the fluid (water in this paper)
φ = angular position around impeller
ω, ω_S = rotating speed, specific speed $\omega_S=\omega Q_N^{1/2}/(gH_N)^{3/4}$
ψ = head coefficient $\psi=gH/(U_2^2/2)$

References

[1] Brennen, C. E., 1994, *Hydrodynamics of Pumps*, Oxford University Press and CETI Inc.
[2] Adkins, D. R., and Brennen, C. E., 1988, “Analysis of Hydrodynamic Radial Forces on Centrifugal Pump Impellers,” ASME J. Fluids Eng., **110**, pp. 20–28.
[3] Dong, R., Chu, S., and Katz, J., 1997, “Effect of Modification to Tongue and Impeller Geometry on Unsteady Flow, Pressure Fluctuations and Noise in a Centrifugal Pump,” ASME J. Turbomach., **119**, pp. 506–515.
[4] Kaupert, K. A., and Staubli, T., 1999, “The Unsteady Pressure Field in a High Specific Speed Centrifugal Pump Impeller. Part I: Influence of the Volute,” ASME J. Fluids Eng., **121**, pp. 621–626.
[5] Chu, S., Dong, R., and Katz, J., 1995, “Relationship Between Unsteady Flow, Pressure Fluctuations, and Noise in a Centrifugal Pump-Part B: Effects of Blade-Tongue Interactions,” ASME J. Fluids Eng., **117**, pp. 30–35.
[6] Lakshminarayana, B., 1991, “An Assessment of Computational Fluid Dynamic Techniques in the Analysis and Design of Turbomachinery-The 1990 Freeman Scholar Lecture,” ASME J. Fluids Eng., **113**, pp. 315–352.
[7] Croba, D., and Kueny, J. L., 1996, “Numerical Calculation of 2D, Unsteady Flow in Centrifugal Pumps: Impeller and Volute Interaction,” Int. J. Numer. Methods Fluids, **22**, pp. 467–481.
[8] Denus, C. K., and Göde, E., 1999 “A Study in Design and CFD Analysis of a Mixed-Flow Pump Impeller,” ASME-FEDSM-99-6858.
[9] Miner, S. M., 2000, “Evaluation of Blade Passage Analysis Using Coarse Grids,” ASME J. Fluids Eng., **122**, pp. 345–348.
[10] British Standard BS-5316 Part-2, 1977, “Acceptance Tests for Centrifugal, Mixed Flow and Axial Pumps.”
[11] González, J., 2000, *“Modelización Numérica del Flujo no Estacionario en*

Bombas Centrífugas. Efectos Dinámicos de la Interacción entre Rodete y Voluta,'' Ph.D. thesis (in Spanish), Universidad de Oviedo, Spain.

[12] Kline, S. J., 1985, ''The Purposes of Uncertainty Analysis,'' ASME J. Fluids Eng., **107**, pp. 153–160.

[13] Parrondo, J. L., Fernández, J., González, J., and Fernández, L., 2000, ''An Experimental Study on the Unsteady Pressure Distribution Around the Impeller Outlet of a Centrifugal Pump,'' ASME-FEDSM-00-11302.

[14] Longatte, F., and Kueny, J. L., 1999, ''Analysis of Rotor-Stator-Circuit Interactions in a Centrifugal Pump,'' ASME-FEDSM-99-6866.

[15] Blanco, E., Fernández, J., González, J., and Santolaria, C., 2000, ''Numerical Flow Simulation in a Centrifugal Pump with Impeller-Volute Interaction,'' ASME-FEDSM-00-11297.

Rotating Cavitation in a Centrifugal Pump Impeller of Low Specific Speed

Jens Friedrichs
Günter Kosyna
Pfleiderer-Institut für Strömungsmaschinen,
TU Braunschweig,
Braunschweig, Germany

The paper describes an experimental investigation of two similar centrifugal pump impellers of low specific speed. Both impellers show rotating cavitation over a wide range of part load operating points. The occurrence of this phenomenon produces a characteristic shape of creeping head-drop compared to the more usual sudden head-drop at "normal" operation points. The onset of rotating cavitation can be assigned to a certain value of the parameter $\sigma/2\alpha$ meaning the cavity volume in relation to the incidence angle. Optical analysis by video and high-speed camera techniques illustrates the development of this instability mechanism which is mainly driven by an interaction of the cavity closure region and the following blade. Combining these observations and the results of a fourier-transformation the characteristic propagation frequencies of rotating cavitation can be presented for one impeller. [DOI: 10.1115/1.1457451]

Introduction

Cavitation and its related effects are still playing a major rule in design and use of centrifugal pumps. Due to the wide acceptance of the $\mathrm{NPSH}_{3\%}$-criterion for industrial use, the mechanisms of cavitation leading to changes in pump delivery head are of special interest. The character of the head-drop-curves represented by the typical shapes of ''sudden'' head-drop (sometimes with initial head-rise) and ''creeping'' head-drop determines the $\mathrm{NPSH}_{3\%}$-figures and have extensive effects in pump applications. At the Pfleiderer-Institute, Technical University of Braunschweig, several projects have been carried out in this field in the past [1–3]. One new effect of particular interest influencing the head-drop curves is the so-called ''rotating cavitation'' in a centrifugal pump impeller of low specific speed.

Most of the information about rotating or alternating cavitation in the available literature is concerned with this phenomenon occurring in inducers of turbopumps of the H-II and also the ARIANE-V rocket. In 1997 Tsujimoto et al. [4] observed several different modes of rotating cavitation in the mentioned turbopump-inducer. Theoretical analyses were performed by Tsujimoto et al. [5] and Greitzer [6]. Both authors described the mass-flow-gain factor M (increasing cavity volume related to decreasing flow rate) as an important stability parameter. A positive factor M can cause cavitation surge in the pumping system itself or rotating cavitation as an instability phenomenon limited to the impeller.

In another theoretical stability analysis for a cascade, Watanabe et al. [7] demonstrated in 1999 that rotating cavitation basically depends on the ratio of cavitation number to twice the incidence angle ($\sigma/2\alpha$). Huang et al. [8] presented in 1998 an experimental investigation of an inducer with alternating cavitation, including typical head-drop-curves. In 2000 Horiguchi et al. [9] investigated in another cascade analysis the influence of the cascade parameters (solidity and stagger angle) on the onset and development of rotating cavitation. The authors also explained the mechanism of the phenomenon to be caused by an interaction of the local flow near the cavity closure region and the leading edge of the following blade.

Pump Design and Test Facility

At the Pfleiderer-Institute the effect of rotating cavitation was observed in two similar single-stage centrifugal pump impellers. Both impellers were tested in a closed-circuit system with variable system pressure. In order to generate a uniform circumferential pressure distribution at the impeller outlet, a vaneless radial diffuser was used instead of a volute. The diffuser itself was connected to the upstream system by twelve 2.5″ discharge pipes. Figure 1 shows a cross-sectional view of the pump. The impeller shroud and also the shroud-sided casing was made of plexiglas to enable direct observations of the impeller. In Table 1 the design parameters of both impellers are presented. The main differences between both designs is the blade shape. Impeller 1 has blades consisting of one circular arc meaning constant curvature between inlet and outlet. Impeller 2 has blades of two different circular arcs, a smaller one from inlet to nearly half of the chord and a larger one up to the outlet. This impeller-geometry was used to produce at least approximately a 2D flow field on one hand and to ensure a good accessibility for the measurement technique on the other hand.

Pressure Measurements. One blade of each impeller can be fitted with piezo-resistive miniature pressure transducers at different positions along the camber line of the middle span between hub and shroud. These transducers can be used to measure the static pressure on the surface of either the blade suction or the blade pressure side (see [2]). The unsteady pressure signals of eight transducers are transmitted simultaneously using a telemetry system, which allows one to analyze frequencies up to 2.5 kHz. For the detection of rotating effects relative to the impeller four additional transducers were mounted in the impeller hub near the middle of the passage (see Fig. 2).

Optical Measurements. To perform visual analysis of rotating cavitation a digital video camera (CCD-chip) operating in frame integrating mode was used together with a frame-grabber device and a stroboscopic light source. Due to the limited sampling rate, an additional high speed camera with a sampling rate up to 40,000 frames per second was used to record sequences of rotating cavitation. These sequences allowed us to analyze the development of single unsteady cavities during one or more revolutions.

Contributed by the Fluids Engineering Division for publication in the JOURNAL OF FLUIDS ENGINEERING. Manuscript received by the Fluids Engineering Division August 2, 2001; revised manuscript received October 17, 2001. Associate Editor: J. Katz.

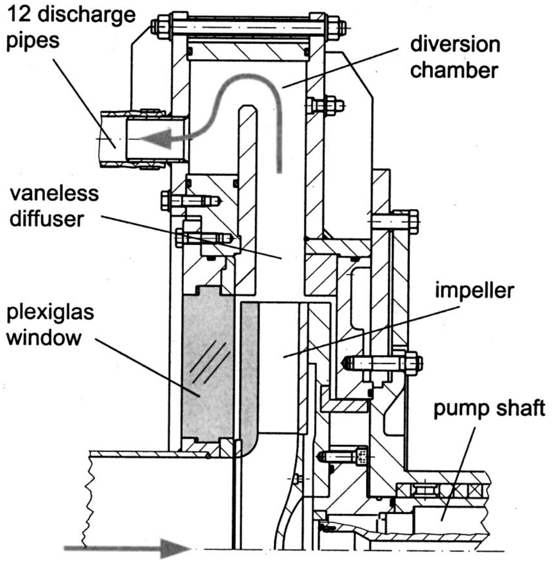

Fig. 1 Cross-sectional view of the test pump

Results and Discussion

Rotating cavitation was observed in both impellers at part load conditions. In impeller 1 the effect occurred at a flow coefficient of about 55% part load and below. In impeller 2 the phenomenon starts at 66% part load. In both impellers the development and characteristic of rotating cavitation was nearly identical. The investigations were mainly carried out at both impellers, but in the following they will be analyzed for impeller 2. Due to the geometric similarities, the physical mechanisms of rotating cavitation derived from impeller 2 should be valid also for impeller 1.

Table 1 Design parameters of both impellers

Impeller		1	2
Blade shape		1-circular-arc	2-circular-arc
Inlet-∅	d_1	260mm	260mm
Outlet-∅	d_2	648mm	556mm
Blade inlet angle	β_1	17°	19°
Blade outlet angle	β_2	20°	23°
Passage width	b	46mm	46mm
Number of blades	z	5	5
Specific speed	n_s	27	27.5
Rotating speed	n	9Hz	9Hz

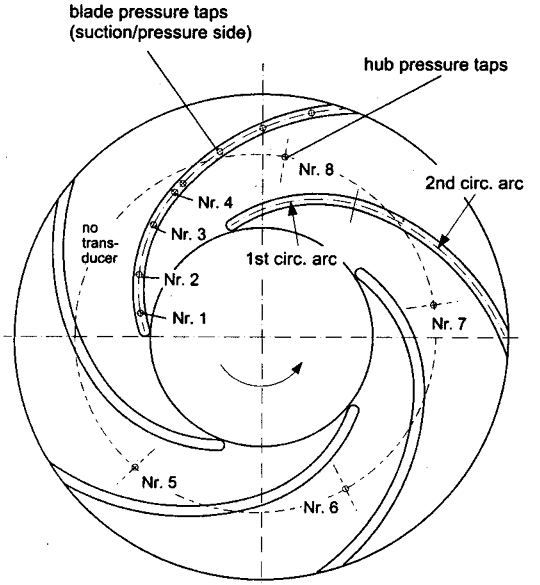

Fig. 2 Plane view of impeller 2

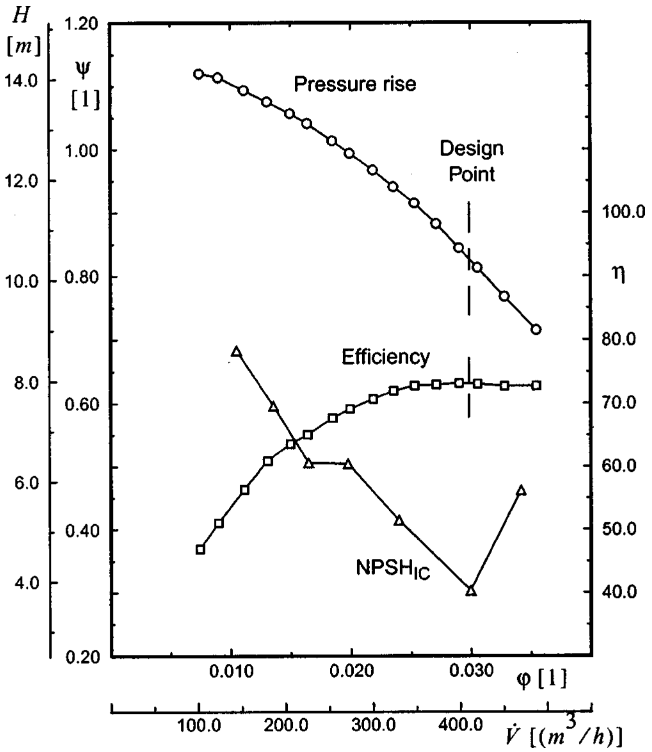

Fig. 3 Impeller 2 characteristic and incipient cavitation

Overall Performance and Head-Drop-Curves. Figure 3 shows the pump performance characteristic of impeller 2 and in addition the NPSH-figures for incipient cavitation (IC) The design point of 412 m^3/h ($\varphi = 0.03$) matches the efficiency characteristic and the NPSH$_{IC}$-curve. At flow coefficients lower than design point, incipient cavitation occurs on suction side, above the design point on pressure side of the blade. At the design point flow coefficient itself cavitation starts nearly simultaneously on both sides of the blade.

The head-drop-curves for the impeller are presented in Fig. 4. At the design flow coefficient and higher flow rates the head-drop-curves show a sudden drop as it would be expected for pumps of low specific speed. For a flow rate of 80% part load a significant pressure rise can be seen before the following sudden-head-drop occurs. This small increase in performance is also a known effect. It can be explained by an additional lift to the blade due to an attached cavity [3]. The video analysis for this operating point confirms that the cavity is still attached to the suction side of the blade.

In the head-drop-curves of 66% part load and lower flow rates the filled symbols indicate the occurrence of rotating cavitation, observed using the stroboscopic light source. Those parts of the curves which are assigned to rotating cavitation show a significant creeping head-drop, beginning just at the point where rotating cavitation occurs. A remarkable fact is, that the phenomenon disappears in the 66% and 55% curve at lower cavitation numbers ($\sigma = 0.3...0.4$). The pressure rise coefficient seems to recover a little just after rotating cavitation has disappeared to show a more classical sudden head-drop, when the cavitation number decreases further.

The observed behavior of creeping head-drop is also well known, mostly for impellers of medium or higher specific speed; although normally no rotating cavitation was reported for those

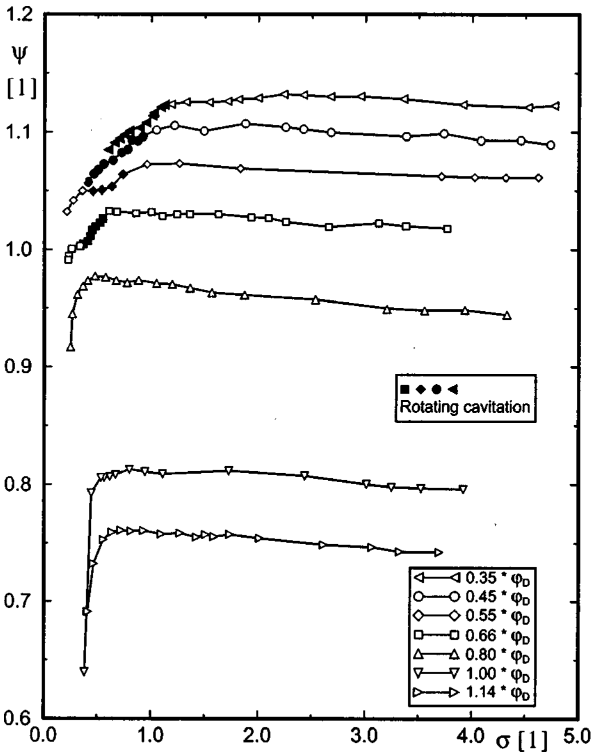

Fig. 4 Head-drop-curves of impeller 2

Table 2 Onset of rotating cavitation described by $\sigma/2\alpha$

Flow rate	$\sigma_{\mathrm{I,Rot}}$	α	$\sigma_{\mathrm{I,Rot}}/2\alpha$
$0.35^{*}\varphi_D$	1.13	14.0°	2.31
$0.45^{*}\varphi_D$	0.94	11.5°	2.34
$0.55^{*}\varphi_D$	0.78	9.5°	2.35
$0.66^{*}\varphi_D$	0.53	6.5°	2.34
$0.80^{*}\varphi_D$	(0.33)	4.0°	(2.33)

machines. Huang et al. [8] presented head-drop-curves of an inducer showing a very similar behavior of creeping head-drop for operating points with occurrence of cavitation oscillation.

Another important result of Fig. 4 is the position of onset of rotating cavitation. Decreasing the flow rate, the cavitation number of beginning rotating cavitation ($\sigma_{\mathrm{I,Rot}}$) increases.

In Table 2 the parameter $\sigma/2\alpha$ for onset of rotating cavitation is shown. The incidence angle α was calculated using a constant meridional velocity without swirl as the inlet condition. The parameter $\sigma/2\alpha$ for the beginning of rotating cavitation is nearly constant for all flow rates. With this result, the phenomenon can be understood as an impeller stability problem, which is driven by the increasing cavity volume (or cavity length) in relation to the incidence angle, according to [5] and [6]. The last row of Table 2 contains the cavitation number for the onset of rotating cavitation at a flow rate of 80% if the parameter $\sigma/2\alpha$ is assumed to 2.33.

At the resulting cavitation number $\sigma_{\mathrm{I,Rot}}=0.33$ the head-drop curve is already within the region of sudden drop, meaning the cavities are highly unsteady and no longer attached to the blade surface. The low cavitation number and the unstable state of the head-drop-curve is probably the reason why no rotating cavitation occurs at this flow rate.

At the Technical University of Darmstadt a scaled model of impeller 2 has been tested at the same Reynolds-number. This impeller shows the same behavior as impeller 2 including the shape of the head-drop-curves and the onset of rotating cavitation. The values of $\sigma/2\alpha$ calculated for onset of rotating cavitation are in a range of 2.50–2.80 for the model-impeller.

Video and High-Speed-Film Analysis. In Fig. 5 different snapshots from a CCD-camera are presented. They were taken during rotating cavitation at a flow coefficient of 45% ($\varphi=0.0136$). The order of the frames is not a time-resolving sequence due to the average sampling rate of 7 Hz. Thus the frames allow one to analyze different states of one blade in rotating cavitation but not their time-dependent development. In comparison, Fig. 6 shows the quasi-steady state of the same flow coefficient just before rotating cavitation starts ($\sigma=1.0...1.1$). In Fig. 5 frame 1 and 2 show an attached cavity with a length similar to Fig. 6 but a very small thickness. Frame 4 shows an even smaller cavity and, similar to frame 2, the phase limit of the cavity according to the blade ahead reaches into the passage. In frames 3, 5, and 6 the

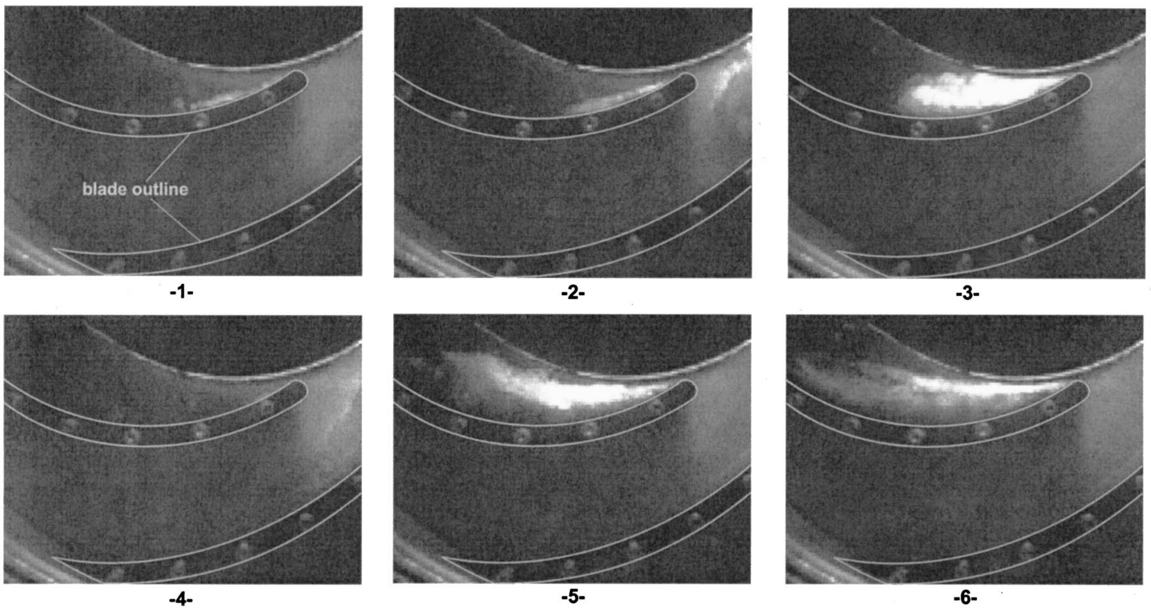

-1- -2- -3-

-4- -5- -6-

Fig. 5 Snapshot of rotating cavitation at 45 percent part load ($\varphi=0.0136$)

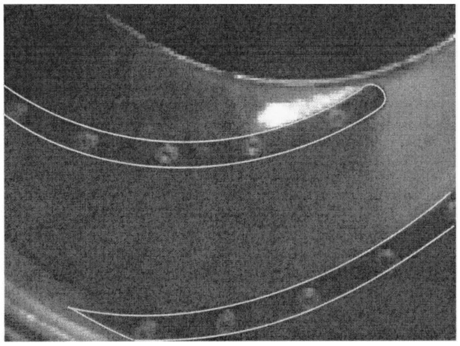

Fig. 6 Quasi-steady state at 45 percent part load

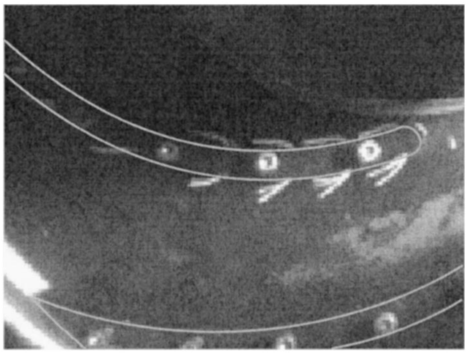

Fig. 8 Quasi-steady state at 45 percent part load

cavities have an extreme thickness and length (in frame 6 more than half the blade length); in 3 the cavity starts to separate, in 5 and 6 it is completely separated.

The same operating point is presented in the snapshots of Fig. 7. The blade is fitted with an array of fiber-probes (3 probes along blade width) to indicate the local flow direction. Due to their negligible inertia and the low significant frequencies of rotating cavitation (see Fig. 10), the probes can be used to get information about the flow direction even in unsteady states. Figure 8 again shows the quasi-steady state before rotating cavitation occurs. (Due to a slightly different angle of view and of light, the cavity seems less bright compared to Fig. 5.)

The state in frame 3 and 6 is similar to the one in frame 5 and 6 of Fig. 5. The suction-side probes also indicate the separation of the cavity. In comparison, the pressure-side probes are orientated at a small angle to the blade, in frame 6 even smaller than in Fig. 8. In frames 1 and 4 the cavity is small and thin; the suction-side probes are attached to the blade while the pressure-side probes are clearly separated. A similar small cavity can be seen in frames 2 and 5 but this time the probes indicate even backflow in the pressure-side passage.

From analysis of Fig. 5 and Fig. 7 two different significant states of rotating cavitation can be described:

(i) A small and very thin cavity on suction side is observed together with a large cavity of the blade ahead, which reaches into the passage. In this passage the flow is dominated by backward orientated components.

(ii) A large cavity on suction side according to an increased local incidence angle means forward flow in the pressure-side passage, probably even with a higher flow rate compared to steady state.

For further analysis in Fig. 9 a sequence of sketches derived from high-speed-film is presented for a flow rate $\varphi = 0.0165$. These sketches are a real time-resolving sequence showing the same blades at each revolution.

At the first revolution blade 1 shows separated cloud cavitation and the following blade 2 a very small attached cavity. One revolution later the cavity of blade 1 is large but attached, while at blade 2 strong cloud cavitation occurs. The next two revolutions (3 and 4) the cavity of blade 1 shrinks and at revolution 5 and 6 the blade shows a small cavity, while the cloud cavitation of blade 2 has developed into an attached cavity. In the following this cavity becomes still smaller (rev. 7 and 8) and a new cloud cavitation develops at blade 1. At revolution 9 a state somewhere between rev. 1 and 2 is reached again.

According to the analysis of Horiguchi et al. [9] and with respect to Fig. 5 and Fig. 7 the mechanism can be explained as follows: A large separated cavity (with cloud cavitation) means

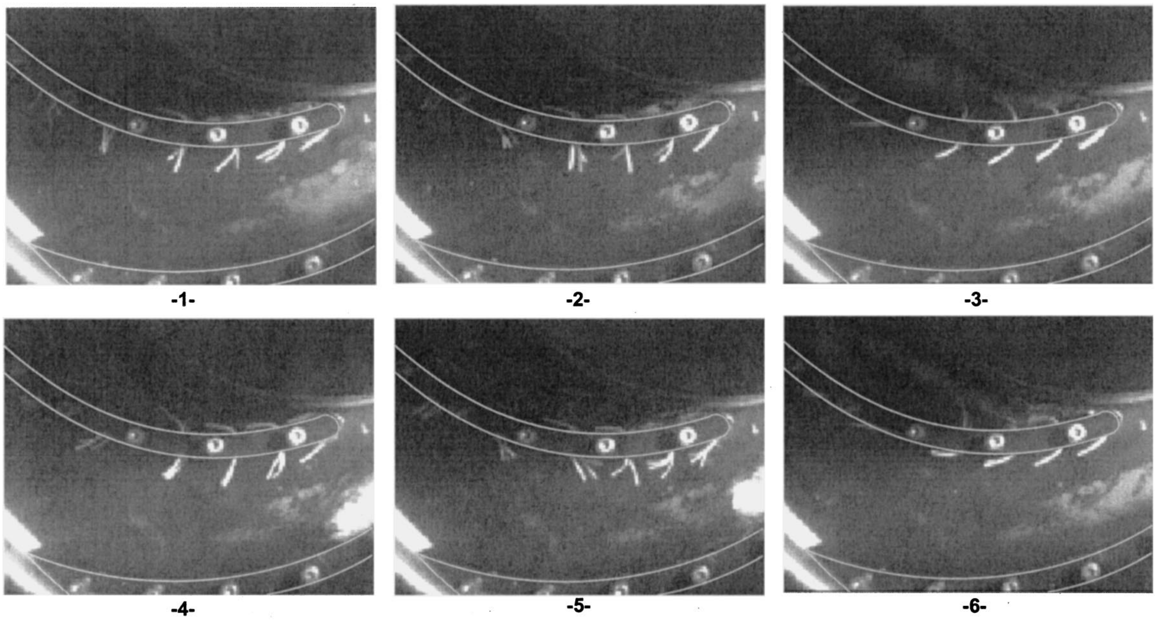

Fig. 7 Snapshots of rotating cavitation at 45 percent part load ($\varphi = 0.0136$), fiber-probe fitted blade

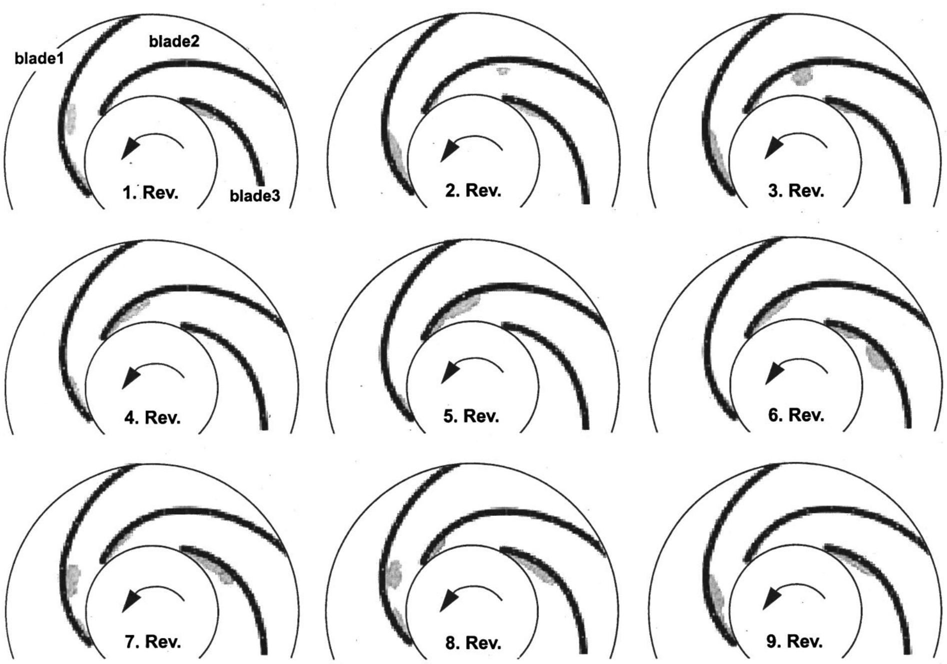

Fig. 9 Sketches of rotating cavitation from high-speed film, $\varphi=0.0165$

blockage for the suction-side passage. Therefore the flow rate in the following passage increases leading to a decrease in the local incidence angle. In addition, the closure region of the larger cavity of the first blade generates a velocity component with direction onto the blade surface which also decreases the incidence angle of the following blade. Thus the following blade shows a very small cavity. If the cavity of the first blade becomes smaller, both effects, namely the blockage and the induced velocity, decreases meaning a rapid increase in the incidence angle of the following blade.

The interaction of the cavity of the first blade and the following blade becomes even stronger if either the cavity becomes larger or the separation angle between cavity and blade increases, both effects leading to an approach of the cavity toward the pressure side of the following blade. This observation matches Table 2, meaning that for an increased incidence angle α of the steady flow the cavitation number σ can be higher to produce the same risk of rotating cavitation.

In developed rotating cavitation two adjacent passages are operating at different points of the impeller characteristic. The blocked passage operates at a point with a lower flow coefficient and the following, unblocked passage at a higher flow coefficient compared to the one according to the current pump operating point [8]. Consequently, the lower flow coefficient means a stronger pressure rise in the passage and the higher flow coefficient means a weaker pressure rise based on the current pump pressure rise (see Fig. 3). The stronger pressure gradient suppresses the development of cloud cavitation further into the passage while the depression of the static pressure rise in the next passage allows the clouds to be carried forward in it.

Once the incidence angle of the second passage has risen and cloud cavitation has developed, these clouds produce increasing blockage in this passage, lowering the flow rate, while the suppressing effect of the pressure gradient in the first passage is leading to an increasing flow rate.

Frequency Analysis. The fast-fourier-transformation of the unsteady pressure signals taken at blade suction side and impeller hub is presented in Fig. 10. For the transducer-position, see Fig. 2. The left side shows the FFT at an operating point just before rotating cavitation occurs, the right side at fully developed rotating cavitation. In the first state (left side) the dominating peak on blade suction side an impeller hub is the impeller rotating frequency of 9Hz. In addition, on blade suction side several frequencies can be seen resulting from the unsteady cavity collapse. As expected, the amplitude of these frequencies depends on the position of each transducer at the blade.

In developed rotating cavitation (right side) more dominating peaks can be found, all of them below 9Hz. They are in very good agreement at blade suction side and impeller hub and they are each shown by all transducers. These new significant peaks have to be assigned to the effect of rotating cavitation, further analysis shows that all of them disappear if rotating cavitation disappears (see Fig. 4, $\varphi=66\%$ and 55%). The frequency of these peaks depends on the flow rate and the state of rotating cavitation. An assignment of the observed frequencies to the mechanisms of rotating cavitation has to take the following aspects into account:

(i) Rotating cavitation propagates against the direction of the impeller (backward in the impeller-relative system); the propagation frequency in the impeller system is low compared to the impeller frequency of 9Hz, see Fig. 9.
(ii) Superimposed with the pure propagation is the frequency of cloud cavitation (Fig. 9); this frequency must be significantly higher than the propagation rate.
(iii) The observation shows that there are two similar cells of rotating cavitation within the impeller; this can also be estimated from Fig. 9. A rotating cycle seen by one blade can be described as follows: small cavity-strong cloud cavitation-large attached cavity.
    Looking at the three adjacent blades at the first time step in Fig. 9, this means that blade 1 is somewhere in the middle of its cycle, while blade 2 is at the beginning and blade 3 is at the end of its cycle. Thus, in the lower half of the impeller there must be one blade being near the beginning of a cycle.
    This observation is confirmed by the investigations at TU Darmstadt (see section, Optical Measurements) where the tested scale-impeller shows also two cells within one impeller revolution.
(iv) A cross-correlation (not presented in this paper) of the hub pressure transducers shows a good signal agreement for the

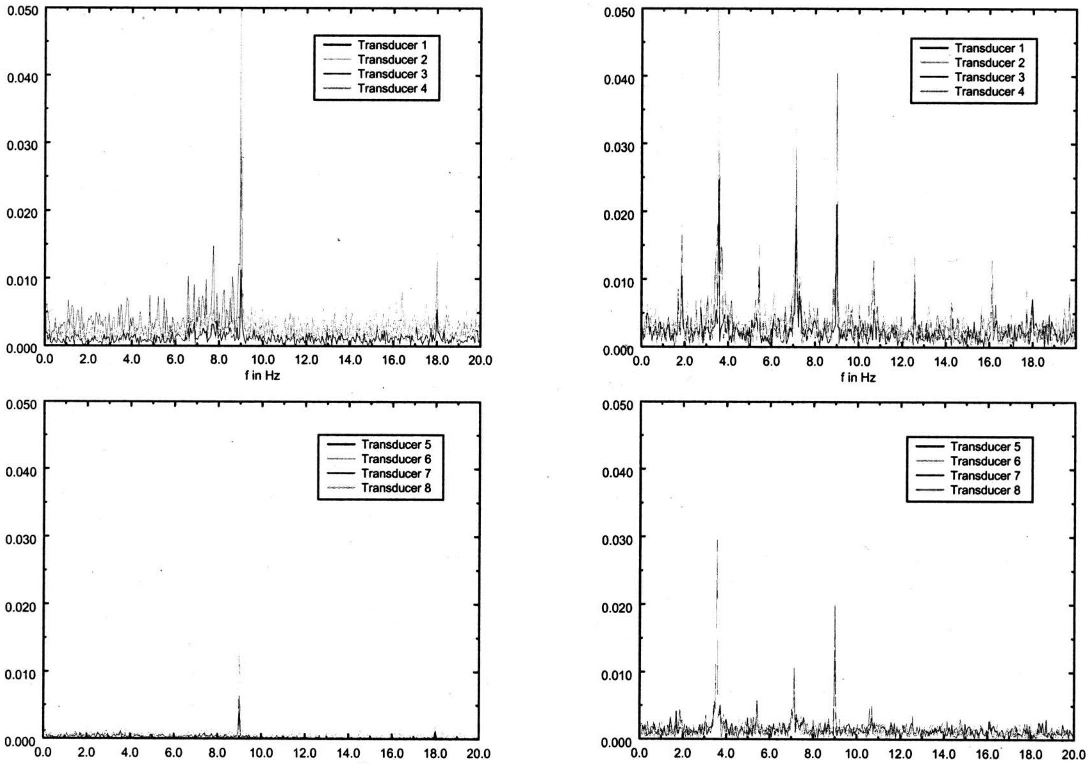

Fig. 10 FFT of pressure signals: Blade suction side (top) and impeller hub (bottom), quasi-steady cavitation (left) and within rotating cavitation (right) at 45 percent part load, ($\varphi=0.0136$)

three adjacent transducer-pairs ($8\rightarrow7, 7\rightarrow6, 6\rightarrow5$) each after $\Delta t_{1,2,3}=0.099$s. Correlating the last and the first transducer ($5\rightarrow8$) the agreement is fairly good for $\Delta t_{45}=0.247$s. This leads to a propagation time of $\Delta t=\Delta t_1+\Delta t_2+\Delta t_3+\Delta t_{45}=0.544$s for one rotation, which also can be found in a correlation of transducer 8 with itself.

Using all these aspects the right side of Fig. 10 can probably be explained as follows: The lowest frequency at this operating point ($f_1\approx1.8$ Hz$\approx1/(0.544$ s$)$) marks the propagation velocity of rotating cavitation. The next peak ($f_2\approx3.6$ Hz) is due to the two cells within the impeller, both propagating with the lower frequency. The other peaks ($f_3\approx5.4$ Hz and $f_4\approx7.2$ Hz) are guessed to be multiple frequencies of the two above mentioned, but they also could be caused by cloud cavitation.

Conclusions

1. Rotating cavitation was observed in two similar impellers of a centrifugal pump of low specific speed. The same phenomenon was also found in a scaled pump running at the same Reynolds number.
2. The occurrence of rotating cavitation was assigned to a typical shape of the head-drop-curves, called creeping-head-drop.
3. For all investigated flow coefficients the onset of rotating cavitation can be described by a constant parameter $\sigma/2\alpha$. That means, at operating points of higher incidence angle (part load conditions) the cavitation number can also be higher and thus the state of cavitation can be weaker to produce the same instability.
4. The propagation of the phenomenon can be explained by an interaction of the cavity (related blockage and velocity component near the cavity closure region) and the leading edge of the following blade. Within one impeller-revolution two cells of rotating cavitation were observed at all operating points.

Acknowledgments

The presented study was carried out in cooperation with the Technical University of Darmstadt and the DFG (Deutsche Forschungsgemeinschaft). The authors would like to thank Mr. M. Hofmann and Prof. B. Stoffel of TFA (TU Darmstadt) for their study on a scale-impeller, supporting the described results over a wide range.

Nomenclature

b = passage width
d = diameter
f = frequency
g = gravity
H = head
M = mass-flow-gain factor
n = impeller rotating speed
n_s = specific speed
p = static pressure
p_ν = vapor pressure
U = upstream mean velocity
$\dot{V}$ = volume flow
z = number of blades
α = incidence angle
β = blade angle
ρ = density
η = efficiency
σ = cavitation number $2*(p_1-p_\nu)/\rho U^2$
φ = flow coefficient $4*\dot{V}/(d_2{}^3\pi^2 n)$

ψ = pressure rise coefficient $2{*}gH/(d_2{}^2\pi^2 n^2)$
1 = inlet
2 = outlet
D = design point
IC = incipient cavitation

References

[1] Spohnholtz, H. H., 1997, ''NPSH-Verhalten von Halbaxial pumpen,'' *Diss. TU Braunschweig, publ. in Mitteilungen des Pfleiderer-Instituts für Strömungsmaschinen, Heft 4,* W. H. Faragallah.

[2] Dreiß, A., 1997, ''Untersuchung der Laufradkavitation einer radialen Kreiselpumpe durch instationäre Druckmessungen im rotierenden System,'' *Diss. TU Braunschweig, publ. in Mitteilungen des Pfleiderer-Instituts für Strömungs maschinen, Heft 4*, W. H. Faragallah.

[3] Dreiß, A., and Kosyna, G., 1997, ''Experimental Investigations of Cavitation-States in a Radial Pump Impeller,'' *Proceedings of the JSME Centennial Grand Congress, International Conference on Fluid Engineering*.

[4] Tsujimoto, Y., Yoshida, Y., Maekawa, Y., Watanabe, S., and Hashimoto, T., 1997, ''Observations of Oscillating Cavitation of an Inducer,'' ASME J. Fluids Eng., **119**, pp. 775–781.

[5] Tsujimoto, Y., Kamijo, K., and Yoshida, Y., 1993, ''A Theoretical Analysis of Rotating Cavitation in Inducers,'' ASME J. Fluids Eng., **115**, pp. 135–141.

[6] Greitzer, E. M., 1981, ''The Stability of Pumping Systems,'' ASME J. Fluids Eng., **103**, pp. 193–242.

[7] Watanabe, S., Sato, K., Tsujimoto, Y., and Kamijo, K., 1999, ''Analysis of Rotating Cavitation in a Finite Pitch Cascade Using a Closed Cavity Model and a Singularity Method,'' ASME J. Fluids Eng., **121**, pp. 834–840.

[8] Huang, J.-D., Aoki, M., and Zhang, J.-T., 1998, ''Alternate Blade Cavitation on Inducer,'' JSME International Journal, Series B, **41**, pp. 1–6.

[9] Horiguchi, H., Watanabe, S., Tsujimoto, Y., and Aoki, M., 2000, ''A Theoretical Analysis of Alternate Blade Cavitation in Inducers,'' ASME J. Fluids Eng., **122**, pp. 156–163.

Takeshi Sano
Mitsubishi Heavy Industries, Ltd.,
Takasago Machinery Works,
2-1-1, Shinhama, Arai, Takasago,
Hyogo 676-8686, Japan

Yoshiki Yoshida

Yoshinobu Tsujimoto

Osaka University, Graduate School of
Engineering Science,
1-3, Machikaneyama, Toyonaka,
Osaka 560-8531, Japan

Yuki Nakamura
Mitsubishi Heavy Industries, Ltd.,
Takasago Research & Development Center,
2-1-1, Shinhama, Arai, Takasago,
Hyogo 676-8686, Japan

Tatsuhito Matsushima
Software Cradle Co., Ltd.,
6-1-1, Nishinakajima, Yodogawa, Osaka,
Osaka 532-0011, Japan

Numerical Study of Rotating Stall in a Pump Vaned Diffuser

This paper treats the flow instabilities in a vaned diffuser by using CFD. A commercial code with the standard κ-ε turbulence model was used for the present work. It was found that the flow instabilities in the vaned diffuser: i.e., rotating stall, alternate blade stall, and asymmetric stall, could be simulated by the present calculations. These instabilities were observed in a range with negative slope of the pressure performance curve of the diffuser. The rotating stall onset flow rate is larger for the case with larger clearance between the impeller and diffuser vanes. [DOI: 10.1115/1.1459076]

Introduction

For low specific speed centrifugal pumps with vaned diffuser, dents in the performance curve are occasionally observed. These dents are often attributed to the flow instabilities in the vaned diffuser with diffuser stall. With the aim of improvement of performance curve instabilities, Hergt et al. [1], and Eisele et al. [2] made experimental observations of the internal flow in vaned diffusers at low flow rate.

The application of CFD code is becoming popular for the investigation of the detailed 3-D flow and unsteady phenomena in pumps. Shi et al. [3] calculated the pressure fluctuation caused by the interaction between the impeller and vaned diffuser. Nohmi et al. [4] analyzed the flow in the vaned diffuser with U-bend and return channel. In addition, Torbergsen [5] could simulate the rotating stall with reverse flow in the axial-type vaned diffuser coupled with a centrifugal impeller.

In previous experimental study on a vaned diffuser (Sano et al. [6]), several types of stall in the vaned diffuser were observed, such as the rotating stall, alternate blade stall, and asymmetric stall. The flow rate, and the amount of the clearance between the impeller and diffuser affected the diffuser flow instabilities, which could be related to the change in the diffuser pressure performance curve.

In the present study, numerical analyses of the flow instabilities in the vaned diffuser were carried out by using a commercial software focusing on the effects of diffuser pressure performance and the impeller/diffuser clearance. In addition, the experiments were carried out for the purpose of visualizing the flow field under the stalled condition, and the results were compared with the calculations.

Calculation Model

Navier-Stokes Code. In present study, a commercial software package was used for the calculation, the code ‘‘SCRYU/Tetra for Windows’’ from SOFTWARE CRADLE Co., Ltd. The transport equations are discretized using a finite-volume method. The code solves the Reynolds averaged Navier-Stokes equations in primitive variable form. The effects of turbulence were modeled using the standard k-ε turbulence model. To make the simulation timely economical, a wall function is used to resolve the wall flows.

Geometry and Boundary Conditions. Figure 1 shows two calculation models used in this study. Model A (for vaned diffuser without impeller) consists of eight vaned diffuser. Inlet vane angle is $\beta_3 = 11.5$ degrees. The diameter of diffuser inlet, D_3, is 155.2 mm, and the diameter of inlet boundary, D_2, is 141.1 mm (for $D_3/D_2 = 1.10$), or 122.2 mm (for $D_3/D_2 = 1.27$). For comparison with Model A with eight vanes, Model A1 and A2 with one and two diffuser channels, respectively, as shown in Fig. 1(*a*), are also considered. In these models, periodic boundary conditions are applied on the internal boundaries.

Model B is a model combined with seven bladed impeller with 22.5 degrees logarithmic spiral blades. The outlet diameter of impeller, D_2, is the same as that of the inlet boundary of Model A for comparison, so that $D_3/D_2 = 1.10$ or 1.27. The rotating impeller grid and stationary diffuser grid are connected using the discontinuous coupled grids (moving grid method) (Jaworski et al. [7]). Eight black dots (No. 1–8) in Figs. 1(*a*), (*b*) show the locations of the reference pressure, p_3, at the diffuser inlet for each diffuser channel. Both models have the same outlet boundary diameter $D_4 = 238.4$ mm.

The original code is for 3-D analysis. Time saving calculations are carried out in the present study using the following methods. Only one element is used in the thickness direction (thickness is constant 3.0 mm), and slip boundary conditions are applied on sidewalls, while non-slip conditions are applied on impeller/diffuser vane surface with wall function. So, it is possible to say

---

Contributed by the Fluids Engineering Division for publication in the JOURNAL OF FLUIDS ENGINEERING. Manuscript received by the Fluids Engineering Division August 1, 2001; revised manuscript received January 4, 2002. Associate Editor: J. Katz.

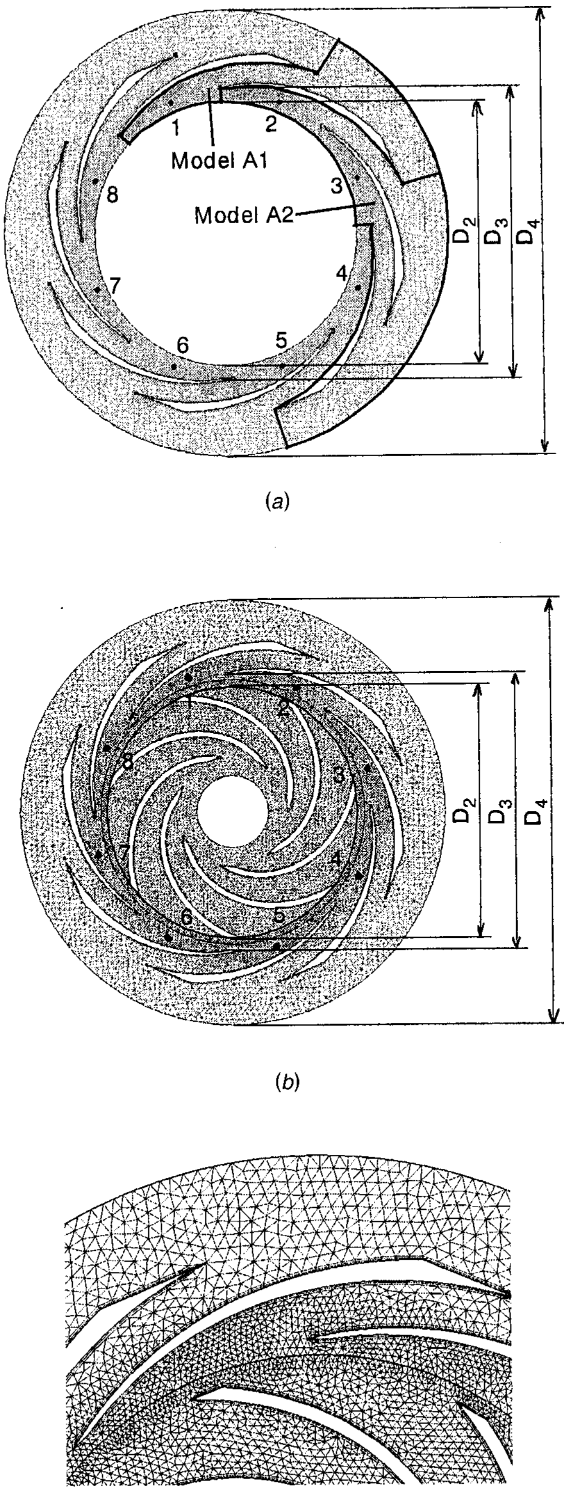

Fig. 1 Calculation model. Eight black dots, No. 1–8, show the locations of pressure reference points at diffuser inlet (p_3). (*a*) Model A, A1, and A2; (*b*) Model B; (*c*) magnification of the computational grid around the diffuser inlet

that these calculations are close to the two-dimensional ones. Constant pressure ($p_4=0$) is assumed on the outlet boundary. For Model A, a prescribed uniform swirl flow with flow angle (β) is assumed at the calculation inlet boundary. For Model B, a uniform radial flow with flow rate (ϕ) is assumed at the inlet boundary. The Reynolds number, $\mathrm{Re}=D_2u_2/\nu$, was about 10^5 throughout the present study. Unstructured 3×10^4 grids are used for Model A, with similar density grids for Model A1 and A2. For Model B, 6×10^4 grids are used. To improve the computational accuracy, smaller grid is used in the region between impeller discharge and diffuser inlet, as shown in Fig. 1(*c*). The grid density in this region is higher than that in other regions. In addition, to examine the grid size, double density grid model with 13×10^4 grids for Model B was calculated. The results calculated with fine grid were almost the same as original ones. Unsteady calculation with Courant number equal to one was performed in this study. When all varieties become constant in time or show the stable oscillation, we regarded that state as the answer for the prescribed boundary and initial conditions.

Results and Discussions

Flow Simulations of Vaned Diffuser Without Impeller (Model A, A1, and A2). The pressure performance of the diffuser is represented by the diffuser outlet static to diffuser inlet total pressure coefficient, ψ_d, defined by the following equation:

$$\psi_d=\frac{p_{3t}-p_4}{\rho v_{\theta 3}^2} \tag{1}$$

where p_{3t} is the total pressure at diffuser inlet reference points shown in Fig. 1, and p_4 is the static pressure at the outlet boundary, $v_{\theta 3}$ is the circumferential velocity at the diffuser inlet. Note that $v_{\theta 3}$ is used as the reference velocity. The 2-D linear stability analysis using an actuator disk model (Yoshida et al. [8]) shows that the rotating stall occurs in the range where the slope of $\psi_d-\phi$ plot is negative.

The diffuser pressure performances, ψ_d, versus flow angle, $\tan\beta/\tan\beta_3$, for each diffuser channel are shown in Fig. 2. Upper figures in Fig. 2 show the results for Model A1 and A2. Lower figures show for Model A with the results of Model A1 for comparison.

In case of $D_3/D_2=1.10$ on Model A2, the pressure in each channel is different with each other in the range where the slope of ψ_d for Model A1 is negative. For Model A, the pressures in eight channels differ in the same flow range. However, no propagation was observed. This is herein called an "asymmetric stall." Figure 3 shows a typical flow field of the asymmetric stall, for $D_3/D_2=1.10$, $\tan\beta/\tan\beta_3=0.3$. A high-pressure region occupies the range from the throat to the inlet of Channel 1, and the pressure at inlet in Channel 2 is lower than that in Channel 1. A reversed flow is observed in Channel 1, but not in Channel 2. The outward flow from the inlet boundary is blocked by the flow reversal in Channel 1, and the flow turns into the Channel 2 through the narrow clearance between the diffuser leading edge and inlet boundary. This "leakage flow" is accelerated around the clearance, and the pressure at the inlet of Channel 2 is lower than that in Channel 1. In the experimental study about eight vaned diffuser (Sano et al. [6]), "alternate blade stall" was observed; i.e., the inlet pressure varies high and low in alternate channels. The flow pattern and the pressure distribution in the experiment were very close to the asymmetric stall observed in Model A2 with two channels periodic boundary condition.

In the case of $D_3/D_2=1.27$ with wider clearance between the diffuser and inlet boundary, two types of flow instabilities were observed in the range with the negative slope of ψ_d for Model A1. The asymmetric stall was observed only at condition *d* ($\tan\beta/\tan\beta_3=0.3$), and the rotating stalls with one cell were observed at the conditions *a*, *b*, *c*, and *e* in Fig. 2(*b*). Figure 4(*a*) shows the cross spectrum of the pressure fluctuations in two adjacent channels, shown in terms of propagation velocity ratio for various flow conditions. In this figure, horizontal axis shows the propagation speed of stall cell (v_p) normalized by tangential velocity at inlet boundary ($v_{\theta 2}$). Figures 4(*b*) and (*c*) show the temporal waveform of the inlet pressure (p_3) under the forward ro-

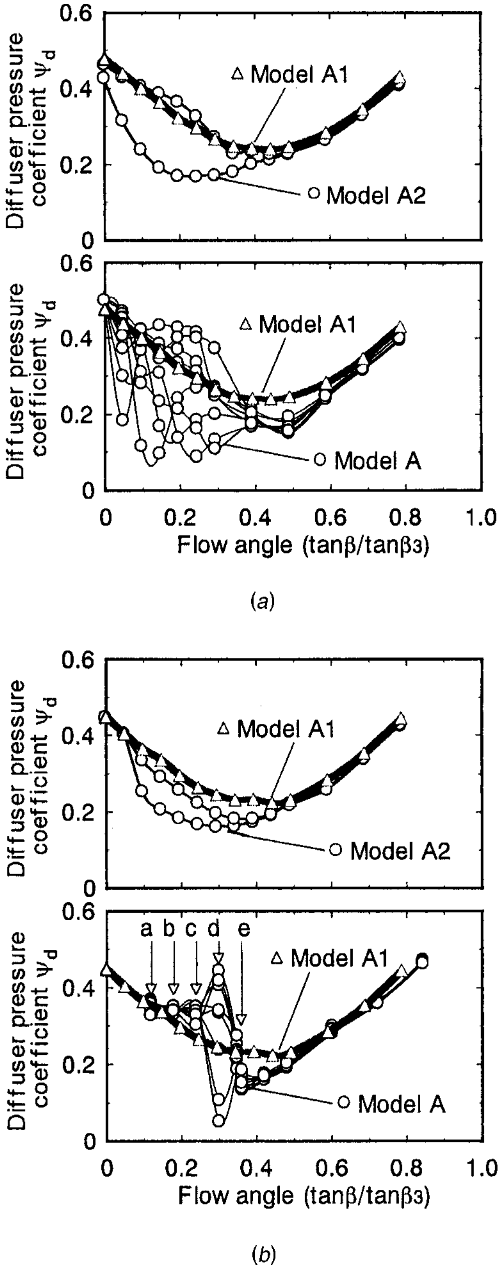

Fig. 2 Diffuser pressure performances for each channel. Upper figures show the results of periodic calculation (Model A1, and A2). Lower figures show those of Model A with Model A1 for comparison. (*a*) $D_3/D_2=1.10$; (*b*) $D_3/D_2=1.27$

tating stall ($v_p/v_{\theta 2}>0$) at condition *b*, and the backward rotating stall ($v_p/v_{\theta 2}<0$) at condition *e*, respectively. Forward rotating stalls were observed also at conditions *a* and *c*. If we consider the asymmetric stall to be a kind of the rotating stall with zero propagation speed ratio, we can say that the propagation speed ratio increases as the flow rate decreases.

From these numerical results for the vaned diffuser without impeller, it was found that the flow instabilities in the vaned diffuser, such as rotating stall and asymmetric stall, occur when the slope of the diffuser pressure coefficient, ψ_d is negative. As we increase the flow rate through a diffuser channel with constant circumferential velocity in the range with negative slope of ψ_d, the diffuser pressure recovery increases and the diffuser inlet pressure decreases if the diffuser outlet pressure is kept constant. Then, the flow toward the channel increases further. This is the principal reason that the flow instabilities in the vaned diffuser occur depending on the slope of the diffuser pressure coefficient, ψ_d.

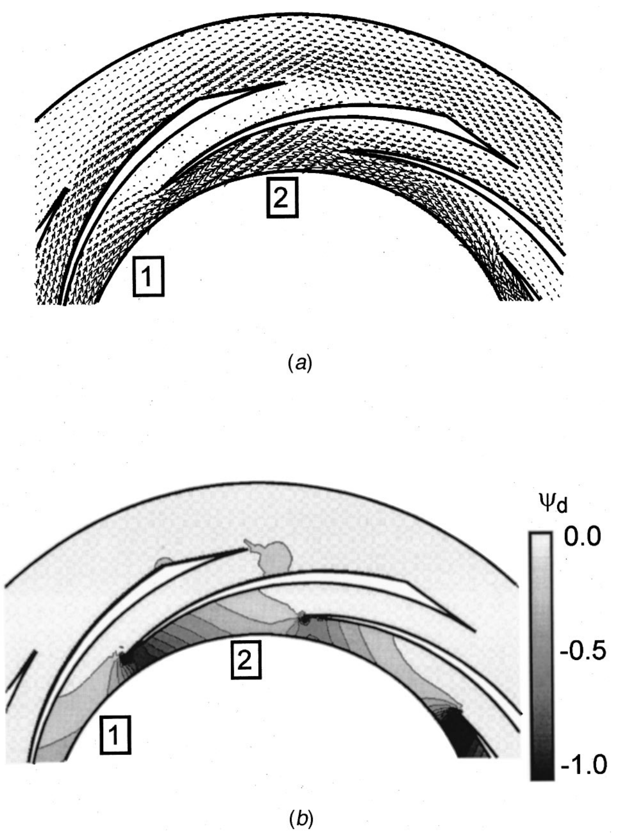

Fig. 3 Flow field under the asymmetric stall condition (Model A, $D_3/D_2=1.10$, $\tan\beta/\tan\beta_3=0.3$). Flow pattern is different between Channel 1 and Channel 2. (*a*) Velocity vector; (*b*) Pressure contour

Flow Simulations of Vaned Diffuser With Impeller (Model B). Flow simulations of a vaned diffuser with seven bladed impeller and outlet diameter, D_2, were carried out for $D_3/D_2=1.10$ and 1.27. Diffuser pressure coefficient, ψ_d, impeller inlet total to diffuser inlet static pressure coefficient, ψ_s, and impeller inlet total to diffuser outlet static pressure coefficient, ψ, are shown in Fig. 5. ψ_s, and ψ are defined as the following equations:

$$\psi_s=\frac{p_3-p_{1t}}{\rho u_2^2} \tag{2}$$

$$\psi=\frac{p_4-p_{1t}}{\rho u_2^2} \tag{3}$$

where u_2 is the peripheral speed of the impeller outlet, and p_{1t} is the total pressure at the inlet boundary. The diffuser pressure performance, ψ_d, for Model A1 is also shown in the upper figures in Fig. 5 for reference. Flow angle $\tan\beta$ for Model A1 was converted into the flow coefficient ϕ in Fig. 5 by using the Euler head obtained by two-dimensional singularly method.

For both $D_3/D_2=1.10$, and 1.27 with Model B, the rotating stalls were observed in the range where ψ_d for Model A1 has negative slope. The propagation speed ratio Ω_p/Ω (Ω_p: rotating stall propagation speed, Ω: impeller rotational speed) of the observed rotating stall is also shown in the figures. At several flow rates, asymmetric stall was observed simultaneously with the rotating stall. However, the magnitude of pressure deviation of the

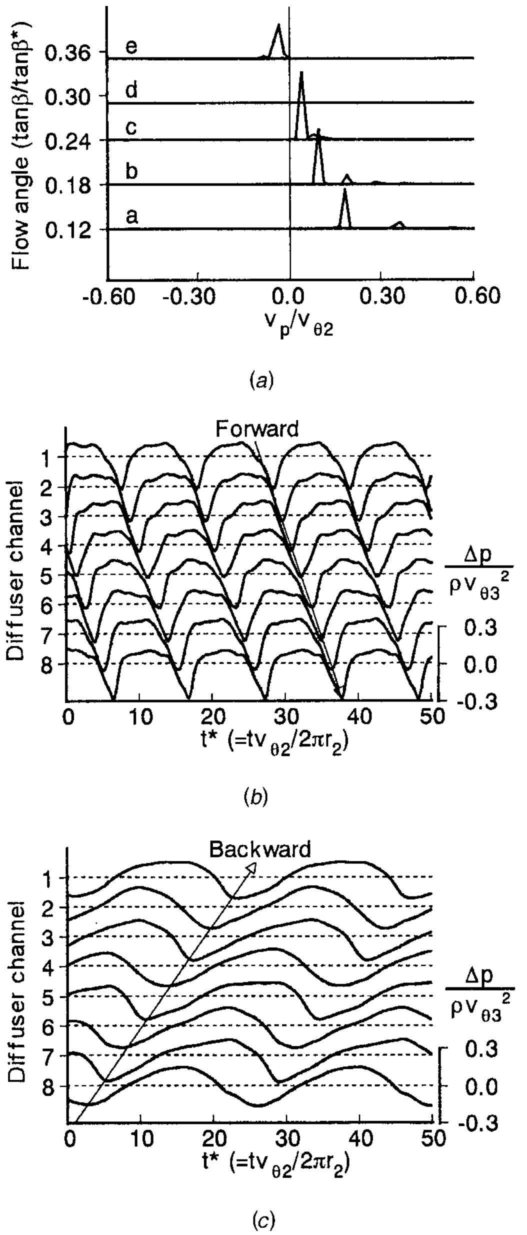

Fig. 4 Propagation speed and temporal wave form of the pressure fluctuation caused by forward/backward rotating stall at several flow rates (Condition a to e) shown in Fig. 2(*b*), for $D_3/D_2=1.27$ (Model A). (*a*) Propagation speed $v_p/v_{\sigma 2}$; (*b*) forward rotating stall for tan β/tan $\beta_3=0.18$ (condition b); (*c*) backward rotating stall for tan β/tan $\beta_3=0.35$ (condition e)

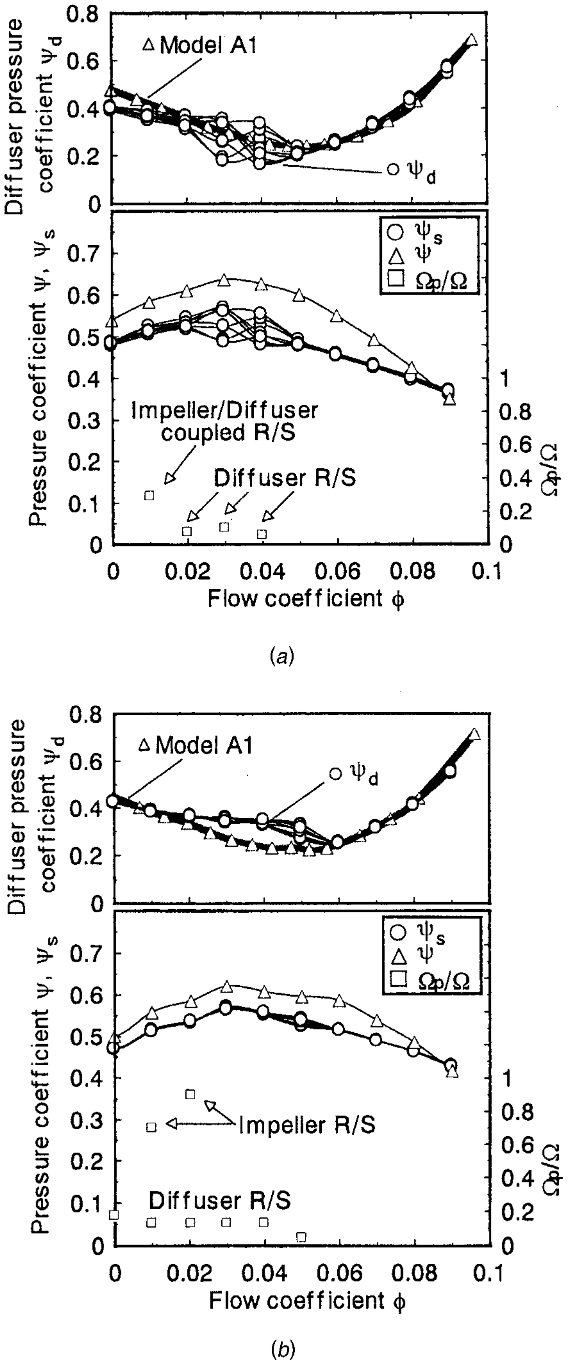

Fig. 5 Pressure performance and propagation speed ratio of rotating stalls (Model B). Diffuser pressure performance of Model A1 is shown for comparison. (*a*) $D_3/D_2=1.10$; (*b*) $D_3/D_2=1.27$

asymmetric stall is less than that observed in Model A. From the comparison between Model A (Fig. 2), and Model B (Fig. 5), it was found that the rotating stall occurs more easily in Model B. This can be explained as follows. For Model A, the velocity at the inlet boundary is kept constant irrespective of the pressure recovery in the diffuser. However, for Model B, the flow at the diffuser inlet can respond to circumferential pressure distribution developed by non-identical flow condition in the diffuser. This flow re-distribution at the diffuser inlet is considered to be the cause of the smaller pressure non-uniformity for Model B with the impeller. The rotating stall starts to occur at larger flow rate with larger impeller/diffuser clearance ($D_3/D_2=1.27$). This can be explained as follows. With smaller clearance, stabilizing effect of the impeller with negative slope of ψ_s is suppressing the onset of the diffuser rotating stall. However, with larger clearance, the coupling between the impeller and diffuser is smaller, and the diffuser rotating stall starts to occur as soon as the slope of diffuser pressure performance becomes negative.

We observed three types of rotating stall for Model B from the viewpoint of the propagation speed ratio. First one was such a rotating stall with $\Omega_p/\Omega\approx0.10$, second one with about $\Omega_p/\Omega\approx0.3$, and the third one was larger than $\Omega_p/\Omega\approx0.7$. Figure 6 shows the typical flow field under rotating stall with lower propagation speed, for $D_3/D_2=1.10$, $\phi=0.03$, $\Omega_p/\Omega=0.10$, N=2 (N: number of cells).

Figure 6(*a*) shows the pressure fluctuations at the reference

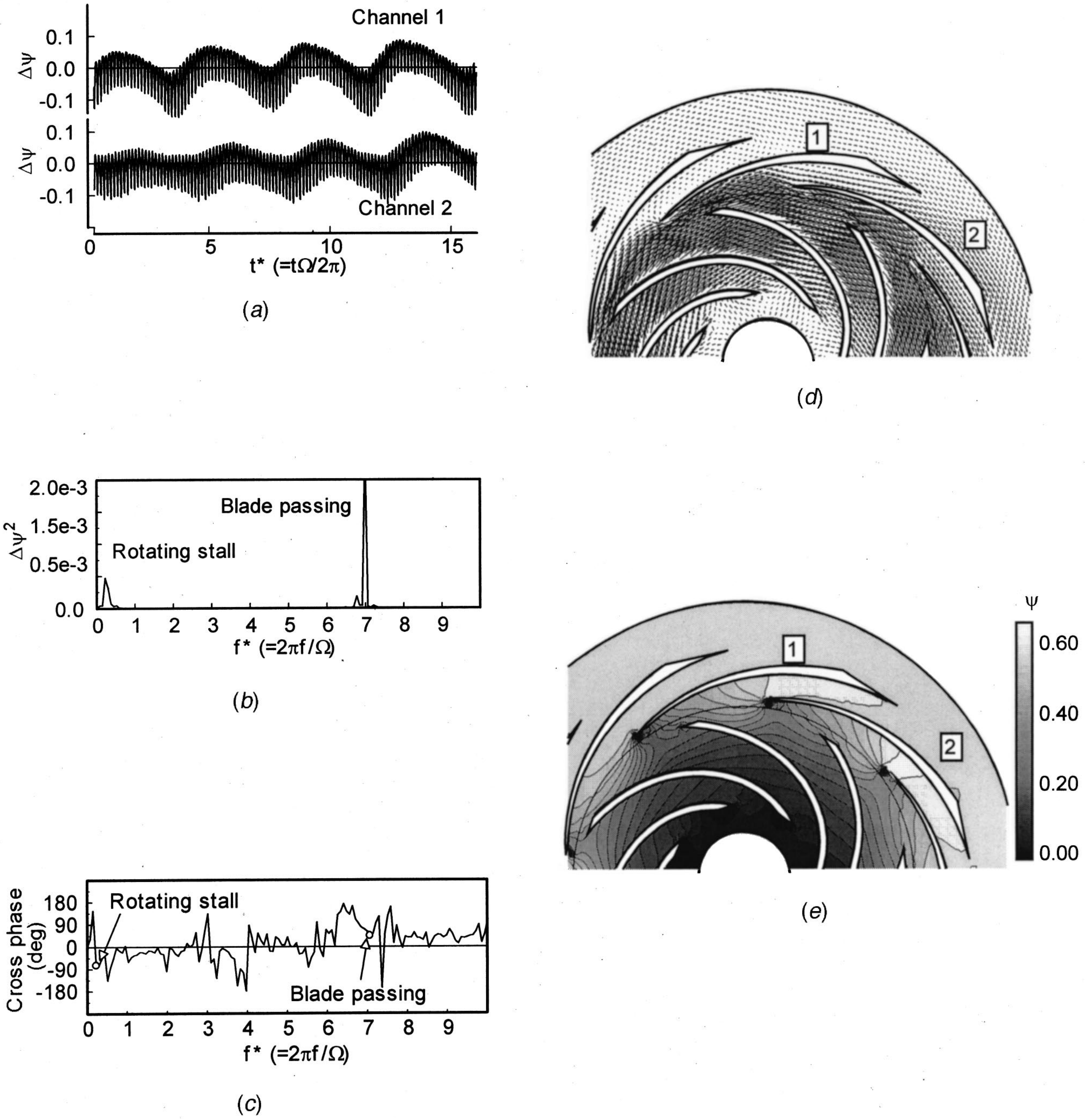

Fig. 6 Pressure fluctuations at the diffuser inlet, absolute velocity vector, and pressure contour around Channel 1 and 2 under the rotating stall obtained by the CFD simulation ($D_3/D_2=1.10$, $\phi=0.03$, $\Omega_p/\Omega=0.10$, $N=2$). (*a*) Pressure fluctuations in Channel 1 and 2; (*b*) cross spectrum of the pressure fluctuations between Channel 1 and 2; (*c*) cross phase delay of the pressure fluctuations between Channel 1 and 2; (*d*) absolute velocity vector; (*e*) pressure contour

points (p_3) located at deferent circumferential positions (separation angle 45 degrees) in two adjacent channels. Figures 6(*b*) and (*c*) show the cross spectrum, and the cross phase delay between these pressure fluctuations. From the temporal waveforms of Channel 1 and 2, it was found that the stall is propagating in the same direction as the impeller rotation. The cross spectrum of pressure fluctuations shows that there are dominant frequencies at $7\times f^*$, and $0.2\times f^*$. These are the blade passing frequency (number of impeller vanes is 7), and the propagating frequency of rotating stall ($N\times\Omega_p/\Omega=0.20$), respectively. The cross phase delay of the frequency $0.2\times f^*$ is about -90 degrees ($=-45$ degrees$\times 2$). From this cross spectrum analysis, it could be found that the rotating stall has two stall cells ($N=2$), and the propagation speed ratio $\Omega_p/\Omega=0.10$. Figures 6(*d*) and (*e*) show the absolute velocity vector and pressure contour. In Channel 1, just under stalled condition, there is a reverse flow from the channel discharge to throat. The higher pressure region in Channel 1 extends to diffuser inlet, like as the asymmetric stall (Channel 1 in Fig. 3). The flow from the impeller turns to the next Channel 2. The reverse flow is not observed in Channel 2, but the velocity in Channel 2 is much higher (jet flow) than the other Channels. And the pressure at the inlet of Channel 2 is lower than that of Channel 1. The reverse flow and jet flow within the diffuser channel under the rotating stall were also observed with the experimental flow visualizations by Hergt et al. [9] and Sinha et al. [10]. The pres-

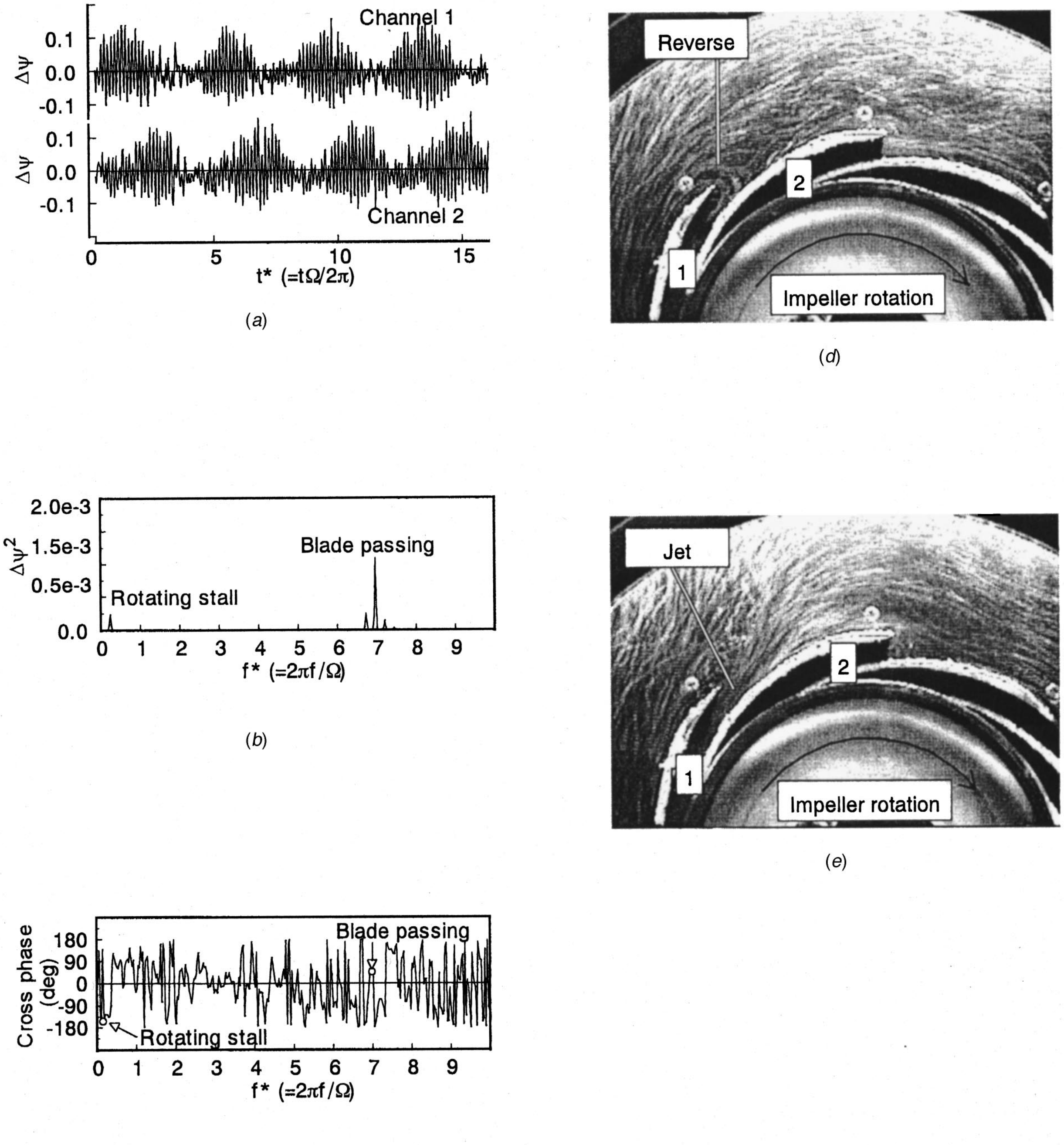

(*a*)

(*d*)

(*b*)

(*e*)

(*c*)

Fig. 7 Pressure fluctuations at the diffuser inlet, and instantaneous pictures around Channel 1 and 2 under the rotating stall obtained by the experiment ($D_3/D_2=1.10, \phi=0.03, \Omega_p/\Omega=0.08, N=3$), uncertainty in $\phi \pm 0.003$, in $\Omega_p/\Omega \pm 0.002$, in $\Delta\psi \pm 0.002$, in phase delay ±3 degrees. (*a*) Pressure fluctuations in Channel 1 and 2; (*b*) cross spectrum of the pressure fluctuations between Channel 1 and 2; (*c*) cross phase delay of the pressure fluctuations between Channel 1 and 2; (*d*) reverse flow at the diffuser outlet; (*e*) jet flow in the channel

sure fluctuation and turbulent flow are limited in the diffuser channels or vaneless region within impeller/diffuser clearance, so that it could be concluded that this is the rotating stall in the vaned diffuser.

Moreover, the rotating stall with higher propagation speed ratio ($\Omega_p/\Omega \approx 0.3$) and one stall cell is observed in the condition of $D_3/D_2=1.10$, at lower flow rate $\phi=0.01$ where the impeller performance curve $\psi_s-\phi$ has positive slope. The turbulent flows, i.e., reverse flow and jet flow, are observed not only in the diffuser channels, but also in the impeller channels. Non-uniform flows in the diffuser and impeller channels caused by the stall are coupled with each other and propagate together. From these results, it is possible to say that this is the impeller/diffuser coupled rotating stall.

In case of larger clearance $D_3/D_2=1.27$, at $\phi=0.01$, and 0.02, where the impeller performance curve, ψ_s, has strong positive slope, we observed two rotating stalls simultaneously. One is with lower propagation speed ratio $\Omega_p/\Omega \approx 0.13$ and one stall cell. Higher turbulence was observed in diffuser channels and vaneless region within impeller/diffuser clearance. The other is with higher propagation speed ratio Ω_p/Ω larger than 0.70 and one stall cell. Higher turbulence was observed mostly at the impeller inlet, and this turbulence region propagated from blade to blade. Hence the former is the rotating stall in the vaned diffuser, and the latter is the rotating stall in the impeller. In this case, these stall cells propagated independently, not coupled at all. This is because the interaction between the impeller and diffuser is smaller than that in case of $D_3/D_2=1.10$.

Comparison With Experimental Results. To confirm these calculation results, experimental investigations were carried out. The geometries of the impeller and diffuser in experimental pump were the same as the computational Model B of $D_3/D_2=1.10$ except the channel height ($b_2=15$ mm). The test impeller has the axial inlet but the impeller has two-dimensional blades. Blade profiles of the impeller and diffuser are constant for height direction. Working fluid is water, and the impeller rotates at 600 rpm, so the Reynolds number, $\mathrm{Re}=D_2u_2/\nu$, in the experiment is 7.1×10^5, although that is 2.4×10^5 in the calculations.

Two types of measurements were conducted to observe the rotating stall. The first is to visualize the flow field in the diffuser channel by using the polystyrene particles with averaged density 1000 kg/m^3, 0.7 mm in diameter as tracers, and digital still camera. The streamlines obtained by taking instantaneous pictures with a fixed shutter speed were examined. The second is to measure the pressure fluctuations in the adjacent diffuser channels (circumferential separation angle 45 degrees). From the cross spectrum between the pressure fluctuations, the propagation speed ratio and the number of rotating stall cells were examined.

Typical pressure fluctuations and visualization at $\phi=0.03$ in the experiment are shown in Fig. 7 compared with the CFD results as shown in Fig. 6. Temporal waveforms of the pressure fluctuations at the diffuser inlet, and the cross spectrum and the phase delay of the pressure fluctuations are shown in Figs. 7(*a*), (*b*), and (*c*), respectively. It was found that the propagating direction is the same as the impeller rotation from the temporal waveforms in two adjacent channels. Two dominant frequencies exist in the cross spectrum, one is rotating stall frequency ($0.24\times f^*$), and the other is blade passing frequency ($7\times f^*$). The cross phase delay of the frequency $0.24\times f^*$ is about -135 degrees ($=-45$ degrees $\times 3$). From this cross spectrum analysis, it was found that this rotating stall has three cells, and propagation speed ratio $\Omega_p/\Omega=0.08$.

Figures 7(*d*) and (*e*) show the pictures at different time. In Fig. 7(*d*), reverse flow from the diffuser discharge to throat was observed in Channel 1, although the flow in Channel 2 is normal. After a few moments from this picture, the region of reverse flow moved to Channel 2. On the contrary, jet flow appeared in Channel 1 as shown in Fig. 7(*e*). These visualized flow patterns and propagation speed ratio were close to those of the vaned diffuser rotating stall in CFD simulations as shown in Fig. 6, although the number of stall cells is different.

At the lower flow rate ($\phi=0.015$) in the experiment, the rotating stall with higher propagation speed ratio ($\Omega_p/\Omega=0.47$) and one stall cell is observed from the cross spectral analysis of the measurements of the pressure fluctuation. Unfortunately, we could not visualize the flow field in the impeller in the relative flame in the experiment. However, this rotating stall could be considered as the impeller/diffuser coupled rotating stall from the similarity in the onset of the flow rate, propagation speed ratio, and the number of stall cell between the experimental result and CFD result at $\phi=0.01$.

Conclusions

From the numerical and experimental results and discussions, the following conclusions can be summarized:

1 The flow instabilities in the vaned diffuser, such as the rotating stall, alternate blade stall, and asymmetric stall, occur in the range with negative slope of the diffuser pressure performance ψ_d.

2 As we increase the clearance between the impeller and the diffuser in the present calculation model, the diffuser rotating stall occurs more easily caused by the decoupling of impeller/diffuser flow.

3 In case of smaller clearance, the impeller/diffuser coupled rotating stall was observed at low flow rate. In case of wider clearance with smaller interaction between the impeller and diffuser, the impeller rotating stall occurs independently from the diffuser rotating stall at low flow rate.

4 The switching between the reverse flow and jet flow in the diffuser channel was observed under the rotating stall condition both in CFD and the experiment.

Acknowledgments

The authors would like to express their sincere gratitude to Mr. Mamoru Abe who assisted in conducting the experiment and calculation as a graduate project at Osaka University.

Nomenclature

b_2 = impeller width
D_2 = diameter of inlet boundary (see Fig. 1(*a*)), or diameter of impeller outlet (see Fig. 1(*b*))
D_3 = diameter of diffuser inlet (see Fig. 1)
D_4 = diameter of outlet boundary (see Fig. 1)
f = frequency
f^* = nondimensional frequency$=2\pi f/\Omega$
N = number of rotating stall cells
p = pressure
Δp = pressure fluctuation
p_{1t} = total pressure at impeller inlet
p_3 = static pressure at diffuser inlet
p_4 = static pressure at outlet boundary
Re = Reynolds number$=D_2u_2/\nu$
r_2 = radius$=D_2/2$
t = time
t^* = nondimensional time$=t\Omega/2\pi$, or $t\nu_{\theta 2}/2\pi r_2$
u_2 = peripheral speed of impeller outlet
v_p = propagation velocity of rotating stall
v_{r2} = radial velocity at impeller outlet
$v_{\theta 2}$ = circumferential velocity at impeller outlet
$v_{\theta 3}$ = circumferential velocity at diffuser inlet
β = flow angle$=\arctan(v_{r2}/v_{\theta 2})$
β_3 = blade angle at diffuser inlet
ϕ = flow coefficient ($=$flow rate$/\pi b_2D_2u_2$)
ν = kinematic viscosity
ρ = density
ψ = impeller inlet total to diffuser outlet static pressure coefficient$=(p_4-p_{1t})/(\rho u_2^2)$
ψ_d = diffuser outlet static to diffuser inlet total pressure coefficient$=(p_{3t}-p_4)/(\rho v_{\theta 3}^2)$
ψ_s = impeller inlet total to diffuser inlet static pressure coefficient$=(p_3-p_{1t})/(\rho u_2^2)$
$\Delta\psi$ = coefficient of unsteady pressure fluctuation$=\Delta p_3/(\rho u_2^2)$
Ω = impeller rotational speed
Ω_p = rotating stall propagation speed

References

[1] Hergt, P., and Starke, J., 1985, "Flow Patterns Causing Instabilities in the Performance Curves of Centrifugal Pumps with Vaned Diffusers," Proceedings of the Second International Pump Symposium, pp. 67–75.
[2] Eisele, K., Zhang, Z., Casey, M. V., Gülich, J., and Schachenmann, A., 1997, "Flow Analysis in a Pump Diffuser-Part1: LDA and PTV Measurements of the Unsteady Flow," ASME J. Fluids Eng., **119**(4), pp. 968–977.

[3] Shi, F., and Tsukamoto, H., 2001, ''Numerical Study of Pressure Fluctuations Caused by Impeller-Diffuser Interaction in a Diffuser Pump Stage,'' ASME J. Fluids Eng., **123**(3), pp. 466–474.

[4] Nohmi, M., and Goto, A., 1998, ''Experimental and Computational Study of the Flow in a Vaned Return Channel of a Low Specific Speed Pump,'' ASME, FEDSM98-4857.

[5] Torbergsen, E. A., 1998, ''Impeller/Diffuser Interaction forces in Centrifugal Pumps,'' Doctor thesis, Norwegian University of Science and Technology.

[6] Sano, T., Nakamura, Y., Yoshida, Y., and Tsujimoto, Y., 2000, ''Alternate Blade Stall and Rotating Stall in Vaned Diffuser-Part1: Effects of Impeller/Diffuser Clearance,'' (in Japanese), Trans. Jpn. Soc. Mech. Eng., Ser. B, **66B**(650), pp. 2545–2552.

[7] Jaworiski, Z., Wyszynski, M. L., and Nienow, A. W., 1997, ''Sliding Mesh Computational Fluid Dynamics-A Predictive Tool in Stirred Tank Design,'' Proc. Inst. Mech. Eng., **211**, Part E, pp. 149–156.

[8] Yoshida, Y., Murakami, Y., Tsurusaki, H., and Tsujimoto, Y., 1991, ''Rotating Stalls in Centrifugal Impeller/Vaned Diffuser Systems,'' ASME, FED-Vol. 107, pp. 125–130.

[9] Hergt, P., and Benner, R., 1968, ''Visuelle Untersuchung der Strömung im Leitrad einer Radialpumpe,'' Schweizerische Bauzeitung, 86. Jahrgang Helt 40, pp. 716–722.

[10] Sinha, M., Pinarbashi, A., and Katz, J., 2001, ''The Flow Structure During Onset and Developed States of Rotating Stall Within a Vaned Diffuser of a Centrifugal Pump,'' ASME J. Fluids Eng., **123**(3), pp. 490–499.

Andrés Tremante
e-mail: atrem@usb.ve

Nathaly Moreno
e-mail: nmoreno@usb.ve

Universidad Simón Bolívar,
Laboratorio de Conversión de Energía Mecánica,
Caracas, Venezuela

Robert Rey

Ricardo Noguera

LEMFI-ESA CNRS 7067
ENSAM-151 bd de l'Hôpital-75013 Paris,
France

Numerical Turbulent Simulation of the Two-Phase Flow (Liquid/Gas) Through a Cascade of an Axial Pump

The main goal of the present work is to establish the analysis of a numerical turbulent simulation of an axial pump cascade under two-phase flow presence of liquid and gas, coupled with the "κ-ε" turbulent model. This knowledge is very important for different applications, for example in the oil industry. Indeed, the transport of two-phase flow (oil and gas) that comes from the well implies the utilization of separation and treatment facilities before pumping. It means that a number of economical resources are involved in this kind of industrial operation. Therefore, depending on the function optimization of this type of two-phase pump, it would permit the substitution of the traditional expensive facilities, in addition to energy cost savings. In order to predict the fluid dynamics characteristics of an axial pump cascade under two-phase flow conditions with a view to improving its performance, the present research will describe a multifluid model in order to solve the momentum equations (Navier-Stokes) coupled with the continuity equation. Here, we will use a modified "κ-ε" turbulent model, taking into account the viscosity of the liquid phase and the compressibility of the gas phase, using the CFD simulator: CFX-4.0. As a consequence of this numerical simulation, we will be able to optimize the design of a cascade of an axial two-phase pump and therefore obtain its optimum point of operation. [DOI: 10.1115/1.1471533]

Introduction

There have been several attempts to develop correlations that predict pump performance in two-phase flow. Most of them have tried to fit the data measured by means of multiplier factors, which do not reflect the physics of the process. This blind search for a "fudge factor" not only is bound to give performance plots with much scatter, but it will give results applicable only to a pump-system configuration operating under the same conditions.

The criticisms expressed above are not intended to mean that all previous work is useless. On the contrary, a great deal of useful data has been reported. The problem is that the lack of knowledge as to what happens inside the pump and how geometry affects the performance makes the correlation of the data difficult. A good understanding of the phenomena would bring confidence to the correlations and would allow, perhaps, the extrapolation of the results to other systems. Therefore, we will briefly introduce a review of the state-of-the-art of two-phase flow in pumps.

Cooper [1] used a homogeneous two-phase flow model to simulate theoretically the flow in turbopump inducers. The principal interest, however, was to model cavitating flows.

Murakami and Minemura [2,3] reported in two papers the effect of entrained air on the performance of a centrifugal pump and the effect of the number of blades. Visual observations were done which in turn allowed them to correlate the bubble size in the impeller passages as a function of homogeneous void fraction and pump speed. The experimental evidence is supported by dynamical analysis of pump head, impeller work, and head losses.

Muench [4] described the use of the energy equation to define pump head in two-phase flow. This method was used to fit the Aerojet Nuclear Company (ANC) pump data. Rohatgi [5] has presented a pump model for two-phase transient flow. The model requires empirical data, i.e., single-phase and two-phase homologous head curves, and the author selected data from ANC.

Heidrick and Hancox [6] contributed a paper on centrifugal pump behavior in steady and transient steamwater flows with low-specific speed. Experiments with both horizontal and vertical inflow of two-phase mixtures were performed for forward and reverse flow. The data presented agree with ANC pump data. Grison and Lauro [7] discussed the possibility of critical two-phase flow in a centrifugal pump from the theoretical and experimental viewpoint.

Mikielewicz et al. [8] presented a semi-empirical two-phase-flow pump model and correlated B&W data by means of the head-loss ratio. Turbomachinery theory was applied to obtain expressions to describe the pump performance. The head-loss ratio is shown to be a function of pump geometry, inlet void fraction, and operation point (flow-coefficient effect).

Wilson et al. [9] has made an extensive review of all the previous work up to 1978.

For prediction of the two-phase flow performance, the methods based on head-loss ratio (Mikielewicz et al. [8], Minemura et al. [10]), homologous curve method (Nilsson [11]), or polar homologous curve method (Minato [12]) are available, after correlating such parameters with the data experimentally obtained. It is, however, desirable to establish a numerical method by which the effects of the design parameters of a pump on its two-phase flow performance can be individually investigated, especially in relation to the development of offshore oil fields (De Donno [13]).

Regarding numerical prediction methods, Furuya [14] has proposed a one-dimensional, incompressible two-fluid model. This model has been extended to a condensable two-fluid model (Furuya and Maekawa [15]) which is successively employed in the studies by Calvin et al. [16] and Noghrehkar et al. [17].

There is also a two-dimensional singularity method by Nishiyama et al. [18] and a three-dimensional method using a quasi-harmonic equation based on a bubbly flow model by Minemura and Uchiyama [19,20]. Weiss [21] also developed a two-

---

Contributed by the Fluids Engineering Division for publication in the JOURNAL OF FLUIDS ENGINEERING. Manuscript received by the Fluids Engineering Division July 27, 2001; revised manuscript received February 20, 2002. Associate Editor: J. Katz.

dimensional singularity potential method and superposed a bubbly flow model to predict the performance of axial pumps and confirmed well with the experimental data (Weiss et al. [21–23]).

However, all these theoretical and numerical methods are obtained by assuming the fluid is inviscid, so that the pump head obtained is a theoretical one, and does not include hydraulic losses.

On the other hand, Minato [13] proposed a simple method to solve the momentum equations of both phases without regard to the changes in void fraction and pressure gradient within the impeller. Fujie [24] has solved the one-dimensional momentum equations for both phases using a friction loss coefficient obtained when the hydraulic torque becomes zero and taking the effect of the transitional flow from the impeller to the stationary volute casing into account.

But the handling of the constitutive equations of the two-fluid model is quite different from others and consideration of the velocity triangle at the impeller exit is not so consistent. Van Den Hove and Geffrage [25] also solve the one-dimensional momentum equations, though they ignored the significant effect of the slip velocity due to finite number of the impeller blades.

Minemura et al. [26] developed a consistent one-dimensional model, by extending Furuya's two fluid model [14], taking into account the related energy changes in the transitional flow from the rotating impeller to the stationary volute casing. This model is also applied to solve the two-phase flow performance of radial flow pump having a low specific speed, and confirmed with the experimental data [10], after investigating the applicability of various and representative constitutive equations for pipe flow.

To grasp analytically the characteristics of axial two-phase flow pumps and to make it possible to improve their performance, the present work describes a consistent multifluid model to solve the turbulent momentum equations coupled with the continuity one, with fluid viscosity and gas-phase compressibility, available in a CFD simulation code, called CFX-4.0. We introduce functions to the code for turbulence energy coefficient (κ) and the energy dissipation rate (ε), which were adjusted to the same scale order of our physical model. These functions allowed obtaining a numerical convergence less than 1E-04 for the residual mass. The numerical results are compared with experimental data for an axial pump obtained in experimental facilities designed and built for these purposes.

Problem Formulation

Multiphase flow refers to the situation where more than one fluid may be present, each possessing its own flow field. Examples are water droplets falling in air, gas bubbles rising in a liquid, steam-water flows in a boiler, oil-gas-water flows in an oil well, etc. We may also model the conveyance of large numbers of solid particles in gas or a liquid by treating the solid particle phase as a separate fluid. This is an alternative to the Lagrangian particle model and is particularly appropriate when the number of particles that are needed in a Lagrangian simulation is large.

From the above examples, we see that the term ''phase'' is applied in a wider sense than its usual usage in thermodynamics. By ''thermodynamic phase'' we mean the familiar distinction between solid, liquid and gaseous phases of the same species. The ''phases'' of a multiphase flow may be quite different chemical species.

Therefore, multiphase flow should not be confused with multicomponent flow. In the latter, the species are mixed at the molecular level. The model equations solve for common velocity and temperature fields, and mass transfer of one species into another is governed by diffusion driven by concentration gradients. In multiphase flows, the species are mixed at much larger scale than molecular length scales. They are given potentially different velocity and temperature fields etc., and these interact via empirically specified ''Inter-Phase Transfer'' terms. For example, if cold particles are injected into a fast flowing stream of hot air, the particles will be accelerated by inter-phase drag, and will be heated up by heat transfer across the phase boundary. Finally in the literature, there are two basic multiphase models available—the multifluid model and the homogeneous model.

The Multifluid Model. In the multifluid model, there is one solution field for each phase separately. Transported quantities interact via inter-phase transfer terms. For example, two phases may have separate velocity and temperature fields, but there will be a tendency for these to equalize through inter-phase drag and heat transfer terms. The multifluid model is solved using the Inter-Phase Slip Algorithm (IPSA) of Spalding [27].

Phases are labeled by Greek indices α, β, γ. The number of phases is denoted by N_β The volume fraction of each phase is denoted by r_α. The generic scalar advection-diffusion equation takes the form:

$$\frac{\partial}{\partial t}(r_\alpha \rho_\alpha \Phi_\alpha) + \nabla \cdot (r_\alpha(\rho_\alpha U_\alpha \Phi_\alpha - \Gamma_\alpha \Delta \Phi_\alpha)) = r_\alpha S_\alpha + \sum_{\beta=1}^{N_\rho} c_{\alpha\beta}(\Phi_\beta - \Phi_\alpha) + \sum_{\beta=1}^{N_\rho} (\dot{m}_{\alpha\beta}\Phi_\beta - \dot{m}_{\beta\alpha}\Phi_\alpha). \tag{1}$$

In this equation, we should note that the term $c_{\alpha\beta}(\Phi_\beta - \Phi_\alpha)$ describes inter-phase transfer of Φ between phases α and β where $c_{\alpha\alpha}=0$, $c_{\alpha\beta}=c_{\beta\alpha}$. Hence the sum over all phases of all inter-phase transfer terms is zero. Also, the term $\dot{m}_{\alpha\beta}\Phi_\beta - \dot{m}_{\beta\alpha}\Phi_\alpha$ only arises if inter-phase mass transfer takes place. $\dot{m}_{\alpha\beta}$ is the mass flow rate per unit volume into phase α from phase β.

We now summarize the equations of continuity and momentum in multiphase flow. These are the continuity equation:

$$\frac{\partial}{\partial t}(r_\alpha \rho_\alpha) + \nabla \cdot (r_\alpha \rho_\alpha U_\alpha) = \sum_{\beta=1}^{N_\rho} (\dot{m}_{\alpha\beta} - \dot{m}_{\beta\alpha}), \tag{2}$$

and the momentum equation:

$$\frac{\partial}{\partial t}(r_\alpha \rho_\alpha U_\alpha) + \nabla \cdot (r\alpha(\rho_\alpha U_\alpha \otimes U_\alpha - \mu_\alpha(\nabla U_\alpha + (\nabla U_\alpha)^Y))) = r_\alpha(B - \nabla \rho_\alpha) + \sum_{\beta=1}^{N_\rho} c_{\alpha\beta}^{(d)}(U_\beta - U_\alpha) + F_\alpha + \sum_{\beta=1}^{N_\rho} (\dot{m}_{\alpha\beta}U_\beta - \dot{m}_{\beta\alpha}U_\alpha) \tag{3}$$

We also have the density algebraic equation of state and constitutive equation for each phase:

$$\rho_\alpha = \rho_\alpha(T_\alpha, p_\alpha) \tag{4}$$

and the algebraic constraint that the volume fractions sum to unity:

$$\sum_{\alpha=1}^{N_\rho} r_\alpha = 1 \tag{5}$$

Equations (1) to (5) represent $5N_\rho + 1$ equations in the $6N_\rho$ unknowns ρ_α, U_α, V_α, W_α, p_α, r_α. We need $N_\rho - 1$ more equations to close the system. These are usually given by algebraic constraints on the pressure, the simplest being that all phases share the same pressure field, namely,

$$p_\alpha = p_1 = p, \quad 2 \leqslant \alpha \leqslant N_\rho \tag{6}$$

Other constraints on the pressures are possible. As an illustrative example, for some gas-solid flows it may be advantageous to use an alternative constraint on pressure to that of Eq. (6). This is achieved by removing the continuous phase pressure from the solid phase. In such cases, the shared pressure gradient term $-r_\alpha \nabla p_\alpha$ is removed from all the momentum equations. In the continuous phase momentum equation the shared pressure gradient term is replaced with $-\nabla p_\alpha$ and no pressure terms are included in the dispersed solid phases.

The Homogeneous Model. The homogeneous model is a simplification of the multifluid model. For a given transport process, it assumes that the transported quantities for that process are the same for all phases:

$$\Phi_\alpha = \Phi, \quad 1 \leqslant \alpha \leqslant N_p \tag{7}$$

for the generic scalar transport Eq. (1). However, the volume fractions are still assumed distinct. Hence, the individual phase continuity Eq. (2) can be solved to determine the volume fractions, but the individual transport Eq. (1) can be summed over all phases to give a single transport equation for Φ:

$$\frac{\partial \rho \Phi}{\partial t} + \nabla \cdot (\rho U \Phi - \Gamma \nabla \Phi) = S \tag{8}$$

where:

$$\rho = \sum_{\alpha=1}^{N_\rho} r_\alpha \rho_\alpha, \quad U = \frac{1}{\rho}\left(\sum_{\alpha=1}^{N_\rho} r_\alpha \rho_\alpha U_\alpha\right), \quad \Gamma = \sum_{\alpha=1}^{N_\rho} r_\alpha \Gamma_\alpha. \tag{9}$$

Here, we should note that the inter-phase transfer terms have all cancelled out. This is essentially a single-phase transport equation, with variable density and diffusivity.

In particular, the homogeneous model for momentum transport assumes that $U_\alpha = U$, $1 \leqslant \alpha \leqslant N_\rho$, and the momentum equation is given by (8) as:

$$\frac{\partial}{\partial t}(\rho U) + \nabla \cdot (\rho U \otimes U - \mu(\nabla U + (\nabla U)^T)) = B - \nabla \rho \tag{10}$$

where:

$$\rho = \sum_{\alpha=1}^{N_\rho} r_\alpha \rho_\alpha, \quad \mu = \sum_{\alpha=1}^{N_\rho} r_\alpha \mu_\alpha. \tag{11}$$

This approximation is good when the flow is drag dominated, that is, $c_{\alpha\beta}^{(d)}$ is very large, and there are no body forces, the phase velocities will tend to equalize over very short spatial length scales. In a flow under gravity, where the phases have completely stratified, for example, a free surface flow, the volume fractions of the phases are equal to one or zero everywhere except at the phase boundaries, and it makes sense to use a single velocity field.

The approximation does not apply to drag dominated multiphase flow under gravity, which is not stratified, for example, droplets falling under gravity in a gas. In this case, the droplets will quickly attain a fixed settling velocity where the inter-phase drag balances the differences in body forces. However, the phase velocities will not be equal, so the multifluid model should be used, which is the case of the present study for axial pump numerical simulation.

Turbulent Multiphase Flow. The subject of multiphase turbulence modeling is not as well developed as single-phase turbulence modeling. There is no ''industrial standard'' model, like the single-phase $\kappa - \varepsilon$ model, which is known to perform reasonably well to engineering accuracy in a wide range of applications. Therefore, the models implemented are the simplest possible generalization of the single-phase ''$\kappa - \varepsilon$'' and Reynolds stress models to the multiphase situation, with the only modification being the possible inclusion of Sato's (1975) model for bubble induced turbulence. (The unmodified models will almost certainly have serious shortcomings in almost any realistic physical situation. In the description of the ''$\kappa - \varepsilon$'' model below, we describe these shortcomings, with some suggestions on how the user may overcome them.)

In the simple unmodified multifluid ''$\kappa - \varepsilon$'' model, it is allowed that individual phases could be declared turbulent or laminar. We assume that the eddy viscosity hypothesis holds for each turbulent phase; hence an effective viscosity governs molecular and turbulent diffusion of momentum:

$$\mu_{\alpha \text{eff}} = \mu_\alpha + \mu_{T\alpha}, \tag{12}$$

where

$$\mu_{T\alpha} = C_\mu \rho_\alpha \frac{{k_\alpha}^2}{\varepsilon_\alpha}. \tag{13}$$

Turbulent dispersion of volume fraction can be modeled using the eddy diffusivity hypothesis:

$$\frac{\partial}{\partial t}(r_\alpha \rho_\alpha) + \nabla \cdot (r_\alpha \rho_\alpha U_\alpha - \Gamma_\alpha \nabla r_\alpha) = \sum_{\beta=1}^{N_\rho} (m_{\alpha\beta} - m_{\beta\alpha}) \tag{14}$$

where

$$r_\alpha = \frac{\mu_{T\alpha}}{\sigma_\alpha} \tag{15}$$

and σ_α is the turbulent Prandtl number. This assumes that the equations are time averaged. More often, when using Favre averaging, the turbulent dispersion force models this effect and no diffusion term is needed in the volume fraction equation.

The transport equations for κ and ε in a turbulent phase are assumed to take the same form as the generic scalar advection-diffusion Eq. (1):

$$\frac{\partial}{\partial t}(r_\alpha \rho_\alpha \kappa_\alpha) + \nabla \cdot \left(r_\alpha \left(\rho_\alpha U_\alpha \kappa_\alpha - \left(\mu_\alpha + \frac{\mu_{T\alpha}}{\sigma_k} \right) \nabla \kappa_\alpha \right) \right) = r_\alpha S_{k\alpha} + \sum_{\beta=1}^{N_\rho} c_{\alpha\beta}^{(k)} (\kappa_\beta - \kappa_\alpha) + \sum_{\beta=1}^{N_\rho} (\dot{m}_{\alpha\beta} \kappa_\beta - \dot{m}_{\beta\alpha} \kappa_\alpha) \tag{16}$$

$$\frac{\partial}{\partial t}(r_\alpha \rho_\alpha \varepsilon_\alpha) + \nabla \cdot \left(r_\alpha \left(\rho_\alpha U_\alpha \varepsilon_\alpha - \left(\mu + \frac{\mu_{T\alpha}}{\sigma_\varepsilon} \right) \nabla \varepsilon_\alpha \right) \right) = r_\alpha S_{\varepsilon\alpha} + \sum_{\beta=1}^{N_p} c_{\alpha\beta}^{(\varepsilon)} (\varepsilon_\beta - \varepsilon_\alpha) + \sum_{\beta=1}^{N_p} (\dot{m}_{\alpha\beta} \varepsilon_\beta - \dot{m}_{\beta\alpha} \varepsilon_\alpha). \tag{17}$$

Standard wall functions are used to extend the model up to the wall, for turbulent phases. If the Sato's pp. 34 model for bubble induced turbulence is included, then Eq. (13) to (19) are only used for the continuous phases. Denoting the continuous phase by α and the dispersed phase by β, the viscosity of the continuous phase in Eq. (12) is replaced by:

$$\mu_{\alpha \text{eff}} = \mu_\alpha + \mu_{T\alpha} + \mu_{T\beta}, \tag{18}$$

where the extra bubble induced turbulence term is given by:

$$\mu_{T\beta} = c_{\mu b} \rho_\alpha r_\beta d |U_\beta - U_\alpha| \tag{19}$$

and d is the bubble diameter. The viscosity of the disperse phase is then given simply as:

$$\mu_{\beta \text{eff}} = \mu_{\alpha \text{eff}} \frac{\rho_\beta}{\rho_\alpha} \tag{20}$$

There is no known sensible default for the turbulent Prandtl number for dispersion of volume fraction, σ_α, when using a time averaged formulation of the equations. Consequently, it can be assumed $\Gamma_\alpha = 0$ unless σ_α is set explicitly. In our case, the turbulent Prandtl number (σ_α) was adjusted taking into account the functions developed for the turbulence kinetic energy (κ) and the energy dissipation rate (ε).

In most physical situations, there will be additional production and dissipation of turbulence, not captured by single-phase source terms S_k, S_ϵ. For example, for two-phase flow of particles in a gas, or of bubbles in a liquid, large particles are known to enhance turbulence due to the production of a turbulent wake behind the particles. On the other hand, small particles are known to suppress turbulence; although, part of this effect can be obtained by using the Sato model.

Single-phase wall functions are known to be inadequate for multi-phase flow near a wall. The use of single-phase wall functions will be safe only if the flow is sufficiently stratified so that mostly only one phase is adjacent to any one wall.

If all phases are declared as turbulent, then the code has the option of declaring a homogeneous model for the transport of κ and ε. This has the advantage of not requiring any specification of the inter-phase transfer terms $c_{\alpha\beta}^{(\mathrm{k})}$, $c_{\alpha\beta}^{(\varepsilon)}$, and in the absence of any knowledge about these, it is perhaps the best thing to do. The homogeneous model assumes $\kappa_\alpha=\kappa$, $\varepsilon_\alpha=\varepsilon$, $1\leqslant\alpha\leqslant N_p$, and it sums Eqs. (16) and (17) to obtain:

$$\frac{\partial}{\partial t}(\rho\kappa)+\nabla\cdot\left(\rho U\kappa-\left(\mu+\frac{\mu_T}{\sigma_k}\right)\nabla\kappa\right)=S_\kappa \tag{21}$$

$$\frac{\partial}{\partial t}(\rho\varepsilon)+\nabla\cdot\left(\rho_\alpha U\varepsilon-\left(\mu+\frac{\mu_T}{\sigma_\varepsilon}\right)\nabla\varepsilon\right)=S_\varepsilon, \tag{22}$$

where:

$$\rho=\sum_{\alpha=0}^{N\rho} r_\alpha\rho_\alpha,\quad U=\frac{1}{\rho}\left(\sum_{\alpha=0}^{N_\rho} r_\alpha\rho_\alpha U_\alpha\right),\quad \mu_T=\sum_{\alpha=0}^{N\rho} r_\alpha\mu_{T\alpha} \tag{23}$$

$$S_\kappa=\sum_{\alpha=0}^{N\rho} r_\alpha S_{\kappa\alpha},\quad S_\varepsilon=\sum_{\alpha=0}^{N_\rho} r_\alpha S_{\varepsilon\alpha}.$$

Results and Discussion

In order to predict the fluid dynamical characteristics of a cascade under two-phase flow conditions with a view to improving its performance, numerical results were obtained for an axial rotor, named 5X, which is a NACA 65 profile, with $C_z=0.288$, $er=1.52$ and $\gamma=80$ deg, as it is shown in Fig. 1.

Four different meshes were developed (5X-α, β, γ, and δ) until the final mesh (5X-Ω) was obtained, in order to ensure mesh independence. This mesh (5X-Ω), with 19200 elements and 28500 nodes (see Fig. 2) was the grid that allows us to obtain a residual mass less than 1.0E-04. The simulation was made in a PC Pentium II 266 MHz.

The numerical results for two-phase flow at low gas fraction GVF over a profile cascade for high stagger angles show an important effect of the gas fraction GVF over the lift and loss coefficients of the profile.

The lift coefficient C_L diminished as the gas fraction GVF augments; in the same order the drag coefficients C_D augments considerably. The influence of the gas fraction is more important for the attack angles α_1 over 82 deg. For angles of attack less than 80 deg there is not effect observed, as is shown in Figs. 3 and 4.

The lift and loss coefficients, C_L and ξ_2, respectively, are strongly influenced for the gas fraction GVF and high angles of attack, but for low angles of attack, in the entire range of gas fraction GVF, there is not an important influence as is shown in Figs. 5 and 6.

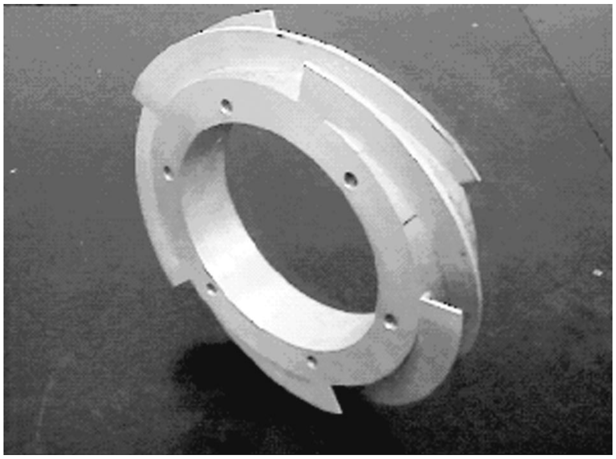

Fig. 1 General view of helico-axial rotor 5X

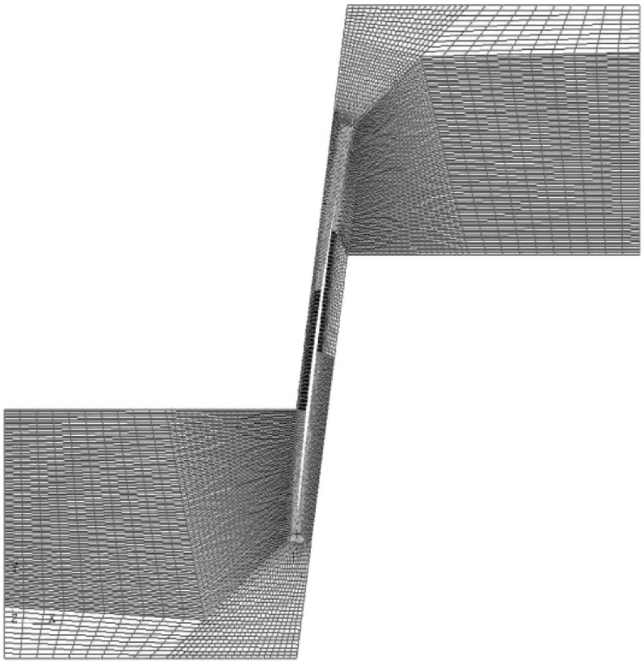

Fig. 2 Final mesh (5X-Ω) (19200 elements and 28500 nodes)

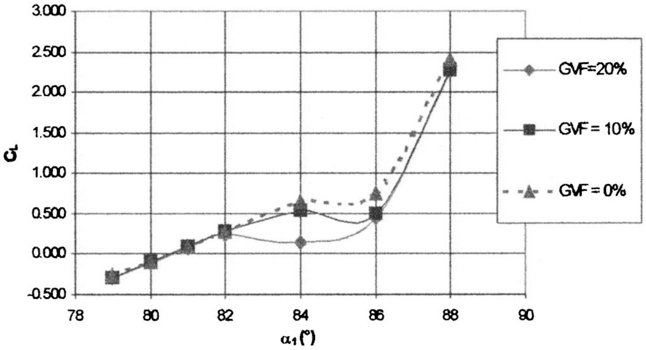

Fig. 3 Lift coefficient as a function of angle of attack for different GVF

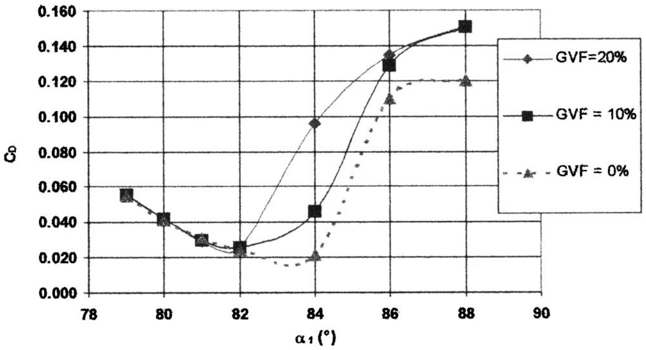

Fig. 4 Drag coefficient as a function of angle of attack angle for different GVF

The numerical results for $\alpha_1=79$ deg and GVF=20 percent show a gas pocket on the lower side and close to the leading edge of the profile (Fig. 7). On Fig. 8 it is observed experimentally, the gas and liquid distribution predicted by the numerical results at the same conditions. It is important to comment about the presence of a gas pocket on the lower side and close to the leading edge and the existence of a liquid pocket on the upper side.

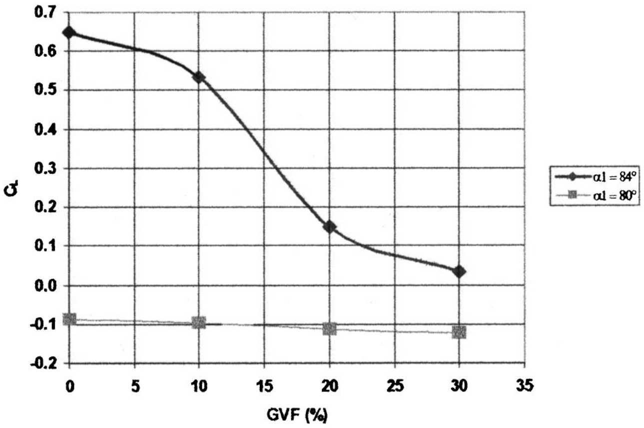

Fig. 5 Lift coefficient as a function of gas fraction GVF for different angles of attack

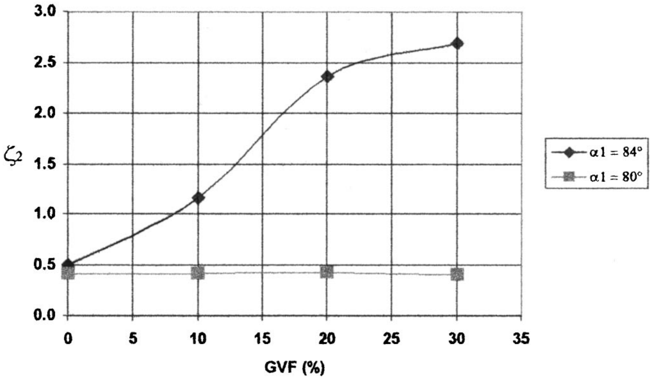

Fig. 6 Loss coefficient as a function of gas fraction GVF for different angles of attack

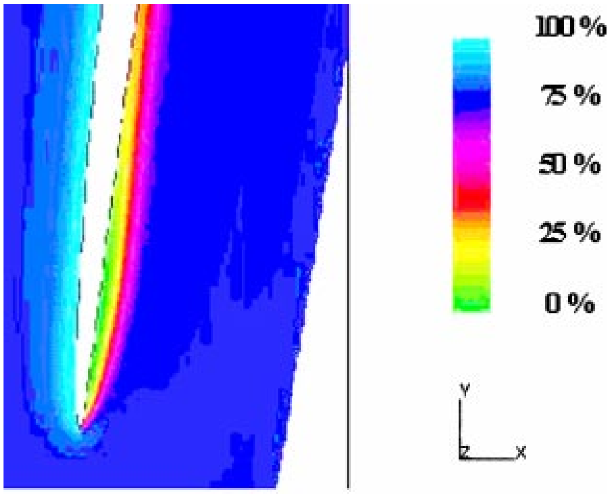

Fig. 7 Concentration of liquid (percent) at leading edge for $\alpha_1 = 79$ deg and GVF = 20 percent

For the same gas fraction GVF and bigger angle of attack α_1 the pocket is developed over a greater surface. For an angle of attack like $\alpha_1 = 84$ deg the gas pocket coats the entire lower side and we observe a stratified flow on the blade passage. (Fig. 9). Figure 10 reproduces experimentally the numerical results observed on Fig. 9. Here the gas pocket coats the entire surface of the lower side, as the liquid coats the upper side.

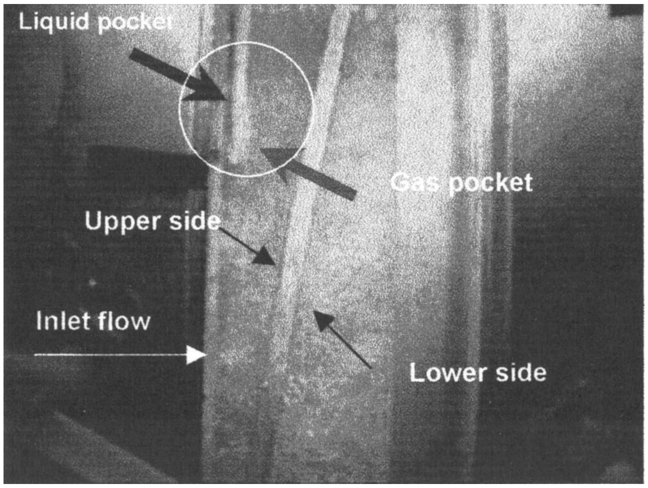

Fig. 8 Gas and liquid distribution for $\alpha_1 = 79$ deg and GVF = 20 percent

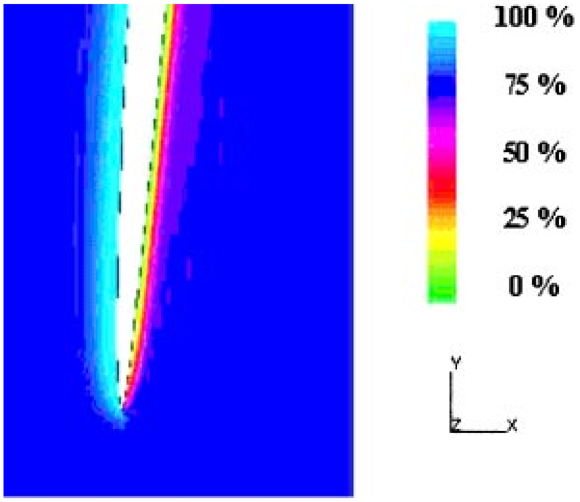

Fig. 9 Concentration of liquid (percent) at leading edge for $\alpha_1 = 84$ deg and GVF = 20 percent

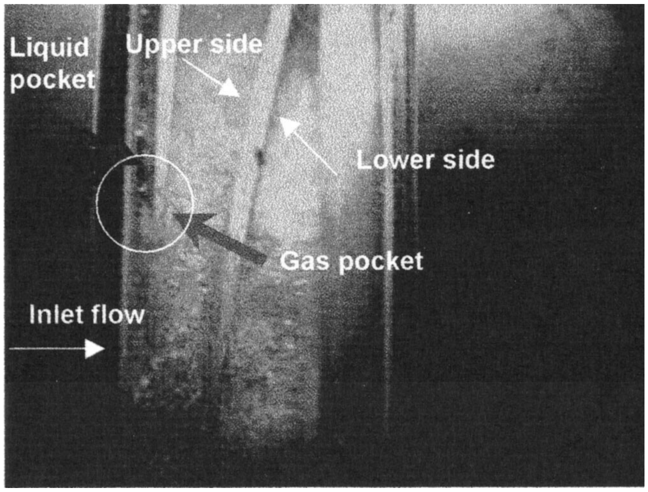

Fig. 10 Gas and liquid distribution for $\alpha_1 = 84$ deg and GVF = 20 percent

This stratified flow explains the augmenting of loss coefficient and the diminishing of lift coefficient for bigger angles of attack. While the phases are separated, the friction loss augmented in the presence of a gas-liquid interface, as we can see in Fig. 5 and 6.

Conclusions

In order to predict the characteristics of axial pumps on two-phase flow this work describes a multifluid model (for low gas fraction) that allows us to resolve numerically the momentum equation for an axial rotor, considering the viscosity of the fluid and the gas compressibility.

The final mesh ($5X$-Ω) (19200 elements and 28500 nodes) allows us to obtain the best approximation with a PC Pentium II 266 MHz.

For a cascade of profile NACA 65 with great stagger angles, the numerical results show the important effect of gas fraction GVF over lift, drag, and loss coefficient, C_L, C_D, and ξ_2, respectively. Also shown is the presence of gas pockets on the lower side. These gas pockets augment their dimensions when the angle of attack is increased.

The experimental results show good agreement with the numerical results and confirm the existence of the gas pockets and the stratified flow in the blade passage.

Acknowledgments

The authors would like to thank the Embassy of France in Venezuela and the National Council of Scientific and Technological Research of Venezuela (CONICIT) for their financial support of this research.

Nomenclature

α = phase
α_1 = angle of attack
β = phase
γ = phase, stagger angle
ρ = density
Φ = function
ξ_2 = profile losses coefficient
κ = turbulence kinetics energy
ε = energy dissipation rate
σ_α = turbulent Prandtl number
Γ = diffusivity
μ = Viscosity
B = body force
c = concentration
C = inter-phase transfer term
C_L = lift coefficient
C_D = drag coefficient
C_μ = constant in eddy viscosity formula
$C_{\mu b}$ = constant in Sato particle induced turbulence model
C_z = lift coefficient of isolated airfoil
d = bubble diameter
er = relative thickness
F = inter-phase non-drag force
m = mass flowrate
N_β = number of phases
p = pressure
r = volume fraction
S = source term
T = temperature
U = velocity
V = velocity
W = velocity

Subscripts

α = relative to phase
$\alpha\beta$ = phase α from phase β
κ = relative to turbulence kinetics energy
ε = relative to energy dissipation rate
eff = effective
T = bubble induced turbulence

References

[1] Cooper, P., 1967, ''Analysis of Single and Two-Phase Flows in Turbopump Inducers,'' ASME J. Eng. Power, **89**, pp. 577–588.
[2] Murakami, M., and Minemura, K., 1974, ''Effect of Entrained Air on the Performance of the Centrifugal Pump,'' Bull. JSME, **17**, pp. 1047–1055.
[3] Murakami, M., and Minemura, K., 1974, ''Effect of Entrained Air on the Performance of the Centrifugal Pump,'' Bull. JSME, **17**, 2nd report, pp. 1286–1295.
[4] Muench, R. A., 1976, ''The Prediction of Pump Differential Pressure For Two Phase/Two Component Compressible Flow,'' ASME Paper No. 76-WA/HT-75.
[5] Rohatgi, U. S., 1978, ''Pump Model for Two-Phase Transient Flow,'' ASME Winter Meeting, San Francisco.
[6] Heidrick, T. R., Hancox, W. T., and Nguyen, D., 1978, ''Centrifugal Pump Behavior in Steady and Transient Steam-Water Flows,'' ASME Winter Meeting, San Francisco, pp. 115–121.
[7] Grison, P., and Lauro, J. F., 1978, ''Experimental and Theoretical Investigations About Two-Phase Critical Flow Through a Pump,'' ASME Winter Meeting, San Francisco.
[8] Mikielewicz, J., Gordon Wilson, D., Chan, T., and Goldfinch, A., 1978, ''A Method for Correlating the Characteristics of Centrifugal Pumping Two-Phase flow,'' ASME J. Fluids Eng., **100**, pp. 395–409.
[9] Wilson, D. G., 1979, ''Analytical Models and Experimental Studies of Centrifugal Pump Performance in Two-Phase Flow,'' EPRI report NP-677.
[10] Minemura, K., Murakami, M., and Katagiri, H., 1985, ''Characteristics of Centrifugal Pumps Handling Air-Water Mixtures and Size of Air Bubbles in Pump Impellers,'' Bull. JSME, **28**, pp. 2310–2318.
[11] Nilsson, K. A., 1977, ''LWR Recirculation Pump Performance under Two-Phase Flow Conditions,'' Proceedings Cavitation & Polyphase Flow Forum ASME, Vol. 1, pp. 39–45.
[12] Minato, A., 1988, ''Analysis of Heat and Torque of Centrifugal Pumps in Two-Phase Flow,'' Journal of Atomic Energy Society of Japan, **30**, pp. 633–642.
[13] De Donno, S., 1985, ''The S.B.S. Project-Development of a Subsea Booster System for the Exploitation of Deep Water Oil Fields,'' Proceedings of 5th Deep Offshore Technology, Houston, pp. B2-d49-d69.
[14] Furuya, O., 1985, ''An Analytical Model for Prediction of Two-Phase (Non-condensable) Flow Pump Performance,'' ASME J. Fluids Eng., **107**, pp. 139–147.
[15] Furuya, O., and Maekawa, S., 1987, ''An Analytical Model for Pump Performance in Condensable Two-Phase Flows,'' EPRI NP-5529M.
[16] Calvin, E. S., 1992, ''Incorporation and Evaluation of a Generalized Two-Phase Degradation Model for Centrifugal Pumps in the RELAP5 Code,'' Proceedings 5th International Topical Meeting on Reactor Thermal Hydraulics, Vol. 2, pp. 308–313.
[17] Noghrehkar, G. R., Kawaji, M., Chan, A. M. C., Nakamura, H., and Kukita, Y., 1995, ''Investigation of Centrifugal Pump Performance Under Two-Phase Flow Conditions,'' ASME J. Fluids Eng., **117**, pp. 129–137.
[18] Nishiyama, H, 1989, ''Flow Analysis of a Centrifugal Impeller in Bubbly Water Using Field Singularity Method,'' Proceedings of the 10th Australasian Fluid Mechanics Conference, Sydney, pp. 14.37–40.
[19] Minemura, K., and Uchiyama, T., 1993, ''Three-Dimensional Calculation of Air-Water Two-Phase Flow in Centrifugal Pump Impeller Based on a Bubbly Flow Model,'' ASME J. Fluids Eng., **115**, pp. 766–771.
[20] Minemura, K., and Uchiyama, T., 1994, ''Three-dimensional Calculation of Air-Water Two-Phase Flow in Centrifugal Pump based on a Bubbly Flow Model with Fixed Cavity,'' JSME International Journal Series B, **37**, pp. 726–735.
[21] Weiss, P., Rey, R., Noguera, R., and Bakir, F., 1994, ''Two-Phase Flow in Pumps,'' The Second Symposium on Cavitation, Vol. 3, pp. 427–432.
[22] Weiss, P., Rey, R., and Noguera, R., 1995, ''Pumping Problems when Conveying Two-Phase Mixtures—Experiments and Modeling,'' Proceedings of the Third Caribbean Congress on Fluid Dynamics and of the third Latin-American Symposium on Fluid Mechanics, Caracas, Vol. 2, pp. 243–248.
[23] Weiss, P., Rey, R., and Noguera, R., 1995, ''Experiments and Modeling in pumping Two Phase mixture,'' Proceedings of the 6th Asian Congress of Fluid Mechanics, Singapore.
[24] Fujie, H., 1985, ''A Study on Performance of Centrifugal Pumps Driven in Two Phase Flow,'' Trans. JSME, **51**, pp. 3754–3759.
[25] Van Den Hove, P., and Geffraye, G., 1992, ''The CATHARE Code one-dimensional Pump Method,'' Proceedings 5th International Topical Meeting on Reactor Thermal Hydraulics, pp. 1129–1137.
[26] Minemura, K., Uchiyama, T., Shoda, S., and Egashira, K., 1998, ''Prediction of Air-Water Two-Phase Flow Performance of a Centrifugal Pump Based on one-dimensional Two-Fluid Model,'' ASME J. Fluids Eng., **120**, pp. 327–334.
[27] Spalding, D. B., 1983, ''Developments in the IPSA Procedure for Numerical Computation of Multiphase Flow Phenomena with Inter-Phase Slip,'' *Numerical Properties and Methodologies in Heat Transfer*, Hemisphere, London, pp. 421–436.

Richard B. Medvitz
e-mail: rbm120@psu.edu

Robert F. Kunz

David A. Boger

Jules W. Lindau

Adam M. Yocum

Applied Research Laboratory,
The Pennsylvania State University,
University Park, PA 16804

Laura L. Pauley
Department of Mechanical Engineering,
The Pennsylvania State University,
University Park, PA 16802

Performance Analysis of Cavitating Flow in Centrifugal Pumps Using Multiphase CFD

A multi-phase CFD method is used to analyze centrifugal pump performance under developed cavitating conditions. The differential model employed is the homogeneous two-phase Reynolds-Averaged-Navier-Stokes equations, wherein mixture momentum and volume continuity equations are solved along with vapor volume fraction continuity. Mass transfer modeling is provided for the phase change associated with sheet cavitation. Using quasi-3D (Q3D) analysis, steady and time-dependent analyses were performed across a wide range of flow coefficients and cavitation numbers. Characteristic performance trends associated with off-design flow and blade cavitation are observed. The rapid drop in head coefficient at low cavitation numbers (breakdown) is captured for all flow coefficients. Local flow field solution plots elucidate the principal physical mechanisms associated with the onset of breakdown. [DOI: 10.1115/1.1457453]

Introduction

Cavitation physics play an important role in the design and operation of many liquid handling turbomachines. In particular, cavitation can give rise to erosion damage, noise, vibration and hydraulic performance deterioration. Accordingly, a large body of research has been performed toward understanding the physics of, designing away from, and designing to accommodate the effects of cavitation.

In many pump applications, large scale developed, or ''sheet'' cavities form on the blade and endwall surfaces when the pump operates off design flow or at low system pressure. In addition to erosion and noise implications, if these cavities become large, they exhibit significant unsteadiness and can vary significantly in extent from blade to blade. These effects conspire to generate potentially damaging vibration due to nonuniform loading around the annulus. Additionally, for low enough cavitation numbers, hydraulic efficiency, flow coefficient and head coefficient can decrease. Ultimately, cavitation breakdown can occur as characterized by a very rapid decrease in impeller head rise coefficient. For these reasons, it is of interest to the pump designer to be able to model large scale cavitation.

Potential flow methods have been employed for decades to model large cavities in a variety of liquid flow systems including pumps. These methods treat the fluid flow outside the bubble as potential flow, while the shape and size of the bubble itself are determined from dynamic equilibrium assumptions across the bubble-liquid interface, with bubble shape family and/or closure conditions also provided. Adaptations of such methods remain in widespread use today due to their inherent computational efficiency, and their proven effectiveness in predicting numerous first order dynamics of sheet- and super-supercavitating configurations, but they retain the limitations of a potential flow model applied to a flow with complex bubble geometries and inherent vortical structures. Recently, more general CFD approaches have been developed to analyze these flows. In the pump application area, Hirschi et al. [1] employed a single-phase RANS methodology wherein the cavity boundary is treated as a constant pressure slip surface, with the cavity geometry defined from bubble dynamics and closure condition modeling. In the past several years several research groups ([2–5], for example) as well as commercial CFD vendors, have introduced large scale cavitation models (for pumps and other applications) wherein the entire flow path is treated using the same differential model, with phase change incorporated to account for the generation and condensation of the cavitation bubble. This is the approach taken here.

In particular, the authors have recently developed a multiphase CFD methodology with applications focused on sheet- and supercavitating flows about underwater vehicles [6–9]. As this capability has been matured and validated for that class of applications, we have begun to pursue developed cavitation in turbomachinery. This paper summarizes our capabilities and results in this area to date.

The paper is organized as follows: The theoretical formulation of the method is briefly summarized, including baseline differential model, specific physical models and numerical methods. The results of the Q3D analyses for a 7-blade impeller operating across a range of flow coefficients and cavitation numbers are then presented.

Theoretical Formulation

Governing Equations and Physical Modeling. A two-phase differential formulation is adopted where individual equations are provided for the transport, generation, and destruction of volume fraction of liquid (which can exchange mass with vapor), and the mixture volume. A mixture momentum equation is also provided. The governing differential equations, cast in Cartesian tensor form, in a frame of reference rotating with constant angular velocity, ω_i, are given as:

$$\left(\frac{1}{\rho_m\beta}\right)\frac{\partial p}{\partial\tau}+\frac{\partial u_j}{\partial x_j}=(m^{\cdot +}+m^{\cdot -})\left(\frac{1}{\rho_l}-\frac{1}{\rho_v}\right)$$

$$\frac{\partial}{\partial t}(\rho_m u_i)+\frac{\partial}{\partial\tau}(\rho_m u_i)+\frac{\partial}{\partial x_j}(\rho_m u_i u_j)$$

$$=-\frac{\partial p}{\partial x_i}+\frac{\partial}{\partial x_j}\left(\mu_{m,t}\left[\frac{\partial u_i}{\partial x_j}+\frac{\partial u_j}{\partial x_i}\right]\right)$$

$$-\rho_m\varepsilon_{ijk}\omega_j\varepsilon_{klm}\omega_l x_m-\rho_m 2\varepsilon_{ijk}\omega_j u_k \qquad (1)$$

$$\frac{\partial\alpha_l}{\partial t}+\left(\frac{\alpha_l}{\rho_m\beta^2}\right)\frac{\partial p}{\partial\tau}+\frac{\partial\alpha_l}{\partial\tau}+\frac{\partial}{\partial x_j}(\alpha_l u_j)=\left(\frac{\dot{m}^{+}}{\rho_l}+\frac{\dot{m}^{-}}{\rho_l}\right)$$

Contributed by the Fluids Engineering Division for publication in the JOURNAL OF FLUIDS ENGINEERING. Manuscript received by the Fluids Engineering Division March 27, 2001; revised manuscript received October 16, 2001. Associate Editor: Y. Tsujimoto.

where mixture density and turbulent viscosity are defined by:

$$\rho_m = \rho_l \alpha_l + \rho_v \alpha_v , \quad \mu_{m,t} = \frac{\rho_m C_\mu k^2}{\varepsilon} \tag{2}$$

In the present work, the density of each constituent is taken as constant. This approximation neglects the potentially significant decrease in mixture sound speed in homogeneous mixtures, which is well known to give rise to compressibility effects associated with cavitation damage. The authors have pursued compressible flow analysis in some of our other multiphase work [11], and our experience is that the global dynamics of these effects (i.e., as would manifest in bulk performance parameters) is not significantly affected.

Equations (1) represent transport/generation of mixture volume, mixture momentum, and liquid phase volume fraction, respectively. Physical time derivatives are included for transient computations. The formulation incorporates preconditioned *pseudo*-time-derivatives ($\partial/\partial\tau$ terms), defined by parameter β. As discussed in [11], this parameter ($\beta/V_{\mathrm{ref}} \cong 50$ in the present studies) characterizes the propagation speed of errors at each physical time step and scales the artificial dissipation inherent in convection term discretization.

The formation and collapse of a cavity is modeled as a phase transformation. Mass transfer is modeled as finite rate interfacial processes:

$$\dot{m}^- = \frac{C_{dest} \rho_l \alpha_l MIN[0, p - p_v]}{(1/2 \rho_l U_\infty^2) t_\infty}$$

$$\dot{m}^+ = \frac{C_{prod} \rho_l \alpha_l^2 (1 - \alpha_l)}{t_\infty} \tag{3}$$

where $\dot{m}^+$ and $\dot{m}^-$ represent evaporation and condensation, respectively. C_{dest} and C_{prod} are model constants ($C_{\mathrm{dest}} = 100$, $C_{\mathrm{prod}} = 1000$) obtained through experience and validation studies summarized in [6,9]. A high Reynolds number form k-ε model with standard wall functions is implemented to provide turbulence closure. This model and most others have well-documented difficulties with stagnated, high strain and recirculating flows, all of which are embodied in large sheet cavity flows. Our efforts in employing several alternative approaches that have appeared in the literature remain an ongoing research activity, beyond the scope of the present paper, but summarized in some more detail in [6]. Further details on the physical modeling are provided in [6,8].

Numerical Method. The numerical method is evolved from the work of Taylor and his coworkers ([10], for example). The UNCLE code, which served as the baseline platform for the present work, is based on a single phase, finite volume, pseudocompressibility formulation. Third-order Roe-based flux difference splitting is utilized for convection term discretization. An implicit procedure is adopted with inviscid and viscous flux Jacobians approximated numerically. A block-symmetric Gauss-Seidel iteration is employed to solve the approximate Newton system at each pseudo-timestep.

The multiphase extension of the code, designated UNCLE-M, retains these underlying numerics but incorporates additional volume fraction transport and mass transfer, nondiagonal preconditioning, and flux limiting. A temporally second-order accurate dual-time scheme is implemented for physical transients. The turbulence transport equations are solved subsequent to the mean flow equations at each pseudo-time step. The multiblock code is instrumented with MPI for parallel execution based on domain decomposition. Further details on the numerical method and code are available in [7].

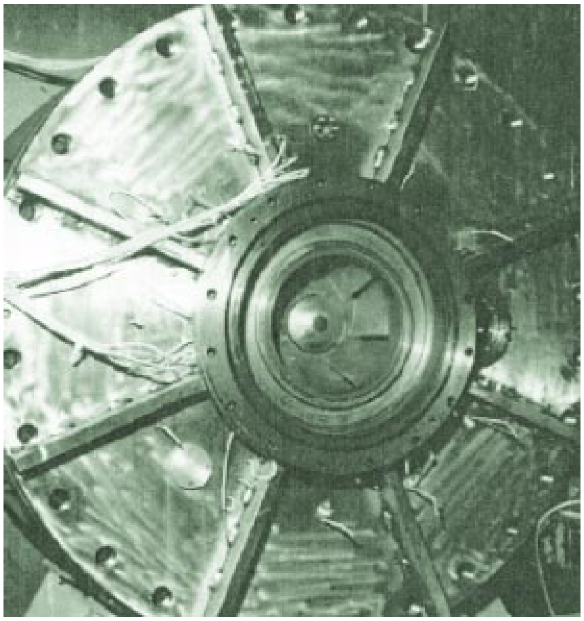

Fig. 1 Photograph of 7-blade impeller during installation in the pump loop facility. Machine rotation is clockwise.

Previous Applications, Validation Status and Analysis Requirements

UNCLE-M has been extensively used and validated for natural and ventilated sheet- and super-cavitation about external flow configurations. Of particular relevance here is that the code has been shown to predict bubble size parameters, drag, and vapor/vorticity shedding characteristics for natural cavitation about numerous axisymmetric configurations with good accuracy [6–9].

Also important is our finding that such analyses require significantly higher discretization fidelity compared to single phase analyses. Specifically, finer wall normal and streamwise grid resolution, as well as higher order flux discretization (with attendant flux limiting) are required. Failure to accommodate these requirements results in: 1) a smearing of the vapor-liquid interface, especially near the aft end of the bubble (re-entrant flow region), 2) too small a cavity for a given cavitation number, and 3) steady-state results instead of the physically observed rich unsteady behavior (again, in particular, in the cavity re-entrant region).

Quasi-3D Analysis

The ultimate goal of this research is to establish a validated three-dimensional capability for the prediction of cavitation in pumps. As discussed above, accurate analysis requires significant grid resolution, accurate numerics, and often a time-accurate solution strategy. Therefore, as we evolve our capability in this area, we have first pursued Q3D modeling wherein a nominal midspan blade-to-blade streamsheet is analyzed. This level of modeling has been widely used in turbomachinery design and analysis for centrifugal machines ([11,12], for example). In centrifugal pumps, quantitative efficiency and off-design head performance cannot be captured with high accuracy since 3D effects including secondary flows are not incorporated. However, Q3D methods are usefully and widely employed in design and assessment studies.

The fully-three-dimensional relative frame code is adapted to perform Q3D analysis as follows: A throughflow design code developed by the fifth author is used to determine meridional streamsheets through the pump. Two nominally midspan streamsheets are extracted and imported into GRIDGEN [13]. The intersection of these streamsheets and the 3-D blade is determined

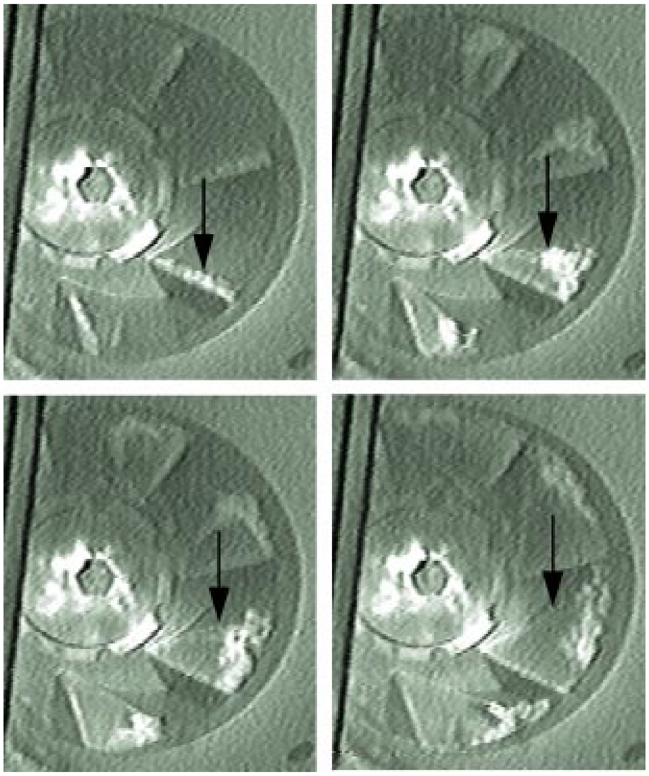

Fig. 2 Video frames of 7-blade impeller during design flow coefficient operation at successively lower cavitation numbers. Approximate midspan cavity trailing edge location is indicated. Machine rotation is clockwise.

within GRIDGEN and a structured multiblock grid is built bounded by the streamsheets and the blade intersection boundaries. An O-block is wrapped around the blade and multiple H-blocks are employed to retain good grid orthogonality and load balancing.

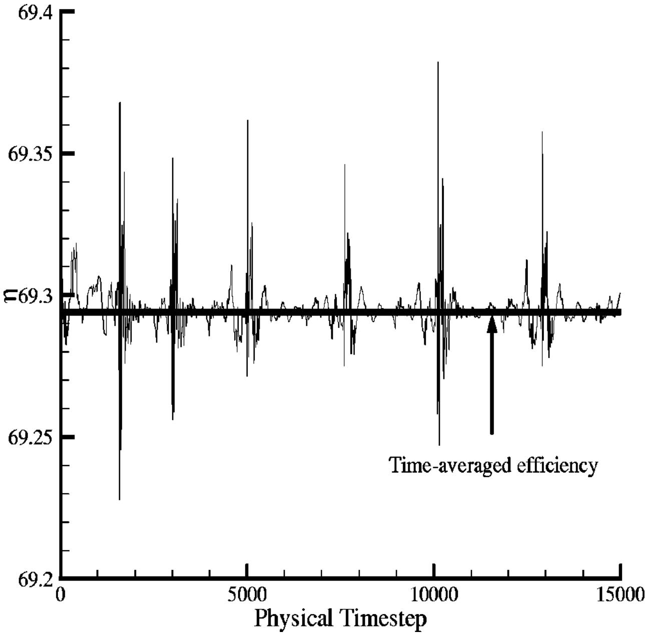

Fig. 3 Efficiency versus physical timestep for transient analysis, $\phi/\phi_{\text{design}}=1.0$, $\sigma=0.200$, $\Delta t/t_{\infty}=0.002$, $\bar{\eta}=69.29$

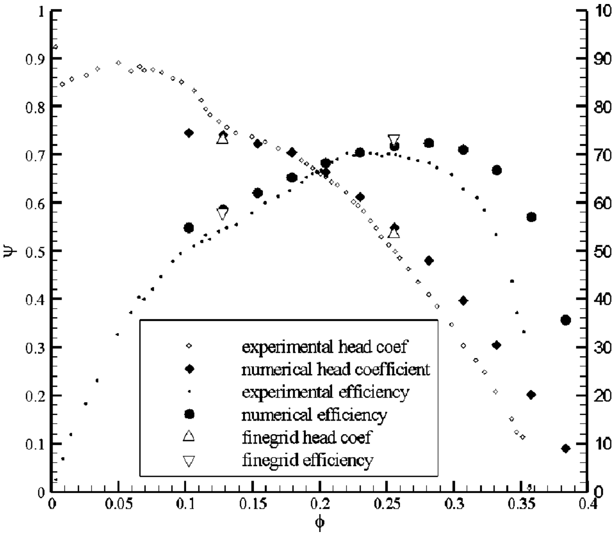

Fig. 4 Comparison of experimental and computational head coefficient and efficiency versus flow coefficient. Data plotted for both fine and coarse grids

Two layers of cells are used in the spanwise direction (i.e., three vertex planes) so that second order accuracy can be retained for convection fluxes. A slip surface boundary condition is imposed on the upper and lower surfaces of the computational domain. Since these surfaces are defined as streamsheets, transport fluxes across these boundaries are set to zero and pressure on these boundaries is determined explicitly from a discrete approximation to the momentum equation dotted into the stream sheet surface

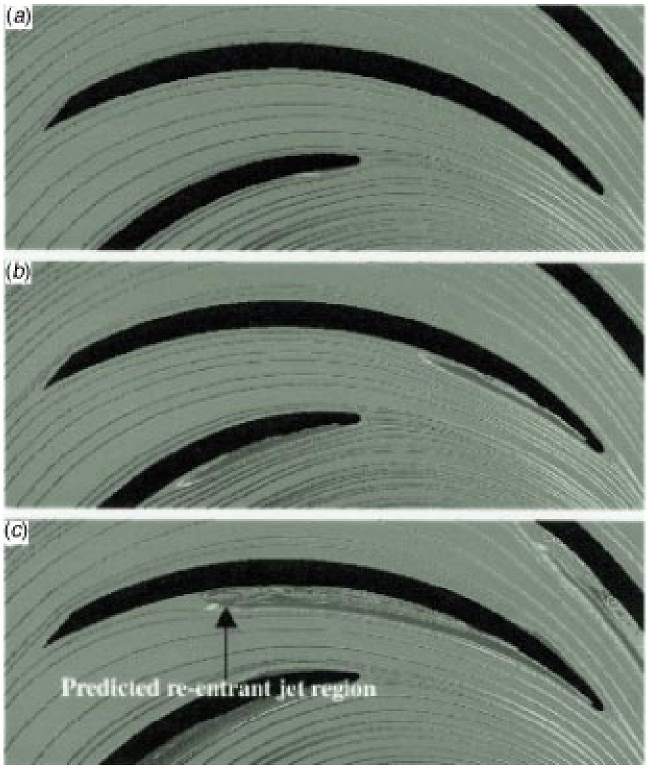

Fig. 5 Streamlines and contours of volume fraction for $\phi/\phi_{\text{design}}=0.8$. (a) $\sigma=0.547$, (b) $\sigma=0.238$, (c) $\sigma=0.154$. Re-entrant jet regions indicated with arrows. Machine rotation is clockwise.

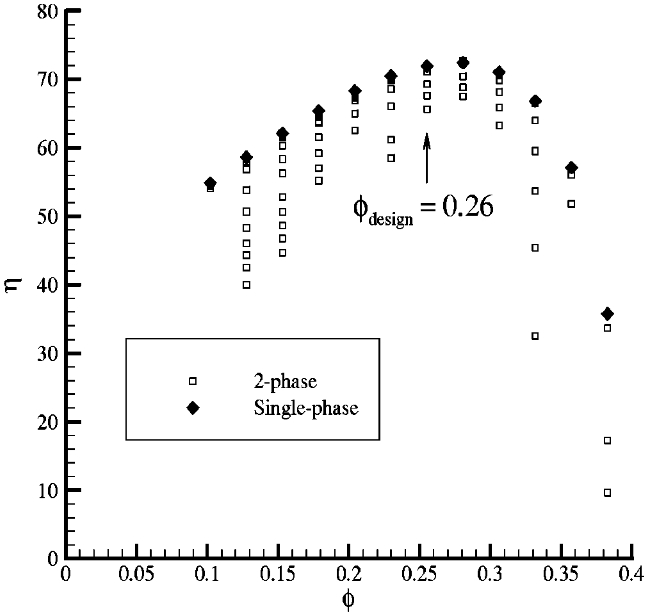

Fig. 6 Predicted efficiency versus flow coefficient for single-phase and multi-phase analyses

normal. At the inflow boundary, velocity components are fixed, with pressure extrapolated from the interior of the computational domain. At the outflow boundary velocity components are extrapolated, with pressure fixed at an arbitrary value of 0. Periodic boundaries are employed along the low and high tangential surfaces. Zero relative velocity slip is imposed on blade surface boundaries, with pressure extrapolated from the cell adjacent to the wall.

For the single passage Q3D analyses presented in this paper, an 8 block, 36,288 vertex mesh was employed (12,096 vertices on each of the three spanwise planes). The calculations were carried out on several different computer systems using 8 processors in each case.

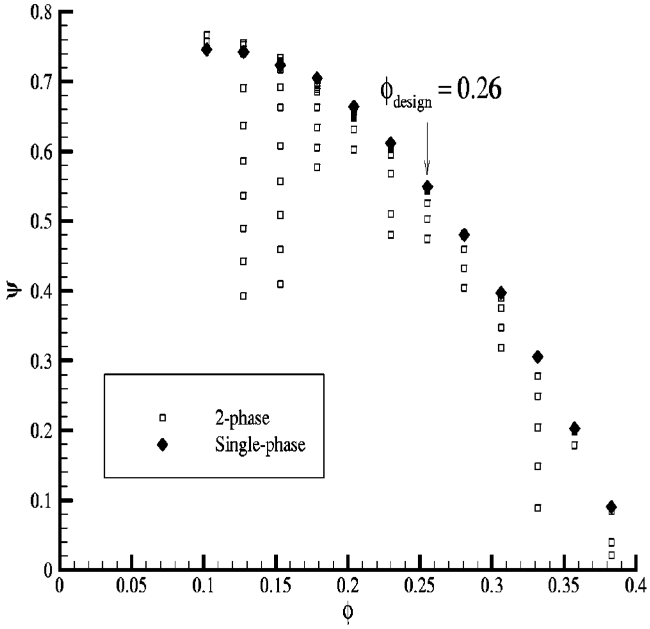

Fig. 7 Predicted head coefficient versus flow coefficient for single-phase and multiphase analyses

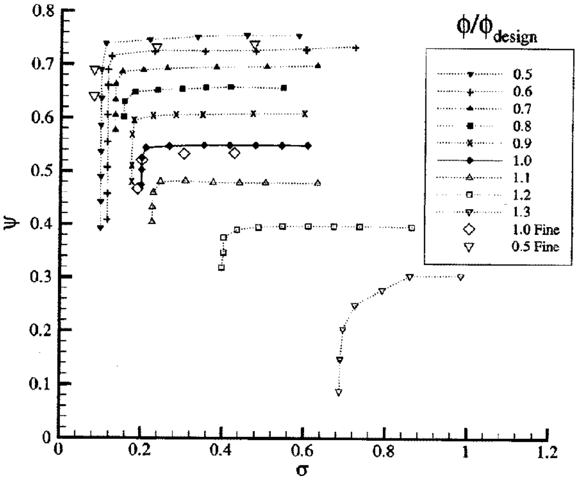

Fig. 8 Predicted head coefficient versus cavitation number for various nondimensional flow coefficients. Data plotted for both fine and coarse grids.

Test Case Considered

The pump analyzed was tested at the Pennsylvania State University Applied Research Laboratory, in the 12 in. water tunnel reconfigured as a pump test facility [14]. The performance of a backswept 7-blade impeller was tested at a variety of single phase and cavitating operating conditions. A photograph of the 7-blade impeller analyzed computationally here, is illustrated in the pump loop during installation in Fig. 1.

Figure 2 shows several video frames of this impeller operating at design flow coefficient, at successively lower cavitation numbers (optical access obtained through a prism mounted externally on viewing windows upstream of impeller). Clearly identified in these figures is a growing sheet cavity on the suction surface, that increases in length with span and extends onto the shroud. The approximate locations of the cavity trailing edge at midspan are indicated in the figure.

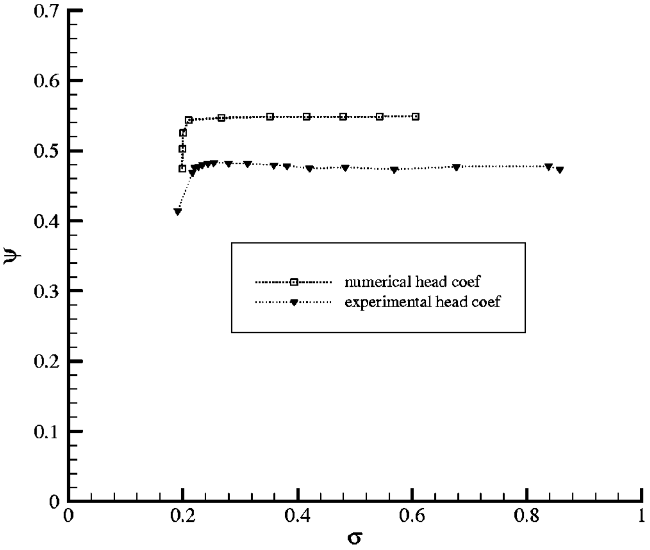

Fig. 9 Numerical results versus experimental results of head coefficient versus cavitation number at design flow coefficient

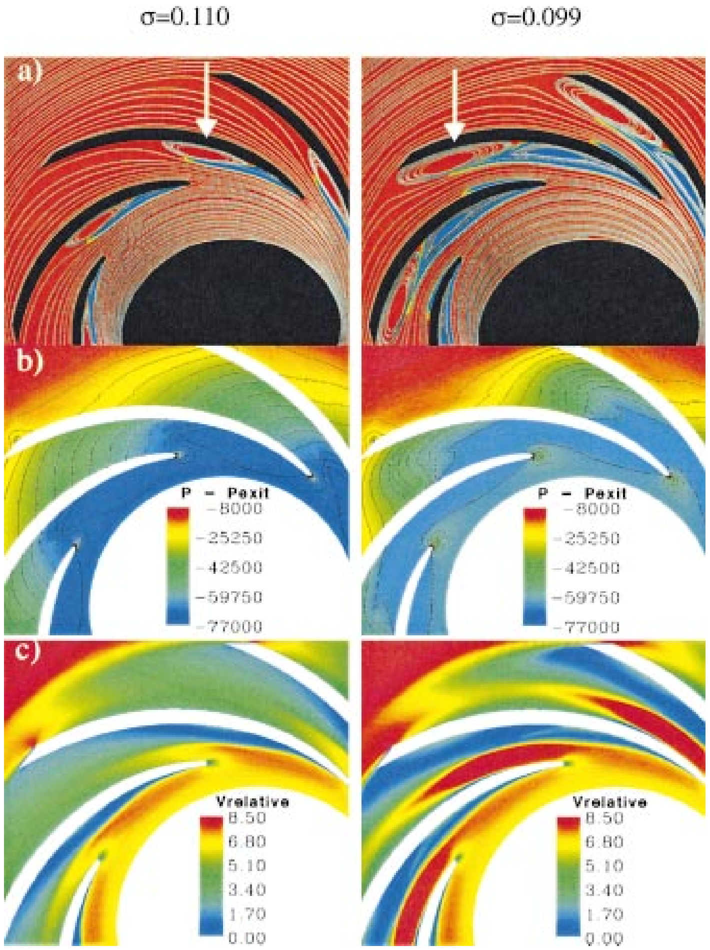

Fig. 10 Predicted instantaneous field variables for $\phi/\phi_{\text{design}}=0.5$, $\sigma=0.110$ and 0.099. (a) Volume fraction contours and streamlines, (b) pressure contours, (c) relative velocity magnitude contours. Re-entrant jet regions indicated with arrows. Machine rotation is clockwise.

Results and Discussion

Quasi-Three-Dimensional Results. A total of 97 Q3D runs were performed covering operating conditions which span $0.4 \leq \phi/\phi_{\text{design}} \leq 1.5$, $0.099 \leq \sigma \leq 1.512$. Steady-state solutions were obtained for most of the cases, but for cases run at low cavitation number and/or low flow coefficient, large sheet cavities develop and large scale unsteadiness is predicted near the aft end of these structures (re-entrant jet region). For these cases, the steady-state runs do not converge but are used to initialize a time accurate simulation. In these cases, reported performance parameters are time-averaged quantities as illustrated in Fig. 3. There, predicted efficiency is plotted versus physical timestep for a time-accurate analysis, $\phi/\phi_{\text{design}}=1.0$, $\sigma=0.200$, $\Delta t/t_\infty=0.002$. The time averaged efficiency, $\eta=69.29$, is also indicated.

In what follows, four parameters are used to define the operating point and performance of the pump. These are the cavitation number, flow coefficient, head coefficient and efficiency, which are defined here as:

$$\sigma \equiv (p_\infty - p_v)/\tfrac{1}{2}\rho_l V_{ref}^2 \tag{4}$$

$$\phi \equiv V_{x,inlet}/U_{tip} \tag{5}$$

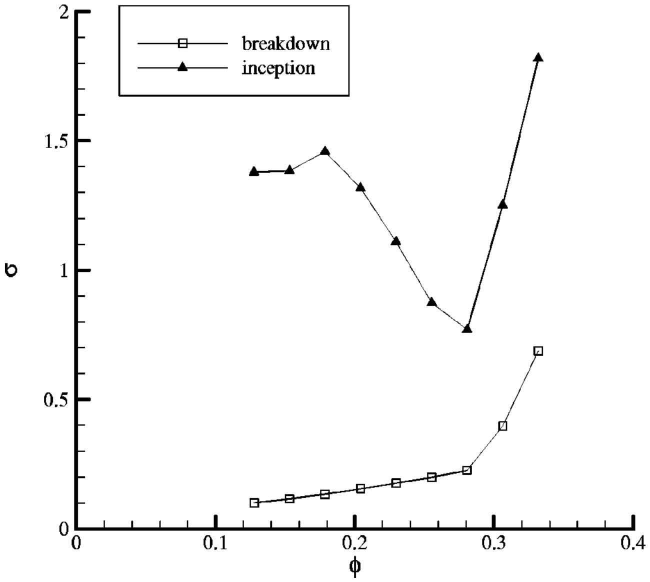

Fig. 11 Predicted cavitation inception and breakdown points versus flow coefficient

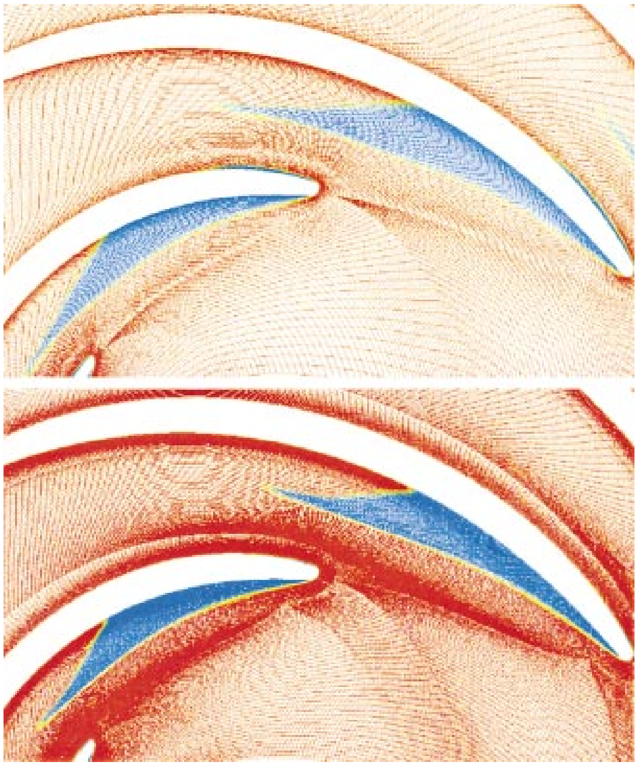

Fig. 12 36,288 and 129,465 vertex meshes employed for grid refinement studies. Predicted cavitation bubbles represented as contours of liquid volume fraction for $\sigma=0.82$, $\phi=0.50$.

$$\psi\equiv\left[\left(\frac{\int p(\vec{v}\cdot d\vec{A})}{\int(\vec{v}\cdot d\vec{A})}\right)_{outlet}-\left(\frac{\int p(\vec{v}\cdot d\vec{A})}{\int(\vec{v}\cdot d\vec{A})}\right)_{inlet}\right]\Big/\ \rho_l U_{tip}^2 \qquad (6)$$

$$\eta=\frac{(\int p(\vec{v}\cdot d\vec{A}))_{outlet}-(\int p(\vec{v}\cdot d\vec{A}))_{inlet}}{\vec{\omega}\cdot\vec{T}} \qquad (7)$$

where $(\vec{v}\cdot d\vec{A})$ is the mass flux through nominal impeller inlet and outlet computational planes and $\vec{T}$ is the total torque exerted on the fluid by the blade through pressure and viscous forces. The reference pressure, p_∞, is taken as that measured or computed upstream of the impeller in the entrance pipe section of the pump loop. (Note that static pressure is used in the head and efficiency definitions to conform to experimental measurements.) For all of the computations carried out here, the flow coefficient is specified, that is, inlet velocity and machine rotation rate are input parameters. The implications of this on cavitation breakdown predictions is discussed below.

In Fig. 4, single phase experimental and computational performance curves are presented for the impeller. Despite the Q3D nature of the analysis and the attendant difficulty in defining consistent pressure values between experiment and computation, predicted head coefficient and efficiency versus flow coefficient compare reasonably well.

Figure 5 illustrates the general nature of the multiphase Q3D analyses. There, predicted streamlines and volume fraction contours are plotted for $\phi/\phi_{\text{design}}=0.8$, at three cavitation numbers, $\sigma=0.547$, 0.238, and 0.154, which correspond to incipient, developed and near-breakdown cavitation numbers for this case. Clearly observed in these plots is the development of a cavitation bubble on the suction surface, which increases in size as the cavitation number is decreased. At low cavitation number, a re-entrant flow is observed near the cavity trailing edge, and some pressure surface cavitation is evident as well.

Figures 6 through 8 show predicted cavitating performance curves. In Fig. 6 hydraulic efficiency is plotted versus flow coefficient for a range of flow coefficients, $0.4\leq\phi/\phi_{\text{design}}\leq1.5$. For each flow coefficient, a single phase calculation was performed. The inception cavitation number is then computed from Eq. (4) setting p_v to the minimum single phase pressure on the blade. From there, the cavitation number, which is an input parameter to the code, is successively lowered and the code rerun (time accurately if required as discussed above). This process was repeated at each flow coefficient until significant performance degradation was observed. As seen in the figure, the CFD analysis returns efficiency levels of up to twenty points lower than for single phase.

In Fig. 7 head coefficient is plotted versus flow coefficient for the same range of flow coefficients and cavitation numbers. Again, very significant head deterioration is returned by the code for low cavitation numbers, especially at off-design flow. In order to interpret these results more clearly, the same data is plotted as head coefficient versus cavitation number in Fig. 8. There it is seen that for each operating flow coefficient a critical cavitation number is reached below which the head coefficient drops dramatically with further reduction in cavitation number. This figure exhibits the familiar appearance of cavitation breakdown trends. Figure 9 shows a comparison of experimental and computed head coefficient versus cavitation number at design flow coefficient. Though quantitatively overpredicting single phase head, due most likely to the Q3D nature of the analysis, the cavitation breakdown number and the ''suddenness'' of the drop-off is captured. From the qualitatively correct trends observed in Fig. 8 and the reasonable quantitative comparison observed in Fig. 9, it is concluded that the analysis is indeed capturing principal physical elements of cavitation breakdown.

To pursue this further we examine some local flow field solution plots. Figure 10 shows elements of two low flow ($\phi/\phi_{\text{design}}=0.5$) simulations with significant cavitation. In Fig. 10(*a*), instantaneous (i.e., at a time step) predicted streamlines and liquid volume fraction contours are presented for cavitation numbers of $\sigma=0.110$ and 0.099, which correspond to operating conditions just before and well into predicted cavitation breakdown ($\psi=0.739$ and 0.586, respectively, in Fig. 8). Just before breakdown a significant two-phase region is observed on the suction side, with an attendant large recirculation (re-entrant jet) at the aft end of the bubble. As the cavitation number is lowered only slightly more ($\Delta\sigma=0.011$), the bubble grows explosively, blocking more than half of the passage. Figures 10(*b*) and 10(*c*) illustrate the significant decrease in passage pressure rise and significant increase in local relative velocity magnitude associated with this near-choking condition.

Although these plots elucidate the principal physical mechanisms associated with the *onset* of cavitation breakdown, they should not be over-interpreted. In pumping systems, the operating point for the pump is defined by the intersection of the pump head-flow characteristic (which is a function of cavitation number) and the pump loop or pumping system characteristic (which is generally fixed). If the pump begins to cavitate significantly, both head rise *and flow rate* will drop. Well into breakdown, the resulting system dynamics can be highly unsteady, and these dynamics are not captured here since flow coefficient is a fixed parameter. In the future we plan to incorporate a quasi-steady analysis of the pump coupled with the system which should predict a change in the flow rate as well.

A final representation of the multiphase Q3D simulations is provided in Fig. 11. There, inception (defined for the mass transfer modeling employed here from Eq. (4) with p_v set to the minimum single phase pressure on the blade) and breakdown cavitation numbers are plotted versus flow coefficient. Again standard trends for these parameters are observed.

Assessment of Grid Resolution Effects. In order to ascertain the influence of discretization errors on the foregoing Q3D analyses, a grid refinement study was carried out for 8 selected operating points. Specifically, a new 8 block, 129,465 vertex mesh was employed (versus 36,288 previously). Figure 12 illustrates the predicted cavitation bubble for $\sigma=0.82$, $\phi=0.50$. The cavitation bubble size and shape are seen to be very similar for the two meshes. Figure 8 includes the head coefficient versus cavitation number for these eight additional fine grid simulations. The pump head rise coefficient and cavitation breakdown number are seen to be only very slightly influenced by the grid at this level of refinement.

Conclusion

A homogeneous multi-phase CFD method was applied to analyze centrifugal pump flow under developed cavitating conditions. Quasi-three-dimensional analysis was used to model a 7-blade pump impeller across a wide range of flow coefficients and cavitation numbers. Performance trends associated with off-design flow and blade cavitation, including breakdown, are observed that compare qualitatively with experimental measurements. Local flow field solution plots were presented that elucidate the principal physical mechanisms associated with the onset of breakdown.

As this work continues the authors are pursuing improvements to three elements of the method including: 1) adapting mass transfer models, Eq. (3), to accommodate thermal effects on cavitation breakdown, 2) implementing time-varying pressure and mass flow boundary conditions that accommodate pumping system dynamics and 3) maturing/validating fully three- dimensional capability.

Acknowledgments

The first author's thesis program was supported under an Exploratory and Foundational program scholarship at the Pennsylvania State University Applied Research Laboratory. This work was supported in part by a grant of HPC resources from the Arctic Region Supercomputing Center and in part by a grant of SGI Origin 2000 HPC time from the DoD HPC Center, Army Research Laboratory Major Shared Resource Center.

c = blade chord length
C_μ, C_{dest}, C_{prod} = turbulence and mass transfer model constants
k = turbulence kinetic energy
$\dot{m}^+ + \dot{m}^-$ = mass transfer rates
p = pressure
Re = Reynolds number
t, t_∞ = time, mean flow time scale (c/U_{tip})
$\vec{T}$ = total torque exerted by blade
U_{tip} = blade tip speed
u_i = Cartesian velocity components
V_{ref}^2 = reference velocity $(U_{tip}^2 + V_{x,inlet}^2)$
x_i = Cartesian coordinates
α = volume fraction
β = preconditioning parameter
$\varepsilon, \varepsilon_{ijk}$ = turbulence dissipation rate, permutation tensor
η = pump hydraulic efficiency
θ = angular coordinate
μ = molecular viscosity
ρ = density
σ = cavitation number
τ = pseudo-time
ϕ = flow coefficient
ψ = head coefficient
ω_i = machine angular velocity

Subscripts, Superscripts

i, j, k, l, m = Cartesian tensor indices
l = liquid
m = mixture
t = turbulent
v = vapor

References

[1] Hirschi, R., Dupont, Ph., Avellan, F., Favre, J.-N., Guelich, J.-F., and Parkinson, E., 1998, "Centrifugal Pump Performance Drop Due to Leading Edge Cavitation: Numerical Predictions Compared With Model Tests," ASME J. Fluids Eng. **120**, No. 4, pp. 705–711.
[2] Ahuja, V., Hosangadi, A., Ungewitter, R. and Dash, S. M., 1999, "A Hybrid Unstructured Mesh Solver for Multi-Fluid Mixtures," AIAA 99-3330, 14th Computational Fluid Dynamics Conference, Norfolk, VA, June.
[3] Chen, Y., Heister, S.D., 1994, "Two-Phase Modeling of Cavitated Flows," ASME FED-Vol. 190, pp.299–307.
[4] Merkle, C. L., Feng, J. Z., and Buelow, P. E. O., 1998, "Computational Modeling of the Dynamics of Sheet Cavitation," 3rd International Symposium on Cavitation, Grenoble, France.
[5] Song, C., He, J., 1998, "Numerical Simulation of Cavitating Flows by Single-phase Flow Approach," 3rd International Symposium on Cavitation, Grenoble, France.
[6] Kunz, R. F., Boger, D. A., Stinebring, D. R., Chyczewski, T. S., Gibeling, H. J., and Govindan, T. R., 1999, "Multi-phase CFD Analysis of Natural and Ventilated Cavitation About Submerged Bodies," ASME Paper FEDSM99-7364.
[7] Kunz, R. F., Boger, D. A., Stinebring, D. R., Chyczewski, T. S., Lindau, J. W., Gibeling, H. J., Venkateswaran, S., and Govindan, T. R., 2000, "A Preconditioned Navier–Stokes Method for Two-Phase Flows with Application to Cavitation Predication," Comput. Fluids **29**, No. 8, pp. 849–875.
[8] Kunz, R. F., Lindau, J. W., Billet, M. L., and Stinebring, D. R., 2001, "Multiphase CFD Modeling of Developed and Supercavitating Flows," VKI Special Course on Supercavitating Flows, Feb.
[9] Lindau, J. W., Kunz, R. F., and Gibeling, H. J., 2000, "Validation of High Reynolds Number, Unsteady Multi-Phase CFD Modeling for Naval Applications," presented at the 23rd Symposium on Naval Hydrodynamics, Val de Reuil, France.
[10] Taylor, L. K., Arabshahi, A., and Whitfield, D. L., 1995, "Unsteady Three-Dimensional Incompressible Navier-Stokes Computations for a Prolate Spheroid Undergoing Time-Dependent Maneuvers," AIAA Paper 95-0313.
[11] Jorgenson, P. C. E., and Chima, R. V., 1989, "Explicit Runge-Kutta Method for Unsteady Rotor-Stator Interaction," AIAA J. **27**, No. 6, pp. 743–749.
[12] Nakamura, S., Ding, W., and Yano, K., 1998, "A 2.5D Single Passage CFD Model for Centrifugal Pumps," ASME Paper FEDSM98-4858.
[13] Gridgen User Manual, 1999, Version 13.3, Pointwise.
[14] Meyer, R. S., and Yocum, A. M., 1993, "Pump Impeller Performance Evaluation Tests for a Parametric Variation of Geometric Variables," ARL Technical Memorandum 93-125.

Nam-Trung Nguyen
Assistant Professor,
Mem. ASME

Xiaoyang Huang
Associate Professor

Toh Kok Chuan
Associate Professor,
Mem. ASME

School of Mechanical and Production
Engineering,
Nanyang Technological University,
Singapore 639798

MEMS-Micropumps: A Review

Microfluidics has emerged from the MEMS-technology as an important research field and a promising market. This paper gives an overview on one of the most important microfluidic components: the micropump. In the last decade, various micropumps have been developed. There are only a few review papers on microfluidic devices and none of them were dedicated only to micropumps. This review paper outlines systematically the pump principles and their realization with MEMS-technology. Comparisons regarding pump size, flow rate, and backpressure will help readers to decide their proper design before starting a microfluidics project. Different pump principles are compared graphically and discussed in terms of their advantages and disadvantages for particular applications. [DOI: 10.1115/1.1459075]

1 Introduction

Microelectromechanical systems (MEMS) have enabled a wide range of sensors and actuators to be realized by allowing nonelectrical devices onto microchips. In the early years of MEMS-development, fluidic components were among the first devices which were realized in microscale using silicon technology. The most common components were: flow sensors, microvalves and micropumps. With the growing importance of genomics, proteomics, and the discovery of new drugs, microfludic systems became hot research objects. The field of microfluidics expanded to the development of numerous micro devices: filters, mixers, reactors, separators. New effects such as electrokinetic effects, acoustic streaming, magnetohydrodynamic effect, electrochemical, and more, which previously were neglected in macroscopic applications, now gained their importance in microscale.

A recent report of System Planning Corporation [1] estimated a microfluidics market of 3 to 4.5 billions US$ and an annual growth rate for scales of 25 percent–35 percent. The report considered four types of microfluidic devices: fluid control devices, gas and liquid measurement devices, medical testing devices, and other devices. The report figured out that the most promising microfluidics products are devices for DNA, protein analysis, and drug discovery.

Since the establishment of the term ‘‘microfludics,’’ several excellent review papers on microfluidic devices have been published. Gravesen et al. gave a general overview on fluidic problems in micro scale [2]. Shoji and Esashi discussed microfluidics from the device point of view and considered micropumps, microvalves and flow sensors [3]. Ho and Tai discussed the MEMS-applications for flow control in the macroscopic domain [4]. Elwenspoek et al. summarized their works on microfludics in [5]. Stemme discussed microfluidic devices under such categories: passive devices (channel, valves, filters), flow sensors, and diaphragm pumps [6]. Zengerle and Sandmaier concentrated on microvalves, micropumps and their commercialization strategy [7]. Since the field has been growing rapidly, it’s very difficult to cover all kinds of microfluidic devices in a single review. In contrast to the previous reviews, this paper only deals with micropumps and discusses their design methodology as well as the development of pump designs in the published examples. The design methodology will cover two main aspects: the pump principles and their comparison. With this concept, the paper tries to give a general view on micropumps, and to help microfluidics designers making their development decision easily.

Using the micromachining technology, a wide range of microdevices has been realized. The most important micromachining techniques are bulk micromachining, surface micromachining, and LIGA technology. Bulk micromachining uses the starting substrate (a silicon wafer) as device material. Surface micromachining is performed on the surface of a substrate, the substrate itself usually doesn’t have a function in devices. LIGA-technology (German acronym for Lithographie Galvanoformung Abformung) creates high aspect ratio structures using X-ray lithography and electroplating. A short description of these technologies was given in [4]. Many MEMS-devices combine two or more of the above techniques. A new trend, especially for microfluidic devices, uses plastic as device material. The common machining technologies for these devices are micro plastic molding or hot embossing. Combining with on-going investigation of polymer microelectronics, plastic microdevices promise a low-cost alternative to their silicon counterparts.

2 Pump Principles

In contrast to another MEMS-devices, micropumps are one of the components with a largest variety of operating principles. Like other MEMS-applications, the first approach made by researchers was the micromachining realization of well-known principles from the macroscale. Micropumps can be divided in two mean categories: mechanical pumps and nonmechanical pumps.

The first category usually utilizes moving parts such as check valves, oscillating membranes, or turbines for delivering a constant fluid volume in each pump cycle [8]. The second category adds momentum to the fluid for pumping effect by converting another energy form into the kinetic energy. While the first category was mostly used in macroscale pumps and micropumps with relatively large size and large flow rates, the second category discovers its advantages in the microscale. Since the viscous force in microchannels increases in the second order with the miniaturization, the first pump category cannot deliver enough power in order to overcome its high fluidic impedance.

For flow rates larger than 10 ml/min, miniature pumps or macroscale pumps are the most common solution. The typical operation range of positive displacement micropumps lies between 10 μl/min to several ml/min. For flow rates less than 10 μl/min, alternative dynamic pumps are needed for accurate control of these small fluid amounts. With these flow rates, most of the pumps are working in the range of Reynolds number from 1–100, and therefore in a laminar regime.

All the pump principles, which were realized recently in microscale, are discussed in details in the following subsections.

2.1 Mechanical Pumps. All mechanical pumps require a mechanical actuator, which generally converts electric energy into mechanical work. The comparison of mechanical works generated

---

Contributed by the Fluids Engineering Division for publication in the JOURNAL OF FLUIDS ENGINEERING. Manuscript received by the Fluids Engineering Division August 7, 2000; revised manuscript received November 7, 2001. Associate Editor: Y. Matsumoto.

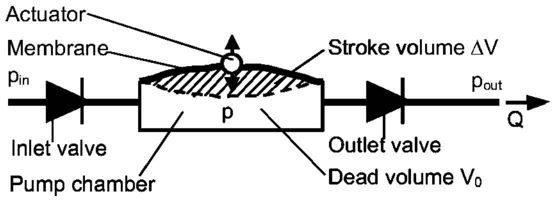

Fig. 1 General structure of a micro check-valve pump

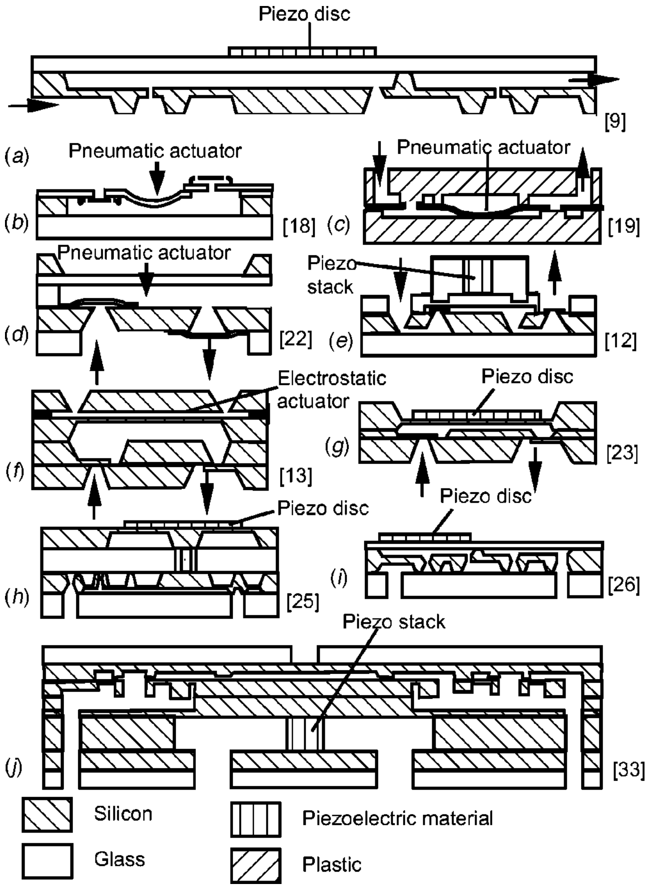

Fig. 2 Check-valve micropumps: (*a*) piezoelectric actuator with ring mesa valves; (*b*) pneumatic actuator with polyimide disk valves; (*c*) pneumatic actuator with membrane valves; (*d*) pneumatic actuator with rubber membrane and parylene disk valves; (*e*) piezoelectric actuator with polysilicon disk valves; (*f*) electrostatic actuator with silicon cantilever valves; (*g*) piezoelectric actuator silicon cantilever valves; (*h*, *i*, *j*) piezoelectric actuator with ring mesa valves.

by different pumps is discussed later in this paper. Shoji [3] divided actuators into two mean categories: external actuators and integrated actuators.

External actuators include: electromagnetic actuators with solenoid plunger and external magnetic field, disk type or cantilever type piezoelectric actuators, stack type piezoelectric actuators, pneumatic actuators, and shape memory actuators. The biggest drawback of external actuators is their large size, which restricts the size of the whole micro-pumps. The advantage is the relatively large force and displacement generated by external actuators.

Integrated actuators are micromachined with the pumps. Most common integrated actuators are electrostatic actuators, thermopneumatic actuators, electromagnetic actuators, and thermomechanic (bimetallic) actuators. Despite their fast response time and good reliability, electrostatic actuators cause small force and very small stroke. With special curved electrodes, electrostatic actuators are suitable for designing micropumps with very low power consumption. Thermopneumatic actuators generate large pressure and relatively large stroke. This actuator type was therefore often used for mechanical pumps. Thermopneumatic actuators and bimetallic actuators require a large amount of thermal energy for their operation, and consequently, consume a lot of electric power. High temperature and complicated thermal management are further drawbacks of these actuator types. Electromagnetic actuators require an external magnetic field, which also restricts the pump size. Their large electric current causes thermal problems and high electric energy consumption.

Check-Valve Pumps. Check-valve pump is the most common pump type in the macroscale. The first attempts in designing a micro pump were the realization of check-valve pumps. Figure 1 illustrates the general principle of a check-valve pump. The pump consists of:

- An actuator unit; a pump membrane that creates the stroke volume ΔV,
- A pump chamber with the dead volume V_0,
- Two check-valves, which start to be opened by the critical pressure difference Δp_{crit}.

Richter et al. [16] determined the operation conditions of a check-valve pump as:

- Small compression ratio ε which is the ratio between the stroke volume and the dead volume $\varepsilon = \Delta V / V0$,
- High pump pressure p ($|p - p_{\mathrm{out}}| > p_{\mathrm{crit}}, |p - p_{\mathrm{in}}| > p_{\mathrm{crit}}$).

Following design rules can be used in order to fulfill the above conditions:

- Minimize the critical pressure Δp_{crit} by using more flexural valve design or valve material with small Young's modulus,
- Maximize the stroke volume ΔV by using actuators with large stroke or more flexible pump membrane,
- Minimize the dead volume V_0 by using thinner spacer or wafer,
- Maximize the pump pressure p by using actuators with large forces.

The terms for passive microvalves used in this paper were defined by Shoji in [3]. One of the first micropumps made in silicon was presented by van Lintel [9]. The pump had check-valves in form of a ring diaphragm, which was relatively stiff and need a large lateral area. That makes one valve consume a large silicon area, which has almost the same size of a pump chamber, Fig. 2(*a*). The same valves were also used in the pumps reported in [10] and [11], which had thermopneumatic actuators instead of piezodisks. The next improvement was the pump presented by Shoji [12], which had check-valves made of polysilicon by using surface micromachining. The valve is a disk supported by four thin polysilicon beams. This design allows small valves to be integrated under the pump chamber. Zengerle [13,14] presented another small and more flexible design. The valve has a form of a cantilever, Fig. 2(*f*). Koch et al. [15] and Wang et al. [16] proposed the same valve type in their micropumps.

Another way to make check-valve flexible is using material with smaller Yong's modulus. Table 1 compares the common materials used for check-valves in micro pumps. Polyimide, polyester, and parilene is one order more flexible than silicon. Pumps presented by Shomburg et al. [17,18] used polyimide as material for the disk valve (Fig. 2(*b*)). The pump reported in [19] and that presented by Kaemper et al. [20] had polyimide ring diaphragm valves (Fig. 2(*c*)). A similar design using polyester valve was reported by Boehm et al. [21]. In the pump presented by Meng et al. [22], the disk valve was realized in parylene (Fig. 2(*d*)).

The next optimization is to fabricate the pump membrane with flexural material like polyimide [19] (Fig. 2(*c*)) or silicone ruber [22] (Fig. 2(*d*)). These membranes require small actuating pres-

Table 1 Young's modulus of different materials

Material	Young's Modulus (GPa)
Stainless steel	~240
Silicon	~200
Silicon nitride	~300
Polyimide	~10
Parylene	~3
Silicone ruber	~0.0005

sure and have large deflection as well as large stroke volume. This type of membrane is suitable for pneumatic or thermopneumatic actuators.

Using thinner spacer or thinner wafer for the pump chamber can minimize the dead volume. The pump presented by Zengerle [13] (Fig. 2(*f*)) was in this way improved in the version presented by Linnemann et al. [23]. The middle wafer was polished and thined to 70 micron. As a result, the compression ratio increased from 0.002 to 0.085 [24]. The improved pump design was able to pump gas and was self-priming. The design of van Lintel [9] (Fig. 2(*a*)) was improved from the later version [25] (Fig. 2(*b*)) and had a compression ratio of 1.15. This pump was self-priming and insensitive to ambient pressure because of the implementation of a special pump membrane limiter. Another good design, which minimizes the dead volume in the Linnemann's pump, was combining the check-valve with the pump chamber realized by Gass et al. [26,27] (Fig. 2(*i*)).

Table 2 lists the most important parameters of the above check-vale pumps and those reported in [28–33]. The pump designs depicted in Fig. 2 also illustrate the "evolution" in designing check-valve micropumps. The development shows clearly how the pump chamber becomes smaller, and how the check-valves and the pump membrane become more flexible. Most of the developed micropumps tend to have a piezoelectric disk as actuator, which is reasonable for the performance and size needed for this pump type.

Peristaltic Pumps. As opposed to check-valve pumps, peristaltic pumps don't require passive valves for the flow rectification. The pump principle is based on the peristaltic motion of the pump chambers, which squeezes the fluid into the desired direction. Theoretically, peristaltic pumps need 3 or more pump chambers with reciprocating membrane. Most of the realized pumps have 3 chambers. Some pumps were designed with active valves, which in fact represent pump chambers, also belong to the category of peristaltic pumps. The optimization strategies are maximizing the compression ratio and increasing the number of pump chambers (Table 3).

Table 2 Typical parameters of check-valve micropumps (values for water, except [18] for air)

Ref.	Author	Year	Chamber size (μm)	Chamber height (μm)	Max. Deflec -tion (μm)	Max. Flow Rate (μl/min)	Max. Back Pressure (Pa)	Typ. Frequency (Hz)	Technology	Actuator
[9]	van Linten	1988	12500	130		8	9800	1	Bulk, anodic bonding	Piezoelectric
[10]	van den Poll	1990	7500	273	23	30	4000	0.5	Bulk, anodic bonding	Thermopneumatic
[11]	Lammerink	1993	7500	261	23	58	2940	5	Bulk, anodic bonding	Thermopneumatic
[12]	Shoji	1990	5000		-	20	14700	40		
[13]	Zengerle	1992	4000	425	4	70	2500	25	Bulk, adhesive bonding	Electrostatic
[14]	Zengerle	1995	4000	425	5	850	31000	1000	Bulk, adhesive bonding	Electrostatic
[15]	Koch	1998	4000	380	1.7	150	2000	200	Bulk, adhesive bonding	Piezoelectric
[16]	Wang	1998	5000	370	-	365	2380	25	Bulk, adhesive bonding	Piezoelectric
[18]	Schomburg	1993	5000	100	100	44	3800	5	LIGA	Pneumatic
[20]	Kaemper	1998	10000	-	30	400	210000	50	LIGA	Piezoelectric
[21]	Boehm	199	10000	200	-	2100	11000	100	Plastic Molding	Piezoelectric, Electromagnetic
[22]	Meng	2000	7000	400	-	13000	5900	12	Bulk, Silicone	Pneumatic, Electromagnetic
[23]	Linneman	1998	5700	15	15	1300	90000	200	Bulk, direct bonding	Piezoelectric
[25]	Maillefer	1999	4000		-	4	35000	2	Bulk, anodic bonding	Piezoelectric
[26]	Gass	1994	14000	2.00E-04		100	9000	40	Bulk, anodic bonding	Piezoelectric
[28]	Dario	1996	10000	1500	-	780	5500	264	Plastic Molding	Electromagnetic
[29, 30]	Guo	1996	6000	-	100	40		2	Precision Eng.	ICPF
[31]	Accoto	1998	10000		-	600	9800	2	Precision Eng.	Piezoelectric
[32]	Benard	1997	8400	450	-	50	519	1	Bulk, adhesive bonding	Shape-memory-alloy
[33]	Li	2000	3600	18	18	1400	300000	3500	Bulk, direct bonding	Piezoelectric

Table 3 Typical parameters of peristaltic micropumps (values for water)

Ref.	Author	Year	Chamber size (μm)	Chamber height (μm)	Max. Defl. (μm)	Max. Flow Rate (μl/min)	Max. Back Pressure	Freq. (Hz)	Technology	Actuator
[34]	Smits	1988	5000	-		100	5880	15	Bulk micromach.	Piezoelectric
[35]	Shinoharal	2000	10000	400		40	2450	1	Bulk, anodic bonding	Piezoelectric
[36]	Judy	1992	400	4	4		-	-	Surface micromach.	Electrostatic
[37]	Folta	1992	1000	10	10	7	-	20		Thermopneumatic
[38]	Mizoguchil	1992	800	18	35	3	4822	3	Buk micromach.	Thermopneumatic
[39]	Grosjean	1999	500	60	60	4.2	3447	2	Bulk, Precision eng.	Thermopneumatic
[40]	Cabuz	1999	800	500	500	8000	-	100	Plastic Molding	Electrostatic

Since a peristaltic pump doesn't require high chamber pressure, the most important optimization factors are the large stroke volume and the large compression ratio. The first peristaltic micro pump presented by Smits [34] (Fig. 2(*a*)) had piezoelectric actuators and pump chambers etched in silicon. Shinohara et al. [35] presented a similar design with the same performance.

Judy [36] proposed a pump, which utilized surface micromachining and electrostatic actuators (Fig. 2(*b*)). The pump chamber, and consequently the dead volume, can be kept very small. No results for maximum flow rate and backpressure were reported for this pump.

The pump reported by Folta et al. [37] (Fig. 2(*c*)) used thermopneumatic actuators, the pump chamber height was 10 micron. However, the heat loss caused by the good thermal conductivity of silicon minimized the thermopneumatic effect and increased the power consumption.

Mizoguchi et al. [38] (Fig. 2(*d*)) also used thermopneumatic actuators for driving 4 pump chambers, the pump had external laser light as heat source. Similar to the methods discussed in the previous section, Grosjean et al. used silicone rubber in order to form the pump membrane [39] (Fig. 2(*e*)). With external pneumatic sources, the pump could generate a flow rate up to 120 μl/min. In thermopneumatic operation, the pump only delivered few μl/min like the similar designs in [37] and [38].

The pump presented by Cabuz et al. [40] increased the compression ratio to 10 by using curved pump chambers and flexible plastic pump membrane for electrostatic actuation. The numerous pump chambers were designed by using a three-dimensional array structure (Fig. 2(*f*)). With these optimization measures, the pump was able to deliver 8 ml/min with only 75 V drive voltage and 4 mW electrical power (Fig. 3).

Valveless Rectification Pumps. The structure of valveless rectification pumps is similar to those of check-valve pumps. The only difference is that instead of using check-valves the pumps use diffuser/nozzle or valvular conduit structures for flow rectification. Maximizing the stroke volume and minimizing the dead volume can optimize this pump type.

Stemme [41] presented the first pump with diffuser/nozzle structures. The pump was fabricated in brass using precision machining (Fig. 4(*a*)). Further development of this pump leads to the flat design in silicon [42–44] (Fig. 4(*b*)). Using small opening angles (7–15 deg), the flow is pumped out of the diffuser structure (Fig. 2(*a*)). With deep reactive ion etching (DRIE), small chamber height, and consequently small dead volume and large compression ratio were achieved.

The pump effect appears in the opposite direction if the opening angle is large. The pump presented by Gerlach had an opening of 70.5 deg, which is determined by the ⟨111⟩ surface freed with anisotropic wet etching [45–47] (Fig. 4(*c*)). This pump design was optimized in the work of Jeong and Yang [48]. The stroke volume was increased by using the thermopneumatic actuator and corrugated pump membrane. Ullman gave in [49] a theoretical analysis of diffuser/nozzle pumps.

Forster et al. [50,51] applied the valvular conduits structure which was first invented by Tesla [52] in micro scale. The inlet/outlet structures shown in Fig. 5 cause the rectification effect without check-valves. This pump type can be realized easily in silicon with DRIE-technology.

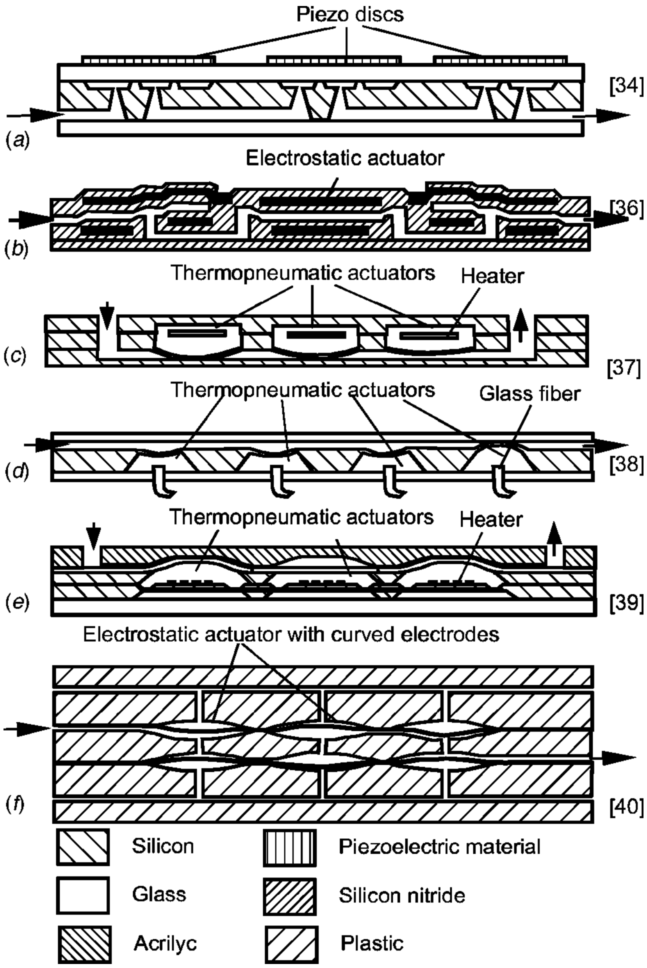

Fig. 3 Realization examples of peristaltic micropumps (not to scale): (*a*) piezoelectric actuators with glass membrane; (*b*) electrostatic actuators with polysilicon membrane; (*c*) thermopneumatic actuators with silicon membrane; (*d*) thermopneumatic actuators with silicon membrane and fiber guided laser as heat source; (*e*) thermopneumatic actuators with rubber membrane; (*f*) electrostatic actuators with curved electrodes.

Another approach of valve-less pumping was proposed by Stehr et al. [53,54]. The pump principles were called the elastic buffer mechanism (Fig. 6(*a*)) and the variable gap mechanism (Fig. 6(*b*)). This pump type is able to pump liquids in two directions depending on its drive frequency. Nguyen et al. also demonstrated the pump effects in a similar structure [55] (Fig. 6(*c*)).

Maysumoto et al. [56] presented another valveless concept by using the temperature dependency of water viscosity. The fluidic impedance at the outlet and the inlet are modulated by means of heat. The heating cycles were synchronized with the pump frequency. Table 4 lists the most important parameters of the discussed valveless rectification micro pumps.

Rotary Pumps. Another mechanical pump type, which can be realized with micro machining technique, is the rotary pump. The rotary pump has a big advantage of pumping highly viscous fluids (Table 5).

Ahn et al. [57] (Fig. 7(*a*)) presented a micropump with a microturbine as rotor in an integrated electromagnetic motor. The pump simply adds momentum to the fluid by means of fast moving blades. The rotor, stator, and coils are fabricated by electroplating of iron-nickel alloy. The high aspect ratio structures were fabricated at a low cost by using conventional photolithography of polyimide.

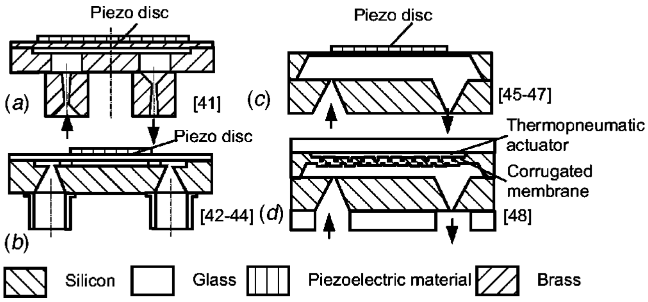

Fig. 4 Realization examples of valveless rectification micro pumps (not to scale): (*a*) piezoelectric actuator with external diffuser/nozzle elements; (*b*) piezoelectric actuator with planar integrated diffuser/nozzle elements; (*c*) piezoelectric actuator with vertical diffuser/nozzle elements; (*d*) thermoelectric actuators with corrugated membrane and vertical diffuser/nozzle elements.

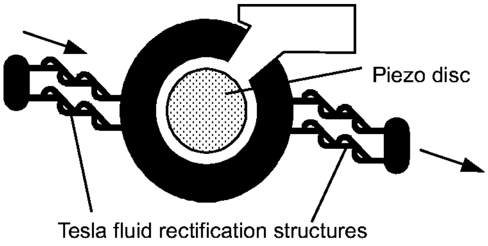

Fig. 5 Valvular conduit pump

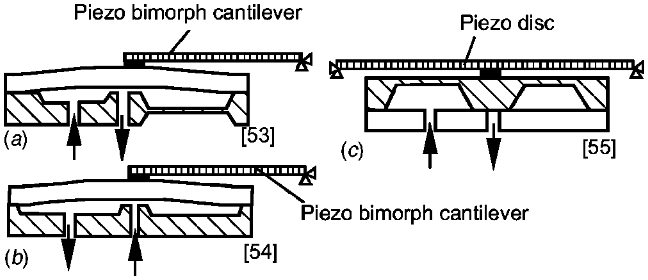

Fig. 6 Other valveless pumps

Table 4 Typical parameters of valveless rectification micropumps

Ref.	Author	Year	Chamber size (μm)	Chamber height (μm)	Max. Deflection (μm)	Max. Flow Rate (μl/min)	Max. Back Pressure	Typ. Freq. (Hz)	Technology	Actuator
[41]	Stemme	1993	19000	-	13	16000	7840	110	Prezision eng.	Piezoelectric
[4-44]	Olsson	1995	5000	80	13	1200	16000	1400	Plastic Molding	Piezoelectric
[45-47]]	Gerlach	1995	5000	430	45	400	3200	3500	Bulk	Piezoelectric
[48]	Jeong	1999	4000	115	100	14		4	Bulk	Thermopneumatic
[50]	Forster	1995	6000	156		900	14700	3700	Bulk, deep RIE	Piezoelectric
[53, 54]	Stehr	1996	5300	425	40	900	6000	50	Bulk	Piezoelectric
[55]	Nguyen	1998	4500	425	15	80	5000	110	Bulk	Piezoelectric
[56]	Matsumoto	1999	5000	250		5.5		5	Bulk	Piezoelectric

Table 5 Typical parameters of rotary pumps (typical size is the size of the turbine or the gear wheel)

Ref.	Authors	Year	Typ. Size (μm)	Chamber height (μm)	Max. Flow Rate (μl/min)	Max. Back Pressure	Rotation speed (rpm)	Technology	Actuator
[57]	Ahn	1995	500	160	24	10000	5000	Bulk	External motor
[58]	Doepper	1997	596	500	55	12500	2250	LIGA	Integrated motor

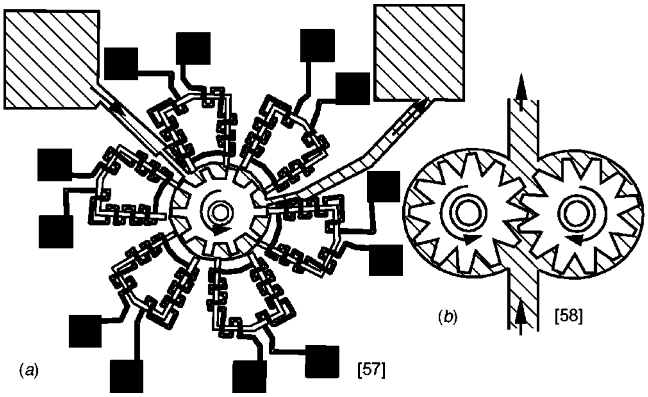

Fig. 7 Rotary pumps

The micropump presented by Doepper et al. [58] (Fig. 7(*b*)) had two gear wheels made of iron-nickel alloy with LIGA-technique. An external motor drove the gear. The gears forced the fluid along by squeezing it to an outlet. Actuating by means of an external magnetic field is possible, but it is so far not reported. Mass production of this pump can be realized with plastic molding.

Ultrasonic Pump. Ultrasonic principle is a gentle pump principle with no moving parts, heat and strong electric field involved. The pump effect is caused by the acoustic streaming, which is induced by a mechanical traveling wave (Fig. 8(*a*)). The mechanical wave can be a flexural plate wave (FPW) [59,60] or a surface acoustic wave [61,62]. The mechanical waves are excited by interdigitated transducers (IDT, Fig. 8(*b*)) placed on a thin membrane coated with piezoelectric film [59,60] or on a piezoelectric bulk material [61,62]. The pumps have a thin flow layer of about 20 micron (for water) (Fig. 8(*a*)), and are therefore also suitable for particle separation applications. Using curved IDT, locally sample concentration can be achieved with this kind of pump.

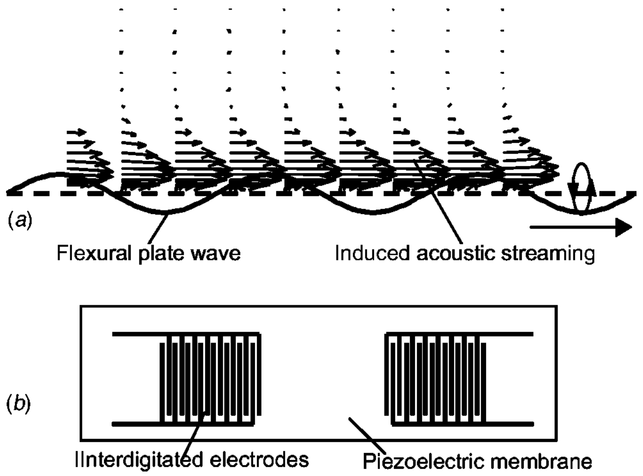

Fig. 8 Ultrasonic pumps

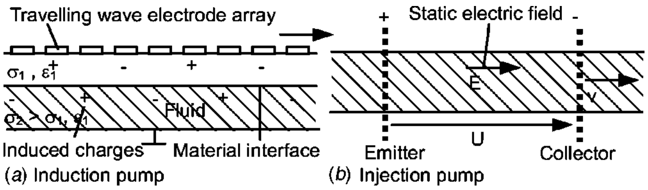

Fig. 9 Principles of electrohydrodynamic pumps

2.2 Nonmechanical Pumps

Electrohydrodynamic Pumps. Electrohydrodynamic (EHD) pumps are based on electrostatic forces acting on dielectric fluids. The force density F acting a dielectric fluid with free space-charge density q_f in an inhomogeneous electric field E is given as [63]:

$$F=\underbrace{q_f E}_{\text{Colombforce}}+\underbrace{P\cdot\nabla E}_{\text{Kelvin polarization force}}-\underbrace{\frac{1}{2}E^2\nabla\varepsilon}_{\text{Dielectricforce}}+\underbrace{\nabla\left(\frac{1}{2}\rho\frac{\partial\varepsilon}{\partial\rho}E^2\right)}_{\text{Electrostrictive force}} \tag{1}$$

where ε is the fluid permittivity, P is the polarization vector, and ρ is the mass density. EHD pumps can be categorized into two main types: the EHD induction pump and the EHD injection pump.

The EHD induction pump is based on the induced charge at the material interface. A traveling wave of electric field drags and pulls the induced charges along the wave direction (Fig. 9(*a*)). The first micromachined EHD induction pump was presented by Bart et al. [63], similar designs were reported by Fuhr et al. [64–67] and Ahn et al. [68]. A fluid velocity of several hundred micron per second can be achieved with this pump type. For better pumping effect, a temperature gradient and consequently a conductivity gradient across the channel height was generated by an external heat source and heatsink (Peltier element) [67].

In the EHD injection pump, the Colomb force is responsible for moving ions injected from one or both electrodes by means of electrochemical reaction (Fig. 9(*b*)). Richter et al. demonstrated this pump principle with micromachined silicon electrodes [69,70]. The pressure gradient bults up in the electric field causes the pump effect. Furuya et al. used electrode grids, standing perpendicular to device surface, in order to increase the pressure gradient [71]. The pump can deliver 0.12 ml/min with a drive voltage of 200 V. Table 6 lists the most important parameters of the EHD-pumps discussed above.

Electrokinetic Pumps. In contrast to the EHD-pumps, electrokinetic pumps utilize the electrical field for pumping conductive fluid. The electrokinetic phenomenon can be divided into electrophoresis and electroosmosis.

Electrophoresis is the effect, by which charged species in a fluid are moved by an electrical field relative to the fluid molecules. The velocity of the charged species is proportional to the field strength E:

$$V=\mu_{\mathrm{ep}}E \tag{2}$$

where μ_{ep} is the electrophoretic mobility of the species. Electrophoresis is used for separation of molecules like DNA molecules.

In contrast to electrophoresis, electroosmosis is the pumping effect of a fluid in a channel under the application of an electrical field. A surface charge exists on the channel wall. The surface charge comes either from the wall property or the adsorption of charges species in the fluid. In the presence of an electrolyte solution, the surface charge induces the formation of a double layer on the wall by attracting oppositely charged ions from the solution. An external electrical field forces the double layer to move.

Table 6 Typical parameters of electrohydrodynamic micropumps

Ref.	Authors	Year	Typ. Size (μm)	Channel height (μm)	Max. Flow Rate (μl/min)	Max. Back Pressure	Principle	Technology
[63]	Bart	1990	500	-			EHD-induction	Bulk
[64-67]	Fuhr	1992-1997	600	50	0.45	-	EHD-induction	Bulk
[68]	Ahn	1998	3000	200	50	220	EHD injection	Bulk
[69, 70]	Richter	1990-1991	3000	-	15000	500	EHD-injecton	Bulk
[71]	Furuya	1996	400	100	0.12		EHDinjection	Bulk

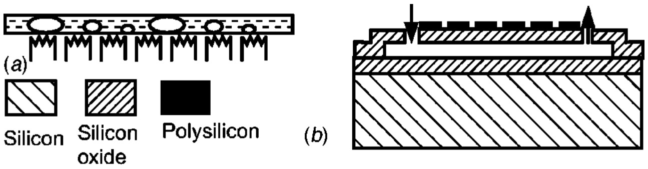

Fig. 10 Phase transfer pumps

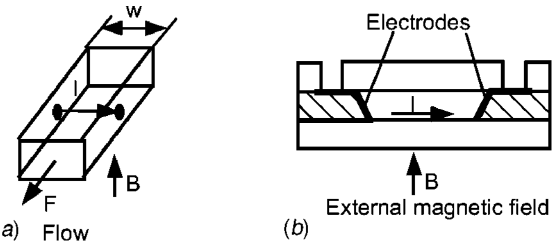

Fig. 12 Magnetohydrodynamic pump: (*a*) schematic of concept, (*b*) design example, fluid flows out of page plane

Due to the viscous force of the fluid, the whole fluid in the channel moves with a flat velocity profile (plug flow):

$$V=\mu_{eo}E \tag{3}$$

where μ_{eo} is the electroosmotic mobility of the fluid. Due to its nature, the electroosmosis effect was used for pumping fluid in small channels without applying a high external pressure. In micro analysis systems electroosmosis effect is used for delivering buffer solution, and in combination with the electrophoretic effect, for separating molecules. The most common application of electrokinetic pumps is the separation of large molecules like DNA or proteins. The device proposed by Harison et al. [72,73] could generate a fluid velocity of 100 μm/s with a field strength of 150 V/cm. Webster et al. [74,75] uses the gel electrophoresis for separating DNA-molecules in microchannel with relatively low field strength (5 to 10 V/cm).

Phase Transfer Pump. Beside the ultrasonic principle, electrohydrodynamic principle and electrokinetic principle, phase transfer is another principle for pumping fluid in small channels, in order to overcome the high fluidic impedance caused by viscous forces. This principle uses the pressure gradient between the gas phase and liquid phase of the same fluid for pumping it. The realization in microscale is simpler than in other pump types. Takagi et al. [76] presented the first phase transfer pump (Fig. 10(*a*)). The alternate phase change is generated by an array of 10 integrated heaters. The same pump principle was realized with stainless steel and 3 heaters in [77]. Jun and Kim [78,79] fabricated a much smaller pump based on surface micromachining. The pump had 6 integrated polysilicon heaters in a channel with 2 micron height and 30 micron width (Fig. 10(*b*)). The pump is capable to deliver a flow velocity of 160 μl/s or flow rates less than 1 nanoliter per minute.

Electro Wetting Pump. The electro-wetting pump was proposed by Matsumoto et al. [80]. The pump principle uses the dependence of the tension between solid/liquid interface on the charge of the surface. The principle can be used for direct pumping, but no example was reported. Lee and Kim [81] reported a micro actuator based on electro-wetting of mercury drop, which can be used for driving a mechanical pump with check valves as proposed in [80].

Electrochemical Pump. Electrochemical pumps use the pressure of gas bubbles generated by electrolysis water. Bi-directional pumping can be achieved by reserving the actuating current, which makes the hydrogen and oxygen bubbles reacting back to water [82]. The pumped fluid volume can be measured by estimating the gas volume with the measurement of the conductivity between electrodes 2 and 3 (Fig. 11).

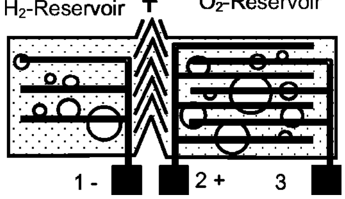

Fig. 11 Electrochemical pump

Magnetohydrodynamic Pump. The pumping effect of a Magnetohydrodynamic (MHD) pump is based on the Lorentz force acted on a conducting solution:

$$F=I\times Bw, \tag{4}$$

where I is the electric current across the pump channel, B the magnetic field strength and w the distance between the electrode (Fig. 12(*a*)). Lemoff et al. [83,84] realized this principle in silicon (Fig. 12(*b*)). The pump was able to generate a not-pulsatile flow like that of EHD-pumps and electrokinetic pumps. A maximum flow velocity of 1.5 mm/s can be achieved (1 M NaCl solution, 6, 6 V). MHD-pumps generate a parabolic velocity profile, similar to a pressure driven flow in channels.

3 Scaling Law for Micropumps

The first question, which arises in dealing with micropumps, is what kind of pump can be actually called a micropump? Is that the size of the pump itself or is that the fluid amount the pump can handle? Since the above question is still unanswered, Fig. 13 illustrates the typical sizes versus the maximum flow rates of the published micropumps listed as references. The pump chamber

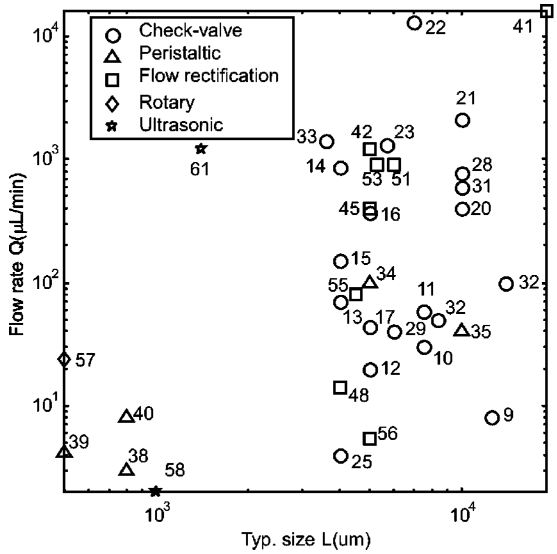

Fig. 13 Flow rate versus typical size for mechanical pumps (the numbers indicate the corresponding references)

Table 7 Typical parameters of phase transfer micropumps

Ref.	Authors	Year	Typ. Size (μm)	Chamber height(μm)	Max. Flow Rate (μl/min)	Max. Back Pressure (Pa)	Typ. Frequency (Hz)	Technology
[76, 77]	Takagi,	1994-1995	180	180	210	-	4	Bulk micromachining
[78, 79]	T. Jun	1996-1998	30	2	5.05	800	1 - 4	Surface micromachining

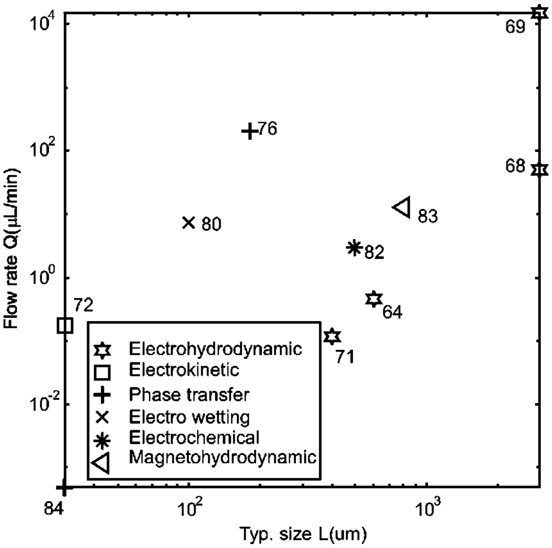

Fig. 14 Flow rate versus typical size for non-mechanical pumps (the numbers indicate the corresponding references)

diameters of mechanical pumps are chosen as the typical sizes. Most of the mechanical pumps have a size between 5 mm and 1 cm, due to their relatively large piezoelectric actuator unit (Table 7). With the use of alternatives such as thermopneumatic actuators [10,19,37,39,48], electro-wetting actuators [80] or electrochemical actuators [82], the pump size can be reduced to less than 100 micron. No mechanical micropump was able to generate a flow rate less than 1 μl/min accurately, due to the large viscous forces and their relatively "large" size.

Figure 14 shows the flow rate-size characteristics of nonmechanical pumps. The channel widths are taken as typical sizes. With nonmechanical principle such as electrohydrodynamic, and electrokinetic pumping, micropumps can penetrate the 1 μl/min limit. Figure 15 depicts the estimated maximum Reynolds number in the reviewed micropumps, it can be seen clearly that most of the pumps have laminar flow characteristics.

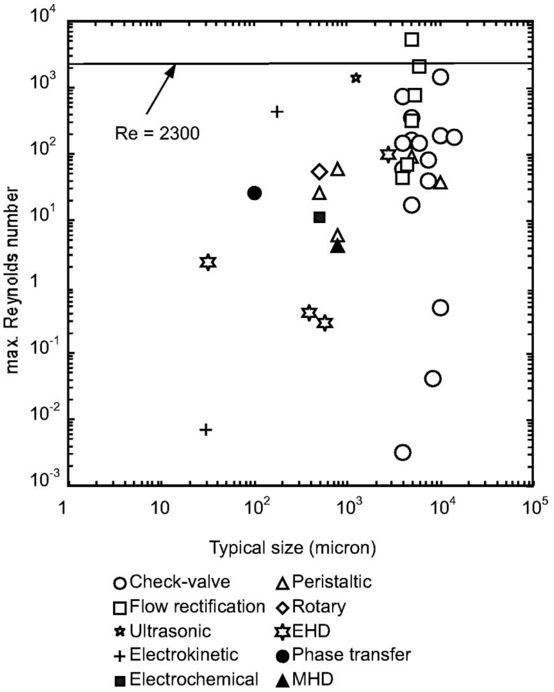

Fig. 15 Maximum Reynolds number versus typical size

Table 8 Maximum energy density of typical actuators in micropumps

Actuator	Maximum energy density	Parameters	Order (J/cm3)
Electrostatic	$\frac{1}{2}\varepsilon E^2$	E: electric field strength ε: dielectric permittivity	0.1 - 1
Thermal	$\frac{1}{2}E(\alpha\Delta T)^2$	α: coefficient of thermal expansion ΔT: temperature difference E: Young's modulus	1 - 10
Magnetic	$\frac{1}{2}B^2/\mu$	B: magnetic field strength μ: magnetic permeability	1 - 10
Piezoelectric	$\frac{1}{2}E_Y(d_{33}E)^2$	E_Y: Young's modulus E: electric field strength d_{33}: piezoelectric coefficient	0.1 - 1

The next problem of scaling law is the relation between the pumped energy or the mechanical work and the pump size. Table 8 gives an overview about the energy density stored in actuators used for micropumps [85]. Assuming that the energy density in all actuator types doesn't change with the miniaturization, the energy stored in a micropump actuator decreases with three order of the miniaturization. The pumped energy per stroke is given by [41]:

$$E_{\max}=\frac{p_{\max}Q_{\max}}{4f} \tag{5}$$

where $p_{\max}$ is the maximum back pressure and $Q_{\max}$ is the maximum flow rate for a given reciprocating frequency f. This equation can only be applied for mechanical pumps using reciprocating pump membrane. The energy efficiency of a pump is defined as the relation between the energy stored in the actuator and the pumped energy. Assuming that the energy efficiency of mechanical micropumps doesn't change compared to its macroscopic counterpart, the energy delivered by a micropump decreases with three orders of miniaturization.

Figure 16 evaluates the pumped energy of the check-valve pumps, the peristaltic pumps and the flow rectification pumps listed in the reference. The data show clearly that the pumped energy varies between 0.01 and 1 μJ while the pump size is restricted between 0.6 mm and 10 mm. The field figures indicated pumps with piezoelectric actuators. Most of the piezoelectric actuators are external, which leads to the size restriction mentioned above. Smaller thermopneumatic actuators (almost 10 time smaller than piezoelectric actuators) can be integrated in the

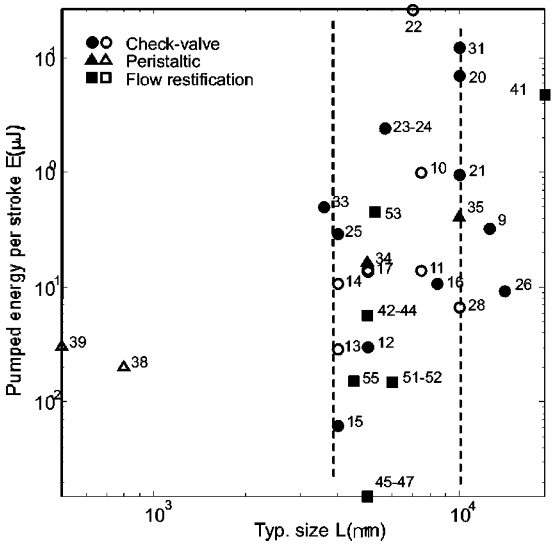

Fig. 16 Pumped energy per stroke versus typical size (filled figures indicate that the pumps use piezoelectric actuators)

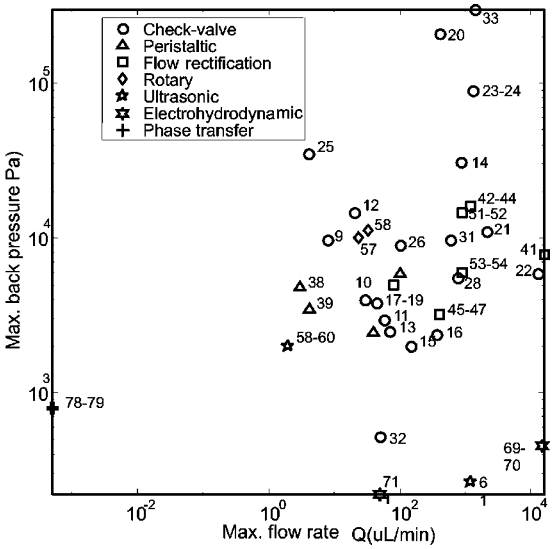

Fig. 17 Maximum back pressure versus maximum flow rate (the numbers indicate the corresponding references)

micromachining process [38,39], but their values of the pumped energy per stroke are also 10 times less than those of piezoelectric actuators. This observation leads to the conclusion that the pumped energy in mechanical pumps also decreases with the miniaturization.

Figure 17 plots the maximum back pressure versus the maximum flow rates. The flow rate is proportional to the average flow velocity, which in turn is proportional to the pressure loss. Figure 15 agrees with this general observation.

Concluding Remarks

The emerging MEMS technology opens new possibilities for fluid machinery in a very distinct length scale, the micron size. In this range, the surface to volume ratio is much larger than that in macro scale, which leads to high viscous forces and restricts down-scaling of well-known mechanical pump principles. Mechanical pumps fill the flow range gap between nonmechanical pumps and classical macro-scale pumps, which ranges between several microliter to several mililiter per minute. We need nonmechanical pumps for handling flow rates in nanoliter or picoliter per minute ranges. With the emerging biomedical technology, pumps for handling extremely small fluid amounts become more and more important. By integrating pumps with other microfluidic devices as well as sensors, the vision of a lab on chip for biomedical applications and drug discovery will be the reality in the near future. With this goal, the exploration of new pumping principles and their realization with MEMS-technology are and will be huge scientific and engineering challenges.

References

[1] System Planning Corporation, 1999, ''MEMS 1999-Emerging Applications and Markets.''
[2] Gravesen, P., Brandebjerg, J., and Jensen, O. S., 1993, ''Microfluidics-A Review,'' J. Micromech. Microeng., **3**, pp. 168–182.
[3] Shoji, S., and Esashi, M., 1994, ''Microflow Devices and Systems,'' J. Micromech. Microeng., **4**, pp. 157–171.
[4] Ho, C. M., and Tai, Y. Ch., 1996, ''Review: MEMS and Its Application for Flow Control,'' ASME J. Fluids Eng., **118**, pp. 437–447.
[5] Elwenspoek, M., Lammerink, T. S., Miyake, R., and Fluitman, J. H. J., 1994, ''Towards Integrated Microliquid Handling System,'' J. Micromech. Microeng., **4**, pp. 227–245.
[6] Stemme, G., 1995, ''Micro Fluid Sensors and Actuators,'' *Proc. 6. IEEE International Symposium on Micro Machine and Human Science*, pp. 45–52.
[7] Zengerle, R., and Sandmaier, H., 1996, ''Microfluidics,'' *Proc. 7. IEEE International Symposium on Micro Machine and Human Science*, pp. 13–20.
[8] White, F. M., 1986, *Fluid Mechanics*. McGraw-Hill, New York.
[9] van Lintel, H. T. G., van den Pol, F. C. M., and Bouwstra, S., 1988, ''A Piezoelectric Micropump Based on Micromachining in Silicon,'' Sens. Actuators, **15**, pp. 153–167.
[10] van den Pol, F. C. M., van Lintel, H. T. G., Elwonspoek, M., and Fluitman, J. H. J., 1990, ''A Thermopneumatic Micropump Based on Micro-Engineering Techniques,'' Sens. Actuators A, **21–23**, pp. 198–202.
[11] Lammerink, T. S. J., Elwenspoek, M., and Fluitman, J. H. J., 1993, ''Integrated Micro-Liquid Dosing System,'' *IEEE 6th Int. Workshop on MEM-MEMS'93*, pp. 254–259.
[12] Shoji, S., Nakafawa, S., and Esashi, M., 1990, ''Micropump and Sample-Injector for Integrated Chemical Analyzing Systems,'' Sens. Actuators A, **21–23**, pp. 189–192.
[13] Zengerle, R., Richter, A., and Sandmaier, H., 1992, ''A Micromembrane Pump With Electrostatic Actuation,'' *IEEE 5th Int. Workshop on MEMS-MEMS'92*, pp. 31–36.
[14] Zengerle, R., Kluge, S., Richter, M., and Richter, A., 1995, ''A Bi-Directional Silicon Micropump,'' *IEEE 8th Int. Workshop on MEMS-MEMS'95*, pp. 19–24.
[15] Koch, M., Harris, N., Evans, A. G. R., White, N. M., and Brunnschweiler, A., 1998, ''A Novel Micromachined Pump Based on Thick-Film Piezoelectric Actuation,'' Sens. Actuators A, **70**, pp. 98–103.
[16] Wang, X., Zhou, Z., Ye, Z., Li, Y., and Zhang, W., 1998, ''A PZT-Driven Micropump,'' *Proc. of Micro Mechatronics and Human Sience 98*, pp. 269–272.
[17] Rapp, R., Schomburg, W. K., Maas, D., Schulz, J., and Stark, W., 1994, ''LIGA Micropump for Gases and Liquids,'' Sens. Actuators A, **40**, pp. 57–61.
[18] Schomburg, W. K., Fahrenberg, J., Maas, D., and Rapp, R., 1993, ''Active Valves and Pumps for Microfluidics,'' J. Micromech. Microeng., **3**, pp. 216–218.
[19] Schomburg, W. K., Vollmer, J., Buestgens, B., Fahrenberg, J., Hein, H., and Menz, W., 1994, ''Microfluidic Components in LIGA Technique,'' J. Micromech. Microeng., **4**, pp. 186–191.
[20] Kaemper, K. P., Doepper, J., Ehrfeld, W., and Oberbeck, S., 1998, ''A Self Filling Low Cost Membrane Micropump,'' *IEEE 11th Int. Workshop on MEMS (MEMS'98)*, pp. 432–437.
[21] Boehm, S., Olthuis, W., and Bergveld, P., 1999, ''A Plastic Micropump Constructed With Conventional Techniques and Materials,'' Sens. Actuators A, **77**, pp. 223–228.
[22] Meng, E., Wang, X. Q., Mak, H., and Tai, Y. C., 2000, ''A Check-Valved Silicone Diaphragm Pump,'' *IEEE 13th International Conference on Micro Electro Mechanical Systems (MEMS'00)*, pp. 23–27.
[23] Linneman, R., Woias, P., Senfft, C. D., and Ditterich, J. A., 1998, ''A Self-Priming and Bubble Tolerant Piezoelectric Silicon Micropump for Liquids and Gases,'' *IEEE 11th Int. Workshop on MEMS-MEMS'98*, pp. 532–537.
[24] Richter, M., Linnemann, R., and Woias, P., 1998, ''Robust Design of Gas and Liquid Micropumps,'' Sens. Actuators A, **68**, pp. 480–486.
[25] Maillefer, D., van Lintel, H., Rey-Mermet, G., and Hirschi, R., 1999, ''A High-Performance Silicon Micropump for an Implantable Drug Delivery System,'' *IEEE 12th Int. Workshop on MEMS (MEMS'99)*, pp. 541–546.
[26] Gass, V., van der Shoot, B. H., Jeanneret, S., and de Rooij, N. F., 1994, ''Integrated Flow-Regulated Silicon Micropump,'' Sens. Actuators A, **43**, pp. 335–338.
[27] Gass, V., van der Shoot, B. H., Jeanneret, S., and de Rooij, N. F., 1993, ''Integrated Flow-Regulated Silicon Micropump,'' *Proc. of Inter. Conf. on Solid-State Sensors and Actuators Transducers'93*, pp. 1048–1051.
[28] Dario, P., Croce, N., Carrozza, M. C., and Varallo, G., 1996, ''A Fluid Handling System for a Chemical Microanalyzer,'' J. Micromech. Microeng., **6**, pp. 95–98.
[29] Guo, S., Nakamura, T., Fukuda, T., and Oguro, K., 1996, ''Design and Experiments of Micro Pump Using ICPF Actuator,'' *Proc. of Micro Mechatronics and Human Science 96*, pp. 235–240.
[30] Guo, S., Hata, S., Sugumoto, K., Fukuda, T., and Oguro, K., 1998, ''A New Type of Capsule Micropump Using ICPF Actuator,'' *Proc. of Micro Mechatronics and Human Science 98*, pp. 255–260.
[31] Accoto, D., Nedelcu, O. T., Carrozza, M. C., and Dario, P., 1998, ''Theoretical Analysis and Experimental Testing of Miniature Piezoelectric Pump,'' *Proc. of Micro Mechatronics and Human Science 98*, pp. 261–268.
[32] Benard, W. L., Kahn, H., Heuer, A. H., and Huff, M. A., 1998, ''Thin Film Shape-Memory Alloy Actuated Micropumps,'' Journal of MEMS, **7**, No. 2, pp. 245–251.
[33] Li, H. Q., Roberts, D. C., Steyn, J. L., Turner, K. T., Carretero, J. A., Yaglioglu, O., Su, Y. H., Saggere, L., Hagood, N. W., Spearing, S. M., and Schmidt, M. A., 2000, ''A High Frequency High Flow Rate Piezoelectrically Driven MEMS Micropump,'' *Tech. Dig. Solid-State Sensor and Actuator Workshop*, Hilton Head, in print.
[34] Smits, J. G., 1988, ''Piezoelectric Micropump With Three Valves Working Peristaltically,'' Sens. Actuators, **15**, pp. 153–167.
[35] Shinohara, J., Suda, M., Furuta, K., and Sakuhara, T., 2000, ''A High Pressure Resistance Micropump Using Active and Normally Closed Valves,'' *IEEE 13th Int. Workshop on MEMS (MEMS'00)*, pp. 86–91.
[36] Judy, J. W., Tamagawa, T., and Polla, D. L., 1991, ''Surface-Machined Micromechanical Membrane Pump,'' *IEEE 4th Int. Workshop on MEMS (MEMS'91)*, pp. 182–186.
[37] Folta, J. A., Raley, N. F., and Hee, E. W., 1992, ''Design Fabrication and Testing of a Miniature Peristaltic Membrane Pump,'' *Tech. Dig. Solid-State Sensor and Actuator Workshop*, Hilton Head, pp. 186–189.

[38] Mizoguchi, H., Ando, M., Mizuno, T., Takagi, T., and Nakajima, N., 1992, ‘‘Design and Fabrication of Light Driven Micropump,’’ *IEEE 5th Int. Workshop on MEMS (MEMS’92)*, pp. 31–36.

[39] Grosjean, C., and Tai, Y. C., 1999, ‘‘A Thermopneumatic Peristaltic Micropump,’’ *Inter. Conf. on Solid-State Sensors and Actuators (Transducers ’99)*, pp. 1776–1779.

[40] Cabuz, C., Cabuz, E. I., Herb, W. R., Rolfer, T., and Zook, D., 1999, ‘‘Measoscopic Sampler Based on 3D Array of Electrostatically Activated Diagphragms,’’ *Inter. Conf. on Solid-State Sensors and Actuators* (Transducers ’99), pp. 1890–1891.

[41] Stemme, E., and Stemme, G., 1993, ‘‘A Valveless Diffuser/Nozzle-Based Fluid Pump,’’ Sens. Actuators A, **39**, pp. 159–167.

[42] Olsson, A., Stemme, G., and Stemme, E., 1995, ‘‘A Valve-Less Planar Fluid Pump With Two Pump Chambers,’’ Sens. Actuators A, **46–47**, pp. 549–556.

[43] Olsson, A., Enoksson, P., Stemme, G., and Stemme, G., 1997, ‘‘Micromachined Flat-Walled Valve-Less Diffuser Pumps,’’ J. of MEMS, **6**, No. 2, pp. 161–166.

[44] Olsson, A., Stemme, G., and Stemme, E., 1999, ‘‘A Numerical Design Study of the Valveless Diffuser Pump Using a Lumped-Mass Mode,’’ J. Micromech. Microeng., **10**, pp. 34–44.

[45] Gerlach, T., Schoenemann, M., and Wurmus, H., 1995, ‘‘A New Micropump Principle of the Reciprocating Type Using Pyramidic Micro Flow Channels as Passive Valves,’’ J. Micromech. Microeng., **5**, pp. 199–201.

[46] Gerlach, T., and Wurmus, H., 1995, ‘‘Working Principle and Performance of the Dynamic Micropump,’’ Sens. Actuators A, **50**, pp. 135–140.

[47] Gerlach, T., 1998, ‘‘Microdiffusers as Dynamic Passive Valves for Micropump Applications,’’ Sens. Actuators A, **69**, pp. 181–191.

[48] Jeong, O. C., and Yang, S. S., 2000, ‘‘Fabrication and Test of a Thermopneumatic Micropump With a Corrugated p+ Diaphragm,’’ Sens. Actuators A, **83**, pp. 249–255.

[49] Ullmann, A., 1998, ‘‘The Piezoelectric Valve-Less Pump: Performance Enhancement Analysis,’’ Sens. Actuators A, **69**, pp. 97–105.

[50] Forster, F. K., Bardell, R. L., Afromowitz, M. A., Sharma, N. R., and Blanchard, A., 1995, ‘‘Design, Fabrication and Testing of Fixed-Valve Micro-Pumps,’’ *Proc. of ASME Fluids Engineering Division, IMECE’95*, Vol. 234, pp. 39–44.

[51] Bardell, R. L., Sharma, N. R., Forster, F. K., Afromowitz, M. A., and Penney, R. J., 1997, ‘‘Designing High-Performance Micro-Pumps Based on No-Moving-Parts Valves,’’ *Proc. of Microelectromechanical systems (MEMS) ASME, DSC-Vol. 62/HTD-Vol. 354*, pp. 47–53.

[52] Tesla, N., 1920, ‘‘Valvular Conduit,’’ *US patent 1 329 559*.

[53] Stehr, M., Messner, S., Sandmaier, H., and Zengerle, R., 1996, ‘‘A New Micropump With Bidirectional Fluid Transport and Selfblocking Effect,’’ *IEEE 9th Int. Workshop on MEMS (MEMS’96)*, pp. 485–490.

[54] Stehr, M., Messner, S., Sandmaier, H., and Zengerle, R., 1996, ‘‘The VAMP-Anew Device for Handling Liquids or Gases,’’ Sens. Actuators A, **57**, pp. 153–157.

[55] Nguyen, N. T., Schubert, S., Richter, S., and Dötzel, W., 1998, ‘‘Hybrid-Assembled Micro Dosing System Using Silicon-Based Micropump/Valve and Mass Flow Sensor,’’ Sens. Actuators A, **69**, pp. 85–91.

[56] Matsumoto, S., Klein, A., and Maeda, R., 1999, ‘‘Development of Bi-Directional Valve-Less Micropump for Liquid,’’ *Proc. of 12th Int. Workshop on MEMS (MEMS’99)*, pp. 141–146.

[57] Ahn, C. H., and Allen, M. G., 1995, ‘‘Fluid Micropumps Based on Rotary Magnetic Actuators,’’ *IEEE 8th Int. Workshop on MEMS (MEMS’95)*, pp. 408–412.

[58] Doepper, J., Clemens, M., Ehrfeld, W., Jung, S., Kaemper, K. P., and Lehr, H., 1997, ‘‘Micro Gear Pumps for Dosing of Viscous Fluids,’’ J. Micromech. Microeng., **7**, pp. 230–232.

[59] Moroney, R. M., White, R. M., and Howe, R. T., ‘‘Ultrasonically Induced Microtransport,’’ *IEEE 4th Int. Workshop on MEMS (MEMS’91)*, pp. 277–282.

[60] Nguyen, N. T., Meng, A. H., Black, J., and White, R. M., 2000, ‘‘Integrated Flow Sensor for In Situ Measurement and Control of Acoustic Streaming in Flexural Plate Wave Micro Pumps,’’ Sens. Actuators A, **79**, pp. 115–121.

[61] Miyazaki, S., Kawai, T., and Araragi, M., 1991, ‘‘A Piezoelectric Pump Driven by a Flexural Progressive Wave,’’ *IEEE 4th Int. Workshop on MEMS (MEMS’91)*, pp. 283–288.

[62] Kurosawa, M., Watanabe, T., and Higuchi, T., ‘‘Surface Acoustic Wave Atomizer With Pumping Effect,’’ *IEEE 8th Int. Workshop on MEMS (MEMS’95)*, pp. 25–30.

[63] Bart, S. F., Tavrow, L. S., Mehregany, M., and Lang, J. H., 1990, ‘‘Microfabricated Electrohydrodynamic Pumps,’’ Sens. Actuators A, **21–23**, pp. 193–197.

[64] Fuhr, G., Hagedom, R., Mueller, T., Benecke, W., and Wagner, B., 1992, ‘‘Pumping of Water Solutions in Microfabricated Electrohydrodynamic Systems,’’ *IEEE 5th Int. Workshop on MEMS (MEMS’92)*, pp. 25–30.

[65] Fuhr, G., 1997, ‘‘From Micro Field Cages for Living Cells to Brownian Pumps for Submicron Particles,’’ *Proc. of IEEE Micro Mechatronics and Human Science 97*, pp. 1–4.

[66] Fuhr, G., Hagedorn, R., Mueller, T., Benecke, W., and Wagner, B., 1992, ‘‘Microfabricated Electrohydrodynamic (EHD) Pumps for Liquids of Higher Conductivity,’’ Journal of MEMS, **1**, No. 3, pp. 141–145.

[67] Fuhr, G., Schnelle, T., and Wagner, B., 1994, ‘‘Travelling Wave-Driven Microfabricated Electrohydrodynamic Pumps for Liquids,’’ J. Micromech. Microeng., **4**, pp. 217–226.

[68] Ahn, S. H., and Kim, Y. K., 1998, ‘‘Fabrication and Experiment of a Planar Micro Ion Drag Pump,’’ Sens. Actuators A, **70**, pp. 1–5.

[69] Richter, A., and Sandmaier, H., 1990, ‘‘An Electrohydrodynamic Micropump,’’ *IEEE 3rd Int. Workshop on MEMS (MEMS’90)*, pp. 99–104.

[70] Richter, A., Plettner, A., Hofmann, K. A., and Sandmaier, H., 1991, ‘‘A Micromachined Electrohydrodynamic (EHD) Pump,’’ Sens. Actuators A, **29**, pp. 159–168.

[71] Furuya, A., Shimokawa, F., Matsuura, T., and Sawada, R., 1996, ‘‘Fabrication of Fluorinated Polyimide Microgrids Using Magnetically Controlled Reactive Ion Etching (MC-RIE) and Their Applications to an Ion Drag Integrated Micropump,’’ J. Micromech. Microeng., **6**, pp. 310–319.

[72] Harrison, D. J., Manz, A., and Glavina, P. G., 1991, ‘‘Electroosmotic Pumping Within a Chemical Sensor System Integrated on Silicon,’’ *Proc. of Inter. Conf. on Solid-State Sensors and Actuators Transducers’91*, pp. 792–795.

[73] Harrison, D. J., Seiler, K., Manz, A., and Fan, Z., 1992, ‘‘Chemical Analysis and Electrophoresis Systems Integrated on Glass and Silicon Chips,’’ *Tech. Dig. Solid-State Sensor and Actuator Workshop*, Hilton Head, pp. 110–113.

[74] Webster, J. R., Jones, D. K., and Mastrangelo, C. H., 1996, ‘‘Monolithic Capillary Gel Electrophoresis Stage With On-Chip Detector,’’ *IEEE 9th Int. Workshop on MEMS (MEMS’96)*, pp. 491–496.

[75] Webster, J. R., Burns, M. A., Burke, D. T., and Mastrangelo, C. H., 2000, ‘‘Electrophoresis System With Integrated On-Chip Fluorescence Detection,’’ *IEEE 13th Int. Workshop on MEMS (MEMS’00)*, pp. 306–310.

[76] Takagi, H., Maeda, R., Ozaki, K., Parameswaran, M., and Mehta, M., 1994, ‘‘Phase Transformation Type Micropump,’’ *Proc. of Micro Mechatronics and Human Sciences 94*, pp. 199–202.

[77] Ozaki, K., 1995, ‘‘Pumping Mechanism Using Periodic Phase Changes of a Fluid,’’ *IEEE 8th Int. Workshop on MEMS (MEMS’95)*, pp. 31–36.

[78] Jun, T. K., and Kim, C. J., 1996, ‘‘Microscale Pumping With Traversing Bubbles in Microchannels,’’ *Tech. Dig. Solid-State Sensor and Actuator Workshop*, Hilton Head, pp. 144–147.

[79] Jun, T. K., and Kim, C.-J., 1998, ‘‘Valveless Pumping Using Traversing Vapor Bubbles in Microchannels,’’ J. Appl. Phys., **83**, No. 11, pp. 5658–5664.

[80] Matsumoto, H., and Colgate, J. E., 1990, ‘‘Preliminary Investigation of Micropumping Based on Electrical Control of Interfacial Tension,’’ *IEEE 3rd Int. Workshop on MEMS (MEMS’90)*, pp. 105–110.

[81] Lee, J., and Kim, C. J., 1998, ‘‘Liquid Micromotor Driven by Continuous Electrowetting,’’ *IEEE 11th Int. Workshop on MEMS (MEMS’98)*, pp. 538–543.

[82] Boehm, S., Olthuis, W., and Bergveld, P., 2000, ‘‘A Bi-Directional Electrochemically Driven Micro Liquid Dosing System With Integrated Sensor/Actuator Electrodes,’’ *IEEE 13th Int. Workshop on MEMS (MEMS’00)*, pp. 92–95.

[83] Lemoff, A. V., Lee, A. P., Miles, R. R., and McConaghy, C. F., 1999, ‘‘An AC Magnetohydrodynamic Micropump: Tpwards a True Integrated Microfluidic System,’’ *Int. Conf. on Solid-State Sensors and Actuators (Transducers ’99)*, pp. 1126–1129.

[84] Lemoff, A. V., and Lee, A. P., 2000, ‘‘An AC Magnetohydrodynamic Micropump,’’ Sens. Actuators B, **63**, pp. 178–185.

[85] Maluf, N., 2000, *An Introduction to Microelectromechanical Systems Engineering*, Artech House, Boston, p. 95.

Jens Nørkær Sørensen
Associate Professor,
Department of Mechanical Engineering,
Building 403,
Technical University of Denmark,
DK-2800 Lyngby,
Denmark

Wen Zhong Shen
Associate Professor,
Department of Mechanical Engineering,
Building 403,
Technical University of Denmark;
Associate Professor,
Research Center for High Speed Trains,
Changsha Railway University,
China

Numerical Modeling of Wind Turbine Wakes

An aerodynamical model for studying three-dimensional flow fields about wind turbine rotors is presented. The developed algorithm combines a three-dimensional Navier-Stokes solver with a so-called actuator line technique in which the loading is distributed along lines representing the blade forces. The loading is determined iteratively using a blade-element approach and tabulated airfoil data. Computations are carried out for a 500 kW Nordtank wind turbine equipped with three LM19.1 blades. The computed power production is found to be in good agreement with measurements. The computations give detailed information about basic features of wind turbine wakes, including distributions of interference factors and vortex structures. The model serves in particular to analyze and verify the validity of the basic assumptions employed in the simple engineering models.
[DOI: 10.1115/1.1471361]

1 Introduction

Load and performance calculations of wind turbines are today routinely performed by the Blade-Element/Momentum (BEM) method (Glauert [1]). This method is based on dividing the flow in annular control volumes and applying momentum balance and energy conservation in each control volume. The annuli are bounded by stream surfaces that enclose the rotor and extend from far upstream to far downstream. Basic assumptions of the method are that the induced velocity in the rotor plane is equal to one half of the induced velocity in the ultimate wake, and that the flow can be analyzed by dividing the blade into a number of independent elements. For each blade element the aerodynamic forces are obtained using tabulated airfoil data, derived from wind tunnel measurements and corrected for three-dimensional effects. Because the BEM model is simple and very fast to run on a computer, it has gained an enormous popularity and is today the only design code in use by industry. However, owing to limitations of representing all the various flow situations encountered in practice, it has become necessary to introduce different empirical corrections. Such situations include phenomena related to dynamic inflow, yaw misalignment, tip loss and heavily loaded rotors. There exists thus an increasing need to establish experiments and to develop more advanced models to evaluate the basic assumptions underlying the BEM model. Although there today seems to be no realistic alternative that may replace the BEM model as an industrial design tool, more advanced inviscid models have been developed to overcome the limitations of the momentum approach.

One such method is the vortex wake method. In this method the shed vorticity in the wake is employed to compute the induced velocity field. The vorticity may either be distributed as vortex line elements (Miller [2], Simoes and Graham [3], and Bareiss et al. [4]) or as discrete vortices (Voutsinas et al. [5]), with vortex distributions determined either as a prescribed wake or a free wake. A free wake analysis may in principle provide one with all relevant informations needed to understand the physics of the wake. However, this method can be very computing demanding and tends to diverge owing to the intrinsic singularities of vortex lines.

Another method is the asymptotic acceleration potential method (van Holten [6] and van Bussel [7]). This method is based on solving a Poisson equation for the pressure, assuming small perturbations of the mean flow. Compared to vortex wake models, the method is fast to run on a computer. The model has been used to analyze various flow cases, such as dynamic inflow and yawed flow. The main limitation of the model is that it is based on linearized flow equations, hence further development of the technique is required when analyzing flows about rotors subject to high loadings.

Finally, yet another class of inviscid methods is the generalized actuator disk method. This type of model represents a straightforward extension of the BEM model, as it employs tabulated airfoil data along with the conservation laws. The main difference is that the annular independence of the BEM model is replaced by the solution of a full set of Euler or Navier-Stokes equations. Axisymmetric versions of the method have been developed and solved either by analytical/semi-analytical methods (Wu [8], Greenberg [9], Conway [10,11]) or by finite difference/finite volume methods (Sørensen and Myken [12], Sørensen and Kock [13], Madsen [14]). In helicopter aerodynamics similar approaches have been applied by e.g., Fejtek and Roberts [15] who solved the flow about a helicopter employing a chimera grid technique in which the rotor was modelled as an actuator disk, and Rajagopalan and Mathur [16] who modelled a helicopter rotor using time-averaged momentum source terms in the momentum equations. Comparisons with experiments have demonstrated that the method works well for axisymmetric flow conditions and can provide usefull informations regarding phenomena such as dynamic inflow (Sørensen and Kock [13]) and turbulent wake states occurring for heavily loaded rotors (Sørensen et al. [17]). The main limitation of the method is that the forces are distributed evenly along the actuator disk, hence the influence of the blades is taken as an integrated quantity in the azimuthal direction.

To avoid the problem of using corrected or calibrated airfoil data various hybrid viscous/inviscid models have been developed. Sørensen [18] used a quasi-simultaneous interaction technique to study the influence of rotation on the stall characteristics of a wind turbine rotor. Sankar and co-workers (Berkman et al. [19]) developed a hybrid Navier-Stokes/full-potential/free wake method for predicting three-dimensional unsteady viscous flows over isolated helicopter rotors in hover and forward flight. The method has recently been extended to cope with horizontal axis wind turbines (Xu and Sankar [20]). Another hybrid method is due to Hansen et al. [21] who combined a three-dimensional Navier-Stokes solver with an axisymmetric actuator disk model.

Recently, full three-dimensional computations employing the Reynolds-averaged Navier-Stokes (RaNS) equations have been carried out by Ekaterinaris [22], Duque et al. [23], and Sørensen and Michelsen [24]. Although the RaNS methods are able of cap-

---

Contributed by the Fluids Engineering Division for publication in the JOURNAL OF FLUIDS ENGINEERING. Manuscript received by the Fluids Engineering Division November 16, 1999; revised manuscript received November 20, 2001. Associate Editor: U. Ghia.

turing the pre-stall behavior, because of inaccurare turbulence modelling and grid resolution RaNS methods still fail to capture correctly the stall behavior.

To overcome the limitations of the axisymmetric actuator disk model, we here present a new model that combines a three-dimensional Navier-Stokes solver with a technique in which body forces are distributed radially along each of the rotor blades. Thus, the kinematics of the wake is determined by a full three-dimensional Navier-Stokes simulation whereas the influence of the rotating blades on the flow field is included using tabulated airfoil data to represent the loading on each blade. Although a Navier-Stokes solver is employed for studying the global flow field, the flow of interest is essentially inviscid, and viscous effects from the boundary layer are introduced only as integrated quantities through the use of airfoil data. The airfoil data and subsequent loading are determined iteratively by computing local angles of attack from the movement of the blades and the local flow field. The technique we refer to as the actuator line concept. The concept enables us to study in detail the dynamics of the wake and the tip vortices and their influence on the induced velocities in the rotor plane. The main motivation for developing such a model is to analyze and verify the validity of the basic assumptions that are employed in the simpler more practical engineering models.

In Section 2 the mathematical model and the computation algorithm are described. Section 3 describes how the body forces are derived from local blade-element considerations employing tabulated airfoil data. In section 4 numerical results are presented for the flow past a Nordtank 500/41 wind turbine equipped with three LM19.1 blades. First, to validate the code, comparisons between numerical results and experimental data are provided and a study on grid sensitivity is carried out. Good agreement with the measured power curve is found. Next, global flow fields about the rotor are analyzed. Distributions of induced velocities in the rotor plane as well as the structure of the wake are computed. Particularly, it is shown that the model is capable of predicting distinct tip vortices and their location in the wake.

2 Mathematical Model and Numerics

The flow model combines the actuator line concept with a finite difference discretization of the Navier-Stokes equations. The equations are formulated in vorticity-velocity ($\boldsymbol{\omega}-\mathbf{V}$) variables and solved in a cylindrical coordinate system (r, θ, z). The formulation, which is obtained by applying the curl operator on the Navier-Stokes equations in primitive variables (i.e., velocity-pressure) consists of three transport equations for the vorticity components, three definition equations connecting velocity and vorticity, and the continuity equation, as shown below,

$$\frac{\partial \boldsymbol{\omega}}{\partial t} + \nabla\times(\boldsymbol{\omega}\times\mathbf{V}) = -\nu\nabla\times(\nabla\times\boldsymbol{\omega}) + \nabla\times\mathbf{f}_\epsilon, \tag{1}$$

$$\nabla\times\mathbf{V} = \boldsymbol{\omega}, \quad \nabla\cdot\mathbf{V} = 0, \tag{2}$$

where ν is the kinematic viscosity and $\mathbf{f}_\epsilon$ is the loading which is introduced as a body force on the right-hand side of the momentum equations.

When solving Eqs. (1) and (2), continuity is automatically ensured, hence the problem of the pressure-velocity coupling associated with a primitive variables formulation is avoided. The vorticity formulation, on the other hand, is complicated by the additional constraint that the vorticity field has to be solenoidal as well. Furthermore, the scalar representation of Eq. (2) constitutes a set of 4 equations in 3 unknowns and, therefore, comprises an over-determined system that calls for special solution techniques. In Huang and Ghia [25] it was demonstrated that a unique solution of the system is possible provided that the velocity boundary conditions satisfy the constraint of zero mass flow out of the boundaries. In the present work a least-squares method is employed to solve Eq. (2).

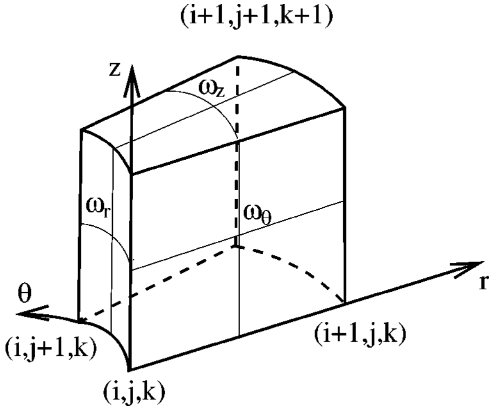

Fig. 1 Staggered grid arrangement

In principle, a solenoidal vorticity field is obtained by writing the transport equations in rotational form. It is important, however, that the discretization in itself does not introduce any artificial production terms due to truncation errors. This problem is solved by employing a staggered grid in which the vorticity components are defined at the face centers of the computational boxes. Thus, denoting by (r_i, θ_j, z_k) the coordinates to the lower left corner point of a computational box, ω_r is located at $(r_i, \theta_{j+1/2}, z_{k+1/2})$, ω_θ is located at $(r_{i+1/2}, \theta_j, z_{k+1/2})$, ω_z is located at $(r_{i+1/2}, \theta_{j+1/2}, z_k)$, and the corresponding transport equations are discretized about the same locations. The staggered grid arrangement is shown in Fig. 1.

Time integration is performed by utilizing a Crank-Nicolson type scheme for the diffusive terms and an explicit Adams-Bashforth discretization of the convection and stretching terms. Employing a notation in which $\mathbf{L}_d$ denotes the diffusive terms and $\mathbf{L}_c$ the convective and stretching terms, Eq. (1) may in short be written as

$$\frac{\partial \boldsymbol{\omega}}{\partial t} - \mathbf{L}_d(\boldsymbol{\omega}) = \mathbf{L}_c(\boldsymbol{\omega}) + \nabla\times\mathbf{f}_\epsilon, \tag{3}$$

which in discretized form reads

$$\frac{2}{\Delta t}\boldsymbol{\omega}^{n+1} - \mathbf{L}_d^{n+1}(\boldsymbol{\omega}) = \frac{2}{\Delta t}\boldsymbol{\omega}^{n} + \mathbf{L}_d^{n}(\boldsymbol{\omega}) + 3\mathbf{L}_c^{n}(\boldsymbol{\omega}) - \mathbf{L}_c^{n-1}(\boldsymbol{\omega}) + 2\nabla\times\mathbf{f}_\epsilon^{n}, \tag{4}$$

where Δt is the time step and superscript 'n' refers to the time at which the operator is evaluated. The spatial discretization is carried out employing central differences for the diffusive terms and the force terms, and the second order upwinding scheme QUICK for the remaining terms. The resulting set of coupled difference equations is solved simultaneously for all vorticity components by an iterative line-relaxation method.

After having advanced the vorticity in time, the velocity field is updated by solving the Cauchy-Riemann equations, Eq. (2), with the newly calculated vorticity on the right-hand side. These equations constitute a set of four first order differential equations. To avoid wiggles from odd-even decoupling the equations are discretized by use of a box scheme. As we are seeking the solution for only three variables, i.e., the velocity components (V_r, V_θ, V_z), the system is overdetermined and the solution is accomplished by employing a least-squares method. This is found by applying the conjugate gradient method on the associated normal equations. In discretized form, Eq. (2) is expressed as:

$$\underline{\underline{A}}\,\underline{V} = \underline{b}, \tag{5}$$

where $\underline{\underline{A}}$ is a $m\times q$ coefficient matrix, $\underline{V}$ is a vector containing q unknown velocity components and the right-hand vector $\underline{b}$ con-

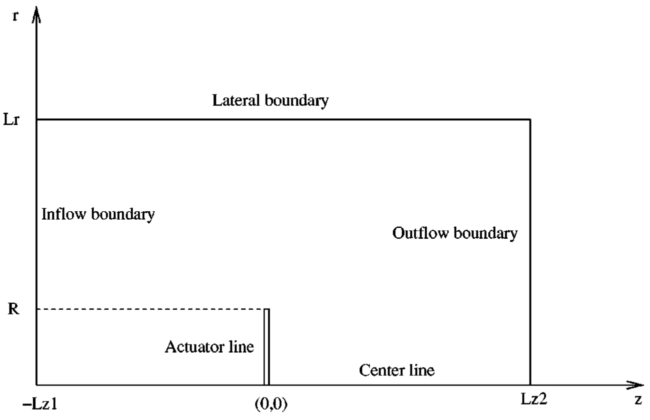

Fig. 2 Cross section of computational domain

tains *m* elements. This system is overdetermined and solved using an iterative least squares method. This is accomplished by replacing Eq. (5) by its normal system

$$(\underline{\underline{A}}^T\underline{\underline{D}}\,\underline{\underline{D}}\,\underline{\underline{A}})\underline{V}=\underline{\underline{A}}^T\underline{\underline{D}}\,\underline{\underline{D}}\,\underline{b}, \tag{6}$$

where $\underline{\underline{D}}$ is a diagonal matrix introduced for the purpose of scaling. The elements on the diagonal of $\underline{\underline{D}}$ are $d_{ii}=\|a_i\|_2$, where a_i denotes the ith row of $\underline{\underline{A}}$. This choice of $\underline{\underline{D}}$ weights all equations equally. It may be noted that solving Eq. (6) is equivalent to minimize the functional

$$I=\frac{1}{2}\int\int\int_v[(\nabla\cdot\mathbf{V})^2+\|\nabla\times\mathbf{V}-\boldsymbol{\omega}\|^2]dv. \tag{7}$$

The solution of Eq. (6) is found by applying a standard conjugate gradient method. Further details about the solution algorithm can be found in Shen and Ta Phuoc [26] and Sørensen et al. [27].

The computational domain is limited by $r\in[0,L_R]$, $\theta\in[0,2\pi/3]$ and $z\in[-L_{z1},L_{z2}]$, where L_R denotes the radius to the lateral boundary, L_{z1} and L_{z2} denote the distances to the upstream and the downstream boundary, respectively, and θ is the azimuthal angle defined positive counter-clockwise. The computational domain is shown in Fig. 2. To reduce the computing time the calculations are carried out in a domain comprising one third of the rotor area by imposing periodicity in the azimuthal direction.

To close the equations, boundary conditions are introduced as follows. At the inflow boundary a constant axial wind velocity is specified. At the outflow boundary downstream the rotor a Neumann condition is imposed for the axial velocity component. At the lateral boundary the radial velocity is put equal to zero. Boundary conditions for the vorticity are everywhere established from the vorticity definition equations. To summarize, the boundary conditions for velocity and vorticity are defined as follows:

Lateral boundary ($r=L_R, 0\leq\theta\leq2\pi/3, -L_{z1}\leq z\leq L_{z2}$):

$$V_r=0,\quad \omega_\theta=-\frac{\partial V_z}{\partial r},\quad \omega_z=\frac{1}{r}\frac{\partial(rV_\theta)}{\partial r}.$$

Inflow boundary ($0\leq r\leq L_R, 0\leq\theta\leq2\pi/3, z=-L_{z1}$):

$$V_z=V_o,\quad \omega_r=-\frac{\partial V_\theta}{\partial z},\quad \omega_\theta=\frac{\partial V_r}{\partial z}.$$

Outflow boundary ($0\leq r\leq L_R, 0\leq\theta\leq2\pi/3, z=L_{z2}$):

$$\frac{\partial V_z}{\partial z}=0,\quad \omega_r=\frac{1}{r}\frac{\partial V_z}{\partial\theta},\quad \omega_\theta=-\frac{\partial V_z}{\partial r}.$$

The boundary conditions are imposed such that the velocity conditions are used in the Cauchy-Riemann system, Eq. (2), and the vorticity conditions are employed in the transport equations, Eq. (1). As the transport equations are written in curl-form, no boundary conditions are necessary for the solution of the ω_z-transport equation at in-and outflow boundaries.

In principle, the flow is inviscid, but in order to stabilize the solution diffusive terms are retained. Thus, an effective Reynolds number is defined as $\mathrm{Re}=V_oR/\nu$, where R is the radius of the rotor and V_o is the undisturbed velocity. It is important to note that the Reynolds number only has a limited influence on the flow behavior, as vorticity is only produced along the lines representing the rotor blades and subsequently convected and diffused away from these. The vorticity sources are introduced into the equations through the body forces appearing on the right-hand side of Eq. (1). It is known from flows past bluff bodies that the drag coefficient and the essential flow behavior do not depend on the Reynolds number, provided that it has reached a certain minimum value (Sørensen et al. [17]).

3 Determination of Body Forces

To determine the body forces acting on the rotor blades we use a blade-element approach combined with two-dimensional airfoil characteristics. In Fig. 3, a cross-sectional element at radius r defines the airfoil in the (θ,z) plane. Denoting the tangential and axial velocity in the inertial frame of reference as V_θ and V_z, respectively, the local velocity relative to the rotating blade is given as

$$\mathbf{U}_{\mathrm{rel}}=(V_\theta-\Omega r,V_z). \tag{8}$$

The angle of attack is defined as

$$\alpha=\phi-\gamma, \tag{9}$$

where $\phi=\tan^{-1}(V_z/(\Omega r-V_\theta))$ is the angle between $\mathbf{U}_{rel}$ and the rotor plane and γ is the local pitch angle. The force per spanwise unit length is

$$\mathbf{f}_{2D}=\frac{d\mathbf{F}}{dr}=\frac{1}{2}\rho U_{\mathrm{rel}}^2c(C_L\mathbf{e}_L+C_D\mathbf{e}_D), \tag{10}$$

where $C_L=C_L(\alpha,\mathrm{Re})$ and $C_D=C_D(\alpha,\mathrm{Re})$ are the lift and drag coefficients, respectively, c is the chord length, and $\mathbf{e}_L$ and $\mathbf{e}_D$ denote the unit vectors in the directions of the lift and the drag, respectively. The lift and drag coefficients are determined from measured or computed two-dimensional airfoil data that are corrected for three-dimensional effects. There are several reasons why it is necessary to correct the airfoil data. First, at separation rotational effects limit the growth of the boundary layer, resulting in an increased lift as compared to two-dimensional characteristics. Various correction formulas for rotational effects have been derived using quasi three-dimensional approaches (see e.g., Snel

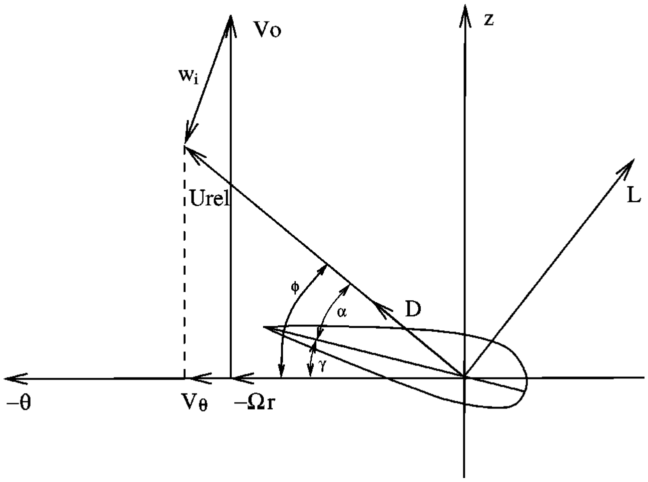

Fig. 3 Cross-sectional airfoil element

et al. [28] and Chaviaropoulos and Hansen [29]). Next, the airfoil characteristics depend on the aspect ratio of the blade. This is in particular pronounced at high incidences where the finite aspect ratio drag coefficient, C_D, is much smaller than the corresponding one for an infinite blade. As an example, for a flat plate at an incidence $\alpha = 90$ deg the drag coefficient $C_D = 2$ for an infinitely long plate, whereas for aspect ratios corresponding to the geometry of a wind turbine blade C_D takes values in the range 1.2–1.3. In Hoerner [30] it is stated that the normal force from a flat plate is approximately constant for $45\,\text{deg} < \alpha < 135\,\text{deg}$, indicating that in this range both C_L and C_D have to be reduced equally. Hansen [31] proposes to reduce C_L and C_D by an expression that takes values in range from 0.6–1.0, depending on the ratio between the distance to the tip and the local chord length. It should be noticed, however, that this is only a crude guideline and that most airfoil data for wind turbine use is calibrated against actual performance and load measurements. This also explains why most manufacturers of wind turbine blades are reluctant to change well-tested airfoil families.

Considering an element of differential size, $dv = r\,dr\,d\theta\,dz$, the force is given by

$$\mathbf{f} = \frac{d\mathbf{F}}{dv} = \frac{\mathbf{f}_{2D}}{r\,d\theta\,dz}. \tag{11}$$

Projecting this vector on the coordinate directions we get

$$f_r = 0, \tag{12}$$

$$f_\theta = \frac{\rho c U_{\text{rel}}^2}{2 r\,d\theta\,dz}(C_L \sin\phi - C_D \cos\phi), \tag{13}$$

$$f_z = \frac{\rho c U_{\text{rel}}^2}{2 r\,d\theta\,dz}(C_L \sin\phi + C_D \cos\phi). \tag{14}$$

The kinematics of the flow may also be expressed in terms of the induced velocity,

$$w_i = (-aV_o, -a'\Omega r), \tag{15}$$

where the axial flow interference factor is defined as

$$a = 1 - \frac{V_z}{V_o}, \tag{16}$$

and the tangential flow interference factor

$$a' = -\frac{V_\theta}{\Omega r}. \tag{17}$$

As the source term in Eq. (1) is given as the curl of the load, it acts as a singular vorticity source along the rotor blades. To avoid singular behavior, $\mathbf{f}_\epsilon$ is formed by taking the convolution of the computed normal load, $\mathbf{f}$, and a regularization kernel, η_ϵ, as shown below

$$\mathbf{f}_\epsilon = \mathbf{f} \otimes \eta_\epsilon,$$

where

$$\eta_\epsilon(r) = \frac{1}{\epsilon^3 \pi^{3/2}} \exp[-(r/\epsilon)^2].$$

Here ϵ is a constant that serves to adjust the strength of the regularization function and r is the distance between the measured point and the initial force points on the rotor. In the case of three blades, the regularized force becomes

$$\mathbf{f}_\epsilon(\mathbf{x}) = \sum_{i=1}^{3} \int_0^R \mathbf{f}_{2D}(r)\,\eta_\epsilon(|\mathbf{x} - r\mathbf{e}_i|)\,dr,$$

where $\mathbf{e}_i$ denotes the unit vector of the blade direction. Denoting the position of the first blade in cylindrical coordinates by (r, θ_o, z_o), the two other positions are given as $(r, \theta_o + 2\pi/3, z_o)$ and $(r, \theta_o + 4\pi/3, z_o)$, respectively. The reason for introducing the function η_ϵ is to distribute smoothly the loading on more than one mesh point. The influence of the parameter ϵ has been studied in Sørensen et al. [17].

4 Results and Discussion

We here compute the global flow field past a 500 kW Nordtank wind turbine equipped with three LM19.1 blades. The turbine has a rotor diameter of 41 m and runs at a tip speed $V_{tip} = 58$ m/s. The blade sections consist of NACA 63-4xx series airfoils on the outer 8 m of the blade and of FFA-W3-xxx airfoils on the remaining inner part. The blade has approximately a linear chord distribution from $r = 4.5$ m to $r = 18.0$ m and is twisted gradually from 0 at the tip to 20 deg at $r = 4.5$ m. The chord and thickness distributions range from about 1.6 m and 53% at $r = 4.5$ m to about 0.1 m and 15% at $r = 20.5$ m, respectively. The airfoil data is based on two-dimensional measurements up to and just beyond stall (see Abbott and Doenhoff [32] and Björck [33]).

For higher incidences, no data are available for these profiles and instead data for NACA 0012 and Göttingen 420 were employed (Riegels [34]). The data were furthermore corrected for three-dimensional effects, as described in Section 3. The data were tabulated at four spanwise stations for incidences ranging from $\alpha = -10$ to $\alpha = 110$ deg. Adaptation to the computational mesh was accomplished by using linear interpolation. The data were kindly provided by Øye (private communication) and are normally used for BEM calculations in the Flex5 aeroelastic code. They were not modified in the present work.

The computations are carried out in a domain in which the inflow and the outflow boundary is located 20 rotor-radii, respectively, upstream and downstream of the rotor. The radial extent of the domain comprises 10 rotor-radii measured from the rotational axis. To capture the gradients of the flow field, grid points are concentrated near the blade tips and stretched in radial as well as in axial direction. The resulting grid consists of 100 grid points in the radial direction, 99 points in the axial direction and 50 points in the azimuthal direction. The mesh is equidistant in the θ-direction, i.e., $\Delta\theta = 0.044$. In the axial direction the grid spacing ranges from $\Delta z = 0.036$ at the rotor plane to about $\Delta z = 1.6$ in the far wake, and in the radial direction the spacing takes values from $\Delta r = 0.022$ near the tip to about $\Delta r = 0.4$ at the lateral boundary. The computations are carried out at an effective Reynolds number of 5000. As discussed earlier, using a low Reynolds number does not have an effect on the flow behavior at the blades, but will cause the wake to become more diffusive. The grid spacing and the value of the used Reynolds number is of course a compromise between accuracy and computing costs.

4.1 Validation of Numerical Model. To validate the numerical model the power yield of the Nordtank wind turbine was computed and compared to measurements. The comparison is shown in Fig. 4 that displays the mechanical power as a function of wind speed. For wind speeds up to about $V_0 = 12$ m/s excellent agreement is found between computed and measured values. At high wind speeds, however, the mechanical power is overpredicted with up to about 5%. This discrepancy is most probably related to inaccurate airfoil data as the induced velocities are almost negligible at high wind speeds. For V_0 greater than 12 m/s the rotor is stalled, and most of the flow on the suction side of the blade is separated. Hence, the airfoil data are subject to severe three-dimensional effects and become less reliable.

To quantify the influence of the employed grid, a computation on a finer mesh consisting of $150 \times 50 \times 148$ points was carried out for $V_0 = 10$ m/s. Comparisons of the force distributions computed by use of the two grids are shown in Fig. 5. Any difference between the two computations are barely seen and we conclude that the original grid is sufficiently fine to ensure accurate solutions.

To ensure that the flow is fully developed in most of the wake we let the computations run to about $t = 20$. With a timestep of $\Delta t = 2 \cdot 10^{-3}$ this corresponds to a total of about 10^4 time steps.

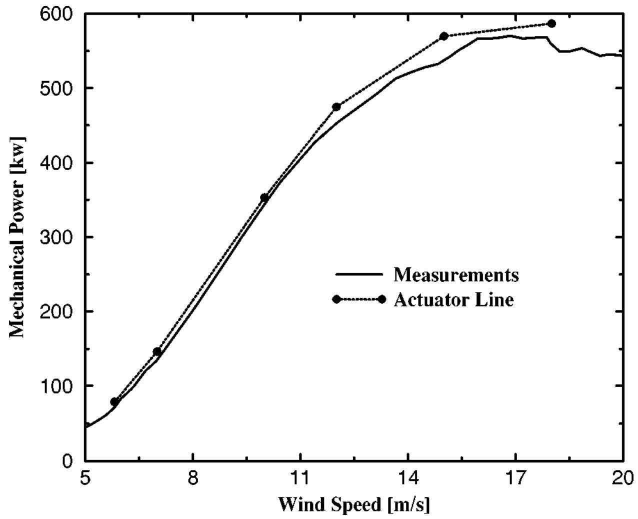

Fig. 4 Comparison of measured and computed mechanical power production for the Nordtank 500/41 wind turbine

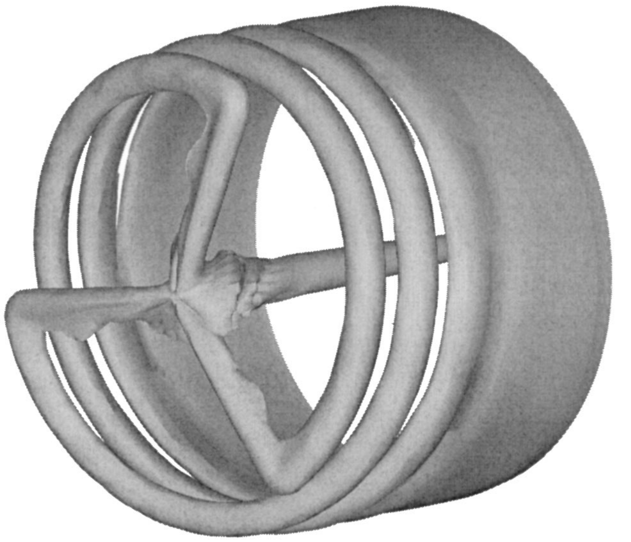

Fig. 6 Computed vorticity field showing the formation of the wake structure at $V_o = 10$ m/s

4.2 Wake Structures. In the following we show some representative numerical results that characterize the wake structure of the rotor. The results shown are computed at a wind speed $V_0 = 10$ m/s, corresponding to a tip speed ratio of 5.8. Figure 6 depicts iso-vorticity contours illustrating the downstream development of the wake vortices. The bound vorticity of the blades is seen to be shed downstream from the rotor in individual vortex tubes. These vortices persist about 2 turns after which they diffuse into a continuous vortex sheet. From experiments it is known that distinct spiral structures are maintained more turns than what is depicted in Fig. 6. It is most likely the combined effect from the low Reynolds number and the somewhat coarse grid downstream of the rotor that causes a too early diffusion of the vortex tubes.

Figure 7 shows the distribution of the axial interference factor, Eq. (16), in the rotor plane. The three blades are seen as lines with a high density of iso-lines, owing to the large changes in induced velocity that takes place across the blades. The number of iso-lines is 30 and the value between two successive lines is equidistant. The values range from -0.15–0.55, with peak values appearing near the mid-section of the blades (with a positive value on one side of the blade and a negative value on the other). The tip vortices appear as localized regions with negative a-values, with a minimum of about -0.11, corresponding to an axial velocity that is 11% higher than the inflow wind speed.

Following a in the azimuthal direction at a constant radius (see Fig. 8), the distribution is seen to be dominated by rather high minimum and maximum values. For the case treated here we compute values of a going from 0.55 on one side of the blade to -0.10 on the other side of the blade, with the mean value located about halfway between two blades. The dramatic jump in a is due to the induction from the bound vorticity located on the blade. To compare the interference factors a and a', defined in Eqs. (16) and (17), with results from BEM or axisymmetric actuator disk models, we compute averaged values from the formulas

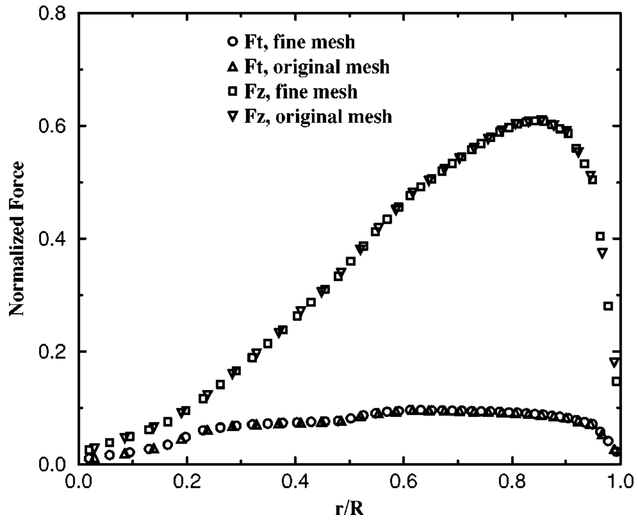

Fig. 5 Comparison of force distributions computed on the original mesh $(100\times50\times99)$ and on the fine mesh $(150\times50\times148)$ at $V_o = 10$ m/s

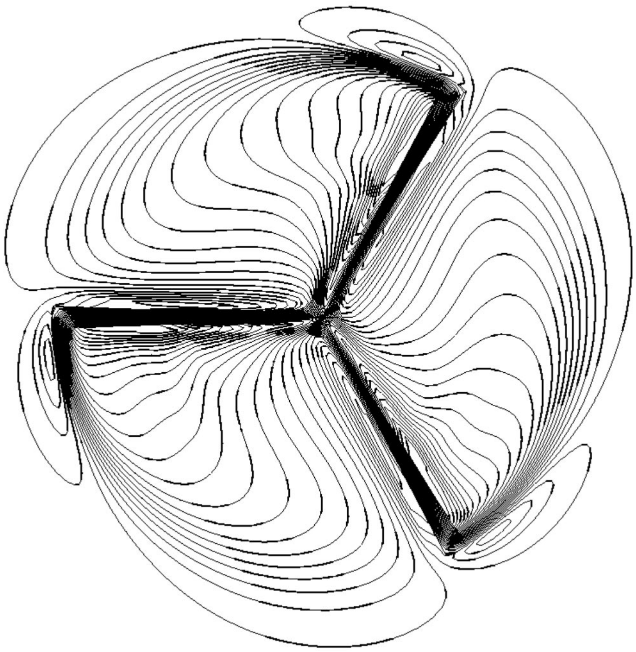

Fig. 7 Distribution of axial interference factor, $a = 1 - Vz/Vo$, in the rotor plane at $V_o = 10$ m/s

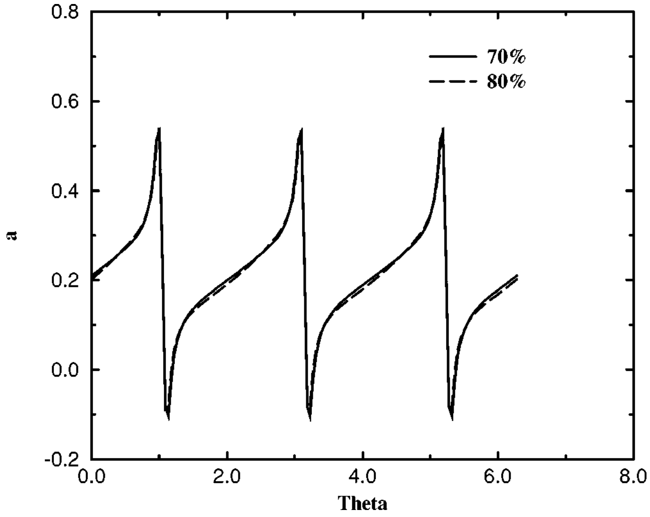

Fig. 8 Azimuthal distribution of axial interference factor, a, at $V_o=10$ m/s. Solid line: Distribution along $r=70\%R$; Dashed line: Distribution along $r=80\%R$

$$\overline{a}(r)=\frac{1}{2\pi}\int_0^{2\pi}a(r,\theta)d\theta,\quad \overline{a'}(r)=\frac{1}{2\pi}\int_0^{2\pi}a'(r,\theta)d\theta. \tag{18}$$

Figure 9 depicts the radial distributions of $\overline{a}$ and $\overline{a'}$. It is seen that $\overline{a'}$ decreases monotonously from a value of 0.4 at $r/R=0.05$ to zero at the tip. In contrast to the smooth behavior of $\overline{a'}$, $\overline{a}$ exhibits local maxima at both $r=0$ and at $r/R=0.75$. Both interference factors exhibit values in the order of 0.1, showing that the induced velocities at $V_0=10$ m/s has a relatively large influence on the performance and the loading of the rotor.

The development of the axial velocity distribution in the wake is depicted in Fig. 10. The velocity distributions are averaged in the azimuthal direction and plotted at axial positions $z/R=0$, 1, 2, and 3. Outside the wake the value of the axial velocity attains the one of the undisturbed wind. A small overshoot is observed at $z/R=2$. For all velocity profiles a distinct minimum occurs at $r=0$. This is caused by the loading on the inner part of the blade that is dominated by large drag forces. The position of the tip vortices (see also Fig. 6) is inferred as dots on the velocity profiles. As can be seen they are generally located midway between the wake and the external flow at the position where the gradient of the axial velocity attains its maximum value.

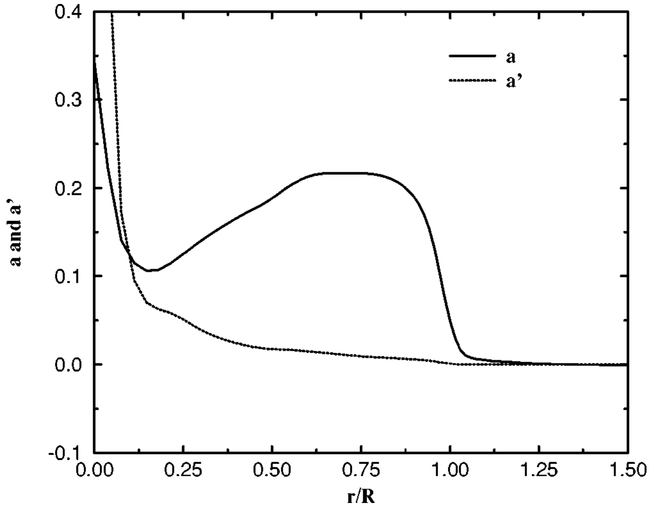

Fig. 9 Radial distributions of averaged interference factors $\overline{a}(r)$ and $\overline{a'}(r)$, defined in Eqs. (16)–(18), computed at $V_o=10$ m/s

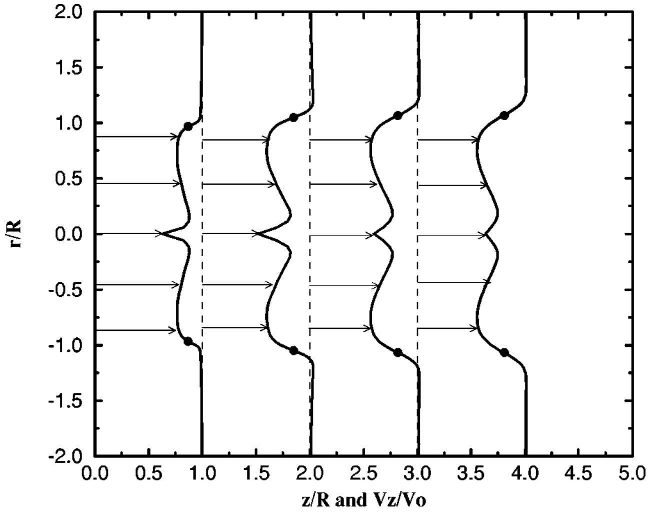

Fig. 10 Distribution of axial velocity for $V_o=10$ m/s. The core of the tip vortices are marked by ●

5 Conclusion

A numerical model for predicting global flow fields about rotors of wind turbines was presented. The model is based on a so-called actuator line concept in which the blade loading, implemented along lines representing the rotor blades, is introduced in the Navier-Stokes equations as body forces.

The model was validated against experiments of a three-bladed 500 kW Nordtank wind turbine. The computed power distribution was found to be in good agreement with experimental results.

The computations demonstrated that the global flow field about the rotor is well represented by letting the loading on the blades be determined by body forces distributed along lines. In the near wake the shed vortices appeared as distinct vortex tubes, although they after about 2 turns are diffused into a continuous vortex sheet.

Useful informations about the structure of the flow field behind the rotor were obtained. In particular, the axial interference factor in the rotor plane and the position of the tip vortices in the immediate wake behind the rotor were analyzed in details.

An important future application of the model will be to analyze the validity of the assumptions underlying simpler practical engineering models, such as the blade-element momentum method. In particular, future applications of the model are planned to focus on tip corrections, curved or tapered blade shapes and yaw misalignment.

Acknowledgments

The work was supported by EFP-98, the Research Program for Renewable Energy under the Danish Energy Agency.

References

[1] Glauert, H., 1963, "Airplane Propellers," *Aerodynamic Theory*, Durand, W. F., ed., Dover, New York.

[2] Miller, R. H., 1983, "The Aerodynamic and Dynamic Analysis of Horizontal Axis Wind Turbines," J. Wind. Eng. Ind. Aerodyn., **15**, pp. 329–340.

[3] Simoes, F. J., and Graham, J. M. R., 1991, "Prediction of Loading on a Horizontal Axis Wind Turbine using a Free Vortex Wake Model," Proc. 13th BWEA Wind Energy Conference, Quarton, D. C. and Fenton, V. C., eds., Mechanical Engineering Publications Limited, London, U.K., pp. 247–254.

[4] Bareiss, R., and Wagner, S., 1993, "A Hybrid Wake Model for HAWT," Proc.

of the Sixth IEA Symposium on the Aerodynamics of Wind Turbines, McAnulty, K. F., ed., ETSU, Harwell, pp. 7.1–7.10.
[5] Voutsinas, S. G., Beleiss, M. A., and Rados, K. G., 1995, ‘‘Investigation of the Yawed Operation of Wind Turbines by Means of a Vortex Particle Method,’’ AGARD Conf. Proc., **552**, pp. 11.1–11.11.
[6] van Holten, Th., 1975, ‘‘The Computation of Aerodynamic Loads on Helicopter Blades in Forward Flight using the Method of the Acceleration Potential,’’ Report VTH-189, Dept. of Aerospace Eng., Delft Univ. of Techn., The Netherlands.
[7] van Bussel, G. J. W., 1995, ‘‘The Aerodynamics of Horizontal Axis Wind Turbine Rotors Explored with Asymptotic Expansion Methods,’’ Doctoral dissertation, Technische Universiteit Delft, The Netherlands.
[8] Wu, T. Y., 1962, ‘‘Flow Through a Heavily Loaded Actuator Disc,’’ Schiffstechnik, **9**, pp. 134–138.
[9] Greenberg, M. D., 1972, ‘‘Nonlinear Actuator Disc Theory,’’ Z. Flugwiss., **20** (3), pp. 90–98.
[10] Conway, J., 1995, ‘‘Analytical Solutions for the Actuator Disk with Variable Radial Distribution of Load,’’ J. Fluid Mech., **297**, pp. 327–355.
[11] Conway, J., 1998, ‘‘Exact Actuator Disk Solution for Non-uniform Heavy Loading and Slipstream Contraction,’’ J. Fluid Mech., **365**, pp. 235–267.
[12] Sørensen, J. N., and Myken, A., 1992, ‘‘Unsteady Actuator Disc Model for Horizontal Axis Wind Turbines,’’ J. Wind. Eng. Ind. Aerodyn., **39**, pp. 139–149.
[13] Sørensen, J. N., and Kock, C. W., 1995, ‘‘A model for Unsteady Rotor Aerodynamics,’’ J. Wind. Eng. Ind. Aerodyn., **58**, pp. 259–275.
[14] Madsen, H. Aa., 1996, ‘‘A CFD Analysis for the Actuator Disc Flow Compared with Momentum Theory Results,’’ Proc. of the 10th IEA Symposium on the Aerodynamics of Wind Turbines, Pedersen, B. M., ed., Department of Fluid Mechanics, Technical University of Denmark, pp. 109–124.
[15] Fejtek, I., and Roberts, L., 1992, ‘‘Navier-Stokes Computation of Wing/rotor Interaction for a Tilt Rotor in Hover,’’ AIAA J., **30** (11), pp. 2595–2603.
[16] Rajagopalan, R. G., and Mathur, S. R., 1993, ‘‘Three Dimensional Analysis of a Rotor in Forward Flight,’’ J. Am. Helicopter Soc., **38** (3).
[17] Sørensen, J. N., Shen, W. Z., and Munduate, X., 1998, ‘‘Analysis of Wake States by a Full-field Actuator Disc Model,’’ Wind Energy, **1**, pp. 73–88.
[18] Sørensen, J. N., 1986, ‘‘Three-level, Viscous-inviscid Interaction Technique for the Prediction of Separated Flow Past Rotating Wings,’’ Ph.D. thesis, AFM Report 86-07, Department of Fluid Mechanics, The Technical University of Denmark.
[19] Berkman, M. E., Sankar, L. N., Berezin, C. R., and Torok, M. S., 1997, ‘‘A Navier-Stokes/full potential/free wake Method for Rotor Flows,’’ AIAA Paper 97-0401.
[20] Xu, G., and Sankar, L. N., 1999, ‘‘Computational Study of Horizontal Axis Wind Turbines,’’ AIAA Paper 99-0042.
[21] Hansen, M. O. L., Sørensen, J. N., Michelsen, J. A., and Sørensen, N. N., 1997, ‘‘A Global Navier-Stokes Rotor Prediction Model,’’ AIAA Paper 97-0970.
[22] Ekaterinaris, J. A., 1997, ‘‘Numerical Simulation of Incompressible Two-bladed Rotor Flow Field,’’ AIAA Paper 97-0398.
[23] Duque, E. P. N., van Dam, C. P., and Hughes, S., 1999, ‘‘Navier-Stokes Simulations of the NREL Combined Experiment Phase II Rotor,’’ AIAA Paper 99-0037.
[24] Sørensen, N. N., and Michelsen, J. A., 2000, ‘‘Aerodynamic Predictions for the Unsteady Aerodynamics Experiment Phase-II Rotor at the National Renewable Energy Laboratory,’’ AIAA Paper 2000–0037.
[25] Huang, Y., and Ghia, U., 1992, ‘‘A Multigrid Method for Solution of Vorticity Velocity Form of 3-D Navier-Stokes Equations,’’ Commun. Appl. Numer. Methods, **8** (10), pp. 707–719.
[26] Shen, W. Z., and Ta Phouc, L., 1997, ‘‘Numerical Method for Unsteady 3D Navier-Stokes Equations in Velocity-vorticity Form,’’ Comput. Fluids, **26**, pp. 93–216.
[27] Sørensen, J. N., Shen, W. Z., and Hansen, M. O. L., 2002, ‘‘A Vorticity-velocity Formulation of the 3D Navier-Stokes Equations in Cylindrical Coordinates,’’ Submitted.
[28] Snel, H., Houwink, R., and Piers, W. J., 1993, ‘‘Sectional Prediction of 3D Effects for Separated Flow on Rotating Blades,’’ Proc. of the ECWEC ’93 Conference, pp. 395–399.
[29] Chaviaropoulos, P. K., and Hansen, M. O. L., 2000, ‘‘Investigating Three-dimensional and Rotational Effects on Wind Turbine Blades by Means of a Quasi-3D Navier-Stokes Solver,’’ ASME J. Fluids Eng., **197**, pp. 330–336.
[30] Hoerner, S. F., 1965, *Fluid-Dynamic Drag*, published by the author.
[31] Hansen, M. O. L., 1999, ‘‘Polar for NACA 63-415 Airfoil,’’ Report ET-AFM-9902, Department of Energy Engineering, Technical University of Denmark.
[32] Abbott, I. H., and Doenhoff, A. E., 1959, *Theory of Wing Sections*, Dover Publications, New York.
[33] Björck, A., 1996, ‘‘A Guide to Data Files from Wind Tunnel Test of a FFA-W3-211 Airfoil at FFA,’’ Technical Report FFA P-V-019, FFA, Bromma, Sweden.
[34] Riegels, F. W., 1961, *Aerofoil Sections*, Butterworths, London.

Jerzy Swirydczuk
Institute of Fluid-Flow Machinery,
Polish Academy of Sciences,
Fiszera 14, 80-952 Gdansk, Poland
e-mail: jsk@imp.gda.pl

Vortex Dynamics of the Stator Wake-Rotor Cascade Interaction

The behavior of turbine stator wakes moving with the flow through a rotor cascade is studied. The stator wake is modeled as a series of active vortices forming part of a von Karman vortex street, the motion of which is determined with the aid of the vortex dynamics theory. The study has recognized basic mechanisms and patterns of the wake-cascade interaction. In particular, it revealed that the course of the interaction depends on initial distribution of the vortices in the wake when it approaches the rotor cascade.
[DOI: 10.1115/1.1467597]

Introduction

Unsteady effects generated by stator wakes transported with the flow through a rotor cascade manifest themselves as local fluctuations of flow parameters, which affect the rotor performance and contribute to the level of losses. Both the scale to which the presence of wakes alters the steady-state pattern of the flow, and direction of its effects are still the matter of discussion. Generally, it is assumed that neglecting unsteady phenomena in a flow machine may lead to the underestimation of its losses [1], but opinions can also be found that in some cases the presence of wakes improves the stage performance by periodical sweeping out the stagnation areas.

Throughout the history, the wake was modeled in many ways, depending on the current state of knowledge on the phenomenon. One of the first models of the stator wake in a rotor cascade was proposed by Meyer [2]. In his model the wake was represented by a regular band of velocity perturbation, the so-called "negative jet," immersed in the otherwise uniform flow. The stator wakes were convected with the main flow and chopped into segments by the downstream rotor cascade. Within the rotor passage, the wake segments kept their initial shapes and continued to behave as negative jets, thus generating secondary velocity fields responsible for fluid transport from the pressure to the suction side of the passage.

Attempts were made to include the ability of the wake to deform on its way through the rotor passage. Smith [3] noted that the circulation around a rotor blade makes the opposite ends of a wake segment move with different velocities. As a consequence, the segment is stretched and sheared, and when the wake leaves the rotor its particular segments form a saw-like structure rather then reunite into the initial continuous shape.

Further attempts to capture the wake deformation based on the potential flow model with a continuous vortex layer of changing intensity shed from the blade trailing edge, following the classical concept proposed by Prandtl and initially implemented for studying unsteady phenomena in the flow past a single airfoil. Lienhart [4] developed a model of the flow through a stage in which the unsteady wakes, shed from both the stator and rotor blades, took into account the relative stator/rotor motion. Once shed to the flow, particular segments of the stator wake moved with the local flow velocity through the rotor cascade, thus making further contribution to unsteady flow effects in the rotor passage. The shapes of the blades were modeled by the vortex layers distributed along blade contours to make them impermeable for the flow. Instantaneous intensities of the layers, being the response to changing flow conditions in their vicinity, were calculated from a set of integral equations. With the aid of computer technique Lienhart simulated successive stages of the wake deformation, and calculated unsteady fluctuations of potential forces generated in each cascade and their dependence on the dimension of the stator/rotor gap.

Krammer [5] modified the model developed by Lienhart by adding two contrarotating rows of vortices along the wake axis to simulate the velocity defect. Thus his wake model, consisting of two types of vortices, was able to combine the potential and viscous effects. He presented the course of wake deformation individually for viscous and potential parts, and calculated their impact on unsteady forces generated on the rotor. By comparing his results with the experiment he proved that neglecting viscous effects when calculating unsteady forces may be only justified for small axial distances.

Despite a discrete representation, the wakes in the above two papers were still treated in a classical manner, as continuous bands of fluid in otherwise inviscid and incompressible flow, with the velocity deficit changing uniformly along the wake axis. Further development in wake modeling was only possible when specialized 3D codes were developed to solve Navier-Stokes (NS) equations for turbulent, compressible, and viscous flows through flow machine stages. In those codes stator wakes were generated as part of the general solution and their characteristics did not have to be assumed a priori. The codes provided opportunities for detail studies of numerous aspects of the stator wake-rotor cascade interaction, including wake deformation [6], profile losses [7], unsteady heat transfer [8], boundary layer transition [9], pressure fields and blade load fluctuations [10], etc. Experimental verification of the obtained results was, generally, good—within accuracy and resolution ranges of the measuring devices used.

Initial unsteady calculations performed with the aid of 3D NS codes made use of relatively coarse grids. As a result, the generated wakes had the shapes similar to those obtained in earlier studies, i.e., regular layers of increased entropy, without visible traces of inner structure. However, experiments intended to take more detailed insight into the stator wakes revealed characteristic, well distinguishable frequencies in the signals recorded in the area occupied by the wake, which testified to the presence of regular structures in there [11,12]. More recent numerical computations performed for isolated stators at sufficiently fine grids and time steps also produced wake patterns, in which easily recognizable were two rows of well-developed vortices, having the structure similar to that of the von Karman vortex street [13–16]. In this context, the natural next step of wake investigations is to examine how the presence of vortices as active structures changes the pattern of the stator-rotor interaction known from earlier NS analyses.

Some attempts to include the vortex dynamics in stator wake-rotor interaction studies have already been published. Valkov and Tan [17] have numerically shown that for selected flow conditions

---

Contributed by the Fluids Engineering Division for publication in the JOURNAL OF FLUIDS ENGINEERING. Manuscript received by the Fluids Engineering Division June 6, 2001; revised manuscript received January 29, 2002. Associate Editor: Y. Tsujimoto.

the wake, initially having the form of a regular layer with Gaussian velocity defect distribution, can roll up into regular vortices before entering the rotor passage.

Sondak and Dorney [18] have simulated numerically the vortex wake shed from stator blades and its further interaction with the rotor cascade. A conclusion from their study was that the presence of the moving rotor affects the stator wake shedding frequency, which reveals a strong energy peak close to the harmonics representing the blade-passing frequency.

Kost et al. [19] have examined experimentally and numerically unsteady flow fields generated by stator wakes passing a HP turbine rotor. Entropy distributions calculated by them downstream of the stator cascade revealed well-developed vortices which generated relatively strong secondary flows in the rotor passage, in the direction from the pressure side to the suction side. These effects were also noticeable in the velocity fields obtained from the measurements.

Hummel [20] continued the numerical studies of the above flow case, with particular interest focused on the stator-rotor wake interaction and its implication to the next stator clocking phenomenon. He presented a schematic of possible distribution and behavior of wake vortex structures behind the rotor trailing edge, in which the dominating role was played by a vortex pair created from the rolled up stator wake. In the two above papers, their authors assess the correspondence between the experimental and numerical results as excellent.

For a continuous wake, as modeled in the majority of the earlier wake interaction studies, the wake characteristics at the rotor inlet are time-independent and successive rotor blades chop off identical wake segments, which are then expected to behave in the same way when passing the rotor passage. This, however, is not true any longer when the wake comprises a sequence of separate, active vortices, observed in the recent publications. At least two factors can be named which make these two kinds of interaction different. First, active structures interact with each other and with the boundaries, as a result their trajectories differ from those estimated on the basis of pure main flow convection. Second, even if vortex wake steady-state parameters, such as strength of the vortices and distances between them, are kept constant, the characteristics of particular wake segments chopped off by rotor blades may differ by an arbitrary parameter, which is the initial distribution of vortices with respect to the chopped-off section at the chopping instant.

The above aspect of the stator wake-rotor interaction cannot be effectively studied using NS codes. The NS equations are believed to capture all phenomena taking place in the flow in given conditions, including shocks, turbulence, large-scale vortices etc. Studying the motion of such fine structures as wake vortices in those circumstances is extremely difficult. The results obtained using the NS codes are affected by both physical and purely numerical agents, and extracting the effects corresponding to an individual agent, the dynamics of wake vortices being the object of the present study, may be burdened with high level of uncertainty. Moreover, the earlier mentioned vortex distribution in the wake segment at the chopping instant is not directly controlled in the NS codes, as it is obtained as part of the solution, and studying the influence of this parameter on the wake dynamics would be ineffective.

To make the vortex dynamics more pronounced and controllable on the background of other effects, in the present study a flow model has been employed which makes full use of the vortex dynamics (VD) theory, developed by Lin for multiply connected regions [21]. Compared to NS analyses, the VD theory provides additional tools, in the form of invariants of motion, to control the process of calculations at a very high accuracy, comparable with analytical solutions. The model bases on a 2D potential flow through an infinite cascade of blades, with the wake represented by vortex singularities. Unlike the previous works with vortex models [4,5], here each singularity in the stator wake represents an independent coherent structure. The main goal of the study is to recognize basic patterns and mechanisms controlling the dynamics of the stator wake vortices in the rotor passage. In order to keep the geometrical and physical conditions of the study within realistic regimes, the geometry of the examined cascade was selected identical with the medium diameter blading cross-section of an HP impulse turbine rotor. The parameters of the flow through the rotor cascade are also typical of the HP turbine stage.

Steady Flow Model

A common strategy in studying the wake deformation with the aid of vortex models is to trace their motion in a series of instantaneous flow images illustrating successive deformation stages, each previous stage creating the input data for calculating the next one. In this context, a factor of crucial significance for the final result is sufficiently high accuracy in evaluating transient stages. The vortex models adopted by Lienhart [4] and Krammer [5] described the velocity field in the vicinity of the blades using the vorticity distributed along the blade contours. In a numerical representation this vorticity is represented by sets of isolated vortices, which is a source of inaccuracy in evaluating instantaneous velocities of the vortices, especially those moving close to the blade contours. To avoid this, in the present study a method of conformal mapping was adopted, in which the singularities used for determining blade shapes are located at a distance from the boundaries. This way a continuous and regular velocity field is created in the entire flow area. Controlled accuracy of solutions obtained using the adopted method is generally believed to reach, asymptotically, the accuracy of analytical solutions.

Mapping Function. The mapping function maps a K-element segment of an infinite linear cascade of blades into a circular cascade of K circles, see Fig. 1. A general formula for this function may be given in a differentiable form of an infinite fraction series [22]:

$$z=\frac{T}{2\pi}\ln\left[\zeta+\sum_{k=1}^{K}\sum_{n=1}^{\infty}C_n e^{i(n+1)(k-1)\phi}\left(\frac{a}{\zeta-\zeta_1 e^{i(k-1)\phi}}\right)^n\right]. \tag{1}$$

The number of blades, K, constituting the transformed cascade segment can be chosen arbitrarily depending, among other factors, on the scale of nonuniformity of the examined phenomenon. Here, the segment consisting of $K=8$ blades was chosen to make it possible to compare instantaneous flow images in several adjacent passages. The choice of K determines the length of the segment as $T=tK$, where t is cascade pitch. The angle between two adjacent circles in the canonical plane is $\phi=2\pi/K$. In practical numerical applications the infinite inner sum is reduced to a limited number of terms, N, the choice of which compromises between the required accuracy and computation time. In the present study a number of $N=20$ terms was assumed, which returned the blade contour mapping error of an order of $10^{-4}-10^{-5}$ over the major part of the blade contour, except a small region of the blade outlet where it rose to 10^{-3}.

Unknown parameters in Eq. (1) are the center of the first circle ζ_1, the circle radius a, equal for all circles, and a series of complex coefficients C_n. In the present study these parameters were calculated using an algorithm based on that developed by Kosma [23], with some modifications introduced to improve the convergence. Definite values of the parameters determining the final formula of the mapping function for the examined cascade are given in the Appendix.

After calculating the unknown parameters of the mapping function, further analyses are performed in the canonical plane ζ. The preliminary part of the present study included a series of steady flow calculations, performed to assess the applicability of the potential flow model to the examined problem.

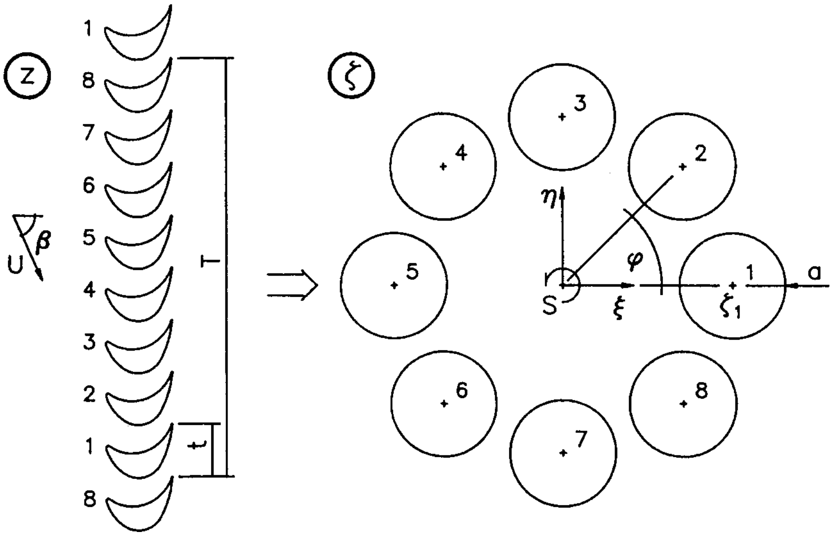

Fig. 1 Rotor cascade mapped into circular cascade of circles

Steady Flow Through Circular Cascade of Circles. The mapping function, Eq. (1), transforms the parallel flow in the physical plane into the flow generated by a source, Q_r, and a vortex, Γ_r, located at origin in the canonical plane—point S in Fig. 1. The strengths of these singularities can be determined from an assumed flow velocity, U, and inlet flow angle, β, in the physical plane as [19]:

$$\text{for vortex:} \qquad \Gamma_r=\frac{UT}{2\pi}\cos\beta \tag{2}$$

$$\text{for source:} \qquad Q_r=\frac{UT}{2\pi}\sin\beta. \tag{3}$$

Similarly to the case of the mapping function, a general differentiable formula for the steady flow complex velocity in the canonical plane can be given in the form of a fraction series [22]:

$$\overline{\nu}(\zeta)=\frac{Q_r-i\Gamma_r}{\zeta}+\sum_{k=1}^{K}\sum_{n=1}^{\infty}D^s_{k,n}\left(\frac{a}{\zeta-\zeta_1 e^{i(k-1)\phi}}\right)^n \tag{4}$$

where $D^s_{k,n}$ are unknown complex coefficients, calculated from the system of equations expressing the condition that the normal velocity be zero along the entire contour of each blade, and the tangent velocity be zero at the circle point corresponding to the blade trailing edge, defined as the point in the vicinity of the cascade exit where the blade camber line crosses the blade contour.

Local flow velocities calculated in the canonical plane are transformed to the physical plane using the standard formula [22]:

$$\nu(z)=\frac{\nu(\zeta)}{\dfrac{dz}{d\zeta}}; \tag{5}$$

where $dz/d\zeta$ is calculated from Eq. (1).

Wake Model

Wake Characteristics. The literature gives little and rather incomplete data on the inner structure and strength of the vortex wake in turbine stages. Generally, the wake is believed to have the structure similar to that of the von Karman vortex street, although Gostelov's visual experiments have shown that other arrangements, like the street of parallel and not alternate vortices, or vortex pairing taking place on one side only, are also possible, especially for supersonic Mach numbers [24]. Even for the classical, alternate structure of the vortex street, vortices constituting the two rows are likely to differ in strength, as was reported by Hummel [20] and can be observed in other patterns of vortex wakes published [15,16]. It should be stressed, however, that the evidence on unequal strength of the vortex rows comes only from numerical studies and has not been confirmed experimentally.

The frequency of stator vortex shedding can vary widely, as it depends not only on basic geometrical and flow parameters, but also on a number of minor details, including the shape and dimension of the blade trailing edge, and the state of boundary layers passing it. The estimations found in the literature place the shedding frequency in real turbines within the range of $5\div50$ kHz [12]. Numerical studies have shown [4–6,18] that in the full stator-rotor configuration this frequency may be affected by upstream potential action of the moving rotor, although the scale of this action on the regular vortex shedding has not been assessed.

The distribution of vortices in the street is not clearly defined. The characteristic h/l ratio (h-distance between the vortex rows in the street, l-distance between two adjacent vortices in one row), as evaluated from the diagrams available in the literature, varies, approximately, from 0.21 to 0.38 [14,15]. The authors offer no information on the strengths of vortices composing the street.

Due to incomplete and incoherent information on the inner structure of the stator wake, in order to obtain wake characteristics which would be considered reliable and representative for the turbine environment a decision was made to reconstruct initial wake parameters from a complementary 3D flow calculation. For this purpose a specialised commercial code FlowER was used, which was developed for computing 3D viscous, compressible flows of steam through turbine stages and sections. The governing relations used in that code have the form of Reynolds-Averaged NS equations for perfect gas, complemented by a modified algebraic model of Baldwin-Lomax to simulate the effects of turbulence. The RANS equations are solved numerically using the Godunov-type upwind differencing, accompanied by a high resolution ENO scheme for calculating convective derivatives, which preserves second-order accuracy everywhere in space and time, and locally third-order accuracy. Convergence of the solution is accelerated by locally using time-stepping techniques, along with a multi-grid algorithm based on the H-type grid refined near walls and leading and trailing edges, and a δ-form implicit operator of Steger & Warming. More detailed description of FlowER can be found in [25]. In the past, the code was positively validated on numerous experimental data sets recorded both on model and real turbines and compressors, and therefore it has been considered a reliable source of information on the flow characteristics in a turbine stage. The code provides opportunities for studying unsteady stator-rotor interactions, in which the wakes are represented by continuous and regular bands of increased entropy. Using this option, a calculation was performed for a stage being the prototype for the rotor geometry examined in the present study. The stage selected for calculation was a typical HP turbine stage operating at the pressure drop of 0.90, inlet temperature 746 K, mass flow rate 165 kg/s, and average reaction 0.15. The 3D calculations, performed on a mesh of 582 420 nodes covering one stator and one rotor passage [26], provided data for evaluating the free stream and wake characteristics at the rotor inlet.

In the wake flow reconstruction, the relative velocity U of the free stream approaching the rotor was equal to 108.6 m/s, and the relative angle β between the free stream velocity and rotor axis was equal to 66.3 deg. In the stator reference frame, the absolute flow inlet angle α, defining the direction of the wake axis, was equal to 79.5 deg. The width h of the wake vortex street was assumed equal to 80% of the width of the wake approaching the rotor in FlowER simulation, to leave some margin for limited radii of the vortices composing the street. The distance l was evaluated from the classical ratio $h/l=0.2806$. The resultant frequency of vortex shedding was equal to about 40 kHz, which was close to the upper limits published in the literature, and realistic when taking into account sharp trailing edges of the stator blades. The wake model assumed regular initial structure of the vortex street, thus neglecting potential disturbances generated by the rotor. There were two reasons justifying such an approach. First, no data on those disturbances were recorded in the FlowER computations, and therefore their possible scale, in terms of both shedding frequency and vortex strength fluctuations, could not be assessed. Literature studies do not provide enough data to reliably model this effect either. Secondly, even if assumed in some arbitrary way, the characteristics of these disturbances would depend on the stator-to-rotor pitch ratio, a parameter which may vary for the same rotor, depending on the stator design. Since the goal of the present study, as formulated in the Introduction, was to provide data on general patterns and mechanisms of the stator wake-rotor cascade interaction, in order to preserve a relatively wide range of applicability of the results to be obtained a decision was made to neglect the potential rotor effect on the creation of stator wake vortices.

Vortex Model. In the potential model the stator wake is represented by two rows of opposite-sign vortices composing a finite section of the von Karman vortex street. The number of wakes in the cascade segment is directly connected with the stator-to-rotor pitch ratio, which in the referential HP turbine stage was equal to 2.36. Simulating such a ratio in the model is technically possible but it would produce different instantaneous wake patterns in each rotor passage and, as a consequence, would provoke certain difficulties in controlling, interpretation, and generalization of the results. Since the study was oriented rather on recognizing general, qualitative regularities of the wake-cascade interaction, an integer ratio of 2 was assumed instead. Along with simpler interpretation, the fact that instantaneous distributions of vortices were identical in every second passage was used for monitoring the accuracy of the performed calculations.

At the beginning of the calculation, a number of wakes, $L=4$, corresponding to the number of stator blades in the rotor cascade segment were positioned upstream of the rotor cascade. The vortices were located along the line parallel to the absolute rotor inlet flow velocity direction assessed from FlowER computation. The first vortex in a wake was placed at a distance g corresponding to the stator-rotor gap in the stage. Once placed, the vortices were transported with the flow through the rotor cascade. For each rotor blade, local velocity fluctuations generated by the passing vortices were compensated by changing blade circulation and simultaneously generating secondary wake vortices downstream of the rotor blades, in order to keep rear stagnation points at the rotor blade trailing edges fixed. It should be stressed here that the only role of the rotor vortices in the model was to keep the blade circulation fluctuations within a reasonable range, and not to model the structure of the rotor wake. Consequently, the behavior of these vortices was not studied.

To include the presence of stator and rotor wakes in the flow, additional components were included in Eq. (4), after which it took the following form:

$$\overline{\nu}(\zeta)=\frac{Q_r-i\Gamma_r}{\zeta}-\sum_{l=1}^{L}\sum_{s=1}^{S}\left[\frac{i\Gamma_0}{\zeta-\zeta_{s,l}^{+}}-\frac{i\Gamma_0}{\zeta-\zeta_{s,l}^{-}}\right]-\sum_{k=1}^{K}\sum_{w=1}^{W}\frac{i\Gamma_{w,k}}{\zeta-\zeta_{w,k}}+\sum_{k=1}^{K}\sum_{n=1}^{N}D_{k,n}\left(\frac{a}{\zeta-\zeta_k}\right)^{n}. \tag{6}$$

In Eq. (6) S is the number of pairs of vortices in a single stator wake. It has to be large enough for the central part of the modelled wake to resemble the behavior of an infinite vortex street. Here, S was assumed equal to 150 which preserved the motion of seven wakes through the rotor passage during the computation. Γ_0 is the strength of a positive vortex in a stator wake, a significant parameter in the present study. Since, to the author's knowledge, no literature data is available on the possible range of the turbine stator wake vortex strength, some preliminary computations were performed before the main part of the study to assess this parameter. As a result, the vortex strength, the same for all vortices-disregarding sign, was chosen as equal to $\Gamma^*=\Gamma/(Uc)=0.005$ (c-stator blade chord). To assess the effect of the vortex strength, complementary computations were performed, for which this parameter was increased four times, to $\Gamma^*=0.02$.

$\zeta_{s,l}^{+}$ and $\zeta_{s,l}^{-}$ are instantaneous locations of the positive and negative vortex, respectively, in the lth stator wake. W is the number of vortices in one rotor wake, $\zeta_{w,k}$ is an instantaneous location of the rotor wake vortex generated in the wth step downstream of the kth blade. All those variables were calculated by the code in each step of computation.

Unlike Eq. (1), the complex coefficients $D_{k,n}$ represent in Eq. (6) the reaction of circles to both steady and unsteady flow components, and had to be calculated in each step.

The velocity ν_i of the ith vortex located at point ζ_i in the canonical plane (here i stands for all indices of both stator and rotor vortices) was calculated from Eq. (6) using Helmholtz and Kirchhoff's principle that the vortex does not act upon itself [21]:

$$\overline{\nu_i}(\zeta_i)=\overline{\nu}(\zeta_i)-\lim_{\zeta\to\zeta_i}\frac{i\Gamma_i}{\zeta-\zeta_i}. \tag{7}$$

From the canonical plane the vortex velocities were transferred to the physical plane using the formula [21,27]:

$$\overline{\nu_i}(z_i)=\overline{\nu_i}(\zeta_i)\Big/\left.\frac{dz}{d\zeta}\right|_{\zeta_i}-\frac{i\Gamma_i}{2}\left.\frac{d^2z/d\zeta^2}{[dz/d\zeta]^2}\right|_{\zeta_i}. \tag{8}$$

The derivatives in Eq. (8) were calculated from Eq. (1).

Singular representation of wake vortices makes it impossible to model properly close vortex-vortex and vortex-boundary interaction. To get more realistic properties of the model vortices in those situations, in numerical realization each wake vortex was attributed a core radius proportional to its strength. When two vortices neared each other to a distance closer than the sum of their radii, they were merged by the code. Another assumption was made for vortices nearing the blade contour. A rule recognized from experiments on vortex-body interaction says that the vortex decays much faster when it moves close to a solid obstacle and interacts with its boundary layer than when it is convected with the main stream [28–30]. To qualitatively model this effect, the strength of a vortex approaching the blade to a shorter distance than its core radius was reduced proportionally to the circle area defined by this part of radius which penetrated inside the blade. The main goal of that vortex strength reduction was to avoid unrealistic behavior of vortices moving close to the blade wall. Since the above assumption might look rather arbitrary, a number of other methods of vortex strength modification were examined, including the reduction in direct proportion to the cut-off part of core radius, and one-step vortex annihilation, against the reference case of the motion of vortices without strength reduction. After these tests the method of square-proportion reduction was finally chosen, although it should be mentioned here that the remaining modifications improved the behavior of the wake vortices near the walls to a comparable extent.

Some numerical efforts were made to simulate the motion of the stator wake, consisting of the finite number of vortices, so as to resemble the motion of an infinite vortex street. To achieve this, the flow area was divided into two subregions. In the first subregion, located upstream of the rotor cascade at a distance greater than the stator-rotor gap, the vortices were only allowed to move with the potential flow velocity, while in the second region, surrounding the rotor cascade, all flow velocity components were taken into account in evaluating the instantaneous velocity of a vortex.

Rotor vortices were successively generated in each calculation step. A crucial point of all applications of a vortex method to studying unsteady flows past lifting bodies is the method of finding locations of nascent wake vortices and their strengths in successive steps. Generally, all models take necessary data from instantaneous velocity distributions in the vicinity of the foil trailing edge, but particular realizations of this task depend on the modelling method applied. For methods using conformal mapping, a rather common approach is to find the vortex location first and then evaluate the vortex strength from the Kutta and circulation preservation conditions. A realistic assumption for finding the nascent vortex position is the equation:

$$\overline{s} = \overline{\nu}_n \frac{1}{2} \Delta t \tag{9}$$

where $\overline{s}$ is the distance vector from the blade trailing edge to the nascent vortex, $\overline{\nu}_n$ is instantaneous velocity at the nascent vortex position found, and Δt is time step. Equation (9) is solved in an iterative manner. Physically, it represents the idea to locate the nascent vortex at a distance equal to half of the length of the vortex layer shed from the trailing edge during the time step.

The above procedure was tested in the present study, but it turned out unstable in cases when the flow field in the vicinity of the hypothetical nascent vortex position was seriously affected by the stator vortices passing by. Therefore the procedure was modified using a concept of a regular line emerging from the foil trailing edge, taken from Streitlien and Triantafyllou [31]. The location of a new rotor vortex was found on a spline curve linking the blade trailing edge, and leaving it at the angle of 90 deg, with current locations of six most recent rotor vortices after their displacement in the calculated step, at a distance equal to 1/3 of the spline curve length to the nearest wake vortex already existing in the flow. This procedure was proved more stable, and produced nascent vortex locations smoothly changing to reflect local flow fluctuations.

Computing Procedure and Accuracy

To be in line with the general policy of error minimization, the computing procedure aimed at preserving the highest possible accuracy in evaluating instantaneous locations of the wake vortices. It included the following actions:

(a) reading the geometry of the cascade and mapping function coefficients;
(b) geometry correctness check;
(c) steady flow computation, evaluating steady circulation around blades, checking velocity field accuracy, storing steady flow coefficients;
(d) placing stator wake vortices at their initial positions;
(e) calculating initial positions of nascent rotor wake vortices;
(f) initial unsteady calculations, evaluating strengths of rotor wake vortices and rotor blade circulation changes, checking velocity field accuracy, storing unsteady flow coefficients and distributions of vortices;
(g) moving vortices to new positions;
(h) unsteady calculations, evaluating strengths and positions of rotor wake vortices, and rotor blade circulation changes, checking velocity field accuracy, storing current flow coefficients and distributions of vortices.

Points (g) and (h) were repeated in each step until an assumed number of steps was reached. The dimensionless time step, $\Delta\tau = U\Delta t/c$, was assumed after a number of preliminary tests as equal to 0.0776, which is within the limits assumed for single vortex-airfoil interaction studies [31]. To increase the accuracy of vortex displacement, each main step consisted of five sub steps. In four initial substeps point (h) was calculated without generation of rotor wake vortices. In each individual substep all vortices were moved to their new positions using a predictor-corrector technique.

Unsteady calculations of the vortex motion performed in each step can be clearly divided into two main stages. The first stage leads to the evaluation of the instantaneous flow field. It includes the generation of nascent vortices and calculation of local vortex velocities. In the next stage the vortices are moved to their new positions resulting from their local velocities and the assumed time-step. Each stage included procedures, whose role was to assess the accuracy of the calculations. For the velocity field evaluation, the accuracy tests included the computation of blade circulation and normal velocity distributions along blade contours. Generally, the achieved level of accuracy depends on an assumed number of singularities N in Eq. (6) modeling the reaction of the blades to the flow disturbances. In the present case N was assumed equal to 80 as a tested result of the compromise between accepted accuracy level and computing time length. The circulation accuracy was assessed making use of the fact that the calculations were performed for $K=8$ cascade passages and, at the stator-to-rotor pitch ratio equal to 2, were expected to generate four theoretically identical flow images. Dimensionless differences, $\Delta\Gamma/\Gamma_s$—where Γ_s stands for steady-state rotor blade circulation, in evaluating unsteady circulation for four corresponding blades, were always kept beyond 10^{-7}. Normal velocity components, calculated in 360 points along each blade contour, were of an order of 10^{-3}–10^{-4}, only locally increasing to 10^{-2} when a vortex moved too close to the blade. In those cases, however, the action described in the previous section took place to reduce the vortex strength.

Evaluating the error of displacing vortices to their new positions is much more difficult. Theoretically, an invariant of vortex motion is the Kirchhoff-Routh function. In a general formula, however, given by Lin for multiply connected regions [21], it has the form of superposition of Routh functions evaluated individually for each vortex in the flow. In the present calculations, coefficients $D_{k,n}$ in Eq. (6) represent total response of the blade to all flow disturbances generated in a step, which makes it impossible to apply them to creating the Kirchhoff-Routh function for the examined flow. To overcome this difficulty, a vortex displacement procedure was used which had been previously tested on cases of limited numbers of foils, for which the creation of the Kirchhoff-Routh function was possible. In those cases the correctness of procedure operation was checked by comparing the vortex displacement performed on the basis of instantaneous vortex velocities with the increment of the Kirchhoff-Routh function [32,33].

Results

Steady Flow Tests. Due to their efficiency, potential flow models were in the past successfully applied for studying vortex

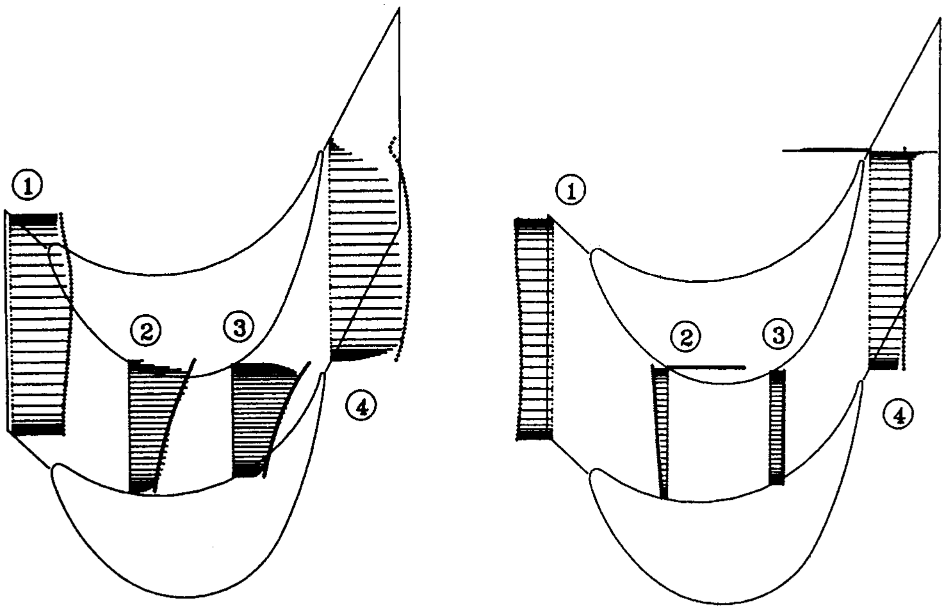

Fig. 2 Distributions of velocity modulus (left) and angle (right) along rotor passage sections located at $x/c_{ax}=-14.85\%$, 25.73%, 66.52%, and 101.68% from the rotor blade leading edge

interactions with single airfoils. In those cases uniform structure of the free stream, along with the areas of viscous effects strictly limited to the airfoil boundary layer and vortex cores, justified the use of such a simplified flow model. However, flows through turbine rows are much more complex, with manifold wave configurations, and/or 3D vortex structures like horse-shoe vortices, or channel vortices. Therefore it is highly difficult to assess a priori the scale of deformation imposed by the potential model to the results obtained with its aid, which puts forward a question to what extent these results may describe the phenomena taking place in a real turbine. This aspect of the model was given high attention in the present study. First, the selected cascade, typical of an HP turbine impulse stage rotor, warranted keeping flow velocities within the incompressible fluid regime, at limited reaction level. Then, a series of comparison tests were performed using the results of the FlowER calculation as reference data to assess the range of applicability of the potential model to the examined problem.

The potential flow calculations were performed using as input data the rotor inlet velocity U, and angle β, computed by the code FlowER and averaged at the rotor inlet mid-span. The first test comprised direct comparison of the velocity distributions in the rotor passage. Its results are shown in Fig. 2 as velocity modulus and angle distributions in selected passage sections. The bars in the diagrams represent the data calculated by FlowER, while the crosses stand for the results obtained from the potential model. The velocity angles are measured from the cascade axis, giving negative values when the flow approaches the rotor, and positive at the exit. In each section the presented data well correspond to each other, except for the rotor wake and a narrow area close to the rotor blade suction side where FlowER detected the boundary layer separation, visible as angle changes by 180 degrees. Those effects could not be modeled by the potential flow.

As was already mentioned, a characteristic feature of the methodology used in unsteady flow studies is that the results obtained for one time step make the input data for the next time step. As a consequence, computational errors sum up with time, in many cases significantly affecting the final result. Taking this into account, another test was performed in which instantaneous images of the wakes computed by FlowER were compared with those obtained using the potential model. A sample FlowER-generated wake is shown in Fig. 3 (top). A corresponding potential model

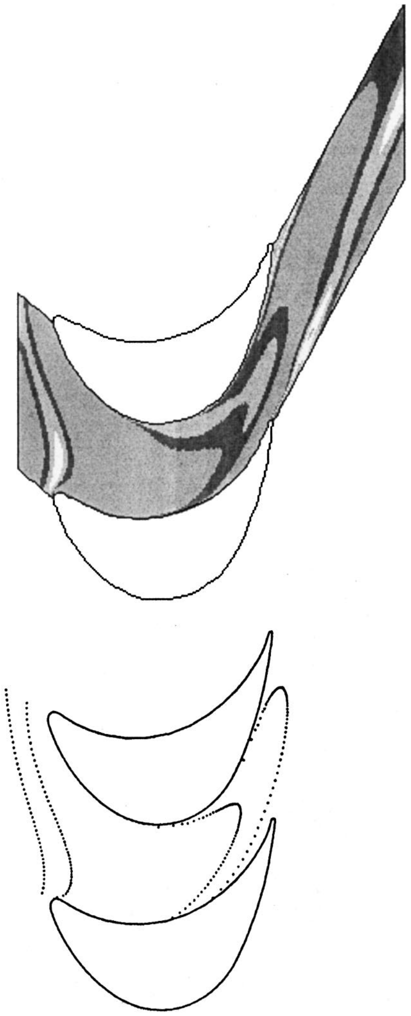

Fig. 3 Wake deformation in the rotor passage: solution by FlowER (top) and potential model (bottom)

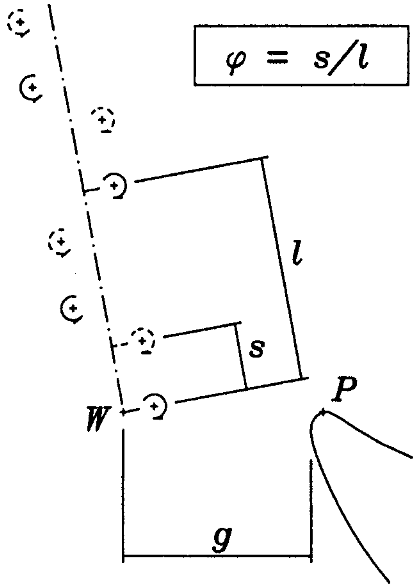

Fig. 4 Phase shift, φ, as the measure of wake vortex position along the wake axis

wake was generated by placing two parallel lines upstream of the rotor to represent initial wake boundaries and then allowing them to convect through the rotor passage. Two instantaneous locations of these pairs of lines, selected so as to correspond to the wake locations generated by FlowER, are shown in Fig. 3 (bottom). The agreement between the both curves is surprisingly good, taking into account all previous comments on the complexity of flow in a turbine stage. Two conclusions can be formulated on the basis of this test. First, it testifies to good credibility of the potential model to determine accurate velocity distributions, and thus to create a realistic pattern of the wake motion through the examined rotor passage. But, on the other hand, it also proves that the wake generated by FlowER at the rotor inlet is highly dissipated, and its further motion through the rotor passage is almost solely controlled by the potential flow. In the examined case this effect visibly results from coarse resolution of the grid used in FlowER computation. Nevertheless, this problem concerns all grid methods and can be formulated as a question about the extent to which the behavior of a stator wake determined using those methods is deformed by the grid resolution applied. The rate of numerical diffusion of all vortex structures is affected by the dimensions of the adopted grid, and a general strategy here is to reach a grid resolution sufficiently fine to consider the obtained results grid-independent. The problem is that wake vortices are extremely fine, compared to other flow structures, like horse-shoe vortices, canal vortices, separation vortices, etc., and extremely fine grids are needed to trace them. So far, there is no indication on how fine the grid should be to obtain grid-independent results for the wake vortices.

Wake-Cascade Interaction. Fixed input parameters for the main body of the wake-cascade interaction studies were inlet flow velocity U, inlet flow angle β, and strengths of the stator vortices Γ_0. The main variable parameter of the study was the phase shift factor, φ, as defined in Fig. 4, which determined the shift in initial locations of the vortices along the stator wake axis with respect to an arbitrary basic distribution.

The vortex distribution marked with solid lines in Fig. 4 was selected as the basic distribution, corresponding to $\varphi = 0.0$. Figure 5 shows a series of instantaneous distributions of stator wake vortices in the rotor passage, illustrating the course of the examined wake-cascade interaction. In the diagrams, the stator wake vortices are represented by small circles, black and white for the positive—counter-clockwise and negative—clockwise rotation, respectively. Series of small crosses, visible downstream of the rotor blades, mark initial segments of the rotor wake. The diagrams also present two sequences of small dots, which represent hypothetical positions of the stator wake vortices in case they moved passively with the potential flow velocity, like the lines in Fig. 3, bottom. The first wake shown in the diagrams of Fig. 5 is in fact the third wake passing the rotor cascade, the two previous being removed as affected by initial non-periodicity.

In the initial diagram, step 33, the wake has approached the cascade. So far the only noticeable effect of activity of the vortices here was reduced velocity of their motion, compared to the potential flow velocity. This effect can be observed as different positions of the active vortices with respect to corresponding passive dots. The reduced velocity of motion of the von Karman vortex street in the flow, resulting from an additional velocity component induced by the street on itself, was first proved, both theoretically and experimentally, by von Karman [34], and its presence here testifies to the correctness of modeling of the wake motion. The next diagrams, steps 36 and 39, show early stages of the wake deformation. Negative vortices composing the central part of the wake segment are accelerated, while those located close to the cut-off end are decelerated. An opposite tendency is observed in the motion of the positive vortices. As a result, the outer vortices of the two rows come closer to each other while the central ones become more distant. All this leads to noticeable segregation of vortices representing opposite rotation signs, with their further motion in two nearly isolated groups, visible in the final diagrams, steps 45 and 48. Of these two groups, only the second group of vortices moves approximately with the velocity predicted by FlowER for the entire wake, while the first group moves faster, contributing to the growing rate of deformation of the inner structure of the wake.

The tendency toward segregation of one-sign vortices offers new data for the interpretation of secondary cross-passage flows, recorded in other studies, which transport the fluid from the pressure side to the suction side of the rotor passage. Initially, the mechanisms responsible for this transport were believed to be negative jets created between the two rows of vortices inside the wake segments [2]. More recent studies based on NS codes revealed significant deformation of the wake, as a consequence of which the jets in their pure form were observed only when the wake was entering the rotor passage. Then, while moving through the passage, the wake rolled up into sequences of opposite-sign rotation structures resembling large vortex pairs, which also generated cross-passage flows, but much wider and occupying much larger area [6,7,19,20]. The present results confirm wake's tendency to create vortex pairs, and point out two main mechanisms driving this process: the flow velocity gradient in the passage, and mutual interaction of the wake vortices.

Beside the basic variant, the study included three more variants of vortex distribution in the wake, denoted by phase shifts, φ, equal to 0.25, 0.5, and 0.75, respectively. The segregation of one-sign vortices and their further motion in nearly isolated groups were recorded for all cases examined. The most spectacular differences between the cases characterized by different φ were observed in the motion of the vortices located close to the cut-off region. These vortices, as a rule, took visibly different trajectories, which in extreme cases led to the separation of isolated vortices from the wake. Characteristic configurations of wakes with isolated vortices are shown in Fig. 6, the top and bottom diagram representing the separation of a positive and negative vortex, respectively. In the both diagrams, showing the instantaneous distributions of vortices in two adjoining passages, the isolated vortex is presented in the upper passage, while two vortex distributions in the lower passage show the initial configuration of vortices at the passage inlet which has led to its separation, and the further motion of the separated vortex in the rear part of the passage.

Chances for recording the wake vortex separation in real tur-

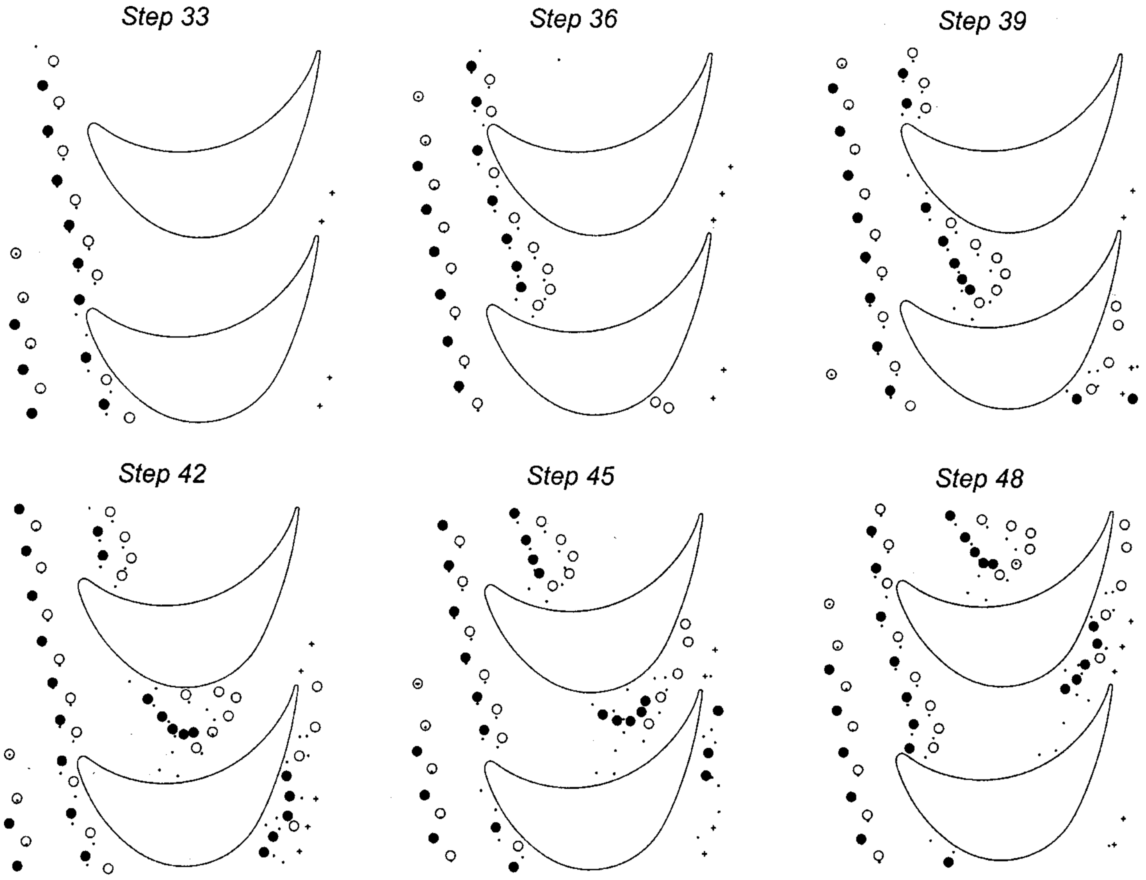

Fig. 5 Stator wake deformation in the rotor passage: $\Gamma^*=0.005$, $\varphi=0.0$

bine flows do not seem high. Vortex-body interaction experiments have shown that vortices moving close to a wall, at a distance comparable with the boundary layer thickness, decay relatively quickly [28–30]. Therefore even for idealized flow conditions in a 2D cascade a separation vortex would most probably decay fast, well before approaching the blade trailing edge. In the 3D row this process would be also accompanied by unavoidable skew of the stator vortex with respect to the rotor blade, which for such small vortex-wall distances would significantly contribute to faster and less uniform vortex decay.

Nevertheless, the above result is believed to be most spectacular, and bringing certain consequences to the methodology of stator wake-rotor studies. It proves and illustrates the existence of mechanisms in the flow which make the stator wake, having steady geometrical and dynamical characteristics, behave in different way in different rotor passages only because of different phase shift in initial vortex distribution. In real wakes this distribution may be generally assumed a stochastic parameter, as for the time being, no evidence has been found to link the timing of generation of a stator wake vortex with the relative stator-rotor location. That means that consecutive segments of the same wake shed from a stator blade may behave in a different way in corresponding rotor passages. Or, in other words, **consecutive segments of identical wakes shed from consecutive, identical stator blades may behave in different way in one and the same rotor passage**.

This last conclusion is important. The overwhelming majority of experimental methods used for studying unsteady wake-cascade interaction assume repeatability of flow parameters recorded at the same point for the same time phase of wake passing. That assumption makes it possible to use the data recorded at different times for creating instantaneous images to illustrate successive stages of behavior of the wake in the rotor passage, which then make the basis for further studies of wake's dynamics, mixing processes, and decay. Using the above methodology, Poensgen and Gallus [35] studied experimentally the interaction of a stator cascade with the vortex street shed from a rotor with cylindrical spokes mounted in front of it. They recorded the wake velocity defect in a series of points located in the stator passage along a stator centerline. They use a data acquisition method based on the triggered time-averaged procedure. After comparing wake velocity defects recorded for the cases with and without stator they found that for the former case the wake velocity defect decreased twice as fast as for the latter one. At the same time, the rotor wake turbulence intensities and turbulence correlations measured in the experiment were less affected by the presence of the stator.

Poensgen and Gallus pointed out two opposite agents affecting the wake development, one of which was stronger mixing effects which led to faster decay of the wake. From the point of view of the present study, however, the conclusion about the rate of wake decay and the mechanism indicated may not be true, as the observed regularity at least in part may have resulted from differences in individual realisations used for reconstructing the general pattern of the wake-cascade interaction. In fact the authors recorded the envelope of all possible realisations of the interaction in given conditions, rather than one sample realisation. If the mechanism of faster dissipation of the wake vortices had been more intensive mixing, it should have manifested itself by corresponding transient increase in the level of turbulence resulting from breaking the primary wake vortices down into smaller structures, as it is suggested by Kolmogorov's vortex cascade law. This correlation was not observed. Moreover, the location of the measuring points in the free-stream region, where viscous effects im-

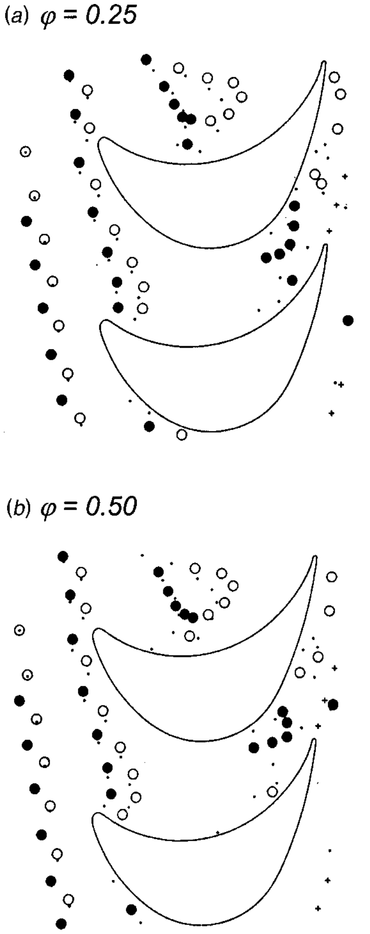

Fig. 6 Isolated vortices separated from the wake: positive (top) and negative vortex (bottom)

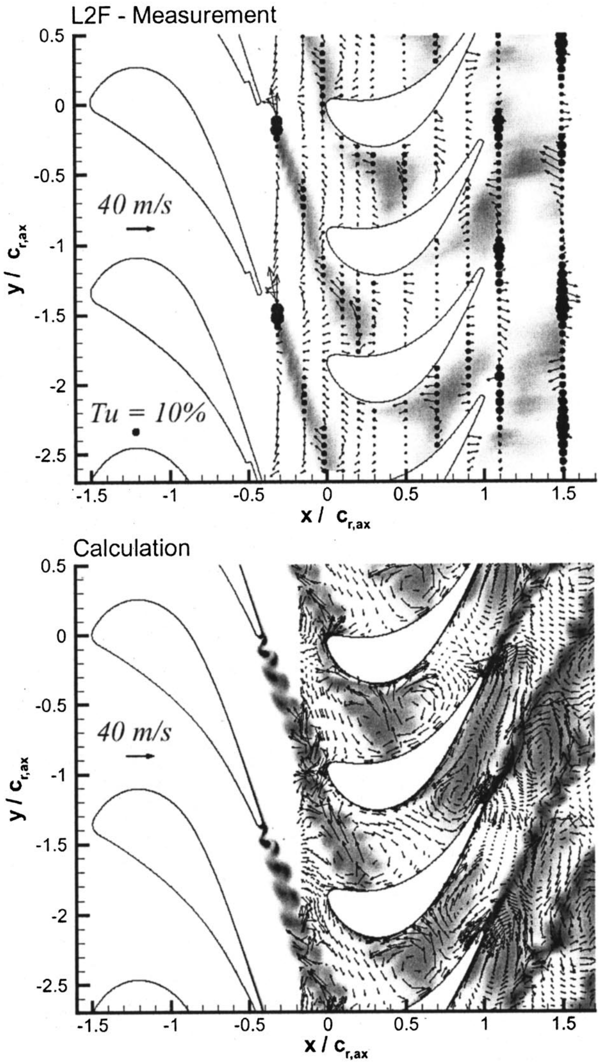

Fig. 7 Comparison of the experimental (top) and calculated (bottom) unsteady flow field generated by the stator wake in the rotor passage (reproduced from [19], courtesy ASME)

posed by the presence of the stator cascade are small, does not seem to provide opportunities for such a dramatic intensification of the dissipation process.

Possible stochastic variations in the realisation of unsteady wake-cascade interaction, suggested by the present VD analysis, could be checked with the aid of the methods, which, like PIV for instance, provide opportunities for recording the entire matrix of flow parameters for the same time. In the context of the present results, such studies are expected to reveal lower rates of the wake decay against the background of higher overall irregularity of the phenomenon, compared to its pattern known from the experiments based on triggered techniques.

To assess the influence of the wake vortex strength on the wake-cascade interaction, a variant was calculated for more intensive vortices, $\Gamma^* = 0.02$. Here, the main features of the wake deformation, such as vortex segregation and different velocities of motion of the vortices composing opposite-sign groups were still recognisable, although less pronounced, as the deformation took faster and more dramatic course. Especially active were the leading vortices which rapidly penetrated into the center of the wake and disorganised its inner structure.

Numerical and Experimental Validation

Wake Deformation. The results presented in the previous chapter illustrate a general pattern of the stator wake deformation in the rotor passage, particular realizations of which may differ, to some extent, from stage to stage due to certain differences in the stage design. Two major factors which may affect the course of interaction are the velocity distribution in the rotor passage, which is responsible for the convective part of the vortex motion, and the strength and initial distribution of vortices in the wake, which control vortex activity on their way through the rotor passage. The present study was performed under the assumption that these differences are only of quantitative, and not qualitative nature.

Although the interest in studying stator wake related unsteady phenomena in a turbine stage has a relatively long history, publications going in their investigations as deep as to recognize inner structure of the stator wake in the rotor passages are, so far, extremely rare. In this context, the results presented by Kost et al. [19] make invaluable material, revealing many new details of the stator wake-rotor interaction. As was mentioned in the Introduction, the authors examined, both numerically and experimentally, the interaction in a full size HP turbine stage, with the air as flowing medium. The wake deformation was traced experimentally by injecting coolant with seeding particles to the flow at the stator blade trailing edge and then recording time-dependent distributions of coolant concentration using LDV. The recorded pattern of the wake deformation was compared with that obtained numerically using a NS code, with entropy playing the role of a marker. Figure 7, reproduced from [19], shows experimental and calculated unsteady flow fields, in which the areas of wake locations are shaded gray. Other details shown in the diagrams

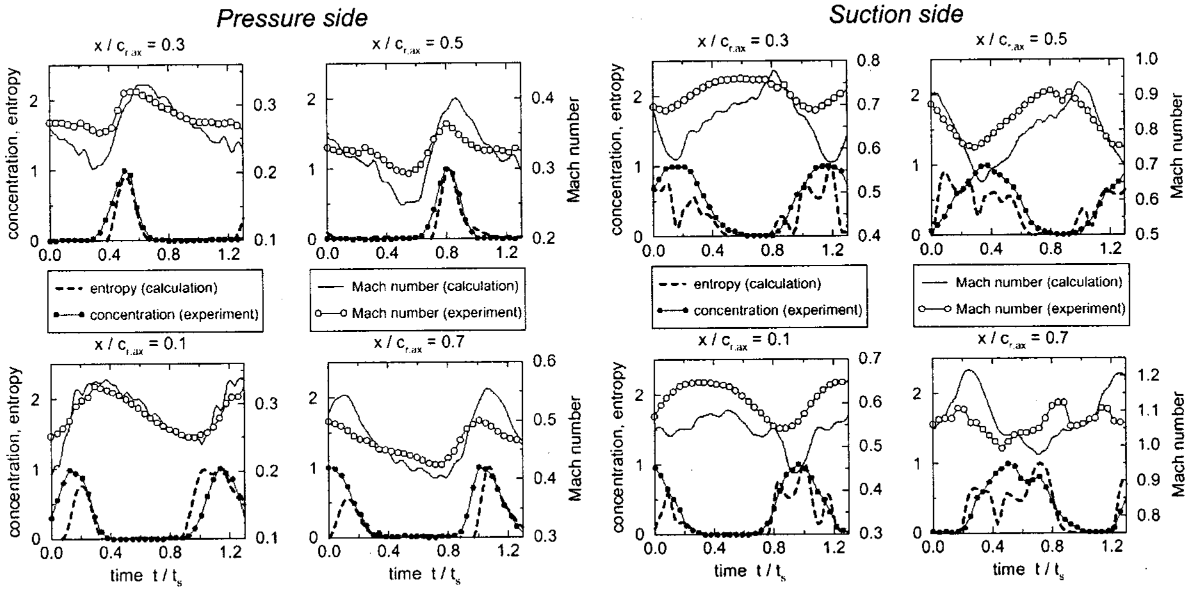

Fig. 8 Comparison of the temporal development of relative flow values at points near the pressure (left) and suction sides (right) of the rotor blade (reproduced from [19], courtesy ASME)

are instantaneous velocity distributions and experimentally recorded turbulence levels, marked as black spots of corresponding dimension.

Flow conditions in the rotor examined by Kost et al. were, in qualitative terms, similar to those assumed in the present VD study. Corresponding axial components differed by about 10 percent. The shapes of the stator and rotor blades in Fig. 7 testify to higher stage reaction, and resulting faster flow acceleration in the rotor passage. The stator wake geometry was qualitatively similar—in Fig. 7 the wake segment flowing through the rotor passage consists of, approximately, 10 vortices, against 14 assumed in the VD analysis, the difference being justified by thicker trailing edge of the stator blade. The stator-to-rotor pitch ratio was equal to 3/2, compared to 2 in the VD case, being a possible source of different effects of the stator-rotor potential-flow interaction. Generally, the data presented in Fig. 7 make good reference material for making qualitative comparisons and testing, in a slightly different environment, the assumed generality of the wake development pattern determined from the VD analysis.

For initial deformation stages, the experimentally recorded wake pattern corresponds well with that predicted by the VD theory. Observed is characteristic thickening of the central part of the wake segment and its further deformation into a boomerang-like shape—compare the coolant cloud in the central passage with the vortex configuration in Fig. 5, step 36, and the coolant cloud in the upper passage with the vortex configuration in Fig. 5, step 42, and also in Fig. 6. The areas of entropy concentration theoretically predicted by the NS solution seem to be slightly less accurate for those cases; the wake, as a whole, occupies the same regions, but the arrangement of the vortices does not reveal proper dynamics. In the first case, the vortex wake widens continuously until it reaches the rotor blade pressure side, and in the second, it takes a shape of a rather irregular triangle. The reason for these differences is not clear, perhaps the use of entropy as a marker was not very fortunate in this case. Hummel [20] in a more detailed numerical analysis of the same flow presented vorticity distributions, which closer resembled the shapes observed in Fig. 7, top, and Figs. 5 and 6. Another regularity observed in the vorticity diagrams presented by Hummel was more intensive rolling-up of the rear, positive vortex row, most likely resulting from its higher intensity, reported by the author, although some tendencies of this type can be also observed in the regular vortex street deformation, as closer concentration of positive vortices, seen in Fig. 5, step 45.

The major difference between the theory and experiment in more advanced stages of the wake development presented in Figs. 5 and 7 is different trajectory of the wake motion. The two theoretical solutions place the wake trajectories close to the suction side of the rotor blade while in the experiment the coolant cloud rather occupies the central part of the passage—compare the vortex configuration in Fig. 5, step 48, and the wake structure in the lower passage in Fig. 7, top and bottom. Indicating possible reasons for this discrepancy would require more detailed knowledge on the flow characteristics in the passage examined by Kost et al., including the velocity distribution in the vicinity of the rotor trailing edge, and wake characteristics.

Velocity Signals. Kost et al. experimentally recorded and numerically evaluated velocity fluctuations in selected points along the rotor passage, at a distance of 1/16 of the rotor pitch from the blade suction and pressure walls. The measuring points were located at dimensionless distances x/c_{ax} equal to 0.1, 0.3, 0.5 and 0.7 from the rotor blade leading edge. Diagrams in Fig. 8, reproduced from [19], show the velocity fluctuations recorded at those points. For the same point locations, velocity fluctuations generated by the VD model were calculated on the basis of instantaneous vortex configurations. It is noteworthy to remark here that the identity of the point locations does not imply the identity of local flow parameters, due to different flow acceleration in the two rotor passages, therefore the comparison of the velocity fluctuations recorded at corresponding points may be of qualitative rather than quantitative nature. The VD results are shown in Fig. 9, in which the lower and upper curves correspond to the pressure and suction sides, respectively. Since the major difference between the experimental and NS-based results in Fig. 8 consists in the fact that the former have been obtained via averaging while the latter represent a single realisation of the examined phenomenon, the VD velocity signals were averaged over four individual realisations defined by the phase shifts equal to 0.0, 0.25, 0.50 and 0.75, thus better simulating the measuring conditions. The individual realisations of the velocity fluctuations, being the source data base for averaging, are also shown in the diagrams as dotted curves.

All velocity fluctuations obtained for the points near the blade

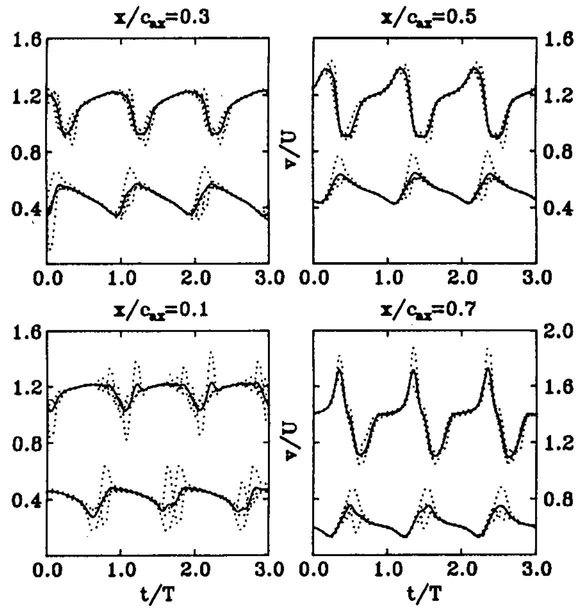

Fig. 9 Velocity fluctuations generated by passing vortex wake at points near the pressure and suction sides of the rotor blade

pressure side are very similar to each other. In each diagram, both in Figs. 8 and 9, they reveal rapid velocity increase followed by slower decrease. An interesting regularity observed in the VD curves is mutual suppression of fluctuations generated by individual realizations, which effectively smoothes down the velocity peaks. This may explain quantitative differences observed in Fig. 8 between the experimental and NS curves, of which the latter, as being represented by a single realization only, reveals more intensive fluctuations. High-intensity fluctuations, observed in individual VD realisations, especially for $x/c_{ax}=0.1$, correspond to the cases of vortex separation shown in Fig. 6. The fact that even such strong fluctuations can be effectively suppressed via averaging is connected here with uniform distribution of phase shift values in particular individual realizations, as a consequence of which the realization revealing an isolated negative vortex had its positive counterpart, of similar qualitative, but opposite quantitative characteristics. The situation in Fig. 9 shows that such fluctuations do not have to be purely stochastic, and can carry valuable information on the flow structure. Unfortunately, this kind of information is totally lost in averaging the signals recorded in real flows, where all irregular or low-frequency fluctuations are eliminated as undesired disturbances.

Good qualitative agreement between all above discussed curves is not surprising. The time-histories of the velocity fluctuations presented in Figs. 8 and 9 for the pressure side points are typical of those generated by the motion of two opposite-sign vortices, or, more generally, of any two well separated groups of one-sign vortices, irrespective of their inner distribution, if only the recording point is sufficiently distant from their trajectories. These two effects, i.e., one-sign vortex segregation, and vortex trajectories located, as a rule, at a distance from the blade pressure side have been demonstrated in the VD analysis. In this context qualitative similarity of the velocity fluctuations predicted by the VD theory to those experimentally recorded suggests that similar processes take place in a real flow.

Although the comparison basically concerns qualitative characteristics of the velocity field generated by the passing wake, a noteworthy quantitative similarity between the experimental and VD results is the fact that for all cases the differences between velocity maximum and minimum peaks are kept within the range of 20–30 m/s.

Velocity fluctuations at points close to the suction side reveal more differences. For $x/c_{ax}=0.1$ and 0.3 the VD curves seems to be closer to those obtained experimentally than the NS solutions. In these two cases the experimental data are smooth, with soft wake generated slopes. The VD curves are also smooth, but especially for $x/c_{ax}=0.1$ reveal fluctuations in the vicinity of the minimum peaks corresponding to the wake passing. A reasonable hypothesis here is that for increased number of realizations used for averaging these fluctuations would vanish, at the same time producing wider and shallower velocity deficit peaks, with softer slopes, similar to those observed in the experiment. The NS velocity time-histories reveal steeper slopes in the vicinity of the wake generated peaks, and are less regular in the remaining part, especially for $x/c_{ax}=0.1$. A possible reason for those effects is a single NS representation of the process, which precludes averaging-connected smoothing. For $x/c_{ax}=0.5$ the NS curve seems to be more accurate than that obtained from the VD analysis. The both curves shown in Fig. 8 reveal regular velocity peaks, sharper for the NS case. Their shapes are qualitatively similar to those recorded at the blade pressure side, which, taking into account that here the recording point is located at a relatively short distance from the hypothetical wake trajectory, may suggest an advanced stage of rolling up of the wake into two large-scale vortices composing the vortex pair, a suggested final structure of the wake deformation [6,7,19,20]. The VD curve also presents a two-peak pattern, but unlike Fig. 8, its slopes neat the peaks are steeper, and between them a softer section is observed for the increasing velocity. This discrepancy may be connected with the fact that the VD analysis does not take into account diffusion of vorticity in the vortex cores, and therefore does not capture accurately the merging of one-sign vortices into a large-scale structure.

For all three cases discussed above, the quantitative agreement between the experiment and VD analysis is rather good. The velocity fluctuations are kept within the limits of 20–30 m/s for $x/c_{ax}=0.1$ and 0.3, and 40–50 m/s for $x./c_{ax}=0.5$. The NS predictions slightly overestimate the scale of possible fluctuations, as equalling, approximately, 50–60 m/s for $x/c_{ax}=0.3$ and 70–80 m/s for $x/c_{ax}=0.5$.

The last case, $x/c_{ax}=0.7$ is most challenging, due to relatively advanced stages of development of the phenomenon, with simultaneous location of the recording point close to the hypothetical trajectory of the wake structures. The two theoretical curves are qualitatively similar to each other in a sense that they both reveal maximum and minimum velocity peaks, with plateau sections in between, more visible for raising velocity part. The peaks in the VD curve are visibly sharper. The agreement of the theoretical curves with the experiment is not as good. The experimental curve reveals two weak maximum peaks in one period, the effect not predicted by the theoretical calculations. Quantitative scales of fluctuations, determined from the VD and NS theories, are, approximately, twice as high, as those recorded in the experiment. A possible factor acting toward worsening of the agreement between the theory and experiment in the examined case is the different trajectory of the experimental wake, which, as seen in Fig. 7, top, moves closer to the center of the passage, while all theoretical considerations place the wake close to the suction side. More detailed analysis of possible reasons for this discrepancy is not possible due to insufficient data on flow characteristics in this area.

Conclusions

The paper presents the study of the interaction between the stator wakes modelled as segments of von Karman vortex streets and the rotor cascade represented by an infinite row of blade profiles, having the geometry typical of an HP impulse turbine stage. Geometrical parameters of the stator wake and inlet conditions for the rotor flow were reconstructed from the preliminary RANS calculations. Along with a number of preliminary tests, intended to assess to applicability of the model to the problem of interest, a series of interaction calculations were performed for different phase shifts defining the initial distribution of vortices in the stator wake. The study has demonstrated that the deformation of the stator wake on its way through the rotor cascade leads to the segregation of two groups of one-sign vortices which then move down the passage along trajectories located, as a rule, close to the rotor blade suction side. Different phase shifts in initial distribution of vortices in the stator wake result in noticeable differences in the wake deformation course, which in extreme cases may lead to the separation of an isolated vortex, whose further trajectory is located close to the rotor blade pressure side.

The course of deformation predicted by the VD analysis was compared to that observed experimentally and analyzed numerically by other researchers in a turbine stage. The comparison revealed good qualitative agreement both with respect to particular stages of the wake deformation and its effects, having the form of velocity fluctuations recorded at selected points near the pressure and suction sides of the rotor blade. It was demonstrated that the VD velocity fluctuation time-histories, when averaged over a number of realisations, were closer to the experimental results that one-realization NS curves.

The VD calculations were performed at a high, controlled level of accuracy, comparable with analytical solutions. The applied flow model secured preservation of invariants of the vortex motion. The generalizing assumptions made at the beginning of the study make it possible to consider the obtained course of the wake deformation a common qualitative pattern of the turbine stator wake behavior in the rotor passage. Since the relations derived from the VD theory are also valid for the NS flow description, this information can be used as a reference for checking correctness and interpreting vortex dynamics related phenomena on the background of other physical and numerical effects in the stator wake-rotor interaction solutions obtained using NS codes.

Of certain significance is the observed relation between the initial distribution of vortices in the wake and their further behavior, as it introduces a stochastic factor to the nature of the stator wake-rotor cascade interaction. Although the vortex dynamics theory clearly presents the existence of that relation and indicates the mechanisms responsible for it, so far there is no sufficient experimental data to assess a possible range of nondeterministic behavior of the wake. Some points discussed in the paper, such as different rates of wake decay and turbulence intensity increase experimentally recorded by Poensgen and Gallus, or better correlation of the averaged VD results with the experiment than those generated by individual NS calculations, suggest that the problem is worth further examining. Possible experimental confirmation of an observable scale of the stochastic aspect of the wake-cascade interaction would lead to some corrections of present assessments concerning the rate of the wake dissipation when it passes the rotor cascade. Along with better and more comprehensive general knowledge on the phenomenon, this direction of wake interaction investigations would have practical aspects, for instance in evaluating clocking effects in simultaneous wake interaction of more than two rows.

Nomenclature

C = complex coefficient in mapping function
D = complex coefficient in velocity function
K = number of blades in mapped rotor cascade segment
L = number of stator wakes
N = number of terms in mapping function fraction series
U = free stream velocity
Q = source strength in canonical plane
S = number of vortex pairs in one stator wake
T = length of mapped cascade segment, wake passing period in rotor passage
W = number of vortices in one rotor wake, number of steps
a = circle radius
c = stator blade chord
g = stator-rotor gap width
h = distance between adjacent vortices in one row of von Karman vortex street
l = vortex street width
s = distance between blade trailing edge and nascent vortex
t = cascade pitch, time
v = local velocity
Γ = vortex strength
α = free-stream inlet angle in stator reference frame
β = free-stream inlet angle in rotor reference frame
ϕ = angle between adjacent circles in canonical plane
φ = phase shift in distribution of wake vortices
τ = dimensionless time, $\tau = tU/c$

Subscripts

ax = axial direction
k = circle number
l = stator wake number
n = mapping function term number, nascent vortex
r = origin
s = steady-state parameter
w = rotor wake number, step number
0 = basic vortex in stator wake
1 = basic circle in canonical plane

Superscripts

$+$ = positive (counter-clockwise) vortex
$-$ = negative (clockwise) vortex
s = steady-state parameter

Appendix

The mapping function used in the present study has a general form of a fraction series, Eq. (1), the coefficients of which are to be determined numerically. Below are given the computed definite values for all unknown parameters in Eq. (1):

Number of profiles in one segment	K	8
Number on terms	N	20
Circle radius	a	0.374803
Location of Circle 1	ζ	(1.198936; 0.022437)

	$C_n.x$	$C_n.y$
1	0.0690310526	0.1355793685
2	−0.1064312275	0.0476350837
3	−0.0004059674	−0.0672603370
4	0.0390495903	0.0168660037
5	−0.0190356093	0.0149892336
6	−0.0051542436	−0.0146191926
7	0.0095019815	0.0009720720
8	−0.0024367562	0.0046313958
9	−0.0015486543	−0.0021768145
10	0.0011753042	0.0001734045
11	−0.0006603038	0.0002220699
12	0.0000038726	−0.0005589232
13	0.0006490103	−0.0000236532
14	0.0000219210	0.0006601034
15	−0.0005658895	−0.0001079551
16	0.0000814274	−0.0002586710
17	0.0000570949	0.0000231256
18	0.0000870961	−0.0000997771
19	0.0000770522	0.0001190673
20	−0.0000751025	0.0000676782

References

[1] Dawes, W. N., 1997, "Current and Future Developments in Turbomachinery CFD," Proceedings, 2nd European Conference on Turbomachinery—Fluid Dynamics and Thermodynamics, Antwerpen, March 5-3.
[2] Meyer, R. X., 1958, "The Effect of Wakes on the Transient Pressure and Velocity Distributions in Turbomachines," ASME J. Basic Eng., **80**, pp. 1544–1552.

[3] Smith, L. H., 1966, ''Wake Dispersion in Turbomachines,'' ASME J. Basic Eng., **88**, Sept., pp. 688–690.

[4] Lienhart, W., 1974, ''Berechnung der instationären Strömung durch gegeneinander bewegte Schaufelgitter und der Schaufelkraftschwankungen,'' VDI-Forschungsheft, **562**, VDI Verlag, Düsseldorf.

[5] Krammer, P., 1982, ''Computation of Unsteady Blade Forces in Turbomachines by Means of Potential Flow Theory and by Simulating Viscous Wakes,'' ASME Paper 82-GT-198.

[6] Korakianitis, T., 1993, ''On the Propagation of Viscous Wakes and Potential Flow in Axial-Turbine Cascades,'' ASME J. Turbomach., **115**, pp. 118–127.

[7] Hodson, H. P., and Dawes, W. N., 1998, ''On the Interpretation of Measured Profile Losses in Unsteady Wake-Turbine Blade Interaction Studies,'' ASME J. Turbomach., **120**, pp. 276–284.

[8] Michelassi, V., Martelli, F., Dénos, R., Arts, T., and Sieverding, C. H., 1999, ''Unsteady Heat Transfer in Stator-Rotor Interaction by Two-Equation Turbulence Model,'' ASME J. Turbomach., **121**, pp. 436–447.

[9] Solomon, W. J., Walker, G. J., and Hughes, J. D., 1999, ''Periodic Transition on Axial Compressor Stator: Incidence and Clocking Effects: Part II—Transition Onset Predictions,'' ASME J. Turbomach., **121**, pp. 408–415.

[10] Dénos, R., Arts, T., Paniagua, G., Michelassi, V., and Martelli, F., 2001, ''Investigation of the Unsteady Rotor Aerodynamics in a Transonic Turbine Stage,'' ASME J. Turbomach., **123**, pp. 81–89.

[11] Sieverding, C. H., and Heinemann, H., 1990, ''The Influence of Boundary Layer State on Vortex Shedding From Flat Plates and Turbine Cascades,'' ASME J. Turbomach., **112**, pp. 181–187.

[12] Cicatelli, G., and Sieverding, C. H., 1997, ''The Effect of Vortex Shedding on the Unsteady Pressure Distribution Around the Trailing Edge of a Turbine Blade,'' ASME J. Turbomach., **119**, pp. 810–819.

[13] Mensink, C., 1996, ''Numerical Prediction of Periodic Vortex Shedding in Subsonic and Transonic Turbine Cascade Flows,'' Int. J. Numer. Methods Fluids, **22**, pp. 881–897.

[14] Currie, T. C., and Carscallen, W. E., 1998, ''Simulation of Trailing Edge Vortex Shedding in a Transonic Turbine Cascade,'' ASME J. Turbomach., **120**, pp. 10–19.

[15] Arnone, A., Marconcini, M., and Pacciani, R., 1999, ''On the Use of Dual Time Stepping in Unsteady Turbomachinery Flow Calculations,'' ERCOFTAC Bulletin No. 42, September, pp. 37–42.

[16] Magagnato, F., 1999, ''Unsteady Flow Past a Turbine Blade Using Non-Linear Two-Equation Turbulence Models,'' Proceedings III European Conference on Turbomachinery: Fluid Dynamics and Thermodynamics, London, March, pp. 221–230.

[17] Valkov, T. V., and Tan, C. S., 1999, ''Effect of Upstream Rotor Vortical Disturbances on the Time-Averaged Performance of Axial Compressor Stators: Part 1-Framework of technical Approach and Wake-Stator Blade Interaction,'' ASME J. Turbomach., **121**, pp. 377–386.

[18] Sondak, D. L., and Dorney, D. J., 1999, ''Simulation of Vortex Shedding in a Turbine Stage,'' ASME J. Turbomach., **121**, pp. 428–435.

[19] Kost, F., Hummel, F., and Tiedemann, M., 2000, ''Investigation of the Unsteady Rotor Flow Field in a Single HP Turbine Stage,'' Proceedings, ASME Turbo Expo 2000, May 8–11, Munich, Germany.

[20] Hummel, F., 2001, ''Wake-Wake Interactions and Its Potential for Clocking in Transonic High Pressure Turbine,'' Proceedings, ASME Turbo Expo 2001, June 4–7, New Orleans.

[21] Lin, C. C., 1943, *On the Motion of Vortices in Two Dimensions*, University Toronto Press, Toronto, Canada.

[22] Prosnak, W. J., 1987, *Computation of Fluid Motions in Multiply Connected Domains*, Wissenschaft+technik series, G. Braun, Karlsruhe, Germany.

[23] Kosma, Z., 1987, ''On an Algorithm for Conformal Mapping of Plane Multiply-Connected Domains,'' Bull. Pol. Acad. Sci.: Tech. Sci., **35**, pp. 41–52.

[24] Gostelov, J. P., 1997, ''Some Unresolved Physical Problems in Two-Dimensional Flows Around Blading,'' *Turbomachinery Fluid Dynamics and Heat Transfer*, Ch. Hah, ed., Marcel Dekker, New York, pp 291–302.

[25] Yershov, S. V., Rusanov, A. V., Gardzilewicz, A., Lampart, P., and Swirydczuk, J., 1998, ''Numerical Simulation of 3D Flow in Axial Turbomachines,'' TASK Quarterly, **2**, pp. 319–348.

[26] Lampart, P., Rusanov, A. V., Yershov, S. V., Swirydczuk, J., and Gardzilewicz, A., 1999, ''Preliminary Investigations of the Effect of Stator-Rotor Interaction on the Characteristics of an HP Turbine Stage,'' Turbomachinery, **115**, pp. 285–296.

[27] Sarpkaya, T., 1989, ''Computational Methods With Vortices—The 1988 Freeman Scholar Lecture,'' ASME J. Eng. Mater. Technol., **111**, pp. 5–52.

[28] Meier, G. E. A., and Timm, R., 1985, ''Unsteady Vortex-Airfoil Interaction,'' Proceedings, AGARD Conference No. 386, Paper 16, 10 p.

[29] Swirydczuk, J., 1990, ''A Visualisation Study of the Interaction of a Free Vortex with the Wake Behind an Airfoil,'' Exp. Fluids, **9**, pp. 181–190.

[30] Swirydczuk, J., Wilder, M. C., and Telionis, D. P., 1993, ''The Interaction of Coherent Vortices With Short Flat Plates,'' ASME J. Fluids Eng., **115**, pp. 590–596.

[31] Streitlien, K., and Triantafyllou, M. S., 1995, ''Force and Moment on a Joukowski Profile in the Presence of Point Vortices,'' AIAA J., **33**, pp. 603–610.

[32] Swirydczuk, J., 1992, ''A Numerical Study of Changes in Flow Conditions Around Two Identical Airfoils Generated by a Moving Vortex Singularity,'' Transactions of the Institute of Fluid-Flow Machinery, **94**, pp. 3–17 (in Polish).

[33] Swirydczuk, J., 1992, ''Modeling the Interaction of a Single Free Vortex with a Limited-Element Cascade of Airfoils by Means of Conformal Mapping,'' Transactions of the Institute of Fluid-Flow Machinery, **94**, pp. 96–111 (in Polish).

[34] von Karman, T., and Rubach, H., 1912, ''Über den Mechanisms des Flüssigkeits-und Luftwiderstandes,'' Physikalische Zeitschrift, **13**, pp. 49–59.

[35] Poensgen, C., and Gallus, H. E., 1991, ''Three-Dimensional Wake Decay Inside of a Compressor Cascade and Its Influence on the Downstream Unsteady Flow Field: Part I—Wake Decay Characteristics in the Flow Passage,'' ASME J. Turbomach., **113**, pp. 180–189.

Detached-Eddy Simulations Over a Simplified Landing Gear

L. S. Hedges
Boeing Commercial Airplanes,
P.O. Box 3707,
Seattle, WA 98124

A. K. Travin
Federal Scientific Center "Applied Chemistry,"
St. Petersburg 197198, Russia

P. R. Spalart
Boeing Commercial Airplanes,
P.O. Box 3707,
Seattle, WA 98124
e-mail: philippe.r.spalart@boeing.com

The flow around a generic airliner landing-gear truck is calculated using the methods of Detached-Eddy Simulation, and of Unsteady Reynolds-Averaged Navier-Stokes Equations, with the Spalart-Allmaras one-equation model. The two simulations have identical numerics, using a multi-block structured grid with about 2.5 million points. The Reynolds number is 6×10^5*. Comparison to the experiment of Lazos shows that the simulations predict the pressure on the wheels accurately for such a massively separated flow with strong interference. DES performs somewhat better than URANS. Drag and lift are not predicted as well. The time-averaged and instantaneous flow fields are studied, particularly to determine their suitability for the physics-based prediction of noise. The two time-averaged flow fields are similar, though the DES shows more turbulence intensity overall. The instantaneous flow fields are very dissimilar. DES develops a much wider range of unsteady scales of motion and appears promising for noise prediction, up to some frequency limit.* [DOI: 10.1115/1.1471532]

1 Introduction

Commercial airplane and engine manufacturers are exploring new technologies to reduce airframe and engine noise in response to ever-increasing requirements to meet new community noise standards. In the landing configuration, a significant portion of the noise generated by an airplane is aerodynamic noise caused by airflow around the extended landing gear. Today's noise-prediction methods are generally highly empirical. Physics-based methods will couple a detailed model of the flow field immediately around the source with an acoustic model, such as Lighthill's equations, for the prediction of the noise radiated to the far field. The flow-field model must include a comprehensive unsteady description of the turbulence, including fluctuations in velocities and wall pressures.

If computing power were not an issue, the method of Direct Numerical Simulation (DNS) would be a natural approach to computing the necessary flow fields [1]. Unfortunately, DNS is too costly by many orders of magnitude at relevant Reynolds numbers. The method of Large-Eddy Simulation (LES) is often and sometimes hugely more cost effective than DNS. With LES, the large and medium noise-producing eddies are captured while the small eddies, which do not contribute as much and are simpler, are modeled with a subgrid scale model [2,3]. However, full-domain LES requires that eddies in the boundary layer be resolved by the grid. This makes LES computationally prohibitive for most geometries of interest when the boundary layers are turbulent [4].

Detached-Eddy Simulation (DES) is a recently developed hybridization of Large-Eddy Simulation and Reynolds-Averaged Navier-Stokes (RANS) [5–8]. The unsteady massively separated regions of the flow are treated with LES. Since the gross mechanisms of the flow such as vortex shedding involve length and time scales much larger than those of the boundary-layer turbulence, the boundary-layer modeling relies on the RANS equations with little loss in the description. The computational requirements for DES are similar to unsteady RANS, but the accuracy of the complete flow field is potentially similar to LES. Results on airfoils [5], cylinders [6], and spheres [7] have been highly encouraging. Few complex geometries have been attempted with DES or LES to date. The method is promising, but quite new.

Solving of the Unsteady Reynolds Averaged Navier Stokes (URANS) equations, often under the name Very-Large-Eddy Simulation, is another approach to simulating the unsteady flow around a bluff body [9,10]. The computing requirement for URANS is manageable up to very high Reynolds numbers. However, the URANS description can be ambiguous. It implies a separation of scales between coherent eddies, which will be resolved, and random eddies, which will be modeled even in the separated region. Few flows fit this description, and often URANS captures none of the coherent eddies. For example, using URANS to model the flow over a sphere does not produce the unsteady behavior observed in the wind tunnel [7]. Modeling the flow over a cylinder with URANS results in a periodic unsteadiness and (typically) a 2D solution with exaggerated vortex shedding rather than the more realistic chaotic 3D unsteadiness [10]. URANS gives a fairly accurate mean flow for a triangle and for a sphere, but not for the cylinder.

In this paper, the methods of DES and URANS using the Spalart-Allmaras turbulence model are applied to a landing-gear truck based on a 31% scale Boeing 757 main landing bogie, as tested by Lazos at the NASA Langley Research Center [11]. The geometry was drastically simplified by eliminating components such as links, tubing, wheel covers, and braking mechanisms. The remaining components are: four smooth wheels, two transverse axles, a longitudinal beam, and a vertical post. The simplicity of the model makes the Lazos geometry excellent for a first attempt at landing-gear simulations.

The goal of the paper is two-fold. First, to compare the simulation results of URANS and DES to experimental results for a complex, massively separated flow-field. The flow around the landing gear is more challenging than the simpler shapes more commonly modeled, and which still pose major difficulties, for URANS and LES. The second goal is to gain an understanding of the nature of the physical modeling obtained with DES and URANS. It has been claimed that URANS resolves the largest coherent scales of motion and models the unresolved random unsteadiness with the turbulent eddy viscosity in a self-consistent manner. That perception of URANS is challenged here.

This study only addresses DES and URANS with the Spalart-Allmaras turbulence model. While both approaches may be sensitive to the underlying RANS model, Strelets [12] showed that DES is insensitive to the RANS model for the backwards facing step. With DES, the massively-separated flow is fundamentally insensitive to the type of RANS model used, as the model is suppressed in these regions. The sensitivity of DES to the RANS

Contributed by the Fluids Engineering Division for publication in the JOURNAL OF FLUIDS ENGINEERING. Manuscript received by the Fluids Engineering Division July 23, 2001; revised manuscript received January 24, 2002. Associate Editor: T. Gatski.

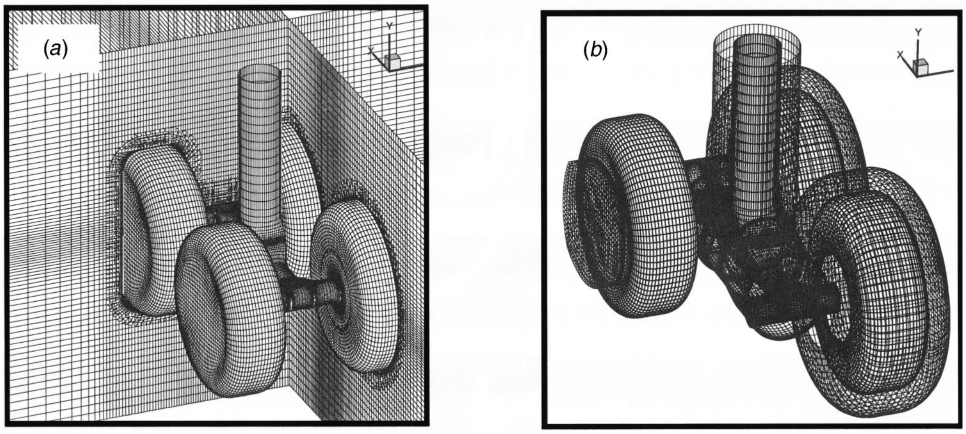

Fig. 1 Surface grids of the internal grid blocks

treatment will likely appear in regions of incipient separation where, in extreme cases, small differences could have a profound effect on the entire flow field.

The type of RANS model used will have a much stronger effect in the URANS calculation as the RANS model remains active in the massively-separated regions. How great the effect is likely depends on the magnitude of the Reynolds stresses associated with unsteady flow when compared to the stresses carried by the model [9].

One-equation models are the simplest models in use today. Without denying that turbulence models other than the Spalart-Allmaras model could perform better for the URANS calculation, we consider that there is no structural reason why a one-equation model should fail in the wake. In the wake of a bluff body the length scale used by the formula of the S-A model, the wall distance, may appear too large. If this were true, the turbulence model would grossly over-predict mixing in the wake. However, this length scale only sets an upper bound for the internal length scale of the model, or mixing length. Effectively, the wall distance becomes irrelevant since the destruction term vanishes. In this region, the S-A model is much less dissipative than a pure mixing length (algebraic) model would have been. It was calibrated in free shear flows with the input length scale set to infinity.

Section 2 of this paper describes the numerical procedures used. Section 3 compares the simulation results to the experimental results. Section 4 contrasts DES and URANS solutions and Section 5 gives a discussion.

2 Simulation Method

The flow around the landing gear was modeled as incompressible and at a Reynolds number, based on wheel diameter, of 6×10^5. The wind-tunnel Mach number was below 0.1 and the Reynolds number was also 6×10^5.

2.1 Governing Equations. The DES formulation used here applies the modified Spalart-Allmaras (SA) RANS model [13], which has a single transport equation, over the whole computational domain. In DES the SA input length scale, which is normally the distance to the wall, is limited by the grid spacing. This turns the RANS model into a LES sub-grid-scale (SGS) model in regions where the grid spacing (multiplied by a constant which is of order 1) is smaller than the distance to the wall. The largest dimension of each grid cell is taken. A more detailed description of DES and the DES model used here is found in references [12] and [6]. Unlike DES, the URANS formulation [14] retains the traditional SA length scale throughout the entire domain. For flows such as this one or past a cylinder and other bluff bodies, the RANS equations do not appear to have a stable steady solution.

The eddy viscosity at the inflow boundary was set to a value five times the molecular viscosity. This caused the turbulence model to be active in all of the boundary layers. Small improvements may be obtained by allowing laminar patches near the front stagnation points on the wheels, and stagnation lines on the axles and post.

2.2 Numerical Procedure. The NTS code. The landing gear calculations were performed with the NTS code written by the Strelets group in St. Petersburg [12]. The grid type is multi-block structured, and the blocks are overset. A hybrid of fifth-order upwind-biased and fourth-order centered difference schemes is used for the inviscid terms. The hybridization is performed by a smooth blending function based on the flow-field. As a result, the upwind method is used in the boundary layers and the irrotational region, and the centered scheme in the LES regions. This is the best compromise, currently, between stability in the RANS and inviscid regions, and low numerical dissipation in the LES region. Time integration is performed with an implicit three-layer second-order-accurate time-stepping scheme. The incompressible Navier-Stokes equations are solved with the Rogers-Kwak method of artificial compressibility and dual time stepping [15]. Airfoil and cylinder DES studies performed with the NTS code have provided remarkably accurate results when compared with experimental data [5,6]. In other cases, the agreement was more modest, but the experimental scatter was much larger, and in general this kind of separated flow is still very challenging for CFD and experiment.

2.3 Grid and Boundary Conditions. The simulations model the landing gear and the wind tunnel test-section walls. The grid is made of thirteen primary blocks, twelve of which are internal. Figure 1(*a*) shows the surface grids and cuts across a few of the blocks. The internal blocks wrap around each of the landing gear components, which is seen better in Fig. 1(*b*). Each wheel is wrapped with one primary block. Another block is used at each wheel to avoid a polar-coordinate singularity at the center of the outside wheel faces. The two axles, beam and post are also each wrapped with one block. The external block covers the entire computational domain, with cut outs, to overlap the internal blocks. Two planes of it are shown in Fig. 1(*a*). The grid has about 2.5 million grid points. The geometry modeled in the simulations is modified slightly from the experimental model at the junction of the vertical post and longitudinal beam.

As an example, the blocks that enclose the wheels each have 90 points around the circumference, and 45 points over the top of the tire. Thirty-one points are normal to the wall, with a first cell spacing of 1×10^{-4} wheel diameters (a$y+$ of about 3). The stretching ratio does not exceed 1.2, and the block extends to a

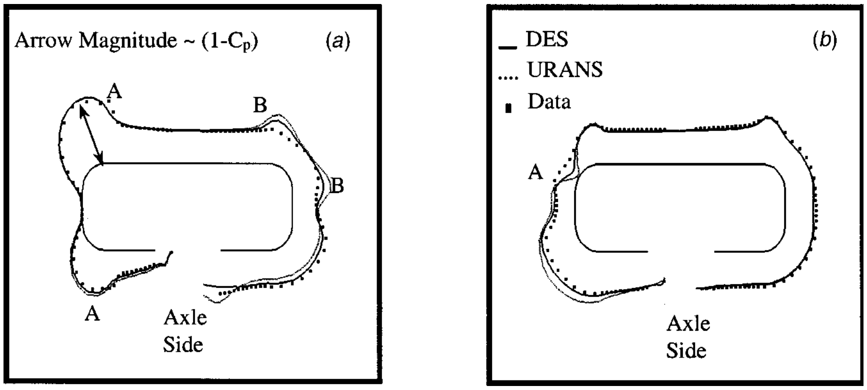

Fig. 2 C_p **around the wheel when placed in the top view. (*a*) Front wheel; (*b*) rear wheel**

distance of 0.115 wheel diameters. The RANS length scale switches to the LES length scale smoothly at a distance of about 0.023 wheel diameters from the surface.

The grid can be loosely viewed as composed of a RANS region and an LES region. Although there is no zonal demarcation, the grid character is quite different in terms of anisotropy and dependence on Reynolds number. For example, the very near-wall regions of the wheel block are RANS regions with very high cell aspect ratios. The outer region of the wheel blocks are LES regions. Near the wall, the grid spacing strongly depends on Reynolds number and is set as it would be for a pure RANS calculation, using wall units. The grid spacing in the LES region depends weakly on Reynolds number, if at all. As much as possible, cubic grid cells are used in the LES regions.

Identical grids and time steps are used for the DES and the URANS calculations. No-slip conditions are applied on the landing gear and slip conditions on the wind-tunnel walls, to save the grid clustering. The model creates a high blockage, but not enough to suspect separation on the tunnel walls. The inflow boundary is placed 3 wheel diameters upstream, and the outflow boundary 7 wheel diameters downstream of the landing gear.

The grid was refined manually after obtaining initial solutions. The refinement was based on visualizations of the flow structures and the level of turbulent viscosity in the LES regions of the DES. A rigorous grid resolution study was prevented by the large computational requirements of the unsteady calculation. Instead, several solutions of varying algorithmic order of accuracy and numerical dissipation were compared with each other. The simulations with upwind/centered differencing, used in this paper, were compared to solutions based entirely on third-and fifth-order upwind difference schemes. The conclusions drawn from this type of comparison are similar to the results of a grid resolution study. The highest order scheme produced visibly finer eddies between the wheels, but the time averaged quantities of the three schemes used were close.

2.4 Simulation Start-Up and Running. A steady Reynolds Averaged Navier-Stokes (SRANS) calculation was used as the starting point for the unsteady calculations. The SRANS calculation allowed the flow field to develop quickly across the domain. Three to four orders of magnitude of convergence was obtained. Once the SRANS solution residuals leveled off, the time-accurate solution was begun. The time step was 0.03, normalized with inflow velocity and wheel diameter. About 10 time units were simulated to remove start-up transients before the time-averaging sample began.

The massively separated flow around the landing gear is chaotic, and the length of simulation time required to ensure a comprehensive time-averaged sample is substantial. At least 100 time units were collected to create a time-averaged data sample. This can be compared with samples of up to 200 time units for the cylinder [6].

The calculations were run on the NAS Origin 2000 computers using an average of 4 nodes. A full run required approximately 1000 hours of wall-clock time.

3 Comparison With Experiment

Lazos tested the landing gear model in the Basic Aerodynamic Research Tunnel (BART) at the NASA Langley Research Center [11]. During that experiment, mean flow characteristics were measured, primarily on and near the wheels. Comparisons between the experiment and the time-averaged numerical predictions of surface pressure are presented first.

3.1 Line Plots of Pressure. Line plots at *X*-, *Y*-, and *Z*-cuts through each wheel allow visual quantitative comparisons between experiment and simulations. The mid *Y*-cut is shown in a top view, the mid *Z*-cut in a side view, and the mid *X*-cut in an end view. The lines around the wheel indicate the magnitude of the pressure coefficient on the wheel surface. The distance from the wall to the line, along the normal to the surface, is $(1-C_p)/10$. When plotted this way, low-pressure regions appear to "pull" on the wheel surface and high-pressure regions appear to "press" against it. The line contacts the surface when the stagnation pressure is reached. Normally, the line never enters the wheel.

The top view of the front wheel is shown in Fig. 2(*a*). At the front of the wheel the pressure is high (the line contacts the wheel). This is expected, as it is the stagnation region. Stagnation pressure is also approached in front of the axle. Both DES and URANS match the pressure very well in this region, which is not very challenging since inviscid physics dominate, and the wake shape, which depends on viscous effects, acts on the flow far downstream of this area. To the sides, the high-curvature wheel edge accelerates the flow rapidly; the line pulls away from the wheel. Here, the numerical calculations over-predict the magnitude of the negative pressure slightly, particularly on the axle side of the wheel. The URANS simulation over-predicts the acceleration slightly more than the DES on that side.

It is evident from the experimental data that the flow separates and rapidly reattaches on both sides of the wheel. This location is labeled with an "A" in Fig. 2(*a*). Considering the Reynolds number, it is likely that the boundary layers separate while still laminar. The boundary layers in the DES and URANS simulations are modeled as fully turbulent and as a result, do not separate. Transition control remains highly challenging with either technique and with any turbulence model, especially when transition and separation mingle [6]. Nevertheless, the DES and URANS pressure profiles are in good agreement with the experimental data

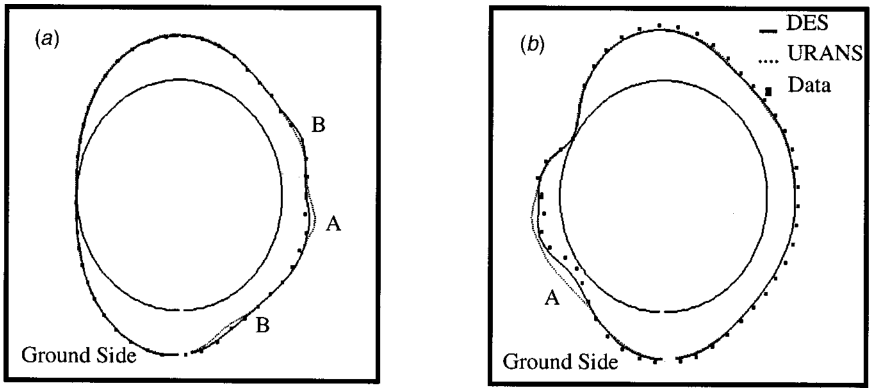

Fig. 3 C_p **around the wheel when placed in the side view. (*a*) Front wheel; (*b*) rear wheel**

along the sides of the wheel, suggesting that the mismatch at the separation bubble does not contaminate the flow downstream.

The furthest aft portion of the front wheel is not close to experiment with either method. The simulations follow the experimental data somewhat, but miss two flow features as indicated with a letter "B." In general, full 3D DNS, LES, and DES have worked quite well on the base regions of bluff bodies [6]. Additional difficulties may arise here for at least two reasons: the interference from the rear wheel, post and axles, and the longer stretch of boundary layer along the wheel, which thickens the boundary layer. DES shows a marginally better agreement than URANS. The complete absence of acceleration at the rear outside tire shoulder, in the experiment, is unexpected. This would happen if the flow were fully separated from the front tire shoulder on, but both experiment and CFD indicate reattachment on the side of the wheel. The boundary layer would have to be very thick compared with the radius of curvature of the tire shoulder to explain the absence of acceleration (recall that in a turbulent boundary layer, most of the velocity difference is located in the near-wall region). A possible explanation for the difference is that the two-dimensional comparison misses the bigger three-dimensional picture. Three-dimensional figures shown below (Fig. 5) reveal an acceleration in the experimental data for planes that are only about 1/10 diameter away from the one chosen for this figure. Thus the cut shown in Fig. 2(*b*) is not typical of this region.

The top view of the rear wheel is shown in Fig. 2(*b*). The aft region of the rear wheel is simulated well by both methods, and here the experiment shows the acceleration. On the other hand, the base pressure is over-estimated by 0.06 in C_p. The front portion of the rear wheel echoes the poor agreement on the aft portion of the front wheel. The distance between the two wheels is only 0.16 diameters, and their width is 0.37. Some discrepancy is seen between simulations and experiment in this region, but the simulations "pick up" most of the flow features. One feature that is captured poorly is again indicated with an "A." The DES prediction is, again, marginally better than the URANS prediction.

The side view of the front wheel is shown in Fig. 3(*a*). The DES pressures compare very well to the experiment almost all around, with a slight deviation on the aft-most point of the wheel (area A). The URANS pressures compare well, but in addition to missing in the aft region, miss at two other locations shown with the letter B.

The side view of the rear wheel is shown in Fig. 3(*b*). The simulations follow the experiment around most of the wheel, but, again, underestimate the negative pressure on the base. Notably, the simulations deviate at the ground side of the front of the rear wheel as indicated by the letter A. This is the region of greatest discrepancy, in terms of resolved flow features, between the numerical and experimental data. The pressure field in the experiment is much more symmetric, top to bottom, than in the CFD. The flow in the experiment impinges on the wheel on both the wing side and ground side, bringing the pressure up near its stagnation level in both spots, whereas the flow in the simulations only impinges on the wheel, in a clear manner, on the wing side. The pressures around the front and rear wheel in an end view are shown in Figs. 4(*a*) and 4(*b*), respectively. The results compare very well. The magnitude of the numerically predicted pressures is slightly higher than the experimental data over the rear wheel. In Fig. 4(*a*) the URANS solution appears to over-accelerate around the front axle (indicated with an "A"). The DES models

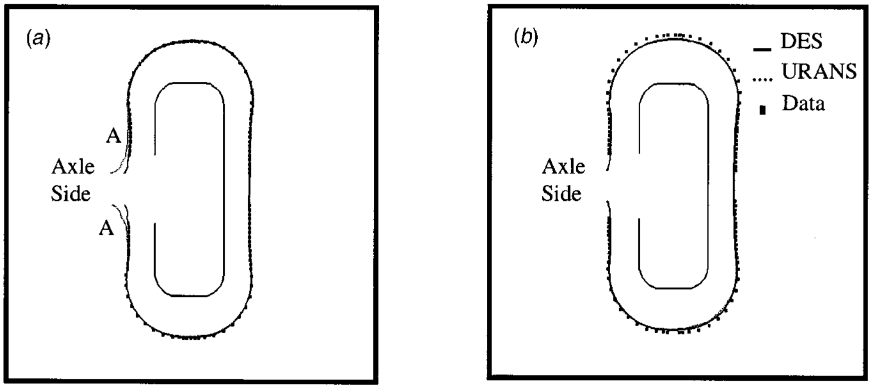

Fig. 4 C_p **around the wheel when placed in the top view. (*a*) Front wheel; (*b*) rear wheel**

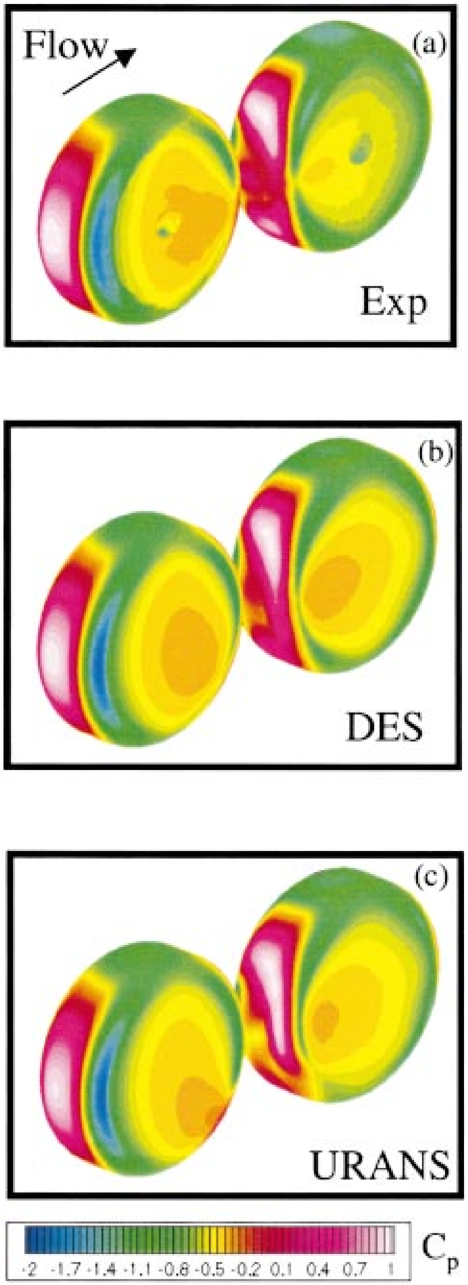

Fig. 5 Pressure coefficient comparison on the front of the wheels

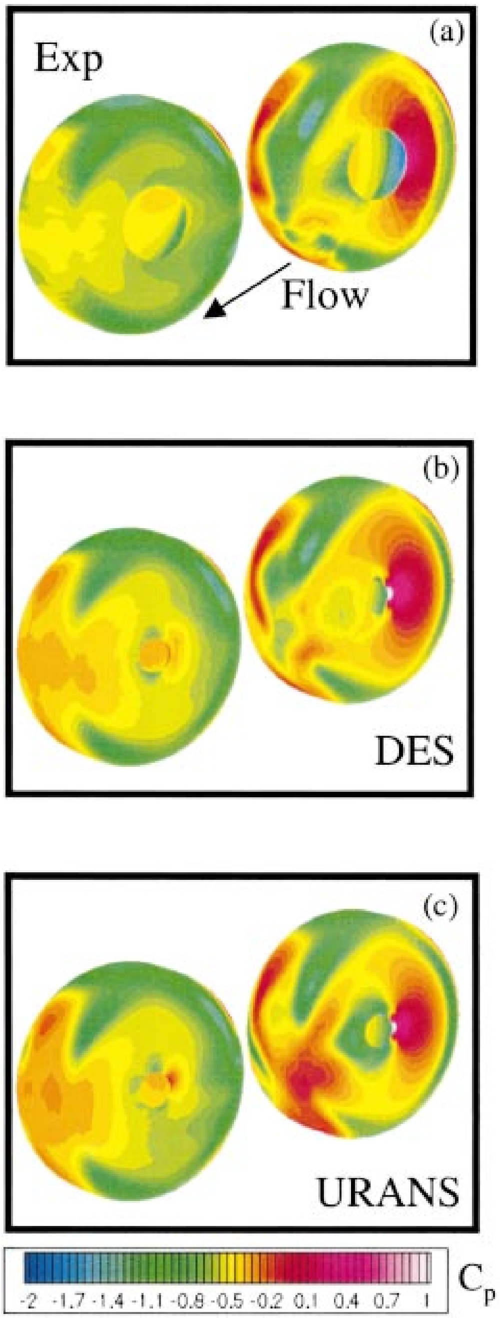

Fig. 6 Pressure coefficient comparison on the back of the wheels

the measurements approaching the axle very well, although the experiment does not reach close enough to be fully certain. The difference between URANS and DES is reminiscent of their behavior over simple cylinders, but exaggerated. This region is inside the wheel's boundary layer, and the pressures do not match those on a 2D cylinder.

Overall, the pressure comparisons between experimental data and both the DES and the URANS predictions are good. Recall that even much simpler geometries such as a single circular cylinder are still challenging. The greatest deviations between the experimental data and the numerical methods occur in the region between the front and rear wheels. Unfortunately, experimental data are not available for other regions that could be acid tests, such as the wakes of the post and axles. The DES matches experiment a little better than URANS.

3.2 Flood Contour Plots of Pressure.

Line plots offer a direct quantitative display of how the pressures compare. Contour plots offer a more qualitative look, but with full coverage. Some flow features are missed by the simple cuts made in Section 3a, but are seen in the flood contour plots. Pressure contours are shown on the wheel surfaces in Figs. 5 and 6 for all three datasets. Figure 5 shows the front and outside of the wheels. Figure 5(*a*) is experiment, Fig. 5(*b*) is DES, and Fig. 5(*c*) is URANS. The axles and post are not shown in the figure, as no experimental measurements were made on these surfaces. The hub side also has a small hole. The smoothness of the data is an indication of the adequacy of the time sample. The residual asymmetry is also an indicator of the adequacy of the time sample. It is of the order of 0.004 in the pressure coefficient.

The DES compares very well to the experiment, accurately

Table 1 Wheel and total landing gear drag and lift coefficients

	Front wheel C_D	Rear wheel C_D	Front wheel C_L	Rear wheel C_L	Total landing gear C_D	Total landing gear C_L
Experiment	0.151	0.161	0.012	0.029	NA	NA
DES	0.127	0.105	0.029	0.015	0.675	0.083
URANS	0.105	0.089	0.045	0.016	0.597	0.123

picking up most of the flow features at the front of the front wheel, in the region dominated by inviscid physics, but also, on the wheel sides and at the front of the rear wheel. The greatest deviation occurs on the ground side, in front of the rear wheel. This was seen in Fig. 3(*b*). The URANS simulation compares less well than the DES. While the URANS ‘‘picks up’’ the same flow features as the DES, some features between the wheels and on the ground side are shifted substantially.

The aft, axle side of the wheels is shown in Fig. 6. The measurement gap around the axle is larger in the experimental data than in the numerical data. This gap opens a view to the ‘‘inside’’ of the hidden part of the wheel, and should not cause confusion. The regions in this figure emphasize viscous effects, compared with those in Fig. 5. Smaller, stronger features are present on the pressure maps, and the DES picks up all of the features (though it misses the pressure magnitude in some spots). The URANS has more trouble, again, particularly on the ground side between the wheels. The deviation that is sustained over the largest area is that the experiment has lower pressures on the aft end of the aft wheel. This is reflected in a drag discrepancy, discussed shortly. While the pressure magnitude is high, the pattern on the aft end of the aft wheel is captured remarkably well.

3.3 Pressure Lift and Drag Coefficients.

The experimental and computational pressures were integrated over the surface of the wheels to give the pressure lift and drag coefficient, shown in Table 1. The side forces are not reported, because of measurement gaps in the pressure. For CFD, averages between the two sides are shown. The discrepancy between the right and left wheels was approximately 5% of the magnitude of the drag coefficient in the computations, or less. The lift discrepancy for the DES was also about 5% of the drag coefficient, creating a more substantial relative difference between the two. The reference area is the wheel diameter, squared. In these units, the frontal area of a wheel is 0.36, and that of the system is very close to 1.

As expected, the wheels generate drag, and a small amount of lift, which is ultimately due to the asymmetry of the post. Wheel drag coefficients based on frontal area are in the 0.3 to 0.4 range, which is closer to that of a sphere than that of a long cylinder. DES underestimates the front wheel drag by 16%, and URANS does so by 30%. Counter-intuitively, the experimentally measured pressure drag is higher for the rear wheel than for the front wheel (these values were not calculated by Lazos [11] but we used his pressure files). The numerical simulations predict a lower drag for the rear wheel than for the front wheel, as when two vehicles are ‘‘drafting.’’ High aft-wheel drag could be attributed, possibly, to interference drag with the post, but there is no compelling reason why this effect would be entirely missed by CFD. The DES rear-wheel drag is lower than the experiment by a surprising 35%, and URANS by 45%. Boundary-layer growth on the walls, which is absent in the CFD because of the slip boundary conditions, could account for only about a 3% growth in dynamic pressure (relative to the upstream plane), and would not be noticeably biased between front and aft wheels.

The drag discrepancy was found to be the result of differences that are almost uniformly distributed around the wheel. We tried to isolate a region of the flow field responsible for the drag difference for the following three reasons. The first was to search for an error; the second was to see if a much larger C_p differences existed away from the cuts we compared in Figs. 2–4; the third was to identify a region that had an unusually high error level, and then refine the grid there and/or detect an intense flow feature such as tight vortex. None of these conjectures were confirmed. There is no clear ‘‘hot spot’’ of disagreement.

The lift is small overall. CFD over-predicts the front-wheel lift and under-predicts the rear-wheel lift. However, the magnitude of the discrepancy is less than that for the drag prediction. While the overall pressure comparisons are quite good, the drag and lift coefficient comparisons are mediocre. DES predicts the forces better than URANS-SA, but we cannot point to any specific flow feature that accounts for it.

4 Detailed Simulation Results

Unsteady simulations produce a wealth of data. Both instantaneous and time-averaged flow fields can be visualized. In this section, instantaneous contour plots of velocity magnitude and vorticity, and time-averaged contour plots of velocity magnitude and Reynolds stresses are used to explore the flow physics and detect differences between the DES and URANS calculations. We also wish to predict the usefulness of these simulations as the basis for noise calculations from first principles. Each of the time-averaged flow fields is data averaged over a period of 100 time units.

4.1 Instantaneous and Time-Averaged Velocity Magnitude.

The instantaneous velocity magnitude is shown in Fig. 7(*a*) for the DES. Contours are shown on an *X*-plane cut just downstream of the model. The unsteady character of the flow field

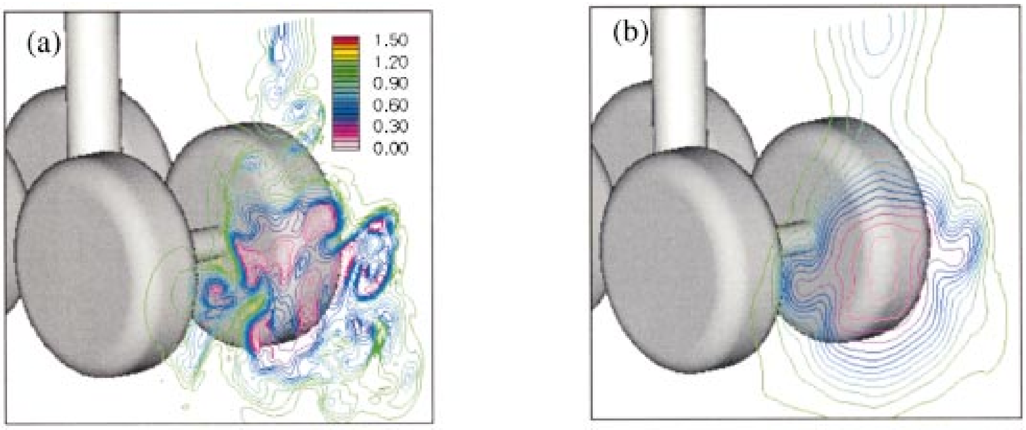

Fig. 7 (*a*) Instantaneous and (*b*) time averaged velocity magnitude, DES

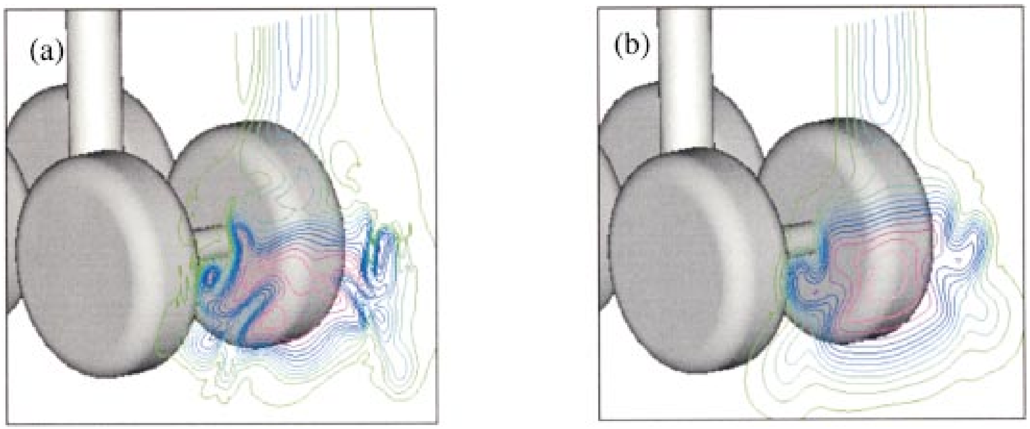

Fig. 8 (*a*) Instantaneous and (*b*) time averaged velocity magnitude, URANS

is revealed by many characteristics visualized here including asymmetry and the large number of small features in the wake region. The flow field also shows many randomly distributed pockets of high-velocity flow in the center region of the wake. This would be out of character with a steady wake, where a smoothly varying momentum deficit is expected.

In contrast, the time-averaged flow field of the DES, in Fig. 7(*b*) is very smooth. The contours were not symmetrized for the figure, and thus give an idea of the adequacy of the time sample.

The residual asymmetry in the velocity reaches 0.07 in the shear layer behind the wheels, which appears to be among the worst areas. There, the U velocity at the points $x=1.4$, $z=+-0.6$ is 0.81 on one side, and 0.88 on the other. On the other hand, the difference is magnified by the high shear rate, and the difference in the shear-layer position is only 0.015 (the velocity at $+0.615$ matches that at -0.6).

In the time-averaged flow field, there are no eddy-like features of any size seen, only the suggestion of streamwise vortices, roughly trailing outside the shoulders of the tires. The center of the wake shows the lowest velocity magnitude.

The instantaneous URANS velocity magnitude contours shown in Fig. 8(*a*) are qualitatively different from the DES contours, being smoother and more symmetric. The center of the wake region contains no marked local velocity peaks. The region of flow aft of the vertical post is particularly smooth and symmetric; animated visualizations reveal that vortex shedding occurs along the entire post in DES, but not in URANS. Overall, the URANS simulation does not include the small-scale eddy content of the DES, and the central region of the wake appears entirely devoid of eddy content.

It is not surprising that the URANS simulation did not capture the smaller scales of the flow-field captured by DES. It was expected that the turbulence model in the URANS simulation would damp out the small-scale features. At $x=1.5$, the URANS eddy viscosity is about 0.004, compared with 0.0007 in the DES (normalized with velocity and diameter); similar ratios are found throughout the wake region. What is worth noting is that the URANS simulation did not capture many of the larger scales or the range of scales captured in the DES. Spectral analysis of the forces on the landing gear sheds some light on the range of scales captured by the URANS simulation and is discussed below.

The velocity magnitude contours for the time-averaged URANS flow field are shown in Fig. 8(*b*) and are exceedingly similar in character to the instantaneous contours, suggesting a much weaker unsteadiness than in DES. Conversely, the URANS time-averaged contours are very similar to those from DES. Differences are seen just downstream of the vertical post where the spreading rate is larger for DES. Additionally, the URANS calculation shows signs of streamwise vortex pairs emitted from around the base of the rear wheels. This is not seen with the DES; again, they could have been diffused. Animations confirm the periodic shedding of large vortices at this location with the URANS, but not with DES. Instead, the DES produces a much smaller amplitude and chaotic type of shedding.

4.2 Instantaneous Vorticity Magnitude Contours. Contours of vorticity magnitude are shown in Figs. 9(*a*) for DES, and 9(*b*) for URANS. Two *Y*-plane cuts are shown, one just above the wheel mid-plane and the other about three-quarters of the way up the vertical post. In the DES, a wide range of spatial scales is seen

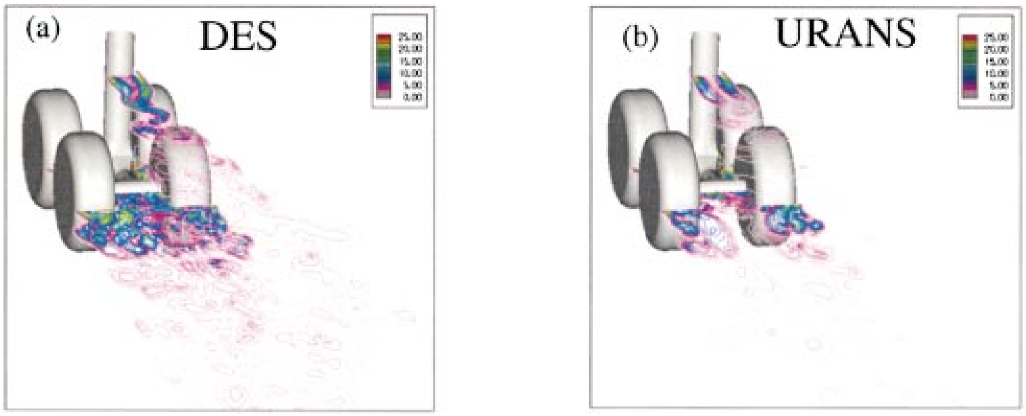

Fig. 9 Instantaneous vorticity magnitude: (*a*) DES, (*b*) URANS

throughout the vicinity of the landing gear. The flow between the wheels is particularly rich with vortical structures. Just downstream of the landing gear, there are many peaks of vorticity, some reach values near 37, normalized with freestream velocity and wheel diameter.

The URANS simulation shows some vortical structure both immediately downstream of the wheels, and well within the truck. As expected, it does not exhibit the same small-scale eddy content as the DES. The URANS vorticity peaks reach values of about 24.

The vortices persist further downstream in DES than in URANS. Their lack of persistence in URANS limits the component interactions as compared with DES. This would have stronger implications if we were studying the effect of the landing-gear wake on a wing flap many unit lengths downstream, for instance.

Both the DES and the URANS simulations shed vortices from the vertical post (as seen in the upper *Y*-plane cut). Yet, the two shed in characteristically different ways. The URANS shedding is highly regular and periodic, and the shear-layer roll-up begins some distance downstream. In comparison, the DES shedding is chaotic and occurs earlier. Exploration of the URANS flow field shows that the URANS shedding is highly two-dimensional along the upper half of the vertical post. The DES flow field is three-dimensional with flow from between the wheels mingling upwards with the vortex shedding. This is not a numerical effect, as the grids and time steps are identical.

Overall, the DES flow-field shows a much more dynamic vortical structure than the URANS flow-field. This is confirmed by numerous other views we made, and animations.

4.3 Total Turbulent Kinetic Energy (TKE).

The resolved energy of the unsteady flow field was calculated as time progressed during the calculations. Its contours are shown in the *Y*-plane cut just above the mid-plane of the wheels for the DES in Fig. 10(*a*). A high level of resolved flow-field unsteadiness is evident between the wheels where the TKE peaks at a value of about 0.27, normalized with freestream velocity. The entire wake region is also energetic, with a peak value of TKE of about 0.15 just downstream of the wheels. The TKE persists for some distance downstream.

Contours of resolved turbulent kinetic energy are shown in the same *Y*-plane cut for URANS in Fig. 11(*a*). The TKE peaks at about 0.17 between the wheels, and at about 0.1 just downstream of them. In general, the resolved TKE for URANS is about half that for DES. The weakness of the TKE in URANS is particularly evident where unsteadiness does not persist, downstream of the landing gear and along the centerline. In these regions, the length scale in the SGS/turbulence model has a wider difference between DES and URANS.

As a side note, the smoothness and symmetry of the TKE and the Reynolds stresses are an indicator of the adequacy of the time-averaged sample obtained. The symmetry is satisfactory behind the model, but good symmetry is not consistently observed between the wheels. This is reminiscent of visual observations of Lazos [11]. He saw the ‘‘footprint’’ of a vortex making very durable migrations between two locations. The simulation may be approximating this ‘‘bimodal’’ behavior.

A higher level of TKE does not in itself indicate a better flow field solution, first because the SGS energy was not included in the TKE magnitude, and second because experimental measurements are not available with which to compare the solution results. Additionally, in a one-equation turbulence model with a simple linear constitutive relation, such as the one used here, the modeled diagonal Reynolds stresses and TKE are inaccurate. In particular, the modeled TKE is too low. Likely, this degrades the URANS results, although in the absence of measurements we have no basis for comparison.

4.4 Resolved and Modeled Reynolds Stresses.

The resolved Reynolds stresses provide insight into the share of the turbulence that is actually simulated. The modeled stresses indicate the level at which the turbulence or SGS model is involved in representing the turbulence that is not resolved by the numerical method. The two can be added and compared between solutions to give an idea of the total level of turbulence, and its sources.

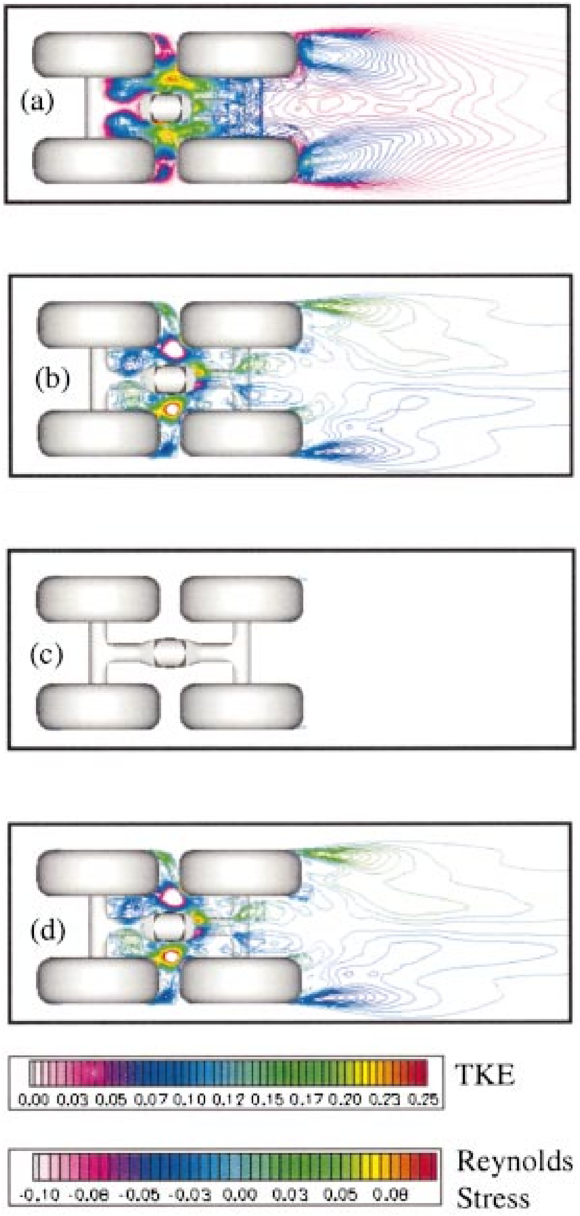

Fig. 10 Time averaged DES cut: (*a*) total kinetic energy, (*b*) resolved Reynolds stress, (*c*) modeled Reynolds stress, (*d*) total Reynolds stress

With DES it is normal for the modeled stresses to dominate in the boundary layers, and then vanish relative to the resolved stresses in the separated regions. It is more so with fine grids, just like in any LES, which makes grid refinement a positive tool to evaluate solutions. In a typical LES of turbulence that conforms to Kolmogorov’s theory, the modeled stress is proportional to the grid spacing, and this behavior was confirmed in a DES of homogeneous turbulence [5]. In those regions, the expectations from URANS are less clear, and the relative magnitudes of resolved and modeled stresses are both highly flow-dependent, and essentially grid-independent, which puts them out of the control of the user. Error estimates are much more difficult to produce.

The resolved $\overline{u'w'}$ Reynolds stress is shown in Fig. 10(*b*) for the Detached Eddy Simulation. Primes denote a fluctuation and

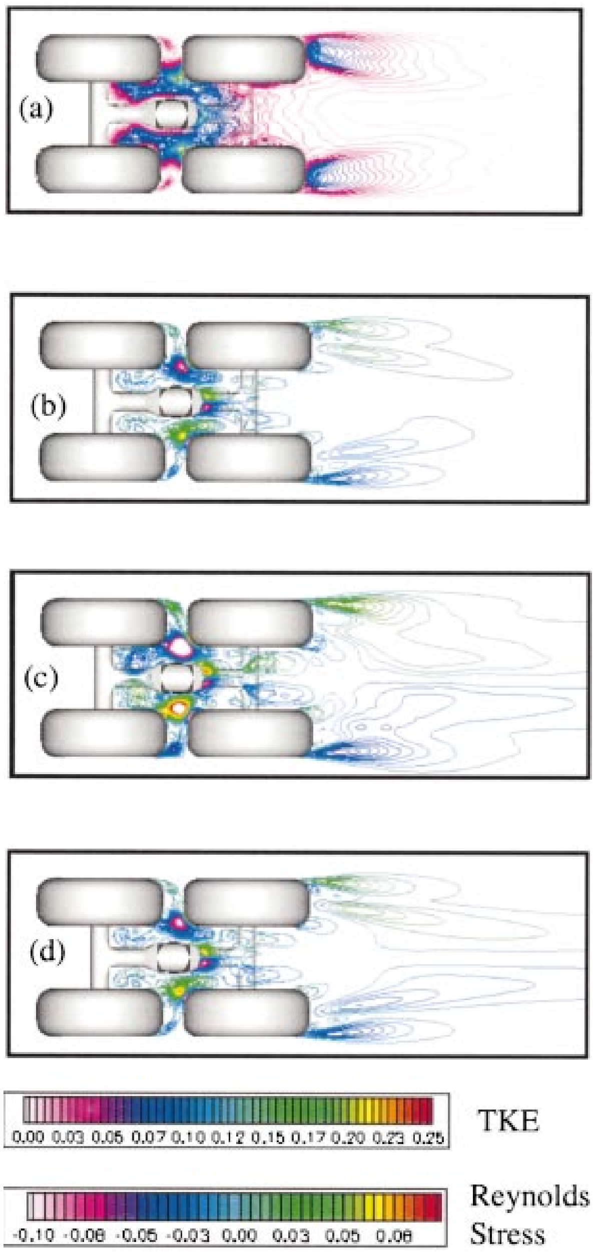

Fig. 11 Time averaged URANS cut: (*a*) total kinetic energy, (*b*) resolved Reynolds stress, (*c*) modeled Reynolds stress, (*d*) total Reynolds stress

the overline a time average. This is the dominant stress in shear layers aligned with the x and z directions, such as those coming off the wheel sides. The resolved stress is predominant between the front wheels and just downstream of the wheels. The Reynolds stress peaks at a value of about 0.13 in-between the wheels and at a value of 0.05 in the wake region (these peak values are confined to the planes displayed in the figures.)

The resolved $\overline{u'w'}$ Reynolds stress is shown in Fig. 11(*b*) for the URANS simulation. As in the DES, the resolved stress also predominates between the front wheels and behind the rear wheels. The Reynolds stress peaks at a value of about 0.07 in between the wheels, and 0.03 in the wake region; this represents about half of the $\overline{u'w'}$ Reynolds stress resolved by the DES.

The modeled $\overline{u'w'}$ Reynolds stress is given by:

$$\overline{-\nu_t\left(\frac{\partial u}{\partial z}+\frac{\partial w}{\partial x}\right)}.$$

Here ν_t is the eddy viscosity [16]. The modeled $\overline{u'w'}$ Reynolds stresses for the DES and URANS simulations are shown in Figs. 10(*c*) and 11(*c*), respectively. This stress does not register in the wheel boundary layers, because it is of the order of 0.003 and the contour-level interval is 0.005. Between the wheels, the modeled stress peaks at a value of 0.003 in DES, and a value of 0.013 in URANS. In the wake region, the modeled $\overline{u'w'}$ Reynolds stress peaks at a value of 0.001 in DES and 0.007 in URANS, which is consistent with the ratios of eddy viscosities presented above. The modeled stress is only about 2 percent of the resolved stress for the DES, but is about 20% of the resolved stress for the URANS simulation.

The sum of the resolved and the modeled $\overline{u'w'}$ Reynolds stress, or total stress, for the DES and URANS simulations are shown in Figs. 10(*d*) and 11(*d*). The total $\overline{u'w'}$ Reynolds stress indicates the level of mixing modeled by the numerical methods, and drives the mean flow. The total level is substantially less in URANS than in DES. The URANS simulation destroys resolved turbulence, without fully compensating for the loss by increasing the turbulent viscosity. This difference gives rise to differences in the mean flow-fields.

The Reynolds stresses were used to access more than just the turbulence characteristics. Initially, the Reynolds stresses offered a ‘‘sanity check’’ of the methods. For example, no sizable resolved or modeled stresses were found outside the wake region of the landing gear. The Reynolds stresses also provide a concrete evaluation of grid resolution in a DES. Any region outside the boundary layer in which the Reynolds stresses tend to be modeled, rather than resolved, would indicate that more grid points are required to accurately capture the unsteady flow field. In that sense, the relative magnitudes of the stresses here are satisfactory.

4.5 Force Spectra. The drag, lift, and side force on the model were collected over the entire simulation time. These unsteady forces give the first approximation to the ‘‘dipole’’ sound, in the low-frequency range. The power spectrum of these forces is shown in Fig. 12 for both simulations.

It was expected that a wide range of spatial scales would be represented by the DES and reflected in a broad spectrum, and that the URANS simulation would capture the amplitude of the larger spatial scales while missing the smaller spatial scales, giving a narrower spectrum. For a cylinder, the URANS spectrum reduces to a few spikes. It turned out that the URANS spectrum is broad for the landing gear, but with a tone. We attribute the breadth of the spectrum to the complexity of the shape, and the fairly tight surface curvature in places forcing ‘‘chaos’’ even on the URANS. We attribute the tone to shedding from the post, since the tone is at a frequency of 1.2 in side force, with the highest level, and a frequency of 2.4 in drag force. The nondimensional frequency 1.2 would be a low one in full scale: about 70 Hz. The corresponding Strouhal numbers based on post diameter are 0.3 and 0.6, respectively, therefore typical of a cylinder with turbulent boundary layers. The DES spectrum lacks the same peaks. Possibly this is because the DES has shedding all along the post, and the interference from the wheels destroys the two-dimensional coherence of the shedding by altering the local natural frequency.

The URANS calculation under-predicts the amplitude of the high frequencies by a significant amount, especially for drag, relative to DES. The DES spectrum is free of strong tones. Noise studies, in general, have indicated that no tones are expected from a clean landing gear truck [16]. In complete geometries, high-frequency tones may come from much smaller items such as brake lines.

The root-mean-square forces, shown in Table 2, echo what the spectra showed. The DES has larger fluctuations especially in the

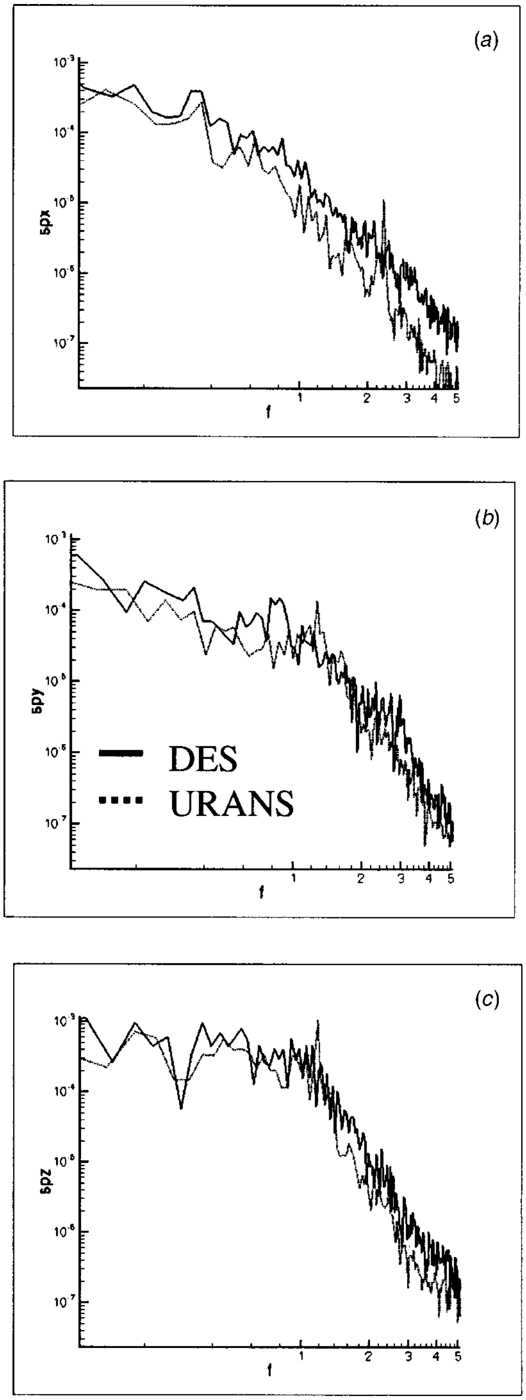

Fig. 12 Total landing gear force power spectrum

drag direction, which would radiate noise in the direction of flight. The rms of the time derivatives of the forces are 4 to 5 times larger than the rms forces, corresponding to non-dimensional dominant frequencies somewhat smaller than 1. The dipole noise at a distance r equals the rms of the time derivative, divided by $(4\pi c r)$ where c is the speed of sound. As a result, the dipole noise for the full-size airplane, at a typical distance of 150 m and typical speed of 150 kt, is about 91 dB, 94 dB and 100 dB in the streamwise, vertical and lateral directions respectively. These numbers exceed a rapid estimate from flight tests conducted with the gear up and then down, which is closer to 87 dB in the vertical direction. However these tests do not distinguish wheel noise from cavity and door noise or interference with the flaps, and our simulations do not include reflection by the wing's lower surface nor a full geometry. Taking the dipole noise from the unsteady forces on the solid may not be very accurate, and more work is in order to extract noise from these simulations.

Table 2 Landing gear RMS of drag, lift, and side force

	RMS Fx	RMS Fy	RMS Fz
DES	0.056	0.052	0.076
URANS	0.028	0.030	0.059

The force frequency spectra corroborate the instantaneous flow-fields discussed above where, on the whole, the scales of motion resolved by URANS both in space and time remain ambiguous [13]. Since the global forces average out much of the pressure fluctuations associated with small turbulent activity, the differences between the forces is weaker than might be expected.

5 Discussion

The turbulent flow around a much-simplified landing-gear truck was calculated using the methods of Detached-Eddy Simulation and the Unsteady Reynolds-Averaged Navier-Stokes Equations with the Spalart-Allmaras turbulence model. The simulations were compared to the test data of Lazos, and the flow fields investigated to determine their suitability for physics-based noise calculations.

Comparison to experiment shows that the simulations predict the pressure over the surface of the wheels with an accuracy that is reasonable considering the presence of multiple bluff bodies and separated regions. Flow features and surface pressure are in good agreement, while the agreement on drag is poor, especially for the aft wheel. Recent simulations of bluff bodies have led to better agreement than this. A repeat of the experiment would be desirable with both field measurements and force measurements with balances.

In the time-average, the DES and URANS-SA flow fields are similar, but DES performed consistently better than the URANS calculation. This conclusion cannot be generalized to include all URANS calculations. It is possible that the URANS solution would turn out better with models more sophisticated than Spalart-Allmaras, but that conjecture is far from being proven in recent literature to our knowledge. Many flow features were well captured only by DES. The two solutions were run on the same grid, and at an equal cost. In the DES, the resolved Reynolds stresses overwhelmed the modeled stresses everywhere except in the boundary layers. This is a measure of success and of sufficient grid density in the LES region, as it indicates that the empiricism contained in the model has very little influence.

The direction for deeper testing of the accuracy will be towards grid and time-step refinement. While we believe our grid is well balanced, there is no doubt that an improvement would be obtained by doubling the grid in all directions, in terms of resolving the smaller flows features. It is very hard to predict how great the improvement would be for global quantities such as drag, or even for the pressure on the wheels, which are large and smooth components. A factor of 16 increase in cost would be required to find out and is prohibitive with today's computing resources.

Unfortunately, without unsteady experimental data, we can not fully ascertain the accuracy of the unsteady simulation behavior. The DES seems more realistic. The force frequency spectra corroborate the instantaneous flow-field observations to some extent. The finite share of the Reynolds stress that is modeled in URANS also gives pause, as it gives the empiricism of the turbulence model a residual role that is difficult to estimate and highly case-dependent.

This is a first attempt at computing the complex flow field around a landing-gear geometry. We have intended to provide enough information in this paper and its references to allow others to address this flow and improve upon the results. High Reynolds number flows with massive separation will be considered routine

CFD tasks in the not so distant future, possibly in the DES framework. The landing gear runs, while manageable, required several months of computing. Improvements in computer power, largely through massive parallelization, have already demonstrated turn-around times on the order of a few weeks for the separated flow behind an F15 and F16 aircraft (J. Forsythe, personal communication, 2001). Turn-around times such as these will make DES realizable on a routine basis.

Acknowledgments

This work was performed under NASA Contract NAS1-97040, Task Assignment No. 13 of the Advanced Subsonic Technology (AST) program. The Fluid Mechanics and Acoustics Division of NASA Langley Research Center managed the task. Dr. Craig Streett was the technical monitor. NASA provided the CPU time. The Boeing Technology Research Center in Moscow supported the second author. We are most grateful to Drs. M. Strelets and M. Shur of the Russian Scientific Center ''Applied Chemistry'' for their ready assistance and fruitful discussions. The authors thank Dr. Bart Singer for his help and comments. Dr. Barry Lazos supplied the geometry and data files. Mr. R. Stoker provided flight-test findings. The reviewers made many helpful suggestions.

Nomenclature

DES = detached eddy simulation
LES = large eddy simulation
RANS = Reynolds averaged Navier Stokes
SRANS = steady Reynolds averaged Navier Stokes
URANS = unsteady Reynolds averaged Navier Stokes

References

[1] Manoha, X. E., Bruno, T., and Sagaut, P., 2000, ''Calculation of Basic Sound Radiation of Axisymmetric Jets by Direct Numerical Simulations,'' AIAA J., **38**(4), pp. 575–583.

[2] Singer, B. A., Lockard, D. P., and Brentner, K. S., 2000, ''Computational Aeroacoustic Analysis of Slat Trailing-Edge Flow,'' AIAA J., **38**(9), pp. 1558–1564.

[3] Avital, E. J., Sandham, N. D., Luo, K. H., and Musafir, R. E., 1999, ''Trailing-Edge Noise Prediction Using Large-Eddy Simulation and Acoustic Analogy,'' AIAA J., **37**(2), pp. 161–168.

[4] Spalart, P. R., 2000, ''Strategies for Turbulence Modelling and Simulations,'' Int. J. Heat Fluid Flow, **21**, pp. 252–263.

[5] Shur, M., Spalart, P. R., Strelets, and M., Travin, A., 1999, ''Detached-Eddy Simulation of an Airfoil at High Angle of Attack,'' Rodi, W., and Laurence, D. eds. 4th Int. Symp. Eng. Turb. Modelling and Measurements, pp. 669–678. May 24, Corsica, Elsevier, Amsterdam.

[6] Travin, A., Shur, M., Strelets, M., and Spalart, P. R., 2000, ''Detached-Eddy Simulations Past a Circular Cylinder,'' Int. J. Flow, Turbulence and Combustion, **63**(14), pp. 293–213.

[7] Constantinescu, G., and Squires, K. D., 2000, ''LES and DES Investigations of Turbulent Flow Over a Sphere,'' AIAA 2000-0540.

[8] Spalart, P. R., 2000, ''Trends in Turbulence Treatments,'' AIAA 2000-2306.

[9] Durbin, P. A., 1995, ''Separated Flow computations with the k-ε-v^2 Model,'' AIAA J., **33**(4), pp. 659–664.

[10] Shur, M. L., Spalart, P. R., Strelets, M. Kh., and Travin, A. K., 1996, ''Navier-Stokes Simulation of Shedding Turbulent Flow Past a Circular Cylinder and a Cylinder with a Backward Splitter Plate,'' G. A. Desideri, C. Hirsch, P. Le Tallec, M. Pandolfi, and J. Periaux, eds, Third ECCOMAS CFD Conference, Paris, Sept., Wiley, Chichester, pp. 676–682.

[11] Lazos, B. S., 2001, ''Mean flow features around the inline wheels of a 4-wheel landing gear,'' AIAA J., **40**(2), pp. 193–198.

[12] Strelets, M., 2001, ''Detached Eddy Simulation of Massively Separated Flows,'' AIAA 2001-0879.

[13] Spalart, P. R., Jou, W.-H., Strelets, M., and Allmaras, S. R., 1997, ''Comments on the feasibility of LES for wings, and on a hybrid RANS/LES approach,'' 1st AFOSR Int. Conf. On DNS/LES, Aug. 4–8, Ruston, LA. In advances in DNS/LES, C. Liu & Z. Liu Eds, Greyden Press, Columbus, OH.

[14] Spalart, P. R., and Allmaras, S. R., 1994, ''A One-Equation Turbulence Model for Aerodynamic Flows,'' La Rech. Aérospatiale, **1**, pp. 5–21.

[15] Rogers, S. E., and Kwak, D., 1990, ''An Upwind Differencing Scheme for the time-accurate incompressible Navier-Stokes Equations,'' AIAA J., **28**(2), pp. 253–262.

[16] Guo, Y., 2001, ''A Statistical Model for Landing Gear Noise Prediction,'' NASA Contract Informal Report, Contract NAS1-97040, Task 2.

Shin Hyung Rhee
Mem. ASME
Postdoctoral Associate;
currently CFD Engineer,
Fluent Inc.,
Lebanon, NH 03766

Fred Stern[1]
Fellow ASME
Professor Mechanical Engineering,
Iowa Institute of Hydraulic Research,
The University of Iowa,
Iowa City, IA 52246
e-mail: frederick-stern@uiowa.edu

RANS Model for Spilling Breaking Waves

A RANS model for spilling breaking waves is developed, which can be implemented with ship hydrodynamics RANS CFD codes. The model is based on the Cointe & Tulin theory of steady breakers. The breaker cross section is assumed triangular with maximum height determined by the theoretical/experimental linear relationship with following wave height. Pressure and velocity boundary conditions are imposed on the dividing streamline between the breaker and underlying flow based on the hydrostatic and mixing layer models. An iterative solution procedure provides a unique solution for specified breaking criteria and simulation conditions. The model is implemented using CFDSHIP-IOWA and validated using spilling breaking wave benchmark data for two-dimensional submerged hydrofoils. As with other current RANS codes, wave elevations are under-predicted. However, for the first time in literature, the breaking wave wake is predicted. Results for total head, mean velocities, and Reynolds stresses are in agreement with available spilling breaking wave benchmark data. [DOI: 10.1115/1.1467078]

1 Introduction

Effects of breaking waves are important in ocean and marine engineering. The processes for initiation of breaking, breaking, and interactions with surroundings are very complex. Many factors affect the initiation of breaking such as wave height and length, vertical pressure gradient, surface tension (especially at laboratory scale), surface shear, and side disturbances. Breaking is three-dimensional (3D) and classified as quasi-steady or unsteady (in a coordinate system moving with the wave) depending on type of breaking, i.e., spilling or plunging, respectively. The physics of spilling and plunging breaking waves are very different, as are their faces. The faces of spilling breaking waves exhibit foam separation regions, whereas the faces of plunging breaking waves exhibit jets. Breaking waves strongly interact with their surroundings, including generation and transport (convection/diffusion/dissipation) of trailing wake, air bubbles, turbulence, and vorticity, modification of breaking and trailing wave heights, other wave systems, bodies (ships and ocean structures) and their boundary layers and wakes, or coastal topography. In addition to Froude number, many factors affect scaling such as surface tension, surfactants, and water quality.

Of interest here is ship hydrodynamics. Important effects include increases in resistance, capsizing, noise production, and signatures [1–3]. The objective is to develop a Reynolds-averaged Navier-Stokes (RANS) model for spilling breaking waves, which can be implemented with ship hydrodynamics RANS CFD codes. The model is based on the Cointe and Tulin [4] (henceforth C&T) theory of steady breakers. The approach can be extended to practical ship flows, but is herein presented and validated for two dimensions (2D) using available spilling breaking wave benchmark data for submerged hydrofoils [5,6].

The paper is organized as follows. Section 2 provides an overview of C&T theory of steady breakers and a review of relevant studies. Some new experimental studies are mentioned, but mostly computational approaches for simulating breaking waves are discussed. Section 3 describes the formulation and iterative solution procedure for the RANS model for spilling breaking waves based on C&T theory. Section 4 describes implementation for 2D submerged hydrofoils using the CFDSHIP-IOWA RANS CFD code. Section 5 presents the simulation conditions, grids, and results, including comparisons with spilling breaking wave benchmark data for wave elevations, total head, mean velocities, turbulence fluctuations, and Reynolds stresses. Lastly, Section 6 mentions concluding remarks with regard to future work, including extensions for practical applications.

2 Related Work

Cointe & Tulin Theory of Steady Breakers. C&T reported an analysis of the steady breaker above a submerged hydrofoil, where experimental data existed [5], and for which they obtained some predictions of breaking and breaker characteristics. Their breaker model consists of an essentially stagnant eddy riding on the forward face of the leading wave in the wave train behind the hydrofoil and held in place by shear stresses acting along the dividing streamline. The breaker eddy contains air entrained at breaking, and the degree of aeration is a parameter of the problem. They applied an idealization of the classical turbulent mixing layer at the onset point of breaker along the dividing streamline and used the velocity reduction at the toe as a parameter of the problem. The model was quantified utilizing independent measurements of the turbulent stresses. They also found that the hydrostatic pressure acting on the dividing streamline underneath the eddy creates a trailing wave, and this trailing wave largely cancels the trailing wave that would exist in the absence of breaking. These findings lead them to the argument that the wave resistance of the hydrofoil manifests itself in the momentum flux of the residual trailing wave plus the breaking resistance, i.e., the momentum flux in trailing wake. C&T demonstrated their theory using linear potential flow method with the surface pressure distribution along the dividing streamline prescribed as the breaker weight.

The simplicity of the theory and the validation shown suggested the authors to consider implementation of the model in RANS CFD codes, which can easily handle mixing layer and hydrostatic pressure on the boundaries.

Experimental Studies. Among the many researches for the deep water surface wave breaking, Duncan [7] is the first documentation of detailed information about 2D spilling breaking waves generated by a submerged hydrofoil, where a NACA0012 foil was towed in a small towing tank at various speeds, angles of attack, and depths of submergence. Duncan [5] later extended his experimental program and showed the relationship between the spilling breaker's geometric parameters and wave dimensions. He observed recirculating aerated water in the breaker, which gives

---

[1] Corresponding author.

Contributed by the Fluids Engineering Division for publication in the JOURNAL OF FLUIDS ENGINEERING. Manuscript received by the Fluids Engineering Division March 28, 2001; revised manuscript received January 3, 2002. Associate Editor: I. Celik

the name eddy-breaker model, and a turbulent wake behind it. He also demonstrated that shear stresses between the breaker and underlying wave produce the trailing turbulent wake and sustain the spilling breaker on the front wave face. Duncan's [5] eddy-breaker model served as a base of C&T theory and eventually of the present model.

Based on experiments similar to Duncan's [5], but with different set-up and conditions, Mori [6] presented velocity and turbulence quantities in the trailing wake for various conditions. He also derived a critical condition for sub-breaking using an instability analysis; for a constant curvature wave, the sub-breaking takes place when the circumferential force is greater than the gravity acceleration, i.e., the pressure gradient in the vertical direction plays a critical role in breaking. He noted that, however, the sub-breaking waves are different from plunging or spilling breaking waves to some extent, since the flows have wrinkle-like waves with turbulence fluctuations and do not have overturning or backward flows.

Battjes and Sakai [8] carried out similar experiments to Duncan's [5], but with different foil geometry, a NACA6024. They measured velocity and turbulence quantities and showed that the trailing wake of a spilling breaker has characteristics similar to that of self-similar mixing layer, which is in accord with C&T theory. However, their wave elevation measurement suggested that it was a hydraulic jump flow after the breaker rather than following waves.

More recent experiments and analysis have focused on the initial breaking process [9–13], surface shape and instantaneous and mean flow field [14], velocity, acceleration, and vorticity [15], radar backscatter for surface roughness [16], and aerated density ratio [17].

Computational Studies. A fair number of studies have been conducted using a wide range of modeling, numerical methods, and applications.

Non-linear potential flow boundary integral methods show good agreement with breaker wave height data using prescribed pressure distributions with represented effects of breaking as done previously by C&T [18,19]. Also, the boundary element methods following Longuet-Higgins and Cokelet [20] could explain the plunging wave breaker. However, it is difficult to explain the wave motion after the initial breaking, which is only the beginning of non-linear breaking wave motion. The Euler equation was solved to simulate the wave profile and velocity vectors of plunging breaking waves in a 2D wave tank [21] and the so-called Smoothed Particle Hydrodynamics (SPH) method with slender body potential flow theory was applied for breaking bow waves around ship hulls [3]; however, the viscous shear and turbulent fluctuations are not taken into account.

Recently, the Navier-Stokes (NS) equations have been solved to simulate breaking waves, where both surface tracking and capturing methods are employed for free-surface solution. For spilling breaking waves, both methods, i.e., tracking and capturing, can be applied, since the free-surface elevation is single valued and surface conforming grids can be regenerated. The physics of primary interest in spilling breaking waves is the initiation of breaking, change of trailing wave form, and the mean and turbulent flow structure in the trailing wake; thereby steady flow formulation of the mathematical equations can be employed [22,23]. For plunging breaking waves, general surface tracking methods cannot be applied. Instead, surface capturing methods, e.g., marker-and-cell (MAC), volume of fluids (VOF), and level set function, have shown promising results for breaking waves in surf zone and hydraulic jump [24–26], in deep water [13,27,28], and around a ship's blunt bow [29]. The physics of primary interest in plunging breaking waves is unsteady development of plunging jets, i.e., deformation, initiation, overturning, merging, air entrainment, and splash-up; thereby unsteady flow formulation should be employed.

For simulations of turbulent flows, although only few studies have considered the effects, several turbulence models, e.g., simple algebraic Reynolds stress model [22], standard [23,27,28] or modified k-ε models [24,25], were used. Effects of free surface on turbulence, which are known to be important as shown for open channel flows [30], submerged jets [31], solid/free surface juncture boundary layer and wake [32], and ocean surface layer [33,34], have yet to be investigated.

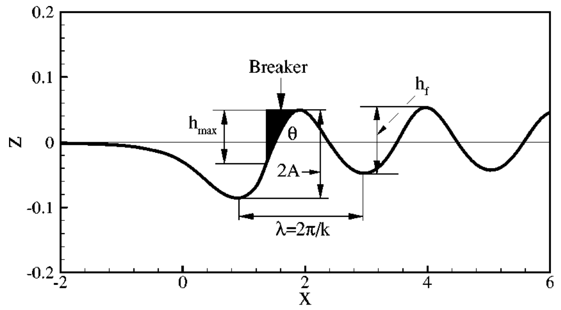

Enlarged view

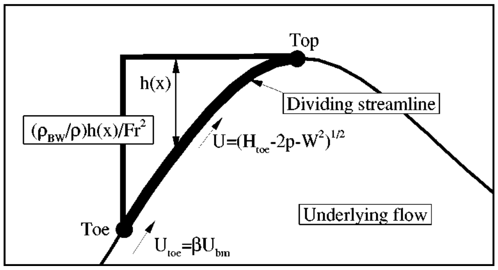

Fig. 1 RANS model for spilling breaking waves

Despite the research described above and also reviewed by Banner and Peregrine [35] and Melville [36], which has explicated various phenomena related to breaking waves, none has yet successfully been applied to spilling breaking waves over a 2D submerged hydrofoil, including prediction of breaker height, following wave height and length, surface shear under the breaker, and trailing wake.

3 RANS Model for Spilling Breaking Waves

Consider a spilling breaking wave using a coordinate system moving with the wave, as shown in Fig. 1. The flow is assumed 2D or a cross section in a 3D strip theory. Present approach is to modify the dynamic free surface boundary condition using C&T theory of steady breakers and an iterative solution procedure. The approach can be implemented with ship hydrodynamics RANS CFD codes using either surface tracking or capturing methods; however, present implementation is for the former.

The breaker shape is assumed triangular with maximum height, $h_{\max}$, determined by the theoretical/experimental linear relationship [4] with following wave height, h_f,

$$h_{\max}=(h_f-\mathrm{Fr}^2)/B \tag{1}$$

where all length scales are nondimensionalized by hydrofoil chord length L, Froude number, $\mathrm{Fr}=U_0/\sqrt{gL}$, is defined by L and characteristic velocity, U_0, and $B\approx-2$ as per C&T's equation (5) with $\beta^2\approx0.5$. The triangular shape of a spilling breaker was shown to be justifiable by Sadovnikov and Trincas [19], in which they demonstrated that the ratio of the triangle area to the experimental breaker area is close to that for all of Duncan's [7] cases. With estimated $h_{\max}$, the location of the breaker toe can be determined assuming that the breaker top is flat and coincides with the wave crest, and the dividing streamline between the breaker and underlying flow is located along the free-surface between the toe and the top.

The pressure distribution along the dividing streamline is specified according to the hydrostatic model

$$p_{toe \leqslant (x,y,z) \leqslant top} = \frac{\zeta + (\rho_{BW}/\rho) h(x)}{\mathrm{Fr}^2} \tag{2}$$

where p $(= p_{\text{static}} + \rho g z)$ is the piezometric pressure normalized by ρU_0^2, ζ is the wave elevation, ρ_{BW}/ρ is the density ratio of aerated breaker to water, and $h(x)$ the breaker height at distance x from the toe. ρ_{BW}/ρ is given, assuming the ideal case of concentrated shear stresses on the breaker surface, between approximately 0.2 for incipient breaking and 0.5 for strong breaking [4].

The streamwise velocity distribution along the dividing streamline is specified according to the mixing layer model. The velocity jump is applied at the toe

$$U_{toe} = \beta U_{bm} \tag{3}$$

where all velocity scales are normalized by U_0, β is the velocity reduction at the toe, and U_{bm} is the streamwise velocity component just upstream of the toe. The value of β is between 0.5 (corresponding to Tollmien's ideal mixing) and 0.7 (based on $\beta^2 \approx 0.5$ in C&T). The steeper the wave is, the smaller β is, i.e., the larger velocity reduction at the toe. Beyond the toe along the dividing streamline the streamwise velocity is specified under the assumption of constant total head

$$U_{toe < (x,y,z) \leqslant top} = \sqrt{H_{toe} - (2p + W^2)} \tag{4}$$

where $H_{toe} = (2p + U^2 + W^2)_{toe}$.

Equations (1)–(4) are readily implemented in ship hydrodynamics RANS CFD codes by modifications of free surface boundary conditions. An iterative solution procedure provides a unique solution for specified breaking criteria and simulation conditions. Starting with the nonbreaking solution, h_f determines $h_{\max}$ according to Eq. (1). A new solution is obtained with the dynamic free surface boundary conditions along the dividing streamline updated according to Eqs. (2)–(4) thereby providing an updated value of h_f. Convergence is achieved when Eqs. (1)–(4) are unchanged.

Implementation of the C&T theory for steady breakers requires breaking criteria, which are not known. For breaking waves over a 2D submerged hydrofoil, correlations have been made with wave steepness $Ak \geqslant 0.31$ [37], forward face slope $\theta \geqslant 17$ deg [5], wave resistance [4,5], and wave vertical pressure gradient [6]. For breaking waves in surf zone, Nadaoka et al. [38] made correlations with wave vertical pressure gradient. At laboratory scale, surface tension is also influential, as shown by Duncan et al. [9], Longuet-Higgins [10], and Lin and Rockwell [11]. Other influences include surface shear [5] and side disturbances [37]. The present results were obtained using simple breaking criteria based on θ or Ak, i.e., breaking was specified for $\theta \geqslant 15$ deg or Ak $\geqslant 0.25$ (see Fig. 1 for definitions). Appropriate values for ρ_{BW}/ρ and β can be set by comparing computed θ and Ak and θ_{crit} and Ak_{crit}, respectively, as discussed in Section 5.

4 Implementation for Two-Dimensional Submerged Hydrofoils

The spilling breaking wave model is implemented using a ship hydrodynamics RANS CFD code with application for 2D submerged hydrofoils. Following describes the RANS CFD code and implementation of spilling breaking wave model.

The unsteady RANS CFD code CFDSHIP-IOWA was used, which was developed at Iowa Institute of Hydraulics Research (IIHR) for ship hydrodynamics applications, especially surface ships and marine propulsors [39–41]. The code was developed for both internal research and external use through transition to universities, governmental laboratories, and industry in support of naval science and technology for general purposes in both research and design [42]. The code was among the better codes for the naval combatant model ship test case at the recent Gothenburg 2000 Workshop on Numerical Ship Hydrodynamics [43].

The code solves the incompressible unsteady RANS and continuity equations in either inertial or non-inertial and Cartesian or cylindrical coordinates. The isotropic eddy viscosity, blended k-ω/k-ε turbulence model [44] is used. A free-surface tracking method is used with non-linear kinematic and approximate dynamic free-surface boundary conditions. The k-ω turbulence model and tracking methods (including the present code as already mentioned) performed well at the Gothenburg 2000 Workshop, although best results were for Reynolds stress turbulence models for the tanker model ship test case and level set methods did well for the container model ship test case. A body force method is used for propulsor modeling. The governing equations are transformed into nonorthogonal curvilinear coordinates using a partial transformation. Second order finite differences are used for both temporal and spatial discretization. The overall solution algorithm follows PISO with pressure Poisson equation derived from the continuity equation. Code and data structures are designed for scalable, parallel, multi-block implementation and ease of second party model subroutine development. General block structures are allowed, including patched, overlaid, and Chimera grids with higher order block interface communication. Message passing interface (MPI) and single program multiple data (SPMD) are used for high performance computing (HPC). Portability is achieved through MPI, the C preprocessor CPP, and the UNIX make utility. A user interface is available in GRIDGEN through a DHTML wizard for setting boundary conditions and run-time parameters. Following provides governing equations and boundary conditions used in the present study in conjunction with discussion of implementation of spilling breaking wave model.

The governing equations are the continuity and RANS equations for viscous incompressible flow, which are written in nondimensional form and using tensor notation

$$\frac{\partial U_i}{\partial x^i} = 0 \tag{5}$$

$$\frac{\partial U_i}{\partial t} + U_j \frac{\partial U_i}{\partial x^j} + \frac{\partial p}{\partial x^i} - \frac{1}{\mathrm{Re}} \nabla^2 U_i - \frac{\partial}{\partial x^j}(-\overline{u_i u_j}) = 0 \tag{6}$$

where $\nabla^2 = \partial^2/\partial x^j \partial x^j$, $U_i = (U,V,W)$ are the Cartesian components of velocity normalized by U_0, and $x^i = (x,y,z)$ are the nondimensional Cartesian coordinates normalized by L, and Reynolds number, $\mathrm{Re} = U_0 L/\nu$, is defined in terms of L, U_0, and kinematic viscosity ν.

The solution domain is shown in Fig. 2 along with the boundary definitions. A two-block, patched-grid topography is used, which conforms both to the body and free-surface, i.e., the upper block comprises the domain above the hydrofoil and free-surface boundary, and the lower block comprises the domain below the hydrofoil and tank-bottom boundary. Although the model problem is 2D, a 3D domain is employed with y (and η in computational domain) as an extra coordinate, since CFDSHIP-IOWA is a 3D code. In order to minimize numerical dissipation, uniform grid spacing is applied in x-direction after 0.5L from the hydrofoil trailing edge.

The boundary conditions are described next with reference to Fig. 2. On the inlet plane S_i, U, V, W, and p are specified as uniform stream and k and ω are specified for zero turbulence. On the body surface S_b, the no-slip condition is imposed. On the symmetry planes S_{sym}, $\partial(U,W,p)/\partial y = V = 0$. On the exit plane S_e, $\partial^2(U,V,W,p)/\partial x^2 = 0$. On the patched boundary S_p, matching condition is imposed. On the tank-bottom boundary S_o, $U = 1$, $V = W = \partial p/\partial n = 0$. On the free-surface S_ζ, the kinematic and dynamic conditions are imposed using a surface tracking approach. The kinematic (stream surface) condition is imposed through solution of the non-linear hyperbolic partial differential equation for ζ using second-order temporal and spatial finite dif-

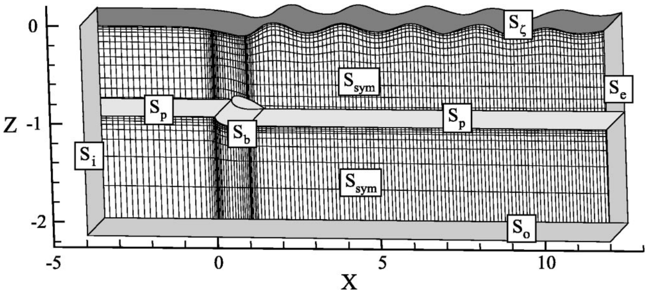

Fig. 2 Solution domain and grid for 2D submerged hydrofoil. (y- and z-coordinates are 10 and 3 times magnified, respectively. Every other grid points are shown.)

ferences along with a simple linear extrapolation contact-line model and variable-order high-pass filter to remove spurious oscillations. The dynamic (continuous stress) condition is imposed under the assumptions of small free surface curvature and gradients of the vertical velocity component, which results in a zero vertical gradient condition for the velocity components and the piezometric pressure boundary condition

$$p=\zeta/\mathrm{Fr}^2 \tag{7}$$

The spilling breaking wave model is implemented through changes to the dynamic free surface boundary condition and the change eventually has an impact on the free surface wave shapes. The zero vertical gradient condition for U is replaced by Eqs. (3) and (4) and the pressure boundary condition (7) is replaced by Eq. (2). The simulations are started with an initial condition of a uniform stream with a flat free surface. Once the solutions for velocity, pressure, and free-surface elevation are converged and the criteria for breaking are met, the spilling breaking wave model is applied and additional iterations are conducted until convergence is obtained.

Only limited verification and validation was done. Verification studies were conducted for iterative and grid convergence; however, quantitative estimates were not made, which is partially justified based on present focus being presentation/demonstration of RANS model for spilling breaking waves and fact that experimental data are also limited and without uncertainty analysis. 200,000 and 10,000 iterations were required for converged solutions before and after the model was applied, respectively. The number of iterations for before model condition is considerably larger than authors' previous experience with free-surface wave development around surface-piercing bodies. However, others have also reported large number of iteration for this type of problem, e.g., Hino [45] reported over 200,000 time steps were needed to get converged solutions. Note that for surface-piercing bodies the free surface is strongly affected by the presence of the body, whereas for submerged bodies it takes a number of iterations for the initially flat free surface to be affected and fully developed by the dynamic pressure variation around the submerged hydrofoil. Several grid sensitivity studies were carried out for one of the cases: the number of grid points in z-direction was doubled while maintaining the first grid spacing off the hydrofoil; the domain extent in the x-direction was doubled while maintaining the grid spacing in the x-direction; and the domain was partitioned with four- and eight blocks. Owing to the slow iterative convergence discussed above, the number of grid points used for grid sensitivity studies were limited. The results were however relatively insensitive to the grid and the solution changes based on wave elevation were less than 6%, which provided evidence that the solutions are not grid sensitive in the range of grids considered. The authors are well aware of the importance of verification and validation and more rigorous studies are recommended for future work.

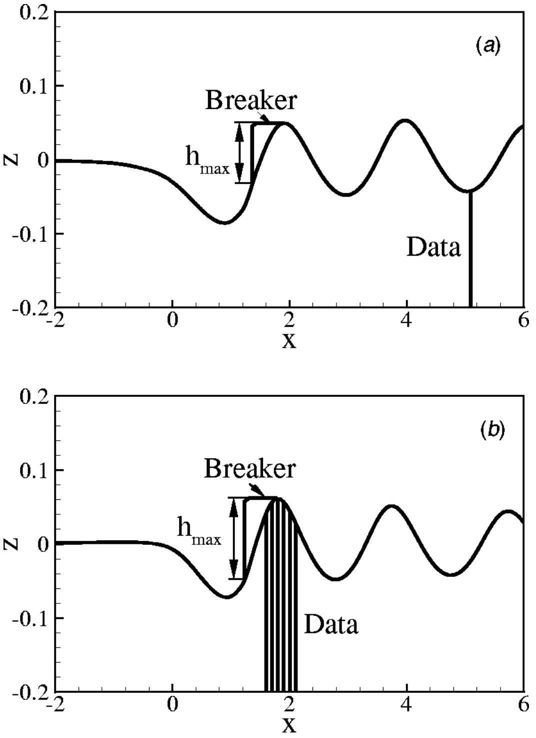

Fig. 3 RANS model spilling breaking wave solutions and experimental data locations: (*a*) Second trough after the breaker for Duncan's [5] case: (*b*) 0.2*L* and 0.1*L* before; on and; 0.1*L*, 0.2*L*, and 0.3*L* after breaker top for Mori's [6] case.

5 Comparison Benchmark Experimental Data

A wide range of conditions corresponding to available spilling breaking wave benchmark data for 2D submerged hydrofoils were considered for evaluation of breaking criteria and prediction of wave elevation, total head, mean velocities, and turbulence quantities. Simulations were performed without the spilling breaking wave model for conditions corresponding to: (1) Battjes and Sakai [8] with a NACA 6024 hydrofoil at angle of attack $\alpha=15$ deg and depth of submergence, Fr, and Re $(d/L,\mathrm{Fr},\mathrm{Re})=(1.05,0.711,2.16\times10^5)$; (2) Duncan [5] with a NACA 0012 hydrofoil at $\alpha=5$ deg and $(d/L,\mathrm{Fr},\mathrm{Re})=(1.29,0.567,1.42\times10^5)$ and $(0.925,0.567,1.42\times10^5)$, and (3) Mori [6] with a NACA 0012

Table 1 Computed θ and Ak, and comparison with breaking criteria

$\theta_{crit}=15$ deg $Ak_{crit}=0.25$	Duncan [5] NACA0012 $\alpha=5$ deg, $d/L=0.925$ Fr=0.567	Battjes and Sakai [8] NACA6024 $\alpha=15$ deg, $d/L=1.050$ Fr=0.771	Mori [6] NACA0012 $\alpha=2$ deg, $d/L=0.633$ Fr=0.441	Mori [6] NACA0012 $\alpha=2$ deg, $d/L=0.633$ Fr=0.606	Mori [6] NACA0012 $\alpha=2$ deg, $d/L=0.700$ Fr=0.551	Mori [6] NACA0012 $\alpha=2$ deg, $d/L=0.700$ Fr=0.571
θ	15 deg	57 deg	17 deg	18 deg	16 deg	18 deg
Ak	0.23	0.76	0.22	0.27	0.24	0.25

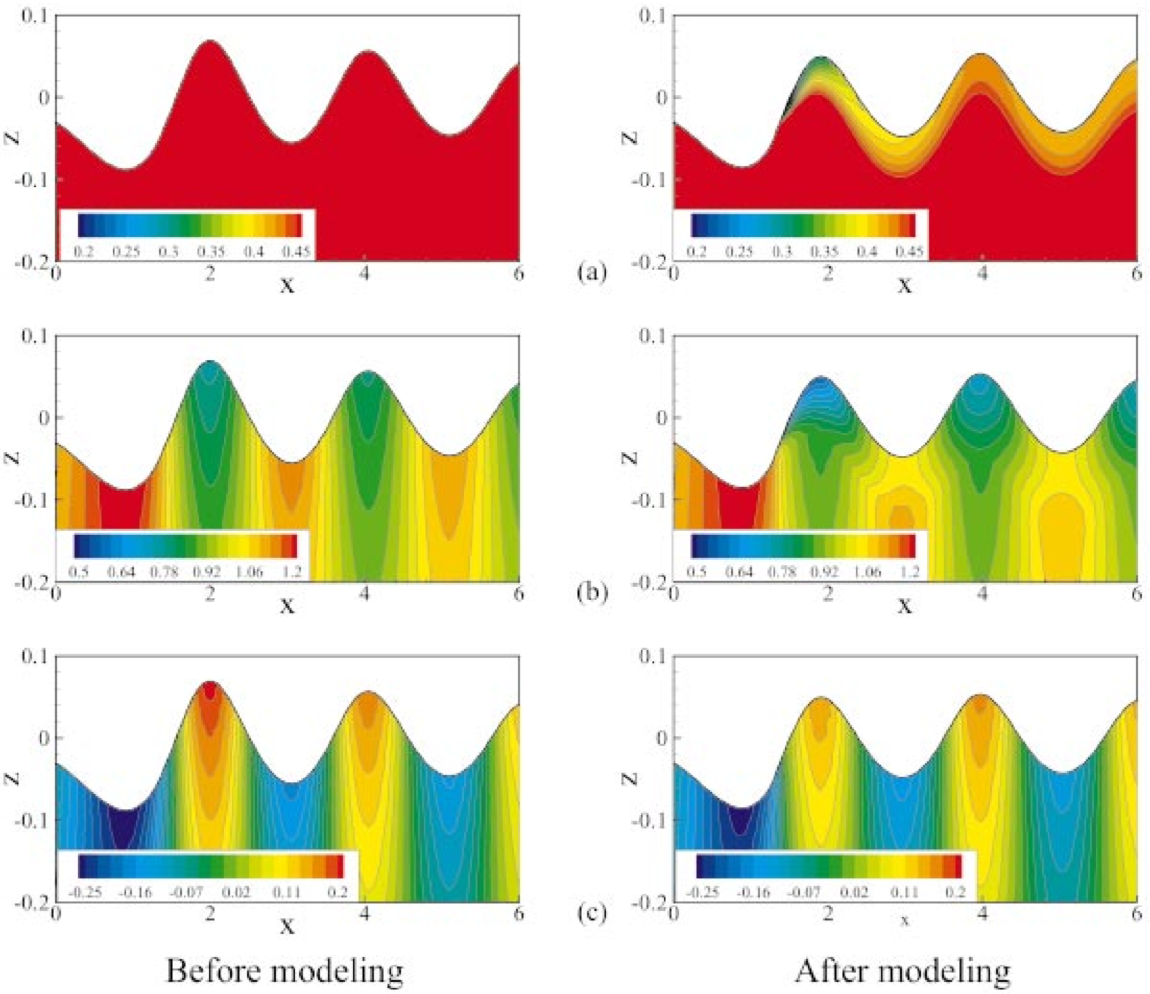

Fig. 4 Contours of total head, streamwise velocity, pressure, eddy viscosity, turbulence fluctuations, and Reynolds stress for Duncan's [5] breaking case $(d/L,\text{Fr},\text{Re})=(0.925,0.567,1.42\times10^5)$: (*a*) Total head; (*b*) streamwise velocity; (*c*) pressure; (*d*) eddy viscosity; (*e*) turbulence fluctuations: $\sqrt{u'^2}$ $(=\sqrt{w'^2})$; (*f*) Reynolds stress: $u'w'$

hydrofoil at $\alpha=2$ deg and $(d/L,\text{Fr},\text{Re})=(0.633,0.441,1.98\times10^5)$, $(0.633,0.606,2.72\times10^5)$, $(0.7,0.551,2.48\times10^5)$, and $(0.7,0.571,2.57\times10^5)$. Simulations were also performed with the spilling breaking model applied for the conditions underlined. Figure 3 shows RANS model spilling breaking wave solutions and data locations for the experiments of Duncan [5] and Mori [6]. Note that facilities and conditions were different for each of the experiments: (1) flume for hydraulic jump conditions; (2) small towing tank for non-breaking, incipient, and breaking; and (3) circulating water channel for incipient breaking. For (1), comparisons were made with data for U, turbulence fluctuation in streamwise direction, $\sqrt{u'^2}$, and Reynolds stress, $u'w'$. Data indicate, however, a hydraulic jump condition, i.e., small following waves and large penetration depth of breaking. Present model converges and predicts small following waves, but not hydraulic jump, which is beyond parameter range and possibly applicability of the present model; therefore, (1) is not considered further. For (2), comparisons are made with data for ζ, U, and $H_d=H_{am}-H_{bm}$, where $H=2p+U^2+W^2$ and H_{am} and H_{bm} are H after and before applying the model, respectively. For (3), comparisons are made with data U, W, $\sqrt{u'^2}$, turbulence fluctuation in depthwise direction, $\sqrt{w'^2}$, and $u'w'$.

The physical domain for (2) is shown in Fig. 2, which is a box with extent $-4\leqslant x\leqslant12$, $0\leqslant y\leqslant1$, and $-2.15\leqslant z\leqslant\zeta$. The numbers of grid points are $316\times5\times51=80{,}580$ and $316\times5\times31=48{,}980$ in the upper and lower blocks, respectively, and 129,560 in total. The x-direction grid spacing at the leading and trailing edge, $\Delta x_{LE/TE}$, is 2.45×10^{-3}, and z-direction grid spacing at the foil surface, Δz_1, and at the free-surface, Δz_{FS}, are 1.0×10^{-4} and 1.0×10^{-2}, respectively. Note that at least five points in y-direction are needed, although it is an extra coordinate, owing to the five-point stencil required for CFDSHIP-IOWA. The physical domain for (3) is the same as Duncan's in x- and y-directions, but different in z-direction such that $-3.00\leqslant z\leqslant\zeta$. The numbers of grid points are $316\times5\times46=72{,}680$ and $316\times5\times46=72{,}680$ in the upper and lower blocks, respectively, and 145,360 in total. $\Delta x_{LE/TE}$, Δz_1 and Δz_{FS} are the same as Duncan's case grid. The grids are generated elliptically using GRIDGEN software.

To confirm the validity of breaking criteria, computations were done without the RANS model for various breaking wave conditions of Battjes and Sakai [8], Duncan [5], and Mori [6]. Table 1 presents computed θ and Ak resulted from various conditions that accompany wave breaking. The breaking wave criteria for the present study are shown in the top left corner of the table. Although Ak's are less than Ak_{crit} (=0.25) in some cases, it shows

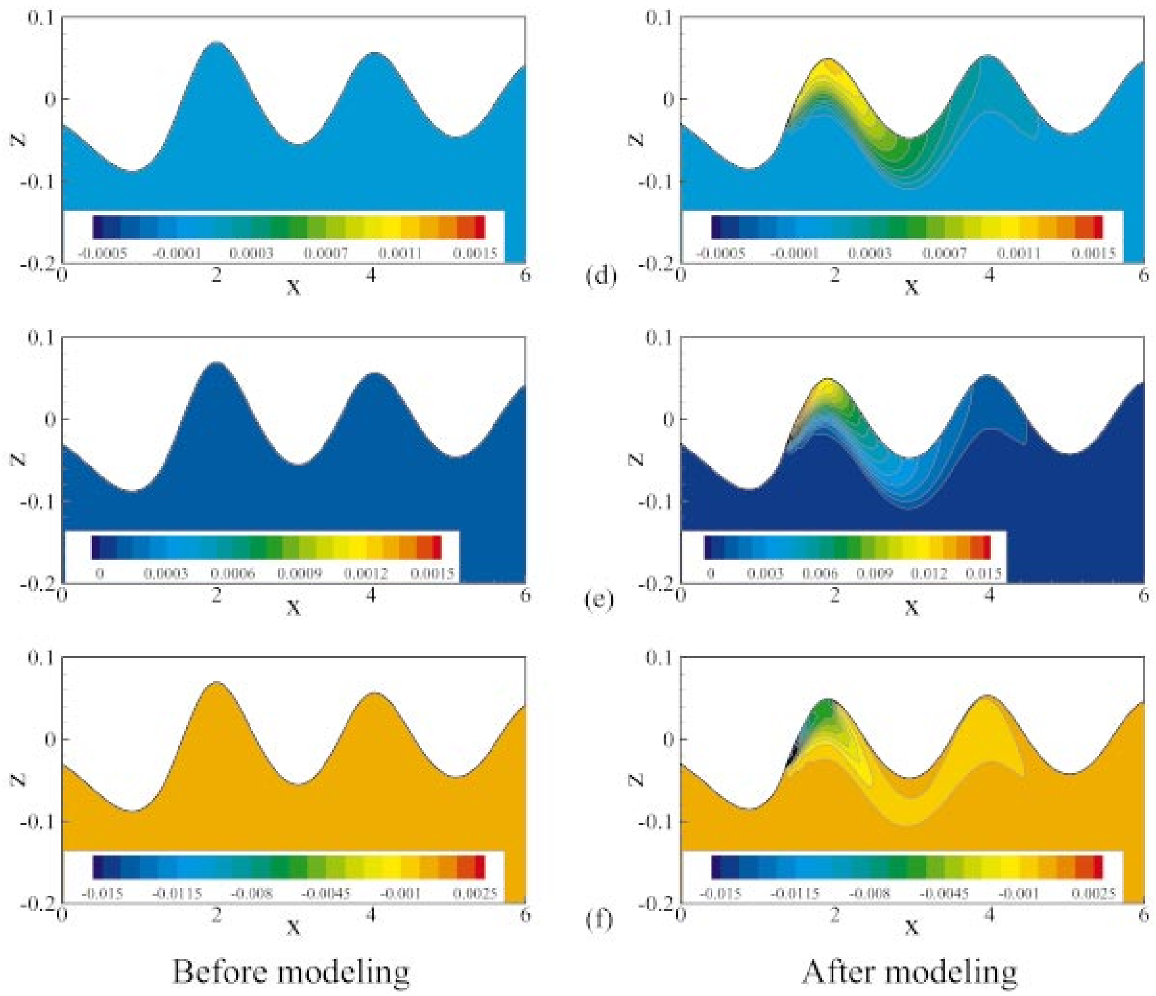

Fig. 4 (**continued**)

that the criteria, i.e., $\theta \geqslant 15$ deg or $Ak \geqslant 0.25$, can predict wave breaking without preliminary knowledge of occurrence of breaking.

Now that the solutions without modeling are obtained, the RANS model is applied to the solutions following the procedure described in Section 3. First, Duncan's [5] breaking wave case, i.e., a NACA 0012 hydrofoil at $\alpha = 5$ deg and $(d/L, \mathrm{Fr}, \mathrm{Re}) = (0.925, 0.567, 1.42 \times 10^5)$, is considered. Since it is rather a mild breaking, the values of ρ_{BW}/ρ $(=0.25)$ and β $(=0.625)$ are chosen to be close to that for incipient breaking condition.

Figure 4 shows contours of total head, H, U, p, eddy viscosity, ν_t, $\sqrt{u'^2}$, $\sqrt{w'^2}$, and $u'w'$ before and after the RANS modeling. The contours of H and U clearly show the defect in the trailing wake, while p does not seem to be affected much. This is expected from the fact that hydrostatic pressure due to the aerated breaker weight is small compared to the pressure that is large enough to generate free-surface waves. The contours of ν_t, $\sqrt{u'^2}$, $\sqrt{w'^2}$, and $u'w'$ show the turbulence generation at the breaker surface and dissipation in the trailing wake, as Duncan [5] and Mori [6] observed in their experiments.

Figure 5 shows the computational results before and after the RANS modeling and comparison with Duncan [5] for ζ, U, and H_d. The profile of ζ shows the effects of breaking in following waves, which are repressed, approximately 5%, wave elevation and shorter, approximately 10%, wavelength. Both these trends are quantitatively predicted and confirm the C&T theory (Fig. 9 in their paper [4]) and measurements by Duncan [5]. However, the breaking wave amplitude is significantly under-predicted and a phase error is evident. Note that this is a spontaneous breaking condition and nonbreaking wave profile measurement data are not available. The defects in U and H_d show good agreement with Duncan [5] in the correct manner both qualitatively and quantitatively, indicating that the present RANS model can properly predict the mean flow defect in the trailing wake relatively far from the breaker, i.e., approximately $3L$ downstream of the breaker top.

The under-predicted breaking wave amplitude, which is widely seen in RANS simulations, can be attributed to both the under-prediction of the suction side pressure and loss of wave energy propagation due to numerical diffusion in z-direction. Figure 6 presents the measured and computed profiles of ζ for nonbreaking condition $(d/L, \mathrm{Fr}, \mathrm{Re}) = (1.29, 0.567, 1.42 \times 10^5)$ of Duncan [5]. The inviscid methods using potential flow theory [18] and Euler equation solution [45] show somewhat over-predicted crests and considerably large phase shifts, which are not desirable in free-surface wave simulations. On the other hand, RANS solution [46] is in phase with the measured wave profile and show under-predicted crests and troughs with the accuracy comparable to that of the present method. These observations support the argument that the wave amplitude under-prediction is a common characteristic in NS/RANS simulations, especially at relatively low Re's, and that the present free-surface wave simulation results are consistent with other NS/RANS results. However, more extensive grid studies are required to verify the sensitivity of the solutions to further grid refinement.

Next, Mori's [6] breaking wave case, a NACA 0012 hydrofoil at $\alpha = 2$ deg and $(d/L, \mathrm{Fr}, \mathrm{Re}) = (0.7, 0.551, 2.48 \times 10^5)$, is consid-

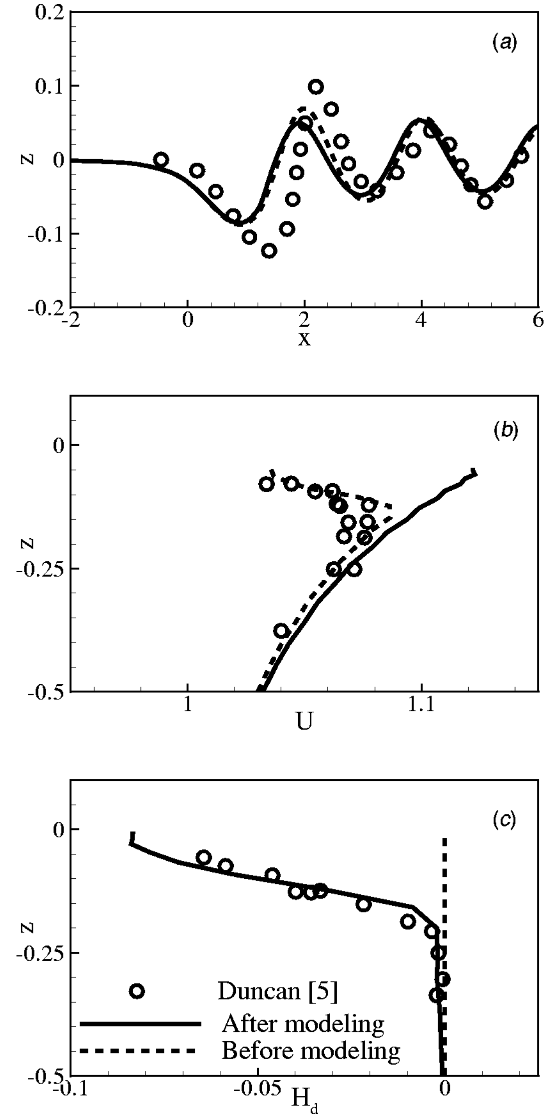

Fig. 5 Wave elevation, velocity, and total head defect for Duncan's [5] breaking case $(d/L, \mathrm{Fr}, \mathrm{Re}) = (0.925, 0.567, 1.42\times10^5)$: (*a*) Wave profile; (*b*) streamwise velocity; (*c*) total head defect.

ered. It is a subbreaking wave condition and therefore selected values for ρ_{BW}/ρ $(=0.25)$ and β $(=0.65)$ are similar to Duncan's, but with slightly larger β considering the less strong breaker eddy. Figure 7 shows the profiles of U and W near the breaker top before and after RANS modeling and comparison with Mori [6].

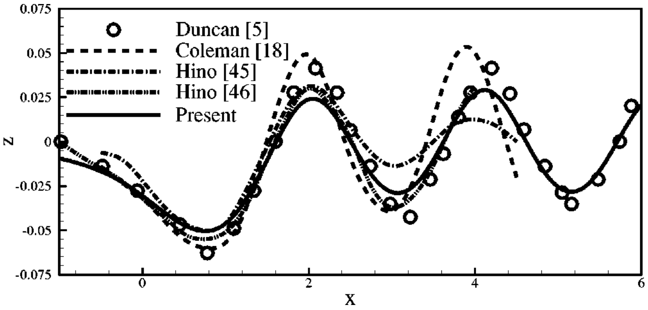

Fig. 6 Measured and computed wave profiles for Duncan's [5] nonbreaking case $(d/L, \mathrm{Fr}, \mathrm{Re}) = (1.29, 0.567, 1.42\times10^5)$

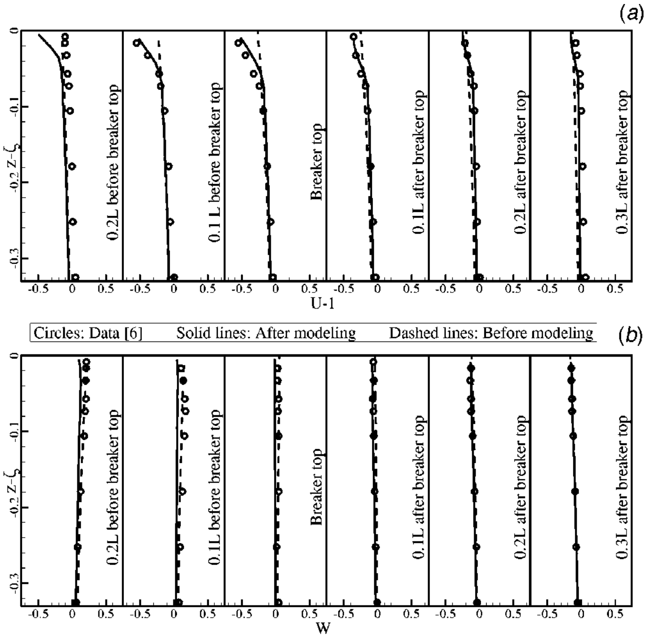

Fig. 7 Profiles of U-1 and W for Mori's [6] breaking case $(d/L, \mathrm{Fr}, \mathrm{Re}) = (0.7, 0.551, 2.48\times10^5)$: (*a*) *U*-1 profiles; (*b*) *W* profiles

The generation and decay of defect in U are clearly shown and the comparison with experimental data is good except at $0.2L$ before the breaker top. The data show considerably smaller defect than the simulations at this distance from the breaker top. Simulations also show reduction in W with poorer agreement with the data than without modeling; however, it should be noted that W profiles are nearly flat and largely unaffected by the breaker and that it is difficult to capture this secondary trend accurately.

Figure 8 presents $\sqrt{u'^2}$, $\sqrt{w'^2}$, and $u'w'$ near the breaker top before and after RANS modeling and comparison with Mori [6]. Note that, due to the linear k-ω model in the present study, both $\sqrt{u'^2}$ and $\sqrt{w'^2}$ are the same and have the value of $\sqrt{2k/3}$, where k here is the turbulence kinetic energy. It is not possible to compare k rather than individual components due to unavailability of data. The generation, decay, and vertical extent of $\sqrt{u'^2}$ show good agreement with experimental data, except again at $0.2L$ before the breaker top and in freestream. The over-prediction is also seen at $0.2L$ before the breaker top as for U profile. The disagreement in free-stream is attributed to the zero free-stream turbulence in the computation. The profiles of $\sqrt{w'^2}$ show qualitative agreement, but with larger over-prediction near the free surface after the breaker top. This over-prediction is clearly due to the effects of free surface on turbulence, which are not accounted for in the present turbulence model, as previously discussed. Lastly, the profiles of $u'w'$ show large over-prediction before and at the breaker top, but show good agreement with experimental data, especially the peak values after the breaker.

For the global prediction by the RANS model, data analysis is carried out to check the balance between three quantities: hydrostatic pressure due to the breaker weight, total shear force on the breaker surface, and momentum deficit at the second trough after the breaker, all of which should be equal according to C&T theory. The three quantities roughly balance each other in both cases (see Table 2), with slightly larger differences in momentum deficit in the wake, apparently due to numerical diffusion in the streamwise direction.

6 Concluding Remarks

A RANS model for spilling breaking waves is developed, which can be implemented with ship hydrodynamics RANS CFD

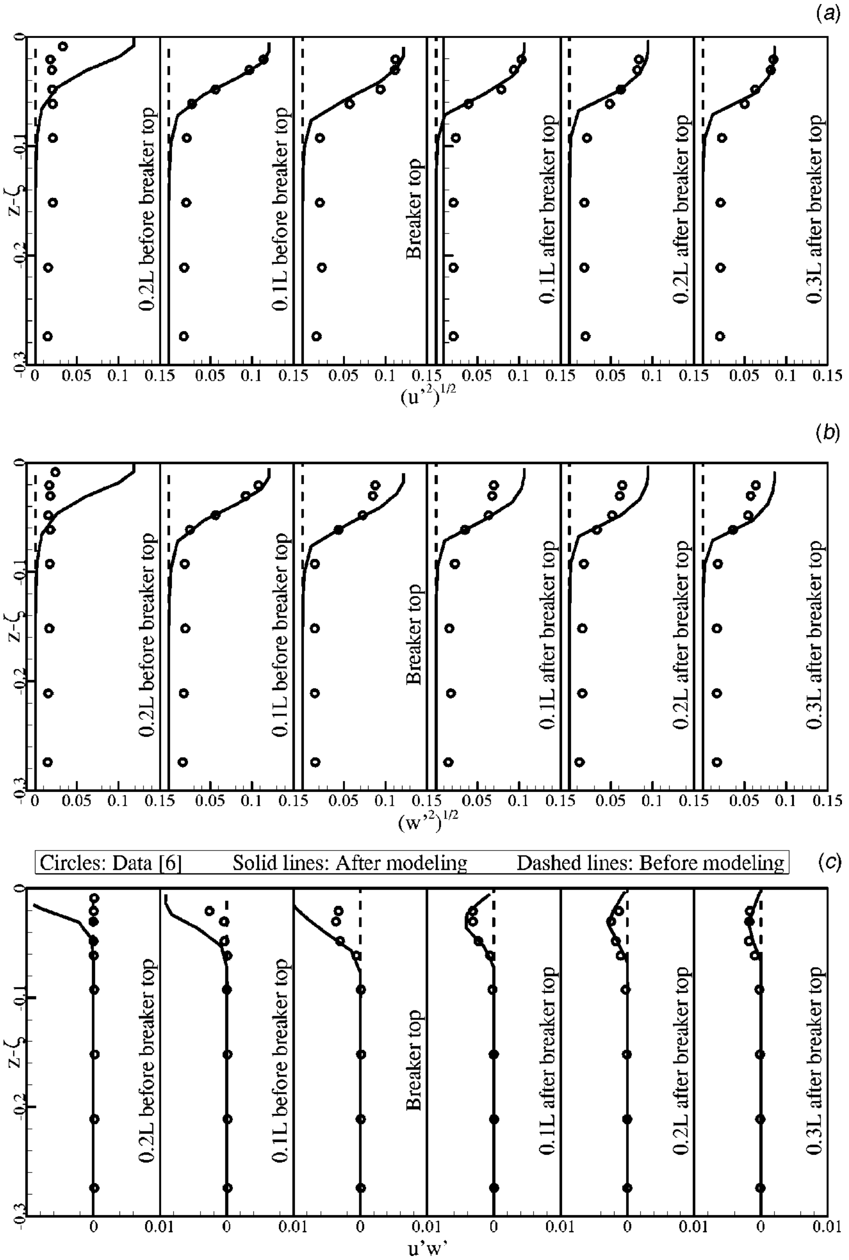

Fig. 8 Profiles of turbulence fluctuations and Reynolds stress for Mori's [6] breaking case $(d/L,\mathrm{Fr},\mathrm{Re})=(0.7,0.551,2.48\times10^5)$: (*a*) Streamwise turbulence fluctuations $(\sqrt{u'^2})$ profiles; (*b*) Depthwise turbulence fluctuations $(\sqrt{w'^2})$ profiles; (*c*) Reynolds stress $(u'w')$ profiles.

codes. The model is based on the C&T theory of steady breakers. The breaker cross section is assumed triangular with maximum height determined by the theoretical/experimental linear relationship with following wave height. Pressure and velocity boundary conditions are imposed on the dividing streamline between the breaker and underlying flow based on the hydrostatic and mixing layer models. An iterative solution procedure provides a unique solution for specified breaking criteria and simulation conditions. The model is implemented using CFDSHIP-IOWA and validated using benchmark spilling breaking wave data for two-dimensional submerged hydrofoils. As with other current RANS codes, wave elevations are under predicted. However, for the first time in literature, the breaking wave wake is predicted. Results for total head, mean velocities, and Reynolds stresses are in agreement with available spilling breaking wave benchmark data. Future work for 2D includes use of nonisotropic turbulence models for effects of free surface on turbulence and rigorous verification and validation (the latter assuming new experimental data becomes available with uncertainty estimates).

Extensions for three-dimensional flows are possible using strip theory such as the one proposed by Tulin and Landrini [3], which

Table 2 Data analysis for global prediction

	Breaker weight	Total shear force	Momentum deficit in wake
Duncan's [5] case	8.77×10^{-3}	1.00×10^{-2}	7.56×10^{-3}
Mori's [6] case	8.55×10^{-3}	8.62×10^{-3}	8.02×10^{-3}

may yield useful results. Similar approaches may also be possible for plunging breaking waves using unsteady RANS with jet boundary conditions. Air entrainment can be included through use of two-fluid models [47]. Breaking criteria remain an important unresolved issue. Experimental data would be useful for improved model parameters and to aid in extensions for three-dimensional and unsteady breakers.

Acknowledgment

This research was sponsored by Office of Naval Research contract N00014-96-1-0018 under the administration of Dr. Ed Rood.

References

[1] Baba, E., 1969, ''A New Component of Viscous Resistance,'' J. of Soc. Naval Archi. Japan, **125**, pp. 23–34.

[2] Longuet-Higgins, M. S., 1996, ''Progress toward Understanding How Waves Break,'' Proc. 21st Sympo. on Naval Hydro., Trondheim, Norway.

[3] Tulin, M. P., and Landrini, M., 2000, ''Breaking Waves in the Ocean and around Ships,'' Proc. 23rd Sympo. on Naval Hydro., Val de Reuil, France.

[4] Cointe, R., and Tulin, M. P., 1994, ''A Theory of Steady Breakers,'' J. Fluid Mech., **276**, pp. 1–20.

[5] Duncan, J. H., 1983, ''The Breaking and Non-breaking Wave Resistance of a Two-dimensional Hydrofoil,'' J. Fluid Mech., **126**, pp. 507–520.

[6] Mori, K.-H., 1986, ''Sub-breaking Waves and Critical Condition for Their Appearance,'' J. of Soc. Naval Archi. Japan, **159**(23), pp. 1–8.

[7] Duncan, J. H., 1981, ''An Experimental Investigation of Breaking Waves Produced by a Towed Hydrofoil,'' Proc. R. Soc. London, Ser. A, **377**, pp. 331–348.

[8] Battjes, J. A., and Sakai, T., 1981, ''Velocity Field in a Steady Breaker,'' J. Fluid Mech., **111**, pp. 421–437.

[9] Duncan, J. H., Philomin, V., Behres, M., and Kimmel, J., 1994, ''The Formation of Spilling Breaking Water Waves,'' Phys. Fluids, **6**, pp. 2558–2560.

[10] Longuet-Higgins, M. S., 1994, ''Shear Instability in Spilling Breakers,'' Proc. R. Soc. London, Ser. A, **446**, pp. 399–409.

[11] Lin, J. C., and Rockwell, D., 1995, ''Evolution of a Quasi-steady Breaking Wave,'' J. Fluid Mech., **302**, pp. 29–44.

[12] Miller, M., Nennstiel, T., Fiaklowski, L., Pröstler, S., Duncan, J., and Dimas, A., 1998, ''Incipient Breaking of Steady Waves,'' Proc. 22nd Sympo. on Naval Hydro., Washington, D.C.

[13] Iafrati, A., Olivieri, F., Pistani, E., and Campana, E., 2000, ''Numerical and Experimental Study of the Wave Breaking Generated by a Submerged Hydrofoil,'' Proc. 23rd Sympo. on Naval Hydro., Val de Reuil, France.

[14] Coakley, D. B., 1997, Surface Shape of Laboratory Generated Steady Breaking Waves, Ph.D. thesis, University of Maryland, College Park, MD.

[15] Chang, K.-A., and Liu, P. L.-F., 1998, ''Velocity, Acceleration and Vorticity under a Breaking Wave,'' Phys. Fluids, **10**, pp. 327–329.

[16] Walker, D. T., Lyzenga, D. R., Ericson, E. A., and Lund, D. E., 1996, ''Radar Backscatter and Surface Roughness Measurements for Stationary Breaking Waves,'' Proc. R. Soc. London, Ser. A, **452**, pp. 1953–1984.

[17] Coakley, D. B., Haldeman, P. M., Morgan, D. G., Nicolas, K. R., Penndorf, D. R., Wetzel, L. B., and Weller, C. S., 2001, ''Electromagnetic Scattering from Large Steady Breaking Waves,'' Exp. Fluids, **30**(5), pp. 479–487.

[18] Coleman, R. M., 1986, ''Nonlinear Calculation of Breaking and Non-breaking Waves behind a Two-dimensional Hydrofoil,'' Proc. 16th Sympo. on Naval Hydro., Berkeley, CA.

[19] Sadovnikov, D., and Trincas, G., 1998, ''Nonlinear Simulation of Breaking Waves with Spilling Breakers by a Boundary Integral Method,'' Proc. 22nd Sympo. on Naval Hydro., Washington, D.C.

[20] Longuet-Higgins, M. S., and Cokelet, E. D., 1976, ''The Deformation of Steep Surface Waves on Water. I. A Numerical Method for Computation,'' Proc. R. Soc. London, Ser. A, **358**, pp. 1–26.

[21] Liou, B., Martinelli, L., Baker, T., and Jameson, A., 1998, ''Calculation of Plunging Breakers with a Fully-implicit Adaptive-grid method,'' 29th AIAA Fluid Dynamics Conf., AIAA-98-2968.

[22] Mori, K.-H., and Shin, M.-S., 1988, ''Sub-breaking Wave: Its Characteristics, Appearing Condition and Numerical Simulation,'' Proc. 17th Sympo. on Naval Hydro., The Hague, The Netherlands.

[23] Lungu, A., Raad, P. E., and Mori, K.-H., 1997, ''Turbulent Early-stage Breaking Wave Simulation,'' ASME FED Summer Meeting, ASME FEDSM97-3404.

[24] Lemos, C.M., 1992, *Wave Breaking: A Numerical Study*, Springer-Verlag.

[25] Lin, P., and Liu, P. L.-F., 1998, ''A Numerical Study of Breaking Waves in the Surf Zone,'' J. Fluid Mech., **359**, pp. 239–264.

[26] Chen, G., Kharif, C., Zaleski, S., and Li, J., 1999, ''Two-dimensional Navier-Stokes Simulation of Breaking Waves,'' Phys. Fluids, **11**, pp. 121–133.

[27] Azcueta, R., Muzaferija, S., Peric, M., and Yoo, S.-D. 1999, ''Computation of Flows around Hydrofoils under the Free Surface,'' Proc. 7th Int. Conf. on Num. Ship Hydro., Nantes, France.

[28] Vogt, M., and Larsson, L., 1999 ''Level Set Methods for Predicting Viscous Free Surface Flows,'' Proc. 7th Int. Conf. on Num. Ship Hydro., Nantes, France.

[29] Miyata, H., Kanai, A., Kawamura, T., and Park, J.-C., 1996, ''Numerical Simulation of Three-dimensional Breaking Waves,'' J. of Marine Sci. and Tech., **1**, pp. 183–197.

[30] Celik, I., and Rodi, W., 1984, ''Simulation of Free-Surface Effects in Turbulent Channel Flows,'' Physicochemical Hydrodynamics, **5**, pp. 217–226.

[31] Walker, D. T., 2000, ''Reynolds-Averaged Models of High Froude Number Free-Surface Jets,'' Proc. 23rd Sympo. on Naval Hydro., Val de Reuil, France.

[32] Sreedhar, M. K., and Stern, F., 1998, ''Non-linear Eddy-viscosity Turbulence Model for Solid/Free-surface Juncture Boundary Layer and Wake,'' ASME J. Fluids Eng., **120**, pp. 354–362.

[33] Craig, P. D., and Banner, M. L., 1994, ''Modeling Wave-enhanced Turbulence in the Ocean Surface Layer,'' J. of Physical Oceanography, **24**, pp. 2546–2559.

[34] Melville, W. K., Veron, F., and White, C. J., 2001, ''The velocity field under breaking waves: coherent structures and turbulence,'' J. Fluid Mech., in press.

[35] Banner, M. L., and Peregrine, D. H., 1993, ''Wave Breaking in Deep Water,'' Annu. Rev. Fluid Mech., **25**, pp. 373–397.

[36] Melville, W. K., 1996, ''The Role of Surface-wave Breaking in Air-sea Interaction,'' Annu. Rev. Fluid Mech., **28**, pp. 279–321.

[37] Stern, F., Hwang, W. S., and Jaw, S. Y., 1989, ''Effects of Waves on the Boundary Layer of a Surface-Piercing Flat Plate: Experiment and Theory,'' J. of Ship Research, **33**(1), Mar, pp. 63–80.

[38] Nadaoka, K., Ono, O., and Kurihara, H., 1997, ''Analysis of Near-crest Pressure Gradient of Irregular Water Waves,'' Proc. 7th Int. Offshore and Polar Eng. Conf., Honolulu, HI.

[39] Paterson, E. G., Wilson, R. V., and Stern, F., 1998, ''Verification/Validation of Steady Flow RANS CFD for Naval Combatant,'' Proc. 1st Marine CFD Applications Symposium, Washington, D.C.

[40] Wilson, R. V., Paterson, E. G., and Stern, F., 1998 ''Unsteady RANS CFD Method for Naval Combatants in Waves,'' Proc. 22nd Sympo. On Naval Hydro., Washington, DC.

[41] Wilson, R. V., Paterson, E. G., and Stern, F., 2000, ''Verification and Validation for RANS Simulation of a Naval Combatant,'' Proc. Gothenburg 2000: A Workshop on Numerical Ship Hydrodynamics, Gothenburg, Sweden.

[42] Iowa Institute of Hydraulic Research, 2001, ''http://www.iihr.uiowa.edu/~cfdship/cfdship-iowa.htm.''

[43] Larsson, L., Stern, F., and Bertram, V., ed., 2000, Proc. Gothenburg 2000: A Workshop on Numerical Ship Hydrodynamics, Chalmers Univ. of Technology, Gothenburg, Sweden.

[44] Menter, F. R., 1994, ''Two-Equation Eddy-Viscosity Turbulence Models for Engineering Applications,'' AIAA J., **32**, pp. 1598–1605.

[45] Hino, T., 1988, ''Numerical Computation of a Free Surface Flow around a Submerged Hydrofoil by the Euler/Navier-Stokes Equations,'' J. of Soc. Naval Archi. Japan, **164**, pp. 17–25.

[46] Hino, T., 1997, ''An Unstructured Grid Method fo Incompressible Viscous Flows with a Free Surface,'' 35th Aerospace Sci. Meeting and Exhibit, AIAA-97-0862.

[47] Carrica, P. M., Bonetto, F. J., Drew, D. A., and Lahey, Jr., R. T., 1998, ''The Interaction of Background Ocean Air Bubbles with a Surface Ship,'' Int. J. Numer. Methods Fluids, **28**, pp. 571–600.

Othon K. Rediniotis
Associate Professor
e-mail: rediniotis@tamu.edu

Jeonghwan Ko[1]
Post Doctoral Research Associate

Department of Aerospace Engineering,
Texas A&M University,
College Station, TX 77843-3141

Andrew J. Kurdila
Professor,
Department of Aerospace Engineering,
Mechanics and Engineering Science,
University of Florida,
Gainesville, FL 32611-6250
e-mail: ajk@aero.ufl.edu

Reduced Order Nonlinear Navier-Stokes Models for Synthetic Jets

While the potential for the use of synthetic jet actuators to achieve flow control has been noted for some time, most of such flow control studies have been empirical or experimental in nature. Several technical issues must be resolved to achieve rigorous, model-based, closed-loop control methodologies for this class of actuators. The goal of this paper is consequently two-fold. First, we seek to derive and evaluate model order reduction methods based on proper orthogonal decomposition that are suitable for synthetic jet actuators. Second, we seek to derive rigorously stable feedback control laws for the derived reduced order models. The realizability of the control strategies is discussed, and a numerical study of the effectiveness of the reduced order models for two-dimensional flow near the jet exit is summarized. [DOI: 10.1115/1.1467598]

1 Introduction

Synthetic jet technology has been recently addressed by many researchers (Amitay et al. [1], Smith et al. [2], Seifert and Pack [3], Chatlynne et al.). It has been suggested that this technology may enable the active modification of the pressure distribution over different surfaces, leading to ''dynamic virtual shaping.'' It has likewise been noted that it may potentially achieve flow separation manipulation, not just separation delay. This possibility could open new horizons in flow control. Indeed, some very promising empirical and experimental studies have provided evidence that synthetic jet actuators can achieve flow separation control. Nevertheless, significant technical barriers remain to be overcome before closed-loop controls based on a rigorous theory can be designed for these devices. For example, low-dimensional physics-based flow models for this class of devices are still lacking. The derivation of rigorous principles by which control laws can be derived that guarantee stability also has yet to be developed. Many researchers have noted the need for reliable, experimentally validated models for these actuators for a range of operating conditions. As an example, this need is exemplified by the work of Joshi et al. [4], where the lack of realistic models of oscillatory blowing actuators is evident. Their work focuses on transition control of the flow between two parallel flat plates. The control algorithm is based on the application of idealized blowing-suction waveforms on the boundary (plates). These waveforms were not derived from actual realistic actuators. Since in an actual implementation of the controller, real actuators will have to be used, the need for models of the actuator-generated flow is evident. Moreover, these models will have to be low-dimensional, since the controller needs to operate in real-time. Joshi et al.'s work, although lacking realistic actuator models, nicely illustrates the benefits that can be gained via rigorous application of control theory to fluid dynamics systems. Most work in the existing literature that illustrates the impressive capabilities of synthetic jets, does so in an experimental and empirical manner and is lacking the use of rigorous control theory (some the present authors' previous work included; Gilarranz and Rediniotis [5], Amitay et al. [1], Smith et al. [2]). For example, let us consider the control of steady separation over a wing or the control of dynamic stall over a helicopter blade, or over the wing of an aircraft during an aggressive high-alpha maneuver. Although significant control authority has been demonstrated with a single synthetic jet located near the leading edge, it is very likely that for complete separation control, distributed control, via multiple synthetic jets on the blade's/wing's leeward side, might be necessary. Moreover, the need for sensing of flow separation/attachment is evident, and closes the control loop. This now becomes a closed-loop, distributed control problem that necessitates the development of rigorous control techniques for nonlinear fluid dynamics systems.

Thus, the goal of this paper is to address two questions of fundamental importance to the eventual realization of closed-loop control via synthetic jet actuators:

1. How may we develop low-dimensional, physics-based flow models for synthetic jet actuators?
2. How amenable to closed-loop control are these reduced order models? In particular, can we state conditions that guarantee the closed-loop stability of (at least) the reduced order system?

We do not claim to have reached exhaustive answers to these questions. Rather we present proposed methodologies, their initial success, their potential as well as their limitations. As in many flow control problems, several aspects of these questions have no simple answer. Often this is due to the fact that the underlying Navier-Stokes equations are inherently nonlinear. However, we will show that proper orthogonal decomposition (POD) methods, which have been used quite effectively to derive low dimensional models of coherent structures in turbulent flows, can be accurate and efficient in reduced order modeling of the open-loop response of two-dimensional, near-field, synthetic jets flows. We do not claim to have achieved a global low-order model for 3-D synthetic jet flows, including all the physics, such as breakdown of the vortex pair and transition to turbulence. Generating such a low-order model is admittedly a vast task, especially if the externally imposed flow that the synthetic jet is trying to control (for example the separated boundary layer flow over a wing that the synthetic jet is attempting to reattach) is included. Nonetheless, the 2-D flow we are considering here, has significant spatial and temporal variation to demonstrate the capabilities and potential of POD order reduction techniques and illustrate the amenability of such flows to POD low-order modeling. We also show that the resulting reduced order model is exponentially output stabilizable,

---

[1] Currently, Senior Researcher, Rocket System Integration Dept., Korea Aerospace Research Institute, jko@kari.re.kr

Contributed by the Fluids Engineering Division for publication in the JOURNAL OF FLUIDS ENGINEERING. Manuscript received by the Fluids Engineering Division October 15, 1999; revised manuscript received October 15, 2001. Associate Editor: P. Raad.

at least under some ideal assumptions. We also note several outstanding questions that must be resolved before these controls can be implemented in realistic control problems.

Related Research. Despite significant progress in diverse disciplines in control theory over the past decade, the control of fluid flow remains one of the most challenging, unresolved problems in the field. The difficulty that arises in deriving rigorous and general methodologies for fluid flows can be attributed to many factors. Perhaps the most significant factors are the inherent nonlinearity of the Navier-Stokes equations that represent the dynamics of the flow, and the high dimensionality of typical approximations of these equations. To help calibrate the complexity of the control task at hand, it can be helpful to consider other classes of nonlinear dynamical systems for which a (nonlinear) control theory is readily available. For example, ''geometric'' methods of nonlinear control, with their foundation in Lie Algebra and differential geometry, have flourished over the past 10 years. The reader is referred, for example, to Isidori [6] and the references therein. Even if the nonlinear control problem at hand is not directly amenable to all the strengths of these geometric approaches, this analysis is often used as a first step in pursuing alternative approaches (Krstic et al. [7]). Still, it is safe to say that the models to which these modern control theories may readily be applied are extremely low dimensional. Typical practical examples in which the geometric methods have been effective are discussed in Sheen and Bishop [8] wherein attitude control is studied, or in Ko et al. [9] where a nonlinear flutter suppression control is derived. In both cases, the number of degrees of freedom of the model is O(10)-O(100) equations. If we acknowledge that reasonable computational fluid dynamics models can require on the order of O(10^6)-O(10^7) degrees of freedom, it is clear that significantly different strategies are required for flow control problems.

A wide spectrum of approaches has been investigated to attempt to codify methods for flow control over the years. These methods differ markedly in the rigor of their treatment of the underlying mathematical control problem, as well as the degree to which the techniques have been validated experimentally or computationally. There is a collection of work that seeks to solve open mathematical problems of control theory associated with fluid flow. In Cuvelier [10], for example, proof of the existence of optimal controls is given for systems of partial differential equations obtained via coupling of the Navier-Stokes and heat conduction equations. The careful, and sometimes incremental, nature of this type of research is illustrated by Gunzburger and Lee [11]. In this paper, the authors derive a mathematically rigorous proof of the convergence of approximations that are applicable to the systems studied in Cuvelier [10]. Thus, the proof of existence of optimal control predates the proof of convergence of approximations for this class of systems by 20 years. Mathematical control theory is characterized by such careful definition of problem and solution. Over the years, careful and rigorous study of mathematical control theory has likewise focused on other specific problems, including control of driven cavity flow (Burns and Ou, [12]), and piezoelectric control of shear layers (Banks and Ito [13]). General studies of the optimal control of the Navier-Stokes equations, for various classes of assumptions (boundary control, distributed control, 2D problems, 3D problems, etc.) can be found in Desai and Ito [14], Ito and Kang [15], Ravindran and Hou [16], Hou and Yan [17], Fattorini and Sritharan [18,19], and Fursikov et al. [20]. While these studies are to be recommended for their rigor, connectivity to experimental verification is often neglected. At the same time, there has been a concerted effort to improve the degree to which rigorous mathematical control theory, in the spirit of the approaches discussed above, can complement and benefit from current research in computational fluid dynamics. Joslin et al. [21] summarizes the use of adjoint and optimality systems for some optimal flow control problems. Emphasis is placed on the numerical requirements and demands imposed for the direct simulation of the resulting set of coupled, nonlinear partial differential equations. This approach is discussed in Joslin [22] to study the interaction between control theory and direct numerical simulation for zero-mass-flux fluidic actuators. This work is particularly relevant to the current paper.

To appreciate the diversity of the approaches taken by researchers to address flow control, the reader is likewise advised to consider the careful experimental work that has appeared in Wygnanski [23]. In Wygnanski [23], studies of boundary layer modification and flow control via oscillatory zero-mass-flux jets is described. While the theoretically precise work in, say, Fattorini and Sritharan [19] does include a single attempt to verify its theory via an experimental protocol, the detailed experimental studies in Wygnanski [23] or Trujillo et al. [24] are carried out without recourse to any mathematical control theory. Thus, the need for the synthesis of rigorous control theory and experimental methods has been noted by several researchers over the years. A key step to this synthesis is the development of lower dimensional descriptions of flow dynamics for control synthesis. For example, the reader is referred to p. 6, Section 5.7 of Bewley et al. [25]. Some authors have proposed ad hoc methods based on neural networks (Cho et al. [26]), or methods based on linearization and order reduction via classical linear system theoretic methods (Joshi et al. [4]).

Additionally, some reduced order methods for flow modeling and control have appeared in the literature over the past few decades. Proper orthogonal decomposition (POD) has been utilized in Aubry et al. [27] to derive low dimensional models for a class of fluid flows. POD is essentially a statistically based order reduction that calculates the singular value decomposition of the covariance operator of output measurements. Recently, Ly and Tran [28] have shown that POD methods can be used effectively for generating a reduced order model for the simulation and control of a class of reactor flows. A similar philosophy, with an experimental orientation, is considered in Corke et al. [29]. In contrast to the POD methods, where the reduced order model is based on optimality criteria, other authors have demonstrated that effective reduced order models can be derived from physical considerations. For example, Ito and Ravindran [30,31] have shown via empirical numerical evidence that reduced order Navier-Stokes simulations can yield accurate reduced order models. This methodology is similar in philosophy to the assumed modes methods of structural mechanics. In fact, the assumed modes methods for order reduction of structural systems have been studied in detail (see for example, Craig [32] or Skelton [33]), and have motivated analogous strategies for the generation of reduced order models for aeroelastic studies (Tang et al. [34]). Finally, there has been recent anecdotal evidence that wavelets and multiresolution methods can provide an avenue for generating reduced order models for flow. Elezgaray et al. [35] study the dynamical systems obtained via periodic-wavelet approximations of prototypical flow equations. Wickerhauser et al. [36] likewise study the effectiveness of generating low dimensional approximations of scalar vorticity fields using wavelets and windowed cosine bases. The authors of this paper have recently studied the use of divergence free wavelets for the order reduction of experimentally collected velocity fields in Ko et al. [37,38].

2 Order Reduction Framework

In this section, we discuss the reduced basis methods, and lay the foundation for the order reduction and control approaches presented in the paper. We will consider viscous, incompressible flows whose dynamic behavior is governed by the Navier-Stokes equations. We seek to find $\vec{V}$ and p such that

$$\begin{aligned} \mathrm{St}\frac{\partial \vec{V}}{\partial t}-\frac{1}{\mathrm{Re}}\Delta \vec{V}+\vec{V}\cdot\vec{\nabla}\vec{V}+\nabla p=f, &\quad \text{in } \Omega\times(0,T) \\ \vec{\nabla}\cdot\vec{V}=0, &\quad \text{in } \Omega\times(0,T) \\ \vec{V}=g, &\quad \text{on } \partial\Omega\times(0,T) \\ \vec{V}(0)=\vec{V}_0, &\quad \text{in } \Omega \end{aligned} \tag{1}$$

where Ω is the fluid domain, $(0,T]$ is the time interval of interest, $\vec{V}$ is the velocity, p is the pressure. Re is the Reynolds number and St is the Strouhal number. In the usual way, we define $L^2(\Omega)$ to be those functions that are square integrable in the domain Ω with norm

$$\|f\|^2_{L^2(\Omega)}=\int_\Omega f(x)dx \tag{2}$$

and by $L^2_0(\Omega)$ those functions in $L^2(\Omega)$ with zero mean. $H^1(\Omega)$ is the Sobolev space of functions whose first weak derivative is in $L^2(\Omega)$.

$$H^1(\Omega)=\left\{f\in L^2(\Omega): \frac{\partial f}{\partial x_i}\in L^2(\Omega), i=1,\ldots n\right\}. \tag{3}$$

By $L^p(0,T;X)$ we mean those X-valued functions that are Bochner integrable with norm

$$\|f\|_{L^p(0,T;X)}=\left\{\int_0^T \|f(t)\|^p_X dt\right\}^{1/p}. \tag{4}$$

In this paper, we will have occasion to use

$$H=\{\vec{V}\in[L^2(\Omega)]^n: \vec{\nabla}\cdot\vec{V}=0 \text{ in } \Omega,\ \vec{V}\cdot\vec{n}|_{\partial\Omega}=0\} \tag{5}$$

and the space that incorporates boundary conditions via the trace of functions on the boundary

$$H_g=\{\vec{V}\in[H^1(\Omega)]^n: \vec{V}|_{\partial\Omega}=g\in H^{1/2}(\Gamma)\} \tag{6}$$

where $H^{1/2}(\Gamma)$ is a Sobolev space of fractional derivative, defined on the boundary Γ. We can write these equations in weak form by introducing the bilinear form

$$a(\cdot,\cdot):[H^1(\Omega)]^n\times[H^1(\Omega)]^n\to R$$

$$a(\vec{U},\vec{V})=\frac{1}{R_e}\int_\Omega(\vec{\nabla}\vec{U}):(\vec{\nabla}\vec{V})dx \tag{7}$$

the bilinear form

$$c(\cdot,\cdot):[H^1(\Omega)]^n\times L^2(\Omega)\to R$$

$$c(\vec{V},p)=\int_\Omega(\vec{\nabla}\cdot\vec{V})p\,dx \tag{8}$$

and, finally, the trilinear form

$$b(\cdot,\cdot):[H^1(\Omega)]^n\times[H^1(\Omega)]^n\times[H^1(\Omega)]^n\to R$$

$$b(\vec{U},\vec{V},\vec{W})=\sum_{i,j=1}^n\int_\Omega U_j\frac{\partial V_i}{\partial x_j}W_i dx. \tag{9}$$

With this notation, the weak form of the governing partial differential equations require that we find

$$\vec{V}\in L^2(0,T;H_g)\cap L^\infty(0,T;H)$$

$$p\in L^2(0,T;L^2_0(\Omega)) \tag{10}$$

such that

$$\left\langle\frac{\partial\vec{V}(t)}{\partial t},\vec{\xi}\right\rangle+a(\vec{V}(t),\vec{\xi})+b(\vec{V}(t),\vec{V}(t),\vec{\xi})-c(\vec{\xi},p(t))$$

$$=\langle f(t),\vec{\xi}\rangle,\quad\forall\vec{\xi}\in[H^1_0(\Omega)]^n$$

$$c(\vec{V}(t),q)=0,\quad\forall q\in L^2(\Omega). \tag{11}$$

Within the context of conventional finite element methods, we choose finite dimensional spaces

$$\mathbf{V}_k\subset[H^1_0(\Omega)]^n$$

$$\mathbf{S}_k\subset L^2_0(\Omega) \tag{12}$$

and seek approximate solutions $\vec{V}_k(t)-\vec{E}(g(t))\in\mathbf{V}_k, p_k\in\mathbf{S}_k$ such that

$$\left\langle\frac{\partial\vec{V}_k(t)}{\partial t},\vec{\xi}_k\right\rangle+a(\vec{V}_k(t),\vec{\xi}_k)+b(\vec{V}_k(t),\vec{V}_k(t),\vec{\xi}_k)-c(\vec{\xi}_k,p_k(t))$$

$$=\langle f(t),\vec{\xi}_k\rangle,\quad\forall\vec{\xi}_k\in\mathbf{V}_k$$

$$c(\vec{V}_k(t),q_k)=0,\quad\forall q_k\in\mathbf{S}_k. \tag{13}$$

Depending on the physical system under consideration, the solution of Eqs. (12)–(13) can be a formidable task indeed. The cardinality of the finite dimensional subspaces $\mathbf{V}_k\times\mathbf{S}_k$ appearing in Eqs. (12)–(13) may be comprised of order of O(10^6) or O(10^7) equations in some applications. Moreover, if these equations appear in the formulation of an optimization, optimal control or design problem, they may need to be solved repeatedly as we seek to minimize some performance functional. As outlined in pp. 108–114 of Gunzburger [39], reduced basis methods have been investigated for over the past decade. More recently, Ito and Ravindran [30,31] have studied the performance of some reduced basis methods in the context of optimization. The essential philosophy behind the approach studied in Gunzburger [39], and Ito and Ravindran [30,31] is straightforward. The full order Navier Stokes equations are solved for a family of N_r solutions. We denote these solutions as

$$\{(\vec{\Psi}_r,\eta_r)\}_{r=1}^{N_r}. \tag{14}$$

Each individual solution $(\vec{\Psi}_r,\eta_r)$ corresponds to a different set of physical conditions. For example, the sequence of solutions $\{(\vec{\Psi}_r,\eta_r)\}_{r=1}^{N_r}$ may correspond to N_r different Reynolds numbers used to generate the solutions. A reduced order model is then sought where the solution is constrained to lie in some subspace of

$$\mathbf{V}_{N_r}\times\mathbf{S}_{N_r}=span\{(\vec{\Psi}_r,\eta_r)\}_{r=1}^{N_r}. \tag{15}$$

Several comments are in order at this point to contrast the spaces $\mathbf{V}_{N_r}$ and $\mathbf{V}_k$. The space $\mathbf{V}_k$ is spanned by a huge number of functions (typically finite element functions), and the functions satisfy homogeneous boundary conditions. In contrast, $\mathbf{V}_{N_r}$ is spanned by a few basis functions, but need not satisfy homogeneous boundary conditions. In fact, for the class of problems we consider, where control is induced via oscillatory blowing, typical reduced order bases comprising $\mathbf{V}_{N_r}$ will not satisfy homogeneous boundary conditions. If we have strong evidence to believe that the solution will vary parametrically in a continuous fashion over the range of parameters used to generate $\mathbf{V}_{N_r}\times\mathbf{S}_{N_r}$, it is anticipated that the reduced order model will be accurate for nearby parameter values. This argument is hardly rigorous. In fact, it avoids all discussion of bifurcation phenomena associated with the infinite dimensional dynamical system. Nevertheless, the empirical evidence in Ito and Ravindran [30,31] has been promising. In a similar fashion, now consider the unsteady Navier-Stokes equations. Some authors have sought to represent the reduced order system by choosing a finite collection of solutions corresponding to different physical parameters and different instants in time. Again, if the total collection of "snapshots" captures the essential modes of the dynamical system, it is hoped that the reduced order system will be a good approximant of the full order system. Provided that the set of basis vectors comprising $\mathbf{V}_{N_r}$ is divergence free, the reduced order problem takes a simpler form. That is, we seek to find $\vec{V}(t)\in\mathbf{V}_{N_r}$ such that

$$\left\langle\frac{\partial\vec{V}(t)}{\partial t},\vec{\xi}\right\rangle+a(\vec{V}(t),\vec{\xi})+b(\vec{V}(t),\vec{V}(t),\vec{\xi})=\langle f(t),\vec{\xi}\rangle,$$

$$\forall\vec{\xi}\in\mathbf{V}_{N_r}\cap\mathbf{V}_k. \tag{16}$$

The pressure field can then be obtained via post-processing, as discussed in Gunzburger [39] and Temam [40]

3 Implementation for Specific Bases

In this section, we discuss the detailed implementation of the reduced order model in Eq. (16) for the synthetic jet actuator described in a later part of the paper. We will restrict our discussion to two-dimensional unsteady incompressible flows. We note that the strong form of the governing momentum equations has been obtained via nondimensional analysis, and is shown as following:

$$\mathrm{St}\frac{\partial\vec{\mathbf{V}}}{\partial t}+(\vec{\mathbf{V}}\cdot\vec{\nabla})\vec{\mathbf{V}}=-\vec{\nabla}p+\frac{1}{\mathrm{Re}}\nabla^2\vec{\mathbf{V}} \tag{17}$$

where

$$\mathrm{St}=\frac{D}{U_{\max}T},\quad \mathrm{Re}=\frac{\rho U_{\max}D}{\mu}. \tag{18}$$

Specifically, we choose the jet orifice diameter as the length scale *D*. The actuator membrane oscillation period is used as the time scale *T*, and the average velocity at the maximum flow rate at the jet orifice, $U_{\max}$, is chosen as the velocity scale. With these definitions, the weak form of the governing equations then requires that

$$\left(\vec{\xi}_i,\mathrm{St}\frac{\partial\vec{V}}{\partial t}+(\vec{\mathbf{V}}\cdot\vec{\nabla})\vec{\mathbf{V}}\right)+(\vec{\xi},\vec{\nabla}p)=\frac{1}{\mathrm{Re}}(\vec{\xi},\nabla^2\vec{\mathbf{V}}). \tag{19}$$

Here $\vec{\xi}_i$ are the general weight functions. We assume that the full velocity vector can be approximately decomposed as

$$\vec{\mathbf{V}}=\vec{V}_M+\vec{V}\approx\vec{V}_M+\sum_{j=1}^{M}y_j(t)\vec{\Phi}_j(x,y) \tag{20}$$

where the basis function $\vec{\Phi}_j=\left\{\begin{smallmatrix}\Phi_{j_x}\\ \Phi_{j_y}\end{smallmatrix}\right\}$ is assumed to be known.

More specifically, each component of the total velocity $\vec{V}=\left\{\begin{smallmatrix}u\\ v\end{smallmatrix}\right\}$ is expressed as

$$u\approx u_M+\sum_{j=1}^{M}y_j(t)\Phi_{j_x}$$

$$v\approx v_M+\sum_{j=1}^{M}y_j(t)\Phi_{j_y} \tag{21}$$

and the time average velocity is given by

$$\vec{V}_M=\frac{1}{T}\int_{t_0}^{t_0+T}\vec{\mathbf{V}}dt. \tag{22}$$

Clearly, since the flow is assumed to be two dimensional and incompressible, it is simple to show that the selected basis must be divergence free

$$\vec{\nabla}\cdot\vec{\Phi}_j=0. \tag{23}$$

Now we consider each of the terms comprising the weak form of the governing equations.

$$(\vec{\xi}_i,\vec{\nabla}_p)=\int_\Omega\vec{\xi}_i\cdot\vec{\nabla}p\,d\Omega=\int_{\partial\Omega}p\vec{\xi}_i\cdot\vec{n}\,ds-\int_\Omega p\vec{\nabla}\cdot\vec{\xi}_i\,d\Omega. \tag{24}$$

If we choose the weight function $\vec{\xi}_i$ such that it is divergence free, then

$$(\vec{\xi}_i,\vec{\nabla}p)=\int_{\partial\Omega}p\vec{\xi}_i\cdot\vec{n}\,ds=[p\vec{\xi}_i]. \tag{25}$$

By substituting the above identities, we obtain the following set of nonlinear ordinary differential evolution equations for the time varying amplitudes $y_i(t)$:

$$\mathrm{St}\frac{dy_i}{dt}=a_i+\sum_{j=1}^{M}b_{ij}y_i+\sum_{j=1}^{M}\sum_{K=1}^{M}c_{ink}y_jy_K-[p\vec{\xi}_i] \tag{26}$$

where

$$a_i=-(\vec{\xi}_i,(\vec{V}_M\cdot\vec{\nabla})\vec{V}_M)-\frac{1}{\mathrm{Re}}(\vec{\nabla}\vec{\xi}_i,\vec{\nabla}\vec{V}_M)+\frac{1}{\mathrm{Re}}[\vec{\xi}_i,\vec{\nabla}\vec{V}_M]$$

$$b_{ij}=-(\vec{\xi}_i,(\vec{V}_M\cdot\vec{\nabla})\vec{\Phi}_j)-(\vec{\xi}_i,(\vec{\Phi}_j\cdot\vec{\nabla})\vec{V}_M)-\frac{1}{\mathrm{Re}}(\vec{\nabla}\vec{\xi}_i\cdot\vec{\nabla}\vec{\Phi}_j)$$

$$+\frac{1}{\mathrm{Re}}[\vec{\xi}_i\vec{\nabla}\vec{\Phi}_j]$$

$$c_{ijk}=-(\vec{\xi}_i,(\vec{\Phi}_j\cdot\vec{\nabla})\vec{\Phi}_K)$$

where the index $i=1,2,\ldots,M$. Using any standard integration scheme to solve these equations, we obtain a set of predicted time histories for the mode amplitudes $y_i(t)$, $i=1,2,\ldots,M$. Carefully note that the governing equations include a boundary flux term expressed in terms of the unknown pressure. This term has arisen from the expansion of the inner product.

$$(\vec{\xi}_i,\vec{\nabla}p)=\int_{\partial\Omega}p\vec{\xi}_i\cdot\vec{n}\,ds-\int_\Omega p\vec{\nabla}\cdot\vec{\xi}_i\,d\Omega. \tag{27}$$

If we choose the weight function $\vec{\xi}_i$ such that it is not only divergence free but also homogeneous at the boundary, then we can drop the pressure term. In our Galerkin projection, the $\vec{\xi}_i$ are the POD basis functions, $\vec{\Phi}_i$. The discussion of POD is given in the next section.

The modifications of the above equations to account for a finite number of controls generated by oscillatory blowing is relatively straightforward. In this case, we define

$$\vec{\mathbf{V}}\approx\vec{V}_M(x,y)+\gamma_1(t)\vec{V}_{c_1}(x,y)+\gamma_2(t)\vec{V}_{c_2}(x,y)$$

$$+\sum_{j=1}^{M}y_j(t)\vec{\Phi}_j(x,y) \tag{28}$$

where $\vec{V}_{c_1},\vec{V}_{c_2}$ are control functions that satisfy

$$\vec{\nabla}\cdot\vec{V}_{c_1}=0,\ \vec{\nabla}\cdot\vec{V}_{c_2}=0. \tag{29}$$

Additionally, we require that

$$\vec{\mathbf{V}}-\vec{V}_M-\gamma_1(t)\vec{V}_{c_1}-\gamma_2(t)\vec{V}_{c_2}=0 \tag{30}$$

on the boundary $\partial\Omega$, so that the basis functions in this case satisfy the divergence free and homogeneous conditions. Of course, the number of control functions is only constrained by physical realizability. We choose two controls for convenience; the generalization to any finite number is obvious. When we substitute the above expressions into the governing equations, and let the $\vec{\xi}_i$ be equal to the POD basis function $\vec{\Phi}_i$, we obtain the following ordinary differential equations for the time-varying amplitude $y_i(t)$, $i=1,\ldots,M$:

$$\mathrm{St}\frac{dy_i}{dt}=a_i+\sum_{j=1}^{M}b_{ij}y_j+\sum_{j=1}^{M}\sum_{K=1}^{M}c_{ijk}y_jy_K+d_{1i}\frac{d\gamma_1}{dt}+d_{2i}\frac{d\gamma_{2i}}{dt}$$

$$+\left(e_{1i}+\sum_{j=1}^{M}f_{1ij}y_j\right)\gamma_1+\left(e_{2i}+\sum_{j=1}^{M}f_{2ij}y_j\right)\gamma_2+h_i\gamma_1\gamma_2$$

$$+g_{1i}\gamma_1^2+g_{2i}\gamma_2^2 \tag{31}$$

where the index $i=1,2,\ldots,M$. The coefficients a_i, b_{ij}, c_{ijk} all have the same definition as in Eq. (26). In addition, we have

$$d_{1i}=-(\vec{\Phi}_i,\vec{V}_{c_1})$$

$$d_{2i}=-(\vec{\Phi}_i,\vec{V}_{c2})$$

$$e_{1i}=-(\vec{\Phi}_i,(\vec{V}_M\cdot\vec{\nabla})\vec{V}_{c_1})-(\vec{\Phi}_i,(\vec{V}_{c_1}\cdot\vec{\nabla})\vec{V}_M)-\frac{1}{\mathrm{Re}}(\vec{\nabla}\vec{\Phi}_i,\vec{\nabla}\vec{V}_{c_1})+\frac{1}{\mathrm{Re}}[\vec{\Phi}_i\vec{\nabla}\vec{V}_{c_1}]$$

$$f_{1ij}=-(\vec{\Phi}_i,(\vec{V}_{c_1}\cdot\vec{\nabla})\vec{\Phi}_j)-(\vec{\Phi}_i,(\vec{\Phi}_j\cdot\vec{\nabla})\vec{V}_{c_1})$$

$$e_{2i}=-(\vec{\Phi}_i,(\vec{V}_M\cdot\vec{\nabla})\vec{V}_{c2})-(\vec{\Phi}_i(\vec{V}_{c2}\cdot\vec{\nabla})\vec{V}_M)-\frac{1}{\mathrm{Re}}(\vec{\nabla}\vec{\Phi}_i,\vec{\nabla}\vec{V}_{c2})+\frac{1}{\mathrm{Re}}[\vec{\Phi}_i\vec{\nabla}\vec{V}_{c2}] \tag{32}$$

$$f_{2ij}=-(\vec{\Phi}_i,(\vec{V}_{c2}\cdot\vec{\nabla})\vec{\Phi}_j)-(\vec{\Phi}_i,(\vec{\Phi}_j\cdot\vec{\nabla})\vec{V}_{c2})$$

$$h_i=-(\vec{\Phi}_i,(\vec{V}_{c_1}\cdot\vec{\nabla})\vec{V}_{c_2})-(\vec{\Phi}_i,(\vec{V}_{c_2}\cdot\vec{\nabla})\vec{V}_{c_1})$$

$$g_{1i}=-(\vec{\Phi}_i,(\vec{V}_{c_1}\cdot\vec{\nabla})\vec{V}_{c_1})$$

$$g_{2i}=-(\vec{\Phi}_i,(\vec{V}_{c_2}\cdot\vec{\nabla})\vec{V}_{c_2}).$$

After we integrate the above equations to obtain the transient amplitudes $y_i(t)$, we can calculate a predicted velocity field $\vec{\mathbf{V}}_G(x,y,t)$ by substituting into Eq. (28)

$$\vec{\mathbf{V}}_G=\vec{V}_M(x,y)+\gamma_1(t)\vec{V}_{c_1}(x,y)+\gamma_2(t)\vec{V}_{c2}(x,y)+\sum_{j=1}^{M}y_j(t)\vec{\Phi}_j(x,y). \tag{33}$$

4 POD Order Reduction of Synthetic Jets

In this section, we outline how proper orthogonal decomposition has been used to generate reduced order models for synthetic jet actuators. In as much as the theoretical foundations of Proper Orthogonal Decomposition (POD) have been discussed elsewhere (Loeve [41], Karhunen [42], Ly and Tran [28]) we focus on the specific protocols employed for the work described in this paper. The POD technique is based on a set of snapshots of the flowfield. In our case, we are interested in the flowfield generated by synthetic jet actuators. We use experimental techniques (PIV) or CFD (FIDAP) to capture the velocity field. Both the experiment and CFD use the same jet geometry and jet membrane operation parameters. We first normalize the velocity field by using the reference scales mentioned earlier. After the snapshots are prepared, we compute the correlation matrix defined as

$$C_{ij}=(1/N)\int_{\Omega}\vec{V}_i(x,y)\cdot\vec{V}_j(x,y)\,d\Omega=(1/N)\int\int_{\Omega}(u_iu_j+\nu_i\nu_j)\,dxdy \tag{34}$$

where $i,j=1,2,\ldots,N$ and

N: total number of snapshots

$\vec{V}_i$: non-dimensional velocity vector at time instance i.

The eigenvalues of the above matrix are solved for, to extract the dominant features (or degrees of freedom):

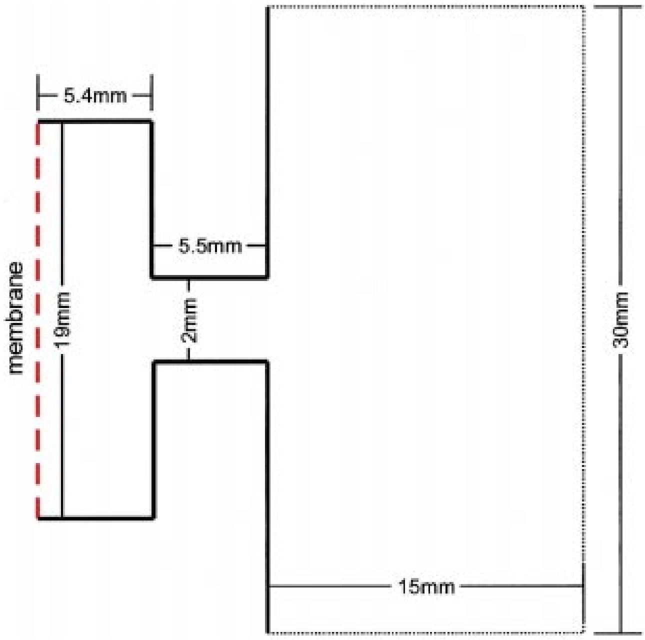

Fig. 1 Computational domain for the simulation

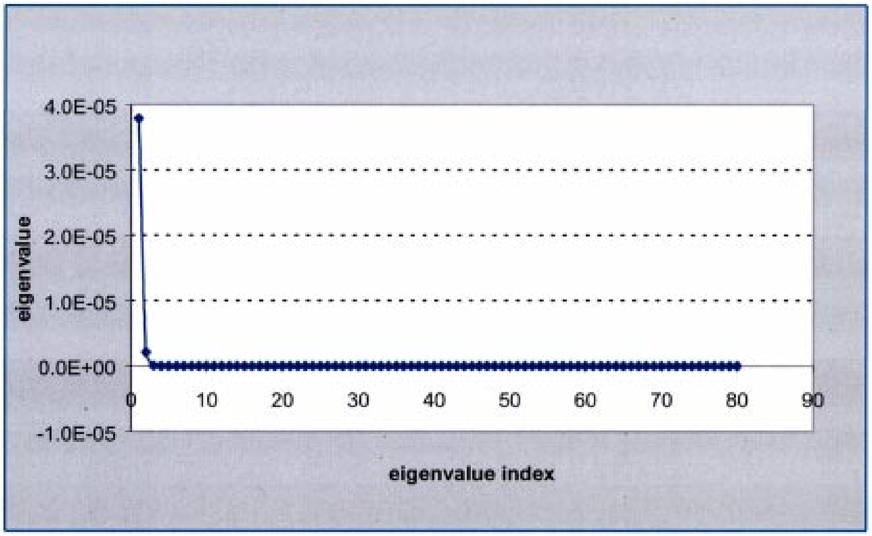

Fig. 2 Eigenvalue distribution

$$CA=\lambda A, \quad A=(a_1,a_2,\ldots,a_N)^T \tag{35}$$

where

$$A^K\cdot A^{K'}=\begin{cases}1/(N\lambda_K), & K=K'\\ 0, & K\neq K'\end{cases}. \tag{36}$$

C is a non-negative symmetric real matrix and has a complete set of orthogonal eigenvectors $A^1, A^2, \ldots, A^N$ with the corresponding eigenvalues $\lambda_1 \geqslant \lambda_2 \geqslant \ldots \geqslant \lambda_N \geqslant 0$.

So the POD basis functions can be expressed as:

$$\vec{\Phi}_K=\sum_{i=1}^{N} a_i^K \vec{V}_i, \quad 1\leqslant K\leqslant N$$
$$(\vec{\Phi}_K,\vec{\Phi}_{K'})=\begin{cases}1, & K=K'\\ 0, & K\neq K'\end{cases} \tag{37}$$

where a_i^K is the ith element of the eigenvector A^K corresponding to the eigenvalue λ_K. It is obvious that the basis functions from definition (37) are divergence free, and the homogeneous boundary condition requirement can be satisfied by constructing a velocity field such that it has homogeneous boundary conditions, as we discussed earlier.

If most of the flow energy is captured in the first M POD modes $(M \ll N)$, then

$$\sum_{i=1}^{M}\lambda_i \cong \sum_{i=1}^{N}\lambda_i. \tag{38}$$

Thus we achieved order reduction, and it is reasonable to approximate the velocity field by using only the first M POD basis functions:

$$\vec{V}(x,y,t)\approx \vec{V}_G(x,y,t)=\sum_{i=1}^{M} y_i(t)\vec{\Phi}_i(x,y)$$
$$=\begin{cases} u_G(x,y,t)=\sum_{i=1}^{M} y_i(t)\Phi_{i_x}\\ v_G(x,y,t)=\sum_{i=1}^{M} y_i(t)\Phi_{i_y}\end{cases} \tag{39}$$

where $\vec{\Phi}_i=(\Phi_{i_x},\Phi_{i_y})$.

Three velocity fields have been involved in our discussions so far: the "exact" field $\vec{V}(x,y,t)$ produced by the numerical simulation (FIDAP) or PIV experiment; the projected field $\vec{V}_P(x,y,t)$ and the predicted field $\vec{V}_G(x,y,t)$. We already discussed $\vec{V}_G$ earlier. $\vec{V}_P(x,y,t)$ is the result of projecting the velocity onto the first M basis functions:

$$\vec{V}_P(x,y,t)\equiv\sum_{i=1}^{M} y_{P_i}(t)\vec{\Phi}_i(x,y)$$
$$\Rightarrow\begin{cases} u_P(x,y,t)\equiv\sum_{i=1}^{M} y_{P_i}(t)\Phi_{i_x}(x,y)\\ v_P(x,y,t)\equiv\sum_{i=1}^{M} y_{P_i}(t)\Phi_{i_y}(x,y)\end{cases}. \tag{40}$$

The projection amplitude $y_{P_i}(t)$ is derived by taking the inner product of the exact velocity field with the basis function $\vec{\Phi}_i$:

$$y_{p_i}(t)=(\vec{V},\vec{\Phi}_i)$$
$$=\int_{\Omega}[u(x,y,t)\Phi_{ix}(x,y)+v(x,y,t)\Phi_{iy}(x,y)]d\Omega.$$

5 Controllability and Output Control

The governing equations in (31) can be expressed in canonical form for nonlinear systems by defining an augmented state vector $\vec{X}(t)\in R^{M+N_c}$ where N_c is the number of controls

$$X_i(t)=y_i(t) \quad i=1\ldots M$$
$$X_{M+j}(t)=\gamma_j(t) \quad j=1\ldots N_c \tag{41}$$

Written as a vector, the states and control vector can be expressed as

$$\vec{X}(t)=\begin{Bmatrix}X_1(t)\\ \vdots\\ X_M(t)\\ X_{M+1}(t)\\ \vdots\\ X_{M+N_c}(t)\end{Bmatrix}=\begin{Bmatrix}y_1(t)\\ \vdots\\ y_M(t)\\ \gamma_1(t)\\ \vdots\\ \gamma_{N_c}(t)\end{Bmatrix},$$
$$\vec{U}(t)=\begin{Bmatrix}u_1(t)\\ \vdots\\ u_{N_c}(t)\end{Bmatrix}=\begin{Bmatrix}\dfrac{d\gamma_1(t)}{dt}\\ \vdots\\ \dfrac{d\gamma_{N_c}(t)}{dt}\end{Bmatrix} \tag{42}$$

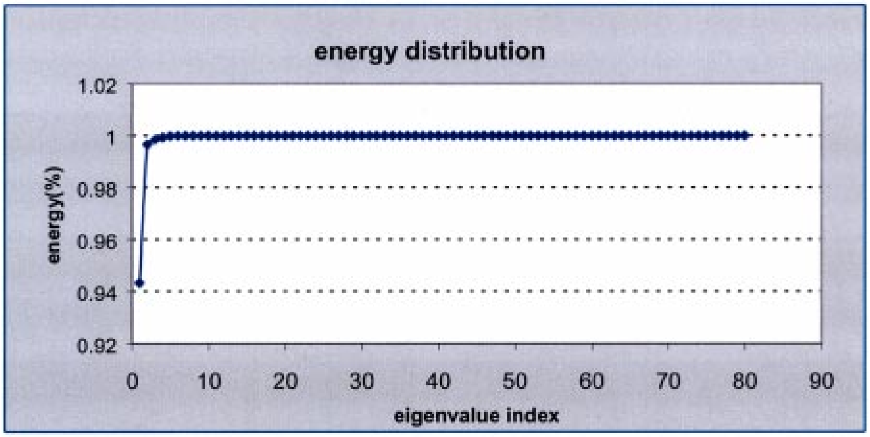

Fig. 3 Energy distribution for eigenvalues

where $u_i(t)$, $i=1,\ldots,N_c$, are the controls. In this case, the governing equations from the last section are written succinctly as

$$\frac{d}{dt}(\vec{X}(t))=\vec{F}(\vec{X}(t))+\vec{G}(\vec{X}(t))\vec{U}(t) \tag{43}$$

where the controls are the time rate of change of the strengths of the jets. The entries of $\vec{F}(\cdot,\cdot):R^{M+N_c}\times R^{+}\rightarrow R^{M+N_c}$ are deduced to be

$$\vec{F}(\vec{X}(t))=\begin{cases} F_i(\vec{X}(t)), & i=1,\ldots,M \\ 0, & i=M+1,\ldots,M+N_c \end{cases} \tag{44}$$

where each of the scalar-valued functions F_i is given by simply re-labeling the entries in the equations derived in the last section, and $R^{+}=[0,\infty)$. The control influence operator $\vec{G}(\cdot)\in R^{M+N_c}\times R^{N_c}$ and control $\vec{U}(t)$ have the following structure

$$\vec{G}(\vec{X}(t))\vec{U}(t)=\begin{bmatrix} d_{1,1} & \cdots & d_{N_c,1} \\ \vdots & & \vdots \\ d_{1,M} & \cdots & d_{N_c,M} \\ 1 & & \\ & \ddots & \\ & & 1 \end{bmatrix}\begin{Bmatrix} u_1(t) \\ \vdots \\ u_{N_c}(t) \end{Bmatrix}$$

$$=\begin{bmatrix} [D]_{M\times N_c} \\ [I]_{N_c\times N_c} \end{bmatrix}\vec{U}(t) \tag{45}$$

where the coefficients $d_{i,j}$ are defined in Eq. (31). It is well-known that the controllability of the nonlinear control problem (43) depends on the definition of the observations

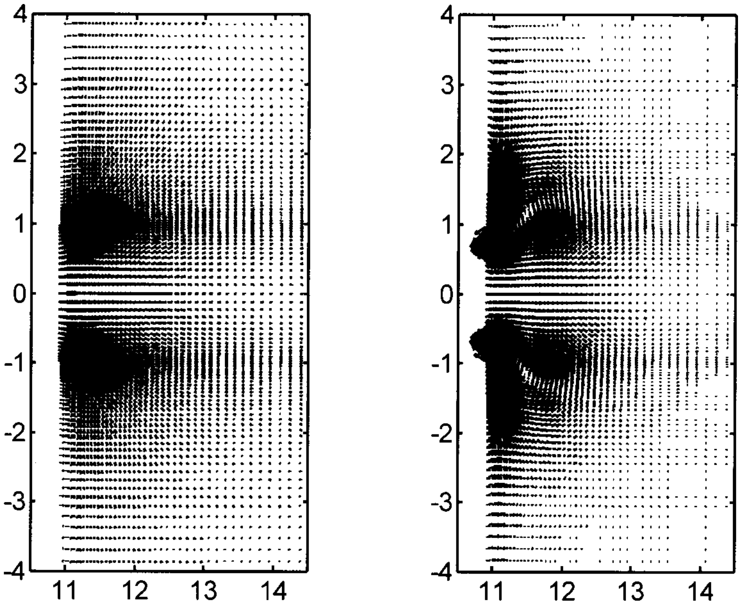

(*a*) First mode (*b*) Second mode

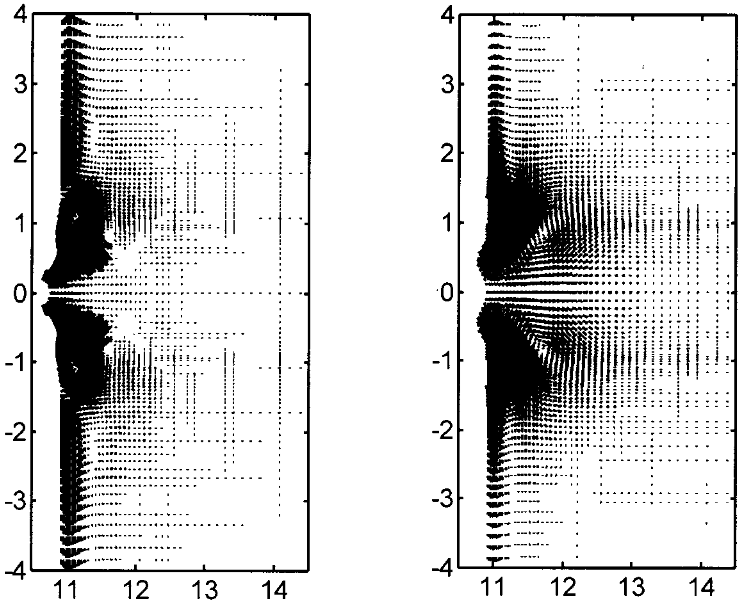

(*c*) Third mode (*d*) Fourth mode

Fig. 4 The first four POD modes

$$\vec{Y}(t)=\vec{H}(\vec{X})=\begin{Bmatrix} Y_1(t) \\ \vdots \\ Y_{N_o}(t) \end{Bmatrix}=\begin{Bmatrix} H_1(\vec{X}(t)) \\ \vdots \\ H_{N_o}(\vec{X}(t)) \end{Bmatrix}. \qquad (46)$$

It is likewise known that questions of controllability can be delicate to address when the number of states, number of controls and number of observations are varied in number and in their nature. Still, we seek justification that the control methodology proposed in this paper, that is control via oscillatory zero-mass-flux jets, is well-motivated. At the very least, we wish to establish that certain ‘‘canonical’’ choices of controls, observations and states lead to well-conceived, controllable systems. To this end, let us suppose that $N_c=N_o=M$. That is, the number of controls, the number of measurements and the number of reduced states are equal. For the sake of illustration, we choose as observations the time-varying amplitudes of the reduced states

$$\begin{Bmatrix} Y_1(t) \\ \vdots \\ Y_M(t) \end{Bmatrix}=\begin{Bmatrix} H_1(\vec{X}(t)) \\ \vdots \\ H_M(\vec{X}(t)) \end{Bmatrix}=\begin{Bmatrix} X_1(t) \\ \vdots \\ X_M(t) \end{Bmatrix}. \qquad (47)$$

Recall that for any scalar-valued function $\lambda(x)$, the (Lie) derivative of $\lambda(x)$ along a vector field $\vec{\nu}(x)$ is given recursively by

$$\begin{aligned} L_{\vec{\nu}}\lambda(x)&=\lambda(x) \\ L_{\vec{\nu}}^{1}\lambda(x)&=\sum_i \frac{\partial\lambda}{\partial x_i}\nu_i(x) \\ &\vdots \\ L_{\vec{\nu}}^{k}\lambda(x)&=\sum_i \frac{\partial(L_{\vec{\nu}}^{k-1}\lambda(x))}{\partial x_i}\nu_i(x) \end{aligned} \qquad (48)$$

The nonlinear system (43) is said to have relative degree $\{r_1,r_2\cdots r_M\}$ at some $\vec{X}_0$ if

(i) $L_{\vec{g}_j}^{0}L_{\vec{F}}^{k}H_i(x)=0$, for all $j=1,\ldots,M$, $k<r_i-1$ and for all $\vec{X}$ in a neighborhood of $\vec{X}_0$, and

(ii) the $M\times M$ matrix,

$$\begin{bmatrix} L_{\vec{g}_1}L_{\vec{F}}^{r_1-1}H_1(x) & \cdots & L_{\vec{g}_M}L_{\vec{F}}^{r_1-1}H_1(x) \\ \vdots & & \vdots \\ L_{\vec{g}_1}L_{\vec{F}}^{r_M-1}H_M(x) & \cdots & L_{\vec{g}_M}L_{\vec{F}}^{r_1-1}H_M(x) \end{bmatrix}$$

is nonsingular at $\vec{X}_0$.

We have the following theorem that guarantees that, at least in this idealized scenario, the nonlinear control problem is well-conceived:

Theorem:

Consider the nonlinear control system associated with the reduced order zero-mass-flux system

$$\begin{aligned} \frac{d}{dt}(\vec{X}(t))&=\vec{F}(\vec{X}(t))+\vec{G}(\vec{X}(t))\vec{U}(t) \\ \vec{Y}(t)&=\vec{H}(\vec{X}(t)) \end{aligned} \qquad (49)$$

where $\vec{X}$, $\vec{Y}$, $\vec{F}(\cdot,\cdot):R^{M+N_c}\times R^{+}\rightarrow R^{M+N_c}$, $\vec{G}(\cdot)\in R^{M+N_c}\times R^{N_c}$, *and* $\vec{U}(t)$ *are defined in Eqs. (41)–(45). If the control functions* $\vec{V}_{c_1}\cdots\vec{V}_{c_M}$ *and test functions* $\vec{\xi}_1\cdots\vec{\xi}_M$ *satisfy*

$$\det|(\vec{\xi}_i,\vec{V}_{c_M})|\neq 0 \qquad (50)$$

then the reduced order nonlinear control system is globally, exponentially output stabilizable.

Proof:

The proof of this theorem is straightforward. If $\det|(\vec{\xi}_i,\vec{V}_{c_M})|\neq 0$, *then*

$$\begin{bmatrix} L_{\vec{g}_1}L_{\vec{F}}^{0}H_1(x) & \cdots & L_{\bar{g}_M}L_{\vec{F}}^{0}H_1(x) \\ \vdots & & \vdots \\ L_{\vec{g}_1}L_{\vec{F}}^{0}H_M(x) & \cdots & L_{\bar{g}_M}L_{\vec{F}}^{0}H_M(x) \end{bmatrix}=[(\vec{\xi}_i,\vec{V}_{c_i})]^T \qquad (51)$$

is nonsingular. The relative degree of the system is $\{r_1,r_2\cdots r_M\}=\{1,1,1,\cdots,1\}$. The global exponential output stabilizability then follows via standard arguments (see Isidori [6]).

Clearly, this theorem represents an idealized scenario. The physical realization of this control methodology would require the real-time measurement of the amplitudes of all reduced order states, as well as the time-varying amplitude of the jet. It is conceivable that modern flow diagnostics will enable the real-time measurement of the time-varying amplitude of the synthetic jet. However, it is problematic as to whether any of the reduced order states, particularly those associated with global POD modes, could be observed in real-time. Furthermore, this theorem says nothing regarding the accuracy of the reduced order model in the closed loop, the applicability of the reduced order model for varying flow regimes or the actual stabilizability of the underlying infinite dimensional system.

With these limitations in mind, however, we view this theorem as a necessary first assessment of the potential of flow control via

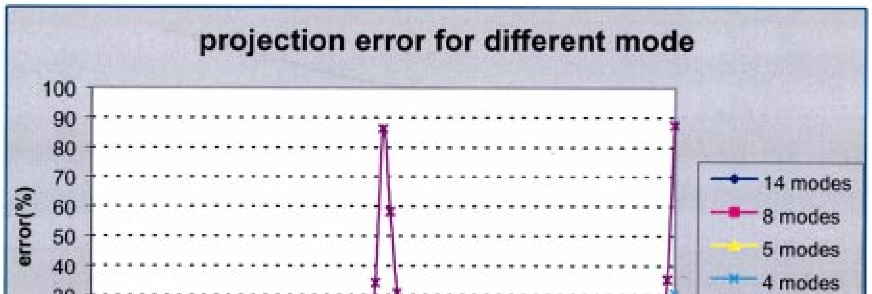

Fig. 5 Projection error for different number of modeS

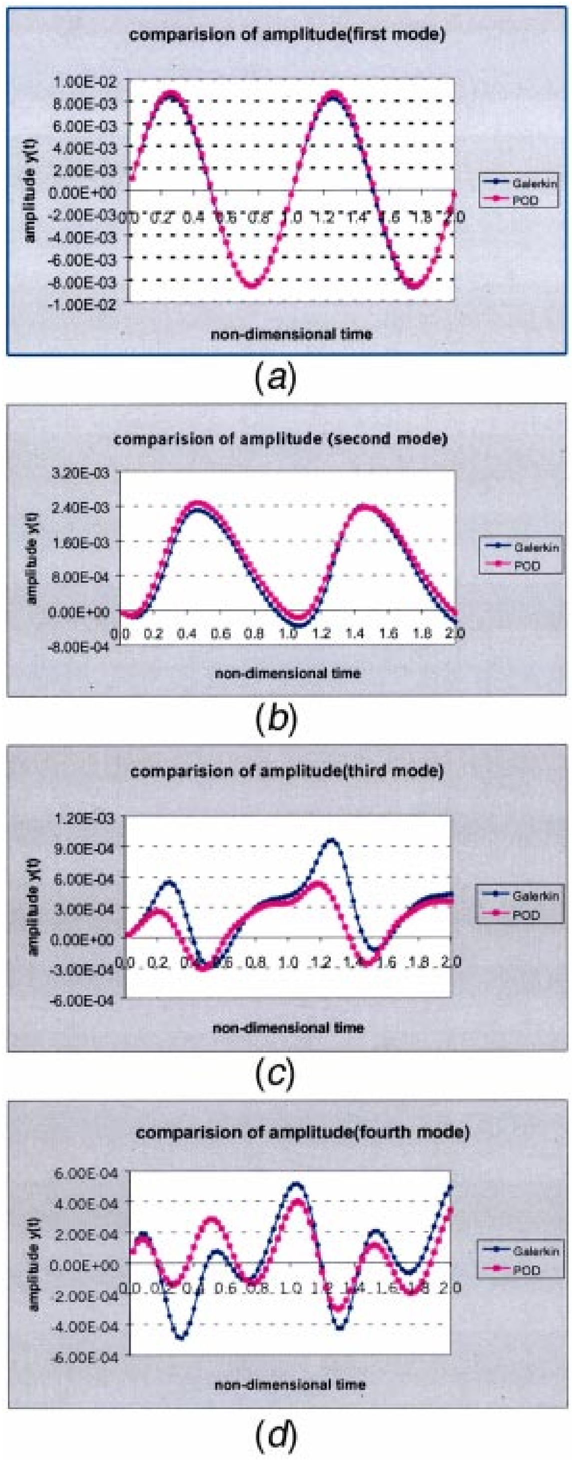

Fig. 6 Comparison of amplitudes for each mode: (*a*) first mode, (*b*) second mode, (*c*) third mode, (*d*) fourth mode

synthetic jets. In addition, further study along the same lines of reasoning should be pursued for realistic observation sets

$$\vec{Y}(t)=\vec{H}(\vec{X})=\left\{\begin{matrix} Y_1(t)\\ \vdots \\ Y_{N_o}(t)\end{matrix}\right\}=\left\{\begin{matrix} H_1(\vec{X}(t))\\ \vdots \\ H_{N_o}(\vec{X}(t))\end{matrix}\right\} \tag{52}$$

that arise from measurements that are realizable.

6 Synthetic Jet Low-Order Modeling

The objective of the work presented in this section is to investigate how "amenable" synthetic jet flows are to order reduction techniques such as POD, and derive low-order dynamic models for synthetic jet flows. For this purpose, FIDAP was used to solve the flowfield for a 2-D synthetic jet, at a Strouhl number of St $=0.175$ and a Reynolds number of Re$=228$. Figure 1 presents the computational domain. The membrane oscillation frequency was 10 Hz, and the velocity at the membrane is modeled as

$$\vec{V}(t)=\left\{\begin{matrix} 6\sin(20\pi t)\\ 0\end{matrix}\right\}(\text{mm/s}). \tag{53}$$

Please note that the above geometry of the computational domain and the operating conditions of the jet are based on water tunnel experiments of synthetic jets at the Department of Aerospace Engineering of Texas A&M University. To make the task more challenging, transient effects were included. With the membrane starting from rest, the first two periods of the flowfield were solved for and 80 snapshots of the flowfield, during these two periods, were used to generate 80 POD modes

$$\vec{\Phi}_i(x,y), \quad i=1,\ldots,80.$$

Figure 2 presents a plot of the eigenvalue magnitudes, while Fig. 3 presents the percentage of the flowfield energy captured by the first M eigenmodes. It is interesting to note that 94% of the flow energy is captured by the first eigenvalue, while the first 5 eigenvalues capture over 99% of the energy. Physically, this can be explained by considering the fact that for this St value, the majority of the flow energy is contained in the two counter-rotating vortices and the forward flow, directed away from the jet exit, which is exactly the flow pattern in the first couple of eigenmodes. The above strongly suggests that this class of synthetic jet flows are very amenable to POD order reduction techniques. The first four POD modes are shown in Fig. 4.

Subsequently, only a few of these modes were used to reconstruct the flowfield at individual time instants, according to Eq. (39). The error between the exact and the projected flowfields, given by Eq. (54), is presented in Fig. 5.

$$\text{Error}=\frac{\|\vec{V}-\vec{V}_P\|_{l_2}}{\|\vec{V}\|_{l_2}}\times 100$$
$$=\frac{\left[\sum_{i,j}\{(u_{i,j}-u^P_{i,j})^2+(v_{i,j}-v^P_{i,j})^2\}\right]^{1/2}}{\left[\sum_{i,j}(u^2_{i,j}+v^2_{i,j})\right]^{1/2}}\times 100. \tag{54}$$

It is noted that the error decreases as the number of modes increases, and that as few as four modes are enough to approximate the flowfield with acceptable errors for control purposes. Subsequently, a dynamical model for the flowfield was derived through the Galerkin projection procedure described earlier. Only four POD modes were considered. For the present application, since the pressure was known everywhere, the velocity decomposition techniques presented earlier (Eq. 28) were not necessary. The Galerkin projection yielded the four amplitudes $y_i(t)$ ($i=1,2,3,4$) corresponding to the four modes. Figure 6 presents the comparison between these mode amplitudes and the amplitudes derived by projecting the exact flowfield onto the four POD modes at each one of the 80 time instants. Very good agreement can be observed. Thus, the derived four-mode dynamical model of the flowfield is:

$$\vec{V}(x,y,t)=\sum_{i=1}^{4} y_i(t)\vec{\Phi}_i(x,y).$$

Qualitative comparisons between the model and the exact flowfield, in the neighborhood of the jet exit where most of the flow complexity resides, are shown in Fig. 7 for four different time

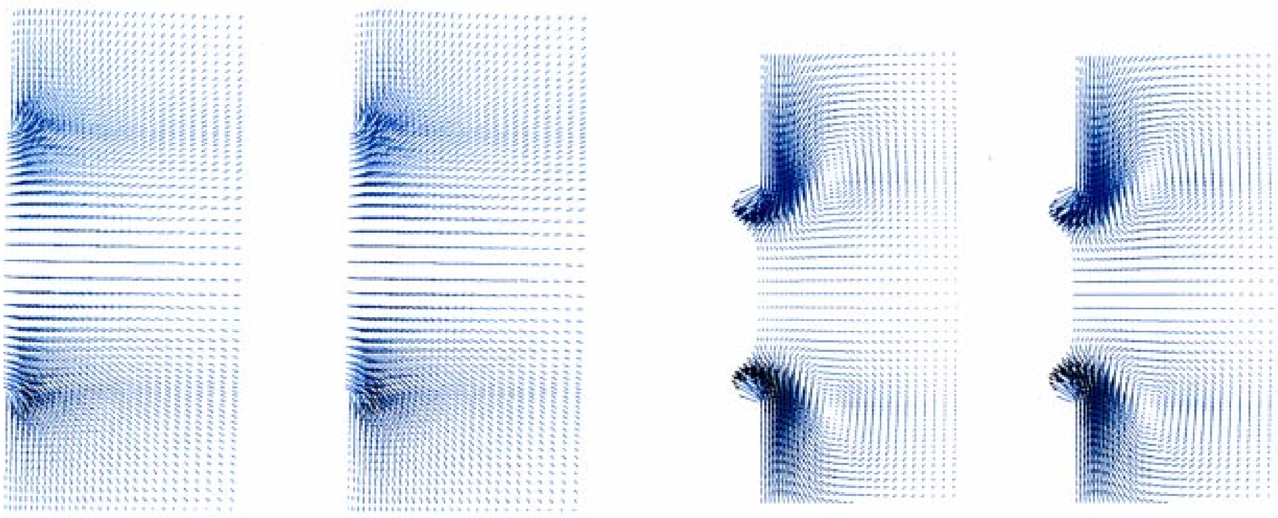

(*a*) at t/T=0.025

(*c*) at t/T=0.525

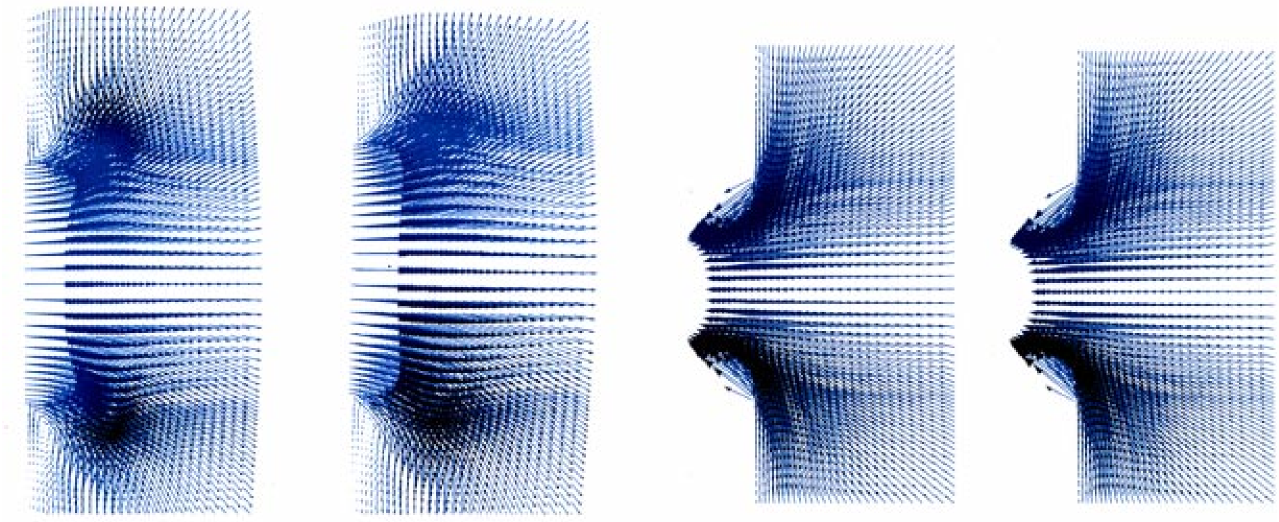

(*b*) at t/T=0.275

(*d*) at t/T=0.775

Fig. 7 Comparison of flow field (left—FIDAP, right—Galerkin): (*a*) t/T=0.025, (*b*) t/T=0.275, (*c*) t/T=0.525, (*d*) t/T=0.775

instants corresponding to $t/T=0.025, 0.275, 0.525, 0.775$. Very good qualitative agreement (and quantitative agreement, to be presented in an upcoming paper) can be observed.

7 Conclusions

In order to enable real-time control of synthetic jet actuated flows, low-order modeling of two-dimensional synthetic jet flows was derived via Proper Orthogonal Decomposition (POD). A dynamical model of the flow was derived via Galerkin projection for specific St and Re values. It was shown that accurate modeling of such flows in the open loop response is possible with as few as four modes. While the current numerical experiments are focused on one set of operating conditions and on the flowfield near the jet orifice, a discussion of how to extend the model for a range of St and Re values will be presented in a forthcoming paper. Controllability of the reduced order models that result from POD approximations was also addressed. It was shown that certain ''canonical'' choices of controls, observations and states lead to well-conceived, controllable systems. In fact, the systems are exponentially output stabilizable under suitably strict assumptions on the set of observations and control functions.

Acknowledgments

This work was supported by the Office of Naval Research under contract number N000014-97-1-0943. Special thanks go to Dr. Allen Moshfegh, the technical monitor of the program, for his support.

References

[1] Amitay M., Smith B. L., and Glezer A., 1998, ''Aerodynamic Flow Control Using Synthetic Jet Technology,'' AIAA Paper No. 98-0208, 36th Aerospace Sciences Meeting & Exhibit, Reno, NV.

[2] Smith, D., Amitay, M., Kibens, V., Parekh, D., and Glezer, A., 1998, ''Modifications of Lifting Body Aerodynamics Using Synthetic Jet Actuators,'' AIAA Paper No. 98-0209, 36th Aerospace Sciences Meeting & Exhibit, Reno, NV.

[3] Seifert, A. and Pack, L., 1999, ''Oscillatory Excitation of Unsteady Compressible Flows over Airfoils at Flight Reynolds Number,'' AIAA Paper No. 99-0925.

[4] Joshi, S. S., Speyer, J. L., and Kim, J., 1997, ''A Systems Theory Approach to the Feedback Stabilization of Infinitesimal and Finite-Amplitude Disturbances in Plane Poiseuille Flow,'' J. Fluid Mech., **332**, pp. 157–184.

[5] Gilarranz, J., Singh, K., Ko, J., Rediniotis, O. K., and Kurdila, A. J., 1997, ''High Frame-Rate, High Resolution Cinematographic Particle Image Velocimetry,'' AIAA Paper 97-0495.

[6] Isidori, A., 1989, *Nonlinear Control Systems*, Springer-Verlag.

[7] Krstic, M., Kanellakopoulos, I., Kokotovic, P., 1995, *Nonlinear and Adaptive Control Design*, Wiley, New York.

[8] Sheen, J.-J., and Bishop, R. H., 1994, ''Adaptive Nonlinear Control of Spacecraft,'' J. Astronaut. Sci., **42**(4), pp. 451–472.

[9] Ko, J., Kurdila, A. J., and Strganac, T. W., 1997, ''Nonlinear Control of a Prototypical Wing Section with Torsional Nonlinearity,'' J. Guid. Control Dyn., **20**(6).

[10] Cuvelier, P., 1976, ''Optimal Control of a System Governed by the Navier-Stokes Equations Coupled with the Heat Equations,'' in W. Eckhaus, ed., *New Developments in Differential Equations*, North-Holland, Amsterdam, pp. 81–98.

[11] Gunzburger, M., and Lee, H. C., 1994, ''Analysis, Approximation, and Computation of a Coupled Solid/Fluid Temperature Control Problem,'' Comput. Methods Appl. Mech. Eng., **118**, pp. 133–152.

[12] Burns, J. A., and Ou, Y., 1994, ''Feedback Control of the Driven Cavity Problem Using LQR Designs,'' *Proceedings of the 33rd Conference on Decision and Control*, pp. 289–294, Lake Buena Vista, FL, Dec.

[13] Banks, H. T., and Ito, K., 1994 ''Structural Actuator Control of Fluid/Structure Interactions,'' Proceedings of the 33rd Conference on Decision and Control, Lake Buena Vista, FL, pp. 283–288.

[14] Desai, M., and Ito, K., 1994, ''Optimal Control of Navier-Stokes Equations,'' SIAM J. Control Optim., **32(5)**, pp. 1428–1446.

[15] Ito, K., and Kang, S., 1994, ''A Dissipative Feedback Control Synthesis for Systems Arising in Fluid Dynamics,'' SIAM J. Control Optim., **32**(3), pp. 831–854.

[16] Ravindran, S. S., and Hou, L. S., 1998, ''A Penalized Neumann Control Approach for Solving an Optimal Dirichlet Control Problem for the Navier-Stokes Equations,'' SIAM J. Control Optim., **36**(5), pp. 1795–1814.

[17] Hou, L. S., and Yan, Y., 1997, ''Dynamics for Controlled Navier-Stokes Systems with Distributed Controls,'' SIAM J. Control Optim., **35**(2), pp. 654–677.

[18] Fattorini, H. O., and Sritharan, S. S., 1992, ''Existence of Optimal Controls for Viscous Flow Problems,'' Proc. R. Soc. London, Ser. A, **439**, pp. 81–102.

[19] Fattorini, H. O., and Sritharam, S. S., 1995, ''Optimal Chattering Controls for Viscous Flow,'' Nonlinear Analysis, Theory & Applications, **25**(8), pp. 763–797.

[20] Fursikov, A. V., Gunzburger, M. D., and Hou, L. S., 1998, ''Boundary Value Problems and Optimal Boundary Control for the Navier-Stokes System: The Two Dimensional Case,'' SIAM J. Control Optim., **36**(3), pp. 852–894, May.

[21] Joslin, R. D., Gunzburger, M. D., Nicolaides, R. A., Erlehbacher, G., and Hussaini, M. Y., 1997, ''Self-Contained Automated Methodology for Optimal Flow Control,'' AIAA J., **35**(5).

[22] Joslin, R. D., 1997, ''Direct Numerical Simulation of Evolution and Control of Linear and Nonlinear Disturbances in Three Dimensional Attachment Line Boundary Layers,'' NASA Technical Paper 3623.

[23] Wygnanski, I., 1997, ''Boundary Layer and Flow Control by Periodic Addition of Momentum,'' 4th AIAA Shear Flow Control Conference,'' Snowmass Village, CO, June 29–July 2, AIAA Paper No. 97-2117.

[24] Trujillo, S. M., Bogard, D. G., and Ball, K. S., 1997, ''Turbulent Boundary Layer Drag Reduction Using an Oscillating Wall,'' *28th AIAA Fluid Dynamics Conference, 4th AIAA Shear Flow Control Conference*, Snowmass Village, CO, June 29–July 2, AIAA Paper No. 97-1870.

[25] Bewley, T. R., Moin, P., and Temam, R., 1997, ''Optimal and Robust Approaches for Linear and Nonlinear Regulation Problems in Fluid Mechanics,'' *28th AIAA Fluid Dynamics Conference, 4th AIAA Shear Flow Control Conference*, Snowmass Village, CO, June 29–July 2, AIAA Paper No. 97-1872.

[26] Cho, Y., Agarwal, R. K., and Nho, K., 1997, ''Neural Network Approaches to Some Model Flow Control Problems,'' 4th AIAA Shear Flow Conference, Snowmass Village, CO, June 29–July 2.

[27] Aubry, N., Holmes, P., Lumley, J. L., and Stone, E., 1988, ''The Dynamics of Coherent Structures in the Wall Region of a Turbulent Boundary Layer,'' J. Fluid Mech., **192**, pp. 115–173.

[28] Ly, H. V., and Tran, H. T., 1998, ''Proper Orthogonal Decomposition for Flow Calculations and Optimal Control in a Horizontal CVD Reactor,'' Technical Report, Center for Research in Scientific Computation, North Carolina State University.

[29] Corke, T. C., Glauser, M. N., and Berkooz, G., 1994, ''Utilizing Low Dimensional Dynamical Systems Models to Guide Control Experiments,'' Appl. Mech. Rev., **47**(6), Part 2, June, pp. 132–138.

[30] Ito, K., and Ravindran, S. S., 1996 ''Reduced Basis Method for Flow Control,'' Technical Report CRSC-TR96-25, Center for Research in Scientific Computation, North Carolina State University.

[31] Ito, K., and Ravindran, S. S., 1997 ''A reduced basis method for control problems governed by PDEs,'' Technical Report CRSC-TR-97-1, Center for Research in Scientific Computation, North Carolina State University.

[32] Craig, R. R., 1981, *Structural Dynamics*, Wiley, New York.

[33] Skelton, R. E., 1988, *Dynamic Systems and Control*, Wiley, New York.

[34] Tang, D., Conner, M., and Dowell, E., 1997, ''A Reduced Order Finite State Aerodynamic Model and Its Application to a Nonlinear Aeroelastic System,'' preprint.

[35] Elezgaray, J., Berkooz, G., Dankowicz, H., Holmes, P., and Myers, M., 1997, ''Local Models and Large Scale Statistics of the Kuramoto-Sivashinsky Equation,'' *Wavelets and Multiscale Methods for Partial Differential Equations*, W. Dahmen, A. Kurdila, and P. Oswald, eds., Academic Press.

[36] Wickerhauser, M. V., Farge, M., Goirand, E., Wesfreid, E., and Cubillo, E., 1994, ''Efficiency Comparison of Wavelet Packet and Adapted Local Cosine Bases for Compression of a Two Dimensional Turbulent Flow,'' *Wavelets: Theory, Algorithms, and Applications*, Chui, C., Montefusco, L., and Puccio, L., eds., Academic Press, pp. 509–532.

[37] Ko, J., Kurdila, A. J., Gilarranz, J. L., and Rediniotis, O. K., 1998, ''Particle Image Velocimetry via Wavelet Analysis,'' AIAA J., **36**(8), pp. 1451–1459.

[38] Ko, J., Kurdila, A. J., and Rediniotis, O. K., 1999, ''Divergence Free Bases and Multiresolution Methods for Reduced-Order Flow Modeling,'' AIAA J., in review.

[39] Gunzburger, M. D., 1989, *Finite Element Methods for Viscous Incompressible Flows: A Guide to Theory, Practice, and Algorithms*, Academic Press, Boston, MA.

[40] Temam, R., 1977, *Navier-Stokes Equations*, North-Holland Publishing Company.

[41] Leove, M., 1945, ''Functions Aleatoire de Second Ordre,'' Compte Rend. Acad. Sci. (Paris).

[42] Karhunen, K., 1946, ''Zur Spektral Theorie Stochasticher Prozesse,'' Ann. Acad. Sci. Fennicae, Ser. A1, Math. Phys., **37**.

[43] Ball, K. S., Sirovich, L., and Keefe, L. R., 1991, ''Dynamical Eigenfunction Decomposition of Turbulent Channel Flow,'' Int. J. Numer. Methods Fluids, **12**, pp. 585–604.

[44] Berkooz, G., Holmes, P., and Lumley, J. L., 1993, ''The Proper Orthogonal Decomposition in the Analysis of Turbulent Flows,'' Annu. Rev. Fluid Mech., **25**, pp. 539–575.

[45] Greenblatt, D. and Wygnanski, I., 1998, ''Dynamic Stall Control By Oscillatory Forcing,'' AIAA 98-0676.

[46] Greenblatt, D., Darabi, A., Nishri, B., and Wygnanski, I., 1998, ''Separation Control By Periodic Addition of Momentum with Particular Emphasis on Dynamic Stall,'' Proceedings Heli Japan 98, Paper T3-4, American Helicopter Society.

[47] Reichert, R. S., Hatay, F. F., Biringen, S., and Huser, A., 1994, ''Proper Orthogonal Decomposition Applied to Turbulent Flow in a Square Duct,'' J. Phys. Fluids, **6**(9), pp. 3086–3092.

[48] Seifert, A., Bachat, T., Koss, D., Shepshelovich, M., Wygnanski, I., 1993, ''Oscillatory Blowing: A Tool to Delay Boundary-Layer Separation,'' AIAA J., **31**(11), pp. 2052–2060.

Bifurcations of Flow Through Plane Symmetric Channel Contraction

T. P. Chiang

Tony W. H. Sheu[1]

Department of Engineering Science and
Ocean Engineering,
National Taiwan University,
73 Chou-Shan Road,
Taipei 106,
Taiwan, R.O.C.

Computational investigations have been performed into the behavior of an incompressible fluid flow in the vicinity of a plane symmetric channel contraction. Our aim is to determine the critical Reynolds number, above which the flow becomes asymmetric with respect to the channel geometry using the bifurcation diagram. Three channels, which are characterized by the contraction ratio, are studied and the critical Reynolds numbers are determined as 3075, 1355, and 1100 for channels with contraction ratios of 2, 4, and 8, respectively. The cause and mechanism explaining the transition from symmetric to asymmetric states in the symmetric contraction channel are also provided.

[DOI: 10.1115/1.1467643]

1 Introduction

There exist many practical applications in which the flow behavior downstream of a sudden geometric contraction is important, with the non-Newtonian flow case being of particular interest. Several investigations have been performed in order to understand the incompressible flow downstream of a channel contraction, which is planar and is normal to the direction of the channel wall. These investigations have been both experimental, see, for example, Durst et al. [1], and numerical, for example, the works of Dennis and Smith [2], Hunt [3], Hawken et al. [4], and Huang and Seymour [5]. The above cited stream function-vorticity analyses employed different ways of avoiding the infinite vorticity at the sharp corners. Investigations into this channel flow allow better understanding of flow separation, re-attachment and recirculation, which are common features in engineering practice. As a result, we conduct a parametric study by varying the Reynolds numbers and the contraction ratios.

When conducting experiments for the flow downstream of a plane, symmetric channel expansion, Cherdron et al. [6] and Sobey [7] observed a larger recirculation region which appeared preferentially at one wall of the channel, thus indicating the existence of a critical Reynolds number, Re_c, above which the flow becomes substantially different from that observed below this value. When the flow is no longer symmetric about the centerline of the channel, a process known as pitchfork bifurcation has been found to occur. Under these circumstances, momentum transfer proceeds between the fluid shear layers. This transfer in momentum, in turn, causes a pressure gradient to form across the channel. Such a pressure gradient may lead to an asymmetric flow. We refer to this phenomenon as the Coanda effect [8]. Numerical simulation of the contraction flow in geometrically symmetric channels has been conducted mostly in a half domain [1–5]. In this paper, we address the bifurcation flow in the full sudden contraction channel.

The remaining sections of this paper are organized as follows. In Section 2, we present the modeling equations with which we will work. This is followed by use of the finite volume discretization method and the segregated solution algorithm. In Section 4, we describe first the computational details and then the numerical results, with emphasis on the effects of contraction ratio and the Reynolds number on the flow asymmetry. Also, the mechanism for the transition from symmetric to asymmetric states is provided. Finally, in Section 5, we provide concluding remarks.

2 The Mathematical Model

In the present investigation, we simulated the flow of an incompressible fluid through a two-dimensional contraction channel. Referring to Fig. 1, the centerline of the channel is positioned at $y=0$. The upstream channel height and the step height are D and $1/2(D-d)$, respectively. The channel height downstream of the contraction is d, leading to a contraction ratio $C=D/d$. The governing equations for simulating this channel flow can be expressed in vector form as:

$$\mathbf{u}\cdot\nabla\mathbf{u}=-\nabla p+\frac{1}{\mathrm{Re}}\nabla^2\mathbf{u}, \tag{1}$$

$$\nabla\cdot\mathbf{u}=0. \tag{2}$$

In the above equations, u and v are the components of the velocity vector $\mathbf{u}$ in the x and y directions, respectively, and p is the static pressure. These primitive variables have been normalized by dividing u and v by the inlet mean velocity, U_{mean}, and p by ρU_{mean}^2, where ρ is the fluid density. The independent variables are non-dimensionalized by the upstream channel height D, leading to the Reynolds number, $\mathrm{Re}=\rho U_{\mathrm{mean}}D/\mu$, where μ denotes the dynamic viscosity.

Upstream of the step plane, the fluid enters the channel at $x=-2.5$, at which a fully developed velocity profile is prescribed as $\mathbf{u}=(6(0.5+y)(0.5-y),0)$. The channel exit is considered to

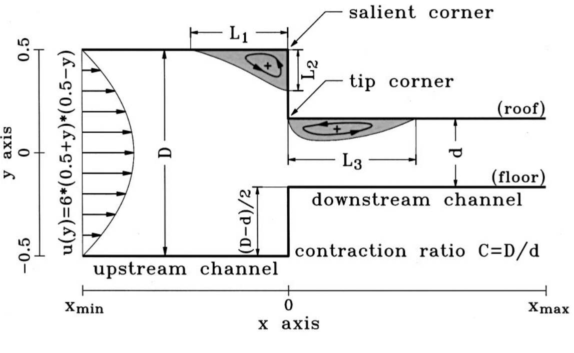

Fig. 1 The geometry and controlling lengths that can characterize the flow reversal in the contraction channel

---

[1] Author to whom all corresondence should be sent.
e-mail: sheu@sccs.na.ntu.edu.tw.

Contributed by the Fluids Engineering Division for publication in the JOURNAL OF FLUIDS ENGINEERING. Manuscript received by the Fluids Engineering Division March 16, 1999; revised manuscript received November 7, 2001. Associate Editor: U. Ghia.

Table 1 The computed separation and reattachment lengths for the case of $C=2$

Length	L_1		L_2		L_3	
Reynolds number Re	1000	2000	1000	2000	1000	2000
Dennis & Smith [2]	0.138	0.182	0.081	0.093	---	---
Hunt [3]	0.154	0.197	0.082	0.094	0.207	0.481
Hawken et al. [4]	0.143	---	0.077	---	0.239	---
Huang & Seymour [5]	0.138	---	0.081	---	0.222	---
Present: 40*20, h = 1/20	0.085	0.145	0.056	0.067	none	none
80*40, h = 1/40	0.162	0.202	0.081	0.093	0.182	0.345
160*80, h = 1/80	0.152	0.198	0.084	0.094	0.254	0.639
320*160, h = 1/160	0.146	0.191	0.083	0.095	0.269	0.606
640*320, h = 1/320	0.142	0.186	0.083	0.094	0.235	0.568
1280*640, h = 1/640	0.140	0.183	0.082	0.094	0.222	0.543

be sufficiently far from the step to allow the flow to have a zero gradient velocity profile. Given this assumption we prescribe zero gradient velocity vector at $x=5$. The no-slip velocity condition is, as a usual, prescribed on the solid walls. In addition to accommodating closure boundary conditions [9], the presently employed primitive-variable formulation can avoid dealing with the corner singularity, which is encountered in the stream function-vorticity formulation.

3 The Numerical Model

As the name of finite volume method indicates, working Eqs. (1)–(2) are integrated in their respective finite volume, each of which are associated with a particular primitive variable and is placed on the centroid of the finite volume. A serious problem, which has been encountered when simulating incompressible Navier-Stokes equations, is checkerboard pressure oscillations. To overcome this difficulty, field variables are stored at staggered grids. Numerical simulation of incompressible Navier-Stokes equations entails another instability, which is evident from the oscillatory velocities, when dominated advective terms are discretized using centered schemes. The loss of convective stability is particularly pronounced in multi-dimensional flow simulations. To fix this problem, we have modified the QUICK scheme of Leonard [10] and implemented it in non-uniform grids to resolve this instability problem and avoid the false diffusion error. Discretization of other derivatives is performed using the centered-scheme for revealing their elliptic characters. For a more detailed representation of the nonuniform flux discretization, see for example Chiang et al. [11].

In solving the finite volume discretized equations for (1)–(2), we abandon the coupled approach due to the need for much more disk storage space compared to the space needed when solving these equations separately by the consistent SIMPLE (or SIMPLE-C) solution algorithm [12]. Use of this algorithm has been found to produce accurate results with a good rate of convergence. The pressure field is solved using the pressure correction method. In the staggered meshes, there are no storage points for the pressure at the domain boundary. As a result, specification of pressure boundary conditions is not needed. The scheme adopted here has been validated against analytic scalar transport equation and Navier-Stokes equations to ensure accuracy in space. The interested reader can refer to Chiang and Sheu [13]. In all the cases investigated, the solution was said to have converged when the global L_2-norm of pressure and velocity residuals reached a value below 10^{-15}. Besides this stringent convergence requirement, it is also demanded that the relative difference of mass flux between the inlet and other arbitrarily chosen cross sections be less than 10^{-10}.

4 Numerical Results

In the present investigation, a computer code was run to simulate the fluid flow through three channels, each of which contains a plane symmetric contraction. The channel geometry is characterized by the dimensionless contraction ratio $C=2$, 4, 8. Reynolds numbers in the wide range of $0.1\leqslant \mathrm{Re}\leqslant 4000$ for the case of $C=2$ and in the range of $0.1\leqslant \mathrm{Re}\leqslant 2000$ for cases $C=4$, 8 were considered in order to allow us to study the Coanda effect. When conducting a numerical simulation, it is important to obtain grid-independent solutions. For this purpose, we will consider rectangular Cartesian grids, which are overlaid uniformly on the region of interest. For the case of $C=2$, grid sizes with $\Delta x=\Delta y=1/20$, 1/40, 1/80, 1/160, 1/320, and 1/640 were used in the grid refinement study. We considered that grid-independent solutions

Table 2 Grid details of Grid-A

C	$x_{\min}$	$x_{\max}$	N-Δx	N-Δy	$(\Delta x_{\min}, \Delta x_{\max})$	$(\Delta y_{\min}, \Delta y_{\max})$
2	-2.5	+5.0	110	130	(0.001, 0.25)	(0.0005, 0.022)
4	-2.5	+5.0	110	180	(0.001, 0.25)	(0.0005, 0.010)
8	-2.5	+5.0	110	180	(0.001, 0.25)	(0.0005, 0.008)

had been obtained when the separation length L_1 and reattachment lengths L_2 and L_3, as schematically shown in Fig. 1, all differed by less than 5% for two successive grids. The finer of the two grids was then chosen to produce the solution.

Table 1 tabulates the computed lengths for flow conditions considered at Re=1000 and 2000. For comparison purposes, other numerical data [2–5] are also included in the table. It can be seen that, for the channel with $C=2$, the agreement between the data is very good. Although very accurate solutions can be obtained, it is fairly expensive to conduct all calculations in the finest grid, which involves 1280 and 640 nodes along the x and y directions, respectively. It is more appropriate to locally refine grids in the region of the contraction and in regions near the solid wall. Use of grids tabulated in Table 2 was shown to produce no observable difference in the velocities obtained from the finest uniform grid. Grid-A consumes only 1/60 of the grid points for the case with the uniform grid size 1/640. In our computational results, more than 100 times the CPU time was saved due to grid reduction without sacrificing the prediction accuracy. To show clearly that the solution indeed remains accurate, we plot the streamwise u-velocity profiles at several x locations. It can be seen from Fig. 2(*a*) that the streamwise velocities computed on the finest uniform grid system for Re=1000 compare very favorably with those computed on the much coarser nonuniform Grid-A. Good agreement is also observed for the case with Re=2000 (Fig. 2(*b*)).

The following analysis was conducted on non-uniform Grid-A to save disk space and CPU time. Two test conditions ($C=2$,Re =426) and ($C=4$,Re=1150), which were experimentally studied by Durst et al. [1], will be considered. As Fig. 3 shows, there is good overall agreement between the computed and measured streamwise u-velocity profiles. A larger discrepancy is observed immediately upstream and downstream of the contraction step, in particular for the case with $C=4$. A check whether this discrepancy arises from non-convergent solutions, we plot in Fig. 4 convergence histories against iterations. Solutions were considered to be convergent as the global pressure and velocity residuals reached a value of 10^{-18}. Having obtained the perfect convergence of the solution, we may attribute the discrepancy between the two-dimensional numerical solutions and three-dimensional experimental data to the flow in z-direction, which is normal to the plane of symmetry. It is worth reminding the reader that the ex-

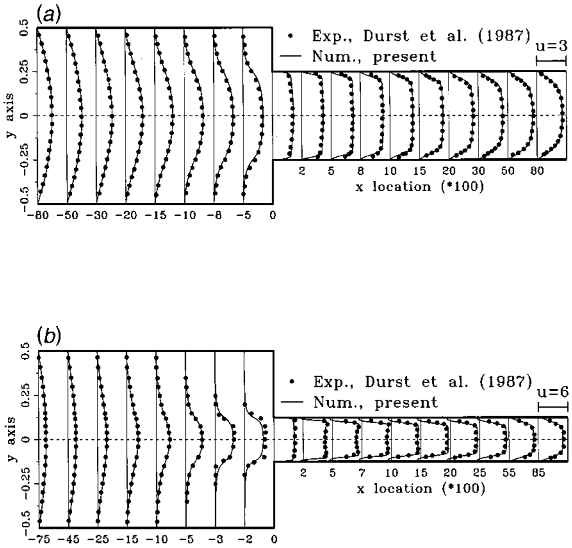

Fig. 3 A comparison of the computed *u*-velocity profiles with the experimental data of Durst et al. [1]. (*a*) *C*=2, Re=426; (*b*) *C*=4, Re=1150.

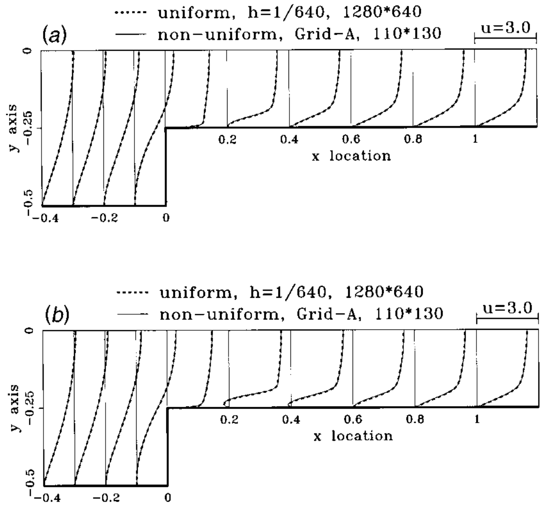

Fig. 2 A comparison of *u*-velocity profiles computed on uniform and nonuniform grids for the case with *C*=2. (*a*) Re =1000; (*b*) Re=2000.

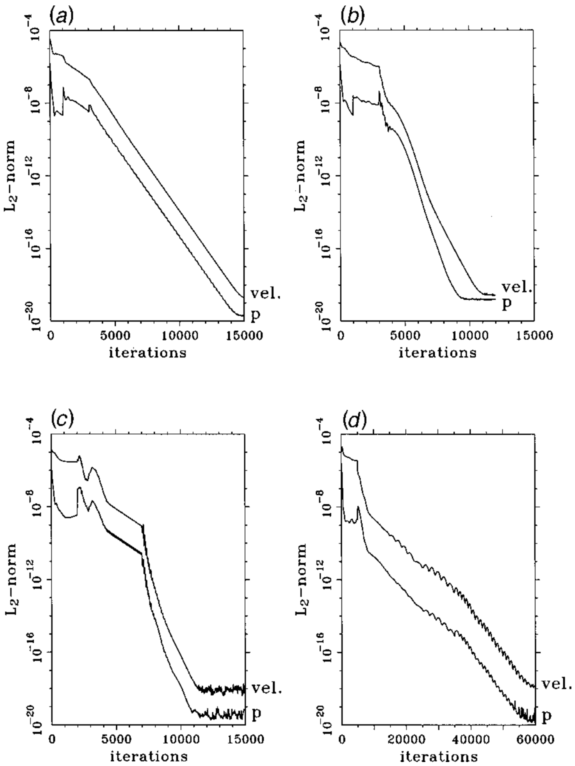

Fig. 4 The plot of residuals reduction, cast in L_2-norm, against iteration numbers for dependent variables. (*a*) *C*=2, Re=426; (*b*) *C*=4, Re=1150; (*c*) *C*=4, Re=2000; (*d*) *C*=8, Re=2000.

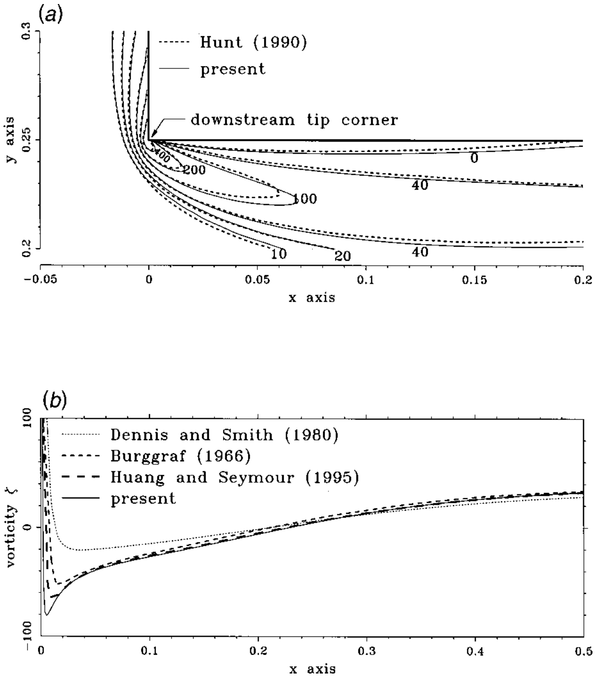

Fig. 5 A comparison of the presently computed vorticity $\zeta = (\partial v/\partial x - \partial u/\partial y)$ with that using the stream function-vorticity formulation for the case of $C=2$ and Re=1000. (*a*) Vorticity contours near the tip corner; (*b*) vorticity distribution along the downstream channel roof/floor.

perimental data of Durst et al. [1] were obtained in a channel, which had a width of $18D$. Showing this width is sufficiently deep to allow the present comparison is beyond the scope of this study. Three-dimensional investigation of this problem is left for future studies.

4.1 Half-Domain Computation. Separation in a contraction channel can be characterized by the recirculation eddies at the upstream salient corner and downstream tip corner. It is, thus, important to select controlling parameters that could well characterize the flow separation. We choose the separation length L_1 and re-attachment length L_2 in a salient corner. While the tip corner separation length existed, its value was too small to be considered. Therefore, only the reattachment length L_3 is considered in the tip corner. Investigations are done by varying the Reynolds number and the contraction ratio. To begin with, calculations from Re $=0.1$ to Re$=4000$ for $C=2$ and Re$=2000$ for $C=4$ and 8 were carried on the half channel by imposing the symmetric boundary condition at the centerline $y=0$ in order to obtain symmetric solutions. These validated half-domain solutions, as schematic in Fig. 5, will be compared with those computed in the full channel for clarifying the presence of bifurcation solutions.

The separation/reattachment lengths L_1 and L_2 of the upstream salient corner eddy are plotted logarithmically against the Reynolds number as shown in Fig. 6. Included in this figure are numerical solutions of Hawken et al. [4] and Dennis and Smith [2] for cases $C=2$ and 4. It is shown that L_1 tends to have a constant value, which is smaller than that of L_2 as Re decreases from 10^0 to 10^{-1}. As Re$>10^0$, lengths L_1 and L_2 are prone to decrease, with the length L_2 being largely decreased. This implies that L_1 has a tendency to reach the value of L_2 as Re approaches to 10^1. A further increase of Re causes L_1 to have a value larger than L_2. When the Reynolds number is further increased up to 10^2, both lengths L_1 and L_2 increase with Re. The L_1 increases at a larger slope. When the Reynolds number becomes larger than 10^1, L_1 is still larger than L_2.

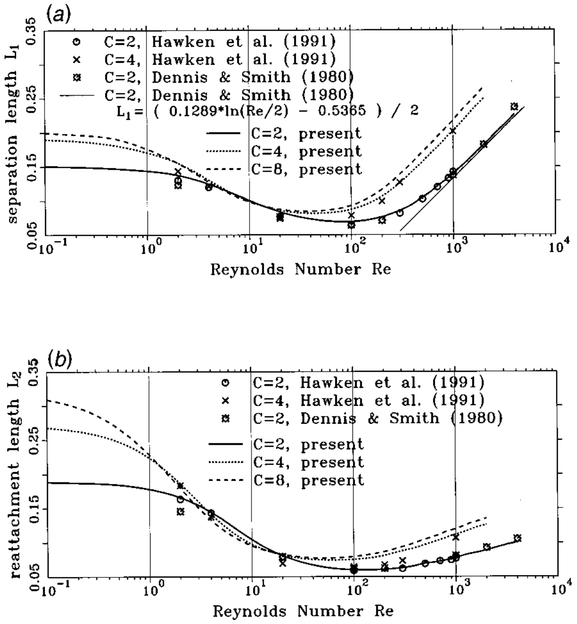

Fig. 6 A comparison of separation/reattachment lengths of upstream salient corner eddy between the present calculation and other numerical data for $C=2$, 4, 8 at different Reynolds numbers. (*a*) Separation length L_1; (*b*) reattachment length L_2.

The downstream tip corner eddy becomes visible as the Reynolds number increases up to Re$\sim 10^2$. The results shown in Fig. 7 reveal that the tip corner reattachment length L_3 varies linearly with the Reynolds number according to $L_3 = a^* \mathrm{Re} - b$, where

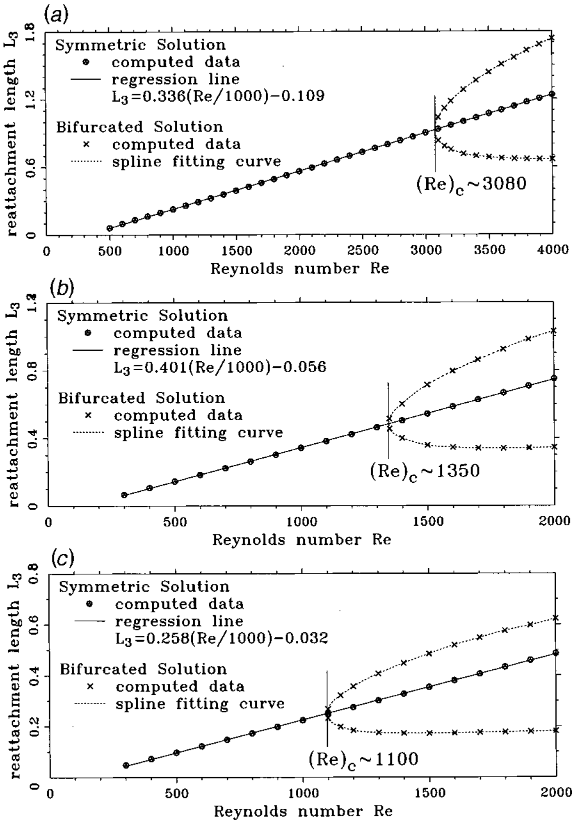

Fig. 7 The plot of reattachment lengths L_3 of downstream tip corner eddy against Reynolds numbers. (*a*) $C=2$; (*b*) $C=4$; (*c*) $C=8$.

Table 3 The computed separation and reattachment lengths. (a) The computed symmetric solution in a half-channel. (b) and (c) reveal bifurcated solutions, in percentage difference relative to (a), in the full-channel computation.

C	Re	L_1			L_2			L_3		
		(a)	(b)	(c)	(a)	(b)	(c)	(a)	(b)	(c)
2	1000	0.140	0.0%	+0.1%	0.078	0.0%	+0.1%	0.228	0.0%	+0.7%
	2000	0.181	0.0%	+0.1%	0.089	0.0%	+0.1%	0.562	0.0%	+0.6%
	2800	0.204	0.0%	+0.1%	0.096	0.0%	+0.1%	0.834	-0.6%	+1.1%
	3200	0.212	-0.5%	+0.6%	0.098	-0.2%	+0.3%	0.969	-22.2%	+21.9%
	3600	0.219	-1.1%	+1.2%	0.099	-0.5%	+0.5%	1.103	-38.7%	+36.6%
	4000	0.227	-1.3%	+1.4%	0.100	-0.6%	+0.6%	1.237	-46.2%	+40.4%
4	500	0.157	0.0%	0.0%	0.097	0.0%	0.0%	0.146	0.0%	+0.7%
	1000	0.202	0.0%	0.0%	0.112	0.0%	0.0%	0.343	-0.1%	+0.8%
	1200	0.214	0.0%	0.0%	0.116	0.0%	0.0%	0.423	-0.6%	+1.2%
	1400	0.225	-0.3%	+0.3%	0.119	-0.2%	+0.3%	0.504	-20.5%	+19.5%
	1700	0.239	-0.6%	+0.6%	0.123	-0.4%	+0.4%	0.626	-45.6%	+37.6%
	2000	0.250	-0.6%	+0.7%	0.126	-0.4%	+0.5%	0.749	-53.9%	+37.4%
8	400	0.156	0.0%	0.0%	0.100	0.0%	0.0%	0.073	0.0%	+1.0%
	700	0.194	0.0%	0.0%	0.112	0.0%	0.0%	0.148	-0.1%	+0.8%
	1000	0.217	0.0%	0.0%	0.120	0.0%	0.0%	0.224	-0.8%	+1.2%
	1200	0.231	-0.3%	+0.3%	0.124	-0.2%	+0.2%	0.275	-33.0%	+29.5%
	1500	0.246	-0.3%	+0.3%	0.130	-0.2%	+0.2%	0.354	-51.2%	+36.9%
	2000	0.267	-0.4%	+0.4%	0.135	-0.3%	+0.3%	0.485	-62.6%	+28.4%

$(a,\ b)=(0.336\times 10^{-3},0.109)$, $(0.401\times 10^{-3},0.056)$ and $(0.258\times 10^{-3},0.032)$ for $C=2$, 4 and 8, respectively. Note that $L_3|_{C=4} > L_3|_{C=8} > L_3|_{C=2}$ when $\mathrm{Re}<1000$. As the Reynolds number becomes larger than 1000, the trend is reversed for $C=2$ and 8. Under these circumstances, $L_3|_{C=4} > L_3|_{C=2} > L_3|_{C=8}$.

4.2 Full-Domain Computation. For clarifying the presence of the well-known pitchfork bifurcation in contraction channel, we conducted analysis on the entire channel. To provide a measure of flow asymmetry, we subtract the half-domain solutions from the full-domain solutions for the lengths L_1, L_2, and L_3. The resulting lengths ΔL_1, ΔL_2, and ΔL_3 are normalized by those obtained on the basis of half-domain analysis. We tabulate L_i and $\Delta L_i/L_i$ $(i=1,2,3)$ by varying the Reynolds number and the contraction ratio in Table 3. The results reveal that when the value of Re is lower than 2800, 1200, and 1000 for $C=2$, 4, and 8, respectively, there exists a stable flow in which the recirculating eddies have the same size on the roof/floor of the channel. Under the circumstances, solutions compare favorably with half-domain solutions in the sense that the difference between two sets of data is less than 0.1% for lengths L_1 and L_2 and 1% for length L_3. This is not the case as Re continuously increases, in particular for the reattachment length L_3. The difference between half- and full-domain calculations can be as high as 1% for L_1 and L_2 and over 20% for L_3 as the value of Re is larger than 3200, 1400, and 1200 for $C=2$, 4, and 8, respectively.

Note that the critical Reynolds numbers for pitchfork bifurcation fall into the ranges of $2800<\mathrm{Re}<3200$, $1200<\mathrm{Re}<1400$, and $1000<\mathrm{Re}<1200$ for $C=2$, 4, and 8, respectively. The larger the contraction ratio, the easier the bifurcation sets in. In this study, we plot the value of L_3 on the channel roof/floor from solutions computed in the full channel to determine critical Reynolds numbers. We then determine the intersection point of the resulting parabola, as shown in Fig. 7, with the line computed under the half-domain calculations. The critical Reynolds numbers are obtained as 3080, 1350, and 1100 for channels with $C=2$, 4, and 8, respectively. To confirm the bifurcated solutions are indeed the convergent solutions, we plot in Figs. (4*c*) and (4*d*) the residuals against iterations for flows with $\mathrm{Re}=2000$ in channels with $C=4$ and 8, respectively.

When the Reynolds number is larger than its critical value, it is seen from Fig. 8 that the streamwise *u*-velocity profiles become asymmetric with respect to the centerline, with the detached flow being directed toward either one of the channel wall. The streamline plots show that one recirculation region immediately downstream of the tip vortex becomes larger at the expense of the other.

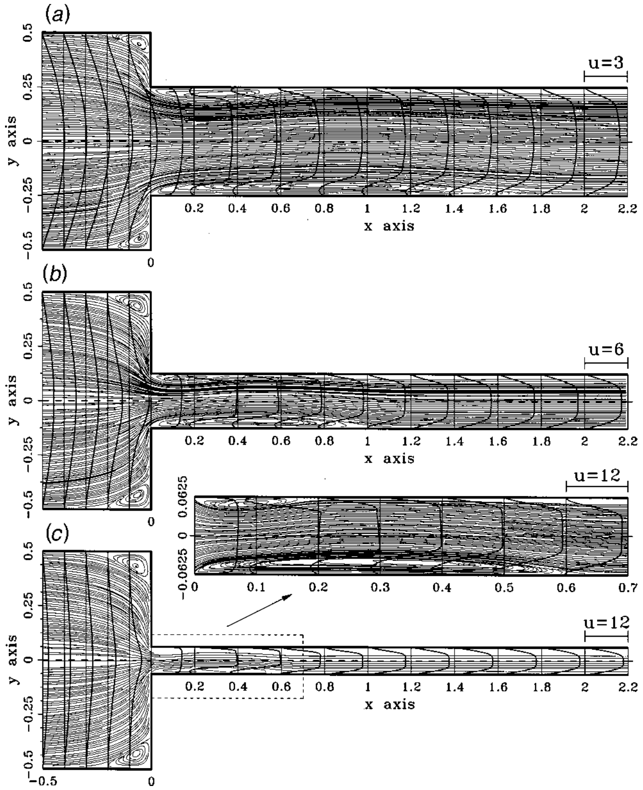

Fig. 8 The plot of streamlines and *u*-velocity profiles to reveal the presence of Coanda effect. (*a*) *C*=2, Re=4000; (*b*) *C*=4, Re=2000; (*c*) *C*=8, Re=2000.

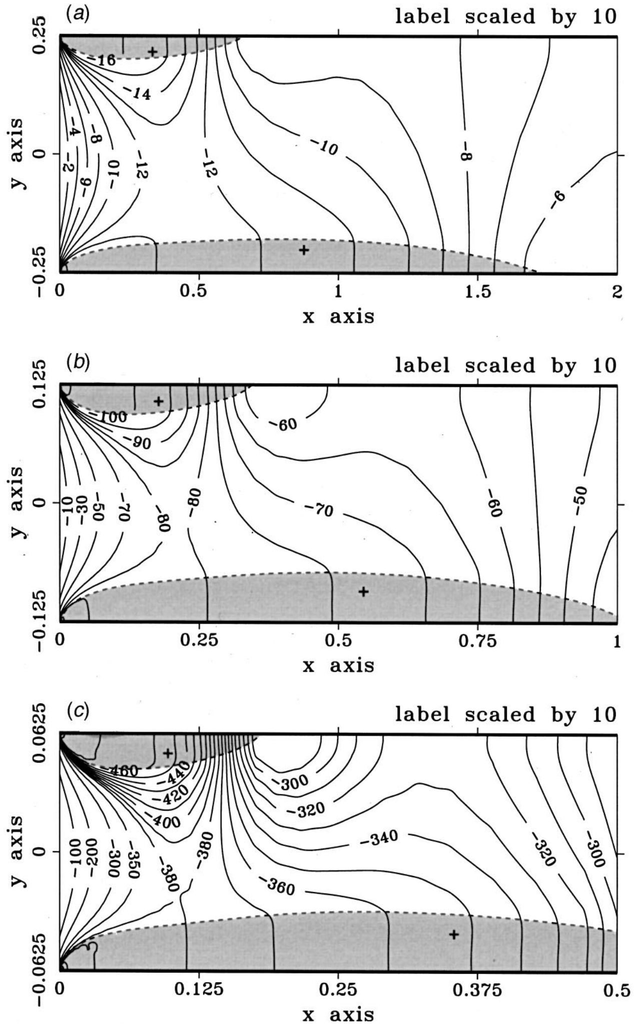

Fig. 9 The plot of pressure contours to reveal the pressure gradient setup in the channel. (*a*) *C*=2, Re=4000; (*b*) *C*=4, Re=2000; (*c*) *C*=8, Re=2000.

Since the flow pattern is asymmetric with respect to the channel centerline, a process known as bifurcation occurs. Under this circumstance, momentum transfer between the fluid shear layers sets in. The momentum exchange in the direction from the larger eddy to the smaller eddy leads to a shear layer at one boundary of the channel. The roof (smaller) eddy acquires momentum at the expense of the other floor boundary layer. As a result, a pressure gradient is formed across the channel. As Fig. 9 shows, the pressure distribution can cause the asymmetric flow to occur. When the Coanda effect occurs, the shear layer with the greater momentum attaches to the channel wall more rapidly than does the layer with less momentum. We can say in mathematical terms that bifurcation occurs and multiple stable solutions to the Navier-Stokes equations may coexist [14]. Here, we provide readers a clear picture of asymmetric solutions for the primary velocity component u, pressure p and their derivatives with respect to x and y. Figure 10 plots solutions at the streamwise location $x=0.1$ for the flow with Re=2000 in a suddenly contracted channel with $C=4$. Clearly seen from this figure is that the computed convergent solution does show flow asymmetry. An increased velocity is in company with a decreased pressure.

Other measures of the flow asymmetry and the critical Reynolds number can be obtained by computing the asymmetry-energy, $I=\int_0^{x_{\max}} v^2|_{y=0}dx$, along the centerline of the channel. It can be seen from Fig. 11 the bifurcation diagram, obtained on the basis of the asymmetry-energy, that the value of I is a nominal zero below the critical Reynolds number. Above the critical Reynolds number, at which the so-called pitchfork bifurcation appears, the flow apparently becomes asymmetric in the sense that I increases by a factor of $10^2 \sim 10^3$ times of that below the critical value. At the critical points seen in Fig. 11, $dI/d\,\mathrm{Re}$ takes the maximum value. This implies that ahead of the critical point $d(dI/d\,\mathrm{Re})/d\,\mathrm{Re}<0$ while behind the critical point $d(dI/d\,\mathrm{Re})/d\,\mathrm{Re}>0$. The critical Reynolds numbers determined in this way are 3070, 1360, and 1100 for channels with $C=2$, 4, and 8, respectively. A comparison of Figs. 7 and 11 reveals that critical Reynolds numbers determined by the above two means are, in essence, identical. It can be concluded that Re=3075, 1355 and 1100 (obtained from the mean value of two criteria) are the critical Reynolds numbers for channels with $C=2$, 4 and 8, respectively. For further confirming of the validity of these critical Reynolds numbers, we have specified a slightly asymmetrical initial velocity at the channel inlet by increasing and decreasing the streamwise velocity by 1% at the upper and lower parts of the inlet velocity profile. Based on the critical Reynolds numbers, namely, 1355, 1100, for channels with $C=4$ and 8, we have considered Re=1300 and 1050 to check the influence of asymmetric inlet flow on the flow asymmetry. Given 1% inlet asymmetry in velocity profile, the downstream asymmetry in L_3 is about 1% for the case of Re=1050 and $C=8$. For the case of Re=1300 and $C=4$, 1% asymmetry in inlet velocity causes only 0.5% difference in the downstream length L_3. This indirectly justifies the obtained critical Reynolds numbers.

As pointed out in the work of Darbandi and Schneider [15], the peak value of the downstream streamwise u-velocity profile does not occur at the centerline of the channel. Take the case of $C=8$ as an example; overshoots in the velocity profile can be observed for Re=500 and 1000, as seen in Fig. 12, owing to the flow

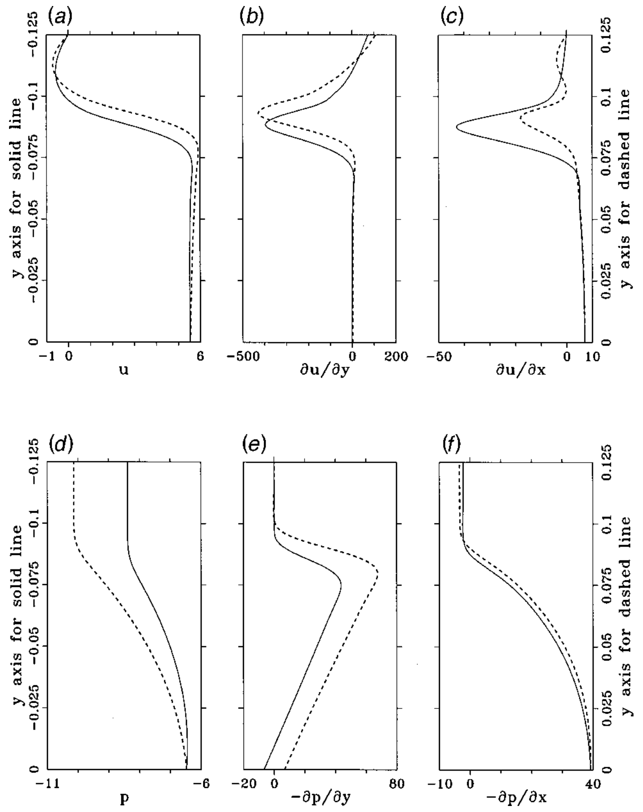

Fig. 10 An illustration of asymmetric solution profiles computed at $x=0.1$ for the case with Re=2000 and $C=4$. (*a*) u; (*b*) $\partial u/\partial y$; (*c*) $\partial u/\partial x$; (*d*) p; (*e*) $-\partial p/\partial y$; (*f*) $-\partial p/\partial x$.

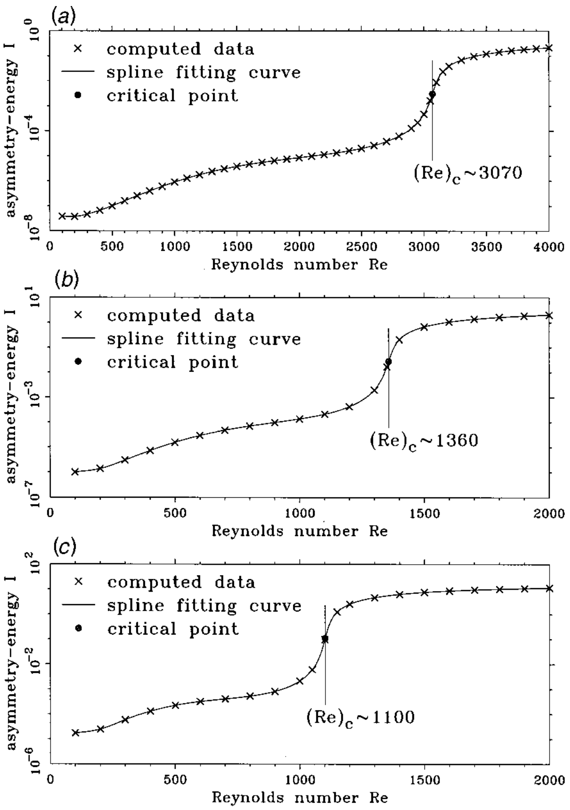

Fig. 11 The plot of asymmetry-energy values against Reynolds numbers in channels of different contraction ratios. (*a*) $C=2$; (*b*) $C=4$; (*c*) $C=8$.

separation from the channel roof and floor. In the light of conservation principle, the flow velocity must be increased in regions adjacent to flow separation to conserve the mass. This overshooting velocity diminishes as the flow gradually develops into the fully developed profile.

4.3 Mechanism Leading to Transition From Symmetric to Asymmetric States. How a flow evolves from symmetric to asymmetric states in a symmetric channel has been a subject of academic importance for many years. Recently, Hawa and Rusak [16] provided a physical mechanism to explain the transition of laminar flows from symmetric to asymmetric equilibrium states in a symmetrically expanding channel. They pointed out that the stability mechanism is a result of the interaction between the destabilizing upstream convection effects by the asymmetric perturbation and the combined stabilizing effects of the viscous dissipation and the downstream convection of perturbations by the base symmetric flow. We believe, however, that the observed asymmetric disturbance originates from imperfections, such as any sort of asymmetries in the channel geometry and the incoming flow conditions in the experiment.

In this paper, we provided a numerical mechanism to explain the transition from symmetric to asymmetric states in a symmetric contraction channel. The errors intrinsic to the nature of the computer itself happen because any computer has a finite precision. Many floating-point numbers cannot be represented exactly when the representation uses a number base 2 on digital computers. As a result, these values must be approximated by one of the nearest representable values; the difference is known as the machine round-off error. Unlike the real system in algebra, which is continuous, a floating-point system in computer has gaps (spacing) between each number. Because the same number of bits is used to represent all normalized numbers (the fractional part), the smaller the exponent the greater the density of representable numbers and the smaller the spacing between two consecutive numbers [17]. This implies that the results of (0.2-0.1) and (1.2-1.1) are different in computer arithmetic even though these quantities are algebraically equal. While the machine round-off errors and/or the spacing between two consecutive numbers, an analogy to the experimental surface roughness, are static in nature, they are asymmetrically distributed.

Due to the inevitable cancellation error (i.e. the error in adding a series of numbers with terms in decreasing order) and subtractive cancellation error (i.e., the error in subtracting two nearly equal numbers with the same sign), the associative and distributive laws are no longer valid in floating-point arithmetic [18], implying that arithmetic in computer is direction-biased. It is, thus, impossible to retain the computational symmetry. The solutions computed from the channel roof/floor to the symmetry-plane may not be equal to those computed from the symmetry-plane to the channel floor/roof (even though they are algebraically equal). In addition, the employed alternating direction implicit (ADI) solution algorithm is asymmetric in the implementation. When the Reynolds number is fairly low, any asymmetric disturbance may be decayed by viscous dissipation and the flow symmetry can be stably maintained. As the Reynolds number is increased, the symmetric flow is less stable and the resulting discrete system may become ill conditioned. Such a system is very sensitive to small changes in input and produces large changes in the output, owing to the propagation of small errors into increasingly larger ones. At high Reynolds numbers, the resulting asymmetries, while fairly small, will propagate and grow and, finally, cause the asymmetric solutions to occur. According to the works of Hawa and Rusak [16], as the asymmetric disturbances grow in time for the Reynolds number beyond its critical value, the combined convection effect of the vorticity perturbation by the axial velocity perturbation creates a stabilizing influence that stops the growth of the

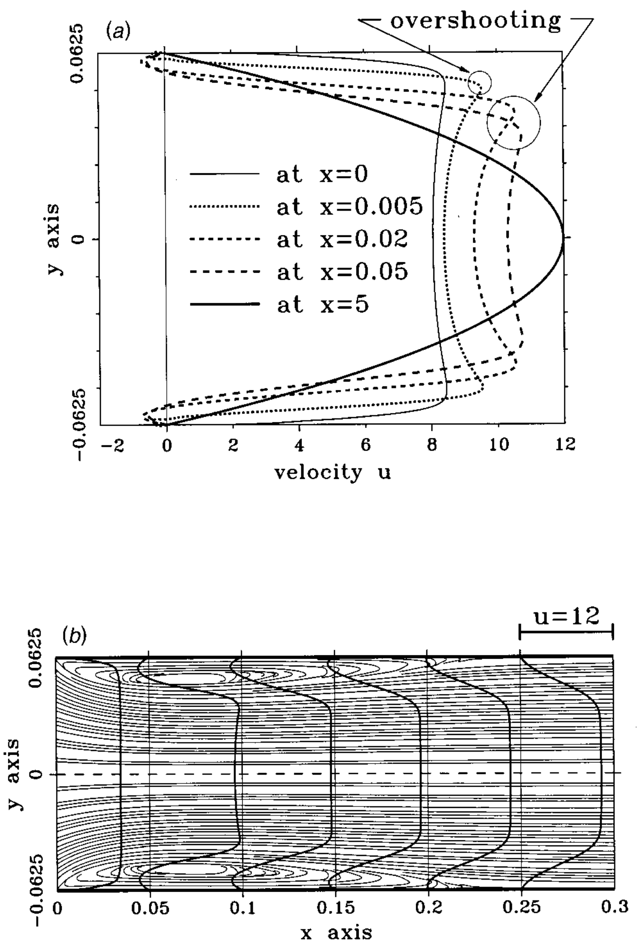

Fig. 12 The streamlines and *u*-velocity profiles for the channel with the contraction ratio of 8. (*a*) Re=500; (*b*) Re=1000.

perturbation and establishes the asymmetric steady state. In conclusion, we believe that the asymmetric error, originated from uneven REAL-representation in computer and from the use of the direction-biased computation, causes the transition from symmetric to asymmetric states to occur in the presently investigated contraction channel.

5 Concluding Remarks

Computational investigations have been performed to study flow bifurcation in the symmetric planar contraction channel. The results obtained at different channel contraction ratios and Reynolds numbers clearly confirm that the pitchfork bifurcation can be present. Our finding is that asymmetric solutions, manifested by unequal tip corner reattachment lengths at the channel floor/roof, can be stably maintained in cases when the Reynolds number exceeds its critical Reynolds number. Another way to determine the critical Reynolds number is to plot the asymmetry-energy along the centerline of the channel for each investigated Reynolds number. Mechanism leading to bifurcated solutions is also provided.

Acknowledgment

This work is under the support of National Science Council of Republic of China, NSC90-2611-E002-017.

References

[1] Durst, F., Schierholz, W. F., and Wunderlich, A. M., 1987, "Experimental and numerical investigations of plane duct flows with sudden contraction," ASME J. Fluids Eng., **109**, pp. 376–383.
[2] Dennis, S. C. R., and Smith, F. T., 1980, "Steady flow through a channel with a symmetrical constriction in the form of a step," Proc. R. Soc. London, Ser. A, **372**, pp. 393–414.
[3] Hunt, R., 1990, "The numerical solution of the laminar flow in a constricted channel at moderately high Reynolds number using Newton iteration," Int. J. Numer. Methods Eng., **11**, pp. 247–259.
[4] Hawken, D. M., Townsend, P., and Webster, M. F., 1991, "Numerical simulation of viscous flows in channels with a step," Comput. Fluids, **20**, pp. 59–75.
[5] Huang, H., and Seymour, B. R., 1995, "A finite difference method for flow in a constricted channel," Comput. Fluids, **24**, pp. 153–160.
[6] Cherdron, W., Durst, F., and Whitelaw, J. H., 1978, "Asymmetric flows and instabilities in symmetric ducts with sudden expansions," J. Fluid Mech., **84**, pp. 13–31.
[7] Sobey, I. J., 1985, "Observation of waves during oscillating channel flow," J. Fluid Mech., **151**, pp. 395–426.
[8] Wille, R., and Fernholz, H., 1965, "Report on the first European Mechanics Colloquium, on the Coanda effect," J. Fluid Mech., **23**, pp. 801–819.
[9] Ladyzhenskaya, O. A., 1963, *Mathematical Problems in the Dynamics of a Viscous Incompressible Flow*, Gordon & Breach, New York.
[10] Leonard, B. P., 1979, "A stable and accurate convective modeling procedure based on quadratic upstream interpolation," Comput. Methods Appl. Mech. Eng., **19**, pp. 59–98.
[11] Chiang, T. P., Hwang, R. R., and Sheu, W. H., 1996, "Finite volume analysis of spiral motion in a rectangular lid-driven cavity," Int. J. Numer. Methods Fluids, **23**, pp. 325–346.
[12] Van Doormaal, J. P., and Raithby, G. D., 1984, "Enhancements of the SIMPLE method for predicting incompressible fluid flows," Numer. Heat Transfer, **7**, pp. 147–163.
[13] Chiang, T. P., and Sheu, W. H., 1997, "Numerical prediction of eddy structure in a shear-driven cavity," Computational Mechanics, **20**, pp. 379–396.
[14] Fearn, R. M., Mullin, T., and Cliffe, K. A., 1990, "Non linear flow phenomena in a symmetric sudden expansion," J. Fluid Mech., **211**, pp. 595–608.
[15] Darbandi, M., and Schneider, G. E., 1998, "Numerical study of the flow behavior in the uniform velocity entry flow problem," Numer. Heat Transfer, **34**, pp. 479–494.
[16] Hawa, T., and Rusak, Z., 2001, "The dynamics of a laminar flow in a symmetric channel with a sudden expansion," J. Fluid Mech., **436**, pp. 283–320.
[17] Bush, B. M., 1996, *The Perils of Floating Point*, http://www.lahey.com/float.html, Lahey Computer System, Inc.
[18] Ueberhuber, C. W., 1997, *Numerical Computation 1: Methods, Software, and Analysis*, Springer-Verlag, Berlin Heidelberg.

Lionel Mathelin

Françoise Bataille
e-mail: daumas@cethil.insa-lyon.fr

André Lallemand

Institut National des Sciences
Appliquées de Lyon,
Centre de Thermique de Lyon, UMR 5008,
Bât. S. Carnot, 20 av. A. Einstein
69621 Villeurbanne cedex, France

The Effect of Uniform Blowing on the Flow Past a Circular Cylinder

This work describes blowing through the whole surface of a porous circular cylinder for the control of the near wake dynamics and the thermal protection of the surface. The flow past the cylinder is numerically studied and the blowing is modeled. Comparisons with experimental data are used for validation. It is shown that the blowing tends to increase the boundary layer thickness, to promote its separation and to decrease the viscous drag induced. Similarly, the convective heat transfer is lowered, and in the case of a nonisothermal blowing, the surface is very effectively protected from the hot free stream flow. The near wake is also affected. The vortex shedding frequency is shown to decrease when blowing occurs and a qualitative model is presented to identify the different mechanisms. [DOI: 10.1115/1.1467919]

1 Introduction

The study of bluff-body flows has been a subject of interest for several decades and has received a considerable amount of work since the pioneering studies of Strouhal [1] who observed the vortex shedding from a cylinder. Because of its conceptual simplicity, it is used as a reference case for the test of fluid mechanics theories or new numerical methods. Nevertheless, the physical problem, which involves boundary layer separation, reattachment, shear layers, recirculating flows and vortex shedding, is complex and has been addressed by many authors who have shed light on several aspects including drag crisis, recirculating bubbles behavior, onset of the three-dimensionality, end effects, base pressure or wake instability properties. Zdravkovich [2], as well as Williamson [3], provides the reader with a rich review of all related phenomena. Most of the investigations were experimental, using various techniques such as hot-wire anemometry, Particle Image Velocimetry, shadowgraph/schlieren systems and more recently Laser Doppler Anemometry and phase-averaging. Until the last thirty years, numerical research was only feasible with a manual solution of the Navier-Stokes equations [4–6], which limited the simulations to very low Reynolds numbers. Theoretical models were the most efficient way of predicting the flow properties. Nevertheless, the drag and the base pressure behavior in the steady regime ($Re<49$) were correctly reproduced. Since the seventies, powerful computers steadily allowed for higher complexity, and higher Reynolds number solutions. The unsteady behavior [7,8] and the onset of the three-dimensionality [9–11] were successfully simulated. Today, numerical computations give valuable insights in phenomena difficult to investigate experimentally such as the vorticity field or the three-dimensional modes (see [12–18] for a rich overview) and can even predict new phenomena (mode C [19]).

The wake dynamics control is of primary interest for the fundamental knowledge of phenomena attached to the vortex shedding and has received a great deal of work in recent years because of its wide range of applications: vibration control, dynamic stall, lift and drag control, reduction of acoustic phenomena ([20–23] among many others). The onset of vortex shedding and its frequency can be shifted and even suppressed by a very small intrusive cylinder located in the near wake of the bluff body to be controlled [24], or by forcing the cylinder to oscillate and with the use of the lock-in effect [25–28]. Other ways to achieve the suppression of the shedding are heating of the cylinder surface to modify the local flow properties [29,30] or the use of localized discrete steady or unsteady blowing or suction to change the circulation around the bluff body or the pressure distribution along its surface [31–38]. Finally, external excitation through loudspeakers driven by a control probe located in the wake in open or closed-loop scheme can also be used [39].

Still, work remains to be carried out on the wake dynamics control. In particular, a secondary fluid injection through a solid surface has received relatively little attention in the past. Most research has been concerned with flat plate configurations, mostly for thermal protection purposes [40]. The circular cylinder with blowing was investigated through the pioneering experimental work of Johnson and Hartnett [41], while Eckert and Livingood [42] derived a theory, based on similarity to wedge flows, for the prediction of the convective heat transfer coefficient along an arbitrary bluff body surface. Most studies on wall protection deal with the technique of film cooling or discrete injection through holes. Nevertheless, it has long been known that blowing through a porous matrix is much more efficient than film cooling in terms of coolant flow rate required for the same thermal protection [43], though some additional difficulties (affordable pressure drop) are to considered.

To our knowledge, no case of blowing through a porous cylinder with heat transfer has been studied. In this work, we will consider a flow around a porous circular cylinder, with a Reynolds number varying from 10–7000, based on the outer cylinder diameter and upstream properties, allowing for a study in laminar and turbulent regimes. The temperature of the main flow can vary from ambient to 200°C. A numerical approach is used in this work and the blowing through the porous wall is modeled. When possible, comparisons with data in the literature and experimental work has been done to validate our numerical results.

The configuration studied is shown in Fig. 1. The porous cylinder is in a cross-flow, and the blowing is normal to the surface and applied all along the cylinder wall. In this paper, we are interested in a 2-D configuration, even if 3-D effects are known to occur in this range of Reynolds numbers ([3,13,44–46], among many others). Three-dimensional modes are beyond the scope of this study and we only focus on the blowing influence on the dynamics and the thermal behavior in the attached boundary layer and the near wake of the circular cylinder in crossflow since 3-D simulations have shown that the blowing influence is essentially a 2-D phenomenon. After the numerical methods and the blowing model are presented in Section 2, the steady regime is investigated in Section 3 through the study of the recirculating region and its dependence on blowing. Next, the unsteady regime is considered in Section 4, and the dynamical and thermal profiles are presented. The blowing impact on the surface temperature and the forces acting on the bluff body are also addressed. The dynamics are

---

Contributed by the Fluids Engineering Division for publication in the JOURNAL OF FLUIDS ENGINEERING. Manuscript received by the Fluids Engineering Division September 25, 2000; revised manuscript received November 3, 2001. Associate Editor: D. R. Williams.

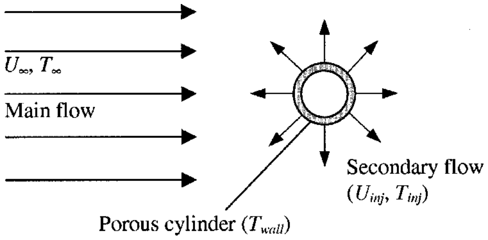

Fig. 1 Schematic of the studied configuration.

studied through the vortex shedding frequency evolution and a qualitative model is used for predicting the shedding frequency through the near wake study.

2 Physical and Numerical Model of the Blowing

2.1 Numerical Approach. A 2-D finite-volume Navier-Stokes solver for both structured and unstructured grids was applied. Extensive grid resolution tests were conducted to check the grid validity. More than twenty different meshes were used with various features including node density, computational domain extent, cell types, and grid structure. The cell number around the cylinder surface was varied from 80–3000 and no significant changes in fundamental results, such as in the Strouhal number or the boundary layer separation angle, occurred. Particular attention was paid to cells' skewness and grid smoothness.

The grid finally retained for most computations is shown in Fig. 2. This choice is based on CPU time requirement, comparisons with experiments for global parameters whenever possible and physical considerations on boundary layer evolution criteria. It consists in a 50,000-triangular cell unstructured grid, which allows the grid density to easily vary compared to quadrilateral cells. This represents the best trade-off between result accuracy and running time. Computational domain is approximately 5 *D* long upstream of the cylinder axis and 15 *D* downstream, with *D* the cylinder diameter. The width is 10 *D* leading to a blockage ratio of 10%. The domain extent has been chosen to keep the blockage ratio and the number of cells to a reasonable level and to allow comparisons with experimental data obtained from our wind tunnel (see [46]). Nevertheless, some particular results have been checked using some other meshes to ensure result independence from the numerical grid. The blockage phenomenon, the computational domain extension, and the inlet/outlet boundary conditions were varied and an extended mesh comprising 242,000 cells, 55 *D* long, 21 *D* wide and 4.8% blockage ratio was also tested. The blowing phenomenon has also been simulated to an actual scale, meshing down to the actual pore size, 30 μm wide, leading to more than 3000 cells along the cylinder surface and 165,000 cells for the entire mesh. Again no difference could be noted.

The numerical results are obtained using a general-purpose RANS code (Fluent). The code was run on several platforms. For some machines, the measure of sustained performance on a large linear algebra problem is indicated [47,48]. A DEC PWS clocked at 433 MHz (588 MFlops), featuring 192 Mo in RAM and a bi-Pentium III 550 MHz PC with 512 Mo of RAM were used leading to a CPU time requirement for a turbulent nonisothermal unsteady case of the order of 120 seconds per time step or 10 days for a complete simulation from a uniformly initialized field. A cluster of DEC 4100 workstations clocked at 400 MHz (9.5 GFlops) was also used, allowing for efficient parallel processing. Finally, a CRAY T3E superscalar computer (112 GFlops), with 256 EV5 processors was also used for large scale computations.

Specified static pressure and turbulence properties are applied at the inlet, whereas a specified mass flow rate is imposed at the outlet. Although the latter is not a nonreflective boundary condition, it was checked not to cause upstream disturbances. In particular, the Strouhal number evidenced no change compared to a case where the growing vortex street has not reached the numerical domain exit yet. Lateral boundary conditions are defined as symmetric planes. Again, wall boundary (i.e., no slip) conditions for the lateral surfaces lead to no change on the global parameters such as the Strouhal number, but the lateral growing boundary layers make the blockage ratio increase slightly. The cell density in the immediate vicinity of the cylinder was set to ensure the boundary layer would be accurately resolved, i.e., at least six cells must be located within.

The governing equations are solved on a triangular staggered grid. Convection terms are evaluated using an upwind second-order scheme, and the diffusion terms using a central second order formulation. This discretization scheme applies to all variables including the Reynolds stresses. For Reynolds numbers below 49, the simulations lead to a steady flow and two recirculation bubbles occur at the rear of the cylinder. Above Re=49, the flow becomes unsteady and the computations are carried-out using the unsteady Navier-Stokes formulation. The time discretization scheme is second-order implicit accurate with the time step adjusted to get more than 800 time steps per shedding period, leading to a non-dimensional time step δt^*, defined as $\delta t^* = \delta t U_\infty / D$, of the order of 3.10^{-3}. Tests carried-out with 2000 time steps per Strouhal period led to identical results. Twenty iterations were typically imposed between each time step to ensure that all variable residues decrease at least by a factor of 50 within the time step and reach a steady level. Pressure-velocity coupling was achieved using the SIMPLEC algorithm [49]. Additional tests on the numerical modeling involved a double-precision simulation, allowing for very low residues. Computations were run until at least 10 periods

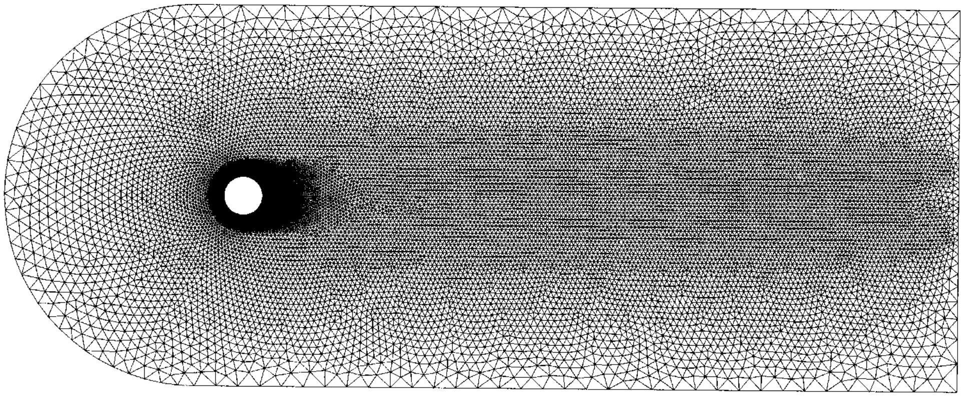

Fig. 2 Grid used for most computations: 50,000 cells, triangular mesh, 20 *D* long and 10 *D* wide.

of shedding occurred after the initial transition time and the vortex shedding was monitored by plotting the velocity at a point arbitrarily located within the wake as a function of time.

2.2 Computational Methods

2.2.1 Governing Equations. To solve the flow, including heat transfer, the time-dependent continuity, Navier-Stokes and energy governing equations were used:

$$\frac{\partial}{\partial t}\rho+\frac{\partial}{\partial x_i}(\rho\mathcal{U}_i)=0 \tag{1}$$

$$\frac{\partial}{\partial t}(\rho\mathcal{U}_i)+\frac{\partial}{\partial x_j}(\rho\mathcal{U}_i\mathcal{U}_j)=-\frac{\partial}{\partial x_i}\mathcal{P}+\frac{\partial}{\partial x_j}\tau_{ij} \tag{2}$$

$$\frac{\partial}{\partial t}(\rho H)+\frac{\partial}{\partial x_i}(\rho\mathcal{U}_i H)=\frac{\partial}{\partial x_i}\left(\lambda\frac{\partial}{\partial x_i}T\right) \tag{3}$$

with $\mathcal{U}$ the instantaneous velocity, H the specific enthalpy, $\mathcal{P}$ the instantaneous pressure, ρ the density, λ the thermal conductivity, and τ_{ij} the stress tensor given by

$$\tau_{ij}=\left[\mu\left(\frac{\partial}{\partial x_j}\mathcal{U}_i+\frac{\partial}{\partial x_i}\mathcal{U}_j\right)\right]-\frac{2}{3}\mu\frac{\partial}{\partial x_l}(\mathcal{U}_l)\delta_{ij} \tag{4}$$

where μ is the molecular viscosity.

Using the Reynolds decomposition $\mathcal{G}=G+g$, the turbulence is treated with a Reynolds Stress Model (RSM) and a low-Reynolds number approach accounting for wall effects. The low-Reynolds number model accounts for the nonequilibrium between production and dissipation of the turbulent kinetic energy within the boundary layer. The exact Reynolds stress transport equation is as follows

$$\begin{aligned}\frac{\partial}{\partial t}(\rho\overline{u_iu_j})&+\frac{\partial}{\partial x_k}(\rho U_k\overline{u_iu_j})\\ &=-\frac{\partial}{\partial x_k}[\rho\overline{u_iu_ju_k}+\overline{p(\delta_{kj}u_i+\delta_{ik}u_j)}]\\ &\quad+\frac{\partial}{\partial x_k}\left[\mu\frac{\partial}{\partial x_k}(\overline{u_iu_j})\right]-\rho\left(\overline{u_iu_k}\frac{\partial}{\partial x_k}U_j+\overline{u_ju_k}\frac{\partial}{\partial x_k}U_i\right)\\ &\quad+\overline{p\left(\frac{\partial}{\partial x_j}u_i+\frac{\partial}{\partial x_i}u_j\right)}-2\mu\overline{\frac{\partial}{\partial x_k}u_i\frac{\partial}{\partial x_k}u_j}.\end{aligned} \tag{5}$$

The turbulent diffusion is modeled using a simplified gradient-diffusion model of Daly and Harlow [50] as follows:

$$-\frac{\partial}{\partial x_k}[\rho\overline{u_iu_ju_k}+\overline{p(\delta_{kj}u_i+\delta_{ik}u_j)}]=\frac{\partial}{\partial x_k}\left(\frac{\mu_t}{\sigma_k}\frac{\partial}{\partial x_k}(\overline{u_iu_j})\right). \tag{6}$$

The turbulent viscosity is given by $\mu_t=\rho C_\mu k^2/\epsilon$ with $C_\mu=0.09$, k the turbulent kinetic energy given by the trace of the Reynolds stress tensor ($k=1/2\,\overline{u_iu_i}$) and ϵ the turbulent kinetic energy dissipation rate defined as

$$\epsilon=\nu\overline{\frac{\partial}{\partial x_j}u_i\frac{\partial}{\partial x_j}u_i} \tag{7}$$

and computed with a model transport equation similar to that of the standard k-ϵ model.

Applying the generalized gradient-diffusion model, Lien and Leschziner [51] derived a value of $\sigma_k=0.82$ for the turbulent Prandtl number for k. For the pressure-strain, the model proposed by Gibson and Launder [52]; Fu et al. [53], and Launder [54,55] is used. It reads:

$$\overline{p\left(\frac{\partial}{\partial x_j}u_i+\frac{\partial}{\partial x_i}u_j\right)}=\Phi_{ij,1}+\Phi_{ij,2} \tag{8}$$

where $\Phi_{ij,1}$ is the so-called "return-to-isotropy" term and $\Phi_{ij,2}$ the "rapid pressure-strain." $\Phi_{ij,1}$ is modeled as

$$\Phi_{ij,1}=-C_1\rho\frac{\epsilon}{k}\left(\overline{u_iu_j}-\frac{2}{3}\delta_{ij}k\right) \tag{9}$$

while the rapid pressure-strain term is modeled as

$$\Phi_{ij,2}=-C_2\left[(P_{ij}+F_{ij}+G_{ij}-C_{ij})-\frac{2}{3}\delta_{ij}(P+G-C)\right] \tag{10}$$

where P_{ij}, F_{ij}, G_{ij} and C_{ij} are, respectively, the stress production, the production by system rotation, the buoyancy production, and the convection term of the Reynolds stress transport Eq. (5). $P=1/2P_{kk}$, $G=1/2G_{kk}$ and $C=1/2C_{kk}$.

In the low-Reynolds approach chosen, C_1 and C_2 are specified as functions of the Reynolds stress invariants and the turbulent Reynolds number, according to the suggestion of Launder and Shima [56]:

$$C_1=1+2.58A\sqrt{A_2}[1-e^{-(0.0067\,\mathrm{Re}_t)^2}]C_2=0.75\sqrt{A} \tag{11}$$

with the turbulent Reynolds number defined as $\mathrm{Re}_t=\rho k^2/(\mu\epsilon)$. The parameter A and the tensor invariants A_2 and A_3 are

$$A=\left[1-\frac{9}{8}(A_2-A_3)\right]\quad A_2=a_{ik}a_{ki}\quad A_3=a_{ik}a_{kj}a_{ji}. \tag{12}$$

a_{ij} is the anisotropic part of the Reynolds stress tensor defined as

$$a_{ij}=-\left(\frac{-\rho\overline{u_iu_j}+\frac{2}{3}\rho k\delta_{ij}}{\rho k}\right) \tag{13}$$

2.2.2 Boundary Conditions Treatment. The near wall modeling consists of a low Reynolds number approach. The viscosity-affected near-wall region is resolved all the way down to the viscous sublayer. The whole domain is subdivided into a viscosity-affected region and a fully-turbulent region, whose demarcation is determined by the wall-distance-based, turbulent Reynolds number Re_d, defined as $\mathrm{Re}_d=\rho\sqrt{k}d/\mu$ where d is the normal distance from the wall at the cells centers.

In the fully turbulent region, *i.e.*, $\mathrm{Re}_d>200$, the RSM model is employed, while in the viscosity-affected near-wall region ($\mathrm{Re}_d<200$), the one-equation model of Wolfstein [57] is used. The momentum and k equations are retained, but the turbulent viscosity, μ_t, is computed from $\mu_t=\rho C_\mu\sqrt{k}l_\mu$. The ϵ field is computed from $\epsilon=k^{3/2}/l_\epsilon$. The length scales that appear are computed from [58]

$$l_\mu=c_l y[1-e^{(-\mathrm{Re}_d/A_\mu)}] \tag{14}$$

$$l_\epsilon=c_l y[1-e^{(-\mathrm{Re}_d/A_\epsilon)}] \tag{15}$$

The constants are $c_l=\kappa C_\mu^{-3/4}$, $A_\mu=70$, $A_\epsilon=2c_l$ where κ is the von Kármán constant ($\kappa=0.42$).

For convenience, all time-averaged quantities are hereafter denoted with a capital letter, omitting the overline.

2.3 Physical Models of a Porous Cylinder Submitted to Blowing. We are here interested in modeling the blowing through a porous circular cylinder in crossflow. It occurs throughout the whole surface of the cylinder, the injection being uniform and normal to the porous wall. Two models were developed to take into account the blowing through the porous material and its impact on the outer flow. In these two models, we directly model the physical phenomena, which take place when blowing occurs instead of introducing additional terms in the flow equations or the wall functions [59–65].

In the first model, hereafter denoted the holes model, the porous surface is considered as a succession of wall segments and holes through which the blown fluid flows. This is supposed to model the physical phenomena as close as possible where the secondary fluid flows through tiny pores. The size of these segments and holes has to be small enough to correctly represent the porous matrix and must be in the same proportion as the considered porosity. This model has been tested and validated in the case of a flat plate [40]. However, it should be noted that it leads to a discontinuous boundary conditions modeling with successive wall and velocity inlet conditions. The number of cells within a pore and a wall segment was varied from 1–3 and from 2–6, respectively, and resulted in no appreciable difference in any characteristic of the boundary layer profiles, vortex shedding frequency or wall temperatures. As mentioned above, a mesh scaled on the physical reality with numerical holes of the same size than the actual pores, was used. This mesh features more than 3000 cells along the cylinder periphery and these tests showed no change in results, allowing a reduction of the refinement degree of the numerical simulations. Nevertheless, as the phenomena linked to a flow around a cylinder involve higher gradients than in the case of a flat plate where the model has been validated, another blowing model was also developed. It has no discontinuities and consists in sources set immediately above the whole impermeable cylinder surface, which account for the blowing impact on the outer flow from the cylinder. These sources have a momentum, mass, and heat source components, adjusted to reflect the actual secondary flow. The momentum direction in each cell is set so that it remains normal to the wall all along the cylinder periphery. As will be seen below, the two models give similar results, allowing us to use the most appropriate for the type of results to be obtained.

3 Steady Regime

3.1 Recirculation Bubbles. For Reynolds number below 49, the flow around a circular cylinder is steady and remains symmetric. Vortex shedding or flow oscillations do not occur at any time and this steady behavior allows us to study the influence of the blowing without having to account for unsteady aspects.

The influence of the blowing on recirculation bubbles is studied in terms of length and shift, as a function of the blowing ratio, *F*, defined as

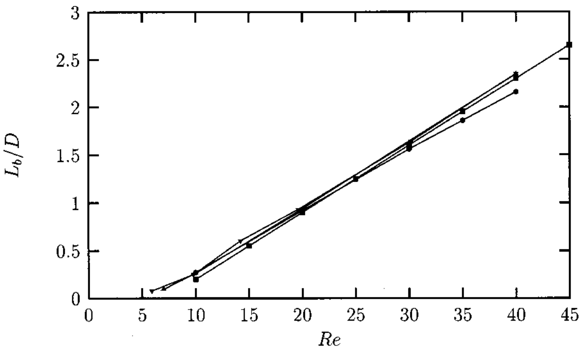

Fig. 3 Recirculation bubbles length evolution with the Reynolds number without blowing.

$$F=\frac{\rho_{inj}U_{inj}}{\rho_\infty U_\infty} \tag{16}$$

where ρ is the density, U the velocity, subscript $_{inj}$ refers to the injected fluid, and $_\infty$ to the main fluid. Initial studies for validation purposes were done for no-blowing cases. It is well-known that recirculation bubbles grow linearly in length when the Reynolds number increases [65–69] until their length is large enough for their equilibrium to become unstable.

From Fig. 3, it is shown that the bubbles grow linearly with the Reynolds number and that this growth is correctly reproduced and collapses well with experimental data from literature. The length, *Lb* (see Fig. 4(*b*) for definition), is taken to be the distance between the front and the rear stagnation point of the bubble as clearly seen in Fig. 4(*a*). No recirculation length is presented for higher Reynolds numbers as the flow is then unsteady and time-averaged bubbles are meaningless. When blowing is applied, the bubbles are pushed away from the back of the cylinder as can be seen from Fig. 4(*b*). They are separated from the cylinder and the blown air impacts on the bubbles and has to flow vertically, either upwards or downwards. Figure 5 shows the evolution of the bubble shift (S/D, see Fig. 4(*b*)) when injection increases for different Reynolds numbers. *S* is defined as the distance from the

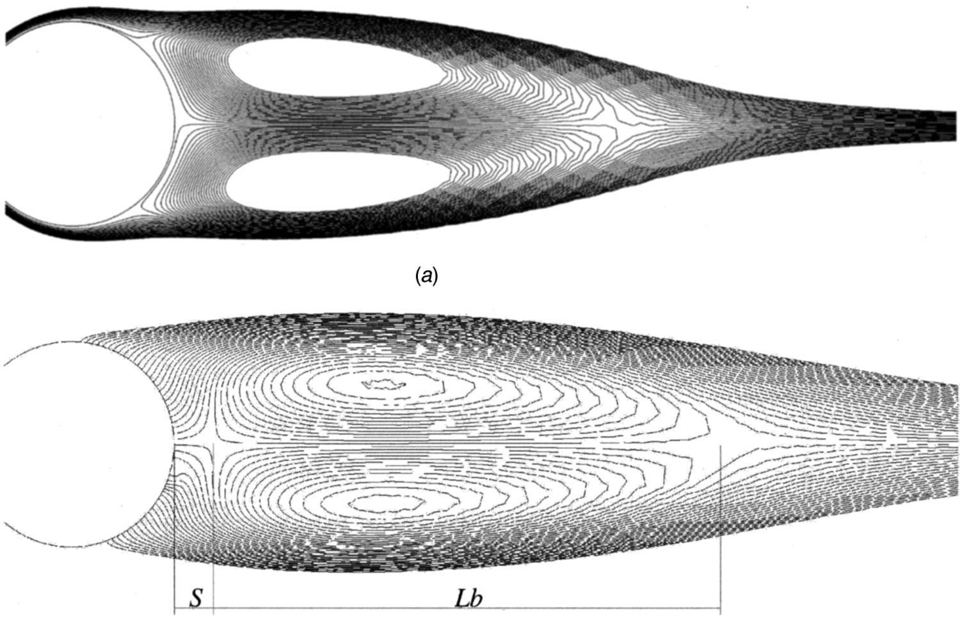

(*a*)

(*b*)

Fig. 4 Recirculation bubbles at Re=40. (*a*) *F*=0 %, (*b*) *F*=5 %.

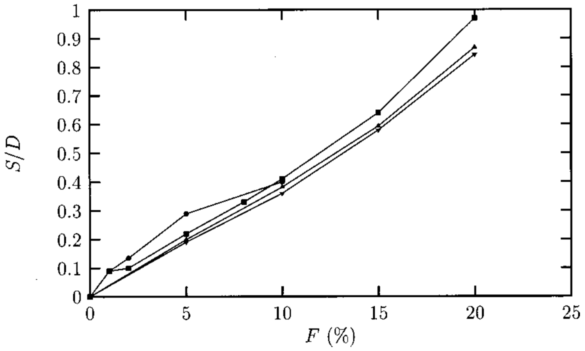

Fig. 5 Evolution of the bubble shift with blowing for different Reynolds numbers. ●, Re=20; ■, Re=30; ▲, Re=35; ♦, Re=40.

rear point of the cylinder to the front bubble stagnation point. It grows approximately linearly with the blowing rate but is independent of the Reynolds number. This shift is due to a change in the rear stagnation point location, set by a momentum equilibrium criterion between the blown fluid and the recirculating flow.

At the rear bubble stagnation point, the blown air and the recirculating flow *x*-momentum moduli are equal. A simple qualitative theory can be derived to deduce the bubble location evolution. In an inviscid flow and neglecting the pressure forces, the momentum balance of the secondary fluid leads to a momentum along the downstream symmetry axis which decreases as 1/*x* if one excludes interactions with the primary flow. Hence, the secondary fluid *x*-momentum at a streamwise distance *x* reads,

$$(\rho\mathbf{U})_x=\frac{R\rho_{inj}U_{inj}}{x}\frac{x}{\|\mathbf{x}\|},\quad x\geqslant R\ \text{(cylinder radius)} \tag{17}$$

while the recirculating flow *x*-momentum is

$$(\rho\mathbf{U})_{recirc}=-(\alpha\rho_\infty+(1-\alpha)p_{inj})\gamma U_\infty\frac{\mathbf{x}}{\|\mathbf{x}\|} \tag{18}$$

where the recirculating bubble temperature is comprised between the main and the secondary flow temperature, ($\alpha\in[0;1]$) and the constant γ is positive as the recirculating velocity is assumed to be proportional to U_∞, i.e., $U_{recirc}=\gamma U_\infty$.

At the rear stagnation point, equilibrium along the **x** direction thus implies

$$(\rho\mathbf{U})_x+(\rho\mathbf{U})_{recirc}=\mathbf{0} \tag{19}$$

or, coming from the blowing parameter definition, *F*, the equilibrium condition reads

$$\frac{RF\rho_\infty U_\infty}{x}-\gamma U_\infty(\alpha\rho_\infty+(1-\alpha)\rho_{inj})=0 \tag{20}$$

or,

$$x=\frac{RF\rho_\infty}{\gamma(\alpha\rho_\infty+(1-\alpha)\rho_{inj})}. \tag{21}$$

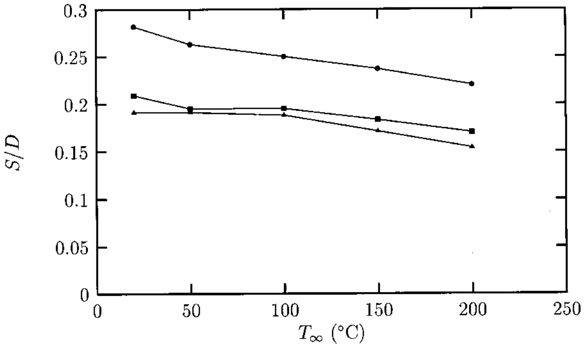

Fig. 6 Evolution of the bubbles shift with the free stream temperature for different Reynolds numbers *F*=5 %; T_{inj}=20°C. ●, Re=20; ■, Re=30; ▲, Re=40.

For an isothermal case, the rear bubble stagnation point location thus shifts downstream linearly with the injection rate and does almost not depend on the Reynolds number (it has been checked that γ is only a slightly increasing function of the Reynolds number). When the main flow gets hotter than the secondary flow, for a constant injection ratio, α remains roughly constant, while ρ_∞ decreases, and the bubble tends to get closer to the cylinder. This is qualitatively confirmed in Fig. 6 where the temperature of the primary flow was varied from ambient (isothermal case) up to 200°C for three Reynolds numbers (20, 30, and 40), while the coolant temperature and the blowing ratio remained the same. It is observed that the shift indeed tends to decrease with a hotter main flow, in full agreement with the qualitative model. However, difficulties in deriving a model for the α and γ constants, and the coarse hypotheses retained, prevent quantitative comparisons.

3.2 Streamlines. Figure 7 exhibits a magnified view of the streamlines of the flow blown from the upstream part of the cylinder only. Figure 7(*a*) is plotted using the holes model while Fig. 7(*b*) uses the sources model. Both figures perfectly collapse, demonstrating that the two models similarly account for the impact of the blowing on the dynamical behavior of the attached boundary layer. It also shows that upstream stream lines, i.e., the upstream flow, are pushed away from the cylinder surface, which illustrates the phenomenon of protection due to blowing. The cylinder is thus isolated from the outer flow by a blowing issued fluid layer.

The only difference between the flow computed from the two models lies in the immediate vicinity above the surface. In the first cell, the streamline direction is not exactly the same for the two models. This is a result of the blowing model. With the holes model, the phenomenon is thought to be as close as possible to the physical reality, where a secondary fluid flows from below the surface and is then governed by the Navier-Stokes equations. On the other hand, the sources model does not consider any secondary flow, but applies a momentum and mass source immediately above the surface. Numerically, this leads to an immediate mixing of the upstream with the flow from sources in the first cell while this is not the case with the holes model where the mixing occurs gradually, as imposed by the fluid equations.

Nevertheless, these small differences are not of primary interest as we are concerned with the general impact of the blowing and not in the exact phenomenon occurring in the immediate vicinity of the wall by the mixing of the two flows. In this work, the aim is to predict the velocity and temperature profiles evolution with blowing or phenomena occurring relatively far from the wall. The two models were used to determine and to study various parameters, and no significant differences were observed in these quantities. Consequently, for sake of convenience, most of the results will be presented with the sources model.

4 Unsteady Regime

When the Reynolds number value increases beyond around 50, the global instability growth rate becomes positive and leads to the vortex shedding phenomenon, called the Bénard-von Kármán vortex street. Simulating this flow configuration requires an unsteady formulation of the Navier-Stokes equations, leading to much larger computation times. The emphasis is put on the modification of the vortex shedding process due to blowing and on the thermal and dynamical wake evolution.

The blowing impact on the critical Reynolds number is far beyond the scope of this study. To allow for direct validation from

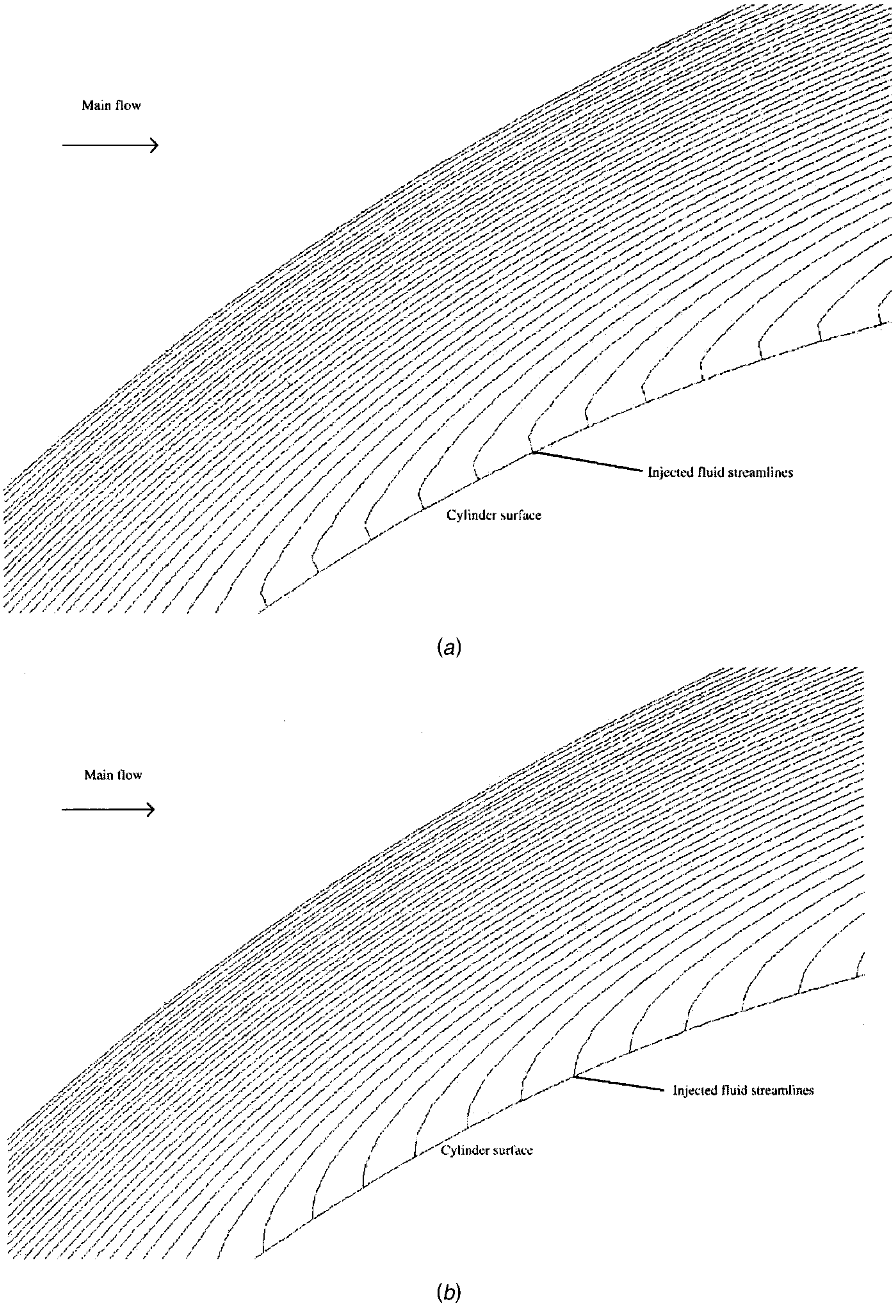

Fig. 7 Secondary fluid path lines in the upstream part of the cylinder. Re=40. (*a*) holes model, (*b*) sources model.

experiments which Reynolds number range is Re $\in[3900;31{,}000]$ and for sake of brevity, only results at a Reynolds number of 3900 are presented.

4.1 Vorticity in the Near Wake. Figure 8 shows a snapshot in time of the vorticity contours at the same phase for a turbulent case without (Fig. 8(*a*)) and with blowing (10%, Fig. 8(*b*)). The contours without blowing are in qualitative agreement with the experimentally obtained photograph for a similar flow (e.g., van Dyke [70]). The vorticity magnitude scale is the same for both figures allowing for direct vorticity level comparison. As will be seen in following sections, the blowing tends to lower all gradients and makes the vorticity magnitude dramatically decrease in the attached boundary layer as seen from the white region within the boundary layer. A certain amount of vorticity is also present at the immediate rear of the cylinder demonstrating the presence of strong recirculating flows. When blowing occurs, this rear vorticity region almost separates from the cylinder and rapidly decays. As will be seen later, the static pressure defect is lower in case of blowing and this effect causes the formation region to increase as clearly illustrated in this figure, where the growing vortex is shifted further away from the back of the cylinder in case of blowing (Table 1).

4.2 Impact on the Force Coefficients. Due to the unsteady behavior of the flow in this range of Reynolds numbers, the lift and drag coefficients, $C_{tD}=F_x/1/2\rho_\infty U_\infty^2$ and $C_L=F_y/1/2\rho_\infty U_\infty^2$, where F_x and F_y are the components of the net force acting on the body, experience oscillations as well. F_x is computed from $F_x=\oint_\Omega -P\mathbf{x}.\mathbf{n}+\oint_\Omega$ (wall shear stress) **x.t** where **n** is the local normal vector from the surface Ω of the body and **t** the tangential

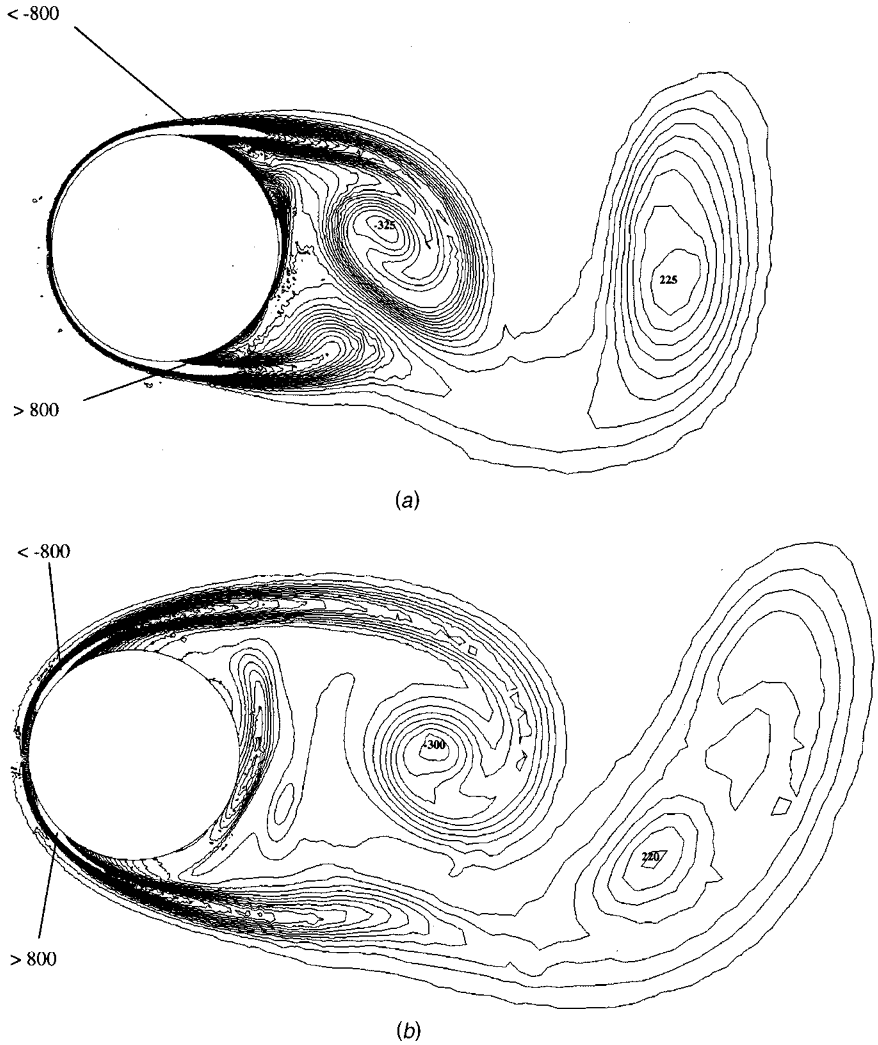

(*a*)

(*b*)

Fig. 8 Near wake vorticity field. Re=3900, (*a*) *F*=0%, (*b*) *F*=10 %. The vorticity levels are indicated.

vector. The relation is similar for the lift expression with a projection on the vertical axis. Their evolution with time is plotted in Fig. 9. The symmetrical character in time of the drag compared to the asymmetrical character of the lift leads to a drag oscillation frequency exactly twice the lift oscillation frequency. Furthermore, the lift coefficient must be zero-centered as the time-averaged lift is nil. This classic test allows a partial check of the numerical simulations validity.

Due to a lower velocity gradient near the surface, the overall viscous drag is expected to decrease with the blowing. This is illustrated in Table 2 where the viscous drag coefficient of the cylinder is reported for different injection rates. It is clear that it rapidly decreases with blowing, leading to many applications. The pressure drag coefficient, also reported, strongly exhibits a blowing dependence, tending to increase as the injection becomes larger. These values are slightly above (20%) the experimentally reported values for no blowing [2]. This is known to be due to the absence of energy transfer into the third direction for 2-D simulations, leading to higher drag and Reynolds stresses [13,71–73]. The pressure drag can be evaluated from Fig. 10, where the pressure coefficient $C_P=(P-P_\infty)/(1/2\rho_\infty U_\infty^2)$ is plotted along the surface for different blowing ratio. In the attached boundary layer region, the pressure coefficient is seen to approximately follow the sinus portion of the potential solution. For $\theta=0$ deg, it remains equal to 1 whatever the blowing ratio, while the front stagnation

Table 1 Maximum shear stress location angle as a function of the blowing ratio. Re=3900.

F (%)	0	1	2	5	10
θ_d (°)	52	50	47	40	40

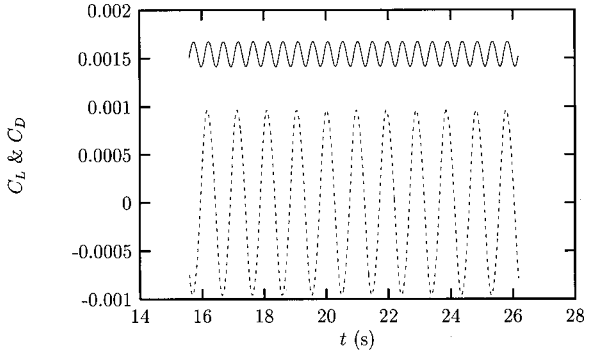

Fig. 9 Force coefficients time history records. Solid line: drag coefficient, dashed line: lift coefficient.

Table 2 Pressure and viscous drag coefficients evolution with blowing. Re=3900.

F (%)	0	1	2	5	10
C_{vD}	0.063	0.050	0.038	0.018	0.009
C_{pD}	1.148	1.429	1.511	1.570	1.652

point moves upstream and separates from the surface. From inviscid considerations, the theoretical pressure coefficient at $\theta=0$ deg can be derived as $C_P(0\,\mathrm{deg})=1-\rho_{inj}/\rho_\infty(U_{inj}/U_\infty)^2$. For the blowing rates considered here ($\leqslant 10\%$), it leads to numerical values very close to 1. For higher angles, the pressure coefficient increases with blowing compared to the no-blowing curve. In that case, some low-momentum fluid is injected into the boundary layer and modifies both the velocity and the pressure field. The same argument can be applied to the near wake, where the velocity defect is lower in case of blowing and makes the pressure rise. Moreover, due to lower gradients in the boundary layer before separation and in the shear layer, and thus lower irreversibilities generated, the pressure in the wake also tends to increase compared to the non-blowing case. Both of these effects, lower velocities and lower irreversibilities, lead to a decrease in the pressure defect at the back of the cylinder. However, the pressure rise at the downstream part of the cylinder is lower than the one on the upstream part and the overall pressure drag coefficient increases with the blowing rate as reported in Table 2.

4.3 Profiles. When blowing occurs, the secondary fluid flows outwards from the surface and has a dramatic influence on the boundary layer dynamics. Figure 11 shows an example of the time-averaged velocity magnitude profile at an angle θ of 65 deg relative to the front stagnation point. The plot direction is vertical, along the h/D variable whose origin is the surface, for convenient comparison with experimental data obtained from hot-wire anemometry in our wind tunnel. Experimental profiles are truncated below a certain distance to the wall due to experimental validity limitations, and also below a certain velocity because of difficulties in calibrating for low velocities (see [74] for full details). An excellent agreement is observed with the experiments whatever the blowing ratio. The impact of the blowing is correctly accounted, hence validating the modelization chosen. The dynamical boundary layer clearly thickens when blowing occurs, and the velocity gradient above the surface is demonstrated to decrease.

Figure 12 shows the velocity magnitude profiles for an angle of 105 deg. The dead fluid zone, below the separated shear layer, is clearly visible. Its height tends to increase with the blowing due to the upstream shift of the boundary layer separation point. The profiles are S-shaped, exhibiting a typical separated shear layer behavior. With blowing, the S-shaped profile becomes less sharp, leading to an increase of the shear layer thickness and a decrease of all gradients.

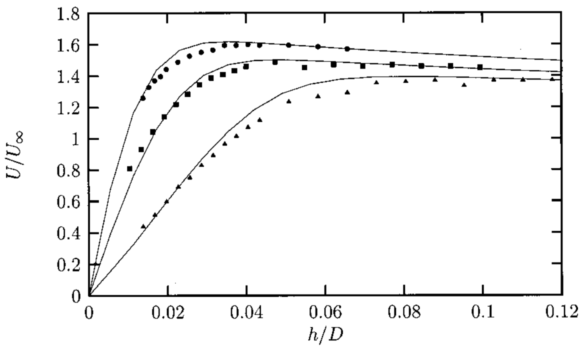

Fig. 11 Velocity magnitude vertical profile. θ=65 deg, Re =3900. Experimental values are the symbols and numerical results are the corresponding solid lines. ●, F=0%; ■, F=2%; ▲, F=5%.

Figure 13 shows the temperature profiles at an angle of 65 deg for different blowing rates. The profiles are plotted along the normal direction. No comparison with our experimental work is possible due to difficulties in handling the cold wire probe for these locations. The thermal behavior is found to be similar to the dynamics. The thermal boundary layer thickens with blowing and the temperature gradient above the surface rapidly decreases, demonstrating the thermal protection effect of the blowing technique. For a 10% injection rate, the profile is also S-shaped, exhibiting a cold fluid zone below the thermal boundary layer. This constant temperature zone thus leads to negligible convective heat transfer coefficients and to a maximum protection.

4.4 Separation Angle. The focus is now put on the evolution of the separation angle with the blowing. Figure 14 shows the time-averaged shear stress along the cylinder surface for different blowing ratii. The separation angle is referred to be the point where the shear stress reaches zero, i.e., where the longitudinal velocity normal gradient at the surface is nil. The unsteady flow dynamics makes the boundary layer to oscillate at the von Kármán frequency. In particular, the front stagnation point and the boundary layer separation point oscillate around their mean value, leading to a nonzero time-averaged shear stress. The separation point is then defined as the time-averaged value of the separation angle.

In case of blowing, the boundary layer is pushed away from the cylinder surface and so is the recirculating flow which induces separation through the adverse pressure gradient. Hence the blowing prevents the shear stress from reaching zero on both sides of

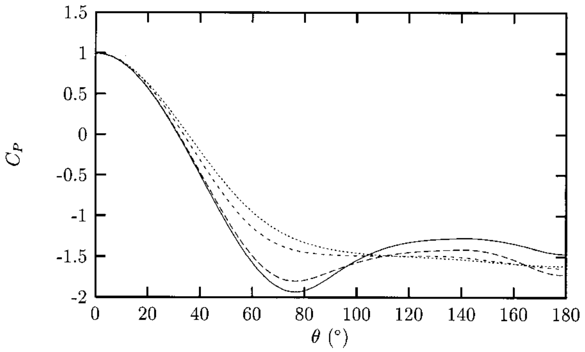

Fig. 10 Pressure coefficient along the cylinder surface as a function of blowing. Re=3900.

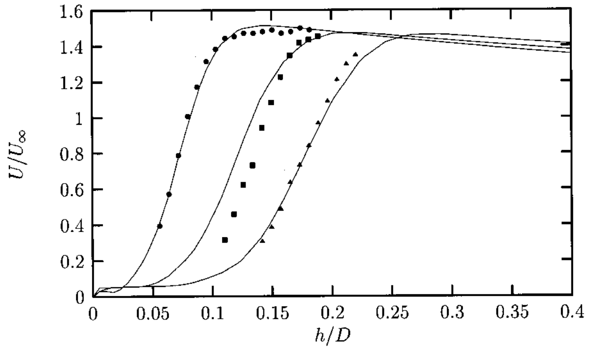

Fig. 12 Velocity magnitude vertical profile. θ=105 deg, Re =3900. Experimental values are the symbols and numerical results are the corresponding solid lines. ●, F=0%; ■, F=2%; ▲, F=5%.

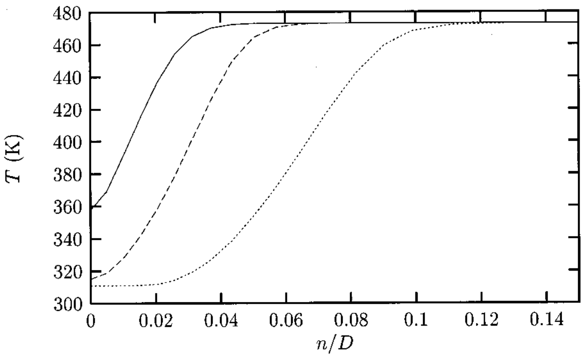

Fig. 13 Temperature normal profile at $\theta=65$ deg for Re $=3900$. Solid line is for $F=2\%$, mid-dash line for $F=5\%$ and dash line for $F=10\%$.

the cylinder at the same time, and solely the in-phase side with the vortex shedding experiences a separation. Thus, no separation angle can accurately be defined.

On could refer to the maximum in the shear stress evolution to study the blowing impact on the separation. The shear stress maximum angle along the cylinder surface is reported in Table 1. It is seen to be shifted upwards, toward lower angle values. This shows the effect of the blowing on the dynamics, which is to promote the boundary layer separation. Blowing thus has a destabilizing effect on the attached boundary layer. The shear stress also tends to decrease all along the surface with blowing. This decrease in the shear stress is consistent with the modification of the velocity gradient above the surface. While its evolution is shifted upstream, it remains qualitatively similar whatever the blowing ratio.

4.5 Temperature Field. The modification of the temperature field in the cylinder near wake due to the blowing is also addressed. This aspect is particularly interesting when a thermally sensitive part is located far downstream of the cylinder. The temperature flow field is plotted in Fig. 15 for $F=1\%$. For visualization convenience, the color scale is set between 450 and 472 K. The vortex cores remain at an almost constant temperature when flowing downstream, due to low thermal diffusion and very little dynamical mixing. Braids between successive von Kármán vortices are clearly visible demonstrating that the temperature closely follows the vorticity patterns. The separated region, appearing in white due to its low temperature, extends far away from the surface beyond the separation point, providing an excellent protection of the downstream side of the cylinder. Recirculation at the back draws hot fluid toward the rear stagnation point. The temperature field is thus seen to be substantially modified far from the cylinder. This allows for lower thermal protection required for downstream parts (e.g., in successive turbine stages).

4.6 Thermal Effectiveness. Similarly to the friction stress, the blowing leads to a thermal stress reduction, decreasing the temperature gradient in the immediate vicinity of the surface. The thermal protection is studied in terms of the dimensionless wall temperature, the thermal effectiveness, η, defined as

$$\eta=\frac{T_\infty-T}{T_\infty-T_{inj}} \tag{22}$$

where T_∞, T, and T_{inj} are the upstream, local, and injected fluid temperature, respectively. Figure 16 shows the thermal effectiveness along the cylinder surface for three blowing ratii using the source model. It is clearly seen that the blowing efficiently protects the cylinder surface even for weak injection rates. The lowest protection is achieved at the front stagnation point. This is consistent with the fact that the boundary layer is squashed onto the surface by the upstream flow, leading to strong gradients and large heat transfer coefficients. A maximum in the thermal effectiveness occurs beyond the separation point whatever the blowing rate due to a cold dead fluid zone located below the separated shear layer. Recirculation at the rear of the cylinder draws back some of the hot fluid from the main flow, which decreases the effectiveness for angles higher than 130 deg.

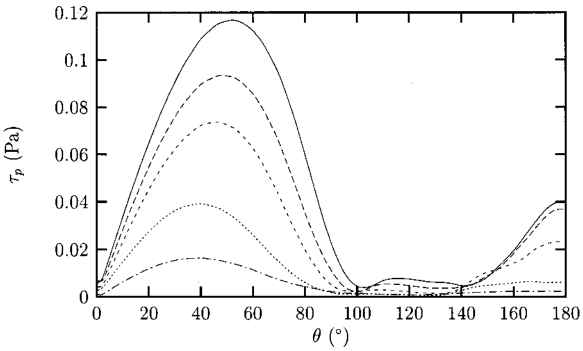

Fig. 14 Shear stress evolution with blowing. Re=3900.

When blowing increases, the thermal protection is enhanced and the effectiveness increases. This is illustrated in Fig. 17 where it is plotted as a function of the blowing ratio for $\theta=65$ deg. Excellent thermal protection is achieved with the blowing and good agreement is found with experimentally obtained data, here again further validating the modeling. It demonstrates that only weak injection rates are necessary to protect walls. For a 1% injection, the thermal effectiveness is already 45%. The experimental limiting value for high blowing rates is not 100% due to radiative heat transfer, which is not accounted in the numerical simulations. As the blowing increases, it rapidly becomes the predominant heat transfer mode and tends to limit the thermal effectiveness, while numerically, only the convective heat transfer coefficient is considered, which rapidly decreases to zero.

Besides the local properties, the blowing is expected to have a dramatic influence on global properties of the wake, downstream of the cylinder. Injecting a secondary fluid through the porous surface tends to increase the apparent diameter and to modify the flow stability. The modification of the vortex shedding process is an important feature for the thermal and dynamical control of the wake in terms of noise generated, intrinsic frequency and vibrations induced, wake stability and interactions, etc. and a detailed study is necessary.

4.7 Vortex Shedding Frequency. The study of the wake instability of the near wake of the cylinder is carried-out from the velocity magnitude time history record at a point located downstream of the cylinder. It is studied in terms of Strouhal number, Sr, defined as $\mathrm{Sr}=fD/U_\infty$ where f is the vortex shedding frequency and U_∞ the upstream velocity magnitude. As the Strouhal number represents the non-dimensional vortex shedding frequency, which is a global instability, the location of the recording point is not an influencing parameter. The frequency is the same throughout the entire flow field, and is present even upstream of the cylinder.

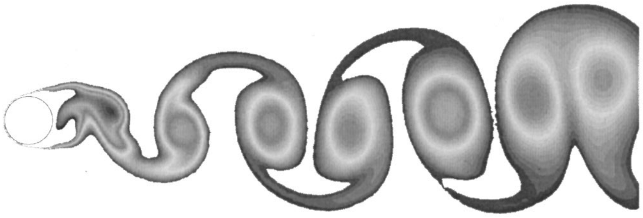

Fig. 15 Temperature field in the wake with the sources model. Re=3900, $F=1\%$, $T_\infty=473$ K.

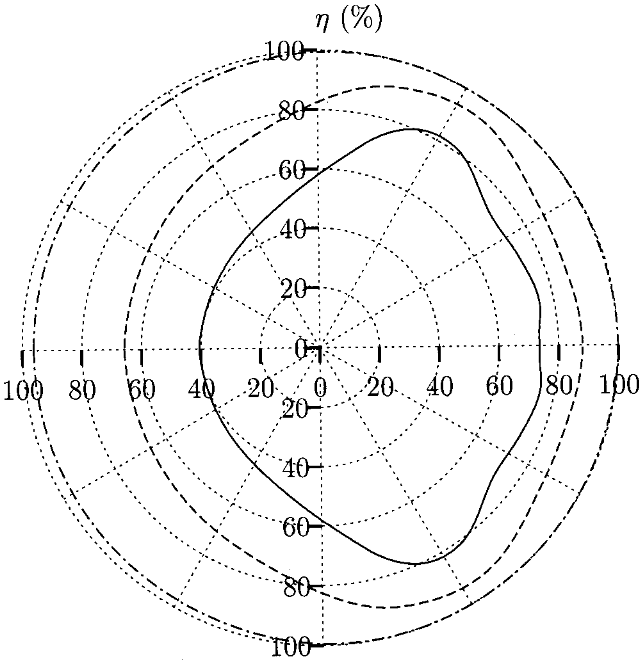

Fig. 16 Effectiveness along the cylinder periphery. Re=3900 From bottom to top: *F*=1, 2, 5%.

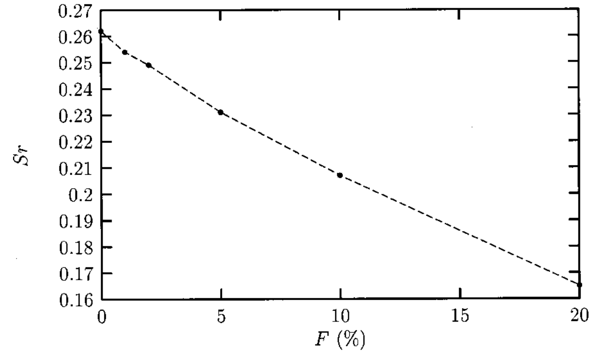

Fig. 18 Strouhal number evolution with blowing. Re=3900.

The blowing impact can be studied through the linear stability theory. Many authors were interested in the modification of the stability patterns by blowing. It has been shown to modify the time-averaged velocity profile in the wake, thus changing the stability properties and the most amplified frequency growth rate [75–77]. The pioneer experimental works of Wood [78] and Bearman [79] studied the modification of the shedding frequency behind an airfoil when base bleed is applied. Several others authors have reported a decrease of the vortex shedding frequency behind bluff bodies with base bleed, but it seems that very few studies are concerned with full blowing, i.e., through the entire surface.

Figure 18 exhibits the evolution of the Strouhal number with the blowing rate at a Reynolds number of 3900. Without blowing, the Strouhal value is found to be 0.262, well above the experimentally reported value of 0.215 [80]. This difference is an intrinsic feature of 2-D simulations, already observed by [13,15,16,22,81]. Mittal and Balachandar [13] have proved that 3-D modes present in experiments "extract" energy from the field, in particular via mode-B vortices, and lead to lower Reynolds stresses than in a purely 2-D configuration as in bidimensional simulation. This effect finally leads to higher Strouhal number than from experiments.

The Strouhal number is seen to approximately decrease linearly with *F*. This result is consistent with the theoretical analysis of Cohen [82] based on a modification of the leading parameter of the laminar attached boundary layer equations, who found a decrease of the boundary layer oscillation frequency with the blowing ratio.

Injecting a low-momentum fluid into the boundary layer leads to lower gradients, both dynamical and thermal. The lower gradients allow for slower dynamics, thus, larger boundary layer and momentum thickness, and lower vortex shedding frequency which is in agreement with the simulation results.

If compared to the experimentally obtained Sr$-F$ relationship [74], the Strouhal number decrease obtained numerically is lower than from experiments, whatever the Reynolds number considered. Very extensive tests were carried-out, both numerically and experimentally, to check-out this difference. The numerical schemes, the cell types, the cells number per hole and wall segment, the numerical domain extent, the pressure-velocity coupling algorithm, the blowing model and the boundary conditions treatment have been checked to have no influence. The blockage ratio was varied using an extended grid and produced same results. The modeling of the blowing, using the two models and the actual size simulation with the dedicated mesh, and the turbulence treatment using a RNG $k-\epsilon$ model, were varied and resulted in no appreciable differences. The separation angle is thought to be a parameter of primary importance for a correct vortex shedding frequency simulation. It is known to be a quantity difficult to accurately capture using classic turbulence models and a more accurate one should be necessary. However, even with the simple

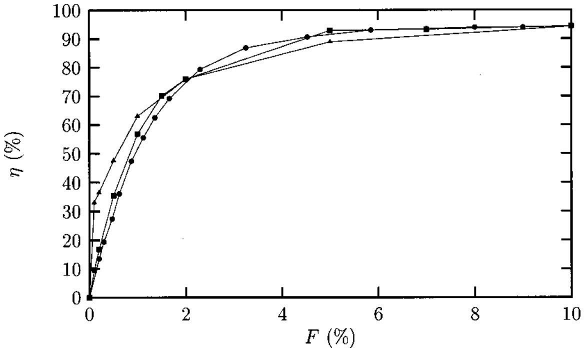

Fig. 17 Effectiveness as a function of blowing. θ=65 deg, Re =3900. Squares are the experimental data, circles are from the sources model and triangles are from the holes model.

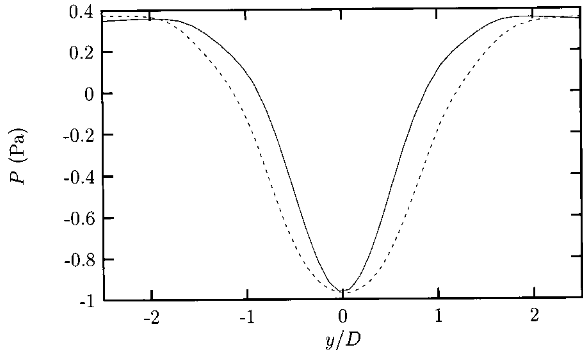

Fig. 19 Static pressure transverse profile in the near wake. Re=3900, *x*/*D*=2.5. The curves are slightly shifted for visualization convenience. Solid line is *F*=0%, dash line is *F*=5%.

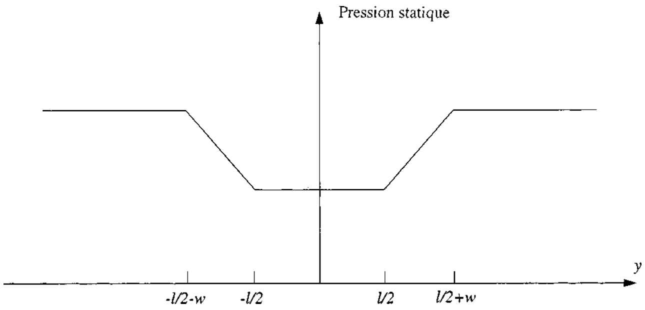

Fig. 20 Schematic of the pressure profile considered for the qualitative model.

blowing modelisation used, the decrease in the shedding frequency is qualitatively reproduced and exhibits the essential phenomena observed from experiments.

The difference with the experiments is not due to 3-D effects, which are not accounted in the simulations. Three-dimensional simulations have been conducted and show no difference in the Strouhal number evolution compared to a 2-D numerical configuration. This justifies the choice of a 2-D approach for studying the blowing impact on the flow dynamics. Although the flow dynamics itself is over-predicted in 2-D, its evolution with blowing is in agreement with 3-D simulations and allows the relative blowing impact to be studied.

4.8 Model for the Strouhal Number Behavior With Blowing. The near wake of the cylinder can also be studied through the static pressure profile along the transverse direction. Figure 19 shows the time-averaged pressure profile, both without and with injection (5%) at $x/D = 2.5$. When blowing occurs, its width tends to increase, which is consistent with the fact that the apparent diameter increases as well. The pressure defect is lower in the case of blowing, as seen in Section 4.2 and the transverse pressure gradient thus decreases. Mathelin et al. [74] derived a simple qualitative model for the prediction of the Strouhal number evolution with blowing. It is based on the analogy between the pressure wake profile and a U-shaped track where a fluid particle would slip from side to side while flowing downstream. The pressure wake is thus modeled in a simple form and the fundamental law of mechanics ($\mathbf{F} = m\gamma$) are applied to the particle and leads to:

$$\frac{\partial P}{\partial_y} dx\, dy = -\rho\, dx\, dy\, \frac{\partial^2 y}{\partial t^2} \tag{23}$$

Figure 20 shows a schematic of the pressure profile model. Simple expression for the Strouhal number was derived and is given by:

$$\mathrm{Sr} = \frac{D}{U_\infty} \sqrt{\frac{w|\partial P/\partial y|_e}{2\rho(16w^2 + l^2)}} \tag{24}$$

where w is the "edge depth" and l the flat band width (see schematic). The pressure gradient is evaluated from the mean edge slope of the pressure defect profile. When applied to the pressure profile shown in Fig. 19, the Strouhal number ratio between the no-blowing and the 5% injection case is 0.90. Using Fig. 18, the ratio effectively reported is 0.88, which is in reasonable agreement with our theoretical value. However, due to the coarse hypotheses retained, this model only gives the trend of the Strouhal number evolution between two blowing rates and should not be used to predict any quantitative value for the Strouhal number itself. It only allows to predict the general behavior of the dynamics in case of blowing. In particular, it is seen that the vortex shedding frequency is directly linked to the pressure gradient, thus exhibiting the analogy between the pressure gradient and the spring strength of an oscillator. In the literature, other oscillator-based models have been proposed to describe some flow phenomena (e.g., formation of spanwise cells [83]).

5 Conclusions

The flow around a porous circular cylinder in a cross-flow when complete blowing is applied has been studied numerically. Both the laminar and turbulent regimes were investigated. The blowing was simulated using two models, which were proved to lead to identical results on global properties such as the boundary layers and the wake dynamics and were validated using experiments. The source model was generally used for smoothness modeling reasons. The blowing has proved to strongly affect the boundary layers, both dynamical and thermal, increasing their thickness and lowering all the gradients by injecting some low-momentum low-temperature fluid. The transfer coefficients thus tend to decrease. This leads to a lower shear stress and convective heat flux, allowing for low viscous drag and an efficient thermal protection when cold fluid is blown and keeping the surface temperature to a reasonable level. Nevertheless, a strong increase in the pressure drag occurs with blowing and leads to an increase in the overall drag with blowing.

Besides the attached boundary layer evolution, the blowing strongly affects the near wake. The vortex shedding frequency decreases with blowing due to slower wake dynamics and a larger formation region. The pressure field was shown to be linked to the vortex shedding frequency. The pressure defect at the back of the cylinder tends to "fill up" with blowing, leading to lower transverse static pressure gradients in the near wake. Using a simple qualitative model, this was proved to be directly connected to the vortex shedding frequency.

It thus appears that the complete blowing can be of primary interest for the wake control (vibrations, suppression of the shedding), the thermal protection (aircraft engine blades) or for the reduction of the viscous drag.

Acknowledgments

Some computational results presented have been performed on a CRAY T3E at the *Institut du Dévelopement et des Ressources en Informatique Scientifique* (IDRIS) and on a workstations cluster at the *Center pour le Dévelopement du Calcul Scientifique Parallèle* (CDCSP) at the Claude Bernard University of Lyon.

Nomenclature

C_{pD} = pressure drag coefficient
C_{tD} = total drag coefficient
C_{vD} = viscous drag coefficient
C_L = lift coefficient
C_P = pressure coefficient
C_μ = constant
D = outer cylinder diameter
d = normal distance to the wall at the cells centers
dx = elementary particle dimension
dy = elementary particle dimension
F = blowing rate, $F = (\rho_{inj} U_{inj})/(\rho_\infty U_\infty)$
$\mathbf{F}$ = force
F_x = drag force
F_y = lift force
f = frequency
H = specific enthalpy
h = vertical coordinate
k = turbulent kinetic energy
Lb = recirculation bubbles length
l = flat band width
l_μ = length scale for μ
l_ϵ = length scale for ϵ
$\mathcal{P}$ = instantaneous pressure
p = fluctuating pressure

R = cylinder radius
Re = Reynolds number, $\mathrm{Re}=(\rho_\infty U_\infty D)/\mu_\infty$
S = shift distance of the recirculation bubbles
Sr = Strouhal number, $\mathrm{Sr}=fD/U_\infty$
Sr_0 = Strouhal number in no-blowing case
T = temperature
t = time
U = mean velocity
$\mathcal{U}$ = instantaneous velocity
u = fluctuating velocity
w = edge depth
x = streamwise coordinate
y = transverse coordinate
z = spanwise coordinate
α = constant
γ = constant
γ = elementary particle acceleration
δ_{ij} = Kronecker symbol
δt = time step
δt^* = nondimensional time step
ϵ = turbulent kinetic energy dissipation rate
η = thermal effectiveness, $\eta=(T_\infty-T)/(T_\infty-T_{inj})$
θ = angle along the cylinder periphery
θ_s = separation angle
κ = von Kármán constant (0.42)
λ = thermal conductivity
μ = dynamic viscosity
ν = kinematic viscosity
ρ = density
σ_k = turbulent Prandtl number for the turbulent kinetic energy k
τ_{ij} = stress tensor
Ω = surface of the cylinder

Subscripts

$\cdot$ = scalar product
∞ = free stream fluid
d = wall distance based
e = edge of the pressure profile
i = discrete variable
inj = injected fluid
j = discrete variable
k = discrete variable
$recirc$ = recirculating fluid
t = turbulent.

Superscripts

$-$ = time-averaged

References

[1] Strouhal, V., 1878, ‘‘Über eine besondere Art der Tonerregung,’’ Ann. Phys. Chem. (Liepzig), Neue Folge, **5**, Heft 10, pp. 216–251.
[2] Zdravkovich, M. M., 1997, *Flow around circular cylinders. Fundamentals*, Oxford University Press.
[3] Williamson, C. H. K., 1996, ‘‘Three-dimensional wake transition,’’ J. Fluid Mech., **328**, pp. 345–407.
[4] Thom, A., 1928, ‘‘An investigation of fluid flow in two dimensions,’’ Aero. Res. Council, Repp. & Memo. 1194.
[5] Thom, A., 1933, ‘‘The flow past circular cylinders at low speeds,’’ Proc. R. Soc. London, Ser. A, **A141**, pp. 651–669.
[6] Kawaguti, M., 1953, ‘‘Numerical solution of the Navier-Stokes equations for the flow around a circular cylinder at Reynolds number 40,’’ J. Photogr. Sci., **8**, pp. 747–757.
[7] Hirota, I., and Miyakoda, K., 1965, ‘‘Numerical solution of Kármán vortex street behind a circular cylinder,’’ J. Meteorol. Soc. Jpn., **43**, pp. 30–40.
[8] Jordan, S. K., and Fromm, J. E., 1972, ‘‘Oscillating drag, lift and torque on a circular cylinder in a uniform flow,’’ Phys. Fluids, **15**, pp. 371–376.
[9] Payne, R. B., 1958, ‘‘Calculation of unsteady viscous flow past a circular cylinder,’’ J. Fluid Mech., **4**, pp. 81–86.
[10] Ingham, D. B., 1968, ‘‘Note on the numerical solution for unsteady viscous flow past a circular cylinder,’’ J. Fluid Mech., **31**, pp. 815–818.
[11] Collins, W. M., and Dennis, S. C. R., 1973, ‘‘Flow past an impulsively started circular cylinder,’’ J. Fluid Mech., **60**, pp. 105–127.
[12] Karniadakis, G., and Triantafyllou, G. S., 1992, ‘‘Three-dimensional dynamics and transition to turbulence in the wake of bluff objects,’’ J. Fluid Mech., **238**, pp. 1–30.
[13] Mittal, R., and Balachandar, S., 1995, ‘‘Effect of three-dimensionality on the lift and drag of nominally two-dimensional cylinders,’’ Phys. Fluids, **7**(8), pp. 1841–1865.
[14] Na, Y., and Moin, P., 1998, ‘‘Direct numerical simulation of a separated turbulent boundary layer,’’ J. Fluid Mech., **374**, pp. 379–405.
[15] Persillon, H., and Braza, M., 1998, ‘‘Physical analysis of the transition to turbulence in the wake of a circular cylinder by three-dimensional Navier-Stokes simulation,’’ J. Fluid Mech., **365**, pp. 23–88.
[16] Breuer, M., 1998, ‘‘Numerical and modelling influences on large eddy simulations for the flow past a circular cylinder,’’ Int. J. Heat Fluid Flow, **19**(5), pp. 513–521.
[17] Bosch, G., and Rodi, W., 1998, ‘‘Simulation of vortex shedding past a square cylinder with different turbulence models,’’ Int. J. Numer. Methods Fluids, **28**(4), pp. 601–616.
[18] Jordan, S. A., and Ragab, S. A., 1998, ‘‘A large-eddy simulation of the near wake of a circular cylinder,’’ ASME J. Fluids Eng., **120**, pp. 243–252.
[19] Zhang, H. Q., Fey, U., Noack, B. R., König, M., and Eckelmann, H., 1995, ‘‘On the transition of the cylinder wake,’’ Phys. Fluids, **7**(4), pp. 779–794.
[20] Dunham, J., 1968, ‘‘A theory of circulation control by slot-blowing, applied to a circular cylinder,’’ J. Fluid Mech., **33**, part 3, pp. 495–514.
[21] Zandieh, A., and Leishman, G. J., 1993, ‘‘Boundary layer pressure measurements on a cylinder with unsteady circulation control,’’ AIAA J., **31**(10), pp. 1769–1776.
[22] Cox, J. S., Rumsey, C. L., Brentner, K. S., and Younis, B. A., 1997, ‘‘Computation of vortex shedding and radiated sound for a circular cylinder,’’ ASME/JSME/MechE/CSME/IAHR 4th symposium in Fluid-Structure Interactions, Dallas, Texas.
[23] Roussopoulos, K., and Monkewitz, P. A., 1996, ‘‘Nonlinear modeling of vortex shedding control in cylinders wakes,’’ Physica D, **97**, pp. 264–273.
[24] Strykowski, P. J., and Sreenivasan, K. R., 1990, ‘‘On the formation and suppression of vortex shedding at low Reynolds numbers,’’ J. Fluid Mech., **218**, pp. 71–107.
[25] Nishioka, M., and Sato, H., 1978, ‘‘Mechanism of determination of the shedding frequency of vortices behind a cylinder at low Reynolds numbers,’’ J. Fluid Mech., **89**, pp. 49–60.
[26] Provansal, M., Mathis, C., and Boyer, L., 1987, ‘‘Bénard-von Kármán instability: transient and forced regimes,’’ J. Fluid Mech., **182**, pp. 1–22.
[27] Rockwell, D., 1990, ‘‘Active control of globally-unstable separated flows.’’ International Symposium on nonsteady fluid dynamics, FED vol. 92, Toronto, Canada.
[28] Nuzzi, F., Magness, C., and Rockwell, D., 1992, ‘‘Three-dimensional vortex formation from an oscillating, non-uniform cylinder,’’ J. Fluid Mech., **238**, pp. 31–54.
[29] Masuoka, T., Takatsu, Y., Naganuma, K., and Tsuruta, T., 1998, ‘‘Suppression of the Kármán vortex street by wake heating,’’ Heat Transfer 1998, 11th IHTC, 5, Kyongju, Korea.
[30] Kieft, R. N., Rindt, C. C. M., and van Steenhoven, A. A., 1998, ‘‘The influence of buoyancy on the behavior of the vortex structures in a cylinder wake,’’ Heat Transfer 1998, Proceedings of the 11th IHTC, Vol. 6, Kyongju, Korea.
[31] Inoue, O., Yamazaki, T., and Bisaka, T., 1995, ‘‘Numerical simulation of forced wakes around a cylinder,’’ ISIJ Int., **16**(5), pp. 327–332.
[32] Hayashi, T., Yoshino, F., and Waka, R., 1993, ‘‘The aerodynamic characteristics of a circular cylinder with tangential blowing in uniform shear flows,’’ JSME Int. J., Ser. B, **36**(1), pp. 101–112.
[33] Roussopoulos, K., 1993, ‘‘Feedback control of vortex shedding at low Reynolds numbers,’’ J. Fluid Mech., **248**, pp. 267–296.
[34] Park, D. S., Ladd, D. M., and Hendricks, E. W., 1994, ‘‘Feedback control of von Kármán vortex shedding behind a circular cylinder at low Reynolds numbers,’’ Phys. Fluids, **6**(7), pp. 2390–2405.
[35] Lin, J.-C., Towfighi, J., and Rockwell, D., 1995, ‘‘Near-wake of a circular cylinder: control by steady and unsteady surface injection,’’ J. Fluids Struct., **9**, pp. 659–669.
[36] Amitay, M., and Cohen, J., 1997, ‘‘Instability of a two-dimensional plane wall jet subjected to blowing or suction,’’ J. Fluid Mech., **344**, pp. 67–94.
[37] Hammond, D. A., and Redekopp, L. G., 1997, ‘‘Global dynamics of symmetric and asymmetric wakes,’’ J. Fluid Mech., **331**, pp. 231–260.
[38] Hernandez, R. H., Baudet, C., and Fauve, S., 2000, ‘‘Controlling the Bénard-von Kàrmàn instability in the wake of a cylinder by driving the pressure at the front stagnation point,’’ Eur. Phys. J. B, **14**, pp. 773–781.
[39] Gillies, E. A., 1998, ‘‘Low-dimensional control of the circular cylinder wake,’’ J. Fluid Mech., **371**, pp. 157–178.
[40] Bellettre, J., Bataille, F., and Lallemand, A., 1999, ‘‘A new approach for the study of the turbulent boundary layer with blowing,’’ Int. J. Heat Mass Transfer **42**, pp. 2905–2920.
[41] Johnson, B. V., and Hartnett, J. P., 1963, ‘‘Heat transfer from a cylinder in crossflow with transpiration cooling,’’ ASME J. Heat Transfer, pp. 173–179.
[42] Eckert, E. R. G., and Livingood, J. N. B., 1953, ‘‘Method for calculation of laminar heat transfer in air flow around cylinders of arbitrary cross section (including large temperature differences and transpiration cooling,)’’ NACA Report 1118, 223–251.
[43] Eckert, E. R. G., and Livingood, J. N. B., 1954, ‘‘Comparison of effectiveness of convection-, transpiration-, and film-cooling methods with air as coolant,’’ NACA TN 3010, Report 1182.
[44] Williamson, C. H. K., 1996, ‘‘Vortex dynamics in the cylinder wake,’’ Annu. Rev. Fluid Mech., **28**, pp. 477–539.

[45] Chyu, O., and Rockwell, D., "Evolution of patterns of streamwise vorticity in the turbulent near wake of a circular cylinder," J. Fluid Mech., **320**, pp. 117–137.

[46] Rodet, J. C., Campolina-França, G. A., Pagnier, P., Morel, R., and Lallemand, A., 1997, "Etude en soufflerie thermique du refroidissement de parois poreuses par effusion de gaz," Rev. Gén. Therm., **37**, pp. 123–136.

[47] Dongarra, J. J., 1992, "Performance of various computers using standard linear equations software," Computer Architecture News, **20**(3), pp. 22–44.

[48] Dongarra, J. J., 1999, "Performance of various computers using standard linear equations software," Report CS-89-85, University of Tennessee.

[49] Vandoormaal, J. P., and Raithby, G. D., 1984, "Enhancements of the SIMPLE method for predicting incompressible fluid flows," Numer. Heat Transfer, **7**, pp. 147–163.

[50] Daly, B. J., and Harlow, F. H., 1970, "Transport equations in turbulence," Phys. Fluids, **13**, pp. 2634–2649.

[51] Lien, F. S., and Leschziner, M. A., 1994, "Assessment of turbulent transport models including non-linear RNG eddy-viscosity formulation and second-moment closure," Comput. Fluids, **23**(8), pp. 983–1004.

[52] Gibson, M. M., and Launder, B. E., 1978, "Grounds effects on pressure fluctuations in the atmospheric boundary layer," J. Fluid Mech., **86**, pp. 491–511.

[53] Fu, S., Launder, B. E. and Leschziner, M. A., 1987, "Modeling strongly swirling recirculating jet flow with Reynolds-stress transport closures," 6th Symposium on Turbulent Shear Flows, Toulouse, France.

[54] Launder, B. E., 1989, "Second-moment closure and its use in modeling turbulent industrial flows," Int. J. Numer. Methods Fluids, **9**, pp. 963–985.

[55] Launder, B. E., 1989, "Second-moment closure: present . . . and future?," Int. J. Heat Fluid Flow, **10**(4), pp. 282–300.

[56] Launder, B. E. and Shima, N., 1989, "Second-moment closure for the near-wall sublayer: Development and application," AIAA J., **27**(10), pp. 1319–1325.

[57] Wolfstein, M., 1969, "The velocity and temperature distribution of one-dimensional flow with turbulence augmentation and pressure gradient," Int. J. Heat Mass Transf., **12**, pp. 301–318.

[58] Chen, H. C., and Patel, V. C., 1988, "Near-wall turbulence models for complex flows including separation," AIAA J., **26**(6), pp. 641–648.

[59] Stevenson, T. N., 1968, "Inner region of transpired turbulent boundary layers," AIAA J., **6**(3), pp. 553–554.

[60] Simpson, R. L., 1970, "Characteristics of turbulent boundary layers at low Reynolds numbers with and without transpiration," J. Fluid Mech., **42**, pp. 769–802.

[61] Kays, W. M., 1972, "Heat transfer to the transpired turbulent boundary layer," Int. J. Heat Mass Transf., **15**, pp. 1023–1044.

[62] Landis, R. B., and Mills, F., 1972, "The calculation of turbulent boundary layers with foreign gas injection," Int. J. Heat Mass Transf., **15**, pp. 1905–1932.

[63] So, R. M. C., and Yoo, G. J., 1987, "Low Reynolds number modeling of turbulent flows with and without wall transpiration," AIAA J., **25**, pp. 1556–1564.

[64] Silva-Feire, A. P., 1988, "An asymptotic solution for transpired incompressible turbulent boundary layers," Int. J. Heat Mass Transf., **31**, pp. 1011–1021.

[65] Campolina França, G. A., 1996, "Contribution à l'étude des écoulements pariétaux avec effusion. Application au refroidissement de parois.," Ph.D. thesis, CETHIL, INSA de Lyon.

[66] Grove, A. S., Shair, F. H., Petersen, E. E., and Acrivos, A., 1963, "An experimental investigation of the steady separated flow past a circular cylinder," J. Fluid Mech., **19**, part 1, pp. 60–80.

[67] Acrivos, A., Leal, L. G., Snowden, D. D., and Pan, F., 1968, "Further experiments on steady separated flows past bluff objects," J. Fluid Mech., **34**, pp. 25–48.

[68] Dennis, S. C. R., and Chang, G.-Z., 1970, "Numerical solutions for steady flow past a circular cylinder at Reynolds numbers up to 100," J. Fluid Mech., **42**, pp. 471–489.

[69] Nishioka, M., and Sato, H., 1974, "Measurements of velocity distributions in the wake of a circular cylinder at low Reynolds numbers," J. Fluid Mech., **65**, part 1, pp. 97–112.

[70] Dyke, M. van, 1982, *An album of fluid motion*, The Parabolic Press, Stanford, CA.

[71] Chua, K., Lisoski, A., Leonard, A., and Roshko, A., 1990, "A numerical and experimental investigation of separated flow past an oscillating flat plate," Int. Symposium on Nonsteady Fluid Dynamics, FED 32, J. A. Miller and D. P. Telionis, eds., pp. 455–464.

[72] Tamura, T., Ohta, I., and Kuwahara, K., 1990, "On the reliability of two-dimensional simulation for unsteady flows around a cylinder-type structure," J. Wind. Eng. Ind. Aerodyn., **35**, pp. 275–298.

[73] Mittal, R., and Balachandar, S., 1997, "On the inclusion of three-dimensional effects in simulations of two-dimensional bluff-body wake flows," Symposium on Separated and Complex Flows, ASME FED, Vancouver.

[74] Mathelin, L., Bataille, F., and Lallemand, A., 2000, "Near wake of a circular cylinder submitted to blowing. Part I–II," Int. J. Heat Mass Transf., **44**(19), pp. 3701–3719.

[75] Hannemann, K., and Oertel, Jr., H., 1989, "Numerical simulation of the absolutely and convectively unstable wake," J. Fluid Mech., **199**, pp. 55–88.

[76] Oertel, Jr., H., 1990, "Wakes behind blunt bodies," Annu. Rev. Fluid Mech., **22**, pp. 539–564.

[77] Schumm, M., Berger, E. B., and Monkewitz, P. A., 1994, "Self-excited oscillations in the wake of two-dimensional bluff bodies and their control," J. Fluid Mech., **271**, pp. 17–53.

[78] Wood, C. J., 1964, "The effect of base bleed on a periodic wake," J. R. Aeronaut. Soc., **68**, pp. 477–482.

[79] Bearman, P. W., 1967, "The effect of base bleed on the flow behind a two-dimensional model with a blunt trailing edge," Aeronaut. Q., **18**, pp. 207–224.

[80] Cardell, G. S., "Flow past a circular cylinder with permeable splitter plate," 1993, PhD thesis, Caltech, p. 257.

[81] Mittal, R., and Balachandar, S., "On the inclusion of three-dimensional effects in simulations of two-dimensional bluff-body wake flows," 1997, ASME Fluids Engineering Division Summer Meeting, Vancouver, Canada, June 22–26, pp. 8.

[82] Cohen, R. D., 1991, "Predicting the effects of surface suction and blowing on the Strouhal frequencies in vortex shedding," JSME Int. J., Ser. II, **34**(1), pp. 30–38.

[83] Noack, B. R., Ohle, F., and Eckelmann, H., 1991, "On cell formation in vortex streets," J. Fluid Mech., **227**, pp. 293–308.

Two-Phase Eulerian/Lagrangian Model for Nucleating Steam Flow

A. G. Gerber
Department of Mechanical Engineering,
University of New Brunswick,
Fredericton, N.B.,
Canada, E3B-5A3

This paper describes an Eulerian/Lagrangian two-phase model for nucleating steam based on classical nucleation theory. The model provides an approach for including spontaneous homogeneous nucleation within a full Navier-Stokes solution scheme where the interaction between the liquid and gas phases for a pure fluid is through appropriately modeled source terms. The method allows for the straightforward inclusion of droplet heat, mass, and momentum transfer models along with nucleation within complex flow systems as found, for example, in low pressure steam turbines. The present paper describes the solution method, emphasizing that the important features of nucleating steam flow are retained through comparison with well-established 1-D solutions for Laval nozzle flows. Results for a two-dimensional cascade blade and three-dimensional low pressure turbine stage are also described. [DOI: 10.1115/1.1454109]

Introduction

A number of numerical studies, over the past several decades, have been directed toward modeling two-phase flow behavior of nucleating steam. Much of this modeling work was initially conducted on Laval nozzles, for which experimental data was more readily available (Gyarmathy and Meyer, [1]; Hill, [2]), assuming simplified one-dimensional flow conditions. Later studies examined two-dimensional flow in turbine cascades, with more sophisticated numerical models used to handle the additional dimension (Bakhtar and Tochai [3]; Young [4,5]; White and Young [6]; Bakhtar et al. [7]; White et al. [8]). In this regard the numerical approach most often used has been the inviscid time-marching scheme of Denton [9] for turbomachinery flows. In these models the dispersed water phase is handled via particle tracking along streamlines; this provides a wetness distribution and hence mixture conditions for the subsequent single-phase inviscid flow calculations. The success of these methods was measured by their ability to predict measured pressure distributions and droplet sizes, which in most cases is quite good for pressure conditions less than one atmosphere.

The use of a single-phase time-marching scheme, the assumption of inviscid flow, and the restriction of particle tracking along streamlines, places limitations on extending these methods to more complex flow conditions involving nucleating steam. Such flow conditions may involve the interaction of small nucleated droplets with larger droplets in the domain (where slip forces must be included in determining the large droplet motion), droplet fragmentation/coalescence, and droplet/wall interaction including moisture collection. The inclusion of turbulence effects on the droplet motion may also be of value.

To extend the modeling of nucleating steam to 3-D flows with additional complexity in droplet models, the present model was implemented within a finite-volume/finite element viscous Navier-Stokes CFD solver, using a two-phase approach for modeling the interaction between the gas and liquid phases. The two-phase approach involves modeling the heat, mass, and momentum transfer between the phases explicitly through appropriate source terms. This is opposed to a single-phase approach, where dependent solution variables and properties, for both phases, are averaged using mixture relations based on the wetness distribution determined from the Lagrangian tracking solution. The use of a two-phase approach has the potential for incorporating much more complex droplet models, since the two phases do not have to share the same velocity field (Gerber [10]).

Governing Conservation Equations for Mass, Momentum, and Energy

Flow processes where homogeneous nucleation occurs can be characterized by rapid expansion, where moisture creation by heterogeneous nucleation is too slow to maintain equilibrium conditions (due to small cumulative particle surface area), and reversion to equilibrium must then occur through the spontaneous formation of the droplet phase. The process leading up to the nucleation event involves the supercooling of the gas phase as thermodynamic conditions pass the saturation line. The supercooling of the gas, defined as the difference between saturation temperature at the local pressure and the local gas temperature, continues until a threshold is reached (typically 30–50 K for low pressure steam), and moisture is spontaneously formed from minute liquid clusters in the flow. The process is then followed by rapid recovery of the thermodynamic conditions to near saturation conditions.

The droplet nucleation event occurs rapidly once critical supercooling is reached and involves a very rapid growth in droplet size (and mass). At present, the most accurate and efficient manner to model the sudden appearance of moisture and its interaction with the gas phase, is within a Lagrangian frame of reference. The gas phase, as the continuous phase, is modeled in the Eulerian frame of reference. Interaction between the phases, in the present model, is through appropriately modeled interphase source terms.

Gas Phase in the Eulerian Frame of Reference

Mass and Momentum. The governing equations for mass and momentum are solved in a coupled manner, and for the present model can be shown in tensor form as

$$\frac{\partial \rho}{\partial t}+\frac{\partial}{\partial x_j}(\rho u_j)=S_m \tag{1}$$

$$\frac{\partial}{\partial t}(\rho u_i)+\frac{\partial}{\partial x_j}(\rho u_j u_i)=-\frac{\partial P}{\partial x_i}+\frac{\partial \tau_{ij}}{\partial x_j}+S_{ui}. \tag{2}$$

where the source terms, S_m and S_{ui}, contain sources representing mass and momentum exchange between the water droplets and the surrounding gas. These will be described in a subsequent section. The source term, S_{ui}, in a rotating frame of reference, also includes appropriate contributions to represent Coriolas and centripetal forces.

Contributed by the Fluids Engineering Division for publication in the JOURNAL OF FLUIDS ENGINEERING. Manuscript received by the Fluids Engineering Division April 14, 2000; revised manuscript received October 29, 2001. Associate Editor: Y. Matsumoto.

Energy. The conservation of total energy, H, in the domain is governed by the conservation equation

$$\frac{\partial}{\partial t}(\rho H)-\frac{\partial P}{\partial t}+\frac{\partial}{\partial x_j}(\rho u_j H)=-\frac{\partial q_j}{\partial x_j}+\frac{\partial}{\partial x_j}(u_i\tau_{ij})+S_h \tag{3}$$

where

$$H=h+\tfrac{1}{2}u_iu_i+\kappa. \tag{4}$$

For a rotating frame of reference the rothalpy, I, is advected instead of H. Rothalpy is defined as

$$I=H-\frac{\omega^2R_\omega^2}{2}. \tag{5}$$

The source term, S_h, models all energy exchange between the liquid and vapor phases.

Turbulence Equations. The nonequilibrium flow model is not dependent on any particular turbulence model, and for the present purposes the standard κ-ϵ model is used. All results to be presented assume smooth walls, along with the assumption of one-way coupling between the gas phase turbulence and dispersed droplet phase. With this latter assumption, the gas phase turbulence is not directly influenced by the presence of droplets (i.e., by modification to the κ-ϵ source terms); however, the motion model for water droplets does include the instantaneous turbulent velocity fluctuations (estimated from mean turbulence quantities as described in the next section) in determining the final droplet trajectory.

Water Particles in the Lagrangian Frame of Reference. At present CFD methods for modeling dispersed two-phase flows fall into two categories, either an Eulerian/Lagrangian or an Eulerian/Eulerian representation of the phases. A full 3D Eulerian/Eulerian approach, in the most simple cases involving heat transfer and one representative droplet size, requires solving an additional four equations for the dispersed phase (u_i, and h). For the wide range of droplets present in condensing systems, many droplet size groups may need to be represented, each with its own velocity (a requirement if the droplets are large) and temperature distribution. The number of equations involved, four additional equations for each group, can rapidly lead to computing times exceeding the Eulerian/Lagrangian approach. In addition, the interaction between the droplet groups must be modeled (a nontrivial problem) since droplets move into and out of size regimes with condensation and evaporation processes. Maintaining strong coupling between these equation groups in transonic flows with shocks can also be problematic. In addition, to resolve the time and spatial scales associated with droplet nucleation and growth, a very fine grid is required.

An Eulerian/Lagrangian model allows the droplet integration to be separated from the grid size, and gas phase time step, allowing for a coarser grid to be employed. Since each droplet group is integrated from its initial creation to a final fate, no special handling is required to account for movement through a wide range of size regimes (other than the appropriate application of heat, mass, and momentum models accunting for Knudsen number regime). The Eulerian/Lagrangian approach suffers from lack of scalability in solution time available with parallel processing; however, it does provide a more direct manner in implementing highly non-linear droplet models. When heat and mass transfer are strongly coupled, as happens during phase change, the coupled ordinary differential equations, representing the heat and mass transfer, are easier to solve. This is especially true since the Lagrangian time step can be changed during integration, for example successive time-step halving, to capture rapidly changing flow conditions. Without time step control such coupled systems cannot be solved without extensive simplifications to the non-linear terms. It should be mentioned that inherent in the Lagrangian approach is the requirement that the volume fraction of the dispersed phases remain low (generally less than one percent), which is not a problem for condensing steam in low pressure turbines.

In light of the large range of droplet sizes and the high degree of interphase coupling, a Lagrangian model describing the motion of a water droplet has been implemented. For the present paper, only freshly nucleated droplets are considered, and therefore a simplified motion model is used that assumes no slip between the droplet and the surrounding gas. This is a reasonable assumption considering that the radius of a freshly nucleated droplet is generally of the order of 10^{-9} m, and may grow to a size in the range of 10^{-7} m within the extent of the solution domain. It is assumed, for the applications to be presented, that the droplets will not grow to a size where slip will become important. This assumption will be relaxed in future studies. In addition, the model accounts for droplet motion in either rotating or stationary frames of reference.

The model also includes the influence of gas phase turbulent fluctuations on the droplet motion. The resulting turbulent dispersion effect is based on an approach developed by Dukowicz [11], where the fluctuating velocity component, u_g', can be computed from turbulence quantities using:

$$u_g'=\Pi(2\kappa/3)^{1/2} \tag{6}$$

which is superimposed on the mean velocity field to compute an instantaneous velocity for the droplet.

In Eq. (6), II represents a normally distributed random number, and accounts for the randomness of turbulence around a mean number. This randomness allows for the gas phase fluctuating component (u_g') at a point to take different values. For time step control during the particle integration the eddy length, l_e, and lifetime, τ_e, are also required and are calculated as follows:

$$l_e=C_\mu^{3/4}\kappa^{3/2}/\epsilon \tag{7}$$

$$\tau_e=l_e/(2\kappa/3)^{1/2} \tag{8}$$

The energy equation describing the thermal behavior of the water droplet, is comprised of a latent energy term, convective heat transfer and a sensible heating term, respectively.

$$l\frac{dm_p}{dt}=4\pi r^2\alpha(T_p-T_g)+m_pc_p\frac{dT_p}{dt} \tag{9}$$

Interphase Source Terms. The influence of the liquid phase on the gas phase equations are through the interphase source terms, S_m, S_{ui}, and S_h. These source terms use water droplet properties consistent with the gas phase equations of state, and are modeled as follows for a control volume

$$S_m=\left\{\sum_m^{mp}\sum_n^{nt}[(\dot m_p)_{mn}^{t+\Delta t}-(\dot m_p)_{mn}^{t}]\right\}\Big/V_{CV} \tag{10}$$

$$S_{u_i}=\left\{\sum_m^{mp}\sum_n^{nt}[(\dot m_p u_{i_p})_{mn}^{t+\Delta t}-(\dot m_p u_{i_p})_{mn}^{t}]\right\}\Big/V_{CV} \tag{11}$$

$$S_h=\left\{\sum_m^{mp}\sum_n^{nt}[(\dot m_p h_p)_{mn}^{t+\Delta t}-(\dot m_p h_p)_{mn}^{t}]\right\}\Big/V_{CV} \tag{12}$$

where the summation is over all m particles that enter the control-volume, and over all n time steps for the particle as it travels through the control-volume. The mass flow associated with a given particle is $\dot m_p$. In Eq. (12) the droplet enthalpy, h_p, is comprised of the bulk internal energy, the surface energy associated with a spherical droplet, and the kinetic energy.

$$h_p=h_b+\frac{3\left(\sigma_p-T_p\dfrac{d\sigma}{dT}\right)}{\rho_p r}+\frac{u_p^2}{2} \tag{13}$$

It is interesting that in the present model the latent heat influence is not explicitly modeled in the energy source term, S_h. The latent heat influence is implicitly accounted for when using consistent thermodynamic properties (between liquid and vapor) when evaluating energy sources.

The term S_{ui} accounts for momentum exchange between the phases due to evaporation or condensation. Since in this study droplets are assumed to remain small with no slip, an interphase drag force contribution is not needed in the calculation of S_{ui}.

Thermodynamic Properties

In modeling nonequilibrium flows supercooled thermodynamic properties are required. Since very little experimental data exists for supercooled properties below saturation, obtaining these properties is accomplished by extrapolating an appropriate equation of state into the meta-stable region. Equations of state based on virial coefficients have been popular in this regard, in part, because they are well behaved when extrapolated into the supercooled region. These equations are also popular because all of the required empirical constants are functions of temperature alone. In Eq. (14) is shown the general form of the virial equation of state used for the results in this paper.

$$P=\rho_g R T_g (B_1+B_2\rho_g+B_3\rho_g^2+B_4\rho_g^3) \tag{14}$$

In particular an equation of state in virial form by Vukalovich [12] is used, and which was tested by Bakhtar and Piran [13] to be suitable for flows with supercooled steam at both high and low pressures. From these equations thermodynamic properties are available over a pressure range from 0.01 bar to 100 bar, and a temperature range from 273.15°K to 1000°K.

Although the present paper emphasizes results at pressures at or below 1 bar, the model has also been applied to high pressure applications (in nuclear steam cycles for example) and hence the requirement for a thermodynamic database applicable at high pressures as well.

Nucleation Model. For nonequilibrium flow calculations there must be a criterion for the onset of nucleation and the appearance of the second phase (liquid). The present model considers only homogenous nucleation in a pure substance and relies heavily on classical nucleation theory (MacDonald [14,15]). The relevant nucleation theory is only briefly presented here.

The essence of the model is that in order for nucleation to occur in a flowing stream undergoing expansion, molecular clusters (the minute embryo of a liquid droplet) must overcome a free-energy barrier, associated with the increase in surface-free-energy of the droplets, for the onset of phase change. As a substance is increasingly supercooled the chances of a molecular cluster moving over the free energy barrier increases. The critical radius when this occurs is equal to:

$$r^*=\frac{2\sigma}{\rho_f \Delta G_b} \tag{15}$$

and becomes increasingly smaller as the level of supercooling increases since ΔG_b, the bulk free energy change, increases with higher levels of supercooling. In Eq. (15) liquid surface tension, σ, for a flat surface is used. The value of ΔG_b depends on the equation of state used, and for the virial equation of state used in the present model it is calculated as follows;

$$\frac{\Delta G_b}{RT_g}=-\ln\frac{\rho_g}{\rho_s(T_g)}+2B_2\{\rho_s(T_g)-\rho_g\}+\frac{3}{2}B_3\{\rho_s^2(T_g)-\rho_g^2\}+\frac{4}{3}B_4\{\rho_s^3(T_g)-\rho_g^3\} \tag{16}$$

where $\rho_s(T_g)$ is the saturated vapor density at the local gas temperature T_g, and B_2, B_3, and B_4 are virial coefficients. With the critical radius known, the free energy change at r^* can be calculated with the following;

$$\Delta G^*=\frac{16\pi\sigma^3}{3\rho f^2(\Delta G_b)^2}=\frac{4}{3}\pi r^{*2}\sigma \tag{17}$$

In the vapor phase there exists a statistically steady-state population of molecular clusters of various sizes. As supercooling increases and r^* becomes smaller there will eventually be enough clusters at the size of r^* (or greater) to start the condensation process and the reversion back to equilibrium. Using a Boltzman-like distribution function to represent the cluster population, combined with the change in free energy at r^*, leads to the equation:

$$J=\frac{q_c}{1+\eta}\left(\frac{2\sigma}{\pi m^3}\right)^{1/2}\frac{\rho_g^2}{\rho_f}\exp\left(-\frac{\Delta G^*}{KT_g}\right) \tag{18}$$

where

$$\eta=2\,\frac{\gamma-1}{\gamma+1}\,\frac{L}{RT_g}\left(\frac{L}{RT_g}-\frac{1}{2}\right) \tag{19}$$

J gives the steady-state number of droplets nucleated per unit volume per unit time. In Eqs. (18) and (19), q_c, is the condensation coefficient (assumed to be one in this paper), K, Boltzman's constant, m, the mass of one water molecule, and, L, the equilibrium latent heat.

It should be noted that no universally applicable nucleation model is yet available for condensing flows, however the general form described here has been successfully used for steam at low pressures by a number of researchers (White [8]; Bakhtar et al. [7]). There is a long standing debate concerning the use of a bulk surface tension in Eqs. (15) and (17) for very small molecular clusters. Since the surface tension appears in the nucleation rate equation, through ΔG^*, to the third power, small changes in its value can strongly influence the resulting value for J. The sensitivity of various nucleation models to σ_b has clearly been shown by Moore et al. [16], where the ratio σ/σ_b had to be adjusted (typically between 0.8 and 1.2) to bring results in-line with the Laval nozzle results. It was found with the present nucleation model, that results for calculations at pressures below 1 bar were better using a $\sigma/\sigma_b=1.1$, and this was used for all of the calculations shown. Future studies may further examine this sensitivity, while the numerical method presented here is not restricted to any particular form of nucleation model.

Droplet Growth Model for Nucleating Particles

Based on the nucleation model just described the quantity of droplets at a location in the continuous gas phase is known, and the rate at which these droplets grow can be derived on the basis of heat transfer conditions surrounding the droplet (Gyarmathy [17]). The equation for the rate of droplet growth is then:

$$\frac{dr}{dt}=\frac{\mathrm{Nu}k_g}{2r\rho_p}\,\frac{(T_p-T_g)}{(h_g-h_p)} \tag{20}$$

where

$$\mathrm{Nu}=\frac{2}{1+1.89Pr^{-1}(1-\nu)\overline{l}/r} \tag{21}$$

and

$$\nu=\frac{RT_s}{L}\left[\beta-\frac{1}{2}-\left(\frac{2-q_c}{2q_c}\right)\left(\frac{\gamma+1}{2(\gamma-1)}\right)\left(\frac{RT_s}{L}\right)\right] \tag{22}$$

In Eq. (20) the sensible heating of the droplet can be neglected, and the droplet temperature related to its size with the following relation (Gyarmathy [17]).

$$T_p=T_s(P)-[T_s(P)-T_g]\frac{r^*}{r} \tag{23}$$

Based on an analysis by Gyarmathy [17], Eqs. (20) and (23) can be used reliably for steam to calculate the rate of droplet growth over molecular and continuum heat transfer regimes (i.e., $0<\mathrm{Kn}<\infty$). The correction to the Nusselt number in Eq. (21) (the factor $1-\nu$), was proposed by White and Young [6] to help improve agreement with experimental condensation results at low pressures (0.1–0.3 bar). The constant β was adjusted for the results in the present paper based on a correlation presented by White and Young [6].

With the droplet motion determined by the gas phase velocity (for small nucleated droplets no-slip is assumed) and the droplet growth and temperature change determined by Eqs. (20) and (23), the droplet contributions to the mass, momentum and energy source terms (S_m, S_{ui}, S_h) can be determined. The final solution provides information on mass-averaged droplet size, wetness levels, and total irreversible losses due to droplet-gas heat transfer. The manner in which these quantities are calculated can be found in Appendix A.

Lagrangian Implementation for Water Droplets

As already described the present model relies on a Lagrangian representation of the water droplet phase. The following describes how the Lagrangian tracking model was implemented for the case of nucleating particles. The particles are injected and tracked through a network of flux-elements, the basic grid element in a finite-element representation of the domain. In Fig. 1 is shown a 2-D representation of a flux-element grid, along with superimposed control-volume boundaries. The gas-phase equations are solved at the control-volume locations. The droplet phase source contributions, during tracking through the domain, are accumulated within flux-elements but distributed equally to all contributing control-volumes in the flux-element at the time the gas phase equations are assembled. This manner in handling the droplet sources, rather than applying sources directly to the control-volumes, was found to improve overall convergence but is also consistent with the calculation of the supercooling level surrounding the droplet. For nucleating particles the supercooling level is the primary driving potential for source term generation, and is calculated as a weighted average for the flux-element using shape functions and neighboring control-volume values (see Eq. (25)).

Prior to solving the Eulerian equations the nucleation rate, Eq. (18), is calculated at all flux-elements where local supercooling exists. The local supercooling is calculated as the difference between the saturation temperature, calculated using the local static pressure, and the local gas temperature. If the nucleation rate is high enough to influence the gas phase (in this case assumed to be $J\geqslant 1\times 10^{15}$ droplets/m^3/s), then eight representative particles are injected in the current flux element at the center of the eight octants making up the flux-element. These locations are shown for the 2-D case, where injection is over four octants, in Fig. 1. The mass associated with each of the eight particles, $\dot{m}_p$, is determined by the equation:

$$\dot{m}_p=\frac{JV_{FE}}{n_p} \tag{24}$$

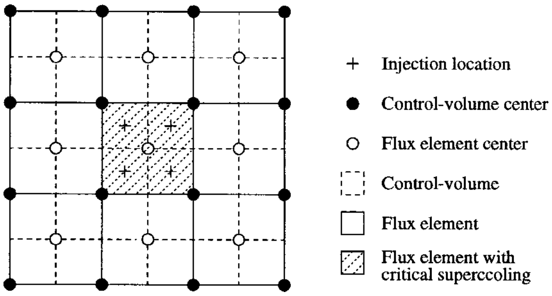

Fig. 1 Schematic describing nucleating particle injection relative to flux-element and control-volume locations

where V_{FE} represents the flux-element volume and n_p the number of particles injected per flux-element (in this case $n_p=8$). The local flow properties, ϕ (such as T_g, ρ_g etc.), used to compute J were computed using the flux-element shape function:

$$\phi=\sum_{i=1}^{n_{CV}} N_i\phi_i \tag{25}$$

where the summation is over the adjacent n_{CV} control-volume values of ϕ. The shape function, N_i, is evaluated using the local (s, t, u) coordinates for the particle relative to the current flux element.

When a particle is injected into the flow (for steady-state calculations) the particle is tracked until some fate is reached, such as impacting a wall, passing into a periodic boundary, exiting the flow domain or reaching a stage interface. For a particular fate, a predetermined action is undertaken such as bouncing or sticking (wall), leaving the domain (outflow), translation/rotation and reinjection (periodic condition), collection/scaling and re-injection (stage interface). In the particular case of a stage interface, the droplet mass is scaled according to the component pitch change followed by random circumferential reinjection.

During a particle's journey to a particular fate it will pass through a succession of flux-elements, with the particle time step governed by a number of parameters as follows:

- The particle cannot travel past a flux-element boundary in any one time step. This enforces integral conservation between the phases.
- The time step is limited by the size of the local turbulent eddy length scale shown in Eq. (7), and the local time scale shown in Eq. (8), when interaction between droplets and turbulence is activated.
- The particle may only travel some user specified fraction of the characteristic flux element length during a time step. This allows the accuracy of the particle tracking integration to be separated from the grid resolution.

A forward Euler integration scheme is used for the particle trajectory. At the beginning of a time step the gas phase properties are determined from the control-volume values by interpolation to the current particle (s, t, u) local grid coordinate using shape functions. The particle properties are determined from the property database based on the particle temperature. The particle size at the end of a time step is predicted by Eq. (20) along with a new particle temperature using Eq. (23). From the change in particle size and temperature, over the time step, the source terms described by Eqs. (10), (11), and (12) can be calculated. Finally, the nonequilibrium irreversible entropy rise, and the droplet size and wetness arrays are updated in a manner described by Eqs. (28)–(31). The droplet integration scheme is repeated until one of the droplet fates is reached.

The choice of the number of particles to inject per flux-element is a balance between better seeding of the flow passing through the flux-element, so that the discrete droplet phase will provide a more continuous representation of the wetness, without adding too much computational overhead. In Figs. 2 and 3 this assumption is tested for the case of a supersonic nozzle and rotor tip cascade respectively, by showing the sensitivity of nucleation rate, pressure profile and wetness variable to the number of particles injected per flux element. From the results it is clear that in the case of the Laval nozzle, where the flow is generally well aligned with the grid, the variables considered are insensitive to the number of particles injected per flux element. However, in the case of the rotor tip cascade, where the flow is not very grid aligned, the use of eight particles per flux element gives significant improvement in the wetness field prediction. In either case, the pressure field and nucleation rate are relatively insensitive to the number of particles injected suggesting that an initial solution can be obtained with $n_p=1$. In practice, an initial solution with $n_p=1$ is

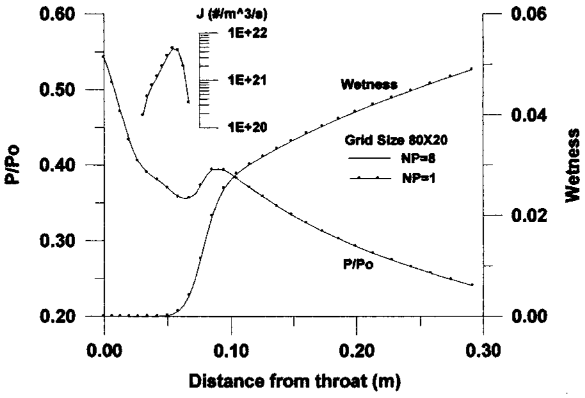

Fig. 2 Centerline nucleation rate, pressure, and wetness predictions using the Laval nozzle of Moore et al. [16] with one and eight droplets injected per flux-element

obtained then $n_p=8$ is used for the final solution, which typically only requires a small number of additional solution iterations for convergence to be reached again.

The appearance of a nucleation front, with considerable heat, mass, and momentum transfer occurring over a short time and distance, introduces a sharp discontinuity in the flow field that needs to be appropriately resolved. Adaptive grid refinement to resolve this discontinuity is a potential solution; however, for the present model ensuring a reasonable grid resolution in the region of the nucleation front is the approach taken. A numerical study is shown in Fig. 4 for a Laval nozzle with condensation during supersonic flow conditions. The course grid resolution is doubled twice over to examine the influence of increasing levels of grid resolution on the nucleation front, pressure and wetness profiles. For the course solution approximately 4 elements span the nucleation front zone, for the middle resolution 8 elements, and for the finest solution 16 elements. As can be seen, the location and magnitude of the nucleation front is relatively insensitive to the grid resolution as is the wetness level; however, the pressure rise is diffused when the grid resolution is low. This sensitivity does point to the need for some grid adaption abilities near the nucleation front; however, for the results presented the 2D cases used grid resolutions similar to the 80×20 case (i.e., approximately 8 elements over the primary nucleation zone). In the case of the 3-D results, because of the grid sizes involved, grid resolutions similar to the 40×10 case are used. Future studies should investigate means to reduce this sensitivity.

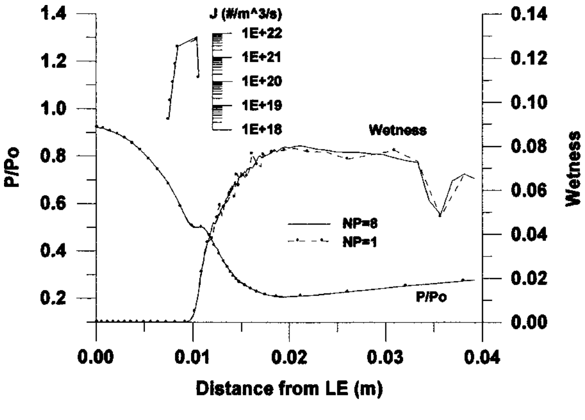

Fig. 3 Centerline nucleation rate, pressure, and wetness predictions using the rotor tip profile of Bakhtar et al. [20] with one and eight droplets injected per flux-element

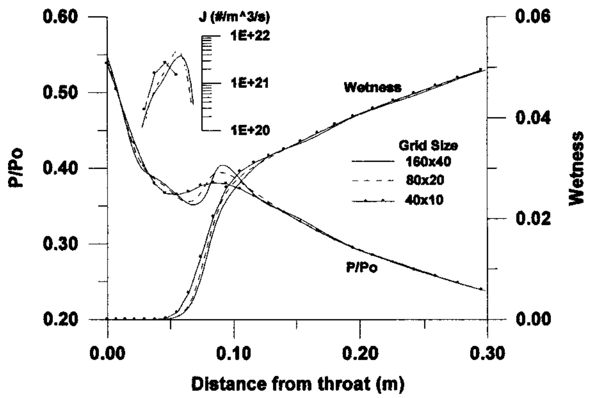

Fig. 4 Centerline nucleation rate, pressure, and wetness predictions using the Laval nozzle of Moore et al. [16] with three levels of grid refinement

CFD Solution Methodology

In addition to the water phase, the gas phase conservation equations are discretized using a conservative finite-volume integration over a control-volume. The discretization of the gas phase equations, in the context of a finite-element representation of the geometry, is as follows for a general scalar ϕ,

$$\rho V_{CV}\left(\frac{\phi-\phi^{o}}{\Delta t}\right)+\sum_{\mathrm{ip}}\dot{m}_{\mathrm{ip}}\phi_{\mathrm{ip}}=\sum_{\mathrm{ip}}\left(\Gamma_{\phi}\frac{\partial\phi}{\partial x_j}\Delta n_j\right)_{\mathrm{ip}}+S_{\phi}V_{CV} \tag{26}$$

where

$$\dot{m}_{\mathrm{ip}}=(\rho u_j\Delta n_j)^{o}_{\mathrm{ip}} \tag{27}$$

and V is the volume of the control volume, the subscript ip denotes an integration point, the summation is over all the integration points of the surface, Δn_j is the discrete outward surface vector, Δt is the time step, the superscripts o means at the old time level. In Fig. 5 is shown the location of the integration points relative to the flux-element and control-volume faces. Source terms are applied over the control-volume, based on Eqs. (10), (11), and (12), and can be linearized into active and passive components.

The assembly of the conservation equations describes the approach used by the commercial software package CFX-TASCflow (used for the present nucleation model development), which uses, as its default, a linear multigrid solver with full coupling between the u_i and P variables along with second-order discretization (Raw [18]). Due to the linear multigrid, solution times scale linearly with problem size.

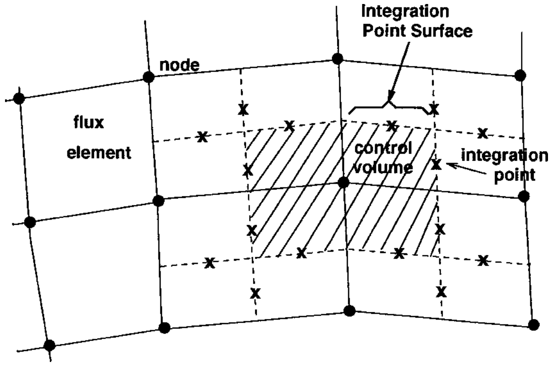

Fig. 5 Finite-volume discretization within a finite-element representation of the geometry

Using an iterative segregated solution approach, the Lagrangian tracking solution of the water droplet phase is first carried out, and the interphase source terms computed based on gas phase conditions at the beginning of the time step. The solution of the scalar turbulence and energy equations are then obtained. The momentum (u_i) and mass (P) equations are then solved as a coupled system and the entire procedure (beginning with the droplet phase) repeated until convergence is reached. The momentum, mass and energy equations are converged to the point where all normalized maximum RMS residuals in the domain are below 10^{-4}. Global balances (between inlet and outlet) for these quantities are typically of the order 10^{-4} to 10^{-5} based on normalizing with known inlet flow conditions.

Laval Nozzle Solution

Considerable amount of theoretical and experimental work for nonequilibrium steam flows has been conducted with Laval nozzles. The following example describes an application of the present model to a Laval nozzle for both nonequilibrium and equilibrium cases.

The present model results were compared to 1-D inviscid flow results based on a nozzle by Gyarmathy and Meyer [1] and presented by Moore and Sieverding [19]. The results show all of the important characteristics typical of homogeneous nucleation in an expanding nozzle, and compare very well with the 1-D inviscid model. In Fig. 6, the Mach number and nucleation front within the Laval nozzle is shown, where the influence of viscous effects near the nozzle wall is apparent. It was found that in the near wall region, supercooling levels decreased, along with the wetness, due to the influence of the boundary layer. Since the present work does not focus on detailed effects occurring when water droplets impact a wall, the droplets in this case (and all other cases to be shown) were allowed to rebound off the wall but with a very small coefficient of restitution. This in effect allowed droplets to move slowly along a wall and equilibriate with the surroundings.

Figure 7 shows the variation in gas supercooling, static pressure, nucleation rate, droplet size, and wetness along the nozzle axis in comparison to the results of Gyarmathy (shown in dashed lines). In order to more effectively compare with 1-D results, relevant quantities from the present model were mass averaged over the nozzle cross-section at various positions along the nozzle passage. For a matter of clarity in Fig. 7, the mass-averaged droplet size becomes significant prior to the point of peak supercooling (and associated maximum droplet nucleation), while wetness remains almost negligible over this portion of the nozzle. This reflects the fact that although droplets are nucleated, and grow rapidly in the supercooled environment, there are not enough of them to influence the overall wetness level. Only once the nucleation rate reaches its peak is there sufficient numbers of droplets to influence the wetness, as seen by the rapid increase in this variable following peak nucleation.

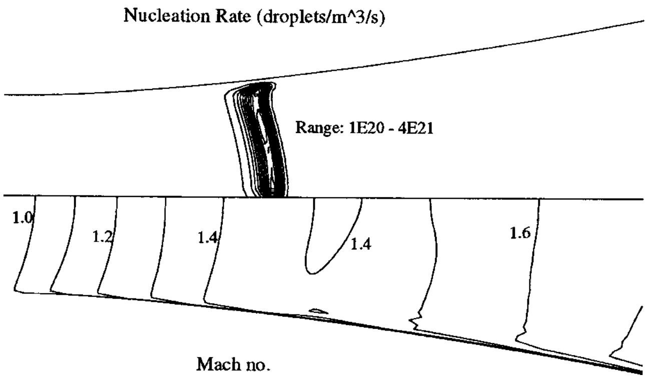

Fig. 6 Nucleation rate and Mach number obtained with the present model. Flow conditions are the same as that described for Fig. 7.

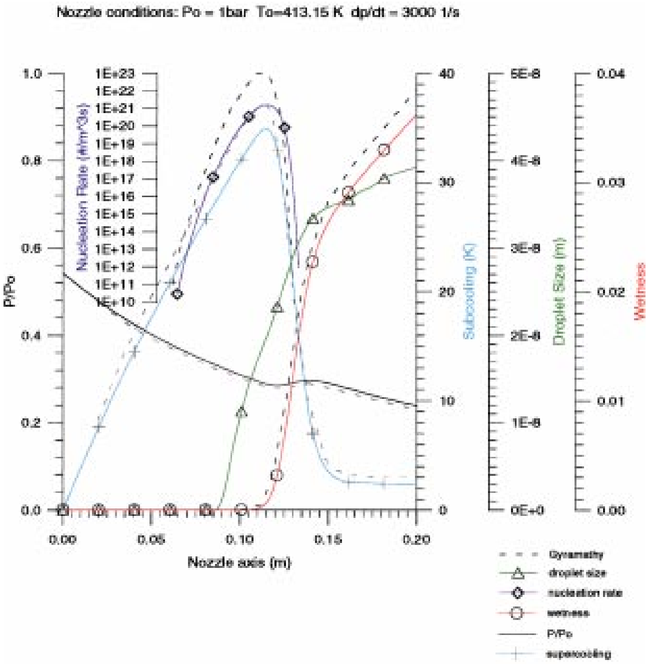

Fig. 7 Comparison with 1-D nonequilibrium solution of Gyramathy and Meyer [1]

Another valuable comparison is with the equilibrium solution, calculated with the same CFD flow code, for the same nozzle geometry and flow conditions used by Gyarmathy and Meyer [1]. In Fig. 8 are shown the wetness, pressure, and temperature levels between the equilibrium and nonequilibrium solutions where it can be seen that, for the equilibrium solution (depicted with dashed lines), wetness forms in the throat region where in the nonequilibrium solution wetness is considerably delayed. As required, the nonequilibrium solution recovers the equilibrium re-

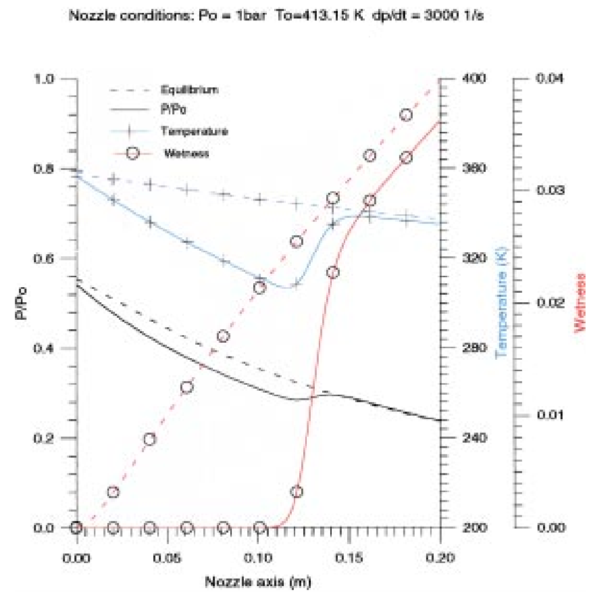

Fig. 8 Nonequilibrium solution compared with the equilibrium solution for the same nozzle and inflow conditions used by Gyramathy and Meyer [1]

Table 1 Verification of calculation of irreversible entropy rise due to nonequilibrium phase change (pc). Subscripts *i* and *o* refer to inflow and outflow conditions, respectively.

Solution Type	s_i (J/KgK)	s_o (J/KgK)	$\Delta s_{eq}= s_o - s_i$	$\Delta s_{neq}= s_o - s_i$	$\Delta s_{pc}= \Delta s_{neq} - \Delta s_{eq}$	Δs_{pc} Eq. 28
Equilibrium (*eq*)	7558.7	7567.9	9.2	N/A	N/A	N/A
Nonequilibrium (*neq*)	7558.7	7579.1	N/A	20.4	11.2	11.2

sult, but with a slightly higher entropy level (resulting in a slightly lower wetness) due to irreversible heat transfer effects, and small level of supercooling at the exit relative to the equilibrium exit temperature. The nonequilibrium static pressure level recovers the equilibrium pressure level following nucleation. The present nonequilibrium model explicitly calculates the irreversible entropy rise using Eq. (28) (see Appendix A). A check on this value can be made by comparing the difference in entropy levels, at the nozzle exit, between the equilibrium and nonequilibrium solutions. These comparisons can be seen in Table 1, where the differences in the mass averaged exit mixture entropy between the equilibrium and nonequilibrium solutions is equal to the irreversible entropy rise calculated using Eq. (28).

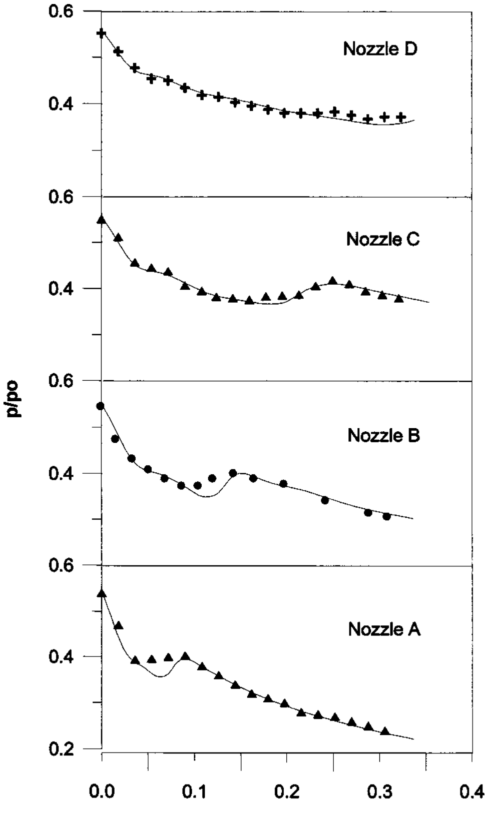

Fig. 9 Centerline pressure levels in a condensing converging-diverging nozzle-present model compared to the results of Moore et al. [16]

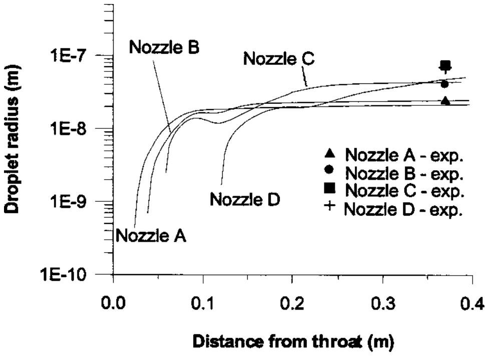

Fig. 10 Centerline mass-averaged droplet size in a condensing converging-diverging nozzle-present model compared to the results of Moore et al. [16]

The present model has also been validated against the experimental data of Moore et al. [16] who obtained centerline pressure distributions and exit droplet sizes for five different converging-diverging nozzle configurations. This set of experimental data is valuable as it provides a combination of pressure data and droplet size information. The nucleation model can only be fully evaluated with both sets of data, since adjustments can be made to the nucleation model parameters (for example using surface tension) relatively easily to induce agreement with pressure data. However, the droplet size is sensitive to the quantity of droplets nucleated for a given amount of supercooling (i.e., the magnitude of *J*), as well as the heat transfer model, and having this additional piece of experimental information allows one to better evaluate the overall accuracy of the model.

In Fig. 9 is shown model results in comparison to centerline pressure distributions, while in Fig. 10 is shown a comparison to droplet sizes at a specified exit location along the centreline of the nozzle. The pressure distributions are reasonably well predicted with the exception of the pressure responses immediately following peak nucleation for Nozzles A and B. In these cases the experimental data suggests the pressure rise should be more diffuse. However, the location and magnitude of the pressure rise is quite good. These results are very similar to the results obtained by previous researchers using this test data (Moore et al. [16], White and Young [6]).

Two-Dimensional Rotor Tip Cascade Solution

A series of experimental studies on condensing steam in a rotor tip cascade was conducted by Bakhtar et al. [20,21] and provides validation data for blade static pressure levels, droplet size, thermodynamic loss and efficiency over a range of expansion ratios and inlet supercooling levels. In Fig. 11 is shown a typical nucleating solution (inflow conditions $P_o = 1$ *bar* and $T_o = 363°K$, and outflow conditions of $P_e = 0.427$ *bar*) using the rotor tip section, and highlights the distribution of the Mach number, supercooling, nucleation rate and droplet size distribution. In this case critical conditions for moisture formation are achieved in the throat region (at transonic flow conditions) at slightly more than 40°K supercooling, with the resulting droplets travelling downstream to reach droplet sizes close to 0.03 μm. As the critical conditions are approached the nucleation rate increases dramatically as seen in Fig. 11, with peak rates approaching the order of 10^{23}.

Additional losses are present in nucleating flows due to the irreversible heat transfer (thermodynamic loss) associated with moisture formation at supercooled conditions. In addition, if during nucleation heat addition to the gas phase is large enough, a condensation shock may be produced in the core flow region introducing additional aerodynamic losses. This additional feature is present, just past the throat region, in the flow depicted by Fig. 11. To highlight the combined effect of these additional losses present with nucleation, in Fig. 12 is shown total pressure profiles, up-

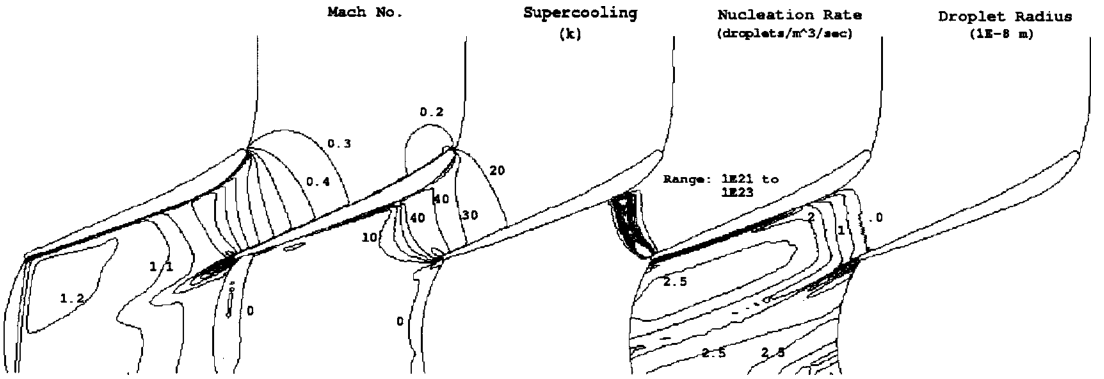

Fig. 11 Typical model predictions for nucleating flow over a two-dimensional rotor tip cascade (Bakhtar [20,21]). Flow conditions $P_o=0.999$ bar, $T_s(P)-T_g=10$ K, and $P_e=0.427$ bar.

stream and downstream of the blade, for the same conditions in Fig. 11 except that one solution has 20°K superheat at the inlet (enough superheat so that flow conditions remain dry). For the superheated downstream profile, the total pressure outside of the wake region (taken at 10 percent chord length past the trailing edge) is near that of the upstream total pressure, indicating that most losses are in the boundary layer and from an oblique shock off of the blade trailing edge. However, in the nucleating case, the core flow region experiences additional thermodynamic (irreversible heat transfer with phase change) and aerodynamic losses (condensation shock) as seen by the reduction in the downstream total pressure level, in regions outside of the wake, compared to the superheated result. These same flow features, deduced from experimental observations, are described in detail by Bakhtar et al. [21].

For further validation of the model a subset of the rotor tip data was used covering expansion ratios ranging from $P_o/P_e=1.83$ to 3.53 with inlet conditions ranging from superheated to 15°K of supercooling. The total pressure inlet condition for all of the calculations was 1 *bar*. The grid size was approximately 10,000 elements determined on the basis of grid sensitivity studies. The subset of experimental data used for comparison correspond to the more extreme flow conditions where the average velocity exiting the cascade was nominally sonic or higher. At a given pressure ratio solutions were obtained with inflow conditions at 20°K superheat and supercooling levels of 5°K, 10°K, and 15°K. The resulting matrix of solutions was then postprocessed to determine aerodynamic and thermodynamic losses, along with droplet sizes, and plotted against expansion ratio and inlet supercooling level. The results are shown in Fig. 13 in comparison to experimental values. For the dry superheated solutions the levels and trends for efficiency and enthalpy loss are well predicted. For the rotor tip cascade under consideration the investigators (Bakhtar et al. [21]) noted the interesting feature of an increase in efficiency at a pressure ratio of 2.33 which was attributed to better aerodynamic performance of the profile under nucleating conditions. The present model captures this increase in efficiency as well as the trend in the reduction in efficiency for a given pressure ratio as inlet supercooling is increased (another conclusion stated by Bakhtar et al. [21]). The trend of increasing losses with increasing pressure ratio is also reflected in the results. The data for efficiencies were reported with an experimental uncertainty of approximately ±0.7 percent (and accounts for some of the scatter in the data presented in Fig. 13); however, in general, the trends reflected by the experimental data are reproduced by the numerical solution including

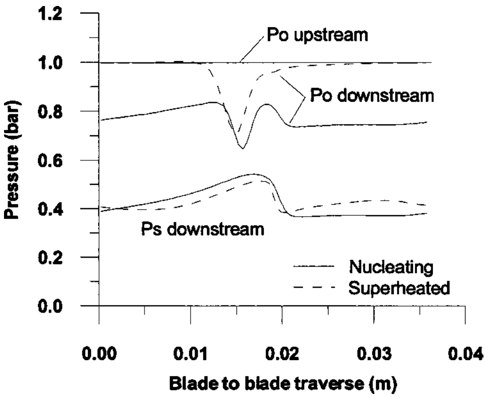

Fig. 12 Total and static pressure profiles (for superheated and nucleating cases) before and after expansion through the rotor tip blade of Bakhtar et al. [20,21]. Flow conditions were $P_o=0.999$ bar and $P_e=0.427$ bar with 20 K superheat and 10 K supercooling respectively at the inlet.

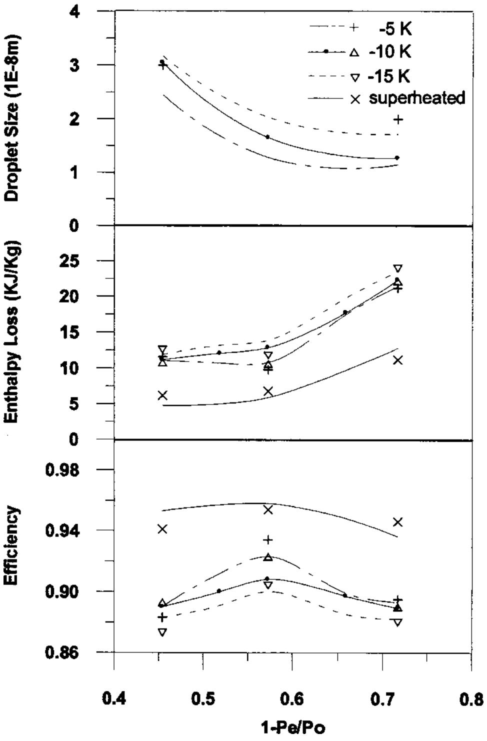

Fig. 13 Component efficiency, enthalpy loss and exit droplet size over a range of inlet supercooling and expansion ratios compared to the experimental data of Bakhtar et al. [21]

the droplet sizes which, for the pressure ratios considered, were reported independent of supercooling level. Comparison to the blade static pressure profile data for these experiments is given in a separate paper (Gerber [22]), in addition, the evaluation of the efficiency and thermodynamic loss followed the approach described by Bakhtar et al. [21].

Three-Dimensional Low Pressure Stage Solution

To show the generality of the method, results for a low pressure stage calculation are shown in Figs. 14 thru 16. The operating speed for the rotor-stator combination was 5000 rpm, with stator inlet total conditions of $P_o = 0.265$ *bar* and $T_o = 328.5$ K (approximately 12°K of supercooling), and rotor exit static pressure of $P_e = 0.0662$ *bar*. The flow path shown is at the hub to shroud mid-span, with stage averaging occurring at the rotor-stator interface. For the flow conditions at mid-span, critical supercooling is reached in the stator passage, with nucleation of sufficient strength to result in a rapid rise in temperature to near equilibrium conditions. The recovery can be seen by the steep gradients in the supercooling field shown in Fig. 14, just after a nucleation index of 22.5 is reached. Equilibrium conditions then persist into the rotor section, with only a few degrees of supercooling remaining in the gas phase. No nucleation of water droplets occurs in the rotor along the mid-span since supercooling is too low. In Fig. 15 the average droplet radius is shown over the mid-span and shows the droplet size varying significantly over the two rotor blade passages. The droplets continue to grow in size through the rotor passage following nucleation in the stator, but at a much slower rate, due to the dropping pressure as energy is extracted from the flow.

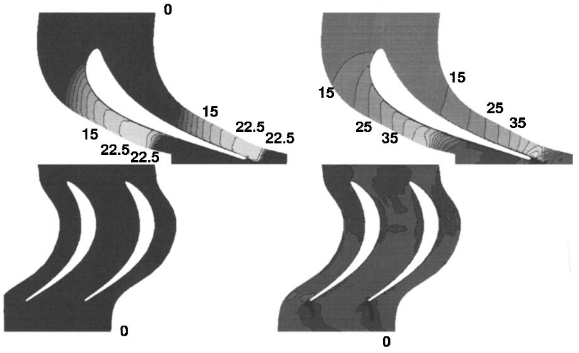

Fig. 14 Low pressure turbine stage calculation results at mid-span. On the left the nucleation index $(n = \log_{10}(J+1))$ is shown with $n_{\min}=0$, $n_{\max}=25$ and $\Delta n = 2.5$. On the right, supercooling $(T_{sc} = T_s(P) - T_g)$ with $T_{sc,\min} = -10$ K, $T_{sc,\max} = 60$ K and $\Delta T_{sc} = 5$ K.

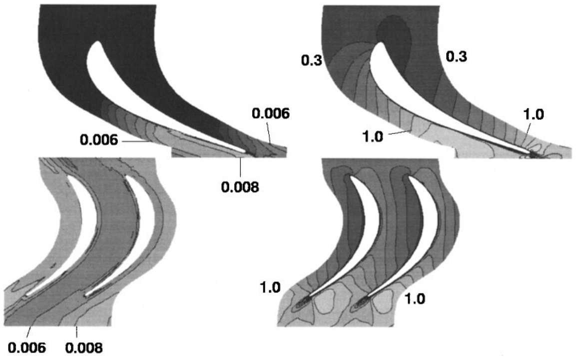

Fig. 15 Low pressure turbine stage calculation results at mid-span. On the left the mass averaged droplet size is shown where $r_{\min}=0$ μm, $r_{\max}=0.012$ μm and $\Delta r = 0.001$ μm. On the right, relative Mach number with $M_{\min}=0$, $M_{\max}=1.4$ and $\Delta M = 0.1$.

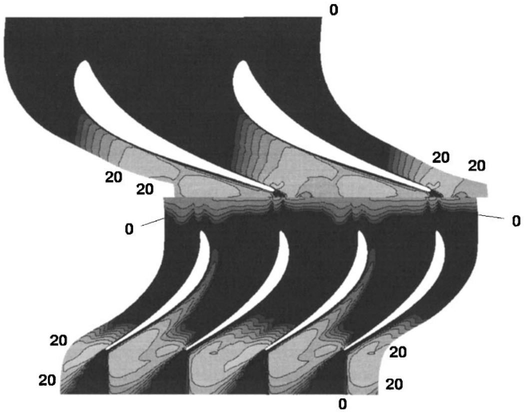

Fig. 16 Low pressure turbine stage results showing nucleation index $(n = \log_{10}(J+1))$ near the shroud. Nucleation index is shown with $n_{\min}=0$, $n_{\max}=25$ and $\Delta n = 2.5$.

Toward the shroud some interesting flow features appear due to the decreasing expansion rate. In Fig. 16 is shown the nucleation index in the flow passage near the shroud. Here it can be seen that droplet nucleation begins in the stator but is not strong enough to bring the flow to equilibrium. The droplets formed in the stator grow rapidly in the sustained supercooled environment as they move into the rotor section, even while the wetness level remains low. Secondary nucleation then occurs toward the rotor tip, but here again the nucleation index, slightly above 20, is still not strong enough to promote a rapid recovery to equilibrium. For this stage calculation the surface of maximum supercooling (i.e., where the nucleation front sits) begins near the hub, crosses the stage interface, and finishes in the rotor near the shroud. This scenario is somewhat as expected for homogeneous condensation in low pressure stage turbines (Skillings et al. [23]). It should be noted that in the present model, droplets nucleated in the stator, and that grow to much larger sizes in the rotor, are still modeled as having no slip even though droplet inertia will begin to influence the droplet trajectory. This is a simplification that will be addressed in future studies. Furthermore, in the wake following the stator (but prior to the rotor/stator interface), the nucleation rate is reduced to zero as expected (see Fig. 16). However, the wake is not conveyed through the rotor/stage interface due to the circumferential stage averaging that also accounts for pitch change. The stage averaging results in a new distribution of supercooling, with associated nucleation, along the length of the inflow into the rotor that affectively washes out the wake. This is an artifact of the commonly employed stage approximation, used to obtain a steady-state solution for what is in fact a unsteady rotor/stator interaction.

At present, there is no experimental data to verify the above predictions, however on a qualitative level the results appear encouraging. In this case the 3-D nonequilibrium calculations are compared to equilibrium solutions, using the same flow code, to check the recovery of equilibrium state conditions. The final mass-averaged exit state for the nonequilibrium run, will be at a slightly higher entropy due to additional irreversible losses (the difference can be measured by Eq. (28)), and a slightly lower wetness, in comparison to an equilibrium run.

Concluding Remarks

A general method has been described for including nonequilibrium phase transition into full Navier-Stokes CFD calculations based on a Eulerian/Lagrangian approach. In this approach the interactions between droplet and vapor are restricted to source terms, and provides a general framework for more advanced droplet models where slip may play an important role. In addition droplet behavior is not restricted to flow along streamlines, and the influence of turbulence on droplet motion and dispersion can be included. The present results, for which nucleated no-slip droplets are only presented, show that the method has promise for modeling complex moisture formation and droplet behavior in three-dimensional systems including stage interfaces. Further work is necessary to reduce the influence of grid resolution near the nucleation front, as well as investigating the implementation of additional droplet models to exploit the source term approach.

Acknowledgments

The support of AEA Technology ESL (Waterloo, ON, Canada) and the Natural Sciences and Engineering Council (NSERC grant 238656-01) of Canada are gratefully acknowledged.

Appendix A

Irreversible Heat Transfer Prediction

The entropy gain due to irreversible heat transfer was calculated directly from the Lagrangian tracking model. As particles were tracked, the entropy gain was accumulated (for the entire flow domain) at each time step and finally normalized by the inlet mass flow, $\dot{m}_i$, based on the expression:

$$\dot{m}_i \Delta s = \sum_{m}^{\mathrm{mp}} \sum_{n}^{\mathrm{nt}} \left[\left(\frac{1}{T_g} - \frac{1}{\tilde{T}_p} \right) (h_g - \tilde{h}_p) \Delta \dot{m}_p \right]_{mn} \tag{28}$$

where

$$\dot{T}_p = (T_p^t + T_p^{t+\Delta t})/2$$

$$\tilde{h}_p = (h_p^t + h_p^{t+\Delta t})/2$$

and $\dot{m}_p$ is the mass flow associated with a particle. For Eq. (28) the summation is over all *m* particles that are injected into the flow domain, and over all *n* time steps for the particle as it travels through the flow domain.

Droplet Size and Wetness Prediction

The mass averaged droplet size, $\overline{r}$, at a flux-element is calculated according to the following equation:

$$\overline{r} = \left\{ \sqrt{\frac{\Sigma_m^{\mathrm{mp}} \Sigma_n^{\mathrm{nt}} (\hat{r}^2 \tilde{\dot{m}}_p \Delta t)_{mn}}{\Sigma_m^{\mathrm{mp}} \Sigma_n^{\mathrm{nt}} (\tilde{\dot{m}}_p \Delta t)_{mn}}} \right\}_{FE} \tag{29}$$

where

$$\tilde{r} = (r^t + r^{t+\Delta t})/2$$

$$\tilde{\dot{m}}_p = (\dot{m}_p^t + \dot{m}_p^{t+\Delta t})/2$$

In addition the wetness, *w*, at a flux-element is calculated from the particle concentration field, *c*, as follows:

$$c = \left\{ \sum_{m}^{\mathrm{mp}} \sum_{n}^{\mathrm{nt}} (\dot{m}_p \Delta t)_{mn} \right\}_{FE} \frac{1}{V_{FE}} \tag{30}$$

$$w = \left(\frac{\rho_g}{c} + 1 \right)_{FE}^{-1} \tag{31}$$

For Eqs. (29) and (30) the summation is over all *m* particles that enter the flux-element, and over all *n* time steps for the particle as it travels through the flux-element.

Nomenclature

B = virial coefficients
c_p = specific heat at constant pressure (J/kgK)
C_μ = $\kappa - \epsilon$ turbulence model constant (0.9)
G = free energy (J/kg)
H = total enthalpy (J/kg)
h = static enthalpy (J/kg)
I = rothalpy (J/kg)
J = nucleation rate (droplets/m$^3 \cdot$s)
k = thermal conductivity (W/m$\cdot$k)
Kn = Knudsen number ($\bar{l}/2r$)
$\bar{l}$ = mean molecular path (m)
l = local latent heat ($h_g - h_p$) (J/kg)
L = equilibrium latent heat (J/kg)
m = mass (kg)
$\dot{m}$ = mass flow rate (kg/s)
Nu = Nusselt number (αD/k)
P = pressure (N/m^2)
Pr = Prandtl number ($c_p \mu / k$)
q = heat diffusion (W/m^2)
q_c = condensation coefficient
r = droplet radius (m)
r^* = critical radius (m)
R_ω = radius of rotation (m)
R = gas constant (J/kg$\cdot$K)
S_h = energy source (W/m$^3 \cdot$s)
S_m = mass source (kg/m$^3 \cdot$s)
S_u = momentum source (N/m^3)
t = time (s)
T = temperature (K)
u = velocity (m/s)
v = specific volume (kg/m^3)
x = spatial dimension (m)

Greek

α = heat transfer coefficient (W/m$^2 \cdot$k)
ϵ = turbulent dissipation (m^2/s^3)
Γ = general diffusion coefficient
γ = ratio of specific heats (c_p / c_v)
κ = turbulent kinetic energy (m^2/s^2)
ρ = density (kg/m^3)
σ = liquid surface tension (N/m)
τ = stress (N/m^2)
ω = rotational speed (rad/s)

Subscripts

b = bulk properties
e = exit conditions
f = liquid phase
g = gas phase
s = saturation
ij = tensor notation
o = total state condition
p = liquid particle
ip = integration point

References

[1] Gyarmathy, G., and Meyer, H. 1965, ''Spontane Kondensation,'' *VDI Forschungsheft 508*, VDI-Verlag, Dusseldorf.
[2] Hill, P. G., 1966, ''Condensation of Water Vapor During Supersonic Expansion in Nozzles,'' J. Fluid Mech., **25**, Part 3, pp. 593–620.
[3] Bakhtar, F., and Tochai, M. T. Mohammadi, 1980, ''An Investigation of Two-Dimensional Flows of Nucleating and Wet Steam by the Time-Marching Method,'' Int. J. Heat Fluid Flow, **2**, No. 1, pp. 5–18.
[4] Young, J. B., 1984, ''Critical Conditions and the Choking Mass Flow Rate in Nonequilibrium Wet Steam Flows,'' ASME J. Fluids Eng., **106**, pp. 452–458.
[5] Young, J. B., 1992, ''Two-Dimensional, Nonequilibrium, Wet Steam Calculations for Nozzles and Turbine Cascades,'' ASME J. Turbomach., **114**, pp. 569–579.
[6] White, A. J., and Young, J. B., 1993, ''Time-Marching Method for the Prediction of Two-Dimensional, Unsteady Flows of Condensing Steam,'' J. Propul. Power, **9**, No. 4, pp. 579–587.
[7] Bakhtar, F., Mahpeykar, M. R., Abbas, K. K., 1995, ''An Investigation of Nucleating Flows of Steam in a Cascade of Turbine Blading-Theoretical Treatment,'' ASME J. Fluids Eng., **117**, pp. 138–144.
[8] White, A. J., Young, J. B., Walters, P. T., 1996, ''Experimental Validation of

Condensing Flow Theory for a Stationary Cascade of Steam Turbine Blades,'' Philos. Trans. R. Soc. London, **354**, pp. 59–88.

[9] Denton, J. D., 1982, ''An Improved Time-Marching Method for Turbomachinery Flow Calculations,'' ASME paper 82-GT-239.

[10] Gerber, A. G., 2000, ''Nonequilibrium Droplet Interactions in Rapidly Expanding Steam Flow,'' Turbomachinery, Journal of the Turbomachinery Society of Japan, **28**, No. 12, pp. 45–48.

[11] Dukowicz, J. K., 1980, ''A Particle-Fluid Numerical Model for Liquid Sprays,'' J. Comput. Phys., **35**, pp. 229–253.

[12] Vukalovich, M. P. 1958, *Thermodynamic Properties of Water and Steam*, Mashgis, Moscow, 6th edition.

[13] Bakhtar, F., and Piran, M., 1979, ''Thermodynamic Properties of Supercooled Steam,'' Int. J. Heat Fluid Flow, **1**, no. 2, pp. 53–62.

[14] McDonald, J. E., 1962–3, ''Homogeneous Nucleation of Water Vapor Condensation. I. Thermodynamic Aspects,'' Am. J. Phys., **30**, pp. 870–877.

[15] McDonald, J. E., 1962–3, ''Homogeneous Nucleation of Water Vapor Condensation. II. Kinetic Aspects,'' Am. J. Phys., **131**, pp. 31–41.

[16] Moore, M. J., Walters, P. T., Crane, R. I., and Davidson, B. J. 1973, ''Predicting the Fog Drop Size in Wet Steam Turbines,'' Inst. of Mechanical Engineers (UK), Wet Steam 4 Conf., University of Warwick, paper C37/73.

[17] Gyarmathy, G. 1976, ''Condensation in Flowing Steam,'' *Two-Phase Steam Flow in Turbines and Separators*, M. J. Moore and C. H. Sieverding, ed., Hemisphere, pp. 127–189.

[18] Raw, M. J. 1995, ''A Coupled Algebraic Multigrid Method for the 3D Navier-Stokes Equations,'' Proceedings of the 10th GAMM-Seminar Kiel, January 14–16. Notes on Numerical Fluid Mechanics, Vol. 49, Vieweg-Verlag, Braunschweig, Wiesbaden, Germany.

[19] Moore, M. J., and Sieverding, C. H. 1976, *Two-Phase Steam Flow in Turbines and Separators*, Hemisphere.

[20] Bakhtar, F., Ebrahimi, M., and Webb, R. A., 1995, ''On the Performance of a Cascade of Turbine Rotor Tip Section Blading in Nucleating Steam. Part 1: Surface Pressure Distributions,'' Proc. Inst. Mech. Eng., Part C: J. Mech. Eng. Sci., **209**, pp. 115–124.

[21] Bakhtar, F., Ebrahimi, M., and Bamkole, B. O., 1995, ''On the Performance of a Cascade of Turbine Rotor Tip Section Blading in Nucleating Steam. Part 2: wake traverses,'' Proc. Inst. Mech. Eng., Part C: J. Mech. Eng. Sci., **209**, pp. 169–177.

[22] Gerber, A. G. 2000, ''Modeling the Steady and Transient Dynamics of Nucleating Two-Phase Steam Flow,'' Proc. of the 2000 National Heat Transfer Conf., August 20–22, ASME paper NHTC2000-12117.

[23] Skillings, S. A., Moore, M. J., Walters, P. T., and Jackson, R. 1988, ''A Reconsideration of Wetness Loss in LP Steam Turbines,'' Proceedings of the BNES (British Nuclear Energy Society), Conference on Technology of Turbine Plant Operating with Wet Steam, London, pp. 171–177.

Masato Ikegawa
Mechanical Engineering Research Laboratory,
Hitachi, Ltd., 502 Kandatsu, Tsuchiura,
Ibaraki 300-0013, Japan
e-mail: mtikega@merl.hitachi.co.jp

Yoshihumi Ogawa

Ryoji Fukuyama

Power and Industrial Systems Kasado,
Administrative Division, Hitachi, Ltd.,
794 Higashitoyoi, Kudamatsu,
Yamaguchi 744-8601, Japan

Tatehito Usui

Jun'ichi Tanaka

Mechanical Engineering Research Laboratory,
Hitachi, Ltd., 502 Kandatsu, Tsuchiura,
Ibaraki 300-0013, Japan

Direct Simulation Monte Carlo Analysis of Rarefied Gas Flow Structures and Ventilation of Etching Gas in Magneto-Microwave Plasma Etching Reactors

Gas flows in plasma etching reactors for semiconductor fabrication became a chief consideration in designing second-generation reactors with higher etching rates. An axisymmetrical model based on the direct simulation Monte Carlo method has been developed for analyzing rarefied gas flows in a vacuum chamber with the conditions of downstream pressure and gas flow rate. By using this simulator, rarefied gas flows with radicals and etch-products were calculated for microwave-plasma etching reactors. The results showed that the flow patterns in the plasma chamber strongly depend on the Knudsen number and the gas-supply structure. The ventilation of the etch-products in the plasma chamber was found to be improved both for higher Knudsen numbers and for gas-supply structures of the downward-flow type, as compared with those of the radial-flow or upward-flow types. [DOI: 10.1115/1.1459074]

1 Introduction

Highly-integrated semiconductor chips have advanced beyond the ULSI (Ultra Large Scale Integration) level that integrates more than ten million devices, and the width of the wiring has been reduced to submicron dimensions (0.5 μm or less). Several plasma sources operating at low pressures of 10 Pa or less, such as a magneto-microwave or ECR (electron cyclotron resonance) source, a helicon source, and an inductively coupled source, have come to be used for plasma etching reactors and plasma CVD reactors, which can correspond to manufacturing equipment for such minute patterns. Analyses of such issues as the generation and diffusion of plasma in the chamber, the gas flow, the production and diffusion of radicals, and the production and diffusion of etch-products on the substrate in etching reactors, are needed to design plasma equipment and processes. Recently, among these issues the gas flow has attracted the attention of process engineers. The reason is that a uniform supply of reactive gas species onto the entire substrate is required, and high-vacuum etching with high-speed exhaust has been proposed for larger diameter ($>$200 mm) substrates because it improves performance [1].

In the case of plasma etching reactors, volatile etch-products are yielded when reactive species (etchants) etch films on the substrate with the assistance of ion bombardment. Because the etching rate decrease if the etch-products adhere to the substrate again, a gas-flow structure that can exhaust etch-products promptly is necessary. Magneto-microwave plasma-etching reactors have been developed and used in the semiconductor fabrication lines since the late-1980's. Then improved reactors with higher etching rates came on the market in the mid-1990's. In this paper, we will call the former and the latter as first generation reactor and second generation reactor respectively. The first-generation reactors used a radial-flow gas-supply structure, and the gas-flow structure was not considered in designing these reactors. But the radical and etch-product densities have become higher in second-generation reactors due to the increased etching rate with high-density plasmas, thereby increasing the importance of ventilating the gas in the chamber. Thus, gas-flow structures have been the chief consideration in designing second-generation reactors with higher etching rates.

So far plasma density distribution has been primarily studied [2–4]. Recently, research papers on the effects of gas flow on etching performance have been also published and their number is increasing [5–12]. High-density plasma sources operate typically at pressures less than 3 Pa. In the microwave etching equipment used under low-pressure conditions, the Knudsen number Kn ($=$mean free path/characteristic length, or λ/L) becomes more than 0.01 (0.24) when, for instance, the size L of the chamber is 162 mm and the pressure is 0.15 Pa. The gas flow must be analyzed not as a continuous flow but as a transitional flow. Therefore, rarefied-gas-flow analysis is needed to analyze such gas flows. To analyze the rarefied gas flow, the direct simulation Monte Carlo (DSMC) method [13] has been developed for aerodynamics around space vehicles. Recently, the DSMC method has come to be used also for rarefied gas flow problems in the semiconductor fabrication processes.

Several papers have reported research in which the DSMC method is applied to gas-flow analysis in the plasma chambers [5–12]. It was found that the etch uniformity changed significantly depending on the reactivity of the ring surrounding the wafer [6]. The etching process of Al wafer in a commercial apparatus was examined by simulating molecular collisions of reactant and product [7]. The flow field in helicon-plasma reactors was found to only be slightly affected by nozzle location using simulations [8]. The diffusion of etchant to the periphery caused a sharp rise of etching rate near the periphery of the wafer [9]. Moreover, the relationship between etching rate uniformity and gas flow has also been studied from the viewpoints of process chamber diameter effects, wafer location, and exit design on processing uniformity [11]. The effects of the flow rate on the etch-

---

Contributed by the Fluids Engineering Division for publication in the JOURNAL OF FLUIDS ENGINEERING. Manuscript received by the Fluids Engineering Division March 14, 2001; revised manuscript received November 27, 2001. Associate Editor: Y. Matsumoto.

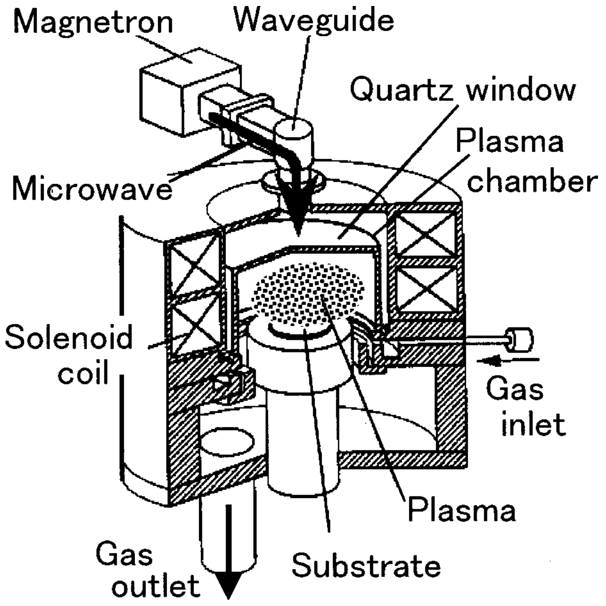

Fig. 1 Schematic of a magneto-microwave plasma etching reactor

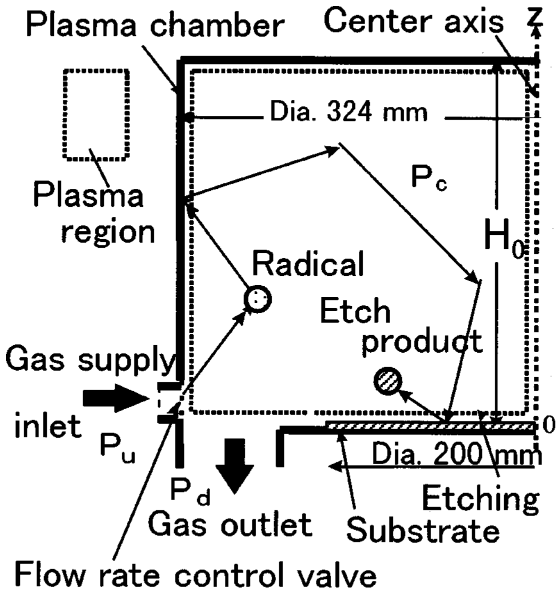

Fig. 2 Calculation model for gas flow in the plasma chamber

product and etchant densities were examined [12]. But they are not concerned on the rarefied-gas-flow structures and the ventilation of the etch-products in the plasma chamber.

We have developed microwave-plasma simulation models, such as a one-dimensional Monte Carlo particle model [14] and a two-dimensional ambipolar diffusion model [15], but these models have not yet accounted for the gas flow. On the other hand, a two-dimensional simulator based on the DSMC method has already been developed for the rarefied-gas-flow analysis of vacuum process equipment [16]. This simulator has been applied to simulate deposition profiles in micron-scale trenches [17]. This simulator was then improved and modified in a program that analyzes an axisymmetrical rarefied-gas-flow with chemical reactions in a chamber under the conditions of flow rate and downstream pressure. This paper reports the results of applying this simulator to gas-flow analysis in a magneto-microwave etching reactor under the development of the second-generation reactor. The fact that the Knudsen number heavily influences the flow pattern has already been reported [18]. Moreover, it has been reported that the gas-supply structure strongly influences the ventilation of the etch-products [19]. The objectives of this paper are to clarify the effect of the gas flow structures on the ventilation of etch-products in detail.

2 Calculation Method

2.1 Calculation Model. A schematic of a magneto-microwave plasma etching reactor is shown in Fig. 1. Microwaves at 2.45 GHz are generated by a magnetron and propagated via a waveguide and into the plasma chamber through a quartz window. Plasma is generated by electron cyclotron resonance (ECR), in which the electrons obtain energy by interacting with the magnetic field generated by solenoid coils. Etching gases, such as Cl_2 or CF_4, are introduced from a gas inlet into the plasma chamber and exhausted from an outlet set at the bottom of the chamber and beyond the perimeter of the substrate.

Figure 2 shows the calculation model for flow analysis of the etching gas in the plasma chamber. The calculation domain is the left half of the cylindrical plasma chamber such that right edge of the domain is the center axis of the chamber. The waveguide (not shown in the figure) is connected with the upper part of the plasma chamber, and the substrate is set on the bottom. The gas inlet for the reactive gas is installed on the lower sidewall of the chamber, and the gas outlet is installed at the bottom, beyond the perimeter of the substrate. The shape of the gas outlet is cylindrical slit, and two different shapes of the gas inlet are examined in addition to the shape in Fig. 2 in this paper.

A rarefied gas-flow simulator [16] for a low-pressure vessel was modified into an axisymmetrical one. DSMC is a method that can solve flow fields by calculating molecular flights and collisions, in cells with sizes smaller than the mean free path, for hundreds of thousands of molecules in each calculation time step. The simulator uses the ‘‘partial region method’’ [16] to briefly calculate the reflections of molecules on the walls. The flights and the molecular collisions of gas molecules are calculated sequentially in a small time interval (time step) Δt. Here Δt is set to be smaller than the mean collision time of molecules. In the simulator, starting from an initial condition, molecular movements in the plasma chamber are calculated in time step Δt.

The etching gas is supplied from the gas inlet, fills the plasma chamber, and is exhausted from the gas outlet. For a flow of mean velocity $(U,0,0)$ in an equilibrium gas, the probability density function $f_{in}(C)$ of the molecular velocity $C(\pm u,v,w)$ (provided that $u>0$), for molecules flowing into the flow fields from the upstream or downstream boundaries, is

$$f_{in}(C)=\frac{2u}{\pi C_m^4 K}\exp\left[-\frac{1}{C_m^2}\{(u\mp U)^2+v^2+w^2\}\right], \qquad (1)$$

where

$$K=\exp\left(-\frac{U^2}{C_m^2}\right)\pm\sqrt{\pi}\frac{U}{C_m}\left\{1\pm\operatorname{erf}\left(\frac{U}{C_m}\right)\right\}; \qquad (2)$$

plus or minus signs indicate upstream or downstream, respectively;

C_m = $\sqrt{2kT/m}$ is the most probable molecular speed;
k = Boltzmann’s constant;
T = the gas temperature upstream or downstream;
m = the molecular mass;

and

erf = the error function.

The number of incoming molecules per cross-sectional area A during a time step Δt from the upstream or downstream boundaries is given by the following equation:

$$N_{in}=\frac{nC_mK}{2\sqrt{\pi}}\Delta tA, \quad (3)$$

where n is the number density upstream or downstream.

The inlet and outlet flow conditions are set by using the successive estimation flow velocity (SEFV) method [16]. In addition, the flow rate is adjusted by using a virtual flow-rate control valve. Conventionally, the flow rate had to be set by changing the upstream pressure by trial and error in the DSMC method because the flow rate was obtained after calculation. Here, a virtual upstream region is designated upstream, and the virtual valve is set on the wall of the plasma chamber at the gas inlet. Some incoming molecules from the gas inlet are reflected diffusely at the valve, with rejection occurring when the flow rate exceeds a set value. In this way, the flow can be calculated based on the conditions of the outlet pressure and the flow rate, which are commonly used in designing industrial vacuum chambers.

In semiconductor manufacturing processes, aluminum and polysilicon films are often etched by chlorine gas. A gas pressure of around 1 Pa is used to etch aluminum films, and it is estimated that in terms of chemical etching, the chlorine radical Cl is the main etchant under this pressure condition [20]. It can then be assumed that the etching rate is determined by the flux of this radical onto the substrate with a uniform ion flux distribution. The models of dissociation and etching reaction are simplified to generalize the results.

The reaction scheme for etching aluminum by Cl_2 is as follows:

$Cl_2+e\rightarrow 2Cl$ (Dissociation in the plasma; e is an electron)

$3Cl+Al\rightarrow AlCl_3\uparrow$ (aluminum film etching reaction).

The reaction scheme for etching polysilicon film by Cl_2 is as follows:

$4Cl+Si\rightarrow SiCl_4\uparrow$ (polysilicon film etching reaction).

Here, the chlorine atom Cl is the radical, and $AlCl_3$ and $SiCl_4$ are the etch-products. This etching reaction model for simulation by the DSMC method is shown schematically in Fig. 2. That is, the molecules of Cl_2 gas supplied to the chamber dissociate into Cl radicals in the plasma area according to the radical dissociation probability P_{rr}. The radical dissociation probability $P_{rr}=1$ means that the dissociation occurs when the every Cl_2 molecule enters into the plasma region. Therefore, the results may be equivalent to ones obtained by using Cl as a source gas. When Cl radicals reach the surface of the substrate by diffusion and flow, they initiate the etching reaction according to the etching reaction probability P_{re}, and the etch-products $AlCl_3$ or $SiCl_4$ are then discharged to the chamber. The plasma region is assumed to spread throughout the entire chamber as shown in Fig. 2. Because the plasma in a magneto-microwave reactor is designed to extend throughout the entire chamber, this assumption is appropriate.

Because the gas and film for etching depend on specific semiconductor fabrication processes, etching equipment must be extensible to a variety of conditions since the types of radicals and etch-products vary depending on the processes. Compatibility with many kinds of processes in the same chamber structure is desirable for equipment in this industry. To investigate general characteristics common all processes, all three kinds of particles in the chamber (reactive gas molecules, radicals and etch-products) are assumed to be monatomic molecules with the same mass and molecular diameter as Cl_2. Moreover, the etching reaction probability P_{re} and radical dissociation probability P_{rr} are both assumed to be 1.0. These assumptions also lead to a simplification of the numerical procedure. (In the last section of this paper, the effect of P_{re} will be examined.) We assume that particles are reflected diffusely by the chamber wall, and that particles other than the radicals causing the etching reaction are reflected diffusely by the substrate. The temperatures of the chamber and substrate are assumed to be the same as that of the gas which flows in.

Incident molecules flowing in the virtual upstream area are all Cl_2 molecules from the parent gas, so that the densities of radicals and etch-products are zero in this region. However, the densities of the species downstream cannot be given at the beginning of the calculation because they are obtained as results of the calculation. The densities of species at each time step for incident particles from downstream are then determined according to a method similar to the SEFV method [16] mentioned previously. The concentrations of incoming molecules from the outlet are determined at each time step, as in the SEFV method. Accordingly, the concentrations of the molecules exhausted from the outlet are checked at each time step and then used as the concentrations of the incoming molecules for the next time step. After the flow and concentrations in the plasma chamber reach steady-state, the concentrations at the outlet, which are calculated from the ratios of each species to the accumulated number of exhausted molecules, are as the concentrations of the incoming molecules for the next time step. The expected result (the normal-direction differentiation is 0) is finally obtained at the downstream boundary with no change in density.

Next, molecular collisions are calculated in each cell by its collision probability. Molecular collisions in diluted gas are overwhelmingly like binary collisions involving just two molecules. The molecular collision calculations are based on the maximum collision number method with a hard-sphere molecular model [21].

It is necessary to promptly exhaust etch-products that may decrease the etching rate by adhering to the substrate again. To evaluate the effect of removing etch-products around the substrate, the ventilation rate R_{ven} is defined as follows, as a function of the numbers of incident radicals and etch-products on the substrate, N_r and N_p, respectively:

$$R_{ven}=\frac{N_r}{N_r+N_p}. \quad (4)$$

Here, a large ventilation rate R_{ven} means that etch-products will be removed from the area around the substrate, and the etching rate will improve.

The mean free path λ_0 of Cl_2 gas at a pressure of 0.67 Pa and a temperature of 293 K is 4.47 mm. This means that the molecular diameter is 5.51×10^{-10} m. The time step Δt is set to be 0.25 λ_0/C_m. A cell size is set as smaller than the mean free path, and in the following calculations the maximum number of simulation molecules and cells in the chamber are 600,000 and 24,000. The calculation is continued until the flow and density reach steady-state and afterwards the statistical error of each physical property's value becomes sufficiently small.

The calculation time by using a workstation with a 180-MHz of CPU is about 40 hours/case.

2.2 Influence of Knudsen Number on Rarefied Gas-Flow Structures.

As shown in Figs. 1 and 2, the radial-flow gas-supply structure in this model has the gas inlet installed on the lower sidewall of the chamber, while the gas outlet is installed at the bottom, beyond the perimeter of the substrate. The inlet has the shape of cylindrical slit as shown in Fig. 1. Under such conditions, the gas-flow patterns are examined with the Knudsen number changed by changing the gas pressure.

2.3 Influence of Gas-Supply Structure on Gas-Flow Pattern.

Because etching is used in several different processes on semiconductor fabrication lines, the gas pressure depends on the process conditions. Therefore, it is undesirable to design gas pressure in the equipment only from the viewpoints of improving the gas-flow pattern and the ventilation rate of etch-products, because this narrows the application of the equipment. It is preferable to change the gas-supply structure and improve the ventilation rate by implementing a better gas-flow pattern. When diffusion is predominant in the transport of gas species, the effect of ventilation does not change, even if the gas-flow pattern is changed. However, the Peclet number, Pe, (UL/D, where U is the flow velocity, L is the characteristic length, and D is the diffusion coefficient),

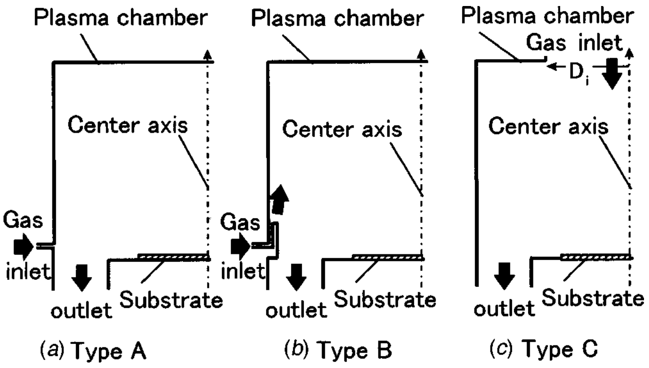

Fig. 3 Gas-supply structures, (*a*) Type A (radial flow), (*b*) Type B (upward flow), and (*c*) Type C (downward flow)

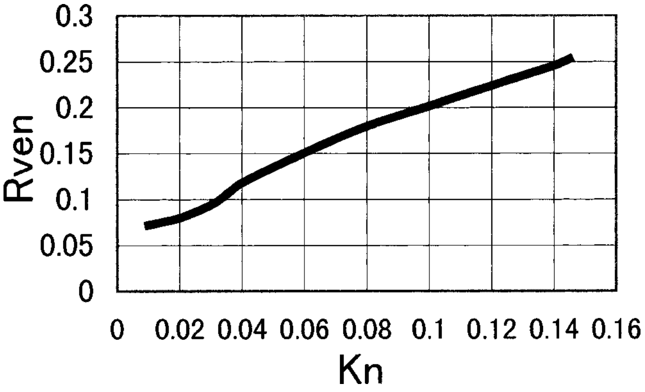

Fig. 5 Ventilation rate R_{ven} and Knudsen number Kn for Type A

which gives the ratio of convective to diffusive mass transport, is around 1.0 under the conditions of a flow rate of 100 $\mathrm{cm}^3\,\mathrm{min}^{-1}$, a pressure of 0.67 Pa, and a chamber diameter of 324 mm. This means that both flow and diffusion are effective for transportation, and it is thought that the gas-flow pattern influences the exhausting of etch-products under such low-pressure conditions. Three types of gas-supply structures are investigated, as shown in Fig. 3: a radial-flow structure (Type A); an upward-flow structure (Type B); and a downward-flow structure (Type C). The gas inlets for Type A and B have a shape of a cylindrical slit, and the gas inlet for Type C has a shape of a circular hole. The chamber height H_0 is 210 mm.

3 Results and Discussions

3.1 Knudsen Number and Rarefied Gas-Flow Pattern. Figures 4(*a*) and (*b*) show the distributions of the velocity vector in the radial-flow gas-supply structure (Type A) for two different Knudsen numbers and pressures with a constant flow rate (40 $\mathrm{cm}^3\mathrm{min}^{-1}$). The Knudsen number Kn is defined by using the chamber radius ($R=162$ mm) and the chamber pressure P_c. The chamber pressure P_c was averaged in the chamber. When Kn is 0.09, the flow velocity vector has a circulation flow pattern, as shown in Fig. 4(*a*). However, for Kn of 0.009, the pattern shows stagnation pattern such that the direction of the flow velocity vector becomes erratic, as shown in Fig. 4(*b*). In this case, the flow enters from the gas inlet and turns directly toward the outlet. This flow pattern is the same as that obtained from an analytical result for continuous fluid flow. The ratio of the flow velocity in the z-direction at the center axis at the height of $z=100$ mm to that at the outlet, v_{zc}/v_{z0}, is 0.34 for (*a*) and less than 0.05 for (*b*). The circulation flow is obviously strong in Fig. 4(*a*). The velocity at the gas inlet is less in Fig. 4(*b*) than that in Fig. 4(*a*). This is due to the decrease in volume flow rate resulting from the increase in pressure.

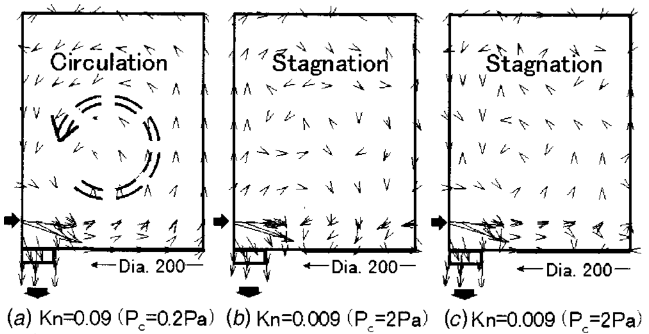

(*a*) Kn=0.09 (P_c=0.2Pa) (Q=40cm³/min) (*b*) Kn=0.009 (P_c=2Pa) (Q=40cm³/min) (*c*) Kn=0.009 (P_c=2Pa) (Q=400cm³/min)

Fig. 4 Velocity-vector distribution for Type A: (*a*) Kn=0.09 (*Q*=40 $\mathrm{cm}^3\,\mathrm{min}^{-1}$), (*b*) Kn=0.009 (*Q*=40 $\mathrm{cm}^3\,\mathrm{min}^{-1}$), (*c*) Kn=0.009 (*Q*=400 $\mathrm{cm}^3\,\mathrm{min}^{-1}$)

A decrease in the Knudsen number more strongly promotes the formation of a stagnation flow than does a decrease in the flow velocity at the gas inlet. The reason is that the pattern of this stagnation flow does not disappear even at ten times the flow rate, as in Fig. 4(*c*). When the Knudsen number is changed under the condition of a constant mass-flow rate, the Reynolds number does not change. However, when the Knudsen number is changed by changing chamber size, the flow pattern should not be compared because in this case the Reynolds number does change. In the latter case, the Reynolds number does not change if the mass-flow rate is changed in inverse proportion to the Knudsen number. Therefore, the influence of changing the Knudsen number by changing the chamber size on the flow pattern can be seen by comparing Figs. 4(*a*) and (*c*).

Figure 5 shows the relationship between ventilation rate R_{ven} and Knudsen number Kn at a constant flow rate. These results clarify that etch-products are exhausted promptly at larger Knudsen number (that is, lower pressure), increasing the ventilation rate R_{ven}. The Cl_2 gas molecules of the parent gas are dissociated and hardly exist in the chamber because the radical dissociation probability P_{rr} is 1.0 in the calculation, so most of the molecules that collide with the substrate are radicals and etch-products. This corresponds to the conditions of a higher-density plasma. The dissociation probability strongly depends on the process conditions, such as plasma density, gas pressure and kind of gas. For the sake of simplifying the phenomena and comprising more different kinds of etching processes, the dissociation probability was assumed as 1.0.

It is also asserted that the model of the simulation in this paper can be applied to the etching of aluminum besides silicon. Silicon is rather strongly influenced by incidence distribution of ion than aluminum. Aluminum is said that the influence of incidence distribution of radical is stronger than ion. It is also said that both Cl_2 and Cl can etch aluminum [22]. Therefore it is considered that the results under the condition of the dissociation probability $P_{rr}=1$ is fitted for aluminum etching. However, degree to which the incidence of etch-products on the wafer causes etching-rate decrease is similar for aluminum and silicon.

The reason why the absolute value of the ventilation rate is small (0.5 or less) is that because the etching reaction probability P_{re} on the substrate is 1.0, the radical density there is decreased. The effect of the Knudsen number on the ventilation rate is similar, although in actual equipment P_{rr} and P_{re} are depend on the film properties and the density of the plasma.

3.2 Gas-Supply Structure and Flow Pattern. Figure 6 shows the distributions of the flow velocity vector for each of the gas-supply structures, Type A, Type B, and Type C (D_i

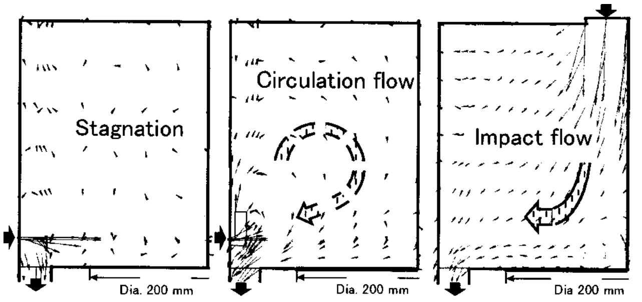

(*a*) Type A (*b*) Type B (*c*) Type C

Fig. 6 Velocity vector distributions for the three gas-supply structures (Kn=0.03)

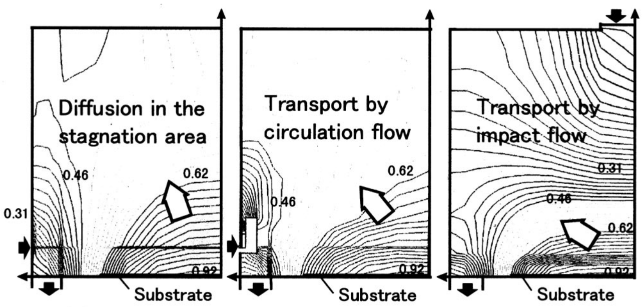

(*a*) Type A (*b*) Type B (*c*) Type C

Fig. 8 Etch-product concentration contours for the three gas-supply structures (Kn=0.03) (normalized by the maximum)

=70 mm), under the conditions of a flow rate of 100 $\mathrm{cm}^3\,\mathrm{min}^{-1}$ and a pressure of 0.67 Pa. Type A, Type B, and Type C, the gas-flow patterns are stagnation, circulation, and impact flow, respectively. The flow pattern for Type A is stagnation because Kn is 0.03.

Because gas inlet is bent upward for Type B, the flow pattern is circulation as the gas rises along the sidewall and then descends toward the outlet from the middle of the chamber. For Type C, the flow descends along the center axis toward the substrate, collides with the substrate and then turns toward the outlet. This shows that in fact the gas-flow pattern in the chamber does depend greatly on the gas-supply structure.

As shown in Fig. 7, the simulation results for ventilation rate R_{ven} are also compared with experiment results for etching rate ER obtained by using an experimental etching reactor. The experiment results were obtained for a nonpatterned polysilicon film. The results show that R_{ven} improves in the order of Type A, B, and C, and this trend agrees with that of the experimental results for ER. The ventilation rates and etching rates are normalized by the ventilation rate R_{venA} and etching rate ER_A for Type A. By changing the flow pattern from a radial one to an impact one, the etch-products around the substrate are promptly exhausted and the etching rate is improved.

Simulation results for the concentration distributions of etch-products in the chamber for each of the three gas-supply structures are shown in Figs. 8(*a*), (*b*), and (*c*). The concentration of etch-products near the substrate decreases in the order of the radial-flow structure (Type A), the upward-flow structure (Type B), and the downward-flow structure (Type C). Because the flow pattern in the chamber is stagnation for Type A, etch-products are transported to the outlet only by diffusion as shown by the large arrow in Fig. 8(*a*). For Type B, etch-products that diffuse up to the middle of the chamber by the diffusion are transported to the outlet by circulation flow. It is thought that for Type C, etch-products are exhausted effectively by a flow that goes from the upper side to the lower side and then collides with the substrate. Its etching-rate uniformity was also confirmed separately [23]. Thus, the downward-flow gas-supply structure (Type C) was adopted for a new reactor design.

3.3 Influences of Gas-Inlet Diameter, Pressure, Flow Rate, and Etching Reaction Probability for the Gas-Supply Structure Type C. Figure 9 shows simulation results for the relationship between the ventilation rate R_{ven} and the gas-inlet diameter D_i for Type C ($Q=150\,\mathrm{cm}^3\,\mathrm{min}^{-1}, P_c=0.67\,\mathrm{Pa}$). It is understood that there is an optimized gas-inlet diameter D_i for which the ventilation rate is maximized. When D_i is large, gas flows directly from the gas inlet to the outlet, the flow velocity near the substrate decreases, and the effect on the substrate of exhausting the etch-products worsens. On the other hand, when D_i is too small, R_{ven} decreases because the area where the flow velocity is fast becomes localized and the etch-products from the entire substrate cannot be exhausted sufficiently.

Figure 10 shows the influence of the flow rate Q and the chamber pressure P_c on the ventilation rate R_{ven} for a gas-inlet diameter D_i of 175 mm. It is understood that the influence of pressure on the ventilation rate is large even for Type C as well as Type A as shown in Fig. 5. The ventilation rate R_{ven} decreases with higher pressure or lower flow rate, although the influence of flow rate is smaller than that of pressure. The reason for this is that both the amount of etch-products and the amount of radicals incident on the substrate increase when the flow rate increases.

Figure 11 shows simulation results for the mean-residence time τ_s from when etch-products are discharged from the substrate until they are exhausted through the outlet. The mean-residence time τ_s decreases with lower pressure or higher flow rate. It can also be

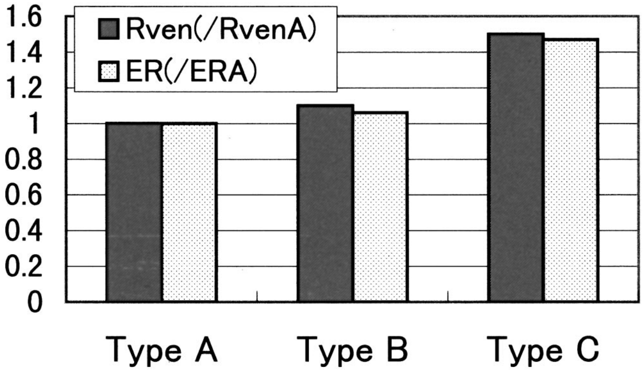

Fig. 7 Effect of gas-supply structure on ventilation rate R_{ven} (by simulation) and etching rate ER (by experiment)

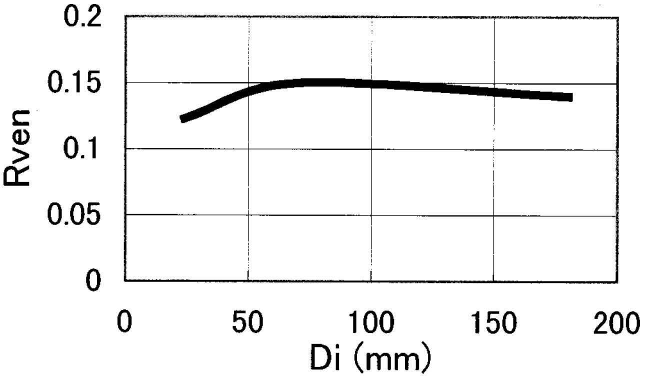

Fig. 9 Effect of gas-inlet diameter D_i for the downward-flow gas-supply structure (Type C) on ventilation rate R_{ven} ($Q=150\,\mathrm{cm}^3\,\mathrm{min}^{-1}, P_c=0.67\,\mathrm{Pa}$)

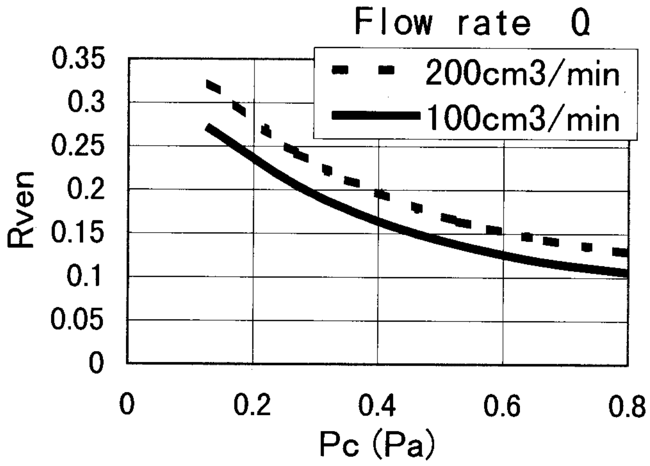

Fig. 10 Effect of chamber pressure P_c on ventilation rate R_{ven} for the downward-flow gas-supply structure (Type C) ($D_i = 175$ mm)

estimated macroscopically as the time over which the density is reduced by half, such that $\tau_s = 0.697(P_c \cdot V_c)/(Q \cdot P_0)$ (where V_c is the chamber capacity and P_0 is atmospheric pressure), or 0.026 s (for $Q = 200$ cm^3 min^{-1} and $P_c = 0.67$ Pa). This mean-residence time is twice that obtained by simulation. The reason is thought to be that in the simulation etch-products are exhausted efficiently by riding on the stream from the substrate near the outlet, while in the macro calculation the value obtained is an average value of the residence time for all particles throughout the chamber.

Simulation results for the effect of etching reaction probability P_{re} on ventilation rate R_{ven} for Type C are shown in Fig. 12. The gas flow rate is 100 cm^3 min^{-1}, the pressure is 0.5 Pa, and the dissociation probability P_{rr} is 1.0. When the etching reaction probability P_{re} decreases, the ventilation rate R_{ven} increases as the radical flux to the substrate increases and the etch-product flux decreases. The etching reaction probability P_{re} is said to be close to 0.1 for etching silicon with chlorine [24], and 0.2–0.3 for etching aluminum with chlorine [25].

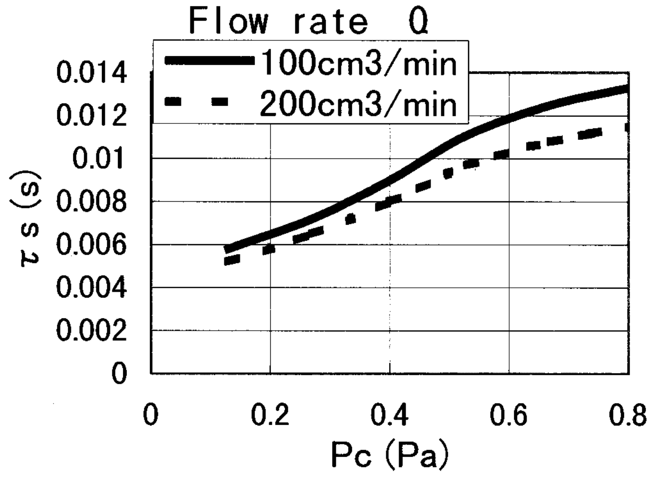

Fig. 11 Effect of gas flow rate Q and chamber pressure P_c on mean residence time τ_c of etch-products (Type C) ($D_i = 175$ mm)

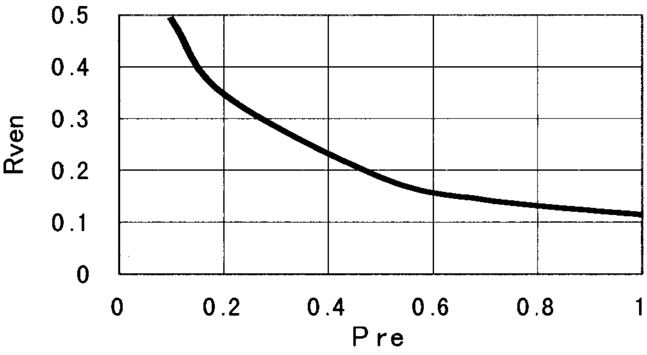

Fig. 12 Effect of etching reaction probability P_{re} on ventilation rate R_{ven} (Type C) ($D_i = 175$ mm, $Q = 100$ cm^3 min^{-1}, $P_c = 0.5$ Pa)

Simulations were done for the magnetomicrowave plasma etching reactor in this paper. It is hard to generalize the gas flow effect in the etching reactors because there are many kinds of etching processes using different gases and films with different plasma reactors. Therefore, we used simple models for the gas dissociation and etching reaction for the sake of simplifying the phenomena and comprising more different kinds of etching processes. This paper focused on the effects of gas flow structures on the ventilation rate (nondimensional factor). There are not large differences of gas-flow conditions among many kinds of high-density plasma etching reactors. Also the pressure (kind of gas) is generalized using Knudsen number. Therefore, it is considered that these results can be applied to other kinds of low-pressure/high-density plasma reactors using helicon source, and ICP, etc.

4 Conclusion

An axisymmetrical model for analyzing the rarefied gas flow in a magneto-microwave plasma process reactor by using the DSMC method with flow rate, downstream pressure was developed, and the effect of various rarefied-gas-flow structures on the removal of etch-products in the etching reactor was examined. As a result, it was determined that the flow pattern and etch-product removal are greatly affected by the Knudsen number and the gas-supply structure. In the case of a radial-flow gas-supply structure, when the Knudsen number is increased, the flow pattern in the chamber changes from stagnation to circulation and the ventilation rate increases. Moreover, it was shown that for a radial-flow gas-supply structure, an upward-flow structure, and a downward-flow structure, the flow pattern in the chamber changes from stagnation to circulation to impact flow, respectively, and the ventilation rate improves with each change. Specifically, the ventilation rate of the downward-flow structure increased to 1.5 times that of the radial-flow structure, and this showed a similar tendency to experimental results for etching rate. Selecting a gas-supply structure from the viewpoint of etch-product removal is important for high-speed etching equipment. Thus, the downward-flow gas-supply structure was adopted in the design for a second-generation magneto-microwave plasma etching reactor with higher etching-rate capability. These results can be also applied to other high-density-plasma, low-pressure etching reactors, such as ICP and helicon plasma reactors.

Nomenclature

C_m = most probable speed of gas atoms
D = diffusion coefficient
D_i = gas-inlet diameter
ER = etching rate
ER_A = etching rate of Type A
f_{in} = probability density function of molecular velocity for molecules flowing into the flow fields from the upstream or downstream boundaries
H_0 = chamber height
Kn = Knudsen number
L = characteristic length
m = molecular mass
n = number density
N_r = radical flux onto the substrate

N_p = etch-product flux onto the substrate
P_c = chamber pressure
Pe = Peclet number
P_0 = atmospheric pressure
P_{rr} = radical dissociation probability
P_{re} = etching reaction probability
Q = flow rate (in normal state)
R_{ven} = ventilation rate
V_c = chamber capacity
u,v,w = velocity components of atoms
λ = mean free path of molecules
τ_s = mean residence time
DSMC = direct simulation Monte Carlo method
ECR = electron cyclotron resonance
ICP = inductively coupled plasma
ULSI = ultra large scale integration
SEFV = successive estimation flow velocity

References

[1] Tsujimoto, K., Kumihashi, T., Kofuji, N., and Tachi, S., 1992, ''High-Gas-Flow-Rate Microwave Plasma Etching,'' Proceedings of Symposium on Dry Process (Oct., 1992 Tokyo), pp. 49–54.

[2] Birdsall, C. K., 1991, ''Particle-in-Cell Charged-Particle Simulations, Plus Monte Carlo Collisions With Neutral Atoms, PIC-MCC,'' IEEE Trans. Plasma Sci., **19**(2), pp. 65–85.

[3] Ventzek, P. L. G., Hoekstra, R. J., and Kushner, M. J., 1994, ''Two-Dimensional Modeling of High Plasma Density Inductively Coupled Sources for Materials Processing,'' J. Vac. Sci. Technol., **B12**(1), pp. 461–477.

[4] Bukowski, J. D., and Graves, D. B., 1996, ''Two-dimensional Fluid Model of an Inductively Coupled Plasma with Comparison to Experimental Spatial Profiles,'' J. Appl. Phys., **80**(5), pp. 2614–2623.

[5] Shufflebotham, P. K., Bartel, T. J., and Berney, B., 1995, ''Experimental Validation of a Direct Simulation by Monte Carlo Molecular Gas Flow Mode,'' J. Vac. Sci. Technol., **B13**(4), pp. 1862–1866.

[6] Economou, D. J., Bartel, T. J. M., Wise, R. S., Lymberopoulos, D. P., and Shufflebotham, P. K., 1995, ''Two-Dimensional Direct Simulation Monte Carlo (DSMC) of Reactive Neutral and Ion Flow in a High Density Plasma Reactor,'' IEEE Trans. Plasma Sci., **23**(4), pp. 581–590.

[7] Serikov, V. V., Kurisawa, S., and Nanbu, N., 1996, ''Profile of Al Etch Rate Estimated from the Analysis of 3-D Rarefied Flow of Cl_2, BCl_3, and $AlCl_3$ In a Commercial Etcher Vacuum,'' **47**(6–8), pp. 1027–1029.

[8] Font, G. I., and Boyd, I. D., 1997, ''Numerical Study of the Effects of Reactor Geometry on a Chlorine Plasma,'' J. Vac. Sci. Technol., **15**(2), pp. 313–319.

[9] Nanbu, K., and Suetani, M., 1997, ''DSMC Analysis of Rarefied Flows of Chlorine in a Parallel-Plate RF Etcher for 300 mm Wafer,'' Reports of the Institute of Fluid Science, Tohoku University, **10**, pp. 283–289.

[10] Johannes, J., Bartel, T., Hebner, G. A., Woodworth, J., and Economou, D. J., 1997, ''Direct Simulation Monte Carlo of Inductively Coupled Plasma and Comparison with Experiment,'' J. Electrochem. Soc., **144**(7), pp. 2448–2455.

[11] Hash, D., and Meyyappan, M., 1997, ''A Direct Simulation Monte Carlo Study of Flow Considerations in Plasma Reactor Development for 300 mm Processing,'' J. Electrochem. Soc., **144**(11), pp. 3999–4004.

[12] Nanbu, K., Morimoto, T., and Suetani, M., 1999, ''Direct Simulation Monte Carlo Analysis of Flows and Etch Rate in an Inductively Coupled Plasma Reactor,'' IEEE Trans. Plasma Sci., **27**(5), pp. 1379–1388.

[13] Bird, G. A., 1976, *Molecular Gas Dynamics*, Clarendon Press, Oxford.

[14] Ikegawa, M., Kakehi, Y., and Kobayashi, J., 1992, ''One-Dimensional Modeling for Magneto-Microwave Plasma Using the Monte Carlo Method,'' Jpn. J. Appl. Phys., **31**(6B), Part 1, pp. 2030–2034.

[15] Tanaka, J., and Ikegawa M., 1994, ''Study of Wave Propagation and Plasma Generation in ECR Plasmas by Numerical Simulation,'' Proceedings of 2nd International Conference on Reactive Plasmas, Jan., Yokohama, pp. 729–732.

[16] Ikegawa, M., and Kobayashi, J., 1990, ''Development of a Rarefied Gas Flow Simulator Using the Direct-Simulation Monte Carlo Method (2-D Flow Analysis with the Pressure Conditions Given at the Upstream and Downstream Boundaries),'' JSME Int. J., Ser. II, **33**(3), pp. 463–467.

[17] Ikegawa, M., Kobayashi, J., and Maruko, M., 1998, ''Study on the Deposition Profile Characteristics in the Micron-Scale Trench Using Direct Simulation Monte Carlo Method,'' ASME J. Fluids Eng., **120**, pp. 296–302.

[18] Ikegawa M., Usui, T., and Tanaka, J., 1994, ''Rarefied Gas Flow Analyses in Plasma Etching Apparatuses Using the Direct Simulation Monte Carlo Method,'' Proceedings of JSME Fluids Engineering Conference, No. 940–53, pp. 271–272 (in Japanese).

[19] Ikegawa, M., Ogawa, Y., Usui, T., and Tanaka, J., 1995, ''Rarefied Gas Flow Analyses in Plasma Etching Apparatuses Using the Direct Simulation Monte Carlo Method (2nd Rep.: Effect of Gas Supply Structure on the Flow Field),'' Proceedings of the 72nd JSME Spring Annual Meeting, No. 95-1, pp. 193–194 (in Japanese).

[20] Danner, D. A., and Hess, D. W., 1986, ''Reaction of Atomic and Molecular Chlorine with Aluminum,'' J. Appl. Phys., **59**(3), pp. 940–947.

[21] Nanbu, K., 1996, ''Stochastic Solution Method of the Boltzmann Equation II. Simple Gas, Gas Mixture, Diatomic Gas, Reactive Gas, and Plasma,'' Reports of the Institute of Fluid Science, Tohoku University, **8**, pp. 77–125.

[22] Edited by Manos, D. M., and Flamm, D. L., 1989, *Plasma Etching—An Introduction*, Academic Press, San Diego, p. 153.

[23] Ikegawa, M., Kobayashi, J., and Fukuyama, R., 2001, ''Effects of Gas-Flow Structures on Radical and Etch-Product Density Distribution on Wafers in Magnetomicrowave Plasma Etching Reactors,'' J. Vac. Sci. Technol., **A 19**(2), pp. 460–466.

[24] Kobayashi, J., Nakazato, N., and Hiratsuka, K., 1989, ''Numerical Simulation for Gas Flow and Mass Transfer in a Dry Etching Chamber,'' J. Electrochem. Soc., **136**, No. 6, pp. 1781–1786.

[25] Tachi, S., 1983, ''Al and Si Etching Mechanism-hot Spot Model,'' Proceedings of 5th Symposium on Dry Process, pp. 8–13.

O. Igra

X. Wu

G. Q. Hu

The Pearlstone Center for Aeronautical Studies,
Department of Mechanical Engineering,
Ben Gurion University of the Negev,
Beer Sheva, Israel

J. Falcovitz

Institute of Mathematics,
The Hebrew University,
Jerusalem, Israel

Shock Wave Propagation Into a Dust-Gas Suspension Inside a Double-Bend Conduit

Using conduits in which a transmitted shock wave experiences abrupt changes in its direction of propagation is an effective means for shock wave attenuation. An additional attenuation of the transmitted shock wave is obtained when the medium contained inside the conduit (through which the shock wave is transmitted) is a suspension rather than a pure gas. The present numerical study shows that adding small solid particles (dust) into the gaseous phase results in sharp attenuation of all shock waves passing through the conduit. It is shown that the smaller the dust particles diameter is, the higher the shock attenuation becomes. Increasing the dust mass loading in the suspension also causes a quick attenuation. By proper choice of dust mass loading in the suspension, or the particles diameter, it is possible to ensure that the emerging wave from the conduit exit channel is a (smooth) compression wave, rather than a shock wave.

[DOI: 10.1115/1.1466457]

Introduction

The propagation of an initially planar shock wave inside a double-bend duct was studied experimentally and theoretically/numerically by Igra et al. [1]. It was shown there that the flow field prevailing behind the transmitted shock wave is highly nonsteady and nonuniform. In addition, the abrupt changes in the flow direction cause rapid attenuation of the transmitted shock wave. It is apparent from those results [1] that very good agreement exists between the recorded wave pattern inside the double-bend conduit and its simulation, as well as between recorded and computed pressure histories. This confirms the reliability of the physical model (Euler equations) and its numerical solution. Falcovitz and Igra [2] studied, numerically, shock wave structure in dusty gas suspension. The aim of the present paper is to investigate by means of numerical simulation the effect of dust suspension on the flow field inside a double-bend conduit, behind the transmitted shock wave. Effects associated with changing the dust particle diameter and the dust loading in the suspension are studied.

Theoretical and Numerical Background

In the present study, a two-fluid model is employed for simulating the gas-particle suspension, where the solid phase is dilute enough to ignore its partial volume and its partial pressure in the suspension. The solid particles are assumed to be rigid spheres, their sole physical interaction with the gas being an exchange of momentum and of heat. Assuming that the carrying gas is inviscid yields that the flow governing equations are the Euler equations expressing conservation of mass, momentum and energy. It is also assumed that the considered compressible gas can be treated as an ideal gas, i.e., it has a simple equation of state. Likewise, the ‘‘particle fluid’’ flow is also governed by the hydrodynamic conservation laws, but for a fluid having zero-pressure. Under these assumptions the governing equations for the considered nonstationary two-phase flow can be written in the Cartesian coordinates (x,y) as:

$$\frac{\partial U}{\partial t}+\frac{\partial F}{\partial x}+\frac{\partial G}{\partial y}=H \tag{1}$$

where U is the vector of unknown flow variables; F, G and H are fluxes in the x- and y-directions and the source terms, respectively which are as follows

$$U=\begin{pmatrix}\rho_g\\ \rho_g u_g\\ \rho_g v_g\\ \rho_g E_g\\ \rho_p\\ \rho_p u_p\\ \rho_p v_p\\ \rho_p E_p\end{pmatrix},\quad F=\begin{pmatrix}\rho_g u_g\\ \rho_g u_g^2+p\\ \rho_g u_g v_g\\ u_g(\rho_g E_g+p)\\ \rho_p u_p\\ \rho_p u_p^2\\ \rho_p u_p v_p\\ \rho_p u_p E_p\end{pmatrix}$$

$$G=\begin{pmatrix}\rho_g v_g\\ \rho_g u_g v_g\\ \rho_g v_g^2+p\\ v_g(\rho_g E_g+p)\\ \rho_p v_p\\ \rho_p u_p v_p\\ \rho_p v_p^2\\ \rho_p v_p E_p\end{pmatrix},\quad H=\begin{pmatrix}0\\ -f_x\\ -f_y\\ -u_p f_x-v_p f_y-q\\ 0\\ f_x\\ f_y\\ u_p f_x+v_p f_y+q\end{pmatrix}$$

The gas is assumed to obey a polytropic equation of state:

$$p=\rho_g R T_g \tag{2}$$

In the equations above, variables p, ρ, T, and u, v are the pressure, density, temperature and velocity components in the x- and y- directions (subscripts g and p refer to the gas and the solid particles, respectively); $E=C_m T+(u^2+v^2)/2$ is the specific total energy (C_v is the specific heat capacity of the gas at constant volume and C_m is the heat capacity of the solid particle material). The source terms on the right side of Eq. (1) create a coupling between the equations governing the flow of the two phases. The viscous interaction between the gas and the solid phase is accounted for by employing the following drag force $\vec{f}$ and a heat exchange rate q:

Contributed by the Fluids Engineering Division for publication in the JOURNAL OF FLUIDS ENGINEERING. Manuscript received by the Fluids Engineering Division January 18, 2001; revised manuscript received December 11, 2001. Associate Editor: E. Graf.

$$f_x = \frac{\pi d^2}{8m}\,\rho_p \rho_g (u_g - u_p)\sqrt{(u_g-u_p)^2+(v_g-v_p)^2}\,C_D$$

$$f_y = \frac{\pi d^2}{8m}\,\rho_p \rho_g (v_g - v_p)\sqrt{(u_g-u_p)^2+(v_g-v_p)^2}\,C_D$$

$$q = \frac{\pi d}{m}\cdot \rho_p\,\frac{\mu C_p}{P_r}\,(T_g - T_p) Nu$$

where m and d are the mass and diameter of a single particle; μ, Pr and C_p are the gas viscosity, Prandtl number and specific heat capacity at constant pressure. In addition, empirical expressions for the drag coefficient C_D and Nusselt number Nu are chosen from the literature. Frequently used expressions are [3]:

$$C_D = 0.48 + 28\ \mathrm{Re}^{-0.85}$$

$$\mathrm{Nu} = 2.0 + 0.6\ \mathrm{Pr}^{1/3}\ \mathrm{Re}^{1/2}$$

$$\mathrm{Re}_s = \rho_g[(u_g-u_p)^2+(v_g-v_p)^2]^{1/2} d/\mu$$

where Re_s is the slip Reynolds number based on the particle diameter. These expressions for C_D and Nu were also employed in Rudinger and Chang [4], Miura and Glass [5], Igra, Elperin and Ben-Dor [6] and many others. Use of similar correlations for C_D and Nu in gasdynamic conservation laws schemes has also been validated by comparison to experiments, e.g., Aizik et al. [7].

Using the operator-splitting technique, Eq. (1) is replaced by the following three conservation laws:

$$\frac{\partial U}{\partial t} + \frac{\partial F}{\partial x} = 0 \qquad (3a)$$

$$\frac{\partial U}{\partial t} + \frac{\partial G}{\partial y} = 0 \qquad (3b)$$

$$\frac{dU}{dt} = H \qquad (3c)$$

Due to the split procedure, the two-dimensional finite-difference scheme for the integration of Eq. (1) can be obtained by applying a sequence of one-dimensional conservation law schemes to Eqs. (3). Moreover, in Eqs. (3a,b), the gas-phase equation is not coupled with the particle-phase equation. The gas Euler equation in conservative form is solved using the GRP scheme [8–10]. The proposed numerical scheme GRP (Generalized Riemann Problem) is especially suitable for producing solutions to compressible flows with shock or contact discontinuities, which characterize shock wave diffraction phenomena. The particle fluid of zero-pressure, however, requires a different numerical method, for example the MacCormack scheme [11] for solving the particle-phase equation. Let L_x and L_y be the one-dimensional operators corresponding to Eqs. (3*a*) and (3*b*), the integration of Eq. (3a,b) for the gas and particles are given, respectively, by:

$$U_g^{n+1} = L_x(\Delta t) L_y(\Delta t) U_g^n \qquad (4)$$

$$U_p^{n+1} = L_x\left(\frac{\Delta t}{2}\right) L_y(\Delta t) L_x\left(\frac{\Delta t}{2}\right) U_p^n \qquad (5)$$

Here, based on the observation in Igra et al. [12], the simplified splitting given in Eq. (4) is adopted since it is more efficient and yields virtually indistinguishable results compared with the more accurate splitting given by Strang [13]. Equation (3*c*) is solved using a predictor-corrector scheme and for each half time-step, its integration is obtained using a predictor step followed by a corrector step,

$$U_{i,j}^{(1)} = U_{i,j}^n + \frac{\Delta t}{2} H_{i,j}^n \qquad (6a)$$

$$U_{i,j}^{n+1/2} = U_{i,j}^n + \frac{\Delta t}{4}(H_{i,j}^n + H_{i,j}^{(1)}) \qquad (6b)$$

All the above schemes are finite-difference schemes of second-order accuracy in time and in space.

The computational domain is a rectangle of 200×60 mm, which is divided into a uniform Cartesian mesh of 600×180 square cells. The validity and accuracy of the two-phase modeling has been confirmed by comparison to shock tube experiments where a planar shock wave has been driven into a dusty gas suspension [14]. Good agreement was observed between the measured shock wave attenuation and the corresponding simulations.

Results and Discussion

In the following the obtained results are compared with a similar pure gas case; the case studied experimentally and numerically by Igra et al. [1]. The investigated flow field is shown schematically in Fig. 1. Items marked as P1, P2, P3, and P4 in Fig. 1 indicate locations at which pressure histories are computed. A sample case from Igra et al. [1] study, obtained for the geometry shown in Fig. 1, is given in Fig. 2. This figure, which includes experimental shadowgraph and schlieren photos (Fig. 2*a*) and the corresponding simulations (Fig. 2*b*), will serve as pure-gas reference for comparison with results obtained for similar dusty flows. The effects caused by the dust presence on the post shock flow are shown in Figs. 3–12. In all cases shown in Figs. 3–5 the dust loading is $\eta = 2$ ($\eta \equiv \rho_{p0}/\rho_{g0}$, which is equal to the dust-gas mass ratio in the suspension) and the particle's diameter is varied from 5 μm in Fig. 3 to 50 μm in Fig. 5. The following dust physical properties are employed in the present computations: $C_m = 1000$ J/(Kg·K) and $\rho_m = 2500$ Kg/m^3 (ρ_m is the dust material density). At $t = 0$ the whole space inside the duct shown in Fig. 1 is uniformly filled with a dusty suspension. In the first 50 mm of the entrance channel to the double-bend duct (not shown in Fig. 1) the transmitted shock propagates in pure air. In all simulations the following initial conditions are used: $P_0 = 0.97$ bar, $T_0 = 296.5$ K and $M_s = 1.347$; with $\gamma = 1.4$ and the molecular weight for air of 29. The entrance boundary conditions prescribe the post-shock air flow, while at the exit (bottom right of Fig. 1) non-reflecting boundary conditions are prescribed.

Comparing results shown in Figs. 3–5 with those obtained for a similar pure gas case (Fig. 2) reveals the following. As could be expected, the smaller the dust particle, the faster is its response to changes in the flow conditions generated by the transmitted shock wave. This leads to a relatively quick relaxation, which eventually brings the suspension to a new equilibrium state. This indeed is the case as is evident from comparing Fig. 3 with Fig. 2(*b*). As is apparent from Fig. 3, where the smallest particles are involved ($d = 5$ μm), the dust's effect on the suspension flow field is extremely fast. It completely alters the wave pattern observed in the pure gas case, which is shown in Fig. 2. The transmitted shock wave in Fig. 3 is weaker than its counterpart in Fig. 2; it has not reached the conduit right vertical wall at $t = 250$ μs while in the pure gas case it is seen reflected from this wall at the considered time. Furthermore, while in the pure gas case, at $t = 250$ μs, a strong reflected shock wave is clearly observed from the conduit bottom; in the case of fine dust particles ($d = 5$ μm shown in Fig. 3 at $t = 250$ μs) the reflected wave from the conduit bottom is a

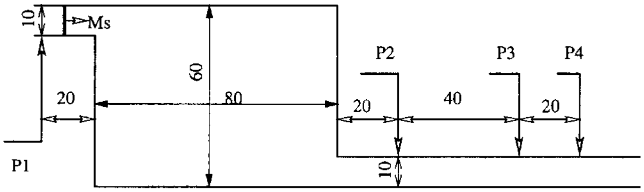

Fig. 1 Schematic description of the investigated conduit. All dimensions are in mm. $M_s = 1.347$, P1, P2, P3 and P4 indicate positions where pressure histories are computed.

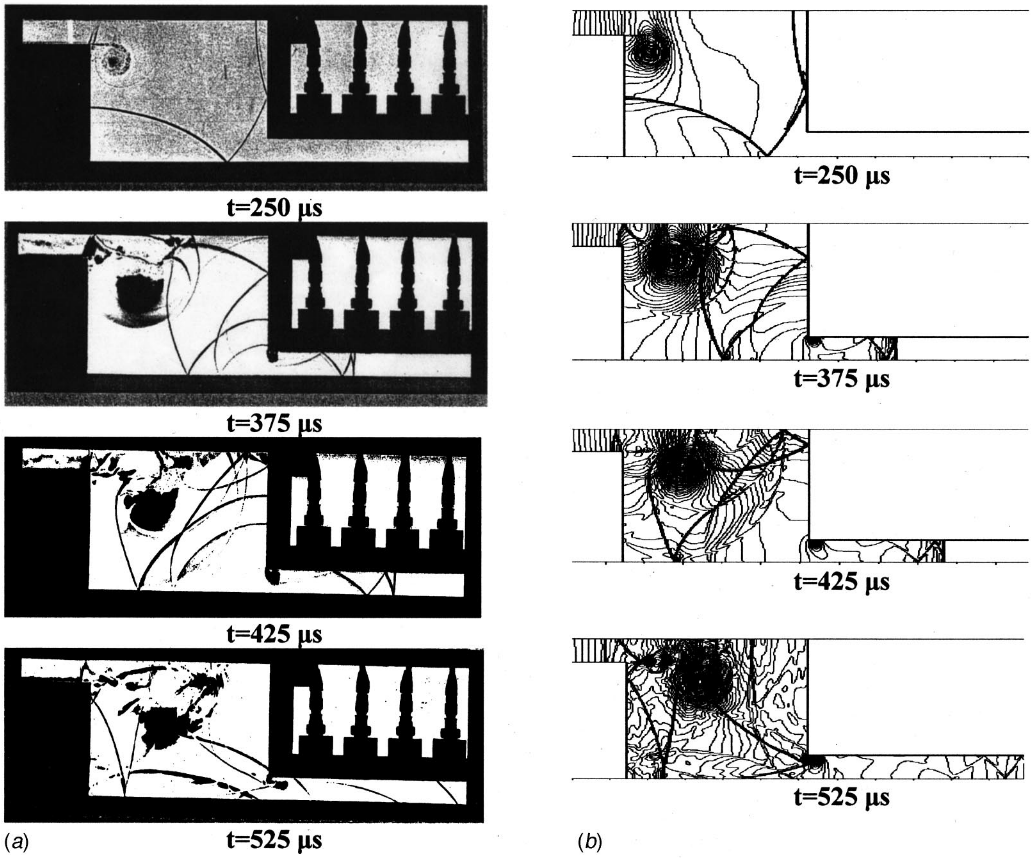

Fig. 2 (*a*) Shadowgraph/schlieren results in pure air. Initial flow conditions are: $P_0=0.97$ bar, $T_0=296.5$ K and $M_s=1.347$. (*b*) Simulations of the flow shown in Fig. 2(*a*).

weak compression wave. It is seen only as a shift in lines of constant density shown in Fig. 3. The strong attenuating effect of the small dust particles is further noticed at late times. While in Fig. 2 strong shock wave reflections from all the conduit's walls are clearly visible, in Fig. 3 the only visible wave is the one engulfing the low-pressure zone generated by the corner-shed vortex. All other waves attenuate to Mach waves, resulting in regions of a fairly uniform flow at the right half of the conduit; see Fig. 3 at $t=525$ μs. At this time no quasi-uniform zones can be detected in the similar pure gas case, as is evident from Fig. 2(*b*). Increasing the diameter of the dust particles results in an increase in their mass and thermal inertia and as a result it takes longer time until the suspension reaches a new equilibrium state behind the transmitted shock wave [3]. This indeed is the case as is evident from comparing Fig. 5 (where $d=50$ μm) with Fig. 2. The suspension shown in Fig. 5 behaves almost like a frozen flow, i.e., the dust presence has almost no effect on the observed wave pattern (in comparison with a similar pure-gas case), during the observed flow duration. Again, the only clearly visible difference is seen in proximity to the corner-shed vortex.

For demonstrating the convergence of the used numerical scheme the case shown in Fig. 4(*a*) was re-computed using a higher grid resolution, i.e., 1200×360 square cells instead of the 600×180 used for obtaining the results shown in Fig. 4(*a*). It is clear from comparing Fig. 4(*a*) with Fig. 4(*b*) that no significant difference is observed due to this change. The almost non-detectable effects associated with changes in the grid size will also be demonstrated subsequently, when pressure histories at various points in the considered duct will de discussed. Throughout the present solution a nonreflecting boundary condition was imposed on the dust particles when they hit the conduit walls. One might ask how the flow and wave pattern would be influenced had the boundary condition been taken as elastic rebound. As is clear

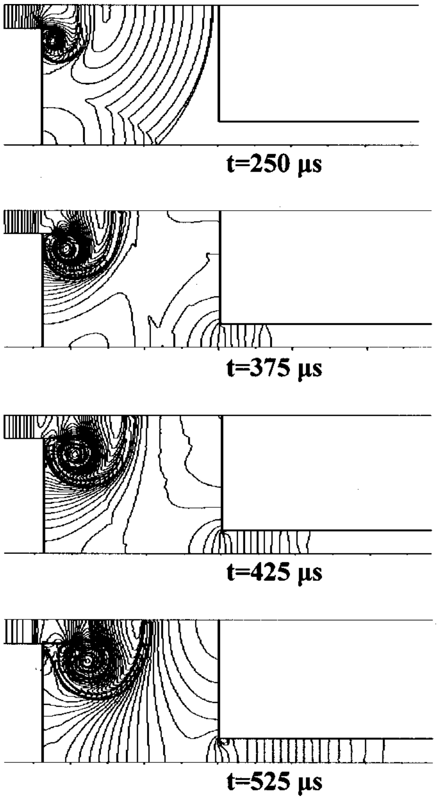

Fig. 3 Flow simulation for dusty gas, $d=5$ μm, $\eta=2$. Initial conditions as in Fig. 2.

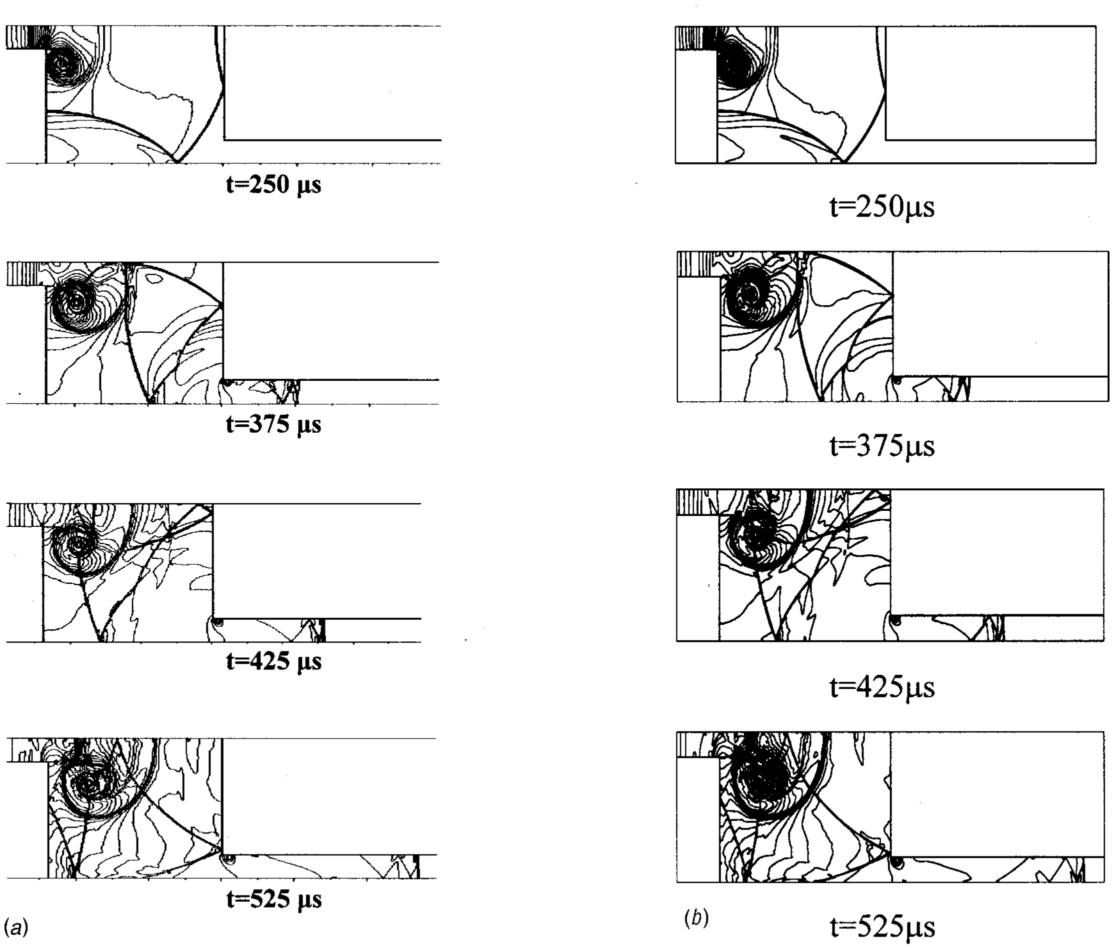

Fig. 4 (*a*) Flow simulation for dusty gas, d=20 μm, η=2. Initial conditions as in Fig. 2. (*b*) Flow simulation as in Fig. 4(*a*) but with double number of grid points; (*c*) flow simulation as in Fig. 4(*a*) but using elastic rebound conditions for the solid particles.

from comparing Fig. 4(*c*) with Fig. 4(*a*) the differences are hardly detectable.

The strong influence that the small dust particles ($d=5$ μm) have on the evolving flow inside the duct can be seen in Fig. 6 where the pressure distributions along the duct's upper wall are shown for different times. A schematic view of the duct geometry (not to true scale) is shown at the top of Fig. 6. For comparison, pressure distribution obtained for a similar pure gas case, at $t=225$ μs, is also shown in this figure. A comparison between the pure and the dusty gas cases shows that in the dusty case, the dust presence causes strong attenuation of the transmitted shock wave. This is clearly seen by comparing the position of the transmitted shock-front, at $t=225$ μs, in the pure gas and in the suspension cases. Simultaneously with the reduction in the propagation velocity of the transmitted shock wave, the pressure jump across the shock front is significantly reduced in the suspension case; it is about 20 percent lower than what is obtained in a similar pure gas case. With progressing time ($t>225$ μs) the transmitted shock wave, in the suspension, is reduced to a compression wave. This process is also visible in Fig. 6.

As mentioned, a noticeable difference between the dusty and the pure gas cases is visible in proximity to the corner-shed vortex; see Figs. 3–5 and 2(*b*). In order to have a clear view of the suspension-flow behavior at this zone the flow field shown as lines of constant density in Fig. 3, at $t=525$ μs, is replotted in Fig. 7. In Fig. 7(*a*), the plot shown in Fig. 3 is repeated using a larger scale. The added dash-dotted line, connecting the two expansive corners of the duct, is to be used as an axis along which the flow variables are to be computed. Figure 7(*b*) shows variations in the suspension pressure and in the gaseous phase density along this line. It is apparent from Fig. 7(*b*) that while the pressure distribution shows a smooth behavior, the gas density plot experiences fast changes while crossing the vortex (points 1, 2, 3, and 4) and the ''interface'' (points 0, 5 and 6); this interface does not exist in the similar pure gas case (in Fig. 2(*b*)). The reason for its existence could be understood from observing Figs. 7(*c*) and 7(*d*). In Fig. 7(*c*) lines of constant spatial dust density are shown. It is clear from this figure that unlike the gaseous phase, in the solid phase there are two zones of almost constant spatial dust density. The two zones of almost constant density are separated by a layer in which large density gradients, in the dust spatial density, takes place. This is confirmed in Fig. 7(*d*) where variations in the dust spatial density along the line connecting the two expansive corners of the duct are shown. It is clear from Fig. 7(*d*) that the transmitted shock wave and the corner-shed vortex push the dust particles downstream generating an almost dust-free zone up to $x\approx 40$ mm. As a result a pronounced increase in the dust spatial density exists in a narrow region, 40 mm$<x<$48 mm. Further downstream an almost constant dust spatial density is observed. The 'interface' observed in the gas density variations (in Fig. 7(*b*) matches the local high density dust layer.

Effects associated with changes in the dust mass loading on the observed wave pattern inside the double bend conduit are shown in Figs. 8–10; in all cases $d=10$ μm. It is evident from comparing these figures with those obtained for a similar pure-gas case (Fig. 2(*b*)) that the amount of dust loading in the suspension has

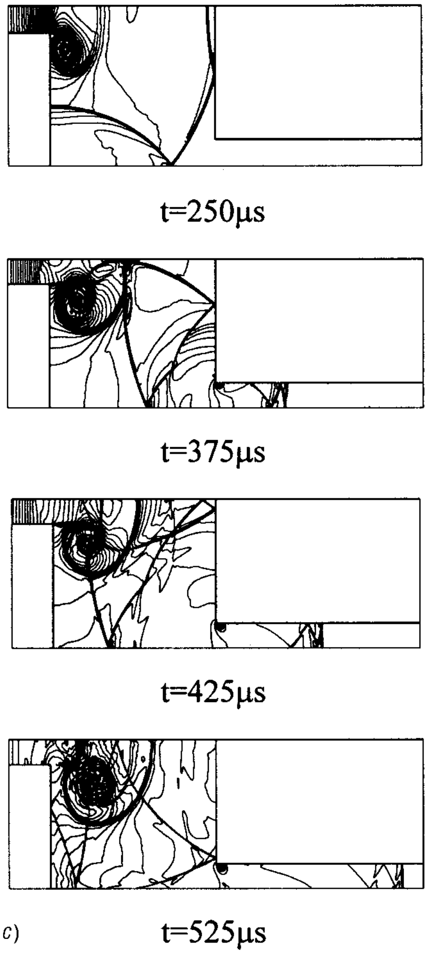

Fig. 4 (***continued***)

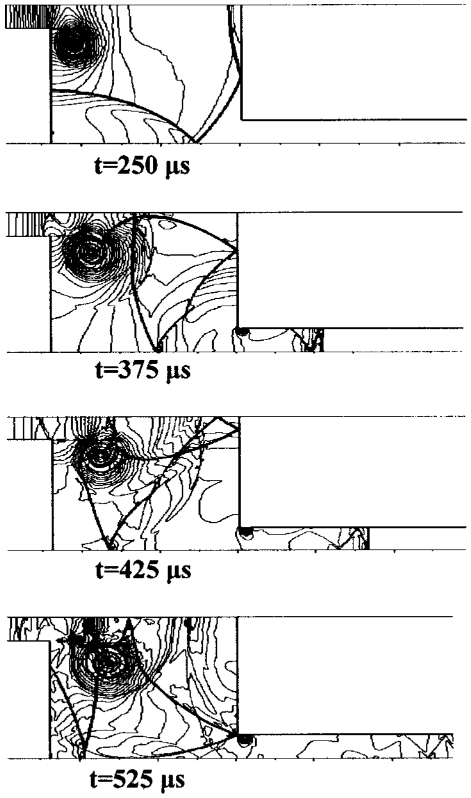

Fig. 5 Flow simulation for dusty gas, d=50 μm, η=2. Initial conditions as in Fig. 2.

strong effect on the flow, and on the wave pattern observed behind the transmitted shock wave. For a relatively low dust loading, $\eta=0.5$, the suspension behaves like a similar pure-gas case throughout the investigated flow duration; see Figs. 8 and 2(*b*). While at early time ($t=250$ μs) the wave pattern shown in Figs. 8 and 2(*b*) is practically the same, at late times differences can be seen. However, the major/strong waves observed in Fig. 2(*b*) can also be found in Fig. 8. The difference between the two flows (pure and dusty gases) will become apparent at late times, at $t \geq 525$ μs, where the dust presence will start affecting the post-shock flow. As seen before, a clear difference is found only around the vortex. Increasing the dust mass loading in the suspension will change the wave pattern. In Fig. 9 the dust loading is raised fourfold, to $\eta=2$. Now the dust is a dominant component in the suspension and its presence has significant effect on the observed wave pattern, although not instantly since the dust particle diameter is not very small ($d=10$ μm). At $t=250$ μs similar wave patterns are seen in both Fig. 9 and Fig. 2. The dust attenuating effect can be observed at this time since in Fig. 9 the diffracted shock wave is seen just as it hits and reflects from the conduit right vertical wall. In Fig. 2(*b*) this shock wave is clearly seen after its head-on collision with the considered wall. At a later time, $t \geq 375$ μs, a very different wave pattern is seen in Fig. 9 and in Fig. 2(*b*). The high dust loading causes fast attenuation of shock waves inside the conduit. This is especially so at late times, see Fig. 9 at $t=525$ μs, where the only strong "wave" seen inside the conduit is the 'interface' engulfing the vortex and separating between the low spatial density zone on the left of the interface and the high spatial density zone on its right. When the dust loading is further increased, to $\eta=5$, the strong wave attenuation is visible from early times. As early as t=250 μs very different wave patterns are seen in the pure-gas case (Fig. 2(*b*)) and in Fig. 10. The diffracting shock wave and its reflection from the conduit bottom are reduced in Fig. 10 to compression waves. In all times shown in Fig. 10 the only visible place where strong density gradients exist are the vortex shed from the expansive

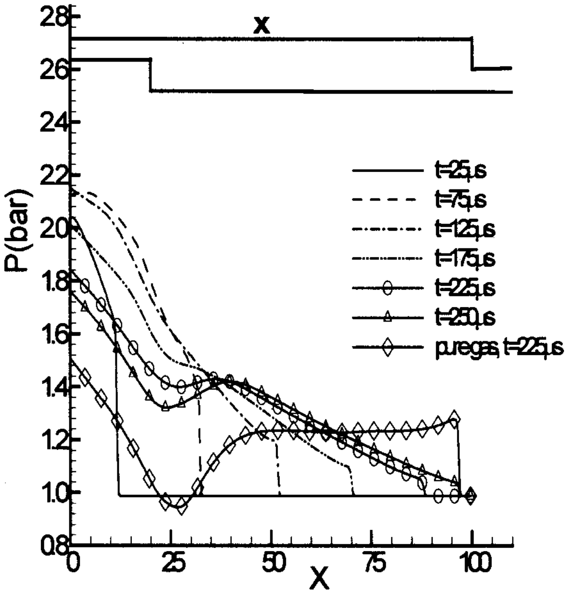

Fig. 6 Pressure variations along the duct upper wall. Initial conditions as in Fig. 2. In the suspension d=5 μm and η=2.

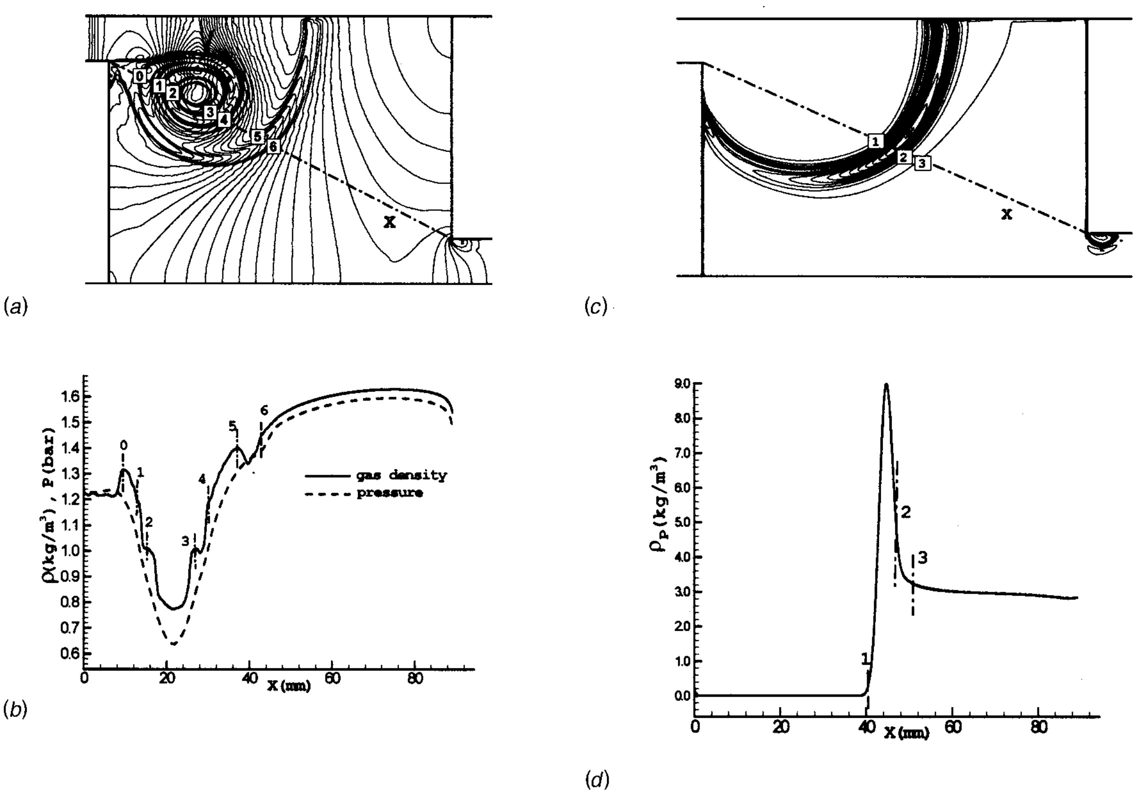

Fig. 7 (*a*) Isopycnics in the gaseous phase. (*b*) Pressure and gas density variations along a line connecting the two expansive corners at t=525 μs, d=5 μm, η=2. (*c*) Isopycnics in the solid phase. (*d*) Spatial dust density variations along a line connecting the two expansive corners at t=525 μs, d=5 μm, η=2. Initial conditions as in Fig. 2.

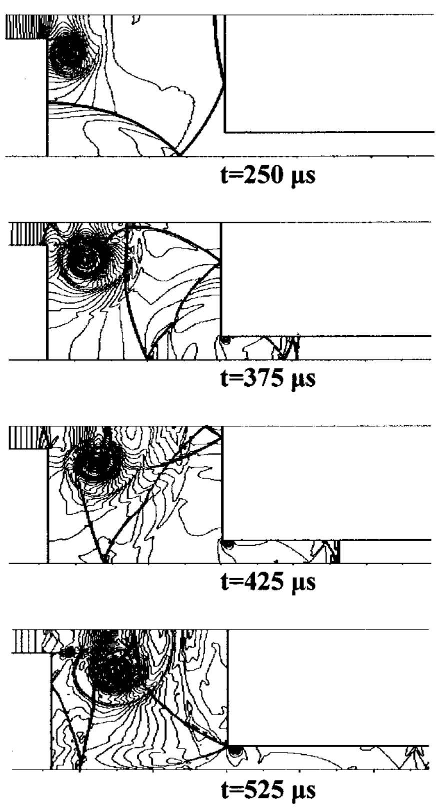

Fig. 8 Flow simulation for dusty gas, η=0.5, d=10 μm. Initial conditions as in Fig. 2.

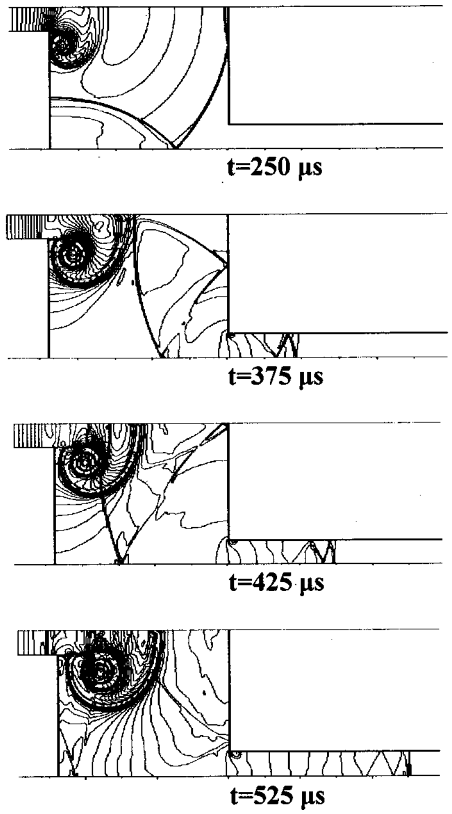

Fig. 9 Flow simulation for dusty gas, η=2, d=10 μm. Initial conditions as in Fig. 2.

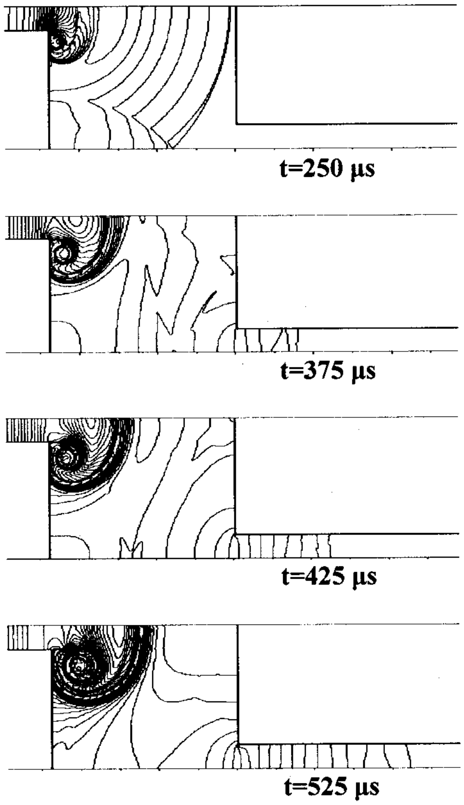
t=250 μs

t=375 μs

t=425 μs

t=525 μs

Fig. 10 Flow simulation for dusty gas $\eta=5$, d=10 μm. Initial conditions as in Fig. 2.

corner and the interface. Again, in the dusty case zones of quasi-uniform flow are visible; in contrast to the pure-gas case in which no quasi-uniform flow regions can be observed.

The effect that changes in the dust mass loading in the suspension have on the computed pressures, at various positions inside the conduit, is shown in Fig. 11. The studied locations are ports P1 to P4 marked in Fig. 1. As could be expected [3,5] when a planar shock wave propagates into a dusty suspension the obtained post shock pressure is higher than that prevailing behind a similar shock wave propagating in a pure gas case. This is also evident from the pressure histories shown in Fig. 11, for port P1, where the pressure behind the planar shock wave entering the conduit is presented. As expected, the higher the dust loading is, the higher the post shock pressure becomes. The pressure immediately behind the shock front is increasing until a maximum is reached; thereafter the pressure is declining due to the low pressure generated by the vortex. In the considered study the flow behind the transmitted shock wave is subsonic and therefore, disturbances progress both upstream and downstream. At late times, outside the investigated time covered in Fig. 11, an equilibrium pressure will be reached. Pressure ports P2, P3, and P4 are located along the exit channel from the conduit shown in Fig. 1. When comparing the pressure jump across the shock front in port P1 with those seen in ports P2 to P4 it is evident that the waves progressing through the double bend conduit experience strong attenuation due to the dust presence. It is therefore expected that upon reaching the conduit's exit the wave is significantly weaker than the strength it had while propagating along the conduit's inlet, at P1. This is clearly visible in the pressure histories shown in Fig. 11. Increasing the dust loading in the suspension not only reduces the pressure jump across the transmitted shock wave, it also change the shock into compression waves for $\eta>2$. In such cases a monotonous pressure increase, toward an equilibrium value, takes place behind the reduced shock wave (a Mach wave; see for $\eta=5$ in Fig. 11).

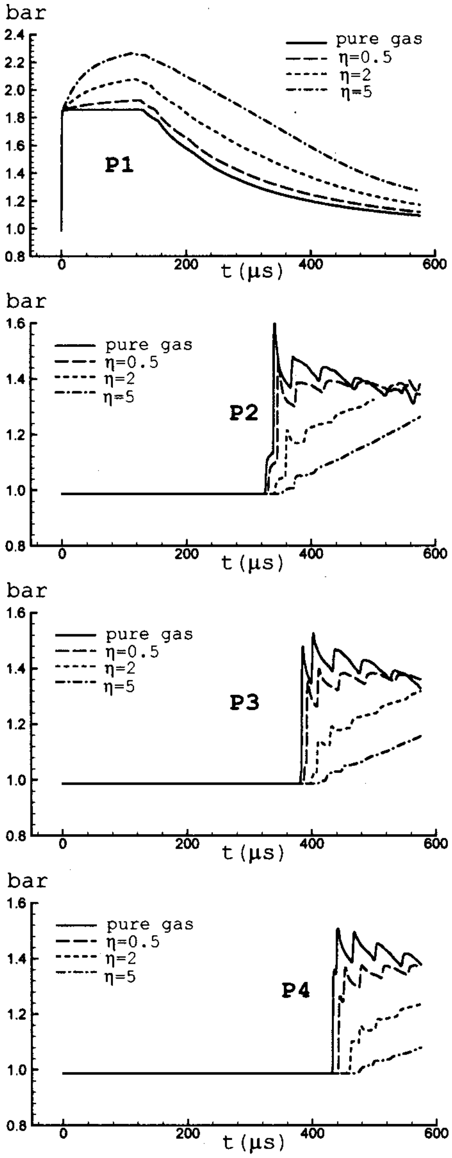

Fig. 11 Effects of changes in the dust loading on obtained pressure histories at ports P1 to P4. d=10 μm. Initial conditions as in Fig. 2.

In the last figure, Fig. 12(*a*), effects on computed pressure histories associated with changes in the dust particle diameter are shown. In all case shown in Fig. 12(*a*), $\eta=2$. As expected in dusty shock waves [5], the entering shock wave (at station P1) experiences a pressure increase, following the sudden jump across the shock front, owing to the deceleration of the flow caused by the solid particles. The smallest the particle diameter is, the higher the post shock pressure becomes. At the exit channel from the considered conduit, ports P2, P3, and P4, the transmitted shock wave is significantly weaker than it was while entering the conduit. The introduction of dust particles into the gaseous phase reduces the pressure jump across the transmitted shock front and the prevailing pressure thereafter, in comparison with a similar pure gas case; see Fig. 12(*a*). It is apparent from Fig. 12(*a*) that the strongest pressure decline is observed in the case of the smallest particles. This is not surprising since all cases shown in Fig. 12(*a*) have the same dust loading. This implies that for the case of small

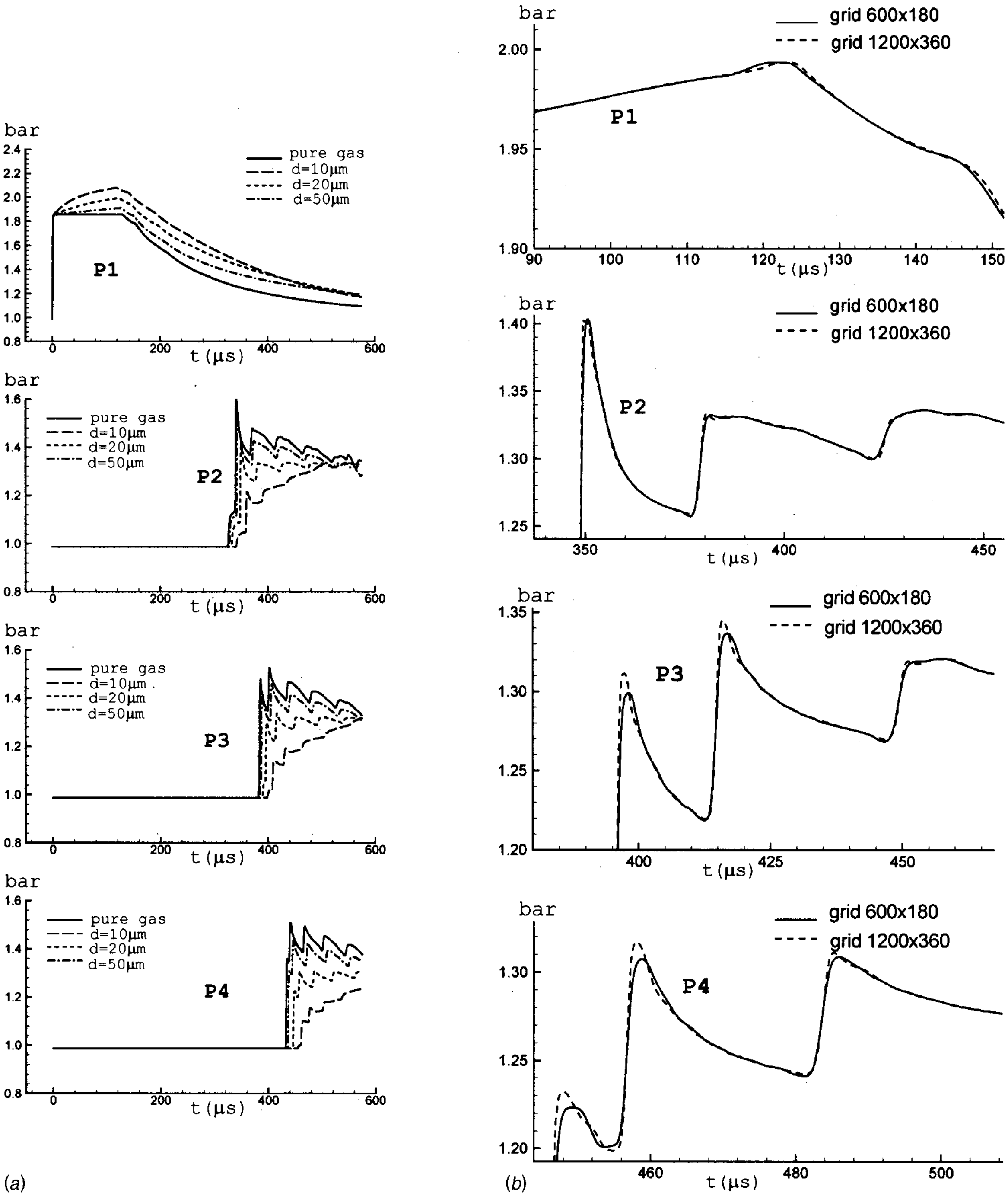

Fig. 12 (***a***) **Effects of changes in the particle diameter on obtained pressure histories at ports P1 to P4.** $\eta=2$**. Initial condition as in Fig. 2(*a*). (*b*) Effects of changes in the grid resolution on the obtained pressure histories for** $\eta=2$ **and** $d=20$ **μm. Initial conditions as is in Fig. 2.**

particle we have the largest number of particles in the suspension. Therefore, the rate of momentum and energy transfer between the two-phases is higher, resulting in larger reduction in the suspension pressure. If a double-bend conduit is employed for reducing the strength of the transmitted shock (or blast) wave a further attenuation, even down to a compression wave, is possible by introducing small solid particles into the air filling the conduit.

It should be noted that in Figs. 11 and 12(*a*) a two steps jump is seen in the pressure signatures shown for ports P2 and P4. The double-jump results from the appearance of two shocks, in different times, at the considered ports. The first is the transmitted shock wave while the second jump is due to the arrival of the shock reflected from the bottom of the duct's exit channel.

For confirming the accuracy and quick conversion of the present solution results shown in Fig. 12(*a*) were repeated for particle diameter of 20 μm using a finer grid, doubling the number of grid points in each direction. When the obtained results were presented using the same scale as in Fig. 12(*a*) no difference between the two could be detected. Therefore, a much finer scale for pressure and time was selected; the obtained results are shown in Fig. 12(*b*). It is clear that doubling the grid's point had practically no effect on the obtained results.

Conclusions

The dust presence has strong effect on the flow and wave pattern developed behind an initially planar shock wave passing through a double-bend conduit. The dust presence causes attenuation of all waves inside the conduit. The smaller the dust particle, the faster all shocks are attenuated. For particles having a diameter of $d=5\ \mu$m almost all shock waves which are present inside the conduit in a similar pure-gas case were attenuated to compression/Mach waves. The only visible strong gradients zone is the interface separating between low and high dust spatial density zones inside the conduit. As a result of the shock waves attenuation to compression/Mach waves in the dusty case ($d=5\ \mu$m), zones of quasi-uniform flow are evident. This is not the case in a similar pure-gas flow field. Changing the dust mass loading in the suspension also has direct effect on the obtained flow field and wave pattern. The higher the dust loading, the faster the shock waves attenuation becomes. In the case where $\eta=5$ the observed behavior is similar to that seen for the small dust particle, e.g., all shock waves were attenuated to compression/Mach waves and quasi-uniform flow zones are observed in the flow field inside the conduit. The dust presence alters the pressure histories inside the conduit. While it causes a pressure increase behind the entering planar shock wave, it reduces the pressure jump across the transmitted wave at the conduit's exit channel. The smaller is the dust particle diameter, the stronger its effect is on the obtained pressure history. Increasing the dust loading results in similar behavior to that seen while reducing the dust diameter. However, faster attenuation is associated with increasing the dust mass loading than in reducing the particle's diameter. It is evident from Fig. 11 that for $\eta=5$ the transmitted shock wave, when it reaches the conduit's exit, is reduced to a compression wave. From Fig. 12 it is noticed that reducing the particle's diameter to 10 μm will significantly reduce the pressure jump across the transmitted shock front, at the conduit's exit, but will not convert it to a compression wave.

Acknowledgment

This research was supported by a Grant from the G.I.F.; the German-Israeli foundation for Scientific Research and Development. Their support is acknowledged with thanks.

References

[1] Igra, O., Wu, X., Falcovitz, J., Meguro, T., Takayama, K., and Heilig, W., 2001, ''Experimental and Theoretical Study of Shock Wave Propagation Through Ducts With Abrupt Changes in the Flow Direction,'' J. Fluid Mech., **437**, pp. 255–282.
[2] Falcovitz, J., and Igra, O., 2000, ''Shock Wave Structure in Dusty Gas Suspension,'' The 14th Mach Reflection Symposium, Sendai, Japan.
[3] Igra, O., and Ben-Dor, G., 1988, ''Dusty Shock Waves,'' Appl. Mech. Rev., **41**, pp. 379–437.
[4] Rudinger, G., and Chang, A., 1964, ''Analysis of Nonsteady Two-Phase Flow,'' Phys. Fluids, **7**, pp. 658–663.
[5] Miura, H., and Glass, I. I., 1983, ''On the Passage of a Shock Wave Through a Dusty-Gas Layer,'' Proc. R. Soc. London, Ser. A, **A385**, pp. 85–105.
[6] Igra, O., Elperin, T., and Ben-Dor, G., 1987, ''Blast Waves in Dusty Gases,'' Proc. R. Soc. London, Ser. A, **A414**, pp. 197–219.
[7] Aizik, F., Ben-Dor, G., Elperin, T., Igra, O., and Mond, M., 1995, ''Attenuation Law of Planar Shock Waves Propagating Through Dust-Gas Suspensions,'' AIAA J., **33**, pp. 953–955.
[8] Ben-Artzi, M., and Falcovitz, J., 1984, ''A Second-Order Godunov-Type Scheme for Compressible Fluid Dynamics,'' J. Comput. Phys., **55**, pp. 1–32.
[9] Ben-Artzi, M., and Falcovitz, J., 1986, ''An Upwind Second-Order Scheme for Compressible Duct Flows,'' SIAM (Soc. Ind. Appl. Math.) J. Sci. Stat. Comput., **7**, pp. 744–768.
[10] Falcovitz, J., and Ben-Artzi, M., 1995, ''Recent Developments of the GRP Method,'' JSME Int. J., Ser. B, **B38**, pp. 497–517.
[11] MacCormack, R. W., 1969, ''The Effect of Viscosity on Hypervelocity Impact Cratering,'' AIAA Paper 69-354.
[12] Igra, O, Falcovitz, J., Reichenbach, H., and Heilig, W., 1996, ''Experimental and Numerical Study of the Interaction Process Between a Planar Shock Wave and a Square Cavity,'' J. Fluid Mech., **313**, pp. 105–130.
[13] Strang, G., 1968, ''On the Construction and Comparison of Difference Schemes,'' SIAM Journal on Numerical Analysis, **5**, pp. 506–517.
[14] Sommerfeld, M., 1985, ''The Unsteadiness of Shock Waves Propagating Through Gas-Particle Mixtures,'' Exp. Fluids, **3**, pp. 197–206.

Michael P. Schultz
Department of Naval Architecture & Ocean Engineering,
United States Naval Academy,
Annapolis, MD 21402

The Relationship Between Frictional Resistance and Roughness for Surfaces Smoothed by Sanding

An experimental investigation has been carried out to document and relate the frictional resistance and roughness texture of painted surfaces smoothed by sanding. Hydrodynamic tests were carried out in a towing tank using a flat plate test fixture towed at a Reynolds number (Re_L) range of $2.8\times10^6-5.5\times10^6$ based on the plate length and freestream velocity. Results indicate an increase in frictional resistance coefficient (C_F) of up to 7.3% for an unsanded, as-sprayed paint surface compared to a sanded, polished surface. Significant increases in C_F were also noted on surfaces sanded with sandpaper as fine as 600-grit as compared to the polished surface. The results show that, for the present surfaces, the centerline average height (R_a) is sufficient to explain a large majority of the variance in the roughness function (ΔU^+) in this Reynolds number range.
[DOI: 10.1115/1.1459073]

Introduction

Many practical engineering applications involve turbulent flows over surfaces that have been smoothed by sanding. Examples range from sailing hulls to models for wind and water tunnels. While a great deal of drag data has been generated for sandgrain roughness (most notably Nikuadse's experiments on monodisperse, closely-packed sand [1]), there are few reliable data for sanded surfaces in which the surface is well documented. This is noteworthy since sanded surfaces form a much larger presence in engineering applications than sandgrain roughness. The purpose, therefore, of the present investigation is to study the frictional resistance of sanded surface roughness.

A large body of basic research has focused on the effect of surface roughness on frictional resistance. Hama [2], Ligrani and Moffat [3], Krogstad and Antonia [4] and many others have investigated the structure of the turbulent boundary layer over rough surfaces. Raupach et al. [5] give a review of much of this work. Studies focusing on the frictional resistance of ship bottom paints have also been made. Grigson [6], Townsin et al. [7], Musker [8], and Lewkowicz and Musker [9] have all investigated these surfaces, and their results indicate that as-sprayed antifouling coatings have significantly higher frictional resistance than a smooth surface. An entire workshop was devoted to the subject of ship hull roughness and drag [10]. However, most of the research into the drag on marine paints has centered on predicting the economic penalty of hull roughness on commercial ships, where sanding is unfeasible.

The mean velocity profile in a turbulent boundary layer can be expressed as:

$$U^+=\frac{1}{\kappa}\ln(y^+)+B+2\,\omega(y/\delta)\Pi/\kappa \tag{1}$$

Clauser [11] noted that for rough wall flows, the log-law intercept is shifted downward and that the shift correlates with k^+, the roughness Reynolds number, defined as the ratio of the roughness length scale, k, to the viscous length scale, ν/U_τ. This downward shift, ΔU^+, called the roughness function, can be used to express the mean velocity profile for rough wall flows:

$$U^+=\frac{1}{\kappa}\ln(y^+)+B-\Delta U^+ +2\,\omega(y/\delta)\Pi/\kappa \tag{2}$$

Hama [2] showed that by evaluating Eqs. (2) and (3) at $y=\delta$, the roughness function could be found by subtracting the rough wall intercept from the smooth wall intercept, B, at the same value of $\mathrm{Re}_{\delta*}$. The roughness function therefore can be expressed as:

$$\Delta U^+=\left(\sqrt{\frac{2}{c_f}}\right)_S-\left(\sqrt{\frac{2}{c_f}}\right)_R \tag{3}$$

It should be noted that Eq. (3) is only valid provided both Π and the velocity defect profile are the same for the rough and smooth walls. The experimental evidence for this is somewhat contradictory. Some research indicates that surface roughness increases Π (e.g. [4]) and alters the velocity defect profile (e.g. [12]), while other studies (e.g. [13]) indicate that these are unchanged by roughness. In the present study, no mean velocity profiles were made. Therefore, the determination of the roughness function required the explicit assumption that Π and the velocity defect profile are unchanged by the roughness to be made. Future studies are planned that will include measurements of the mean velocity profiles over these sanded surfaces.

A universal roughness function for a given class of surfaces can be defined if k is related directly to the surface profile. Nikuradse's [1] pipe flow experiments on closely-packed, uniform sand roughness show that this roughness type has a universal roughness function with k simply being the diameter of the individual sandgrains. The results from Nikuradse's experiments have been used to explain the behavior of generic, naturally occurring surface roughness. This is evidenced by the widespread use of the equivalent sandgrain height, k_s. This parameter is defined as the sandgrain height in Nikuradse's experiment that has the same roughness function in the fully-rough regime as the surface of interest. The use of k_s is attractive because it is simple, but is also problematic because it is not physically related to the surface roughness profile for generic surfaces of engineering interest. Most naturally occurring rough surfaces do not behave like Nikuradse sand surfaces.

Contributed by the Fluids Engineering Division for publication in the JOURNAL OF FLUIDS ENGINEERING. Manuscript received by the Fluids Engineering Division August 14, 2001; revised manuscript received December 31, 2001. Associate Editor: T. Gatski.

Colebrook [14] first demonstrated this in a study of the irregular surface roughness in pipes resulting from the manufacturing process.

Nikuradse's roughness function for uniform sand roughness has led to the critical roughness height concept. This concept states there exists some critical roughness height for surfaces below which there is no increase in drag. This is termed the hydrodynamically smooth condition. In this condition the individual roughness elements are small enough to be completely submerged in the viscous sublayer region of the boundary layer. In order to have a hydrodynamically smooth surface, k^+ must be less than a critical value ranging from 2.25 to 5. For this surface type, if the viscous length scale is known, a critical roughness height may be specified for a surface below which a reduction in roughness height causes no concomitant reduction in drag. A recent paper by Bradshaw [15] questions the existence of a critical roughness height on theoretical grounds. He argues that the roughness function should go asymptotically to 0 in the limit as k^+ goes to 0.

Granville [16] offers three alternative methods for determining the roughness function of a surface experimentally using pipe flow, towed flat plates, and rotating disks, respectively. The procedure given for towed flat plates was used in the present investigation to determine the roughness function. Further details are given in the Results and Discussion section of the paper. It should be noted that ΔU^+ can also be obtained directly by measuring the mean velocity profile over a rough wall. Once $\Delta U^+ = \Delta U^+(k^+, [l])$ for a surface is known, it can be used in a boundary layer code or a similarity law analysis to predict the drag of any body covered with that roughness.

A great deal of effort has been made to correlate the roughness function for a surface with its roughness statistics. This would allow the drag change to be predicted based on knowledge of the surface profile alone. However, development of a universal relationship to correlate the roughness function to the surface roughness length scales has been illusive. Several researchers have attempted to correlate the roughness function with a roughness height and density parameter for relatively simple uniform roughness [17,18]. Koch and Smith [19] and Acharya et al. [12] both looked at the effect of machined roughness on frictional resistance. Acharya et al. found that collapsing the roughness functions for these surfaces to a universal curve using R_a alone was not possible and suggested that the deviation in the slope angles of the roughness might allow better correlation. Both Townsin et al. [7] and Musker [8] have proposed correlations that include roughness height as well as texture. Townsin proposed that a height parameter, h, based on the first three even moments of the profile power spectral density reasonably collapsed the roughness functions for ship hull surfaces. Townsin and Dey [20] give the following formulation for the roughness function of ship hull coatings based on their modified roughness Reynolds number:

$$\Delta U^+ = \frac{1}{\kappa} \ln(1 + 0.18h^+) \tag{4}$$

where

$$h = \sqrt{\alpha m_0 m_2}$$

$$\alpha = \frac{m_o m_4}{m_2^2} \tag{5}$$

$$m_n = \int_{2\pi/Lp}^{\pi/Ls} E \gamma^n d\gamma$$

Musker [8] suggests an alternative roughness scale that incorporates the skewness and kurtosis of the roughness height distribution. Grigson [6] asserts that the statistics of the surface profile alone cannot be relied upon to predict the roughness function. He contends that only experimental testing of the surface of interest allows accurate determination of the roughness function. It is of note that Grigson's results indicate that the roughness functions of some ship hull coatings do not behave as either Nikuradse or Colebrook-type functions and may have multiple inflection points.

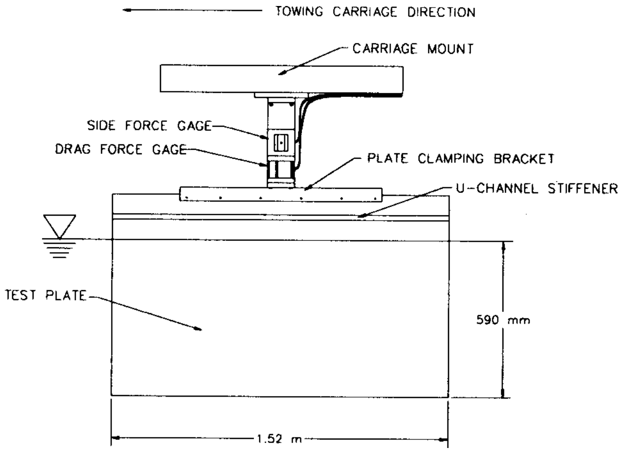

Fig. 1 Schematic of the flat plate test fixture

The goal of the present experimental investigation is to document the frictional resistance and surface roughness of a range of sanded paint surfaces. An attempt to identify a suitable roughness parameter relating the physical roughness and the roughness function for this particular class of surfaces is made. The results are then scaled up to a planar surface using the similarity law procedure of Granville [21] to predict the effect of the present roughness on the frictional resistance of a plate of the order of length of typical sailing vessels.

Experimental Facilities and Method

The present experiments were conducted in the 115 m long towing tank facility at the United States Naval Academy Hydromechanics Laboratory. The width and depth of the tank are 7.9 m and 4.9 m, respectively. The towing carriage has a velocity range of 0–7.6 m/s. In the present investigation the towing velocity was varied between 2.0 m/s–3.8 m/s ($\mathrm{Re}_L = 2.8 \times 10^6 - 5.5 \times 10^6$). The velocity of the towing carriage was measured and controlled using an encoder on the rails that produce 4000 pulses/m. Using this system, the precision uncertainty in the mean velocity measurement was $<0.02\%$ over the entire velocity range tested. The working fluid in the experiments was fresh water, and the temperature was monitored to within ±0.05°C during the course of the experiments using a thermocouple with digital readout. Further details of the experimental facility are given in [22].

Figure 1 shows a schematic of the test fixture and plate. The flat test plate was fabricated from 304 stainless steel sheet stock and measured 1.52 m in length, 0.76 m in width, and 3.2 mm in thickness. Both the leading and trailing edges were filleted to a radius of 1.6 mm. No tripping device was used to stimulate transition. The overall drag of the plate was measured using a Model HI-M-2, modular variable-reluctance displacement force transducer manufactured by Hydronautics Inc. An identical force transducer, rotated 90 deg to drag gage, was included in the test rig to measure the side force on the plate. The purpose of the side force gage was to ensure precise alignment of the plate. This was accomplished by repeatedly towing the plate at a constant velocity and adjusting the yaw angle of the test fixture to minimize the side force. Once this was done, no further adjustments were made to the alignment over the course of the experiments. The side force was monitored throughout to confirm that the plate alignment did not vary between test surfaces. Both of the force transducers used in the experiments had load ranges of 0–89 N. The combined bias uncertainty of the gages is ±0.25% of full scale. Data were gathered at a sampling rate of 100 Hz and were digitized using a

16-bit A/D converter. The length of the towing tank dictated the sampling duration. This ranged from ~30 s of data per test run at the lowest Reynolds number to ~11 s of at the highest Reynolds number. The overall drag was first measured with 590 mm of the plate submerged. This was repeated with 25 mm of the plate submerged in order to find the wavemaking resistance tare. The difference between the two was taken to be the frictional resistance on the two 565 mm wide by 1.52 m long faces of the plate. The tests were repeated ten times for each surface and velocity. The results presented are the means of these runs.

A single test plate was used for all the towing experiments. This was done to ensure that any differences in the drag measured were due to the surface condition of the plate and not small variations in leading edge shape, plate flatness, and other factors that could have varied between multiple test plates. The plate was initially painted with several coats of marine polyamide epoxy paint manufactured by International Paint. This surface condition was termed the ''unsanded'' condition. After hydrodynamic testing, the plate was wet sanded with 60-grit sandpaper. This surface was referred to as the ''60-grit sanded'' condition. Subsequent to hydrodynamic testing under the 60-grit sanded condition, the entire process was repeated for the ''120-grit sanded,'' ''220-grit sanded,'' ''400-grit sanded,'' and ''600-grit sanded'' surface conditions. After hydrodynamic testing of the 600-grit sanded surface the plate was wet sanded up to 1800 grit and polished with a buffing wheel using Maquire's swirl remover polishing compound. This surface is referred to as the ''polished'' condition. All the sanding in the present experiment was carried out by hand with the aid of a sanding block using small circular motions. Prussian blue was used to dye the surface before sanding with finer grit paper to ensure the entire surface was sanded and to reveal the surface scratches left behind by the previous grit so they could be removed. The surfaces were cleaned with water and a soft cloth between surface treatments to remove grit and detritus left behind by the sanding process.

The surface profiles of the test plates were measured using a Cyber Optics laser diode point range sensor (model #PRS 40) laser profilometer system mounted to a Parker Daedal (model #106012BTEP-D3L2C4M1E1) two-axis traverse with a resolution of 5 μm. The resolution of the sensor is 1 μm with a laser spot diameter of 10 μm. Data were taken over a sampling length of 50 mm and were digitized at a sampling interval of 25 μm. Ten linear profiles were taken on each of the test surfaces. A single three-dimensional topographic profile was made on each of the surfaces by sampling over a square area 2.5 mm on a side with a sampling interval of 25 μm.

The roughness statistics were calculated using the linear profiles from each of the surfaces. All were calculated without using a long wavelength cutoff (effectively the cutoff was the sampling length, 50 mm) and using 25 mm, 10 mm, 5 mm, 2 mm, and 1 mm long wavelength filters. The highpass filtering was carried out using a Butterworth digital filter and the long wavelength cutoffs were chosen to be in the range used by Musker [8] and Townsin and Dey [20]. The purpose of the filtering was to remove surface waviness which has little effect on the drag. Musker says that the long wavelength cutoff should be set equal to the size of the large energy-containing eddies near the surface, and he suggests using the Taylor macro-scale. In the present investigation no spatial turbulence correlations were available from which to calculate the Taylor macro-scale, so roughness statistics using a range of long wavelength cutoffs were calculated.

Some of the roughness statistics calculated for the surfaces included the centerline average height, R_a, given as:

$$R_a=\frac{1}{N}\sum_{i=1}^{N}|y_i| \tag{6}$$

It should be noted that all of the roughness statistics are calculated using the centerline as the datum for y. This is defined as the datum at which the average value of y is zero. R_q is the root mean square height given as:

$$R_q=\sqrt{\frac{1}{N}\sum_{i=1}^{N}y_i^2} \tag{7}$$

R_t is the height from the called maximum peak to the minimum trough and is given as:

$$R_t=y_{\max}-y_{\min} \tag{8}$$

R_z is called the ten point height and is given as the mean of the difference of the five highest peaks and the five lowest troughs.

$$R_z=\frac{1}{5}\sum_{i=1}^{5}(y_{\max\,i}-y_{\min\,i}) \tag{9}$$

The correlation length scale, λ_{corr}, is calculated as the distance (j times the sampling interval, L_p) at which the autocorrelation function falls below 0.5. The autocorrelation function is given by:

$$C_j=\frac{\dfrac{1}{N-1-j}\displaystyle\sum_{i=1}^{N-1-j}(y_iy_{i+j})}{\dfrac{1}{N-1}\displaystyle\sum_{i=1}^{N}y_i^2} \tag{10}$$

It should be noted that for the 120-grit and smoother surfaces this value was less than the sampling interval so no accurate estimate could be made. The root mean square slope, sl_{rms}, is given as follows:

$$sl_{rms}=\sqrt{\frac{1}{N-1}\sum_{i=1}^{N-1}\left\{\frac{(y_{i+1}-y_i)}{(x_{i+1}-x_i)}\right\}^2} \tag{11}$$

A similar parameter, the root mean square slope angle, was offered by Acharya et al. [12] as an important one in describing roughness caused by machining on turbine blades. By calculating the power spectral density of the surface waveforms using a fast Fourier transform and the first three even moments of the power spectral density, Townsin's height parameter, h, was calculated using Eq. (4). Musker [8] offers an alternative roughness length scale given by:

$$h'=R_q(1+aS_p)(1+bS_kK_u) \tag{12}$$

His results show that this roughness length scale works well for correlating the roughness function for a range of ship hull coatings when a long wavelength cutoff of 2 mm is used and the constants a and b are taken to be 0.5 and 0.2, respectively.

Uncertainty Estimates

Precision uncertainty estimates for the resistance measurements were made through repeatability tests using the procedure given by Moffat [23]. Ten replicate experiments were made with each of the test plates at each Reynolds number. This was carried out so that the relatively small differences in the frictional resistance between the surface conditions could be identified. The standard error for C_F was then calculated. In order to estimate the 95% precision confidence limits for a mean statistic, the standard error was multiplied by the two-tailed t value ($t=2.262$) for 9 degrees of freedom, as given by Coleman and Steele [24]. The resulting precision uncertainties in C_F were $\leq\pm0.3\%$ for all the tests. The overall precision and bias error was dominated by the systematic error due to the combined bias of the force gages (±0.25% full scale). The resulting overall precision and bias uncertainty in C_F ranged from ±4.8% at the lowest Reynolds number to ±1.4% at the highest Reynolds number. Periodically throughout the experiments, a reference plate was run to check that the resulting mean C_F value was within the precision uncertainty bounds that had been obtained from previous testing with the same surface. This

Table 1 Roughness statistics

Specimen	λ_{FL} (mm)	R_a (μm)	R_q (μm)	R_t (μm)	R_z (μm)	S_k	K_u	λ_{corr} (μm)	sl_{rms}	h (μm)
Unsanded	NF	2.7 ± 0.2	5.0 ± 0.3	39 ± 2	38 ± 2	2.0 ± 0.2	5.0 ± 0.3	127 ± 22	0.113 ± 0.006	2.2 ± 0.3
	10	3.4 ± 0.2	4.8 ± 0.3	50 ± 3	43 ± 3	0.02 ± 0.1	4.8 ± 0.3	118 ± 9	0.113 ± 0.006	2.1 ± 0.3
	1	2.5 ± 0.1	3.4 ± 0.2	28 ± 2	25 ± 2	-0.01 ± 0.1	3.4 ± 0.2	31 ± 1.7	0.112 ± 0.006	1.0 ± 0.1
60-Grit	NF	0.96 ± 0.06	1.63 ± 0.09	12 ± 1.6	11 ± 0.9	1.1 ± 0.1	3.2 ± 0.4	40 ± 7	0.063 ± 0.002	0.24 ± 0.01
	10	1.14 ± 0.07	1.62 ± 0.08	13 ± 1.6	11 ± 0.9	0.61 ± 0.1	2.1 ± 0.5	31 ± 6	0.063 ± 0.002	0.24 ± 0.01
	1	1.05 ± 0.05	1.43 ± 0.07	13 ± 2	11 ± 0.6	-0.21 ± 0.1	1.5 ± 0.2	<25*	0.063 ± 0.002	0.19 ± 0.01
120-Grit	NF	0.58 ± 0.03	1.02 ± 0.04	9.4 ± 0.7	7.6 ± 0.2	1.4 ± 0.2	5.2 ± 1.1	<25*	0.047 ± 0.002	0.10 ± 0.005
	10	0.70 ± 0.02	1.01 ± 0.03	10 ± 0.95	8.1 ± 0.3	0.96 ± 0.09	4.0 ± 1.0	<25*	0.047 ± 0.002	0.10 ± 0.005
	1	0.65 ± 0.03	0.90 ± 0.03	9.2 ± 0.6	7.7 ± 0.2	0.11 ± 0.08	2.5 ± 0.6	<25*	0.047 ± 0.002	0.08 ± 0.005
220-Grit	NF	0.47 ± 0.01	0.86 ± 0.04	8.6 ± 1.5	7.0 ± 0.7	1.8 ± 0.2	7.8 ± 1.9	<25*	0.039 ± 0.002	0.07 ± 0.006
	10	0.59 ± 0.02	0.86 ± 0.04	9.4 ± 1.6	7.7 ± 0.8	1.1 ± 0.2	5.3 ± 1.3	<25*	0.039 ± 0.002	0.07 ± 0.006
	1	0.52 ± 0.02	0.74 ± 0.04	9.1 ± 1.2	7.0 ± 0.7	0.15 ± 0.06	3.9 ± 0.8	<25*	0.039 ± 0.002	0.05 ± 0.005
400-Grit	NF	0.43 ± 0.03	0.77 ± 0.04	8.0 ± 0.5	7.0 ± 0.7	1.8 ± 0.1	8.1 ± 1.6	<25*	0.038 ± 0.001	0.06 ± 0.007
	10	0.52 ± 0.03	0.77 ± 0.04	8.6 ± 0.4	7.7 ± 0.8	1.4 ± 0.2	6.5 ± 1.3	<25*	0.038 ± 0.001	0.06 ± 0.007
	1	0.49 ± 0.03	0.70 ± 0.03	8.1 ± 0.4	7.0 ± 0.7	0.5 ± 0.2	4.3 ± 0.9	<25*	0.038 ± 0.001	0.05 ± 0.003
600-Grit	NF	0.40 ± 0.01	0.73 ± 0.02	7.9 ± 2.6	6.0 ± 0.6	2.1 ± 0.7	15 ± 14	<25*	0.038 ± 0.002	0.05 ± 0.003
	10	0.47 ± 0.02	0.73 ± 0.03	8.4 ± 2.5	6.3 ± 0.6	1.8 ± 0.7	13 ± 12	<25*	0.038 ± 0.002	0.05 ± 0.003
	1	0.47 ± 0.02	0.67 ± 0.03	9.1 ± 2.5	6.5 ± 0.9	0.5 ± 0.3	7.7 ± 6	<25*	0.038 ± 0.002	0.04 ± 0.003
Polished	NF	0.18 ± 0.004	0.30 ± 0.01	2.0 ± 0.3	1.9 ± 0.3	1.15 ± 0.08	3.3 ± 0.3	<25*	0.015 ± 0.001	0.009 ± 0.001
	10	0.21 ± 0.006	0.30 ± 0.01	2.4 ± 0.1	2.1 ± 0.4	0.70 ± 0.07	2.3 ± 0.2	<25*	0.015 ± 0.001	0.009 ± 0.001
	1	0.19 ± 0.004	0.27 ± 0.01	2.6 ± 0.1	2.2 ± 0.1	0.18 ± 0.06	2.1 ± 0.2	<25*	0.015 ± 0.001	0.007 ± 0.001

* - λ_{corr} was < L_s

All uncertainties represent the 95% confidence precision bounds for the measurement

was confirmed in all cases tested. Uncertainty estimates for the roughness statistics were calculated in the same manner and are reported in Table 1.

Results and Discussion

The presentation of the results and discussion will be organized as follows. First, a qualitative discussion of the nature of each of the surfaces tested will be made. The roughness statistics will then be presented. Next the results of the hydrodynamic tests will be presented and discussed. Finally, an attempt will be made to relate the roughness statistics of this class of surfaces to the roughness function, ΔU^+.

Qualitative Description of the Surfaces. In order to better understand the nature of each of the surfaces tested, a qualitative description of each will be made using the three-dimensional topographic profiles shown in Fig. 2. Even cursory inspection of the profiles shows that the surfaces vary greatly. Figure 2(*a*) shows the unsanded surface and indicates that it has relatively large features with a wavelength of up to 1 mm. This is very common in as-sprayed paint surfaces and is often referred to as ''orange peel'' because of the characteristic texture. Figure 2(*b*), which shows the 60-grit surface, indicates that the orange peel has been almost entirely removed by sanding, but linear scratches have been added. These scratches have a width of up to 150 μm and a depth of up to 25 μm. Figure 2(*c*) shows the 120-grit surface. Many of the scratches seen in the 60-grit surface have been removed, and narrower, shallower scratches have been added. It is of note that some of the deeper scratches from the 60-grit surface have not been completely removed and remain as features of up to 150 μm in width, with a depth of up to 10 μm. The 220-grit surface (Fig. 2(*d*)) shows that the scratches from the 60-grit paper have been removed. They have been replaced with finer scale scratches that are much narrower and shallower. The 400-grit and 600-grit surfaces are very similar in nature and for this reason only the 600-grit surface (Fig. 2(*e*)) is presented. The polished surface (Fig. 2(*f*)) shows that many of the small scale peaks and troughs seen in the 400-grit and 600-grit surfaces have been removed.

The evolution of the surface scratches can be more easily seen in plan views of the previous figures. These views for the unsanded, 60-grit, 120-grit, and 220-grit surfaces are given in Fig. 3. Figure 3(*a*) of the unsanded specimen shows the orange peel surface. The 60-grit surface (Fig. 3(*b*)) shows that the orange peel has been removed and linear scratches have been added. Smaller scale scratches are evident in the 120-grit surface (Fig. 3(*c*)) as well as 60-grit scratches that have not been completely removed. By the time the 220-grit paper has been used (Fig. 3(*d*)), only rather small scale features remain.

The quantitative statistics of the roughness surfaces are given in Table 1. The results are presented for processing with no long wavelength filter, a 10 mm long wavelength filter, and a 1 mm long wavelength filter. One item of note is that all of the roughness tested in the present study is quite small compared to the roughness used in a majority of previous studies. Most basic research has focused on roughness large enough to generate turbulent flows in the fully-rough regime, and the studies on ship hull roughness by Musker [8] and others addressed smaller scale transitional roughness with $150\ \mu\text{m} \leqslant R_t \leqslant 600\ \mu\text{m}$ ($5 \leqslant k^+ \leqslant 320$; k^+ based on R_t). For the present study, the range of roughness was $2\ \mu\text{m} \leqslant R_t \leqslant 39\ \mu\text{m}$ ($0.15 \leqslant k^+ \leqslant 5$; k^+ based on R_t). This is important to keep in mind because the differences in drag for the surfaces is expected to be rather small. The change in the roughness statistics for the unfiltered profiles with sanding is shown in Fig. 4. The figure shows that all of the roughness height parameters are reduced with sanding up to 220-grit. At that point, no significant reduction in the roughness height is made by sanding with 400-grit and 600-grit. The polished surface does show a significant reduction in roughness. Figure 2(*f*) shows that this is largely due to a reduction in the isolated protuberances seen in the 220-grit, 400-grit, and 600-grit surfaces.

Test Results. The results of the hydrodynamic tests are shown in Fig. 5. The Schoenherr mean line for smooth plates is shown for comparison [25]. The Schoenherr mean line is given as:

$$\frac{0.242}{\sqrt{C_F}} = \log(\mathrm{Re}_L\, C_F) \tag{13}$$

Table 2 shows the % increase in C_F for the test surfaces compared to the polished surface. The results show that the 60-grit specimen had a significant reduction in C_F from the unsanded surface. A further reduction in C_F was found for the 120-grit specimen compared with the 60-grit surface. A smaller, but significant, reduction in C_F occurred for the 220-grit surface compared with the 120-grit specimen. However, no significant change in C_F was seen for the 400-grit and 600-grit surfaces compared to the 220-grit surface. Inspection of Figs. 2(*d*–2*e*) and Table 1 shows that the roughness on these surfaces is quite similar as well. The polished surface had C_F values that were significantly less than any of the other specimens. The reduction in frictional resistance seems to be due to a reduction in the isolated protuberances (Fig. 2(*f*)) that were seen in the 600-grit surface (Fig. 2(*e*)).

It should be noted that the results could have been affected to varying degree by the influence of the surface roughness and Reynolds number on the transition of the flow to turbulence. The flow was not tripped, so the transition point may have varied between the test cases depending on the surface roughness. Leading-edge and three-dimensional effects could have also had some influence on these results. However, these effects are very difficult to quantify precisely. Overall, it is felt these effects are small since the smooth plate results agree within ~1% with the Schoenherr mean line for frictional resistance in turbulent flow. The fact that the smooth plate results remain a fairly constant percentage lower than the Schoenherr mean line over the range of Reynolds number tested seems to also indicate that the transition point must not vary significantly over the Reynolds number range tested.

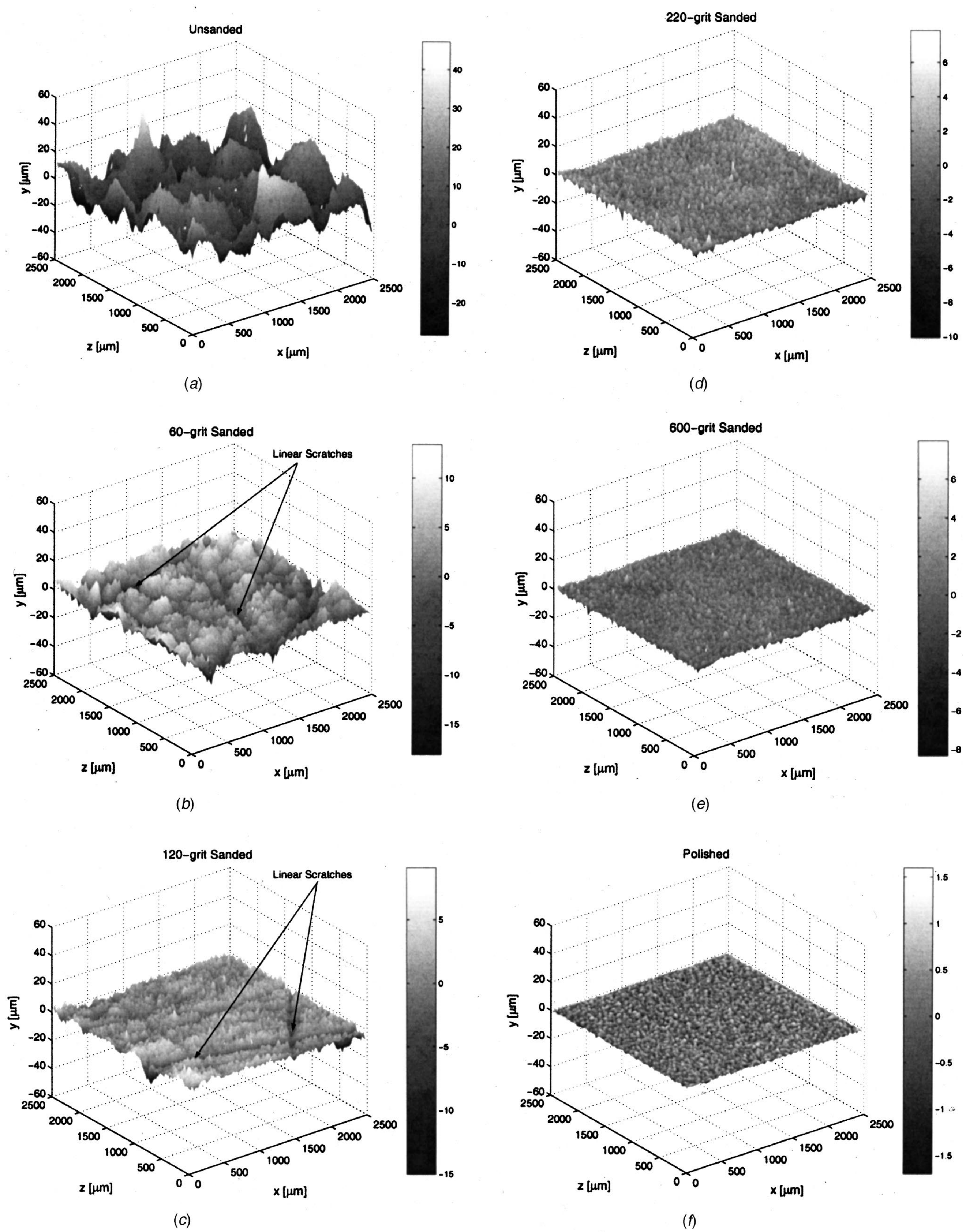

Fig. 2 Surface waveforms for (*a*) the unsanded specimen, (*b*) the 60-grit specimen, (*c*) the 120-grit specimen, (*d*) the 220-grit specimen, (*e*) the 600-grit specimen, and (*f*) the polished specimen. (Uncertainty in the y-direction ±1 μm, *x*- and *z*-directions ±5 μm)

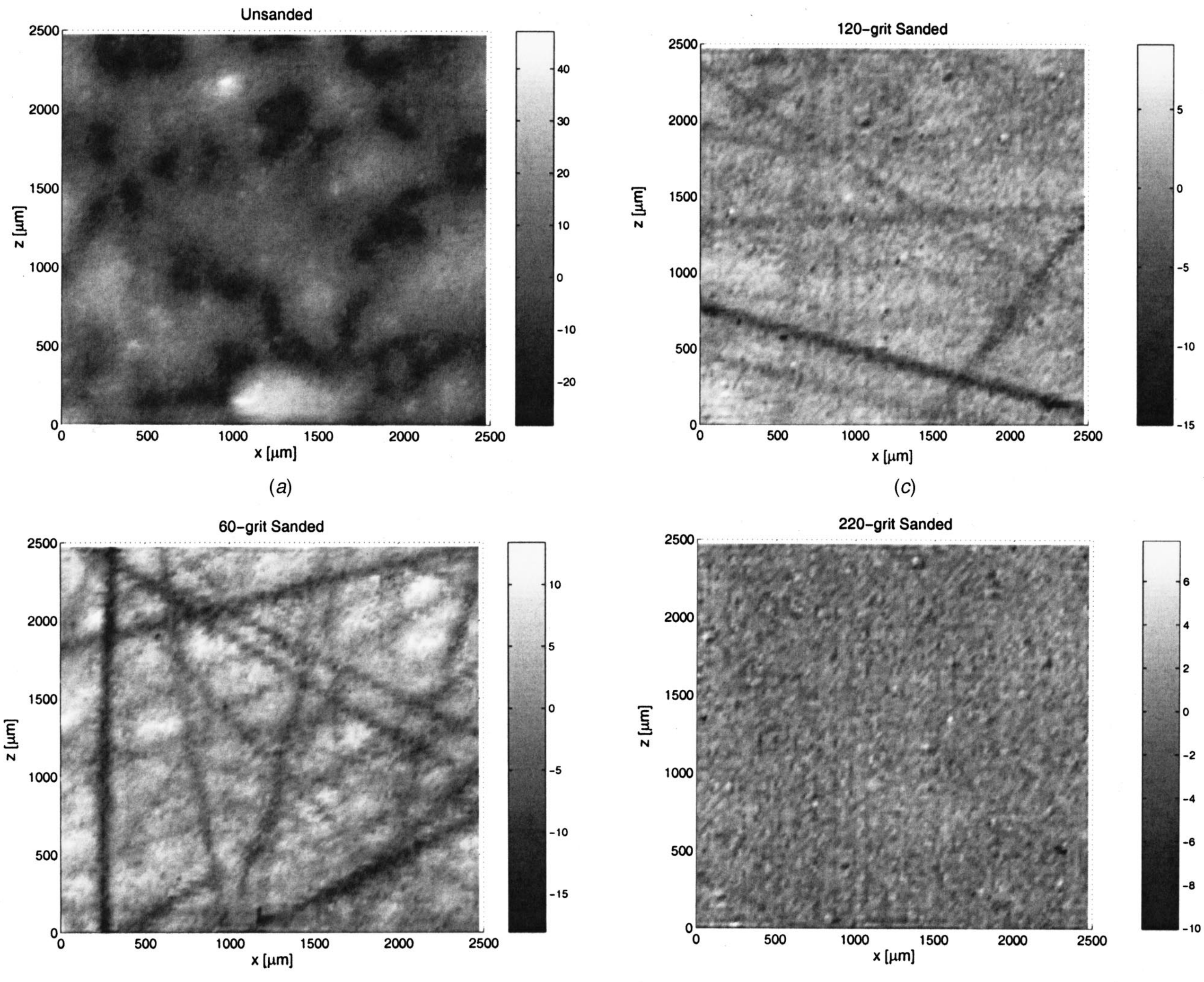

(*a*) (*c*)

(*b*) (*d*)

Fig. 3 Plan view of the surface waveform for (*a*) the unsanded specimen, (*b*) the 60-grit specimen, (*c*) the 120-grit specimen, and (*d*) the 220-grit specimen. (Uncertainty in the y-direction ±1 μm, *x*- and *z*-directions ±5 μm)

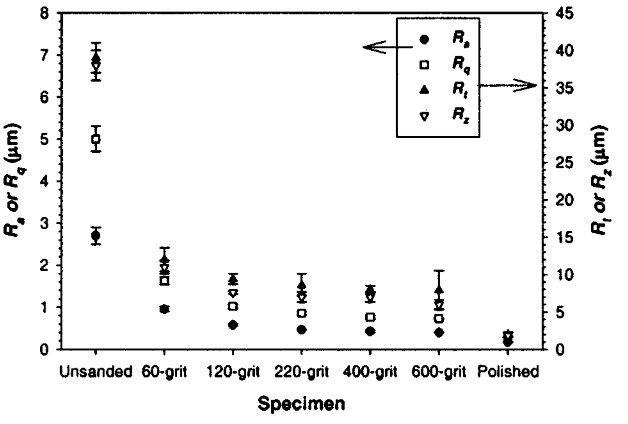

Fig. 4 The effect of sanding on the roughness statistics of the unfiltered profiles. (Error bars represent the 95% confidence limits for the precision uncertainty.)

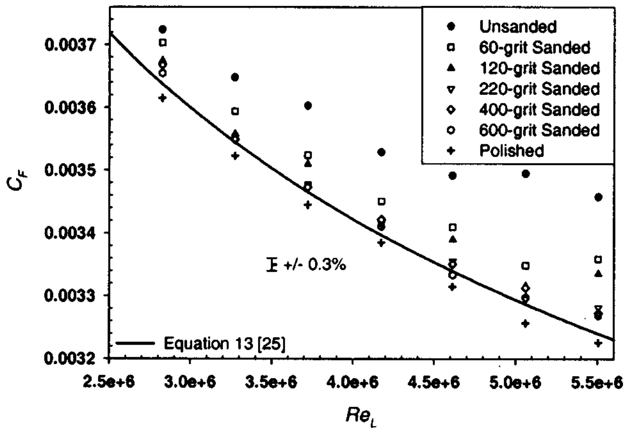

Fig. 5 Overall frictional resistance coefficient versus Reynolds number for all the specimens. (Precision uncertainty ⩽±0.3% at all Reynolds numbers; overall precision and bias ranges from ±1.4% at highest Reynolds number to ±4.8% at lowest Reynolds number.)

Table 2 Increase in overall frictional resistance coefficient for the test specimens compared to the polished surface

Specimen	Average % Increase in C_F	Range of % Increase in C_F
Unsanded	5.0	3.0 – 7.3
60-Grit	2.6	2.0 – 4.1
120-Grit	1.9	1.0 – 3.4
220-Grit	1.2	0.8 – 1.7
400-Grit	1.2	0.7 – 1.7
600-Grit	1.0	0.6 – 1.4

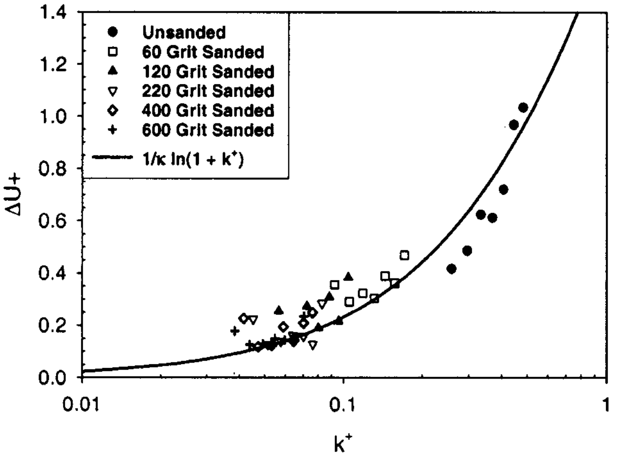

Fig. 6 Roughness function for all specimens. (Overall uncertainty ±0.1 in ΔU^+)

Relation of Roughness Statistics to ΔU^+. Using similarity law analysis, Granville [16] derived an expression to relate the local frictional coefficient, c_f, at the trailing edge of a planar surface to the overall frictional resistance coefficient, C_F, for the same surface. It is given as:

$$\left(\sqrt{\frac{c_f}{2}}\right)_{TE}=\left(\frac{U_\tau}{U_e}\right)_{TE}=\sqrt{\frac{C_F}{2}}\left(1-\kappa\sqrt{\frac{C_F}{2}}\right) \qquad (14)$$

By solving this equation for U_τ, the viscous length scale, ν/U_τ, at the trailing edge of the plate can be obtained. For the present surfaces ν/U_τ ranged from ~ 14 μm at $\mathrm{Re}_L = 2.8\times 10^6$ to ~ 7.6 μm at $\mathrm{Re}_L = 5.5\times 10^6$. The roughness function, ΔU^+, at the trailing edge of the plate can be found using the method of Granville [16] as well. This procedure involves plotting $\sqrt{2/C_F}$ versus $\mathrm{Re}_L C_F$. The roughness function, ΔU^+, is given as the following evaluated at the same value of $\mathrm{Re}_L C_F$ for both smooth and rough walls:

$$\Delta U^+=\left(\sqrt{\frac{2}{C_F}}\right)_S-\left(\sqrt{\frac{2}{C_F}}\right)_R \qquad (15)$$

In the present study, the results for the polished surface were used as smooth plate values. Since the behavior of ΔU^+ at vanishing roughness height did not behave as a Nikuradse-type roughness function, attempts were made to collapse the results to a Colebrook-type roughness function as given by:

$$\Delta U^+=\frac{1}{\kappa}\ln(1+k^+) \qquad (16)$$

All of the roughness length scales in Table 1 were considered including the Musker [8] and Townsin [20] length scales. The best fit of the results to Eq. (16) was obtained using a multiple of the centerline average height, R_a, calculated from the unfiltered profiles as k. With $k = 1.35R_a$, 87% of the variance (i.e., $R^2 = 0.87$) in ΔU^+ could be explained with the Colebrook-type roughness function (Eq. (16)). The results are shown in Fig. 6. It should be noted that >80% of the variance could also be explained for this relatively simple roughness using R_q, R_t, or R_z calculated from the unfiltered profiles. Attempts to use the filtered profile statistics led to larger scatter in the roughness function than the unfiltered profile statistics. This seems to indicate that for sanded surfaces in this Reynolds number range, long wavelength roughness (up to 50 mm) contributes significantly to the increase in frictional resistance.

Using the roughness function obtained for a flat plate, Granville [16] gives a similarity law procedure for calculating the effect of the same roughness on a planar surface of arbitrary length. This was carried out with the present results for surfaces of 4 m and 12 m. These lengths were chosen to be representative of the range of length of sailing vessels for which sanding would be practicable. Using this analysis, significant increases in C_F above the polished plate values were predicted for the surfaces. These increases were of the same order as seen in the present experiments. For example, it was found that the unsanded surface would have an average increase in C_F of 5.0% above a polished surface over a velocity range of 2.3–4.6 m/s (4.5–8.9 knots) at a length of 4 m and an average increase in C_F of 4.5% over a velocity range of 2.6–5.0 m/s (5.1–9.7 knots) at a length of 12 m. Over the same velocity range, the 60-grit surface would have an average increase in C_F of 2.5% at a length of 4 m and an average increase in C_F of 2.3% at a length of 12 m. The increase for the 120-grit surface would be 1.9% at a length of 4 m and 1.6% at a length of 12 m. Both the 220-grit and 400-grit surfaces would have an increase of 1.3% and 1.1% at lengths of 4 m and 12 m, respectively, while the increase for the 600-grit surface would be 1.1% and 1.0% at lengths of 4 m and 12 m, respectively. Due to the three-dimensional nature of the boundary layer flow around a real vessel, however, additional data on actual hull shapes are needed to corroborate these findings. It should also be noted that in the present study significant care was given to ensure that the entire surface was sanded and that no area was missed. This was relatively easy on a small flat surface, but would be much more difficult in practice on a large three-dimensional shape.

Conclusion

Measurements of the roughness and frictional resistance of sanded paint surfaces have been made. The results indicate that as-sprayed, unsanded surfaces can have a significant increase in C_F compared to a polished surface. Smaller, but significant, increases in C_F compared to the polished surface were also noted on surfaces sanded with sandpaper as fine as 600-grit. This increase seems to be due to isolated surface protuberances not completely removed by the sanding process. The roughness function, ΔU^+, shows good collapse to a Colebrook-type roughness function for this class of surfaces when a multiple of the centerline average height ($k = 1.35R_a$) is used as the roughness length scale. Similarity law predictions of C_F on larger planar surfaces of sailing vessel length show that similar increases in C_F can be expected in that range of wetted length as well. Further effort needs to be focused on understanding the effect of roughness on three-dimensional bodies.

Acknowledgments

I would like to thank the Office of Naval Research for financial support under the direction of Dr. Steve McElvaney. Many thanks go to Mr. Steve Enzinger, Mr. Don Bunker, and the rest of the USNA Hydromechanics Lab staff for their valuable help in providing technical support. I also thank Mr. Bill Beaver of the USNA Technical Support Division who provided a great deal of practical insight and never seemed to tire of sanding. I am grateful to Prof. Peter Bradshaw, Prof. Karen Flack, Prof. Ralph Volino, and the anonymous reviewers for reading drafts of the manuscript and offering many helpful comments. I am also indebted to Prof. Michelle Koul for helping with the laser profilometry.

Nomenclature

a, b = constants in Musker's roughness length scale equation
B = smooth wall log-law intercept $= 5.0$
C_F = overall frictional resistance coefficient $= (F_D)/(1/2\rho U_e^2 S)$
c_f = local frictional resistance coefficient $= (\tau_o)/(1/2\rho U_e^2)$
C_j = autocorrelation function
E = power spectral density of surface waveform
F_D = drag force
h = Townsin's roughness height parameter $= \sqrt{\alpha m_0 m_2}$
j = lag in autocorrelation function
k = arbitrary measure of roughness height
k_s = sand roughness height or equivalent sand roughness height
K_u = kurtosis
L = plate length
L_p = overall length of surface profile
L_s = profile sampling interval
$[l]$ = other roughness length scales
m_n = nth moment of the power spectral density
N = number of samples in surface profile
Re_{δ^*} = displacement thickness Reynolds number $= U_e \delta^*/\nu$
Re_L = Reynolds number based on plate length $= U_e L/\nu$
R_a = centerline average roughness height $= (1/N)\Sigma_{i=1}^{N}|y_i|$
R_q = root mean square roughness height $= \sqrt{(1/N)\Sigma_{i=1}^{N} y_i^2}$
R_t = maximum peak to through height $= y_{\max} - y_{\min}$
R_z = ten point roughness height $= \Sigma_{i=1}^{5}(y_{\max\, i} - y_{\min\, i})$
S = wetted surface area
sl_{rms} = root mean square slope of the roughness profile $= \sqrt{(1/N-1)\Sigma_{i=1}^{N-1}\{(y_{i+1}-y_i)/(x_{i+1}-x_i)\}^2}$
S_k = skewness
S_p = average absolute slope of roughness profile
U = mean velocity in the x direction
U_e = freestream velocity relative to surface
ΔU^+ = roughness function
U_τ = friction velocity $= \sqrt{\tau_o/\rho}$
x = streamwise distance from plate leading edge
y = normal distance from the boundary measured from roughness centerline
α = bandwidth parameter $= m_0 m_4/m_2^2$
δ = boundary layer thickness
δ^* = displacement thickness $= \int_0^{\delta}(1 - U/U_e)\,dy$
κ = von Karman constant $= 0.41$
γ = wavenumber $= 2\pi/\lambda$
λ = wavelength
λ_{corr} = correlation length scale
ν = kinematic viscosity of the fluid
Π = wake parameter
ρ = density of the fluid
τ_o = wall shear stress
ω = wake function

Superscript

$+$ = inner variable (normalized with U_τ or U_τ/ν)

Subscript

FL = long wavelength filter
min = minimum value
max = maximum value
R = rough surface
S = smooth surface
TE = trailing edge

References

[1] Nikuradse, J., 1933, ''Laws of Flow in Rough Pipes,'' *NACA Technical Memorandum 1292*.
[2] Hama, F. R., 1954, ''Boundary-Layer Characteristics for Rough and Smooth Surfaces,'' Transactions SNAME, **62**, pp. 333–351.
[3] Ligrani, P. M., and Moffat, R. J., 1986, ''Structure of Transitionally Rough and Fully Rough Turbulent Boundary Layers,'' J. Fluid Mech., **162**, pp. 69–98.
[4] Krogstad, P. Å., and Antonia, R. A., 1992, ''Comparison Between Rough-and Smooth-Wall Turbulent Boundary Layers,'' J. Fluid Mech., **245**, pp. 599–617.
[5] Raupach, M. R., Antonia, R. A., and Rajagopalan, S., 1991, ''Rough-Wall Turbulent Boundary Layers,'' Appl. Mech. Rev., **44**, No. 1, 1991, pp. 1–25.
[6] Grigson, C. W. B., 1992, ''Drag Losses of New Ships Caused by Hull Finish,'' J. Ship Res., **36**, No. 2, pp. 182–196.
[7] Townsin, R. L., Byrne, D., Svensen, T. E., and Milne, A., 1981, ''Estimating the Technical and Economic Penalties of Hull and Propeller Roughness,'' Transactions SNAME, **89**, pp. 295–318.
[8] Musker, A. J., 1980–1981, ''Universal Roughness Functions for Naturally-Occurring Surfaces,'' Trans. Can. Soc. Mech. Eng., **1**, pp. 1–6.
[9] Lewkowicz, A. K., and Musker, A. J., 1978, ''The Surface Roughness on Ship Hulls: Interaction in the Viscous Sublayer,'' *Proceedings of the International Symposium on Ship Viscous Resistance-SSPA Goteborg, Sweden*.
[10] *Proceedings of the RINA International Workshop on Marine Roughness and Drag*, 1990, London, UK.
[11] Clauser, F. H., 1954, ''Turbulent Boundary Layers in Adverse Pressure Gradients,'' J. Aeronaut. Sci., **21**, pp. 91–108.
[12] Acharya, M., Bornstein, J., and Escudier, M. P., 1986, ''Turbulent Boundary Layers on Rough Surfaces,'' Exp. Fluids, **4**, pp. 33–47.
[13] Perry, A. E., and Li, J. D., 1990, ''Experimental Support for the Attached-Eddy Hypothesis in Zero-Pressure Gradient Turbulent Boundary Layers,'' J. Fluid Mech., **218**, pp. 405–438.
[14] Colebrook, C. F., 1939, ''Turbulent Flow in Pipes with Particular Reference to the Transition between Smooth and Rough Pipe Laws,'' Journal of Civil Engineers, **11**, pp. 133–157.
[15] Bradshaw, P., 2000, ''A Note on 'Critical Roughness Height' and 'Transitional Roughness','' Phys. Fluids, **12**, pp. 1611–1614.
[16] Granville, P. S., 1978, ''Similarity-Law Characterization Methods for Arbitrary Hydrodynamic Roughnesses,'' David Taylor Naval Ship R&D Center Report 78-SPD-815-01.
[17] Betterman, R. J., 1966, ''Contribution a L'etude de la Convection Forcee Turbulente le Long de Plaques Rugueuses,'' Int. J. Heat Mass Transf., **9**, pp. 153–164.
[18] Dvorak, F. A., 1969, ''Calculation Turbulent Boundary Layers on Rough Surfaces in Pressure Gradient,'' AIAA J., **7**, pp. 1752–1759.
[19] Koch, C. C., and Smith, L. H., 1976, ''Loss Sources and Magnitudes in Axial-Flow Compressors,'' ASME J. Eng. Power, **98**, pp. 411–424.
[20] Townsin, R. L. and Dey, S. K., 1990, ''The Correlation of Roughness Drag with Surface Characteristics,'' *Proceedings of the RINA International Workshop on Marine Roughness and Drag*, London, UK.
[21] Granville, P. S., 1958, ''The Frictional Resistance and Turbulent Boundary Layer of Rough Surfaces,'' J. Ship Res., **1**, pp. 52–74.
[22] Anon, 1981, ''United States Naval Academy Hydromechanics Laboratory,'' Catalog of Facilities from the *Proceedings of the 16th International Towing Tank Conference*, Leningrad, USSR.
[23] Moffat, R. J., 1988, ''Describing the Uncertainties in Experimental Results,'' Exp. Therm. Fluid Sci., **1**, pp. 3–17.
[24] Coleman, H. W., and Steele, W. G., 1995, ''Engineering Application of Experimental Uncertainty Analysis,'' AIAA J., **33**, No. 10, pp. 1888–1896.
[25] Schoenherr, K. E., 1932, ''Resistances of Flat Surfaces Moving Through a Fluid,'' Transactions SNAME, **40**, pp. 279–313.

The Distortion of a Jet by Coil Inserts

Huy T. Hoang
Graduate Student

Hamid R. Rahai[1]

Mechanical and Aerospace Engineering Department,
California State University, Long Beach,
Long Beach, CA 90840

Results of experimental investigations of the effects of distortion caused by coil inserts on a turbulent jet are presented. The coils have different wire diameters with constant pitch spacing. The ratios of the coil wire diameter to the tube inside diameter, d/D, are 0.06, 0.08, 0.11, 0.13, and 0.16 and the ratio of the pitch spacing to the tube inside diameter, p/D, is 1.2. Results show that the coil inserts enhance the mixing process. At the jet-outlet, mixing enhancement is increased when $d/D<0.1$. However, further downstream, the highest mixing is achieved for the coil with the largest d/D ratio. Results suggest that the streamwise vortices generated by the coil inserts are the mechanism behind the high entrainments and the mixing process. [DOI: 10.1115/1.1470476]

Introduction

Vortex generators or tabs and swirling motions have been used for mixing enhancement in a jet. Bradbury and Khadem [1] seem to be the first to investigate the distortion of a subsonic jet by tabs. Their tabs were square with sides equal to 1/16 of the jet diameter and were placed inside the jet, near its outlet. They investigated the effects of a single and multiple tabs on the centerline mean velocity decay and found a substantial increase in entrainment and mixing processes with multiple tabs, especially when two tabs at 180 degrees spacing are used. They conjectured the stirring action of the trailing vortex motion shed from the tabs as possible mechanism for the enhanced mixing process.

Further studies by Samimy et al. [2] and Zaman et al. [3] on the effects of triangular tabs on the mixing enhancement in both subsonic and supersonic jets have shown that indeed the trailing vortices shed from the sides of the tabs are the mechanism behind the enhanced mixing process.

Another relevant study is by Bell and Mehta [4]. They studied the effects of four different types of spanwise perturbations, placed at the origin of the mixing layer on its downstream development. The perturbation mechanisms were serration, cylindrical pegs, vortex generator, and corrugation. Their results show that except for the serration mechanism, the imposition of the other perturbations results in regular arrays of counter rotating vortices, which enhance the mixing layer growth rate in the near field.

The introduction of swirl on a turbulent jet results in increases in the jet half width, rate of entrainment, and rate of decay of the jet and inducement of pressure fields to balance centrifugal forces. Decay of swirl caused by shear and mixing with surrounding fluid results in an adverse pressure gradient along the jet axis which displaces the location of the maximum mean velocity away from the jet axis (e.g., Rose [5], Lee [6], Chigier and Chervinsky [7], Syred and Beer [8], Lilley [9], Sheen et al. [10]). In combustion systems, mixing enhancement is obtained using a strong swirl which generates a shorter and more intense flame and reduction in NOx formation and in some cases improvements in combustion efficiency (Talagi and Okamoto [11], Gupta et al. [12], and Tangirala and Driscoll [13]). However, a very strong degree of swirl causes excessive entrainment of the surrounding air, resulting in a flame blow out (Ho et al. [14]).

Weak degree of swirl has limited practical application. However, as Gupta et al. [15] have explained, it can be used in characterization of some geophysical phenomena such as fire whirls, dust devils, tornadoes, hurricanes, and water spouts. In combustion, weak degree of swirl causes increase in the fire length, which has practical application in fire whirls and tangentially-fixed boilers.

Swirl in a tube has been produced by tangential injection, twisted tape inserts, wall slots, rotating tubes and spiral riblets (e.g., Babikian et al. [16], Yang et al. [17], Yamplosky et al. [18]). The coil-inserted tube for the present investigation is similar to the spiral riblets. In the present experiments, results are presented for the effects of coil inserts with constant pitch but different wire diameters on a turbulent jet from a round tube. The present study is a continuation of our previous study (Rahai and Wong [19], Rahai et al. [20]) where the coils had constant wire diameter but different pitch spacing. In the previous experiments, the ratios of the pitch spacing to the tube inside diameter, p/D, were 0.4, 0.7, 1.2, and 2.7. Experiments were performed at five axial locations up to 10 orifice diameters. Their results showed that the coils with large pitch spacing caused significant decrease in the maximum mean velocity and increases in the jet half width and turbulent velocities in the jet developing region which are indications of a higher mixing process. These effects were more pronounced when p/D was 1.2.

Experimental Procedure and Techniques

The central tube of the main combustion unit of the combustion laboratory in the Mechanical Engineering Department at California State University, Long Beach was used in the experiment. Figure 1 shows the experimental setup. The central tube is a 3 mm thick tube which has an inside diameter of 12.7 mm and is 102 cm long. The tube has aluminum honeycomb at its inlets for flow conditioning.

Five coils with approximate wire diameters of 0.75, 1.0, 1.4, 1.65, and 2 mm and a pitch spacing of 15.24 mm were used in the experiments. The effective length of the coils was 30.5 cm. The ratios of the wire diameter to the tube inside diameter were 0.06, 0.08, 0.11, 0.13, and 0.16, and the ratio of the pitch spacing to the tube inside diameter was 1.2. Filtered laboratory air, supplied at a steady rate is sent through the tube. The supplied airflow rate is kept at a constant rate of 5.66 m^3/hr. The Reynolds number based on the tube inside diameter and the volume flow rate is 10,187. Measurements are carried out at five axial locations of $X/D=0.1$, 1, 3, 5, and 10 and different radial locations using a TSI double sensor hot wire probe model 1243-T1.5 connected to two channels of TSI IFA-100 intelligent flow analyzer. At each axial location, measurements are carried out twice to obtain the three components of the turbulent velocity and two components of turbulent shear stresses. At each measurement location 50 records where each record contains 2048 sample of data are digitized at a

---

[1] Corresponding author.

Contributed by the Fluids Engineering Division for publication in the JOURNAL OF FLUIDS ENGINEERING. Manuscript received by the Fluids Engineering Division March 21, 2001; revised manuscript received December 17, 2001. Associate Editor: K. Zaman.

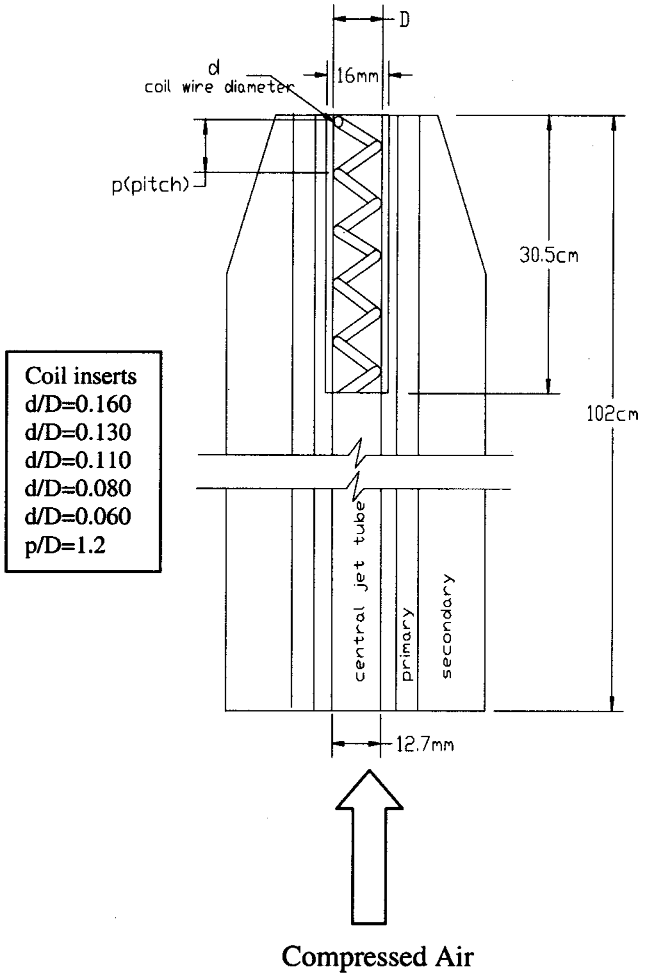

Fig. 1 Experimental setup

sample rate of 6000 samples/s, using a Metra-Byte DAS-20 Analog to digital converter. Digitized data are analyzed using software supplied by Data Ready, Inc.

Results and Discussions

Figure 2 shows radial variation of the normalized axial mean velocity at two axial locations of $X/D=0.1$ and 3. At $X/D=0.1$, the profiles for the smooth tube and the coil-inserted tube with $d/D=0.06$ are Gaussian. The smooth tube profile has a very narrow width. For the coil-inserted tubes, as d/D increases, the mean velocity profiles deviate from the Gaussian shape and have larger widths, which are indications of increased entrainment and mixing. When $d/D=0.16$, the mean velocity profile is approaching a distorted top hat profile where the distortions are due to the wake of the coil insert.

At $X/D=3$, all mean velocity profiles have approached a Gaussian shape and again the largest increase in the width is for the coil-inserted jet with $d/D=0.16$.

Figure 3 shows axial development of the jets half-widths, the normalized maximum mean velocities and the centerline axial turbulence intensity for the smooth and the coil-inserted jets. At $X/D=0.1$, the jet half-widths for the coil inserted jets with $d/D>0.1$ have increased. However, these values decrease to values less than the corresponding value for the smooth jet further downstream up to $X/D=1.0$ where they start to increase and become substantially larger than the jet half width of the smooth jet at $X/D>5$. For the coil inserted jets with $d/D<0.1$, the jet half widths are nearly the same as the jet half width of the smooth tube at $X/D=0.1$ and then they increase downstream to values larger than the corresponding value for the smooth tube. At $X/D\geqslant 10$, the jet half-widths of the coil inserted jets with $d/D\geqslant 0.08$ are nearly the same.

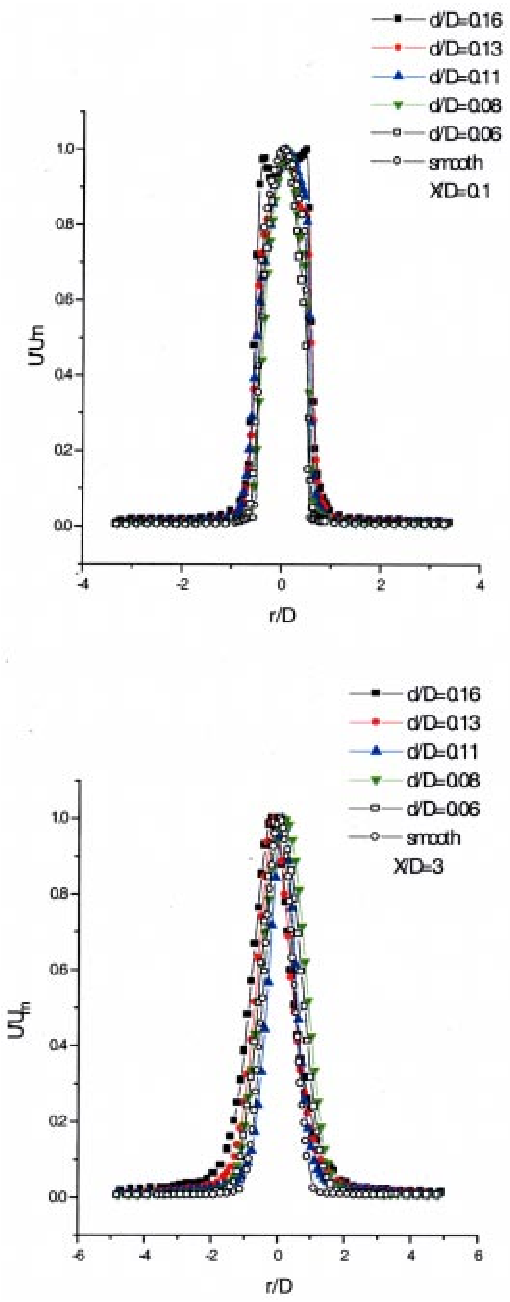

Fig. 2 Radial variation of normalized axial mean velocity at two axial locations. Uncertainty in U/U_0 is ±0.005, in r/D is ±0.05, and in x/D is ±0.05 at 20:1 odd.

There are large decay rates in the normalized maximum mean velocity for the coil- inserted jets as compared to the corresponding decay rate for the smooth jet and the decay rates for all the coil inserted jets are nearly the same for $X/D>3$.

The centerline axial turbulence intensities for the coil inserted tubes are increased substantially in the near field region, as compared with the corresponding values for the smooth tube, and the extend of these increases in the downstream direction depends on the size of the d/D. For coil-inserted jets with $d/D=0.13$ and 0.16, the decay of turbulence intensity starts at $X/D=1$, while for the other coil-inserted jets, the decay process is delayed to further downstream locations.

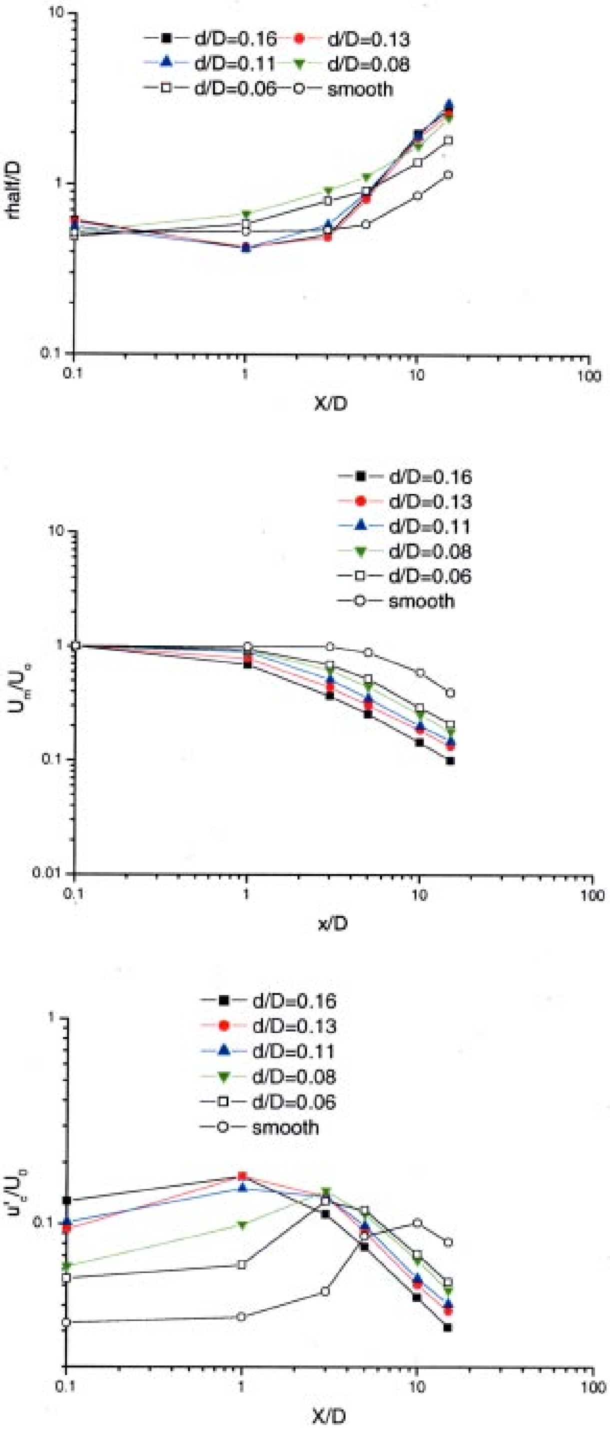

Fig. 3 Axial variation of the jet half widths, the flow center mean velocity and axial turbulence intensity. Uncertainty in rhaf is ±0.05 and in u_c'/U_0 is ±0.02 at 20:1 odd.

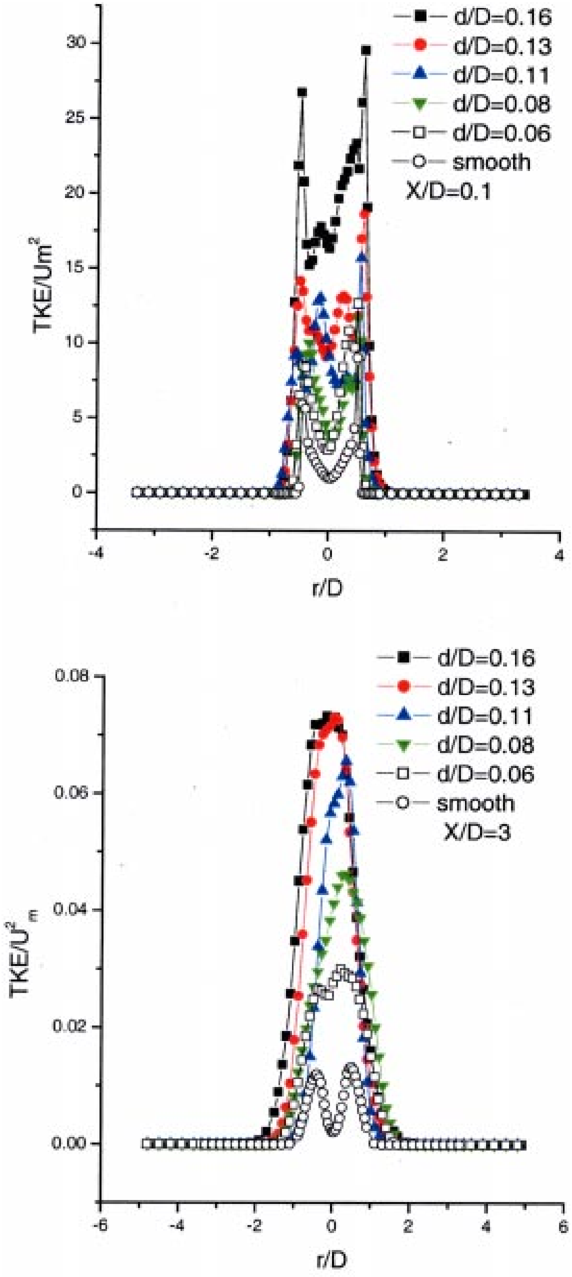

Fig. 4 Radial variation of turbulent kinetic energy, TKE, at two axial locations. Uncertainty in TKE is ±0.0004 at 20:1 odd.

Figure 4 shows radial variation of turbulent kinetic energy at two axial locations of $X/D=0.1$ and 3. The presence of the coils results in increases in the turbulent kinetic energy and the highest increase is for the jet with $d/D=0.16$.

Figure 5 shows radial variation of the normalized swirl velocity at $X/D=0.1$. The velocity profiles show that as d/D increases, the peak of the velocity profiles move more toward the edge of the jet and for the coil inserted tube with $d/D>0.1$, the jet is in a near solid body rotation. For the coil-inserted jets with $d/D>0.1$, the profiles show two additional peaks near the edge of the jets which are due to the wake of the coil inserts.

According to Gupta et al. [15], the swirl number can be estimated as

$$S=\frac{G/2}{1-(G/2)^2}.$$

Here $G=W_0/U_0$. Assuming negligible decay in the swirl velocity between the jet outlet and $X/D=0.1$, the maximum swirl at this location is approximately 0.2 for the coil inserted jet with $d/D=0.16$. This value corresponds to a weak swirl condition.

For the coil inserted tubes with $d/D>0.1$, the results for the swirl velocity indicate the presence of forced vortices in the near field, especially for the coil inserted jet with $d/D=0.16$. Since the swirls generated are weak swirls, they reduce the jet half widths in

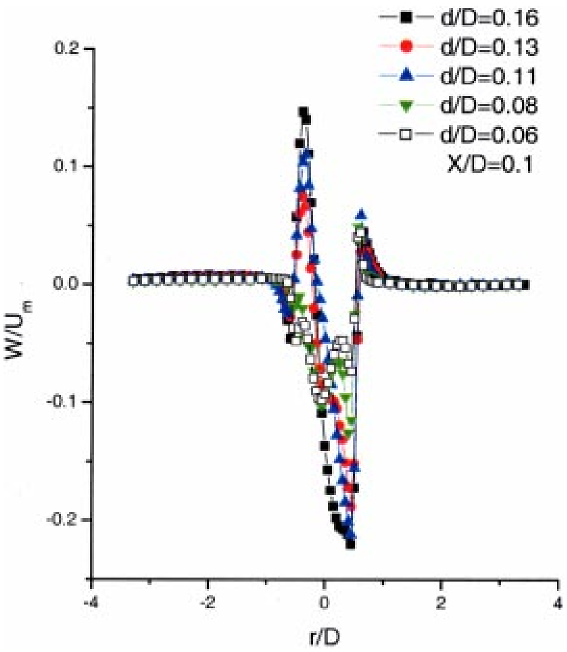

Fig. 5 Radial variation of the swirl velocity near the jet outlet. Uncertainty in W/U_m is ±0.005 at 20:1 odd.

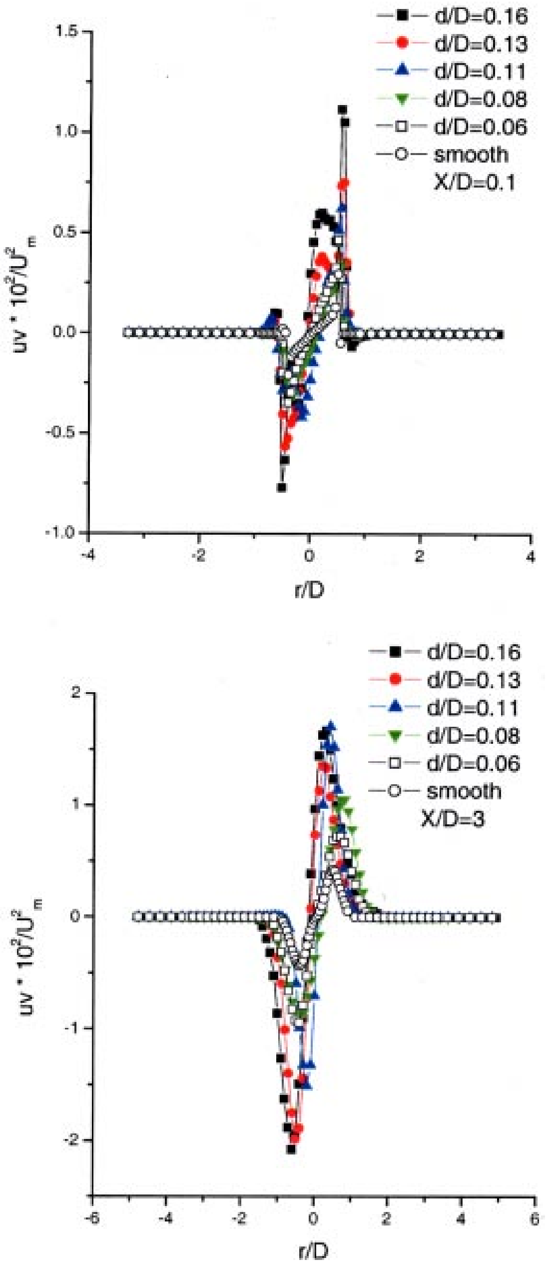

Fig. 6 Radial variation of normalized turbulent shear stress at two axial locations. Uncertainty in turbulent shear stress is ±0.25 at 20:1 odd.

the initial regions of the jets, until further downstream where the free vortices become dominant and increased entrainment and mixing are prevailed. When $d/D<0.1$, the free vortices are the main mechanism behind the mixing immediately downstream of the tube outlet.

Figure 6 shows radial variations of the main turbulent shear stress at the two axial locations of $X/D=0.1$ and 3. The presence of the coils results in increases in the turbulent shear stress, as compared to the corresponding values for the smooth tube. The larger the coil wire diameter, the larger the turbulent shear stress. The azimuthal component of the turbulent shear stress (not shown here) also show increases for the coil-inserted jets, however, since the radial component of the turbulent shear stress is an order of magnitude larger and play a larger role, it is the one that is included here.

At $X/D=0.1$, for the coil-inserted jets with large wire diameters, the shear stress profiles have multi-peaks which are due to the wake of the coil inserts. As mentioned before, for these jets, the weak swirl plays a larger role and the entrainment is less than the other coil-inserted jets. At $X/D=3$, while we have a fully turbulent flow, the increase in the coil wire diameter results in an asymmetry in the turbulent shear stress profile which is more pronounced for the coil with $d/D=0.16$.

Results for further downstream locations (not shown here) show that the shear stress decays rapidly beyond $X/D=3$ and at $X/D=10$, they are reduced by an order of magnitude and the shear stress values for the coil-inserted jets are less than the corresponding value for the smooth tube.

Figure 7 shows power spectra of the axial turbulent velocity for the smooth and coil-inserted jets at the two axial locations of $X/D=0.1$ and 3, along $r=0$. The effects of the coils are seen as increases in the low wave number and decreases in the high wave number flows. These results are also indicative of increased mixing process for the coil-inserted jets due to generation of large eddy structures.

At $X/D=3$, for the smooth jet, the axial turbulent velocity spectrum shows a peak which is an indication of the presence of a coherent structure in the near field region of the jet. Further downstream, results (not shown here) show that this peak has disappeared and the spectra for the coil-inserted jets approach the corresponding spectrum of the smooth jet.

Conclusions

Experimental investigations of turbulent jet from round tubes with coil inserts are performed and results are compared with the corresponding results for a smooth tube. The coils used in the experiments had constant pitch spacing but different wire diameter. The ratio of p/D was 1.2 and the ratios of d/D were 0.06, 0.08, 0.11, 0.13, and 0.16. Results show that when $d/D<0.1$, the coil inserts act like a turbulator, with increased mixing at the jet outlet and downstream. However, when $d/D\geqslant 0.1$, the weak swirl generated by the coil, delay the mixing enhancement until further downstream, before high mixing is achieved.

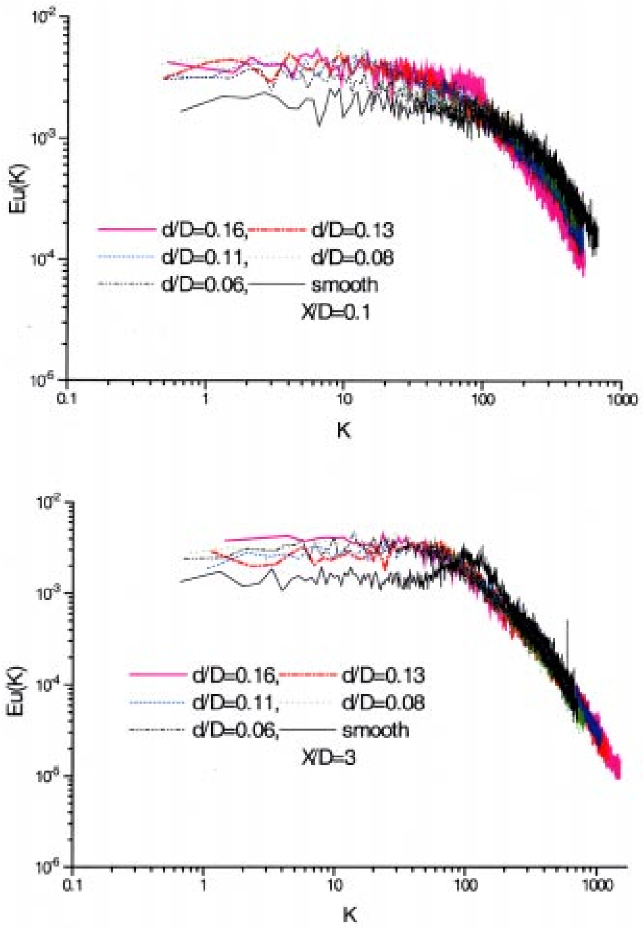

Fig. 7 Spectra of axial turbulent velocity at two axial locations

It has been suggested that the increased mixing in the near field region is mostly due to generation of streamwise vortices, which makes the flow fully turbulent with large entrainment.

Further study is underway to investigate detail flow characteristics of the coil inserted jets in the near field and results will be presented in a future publication.

Acknowledgments

The authors would like to thank Dr. K. Helland of Data Ready for providing the data acquisition software.

Nomenclature

D = tube inside diameter, cm

$E_u(u)$ = axial turbulent velocity spectra, $\dfrac{E_f(u)U_m}{2\pi\overline{u^2}}$

K = wave number, $\dfrac{2\pi f}{U_m}$

U = axial mean velocity, m/s

U_m = maximum mean velocity, m/s

U_0 = maximum mean velocity at $X/d=0.1$ (or tube outlet), m/s

u'_c = rms axial turbulent velocity along the centerline, m/s

$\overline{u^2}$ = mean squared axial turbulent velocity, $\dfrac{m^2}{s^2}$

$\overline{v^2}$ = mean squared radial turbulent velocity, $\dfrac{m^2}{s^2}$

$\overline{w^2}$ = mean squared tangential turbulent velocity, $\dfrac{m^2}{s^2}$

W = swirl (tangential) velocity, m/s

W_0 = swirl (tangential) velocity at $X/D=0.1$ (or tube outlet), m/s

X = axial distance, cm

d = coil wire diameter, mm

f = frequency, Hz

p = pitch spacing, mm

r = radial distance, cm

rhalf = jet half width, cm

S = swirl number

TKE = turbulent kinetic energy, $\dfrac{m^2}{s^2}=1/2(\overline{u^2}+\overline{v^2}+\overline{w^2})$

uv = time averaged turbulent shear stresses, $\dfrac{m^2}{s^2}$

References

[1] Bradbury, L. J. S., and Khadem, A. H., 1975, ‘‘The Distortion of a Jet by Tabs,’’ J. Fluid Mech., **70**, p. 801.

[2] Samimy, M., Zaman, K. B. M. Q., and Reeder, M. F., 1993, ‘‘Effect of Tabs at the Nozzle Lip on the Flow and Noise Field of an Axisymmetric Jet,’’ AIAA J., **31**, p. 609.

[3] Zaman, K. B. M. Q., Samimy, M., and Reeder, M. F., 1994, ‘‘Control of an Axisymmetric Jet Using Vortex Generator,’’ Phys. Fluids, **6**(2), pp. 778–793.

[4] Bell, J. H., and Mehta, R. D., 1993, ‘‘Effects of Imposed Spanwise Perturbations on Plane Mixing-Layer Structure,’’ J. Fluid Mech., **257**, pp. 33–63.

[5] Rose, W. G., 1962, ‘‘A Swirling Round Turbulent Jet,’’ ASME J. Appl. Mech., **29**, pp. 616–625.

[6] Lee, S-L, 1965, ‘‘Axi-symmetrical Turbulent Swirling Jet,’’ ASME J. Appl. Mech., **32**, pp. 258–262.

[7] Chigier, N. A., and Chervinsky, A., 1967, ‘‘Experimental Investigation of Swirling Vortex Motion in Jets,’’ ASME J. Appl. Mech., **34**, June, pp. 443–451.

[8] Syred, N., and Beer, J. M., 1974, ‘‘Combustion in Swirling Flows: A Review,’’ Combust. Flame, **23**, pp. 143–201.

[9] Lilley, D. G., 1997, ‘‘Swirling Flows in Combustion: A Review,’’ AIAA J., **15**(8), pp. 1063–1078.

[10] Sheen, H. J., Chen, W. J., and Jeng, S. Y., 1996, ‘‘Recirculation Zones of Unconfined and Confined Annular Swirling Jets,’’ AIAA J., **34**(3).

[11] Talagi, T., and Okamoto, T., 1981, ‘‘Characteristics of Combustion and Pollutant Formation in Swirling Flames,’’ Combust. Flame, **43**, pp. 69–79.

[12] Gupta, A., Ramavajjala, M., and Taha, M., 1992, ‘‘The Effect of Swirl and Nozzle Geometry on the Structure of Flams and Nox Emission,’’ AIAA Thirteen Aerospace Science Meeting and Exhibit, Reno, NV.

[13] Tangirala, V., and Driscoll, J. F., 1988, ‘‘Temperature Within Non-premixed Flames: Effects of Rapid Mixing Due to Swirl,’’ Combust. Sci. Technol., **69**, pp. 143–162.

[14] Ho, W., Yang, S., and Yang, R., 1990, ‘‘The Advanced Burner Design Project,’’ The Fourteen Annual Conference on Theoretical and Applied Mechanics, Chung LI, Taiwan, R.O.C.

[15] Gupta, A. K., Lilley, D. G., and Syred, N., 1984, *Swirl Flows*, ABACUS Press.

[16] Babikian, D. S., La Rue, J. C., and Rahai, H. R., 1991, ‘‘Characteristics of the Velocity Field in the Central Region of a Spirally Fluted Tube,’’ Paper No. III-3, Proceeding of the Eight Symposium on Turbulent Shear Flows,’’ Sept. 9–11, Munich, Germany.

[17] Yang, S. R., Zai, G. D., and Kim, R. H., 1990, ‘‘Experimental Investigation of a Spiral Turbulator with a Reinforcing Wire as an Augmentator/Cleaner in the Tube Side of Surface Condensers,’’ Proceedings of CSME Mechanical Engineering Forum 1990, University of Toronto, June 3–9.

[18] Yamplosky, J. S., Libby, P. A., and Launder, B. E., and La Rue, J. C. 1984, ‘‘Fluid Mechanics and Heat Transfer of Spiral Fluted Tubing,’’ GA Technologies Report GA-A17833.

[19] Rahai, H. R., and Wong, T. W., 1998, ‘‘Experimental Investigation of Turbulent Jet From Round Ribbed Tubes,’’ Paper No. FEMSM98-4972, 1998 ASME Fluids Engineering Division Summer Meeting, June 21–25, Washington, DC.

[20] Rahai, H. R., Vu, H. T., and Shojaee Fard, M. H., 2001, ‘‘Mixing Enhancement Using a Coil Insert,’’ Appl. Therm. Eng., **21**, pp. 303–309.

Axial and Secondary Flow Study in a 90 Deg Bifurcation Under Pulsating Conditions Using PIV

N. M. Nikolaidis

D. S. Mathioulakis
Assistant Professor
e-mail: mathew@fluid.mech.ntua.gr

National Technical University of Athens,
Department of Mechanical Engineering,
Fluids Section,
9 Heroon Polytechniou, 15710 Zografos,
Athens, Greece

Both axial and secondary flow were experimentally studied in a 90-degree bifurcation of square tubes, under pulsating conditions and equal branch flow rates. The examined peak Reynolds number (Re) was in the range 330–830, and the Womersley parameter (α) between 5 and 15. In the extension of the mother tube during deceleration, axial flow separated from the wall opposite of the 90-degree branch. The formed shear layer rolled up, for higher values of Re and low α, generating discrete vortices. However, for the highest value of α, the shear layer was limited close to the wall, without rolling up, for all the examined Re. During acceleration, all recirculation zones were washed out and the flow became attached before flow peak. In the 90-degree branch during acceleration, a vortex was formed at the bifurcation apex and moved streamwise towards the center of the cross-section where it degenerated. The secondary flow of this branch had the following characteristics: during deceleration two Dean vortices were located close to the outer bend side of the cross-section, and their strength was progressively reduced. A little before flow peak any Dean vortices of the previous phase were destroyed and two new ones were born. Maximum secondary velocities were on the order of 20% higher than the bulk velocity of the branch. [DOI: 10.1115/1.1470478]

Introduction

Numerous studies have been published investigating the flow field in duct bifurcations. These studies have explored their interesting flow features and some have attempted to answer the basic medical question of why branches in the human circulatory system are likely sites for developing arteriosclerosis. Findings have indicated that this disease can be attributed to the wall shear stresses magnitude, due to blood flow, which affects the material of the arteries. For instance, Caro et al. [1] and Ku et al. [2] suggest that this disease initiates at sites of low wall shear stress, whereas Fry [3] proposed that this occurs at sites of high wall shear stress. More references about this apparently contradictory issue are reported in [4]. On the other hand, this fluid mechanics problem is characterized by axial adverse pressure gradients, which cause recirculation zones, and due to the streamline curvature of the fluid entering the tube branches, strong secondary flow appears. Both phenomena are, in general, unstable. Moreover, when the flow accelerates or decelerates, as for example in case of physiological flows, unsteady inertial forces change the whole picture dramatically.

The basic nondimensional parameters involved in the description of the above problem [5] are: (a) the Reynolds number, Re; (b) the so-called Womersley parameter α, defined as $\alpha = \mathrm{R}\sqrt{\omega/\nu}$, where R, is the radius of the duct, ω, the angular frequency of the pulsating flow, and ν, the kinematic viscosity of the fluid; (c) the Dean number, κ, defined as $\kappa = \mathrm{Re}\sqrt{\delta}$, with δ, the ratio of duct radius to its radius of curvature. Of course, the flow field is also dependent on the flow rate ratio of the branches to the mother tube, their cross-sectional area ratio, the angle of the bifurcation, the shape of the cross sections, to mention a few [6].

This work constitutes a continuation of previous works carried out by the same group in an effort to reveal details of the flow field in a 90-degree bifurcation (Fig. 1) under steady conditions (Mathioulakis et al. [7]) and pulsating ones (Schinas and Mathioulakis [8]). The motivation of the present work was to explore axial flow and secondary flow patterns in the same model by performing simultaneous velocity measurements in a great number of points through Particle Image Velocimetry (PIV). To the best of our knowledge this information is missing from the relevant existing literature since the most commonly used experimental techniques employ point to point measurements such as hot film, LDA and ultrasound and ensemble averaging processing for periodic flows which obscure any transient or non periodic flow patterns.

The 90-degree bifurcation was selected for its simplicity, resembling branches of the human circulatory system. For example, this type of asymmetric bifurcation is found in the pulmonary artery with its branches, in the aorta with both renal arteries, and in the aortic arch, from which arteries emanate. The flow in the pulmonary artery and its branches has been studied experimentally in vitro by Yoganathan et al. [9] using LDA under steady conditions and later on by Sung and Yoganathan [10] for a physiological flow rate both experimentally and numerically. It should be remembered that in the above mentioned arterial bifurcations the diameter of the mother tube differs from that of one of the branches, while in our study all tubes were of the same size. More references about studies in duct bifurcations also can be found in [8].

A good effort was given in the present work to study the secondary flow in the branch normal to the mother tube, which was strong due to the relatively high curvature of the streamlines entering this branch. After the pioneer work of Dean [11,12] who analyzed the secondary flow of a curved circular tube, consisting of two counter rotating vortices (the so-called Dean vortices), a great number of studies by others followed. In 1970, Lyne [13], using a perturbation method discovered an additional pair of vortices in the secondary flow in a curved tube for oscillating flows of high Womersley parameter. This was also predicted by Smith [14], solving the flow for an arbitrary but symmetric tube cross-section. These Lyne vortices were rotating in the opposite direction with respect to the Dean vortices so that the fluid was moving towards the center of the curvature at the symmetry plane of the cross-section. This "negative" centrifuging was attributed to the higher values of the pressure gradient compared to the centripetal forces in the central part of the cross section. Conversely, close to

---

Contributed by the Fluids Engineering Division for publication in the JOURNAL OF FLUIDS ENGINEERING. Manuscript received by the Fluids Engineering Division July 27, 2000; revised manuscript received November 27, 2001. Associate Editor: J. Bridges.

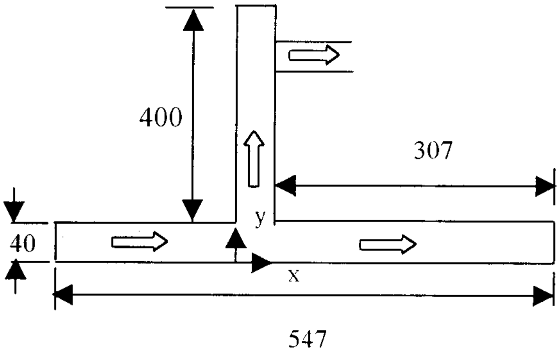

Fig. 1 Bifurcation model. (Dimensions in mm)

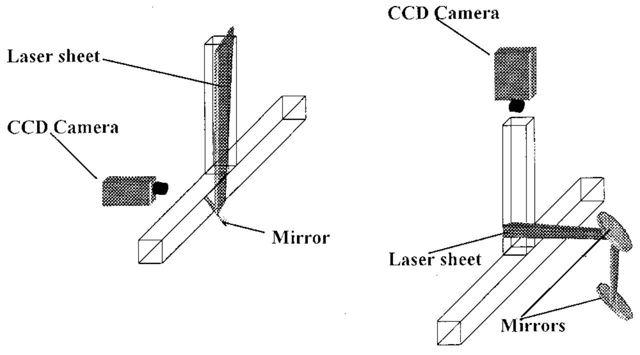

(*a*) (*b*)

Fig. 2 PIV set up. a. Axial flow. b. Secondary flow

the tube walls, the Dean vortices rotating in the opposite direction appeared elongated and thin. Talbot and Gong [15] recorded, by using LDA, the appearance of two pairs of vortices in a curved tube for pulsating flow and $\alpha \geqslant 12.5$. Similar results were obtained numerically by Hamakiotes and Berger [16], Rindt et al. [17], and Sudo et al. [18]. The complexity of this flow is shown in a numerical study by Chang and Tarbell [5] who predicted the number and shape of secondary vortices that would evolve over one time period in the flow in an aortic arch, for a given value of α. The number of vortices appearing simultaneously was as high as fourteen at a particular instant.

The secondary flow has also been examined in curved tubes of rectangular cross-section by many researchers in which, under steady conditions, it has been found that the secondary flow consists of one, two or more pairs of vortices, depending on the aspect ratio and the Dean number. Winters [19] showed that for rectangular cross section curved tubes multiple vortex solutions are unstable to symmetric or antisymmetric perturbations, except the one pair vortex type which is stable. For rectangular ducts of high aspect ratio, Thangam and Hur [20] predicted more pairs of vortices than two, and Kao [21] examined the transition from the two to four vortex structure by increasing the Dean number for various cross-sections.

The flow field in a 90-degree bifurcation with square tubes is presented in the following paragraphs under pulsating conditions by employing PIV, for various combinations of Re and Womersley parameter.

Experimental Apparatus and Methodology

The examined bifurcation model was made of transparent Plexiglas with tubes of square cross section (40×40 mm^2), consisting of a vertical and a horizontal branch (see Fig. 1), the latter being an extension of the mother tube. The Cartesian coordinate system used in order to designate the location of a measuring point has its origin at the bottom of the model (see Fig. 1). The flowing medium was water of a mean temperature of 20°C ($\rho = 0.998$ gr/cm^3, $\nu = 0.01011$ cm^2/s). Major components of the hydraulic loop were two water tanks, a settling chamber to reduce flow disturbances located upstream of the model, and a rotating spherical valve downstream of both branches, in order to introduce unsteadiness to the flow established by gravity. The rotation of the valve and therefore the flow rate waveform were PC controllable by varying the number and duration of the voltage pulses sent to a stepper motor, which moved the valve. In order for the flow to enter the model smoothly, the settling chamber afforded a 25:1 convergent nozzle (based on the area) which was connected to the model by a 2 m long (50 hydraulic diameters) square tube (see also Schinas and Mathioulakis [8]).

Both the axial and secondary flow were measured by PIV. The illumination source was continuous (300 mW Argon-Ion Laser), the thickness of the light sheet was on the average 1.5 mm, the scattering particles were hollow glass spheres (mean diameter 10 μm, density 1.1 gr/cm^3) and the camera was a CCD black and white video camera (SONY imager 752×582 pixel, 25 frames/s) with a 100 mm macro lens, sending pictures to a video recorder (SONY SVO-5800P). Selected pictures (using a DIAQUEST DQ-422+ card) were then transferred from the videotape to a PC, through a frame grabber (TARGA + of TRUEVISION Inc.). Besides this frame grabber there was another one used (FG 4000 of ARCO Ltd) which had the option of digitizing a picture at the time instant that a trigger pulse arrived to it. This was necessary in order to establish a correspondence between the flow rate signals and the stored pictures. More particularly, at a given opening of the valve (say $t=0$), a photodiode sent a triggering pulse both to the FG4000 grabber and a PC, initiating the digitization (via an A/D converter) of both the mother tube flow rate (Fischer-Porter electromagnetic flow meter) and that one of the vertical branch (Carolina electromagnetic flow meter, FM501). Therefore, at $t = 0$, the FG4000 grabber stored a picture along with its time code, which thus allowed the matching of the subsequent pictures to the flow rates.

The velocity vectors were calculated by cross correlating two pictures taken 40 ms apart. The cross correlation function was computed by performing two dimensional FFTs through MATLAB. Its peak was designated by using a Gaussian scheme in both directions of the image plane, in order to increase its accuracy (subpixel accuracy). Maximum error concerning cross correlation peak detection was 0.1 pixel based on artificial image tests. The interrogation windows were 48×48 pixels and a 50% overlapping was employed in both directions. The magnification factors were 11.42 pixel/mm for the axial flow and 14.4 pixel/mm for the secondary flow. Therefore, the maximum error concerning the cross correlation peak detection was 0.22 mm/s for the axial flow and 0.17 mm/s for the secondary flow. More about PIV applications performed by this group are found in Kostis and Mathioulakis [22] and Koutsiaris et al. [23].

Axial flow velocities were measured in the bifurcation plane (normal to z-axis), passing through the center of the tube cross-sections. In order to study the secondary flow in the vertical branch, a piece of transparent Plexiglas was glued to this branch normal to its axis, 40 cm downstream of the bifurcation so that this did not influence the flow at the bifurcation itself (Fig. 1). In a previous study (Mathioulakis et al. [7]) it was observed that the upstream influence of the bifurcation to the flow field is confined in a region of about 1 hydraulic diameter. Thus, it was possible for a camera to record the flow field on a light sheet, being normal to this branch's axis. The orientation of the light sheet for each case was adjusted by plane mirrors (see Fig. 2(*a*, *b*)). As it was shown by Schinas and Mathioulakis, [8] the unsteady flow field in this bifurcation is quite complex and, obviously, presenting velocity vectors in one plane cannot reveal the whole picture of the flow.

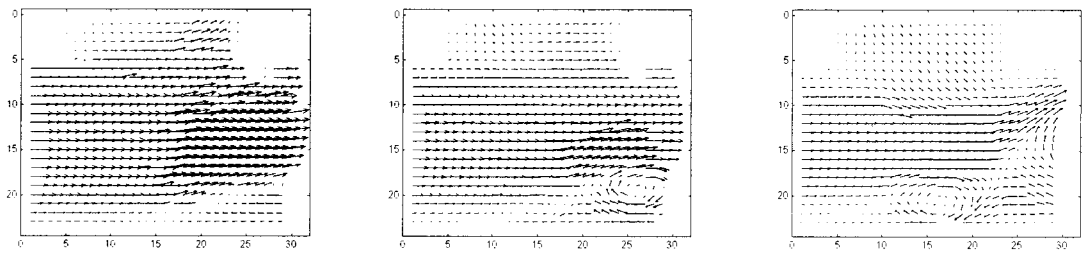

(*a*) t=76s (Q=2lt/min, T=88s) (*b*) t=80s (Q=2lt/min, T=88s) (*c*) t=84s (Q=2lt/min, T= 88s)

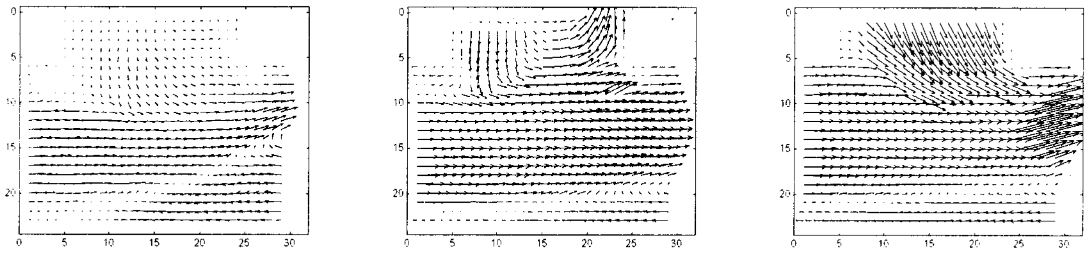

(*d*) t=14s (Q=0.8lt/min, T=88s) (*e*) t=27s (Q=0.8lt/min, T=28s) (*f*) t=0 (Q=2lt/min, T=11s)

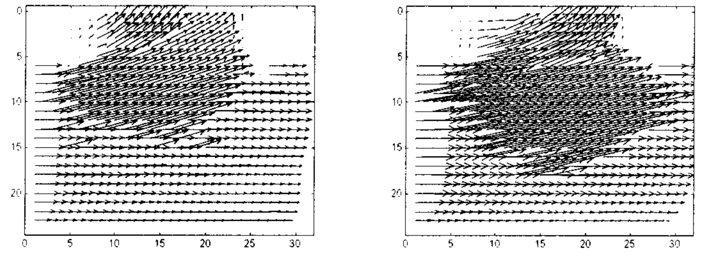

(*g*) t=25s (Q=1.5lt/min, T=88s) (*h*) t=30s (Q=1.5lt/min, T=88s)

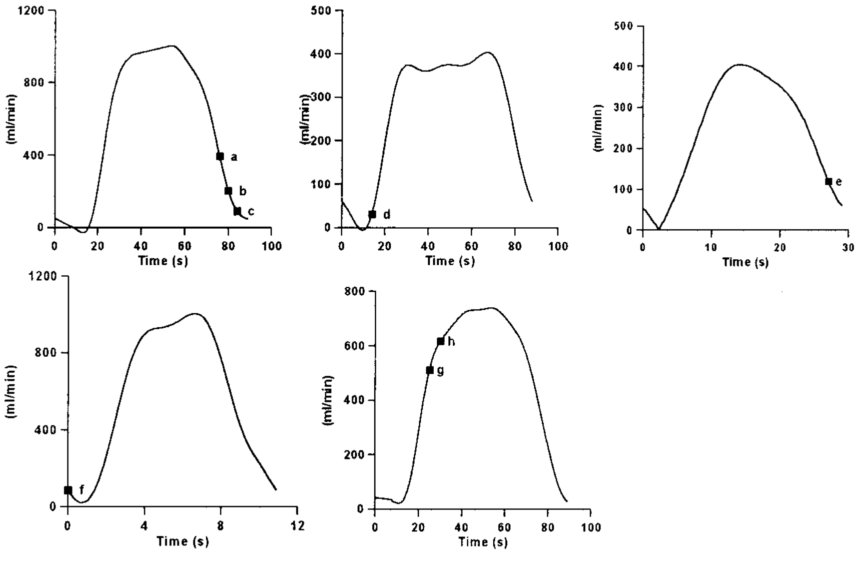

Fig. 3 Axial flow-Horizontal part. Velocity vectors and flow rates. (*a*), (*b*), (*c*): Q=2 lt/min, T=88 s, t=76 s, 80 s, 84 s, (*d*): Q=0.8 lt/min, T=88 s, t=14 s, (*e*): Q=0.8 lt/min, T=28 s, t=27 s, (*f*): Q=2 lt/min, T=11 s, *t*=0, (*g*), (*h*): Q=1.5 lt/min, T=88 s, t=25 s, 30 s

However, in this work a number of combinations of Re and α was examined, instead of only one in our previous study. Moreover, using PIV we were able to explore flow structures in both axial and secondary flow, which was impossible by using LDA point-to-point measurements.

Results and Discussion

The measured velocity vectors of both axial and secondary flow are presented in Figs. 3–5. Due to the unsteadiness of the flow, which varied between zero and a maximum value, each figure

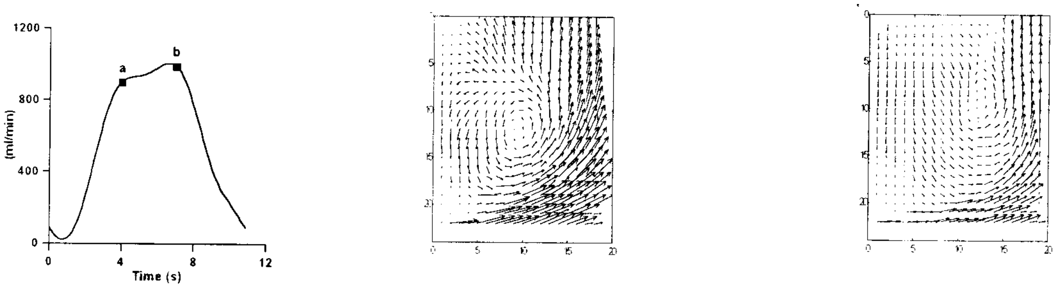

(*a*) t=4s (q=2lt/min, T=11s) (*b*) t=7s (Q=2lt/min, T=11s)

Fig. 4 Axial flow-vertical part. Velocity vectors and flow rate. (*a*), (*b*): Q=2 lt/min, T=11 s, t=4 s, t=7 s.

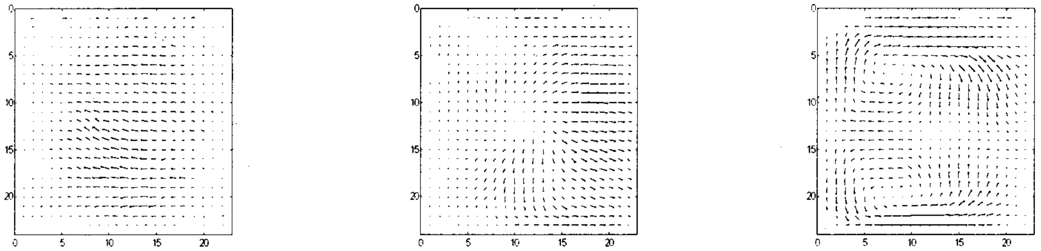

(*a*) t=20s (Q=1lt/min, T=88s) (*b*) t=25s (Q=1lt/min, T=88s) (*c*) t=29s (Q=1lt/min, T=88s)

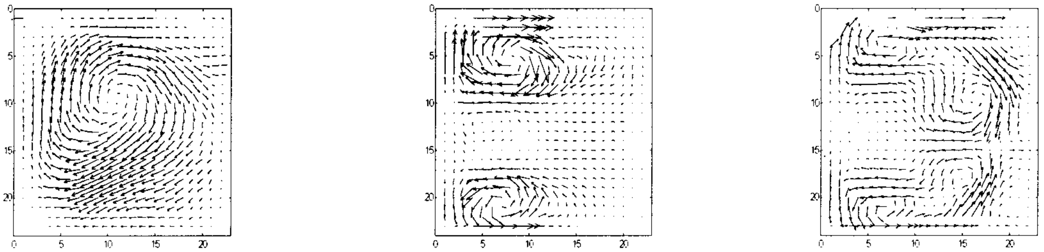

(*d*) t=20s (Q=1.5lt/min T=88s) (*e*) t=74s (Q=1.5lt/min T=88s) (*f*) t=17 (Q=1lt/min T=28s)

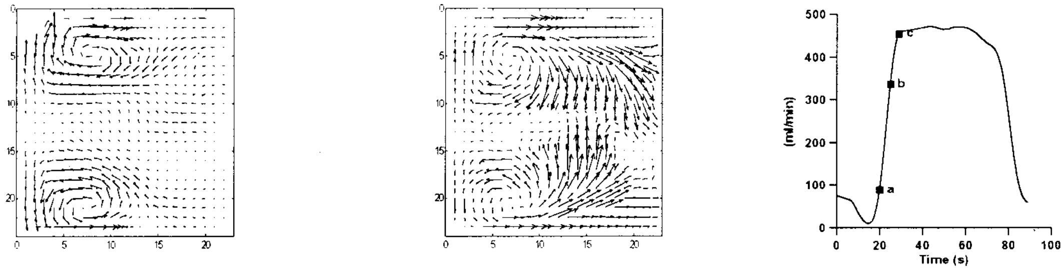

(*g*) t=23s (Q=1.1lt/min T=28s) (*h*) t=8.5s (Q=1.5lt/min T=11s)

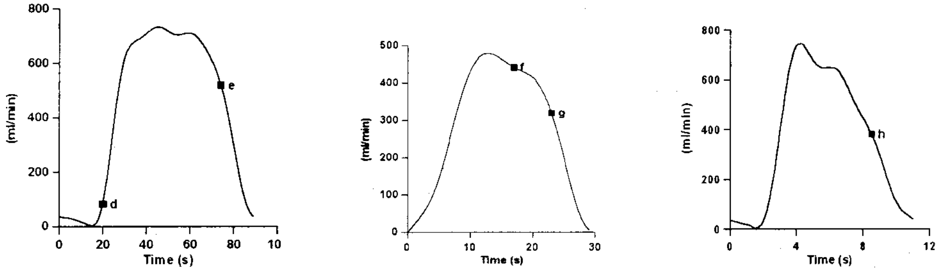

Fig. 5 Secondary flow. Velocity vectors and flow rates, (*a*), (*b*), (*c*): Q=1 lt/min, T=88 s, t=20 s, 25 s, 29 s, (*d*), (*e*): Q=1.5 lt/min, T=88 s, t=20 s, 74 s, (*f*), (*g*): Q=1 lt/min, T=28 s, t=17 s, 23 s, (*h*): Q=1.5 lt/min, T=11 s, t=8.5 s.

Table 1 The length of vector U compared to da

Fig. nr	U/da
3a,b,c	1.7
3d	5
5e	3.3
3f	3.9
3g,h	2.2
4a,b	2

corresponds to a time instant within the period, designated with a letter in the corresponding graph of the vertical branch flow rate. This flow rate was used for reference due to the much faster electromagnetic flow meter of this branch (500 Hz excitation frequency), compared to the relatively slow one of the mother tube (25 Hz excitation frequency). The branch flow rates were adjusted through valves to be equal in the mean within +/−3% of the mother tube flow rate.

It should be mentioned that for all the examined cases the flow patterns were very much repeatable and the presented velocity vectors, resulting from the PIV, are instantaneous and unfiltered.

(a) Axial Flow. Axial flow was studied in both the horizontal and vertical part of the bifurcation. For the horizontal part, the measured region extended between $x = -8$ mm and $x = 48$ mm, namely, starting 8 mm before entering the bifurcation and ending 8 mm inside the horizontal branch. In the vertical branch, this region extended between $y = 40$ mm and $y = 82$ mm, covering a length of about one hydraulic diameter. In order to study the influence of both the unsteadiness and viscosity on the flow field, nine combinations of Reynolds and Womersley parameters were examined. The maximum flow rate of the mother tube, Q, took three values 0.8, 1.5 and 2 lt/min, and T, its period, 88, 28, and 11 s, respectively. According to these values, the maximum Re (where $\mathrm{Re} = Q/b\nu$ and b, the side of the tube cross section) was 330, 618, and 824 (their average values were 198, 355, and 453, respectively) and $\alpha = b/2\sqrt{2\pi/\mathrm{T}\nu}$ (where $b/2$ is the hydraulic radius) was equal to 5.31, 9.42, and 15.02. These values are normally found in physiological flows ([24,25]).

(a1) Horizontal Part. The flow behavior was examined during acceleration, deceleration and flow peak for various combinations of Re and α. In Fig. 3(a–h), the measured velocity vectors are shown in the mid-plane of the bifurcation, in which the flow is from left to right and upwards, and the distance, da, between two adjacent vectors is 24 pixels or 5.25% of b. Since the scaling of the vector's magnitude is not the same for all figures, in order to facilitate any comparisons the length of the velocity vector $U = Q/b^2$ is given in Table 1 for each case as a function of da. The time instant of each figure is shown in the corresponding flow rate graph of the vertical branch.

In this region, during deceleration, negative flow appears close to the bottom wall ($y = 0$) and extends both upwards and upstream as time proceeds. Depending upon Re and α, the formed shear layer either rolls up, being transformed into discrete vortical structures or is straight, intersecting the bottom wall at an angle.

In Fig. 3(a)–3(c) the flow field is shown for Re=824 and $\alpha = 5.31$ ($Q = 2$ lt/min, T=88 s) at three time instants during the deceleration phase. More particularly, at $t = 76$ s (Fig. 3(a)), a shear layer emanates from the bottom wall, generating at a later instant ($t = 80$ s) (Fig. 3(b)) a clockwise vortical structure. The approximate location of the center of this structure is at $x = 42$ mm, and $y = 10.5$ mm and its maximum nondimensional circulation $\Gamma/Ub = 0.48$. The circulation, Γ, was calculated according to its definition by numerically computing the closed line integral of the dot product of the velocity vector times the line element along rectangles, which included the center of the vortex. A similar procedure was followed in a previous work (Wilder, et al. [26]) for the case of vortices shed downstream of a pitching airfoil. While this vortex moves downstream and upwards out of the examined area, another vortex is created at $t = 84$ s (Fig. 3(c)) at an upstream location ($x = 21$ mm, $y = 7.4$ mm) with $\Gamma/Ub = 0.19$. This vortex essentially does not move because of the small flow rate of this phase. However, it is soon diffused, taking the shape of an ellipse whose longer axis is parallel to the model bottom wall. Other flow features at $t = 84$ s are the appearance of a saddle point ($x = 39.9$ mm, $y = 16.8$ mm), the parabolic type profile in the mother tube (left side of the graph) and the negative flow at the entrance of the vertical branch.

Keeping the same value of α, but reducing Re down to 330, there was no vortex generation observed (Fig. 3(d)). For this condition a straight shear layer appears with its zero velocity points being along a line, which at $t = 14$ s intersects the bottom wall at an angle of 25 degrees. It is clear that a reduction of Re is associated with a damping of flow instabilities. In a previous work (Mathioulakis et al. [7]) in the same model and under steady inlet conditions and higher Re=1200, vortex shedding in the same area of the model was very strong.

With Re constant at 330, an increase of α from 5.31 (T = 88 s) to 9.42 (T = 28 s) reduced the width of the negative flow region (Fig. 3(d, e)). When α was further increased to 15.02 (T = 11 s), this region was compressed close to the bottom wall, even for higher values of Re (Re=824) while at the same time no vortices were generated (Fig. 3(f)). Therefore, when increasing the Womersley parameter, unsteady inertial forces overwhelm viscous ones, reducing the influence of the latter only in a thin region close to the tube bottom wall.

During acceleration and before flow peak, vortices and any separated flow regions which have been generated close to flow minimum are washed out. As a result, the flow is attached at the bottom wall before the flow peak for all the examined cases. During this phase, the direction of the flow turns progressively towards the vertical branch, starting at the entrance of this branch and expands both downstream and towards the bottom wall (Fig. 3(g, h)). During deceleration, an opposite process takes place due to flow separation at the bifurcation leading edge, which turns the flow horizontal again. Another point which is noteworthy is the bluntness of the velocity profile during acceleration in the mother tube (left side of Fig. 3(g, h)), compared to the parabolic type profile during deceleration (Fig. 3(a, b, c)). This is attributed to the fact that the low momentum fluid close to the walls reacts more rapidly to the imposed time varying pressure gradient, compared to the central region. Similar behavior has been observed in external flow applications (Mathioulakis and Telionis [27,28]).

At the flow peak plateau, as time goes by a negative flow region appears at the bottom wall and then expands upstream, similar to that region which appears under steady conditions. During deceleration this region expands further upstream due to the imposed adverse pressure gradient. As an example, for Re=824 and $\alpha = 5.31$ when $t \leqslant 15$ s (a little before the onset of flow acceleration) the entire bottom wall mid plane is covered by negative velocities. At $t = 22$ s (before the flow peak), the flow is attached and at about the middle of flow peak plateau ($t = 46$ s) negative flow appears at $x = 27.3$ mm which during deceleration moves upstream. Namely, at $t = 76$ s this is at $x = 18$ mm, four seconds later at $x = 12.6$ mm and six seconds later at $x = 4$ mm. The above estimates are based on measurements which are not shown for reasons of space economy.

(a2) Vertical Part. Since the fluid entering the vertical branch changes its direction by 90 degrees, the streamlines are curved, causing a transverse pressure gradient which points toward the center of the curvature. This pressure gradient, along with the centripetal forces exerted upon the fluid particles, are responsible for the appearance of strong velocities perpendicular to the axial flow of this branch (see following paragraph). Concerning the axial flow characteristics, during acceleration, for all the examined cases, a counter-clockwise vortex is generated at the leading edge bifurcation apex ($x = 0$, $y = 40$ mm), moving stream-

Table 2 The length of vector U compared to ds

Fig. nr	U/ds
5a	10.9
5b	5.3
5c	2.7
5d, e	8.7
5f, g	5
5h	3.7

wise and toward the center of the cross-section. In Fig. 4(*a*) this vortex for Re=824 and $\alpha=15.02$ is shown at $t=4$ s. In the same figure there is negative flow in the lower left part of the examined area. Three seconds later, when the flow starts to decelerate, this vortex has almost degenerated, and negative flow covers more than half of the examined area parallel to the tube wall (Fig. 4(*b*)). The length of the velocity vector *U* is given in Table 1 as a function of the distance, da, of two adjacent vectors. In both figures, the streamwise velocity profiles are highly skewed, taking higher values next to the wall of the bifurcation trailing edge ($x=40$ mm). This velocity skewness is characteristic in tube bends for relatively low Re. Also, it is noteworthy that after the positive flow turns by 90 degrees, the flow has the tendency to move towards the bifurcation leading edge (Fig. 4(*b*)). During deceleration, the width of the negative flow region increases, allowing the flow to enter the branch only from an area close to $x=40$ mm (see Fig. 3(*a*, *e*)).

(b) Secondary Flow. The secondary flow was examined at plane $y=60$ mm, namely 20 mm distal of the vertical branch inlet. The selection of this measuring station was based on the desire to record high secondary velocities which were expected to be here due to the high streamline curvature. This was also predicted by Rindt and Steenhoven [29] in a carotid artery bifurcation, Perktold et al. [30] in a coronary artery branch and Ethier et al. [31] in an end-to-side anastomosis geometry. That is, secondary velocities were strong at the inlet of the branches which died out further downstream. The examined cases of flow rate *Q* were 0.8, 1 and 1.5 lt/min, maximum Re was 330, 412, and 618, and T took the same values as before. Maximum flow rate was 1.5 lt/min, which is smaller than that the maximum flow rate of the axial case, a necessary condition for the particles to remain in the light sheet long enough for the PIV be successful.

Some of the most significant flow features will be presented below, amongst the examined combinations of Re and α. In Fig. 5 the secondary flow velocity vectors are shown, where the distance between two adjacent vectors, ds, is 1.66 mm or 4.15% of *b*. The length of the velocity vector *U* is given in Table 2 as a function of ds. In each figure (5(*a*–*h*)), the side of the cross section to the right is closer to the center of curvature.

For Re=412 and $\alpha=5.31$ ($Q=11$ lt/min, T=88 s), during early acceleration ($t=20$ s) the secondary flow is almost uniformly directed toward the outer bend side ($x=40$ mm) without any Dean vortices being present (Fig. 5(*a*)). At $t=25$ s, almost half of the flow changes its direction by 180 deg moving toward the center of curvature (Fig. 5(*b*)). Apparently this is a result of the arrival of the counter-clockwise vortex having an axis perpendicular to the main flow of this branch and originally generated at the bifurcation leading edge apex (see Fig. 4). A little later and close to the flow peak, two counter-rotating vortices are generated, the so-called Dean vortices (Fig. 5(*c*), $t=29$ s), with centres located toward the outer bend side. As time proceeds, these vortices become more rounded without tails, and the secondary flow is essentially restricted close to the two corners of the tube outer bend. Vortex circulation Γ/Ub, was reduced during deceleration (in all the examined cases), resulting in the following values: 0.293 at $t=70$, 0.277 at $t=76$, 0.164 at $t=84$ s and 0.138 at $t=87$ s. This reduction of vortex strength was anticipated due to the reduction of the flow rate and the resulting lowered centripetal forces. At flow minimum when the flow is almost zero, the Dean vortices existed for about 10 s, but later they dissipated. As it was pointed out by Komai and Tanishita [32] for an intermittent flow in a curved tube, there is secondary flow dissipation during long minimum flow phases, which in turn influences the acceleration phase. Similar conclusions were drawn for Re=330 and $\alpha=5.31$. However, when increasing Re to 618, and keeping α constant, in contrast to previous cases only one clockwise vortex was present during acceleration (Fig. 5(*d*), $t=20$ s) with $\Gamma/Ub=0.272$. At $t=22$ s the strength of this vortex was reduced and as in the previous procedure, two Dean vortices were born before flow peak. During the end of the period, close to flow minimum, the counter-clockwise Dean vortex progressively lost strength (Fig. 5(*e*) $t=74$ s) while the clockwise Dean vortex spread out, moving at the same time towards the center of the cross-section. As a result, only this vortex appears in the subsequent acceleration phase. A similar phenomenon was predicted by Perktold et al. [33] for a carotid siphon model, where a unique secondary vortex was found downstream of a tube bend when at the minimum physiological flow rate. This was the only case among all the cases we studied that one secondary vortex was found. It has to be stressed that repeating the experiment after a few days the same phenomenon was observed.

Increasing α from 5.31–9.42, the basic change in the secondary flow, for all the examined Re, was the existence of two Dean vortices instead of one during acceleration, located closer to the outer bend side. Apparently, the smaller period of the zero flow phase, allows the conservation of vortex circulation in the acceleration phase. This was also verified numerically by Komai and Tanishita [32], who found that the secondary flow in the acceleration phase was reconstructed by residual vortices of the previous deceleration phase. For Re=412 and $\alpha=9.42$ at flow peak, there was an interesting flow pattern consisting of four Dean vortices (Fig. 5(*f*) which lasted until the end of this phase. As it is shown in Fig. 5(*f*) one pair was close to the outer bend and the other pair close to the inner bend. Later on, there were again only two secondary vortices present (Fig. 5(*g*)). It seems that the four vortex pattern is not a stable one. Hamakiotes and Berger [16] in a numerical study predicted four secondary vortices in a curved tube which were present only during acceleration. Of course these vortices, in contrast to our observations, were two Dean and two Lyne type vortices. Also, Winters [19] in a stability analysis of the flow in a rectangular curved tube showed that among multiple vortex solutions the most stable is the two vortex one.

Further increasing α to 15.02 we expected to see the so-called Lyne type vortices predicted by several studies in curved tubes in which these vortices appeared during acceleration but before flow peak, when α is greater than 10 (Munson [34], Chang and Tarbell [5], Sudo et al. [18]). However, the common element of the three flow rates in our experiment for $\alpha=15.02$ was that during acceleration the secondary vortices were not Lyne type and not well shaped. Only during the end of the cycle in the late deceleration phase were the Dean vortices well organised (Fig. 5(*h*), Re=618, $\alpha=15.02$). According to the numerical work of Hamakiotes and Berger [16], on pulsating flow in a curved tube, there were no Lyne vortices predicted when Re was low, independent of the Womersley parameter, which varied between 7.5 and 25. Concerning the magnitude of circulation, this was of the same order as in all the other cases. It should be mentioned that according to a numerical finding of Rindt et al. [17] the secondary vortices for $\alpha=24.7$ were 50 times smaller that those for $\alpha=7.8$ in contrast we found that there was no such tendency. Also, the maximum secondary flow velocities were of the order of 0.6U for all the examined cases, a value 20% higher than the maximum bulk velocity of this branch. LDA measurements in the same model and under steady conditions revealed the same order of secondary velocities (Mathioulakis et al. [7]). Such high secondary flow velocities were also found by Ethier et al. [31] in a 45-degree junction for steady flow.

Conclusions

The flow field in a 90-degree asymmetric bifurcation was studied experimentally using PIV under pulsating conditions and equal mean branch flow rates. The examined peak Reynolds number Re was in the range 330 to 830, and the Womersley parameter α between 5 and 15. In the extension of the mother tube, during deceleration the axial flow separated from the bottom wall opposite of the vertical branch forming a shear layer. For low α (5.31) and low Re (330) the shear layer did not roll up, in contrast to higher Re (618, 824) and low α that was transformed into discrete vortices during flow minimum. Increasing α to 15.02, there was a negative flow region formed close to the bottom wall, without any vortices, independently of Re. Apparently for high α, viscosity effects are limited close to the tube walls, while for low α, any amplification of flow instabilities is associated with a Reynolds number increase. During acceleration, negative flow regions or existing vortices from the previous phase are washed out and, the flow becomes attached prior to flow peak. At the flow peak plateau unsteadiness is diminished, and the flow tends to behave like that one under steady conditions. A negative flow region appears opposite to the vertical branch as in the case of steady flow.

The most characteristic axial flow pattern in the vertical branch is the formation of a vortex at the bifurcation leading edge apex during early acceleration. This vortex moves streamwise and towards the center of the cross section where it degenerates. The streamwise velocity profile is highly skewed with its maximum being close to the outer bend side and negative flow appears close to the inner bend, spreading out during deceleration.

For the secondary flow of the vertical branch, the main conclusions are as follows: For low α and low Re during early acceleration there are no Dean vortices. However, increasing α there are normally present two counter-rotating Dean vortices during this phase. For all the examined cases it is characteristic that before the flow peak any existing vortices are destroyed and two new are born. This phenomenon is associated with the appearance of the vertical branch axial flow vortex, which destroys any secondary flow patterns of the previous phase. During flow peak plateau and deceleration these vortices become more coherent located close to the outer bend side of the cross section. Maximum secondary velocities were on the order of 20% higher than the bulk velocity of this branch. During deceleration, the strength of the vortices is progressively reduced. Yet for higher values of α, the vortices remain part of the flow until the subsequent acceleration phase.

The objective of this work was to provide information about time-dependent flow phenomena in a duct bifurcation. The presented velocity vectors exhibited details of the temporal evolution of the flow field and revealed its complexity. Due to the idealized conditions of the experiment (90-degree bifurcation, equal branch flow rates, equal cross-sectional areas) and the non-circular tubes of the model, these findings cannot be used directly to applications concerning the human circulatory system. However, these results might provide some guidelines for understanding the flow mechanisms in real vascular bifurcations where the blood flow is even more complex, and hopefully assist medicine in facing vascular diseases more effectively.

Acknowledgments

This work was partly supported by the Greek General Secretariat of Research and Technology. Thanks are also extended to the valuable criticism of the reviewers.

References

[1] Caro, C. G., Fitz-Gerald, J. M., and Schroter, R. C., 1971, ''Atheroma and Arterial Wall Shear. Observation, Correlation and Proposal of a Shear Dependent Mass Transfer Mechanism for Atherogenesis,'' Proc. R. Soc. London, Ser. B, **B177**, pp. 109–159.

[2] Ku, D. N., Giddens, D. P., Zarins, C. K., and Glagov, S., 1985, ''Pulsatile Flow and Atherosclerosis in the Human Carotid Bifurcation,'' Rev. Mod. Astron., **5**, pp. 293–302.

[3] Fry, D. L., 1968, ''Acute Vascular Endothelial Changes Associated with Increased Blood Velocity Gradients,'' Circ. Res., **22**, pp. 165–197.

[4] Salzar, R. S., Thubrikar, M. J., and Eppink, R. T., 1995, ''Pressure-Induced Mechanical Stress in the Carotid Artery Bifurcation: a Possible Correlation to Atherosclerosis,'' J. Biomech., **28**(11), pp. 1333–1340.

[5] Chang, L.-J., and Tarbell, J. M., 1985, ''Numerical Simulation of Fully Developed Sinusoidal and Pulsatile (Physiological) Flow in Curved Tubes,'' J. Fluid Mech., **161**, pp. 175–198.

[6] Pedersen, E. M., Yoganathan, A. P., and Lefebvre, X. P., 1992, ''Pulsatile Flow Visualization in a Model of the Human Abdominal Aorta and Aortic Bifurcation,'' J. Biomech., **25**(8), pp. 935–944.

[7] Mathioulakis, D. S., Pappou, Th., and Tsangaris, S., 1997, ''An Experimental and Numerical Study of a 90° Bifurcation,'' Fluid Mech. Res., **19**, pp. 1–26.

[8] Schinas, D., and Mathioulakis, D. S., 2000, ''Pulsating Flow in a 90 Degree Bifurcation,'' ASME J. Fluids Eng., **122**, pp. 569–575.

[9] Yoganathan, A. P., Ball, J., Woo, Y.-R., Philpot, E. F., and Sung, H.-W., 1986, ''Steady Flow Velocity Measurements in a Pulmonery Artery Model with Varying Degrees of Pulmonic Stenosis,'' J. Biomech., **19**(2), pp. 129–146.

[10] Sung, H.-W., and Yoganathan, A. P., 1990, ''Axial Flow Velocity Patterns in a Normal Human Pulmonery Artery Model: Pulsatile in Vitro Studies,'' J. Biomech., **23**(3), pp. 201–214.

[11] Dean, W. R., 1927, ''Note on the Motion of Fluid in a Curved Pipe,'' Philos. Mag., **4**(7), pp. 208–223.

[12] Dean, W. R., 1928, ''The Streamline Motion of Fluid in a Curved Pipe,'' Philos. Mag., **5**(7), pp. 673–695.

[13] Lyne, W. H., 1970, ''Unsteady Viscous Flow in a Curved Pipe,'' J. Fluid Mech., **45**, Part 1, pp. 13–31.

[14] Smith, F. T., 1975, ''Pulsatile Flow in Curved Pipes,'' J. Fluid Mech., **71**, Part 1, pp. 15–42.

[15] Talbot, L., and Gong, K. O., 1983, ''Pulsatile Entrance Flow in a Curved Pipe,'' J. Fluid Mech., **127**, pp. 1–25.

[16] Hamakiotes, C. C., and Berger, S. A., 1990, ''Periodic Flows Through Curved Tubes: the Effect of the Frequency Parameter,'' J. Fluid Mech., **210**, pp. 353–370.

[17] Rindt, C. C. M., van Steenhoven, A. A., Janssen, J. D., and Vossers, G., 1991, ''Unsteady Entrance Flow in a 90° Curved Tube,'' J. Fluid Mech., **226**, pp. 445–474.

[18] Sudo, K., Sumida, M., and Yamane, R., 1992, ''Secondary Motion of Fully Developed Oscillatory Flow in a Curved Pipe,'' J. Fluid Mech., **237**, pp. 189–208.

[19] Winters, K. H., 1987, ''A Bifurcation Study of Laminar Flow in a Curved Tube of Rectangular Cross-Section,'' J. Fluid Mech., **180**, pp. 343–369.

[20] Thangam, S., and Hur, N., 1990, ''Laminar Secondary Flows in Curved Rectangular Ducts,'' J. Fluid Mech., **217**, pp. 421–440.

[21] Kao, H. C., 1992, ''Some Aspects of Bifurcation Structure of Laminar Flow in Curved Ducts,'' J. Fluid Mech., **243**, pp. 519–539.

[22] Kostis, A., and Mathioulakis, D. S., 1997, ''Study of Vortical Structures by Means of Particle Image Velocimetry,'' Proc. Second Greek-Italian International Conference on New Laser Technologies and Applications, SPIE Vol. 3423, pp. 286–290.

[23] Koutsiaris, A. G., Mathioulakis, D. S., and Tsangaris, S., 1999, ''Microscope PIV for Velocity-Field Measurement of Particle Suspensions Flowing Inside Glass Capillaries,'' Meas. Sci. Technol., **10**, pp. 1037–1046.

[24] Bharadvaj, B. K., Mahon, R. F., and Giddens, D. P., 1982, ''Steady Flow in a Model of the Human Carotid Bifurcation, Part-I-Flow Visualization. Part 2-Laser Doppler Anemometer Measurements,'' J. Biomech., **15**, pp. 349–378.

[25] Pedersen, E. M., and Yoganathan, A. P., 1990, ''Axial Flow Velocity Patterns in a Normal Human Pulmonary Artery Model: Pulsatile in Vitro Studies,'' J. Biomech., **23**, pp. 201–214.

[26] Wilder, M. C., Mathioulakis, D. S., Poling, D. R., and Telionis, D. P., 1996, ''The Formation and Internal Structure of Coherent Vortices in the Wake of a Pitching Airfoil,'' J. Fluids Struct., **10**, pp. 3–20.

[27] Mathioulakis, D. S., and Telionis, D. P., 1987, ''Velocity and Vorticity Distributions in Periodic Separating Laminar Flow,'' J. Fluid Mech., **184**, pp. 303–333.

[28] Mathioulakis, D. S., and Telionis, D. P., 1989, ''Pulsating Flow Over an Ellipse at an Angle of Attack,'' J. Fluid Mech., **204**, pp. 99–121.

[29] Rindt, C. C. M., and Steenhoven, A. A. v., 1996, ''Unsteady flow in a Rigid 3-D Model of the Carotid Artery Bifurcation,'' ASME J. Biomech. Eng., **118**, pp. 90–96.

[30] Perktold, K., Hofer, M., Rappitsch, G., Loew, M., Kuban, B. D., and Friedman, M. H., 1998, ''Validated Computation of Physiologic Flow in a Realistic Coronary Artery Branch,'' J. Biomech., **31**, pp. 217–228.

[31] Ethier, C. R., Prakash, S., Steinman, D. A., Leask, R. L., Cough, G. G., and Ojha, M., 2000, ''Steady Flow Separation Patterns in a 45 Degree Junction,'' J. Fluid Mech., **411**, pp. 1–38.

[32] Komai, Y., and Tanishita, K., 1997, ''Fully Developed Intermittent Flow in a Curved Tube,'' J. Fluid Mech., **347**, pp. 263–287.

[33] Perktold, K., Florian, H., Hilbert, D., and Peter, R., 1988, ''Wall Shear Stress Distribution in the Human Carotid Siphon During Pulsatile Flow,'' J. Biomech., **21**, No. 8, pp. 663–671.

[34] Munson, B. R., 1975, ''Experimental Results for Oscillating Flow in a Curved Pipe,'' Phys. Fluids, **18**, pp. 1607–1609.

Concentration Measurements in a Pressurized and Heated Gas Mixture Flow Using Laser Induced Fluorescence

Philippe Guibert
e-mail: guiber@ccr.juss.ieu.fr

William Perrard

Céline Morin

Laboratoire de Mécanique Physique,
Groupe Fluides Réactifs,
Université Pierre et Marie Curie Paris 6-CNRS,
2, place de la Gare de Ceinture,
78210 Saint-Cyr-l'Ecole,
France

The fuel concentration in a pressurized and heated gas mixture flow was measured by LIF (laser induced fluorescence) technique. Diacetyl was used as the fluorescence tracer of fuel and was excited at a wavelength of 355 nm. Influent parameters on the LIF intensity among the equivalence ratio, the environment temperature and pressure, the flow velocity were determined from a parametric study. The technique of plans of experiments with statistical tests and analysis was investigated to determine exactly the preponderant parameters and their influence on the LIF intensity. For the experimental conditions explored in this work, the value of the LIF intensity was calculated by developing a quadratic model. By inversion of the transfer function, the equivalence ratio was deduced with a low mean relative error. [DOI: 10.1115/1.1456462]

Introduction

Laser induced fluorescence (LIF) is a technique widely developed for the study of the mixture formation in internal combustion (IC) engines with the measurements of species concentration, temperature, and the flow visualization [1–4]. Flow fields can be characterized thanks to this technique by providing qualitative or semi-quantitative information. To obtain quantitative measurements in an engine, the fuel concentration, the environment temperature and pressure must be exactly known, the LIF intensity is in fact affected by these parameters. The object of this study is then to investigate LIF experiments in a pressurized and heated gas mixture flow to underline the influent parameters between the temperature, the pressure, the flow velocity, and the fuel concentration on the LIF intensity.

LIF is the light emitted by an atom or molecule following excitation by a laser beam. In a simplified approach, the molecule could be in two levels. The first one of energy E_1 and population N_1 is the ground level, the second one of energy E_2 and population N_2 is the excited level. The excited species reaches an upper electronic energy level. Besides spontaneous emission of light (fluorescence), the molecule can be returned to its original electronic state by different processes: stimulated emission, inelastic collisions with other molecules, that is referred to as "quenching," or to near quantum states by rotational or vibrational energy transfers, internal energy transfer and dissociation of the molecule [1].

According to the laser intensity, two regimes of fluorescence will be characterized. At low laser intensity, when the spectral intensity of the incident laser light is strongly lower than the saturation intensity, the regime is called the "linear fluorescence regime." The LIF signal is then linearly proportional to the incident laser power. Inversely, when the spectral intensity of incident laser light is strongly higher than the saturation intensity, the regime is called the "saturation fluorescence regime." In this work, the regime is linear in energy and the fluorescence flux is then given by the following expression:

$$\Phi = N_0^1 \cdot \frac{A_{21}}{A_{21}+Q_{21}} \cdot I_v \cdot \frac{B_{12}\cdot \varepsilon \cdot \Omega \cdot V_c}{4\pi}. \tag{1}$$

where N_0^1 corresponds with the number density of the absorbing species in the ground state, A_{21} the Einstein coefficient for spontaneous emission (fluorescence), Q_{21} the quenching rate constant, B_{12} the Einstein coefficient for stimulated emission, I_v the spectral intensity of incident laser light, ε the detection efficiency of the collection system, Ω the solid angle of collection optics, and V_c the collection volume.

In the linear regime, the quenching rate constant could be

Table 1 Summary of LIF experiments reported in the literature

Laser source	Dopant	Reference
KrF 248 nm	3-pentanone (2 vol. %)	Neij et al. [3] Johansson et al. [4]
	N,N-dimethylaniline (0.2 vol. %)	Itoh et al. [5] Urushihara et al. [6] Hishinuma et al. [7]
	Toluene (5 vol. %)	Reboux et al. [8, 9]
	3-pentanone (5 vol. %)	Knapp et al. [10]
	Gasoline (10 vol. %)	Kim et al. [11]
	Triethylamine (2 vol. %) / benzene (2.9 vol. %)	Krämer et al. [12]
Nd:YAG 266 nm	3-pentanone (5 vol. %)	Ghandi et al. [13]
	Acetone (17 vol. %)	Fujikawa et al. [2, 14]
XeCl 308 nm	3-pentanone (5 vol. %)	Arnold et al. [15]
	Acetone	Wolff et al. [16]
	Aldehydes (9.1 vol. %)	Swindal et al. [17]
	Fluoranthene (<1 mass %)	Meyer et al. [18]
	3-pentanone (25 vol. %)	Berckmüller et al. [19, 20]
Nd:YAG 355 nm	Diacetyl (2-6 vol. %)	Baritaud & Heinze [21] Deschamps et al. [22, 23] Depussay et al. [24]

Data from Refs. [3–24] are included in Table. with iso-octane as fuel

---

Contributed by the Fluids Engineering Division for publication in the JOURNAL OF FLUIDS ENGINEERING. Manuscript received by the Fluids Engineering Division November 1, 2000; revised manuscript received December 19, 2001. Associate Editor: J. Lasheras.

Table 2 Studies on the influence of pressure and temperature on the LIF intensity for several combinations of fluorescence tracer and excitation wavelength

Reference	Excitation Wavelength	Gas	Dopant	Experimental range
Cruyningen et al. [29]	351 nm	Nitrogen	Diacetyl	P=0.1 MPa T=300 K
Lawrenz et al. [30]	308 nm	Air	Diacetyl Acetone Ethylmethylketone Diethylketone Acetaldehyde Valeraldehyde	P=0-0.5 MPa T=300 K
Grossmann et al. [31]	248 nm	Air Oxygen Nitrogen	Acetone 3-pentanone	P=0-0.5 bar / T=383 K or P=0.1 MPa / T=383-640 K
	277 nm		3-pentanone	
	312 nm		3-pentanone	
Yuen et al. [32]	266 nm	Air Nitrogen Methane Helium	Acetone	P=0-0.8 MPa T=273 K
Fujikawa et al. [2, 14]	248 nm	Iso-octane	Acetone 3-pentanone Toluene Ethyl pentyl ketone Propionaldehyde n-valeraldehyde	P=0.1-1 MPa T=373-573 K
	266 nm		Acetone 3-pentanone Toluene	
Krämer et al. [12]	248 nm	Air	Toluene Xylene 3-pentanone Acetone	P=0.1-1.5 MPa T=423 K
	276 nm			
	312 nm			
Bryant et al. [33]	266 nm	Air	Acetone	P=0.02-0.1 MPa T=240-300 K

Data from Refs. [2], [12], [14], [29–33] are included in Table.

evaluated to make quantitative measurements. However, this rate is sensitive to the pressure, the temperature, and the composition. Quantitative measurements by the LIF technique are then difficult to investigate. LIF technique is essentially used for imaging flow or fuel distributions. In this case, LIF is investigated to characterize qualitatively flow fields. For fuel concentration measurement by LIF, different techniques are usually adopted: either a direct natural fluorescence from the fuel, or a fluorescence from a dopant molecule. The first technique is easily adapted but could be involved errors in the interpretation of results caused by the complex fuel composition. As the majority of fuels do not fluoresce with laser beam in the visible or UV region, the second method is largely developed with the use of dopants or tracers to mark the fuel. Tracers must present satisfactory spectroscopic qualities (low quenching rate by oxygen, limited absorption of the laser beam, good solubility in the fuel, sufficient spectral shift of the fluorescence signal relative to the laser excitation wavelength) and thermodynamic properties (boiling point and latent heat of vaporization similar to the fuel). Two types of dopants, corresponding to the above requirements, are usually used for LIF measurements: aromatic and carbonyl compounds. Fujikawa et al. [2] have evaluated the optimum combination of fluorescence tracer and excitation wavelength which gives the lowest effects of temperature and pressure on LIF intensity. Between ketones, aldehydes and aromatics, acetone and 3-pentanone were selected by the authors in terms of the lowest temperature and pressure dependence on LIF intensity with 266 nm excitation. Aromatics, such as toluene, are strongly quenched by oxygen. Diones present longer excitation and fluorescence band. For example, diacetyl (2,3-butanedione) has an absorption band between 200–480 nm and an emission band between 440–510 nm.

Among all the fuels, iso-octane (trimethyl-2,2,4 pentane) is largely used in LIF measurements for its good transparency to UV light above 250 nm [5]. Moreover, its boiling point corresponds to the 60 percent distillation temperature of gasoline. LIF experiments reported in the literature with this fuel and different dopants are summarized in Table 1.

In experiments reported in Table 1, LIF technique is used for imaging fuel distributions in IC engines, for studying the mixture homogeneity in a single cylinder with the effect of the injection timing, the air/fuel ratio, the engine speed, the swirl and tumble flows, the piston geometry. The dopants listed in Table 1 present satisfactory thermodynamics properties for tracking iso-octane, except fluoranthene with a high boiling point (657 K against 373 K for iso-octane). However, their pumping requires the use of lasers at low wavelength (KrF laser at 248 nm, Nd:YAG laser at 266 nm, XeCl laser at 308 nm). When excited by a laser beam at 355 nm, diacetyl is usually chosen as the tracer in iso-octane [21–24]. Its boiling point of 361 K is close to that of iso-octane. On the other hand, diacetyl decomposes slowly and polymerizes in presence of impurities, that involves a reduction of its effective concentration. Baritaud and Heinze [21] have noticed a decreasing of fluorescence efficiency with time. A fresh mixture of iso-octane and diacetyl must be used for every experiment. After excitation by a laser beam, the diacetyl molecules in the ground state absorb the laser energy and transit to the singlet state. Diacetyl fluoresces then from the first excited singlet state (lifetime: 50 ns, λ: 440–480 nm). Molecules in the singlet state can also transit to the triplet under the perturbation of the spin-orbit coupling [25]. Diacetyl in the triplet state return to the ground state via either intersystem crossing or the phosphorescence transition (lifetime: 1.2 ms, λ: 510–600 nm). Diacetyl molecules may be also deexcited by colliding with other molecules. The quenching rate constant is quite small if these species do not include oxygen. Since phosphorescence and fluorescence differ only slightly in wavelength, both phenomena have been studied extensively for diacetyl [26–28].

The studies reported in Table 2 were investigated to know exactly the temperature and pressure dependence of the LIF intensity. These studies are necessary to determine the influence of preponderant parameters (concentration of oxygen, fuel and tracer, temperature, pressure, flow velocity, laser power . . .) on the LIF signal, before setting about quantitative LIF measurements on IC engines.

In the following sections, the experimental setup developed to follow instantaneously the evolution of the LIF signal, in conditions close to those found in engines, will be described. Then, experimental results will be discussed. A parametric study with the influence of different parameters (dopant volumic fraction, photomultiplier supply voltage, laser power, flow velocity, concentration, pressure, temperature) on the LIF signal will be firstly examined. Finally, from plans of experiments, the significant parameters will be defined. The value of the equivalence ratio could be deduced by inverting a transfer function determined from a quadratic model.

I Experimental Setup

The experimental apparatus (Fig. 1) used to characterize the influence of different parameters, such as pressure, temperature, concentration or velocity on the fluorescence phenomenon consists of a stainless steel tube (external diameter: 16 mm; width: 2 mm) equipped with different sensors and an optical system. The maximum operating pressure of the experimental setup is 0.65 MPa and the maximum temperature is 573 K. The pressure, the temperature, and the gas flow rates are kept constant in time with different regulators installed on the tube composed of four parts.

The first part corresponds with the air circuit, where several sensors control the pressure, the temperature and the volumetric air flow rate. A 5.5 kW electrical heating system regulates the air flow temperature. The second part of the experimental setup concerns the fuel injection in the air flow. The fuel flow rate is controlled by a gearing pump entrained magnetically by a compressed air engine. A large fuel flow rate range (until 1.1 l/min for a pump speed of 6000 rpm) can be explored, and consequently, a large equivalence ratio range (from 0.7 to 1.4). An injector of a domestic fuel boiler is used to introduce and atomize correctly the liquid fuel in the pipe. Two knees of 90 deg allow to homogenize the air-fuel mixture, before being injected into the third part of the experimental set-up, the measurement cell. Pressure and temperature sensors are installed on this cell equipped of three optical quartz windows (10 or 20 mm diameter) for the concentration measurement by LIF. Figure 2 presents in details the optical system for LIF signal measurements. It is composed of a continuous argon laser (300 mW) in UV domain (from 333.6 to 363.8 nm) coupled to an optical fiber (efficiency higher to 80 percent). A focusing lens system gives an incident coherent light beam of 50 μm diameter approximately. A second optical fiber collects the emitted fluorescent signal along the axis perpendicular to the incident light beam. The emitted signal is then filtered to eliminate not only Mie and Rayleigh diffusions (long wave pass filter) but also the phosphorescence signal (from 510 nm for the diacetyl molecule), before reaching a photomultiplier (PM) detector Hamamatsu Side On R4220 supplied in high voltage with an accuracy of 0.2 Volts and a spectral sensibility from 185 nm to 710 nm. After the measurement cell, the experimental setup is composed of the last part concerning the destruction or burning of the air-fuel mixture. A flow rate regulator controls the mixture flow rate and consequently the flow velocity. Below this regulator, the stainless tube widens suddenly to reduce the flow velocity. A pare-flame grid fixes then the flame initiated by a spark plug. On the exhaust pipe, an oxygen sensor calculates the equivalence ratio with an accuracy of 2 percent. This sensor measures the oxygen or carbon monoxide concentration in the exhaust gases, through of the circulation of oxygen ions between two platinum electrodes separated by a ZrO_2 electrolyte [34].

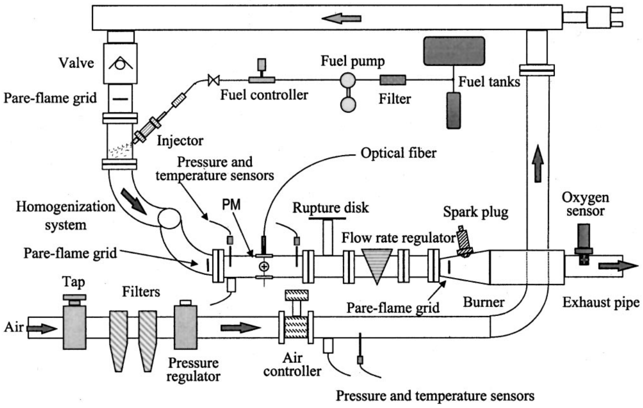

Fig. 1 Experimental setup

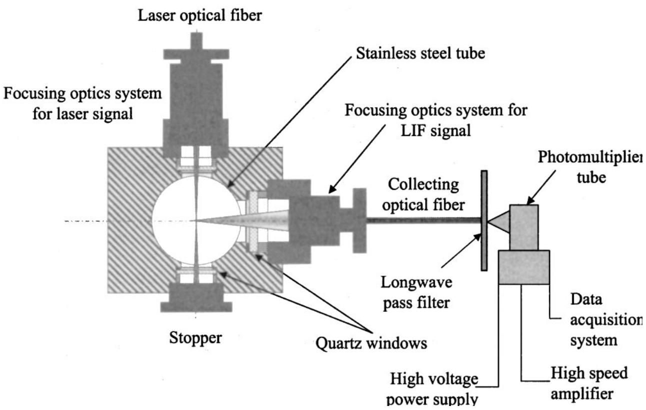

Fig. 2 Optical system for the LIF signal measurement

Table 3 presents equivalence ratio, pressure, temperature and velocity ranges explored in this work. Interactions exist between the parameters controlled on the experimental set up. For example, a flow at a high velocity can not be investigated at a low pressure. Conditions of high temperatures set a minimum air rate to be able to cool the heating element. Concerning the results presented in this paper, diacetyl was chosen as tracer for LIF experiments for its satisfactory thermodynamics and spectroscopic

Table 3 Experimental conditions for the measurement of LIF signal

	Minimum	Maximum	Accuracy
Equivalence ratio	0.7	1.4	2 percent
Pressure (MPa)	0.1	0.65	0.1 percent
Temperature (K)	360	573	0.5 K
Velocity (m/s)	2	30	3.5 percent

properties, when excited by an argon laser at 355 nm. It was mixed at a concentration of 2 percent by volume in iso-octane to produce strong fluorescence signal with little absorption.

II Experimental Results and Discussion

II.1 Parametric Study: Influence of Different Parameters on the LIF Signal. The LIF signal delivered by the photomultiplier could be modified by two groups of parameters. The first one is relative to the physical phenomenon of fluorescence and includes the equivalence ratio, the gas mixture flow temperature and pressure, the flow velocity. The second one concerns the parameters controlled by the experimental setup itself and includes the dopant volumic fraction, the photomultiplier supply voltage and the laser power.

II.1.1 Effect of the Dopant Volumic Fraction, the Photomultiplier Supply Voltage and the Laser Power. As shown in Fig. 3, the evolution of LIF signal versus the laser power presents a linear excitation form in energy for a diacetyl molecule. The two series plotted in Fig. 3 are realized in steady flows for different conditions of temperature, pressure, equivalence ratio, flow velocity and for a diacetyl concentration of 2 percent by volume in iso-octane.

When the photomultiplier supply voltage is fixed to 1000 Volts, a satisfactory compromise is realized between the anode sensitivity and the background noise. The maximum laser power at the output of the optical fiber is set to 280 mW.

A diacetyl volumic fraction between 2–6 percent in iso-octane is usually chosen in LIF experiments [21–24]. When the dopant volumic fraction is low, the laser beam absorption is limited. With the photomultiplier supply voltage and the laser power fixed to 1000 Volts and 280 mW respectively, the amplifier voltage range is totally covered with a diacetyl volumic fraction of 2 percent in iso-octane.

II.1.2 Effect of the Flow Velocity. Equation (1) gives the expression of the fluorescence flux collected by the optical fiber from a two-level model with quenching and without considering phosphorescence phenomenon. In the case of a regime linear in energy, the signal delivered by the photomultiplier is proportional to the spectral density of energy noted U_v:

$$S^{LIF} \approx k_1 \cdot \frac{A_{21} \cdot B_{12}}{A_{21} + Q_{21}} \cdot N_0^1 \cdot U_v \tag{2}$$

With a flow velocity noted V, a cylindrical laser beam of diameter ϕ_{laser}, of height h_{laser} and power P_{laser}, the spectral density of energy received by the diacetyl molecule is given by the following equation:

$$U_v = \frac{4 \cdot P_{laser}}{\pi \cdot h_{laser} \cdot \phi_{laser} \cdot V} \tag{3}$$

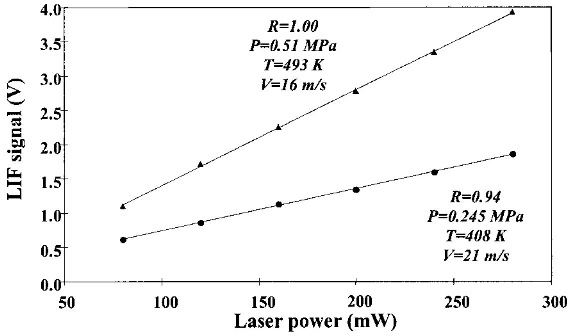

Fig. 3 Evolution of the LIF signal versus the laser power

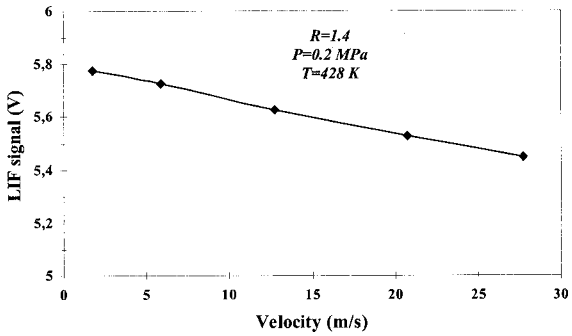

Fig. 4 Evolution of the LIF signal versus the flow velocity

The LIF signal is then inversely proportional to the flow velocity noted V, as expressed in Eq. (4):

$$S^{LIF} \approx k \cdot \frac{A_{21} \cdot B_{12}}{A_{21} + Q_{21}} \cdot N_0^1 \cdot \frac{P_{laser}}{V} \tag{4}$$

As presented in Fig. 4, the flow velocity is not an influent parameter on the LIF signal. For given conditions of equivalence ratio, pressure and temperature, the LIF signal decreases slightly by 0.34 Volts for a flow velocity increasing from 2 m/s to 28 m/s.

II.1.3 Effect of the Equivalence Ratio. When the pressure and the temperature are fixed in the measurement cell to 0.44 MPa and 428 K, respectively, the LIF signal increases linearly with the equivalence ratio increasing, as reported in Fig. 5. This experimental result is in agreement with the expression of the fluorescence flux which depends linearly on the equivalence ratio:

$$\Phi = \frac{\varepsilon \Omega V_c}{4\pi} \cdot \frac{A_{21} \cdot B_{12}}{A_{21} + Q_{21}} \cdot \left(1 - \frac{1}{1 + \frac{R}{R^{sto}} \cdot \frac{M_{air}}{M_{fuel}}} \right) \tag{5}$$

The equivalence ratio measurements are realized according to two methods. For the first five points plotted in Fig. 5, the method consists of modifying the injected fuel flow rate. For the following plotted points, the air flow rate varies. As the same evolution of the LIF signal is obtained by applying either the one or the other method, the LIF signal depends really on the fuel concentration and not only the fuel fraction through the laser beam.

II.1.4 Effect of the Pressure. The LIF signal increases linearly with the pressure increasing for given conditions of temperature and equivalence ratio, as shown in Fig. 6. When the temperature increases from 429 K to 473 K for a pressure and an equivalence ratio fixed to 0.5 MPa and 0.7, respectively, the LIF signal decreases slightly by 0.3 Volts. On the other hand, for the same pressure of 0.5 MPa and a temperature of 473 K, the LIF

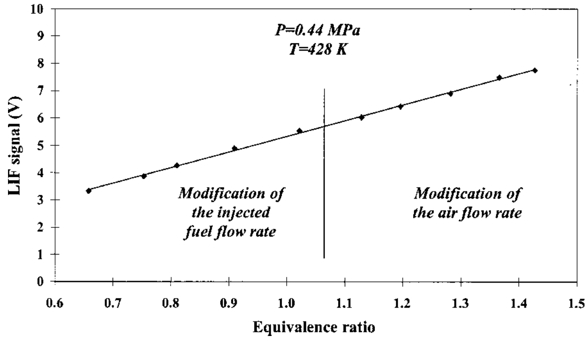

Fig. 5 Variation of the LIF signal versus the equivalence ratio at a pressure of 0.44 MPa and a temperature of 428 K

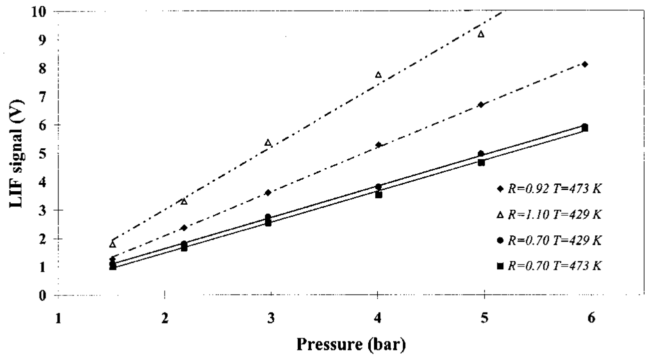

Fig. 6 Variation of the LIF signal versus the pressure at various conditions of equivalence ratio and temperature

signal increases by 2 Volts when the equivalence ratio increases from 0.70 to 0.92. From this parametric study, the equivalence ratio seems to be a more influent parameter than the temperature.

II.1.5 Effect of the Temperature. For constant pressure and equivalence ratio, the LIF signal decreases linearly with the temperature increasing, as presented in Fig. 7. In fact, the fluorescence flux can be expressed as a function of the fuel concentration noted [fuel]:

$$\Phi=\frac{\varepsilon\Omega V_c}{4\pi}\cdot\frac{A_{21}\cdot B_{12}}{A_{21}+Q_{21}}\cdot[fuel] \tag{6}$$

with $[\text{fuel}]=\text{P}_{\text{fuel}}/\text{RT}$ and $\text{R}=8.314\ \text{J}\cdot\text{K}^{-1}\cdot\text{mol}^{-1}$ the universal gas constant

When the quenching rate Q_{21} is neglected in comparison with the Einstein coefficient for fluorescence A_{21}, the evolution of the fluorescence flux versus the temperature is represented by a function $1/x$. For the low temperature range explored in this work, the function $1/x$ can be compared to a linear evolution, as noted experimentally.

From the parametric study, the influent parameters on the LIF signal in the experimental range imposed by the experimental setup have been determined. The equivalence ratio, the pressure, the temperature and their interactions of the first order seem to have an important effect on the LIF signal, which is a linear function versus these three parameters. On the other hand, the flow velocity influence seems to be negligible.

To complete this parametric study, plans of experiments have been investigated to underline the preponderant parameters between the flow velocity, the equivalence ratio, the pressure and the temperature, their interactions and to reduce the large amount of experiments relative to possible values of these parameters. The LIF signal is then expressed as a transfer function from the influent parameters.

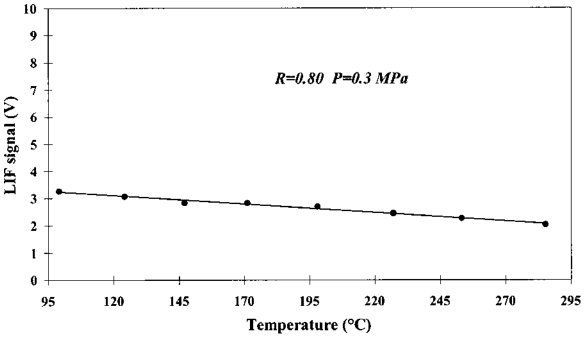

Fig. 7 Variation of the LIF signal versus the temperature at a pressure of 0.3 MPa and an equivalence ratio of 0.80

II.2 Plans of Experiments. To define the preponderant parameters, a statistical analysis is realized from some plans of experiments [35,36]. Three factors are considered simultaneously for experimental abilities: equivalence ratio-flow velocity-pressure (R-V-P plan) or equivalence ratio-pressure-temperature (R-P-T plan).

When the input variables are correctly identified, the physical phenomenon is described by a statistical function from a multilinear regression in a defined experimental range. The linear relation between the physical phenomenon and the input variables is given by Eq. (7):

$$y=\alpha_1\cdot v_1+\alpha_2\cdot v_2+\ \dots+\alpha_j\cdot v_j+\alpha_p\cdot v_p \tag{7}$$

where v_j corresponds to explicative variables (in our case, these variables are the pressure P, the equivalence ratio R, the interactions RT or $\text{T}^2\dots$), α_j are the unknown model coefficients. In our case, Eq. (7) becomes:

$$\begin{aligned}\text{f(R,P,T)}&=\alpha_0+\alpha_1\text{R}+\alpha_2\text{P}+\alpha_3\text{T}+\alpha_{12}\text{R.P}+\alpha_{13}\text{R.T}+\alpha_{23}\text{P.T}\\&\quad+\alpha_{11}\text{R}^2+\alpha_{22}\text{P}^2+\alpha_{33}\text{T}^2\end{aligned} \tag{8}$$

The plan of experiments consists of a test matrix where the columns represent explicative variables and the lines the tests. The hypothesis of the linear model validity can be expressed according to the following equation:

$$y=\sum_{j=1}^{p}\alpha_j\cdot v_j \tag{9}$$

The linear regression provides a fit by optimizing the regression criterion for given actions. The adjustment allows to estimate the mean value of the response for a given combination of explicative variables. The mean value of the response is then estimated from the fit:

$$\hat{y}=\sum_{j=1}^{p}\hat{\alpha}_j\cdot v_j \tag{10}$$

$\hat{\alpha}_j$ are the estimations of α_j. $\hat{y}$ represents the estimation of the mean response. For every test i ($1<i<N$, with N the test number), a difference noted ε_{i} is observed between the value calculated from the adjusted model and the real result:

$$\begin{gathered}y_i=\sum_{j=1}^{p}\hat{\alpha}_j v_j+\varepsilon_i\\ \varepsilon_i=y_i-\hat{y}_i\end{gathered} \tag{11}$$

The coefficients $\hat{\alpha}_j$ are then estimated to minimize an adjustment criterion on ε_{i}, called "the least squared fit":

$$Min\sum_{i=1}^{N}(y_i-\hat{y}_i)^2\ \text{ or }\ Min\sum_{i=1}^{N}\varepsilon_i^2 \tag{12}$$

Using a matrix form, the response is then given by:

$$y=X\cdot\hat{\alpha}+\varepsilon \tag{13}$$

where the response vector (y) has for dimension $N*1$,

the matrix X of explicative variables (v_{ij}) has N lines and p columns,

the vector of estimated coefficients ($\hat{\alpha}$) has for dimension $1*p$,

the residue vector (ε) has for dimension $N*1$.

The expression of the coefficients minimizing the adjustment criterion is:

$$\hat{\alpha}=(X^tX)^{-1}X^ty \tag{14}$$

In a plan of experiments, the causes of the studied phenomenon must be listed and described. These causes are called "actions" and includes the terms "factors" and "interactions," a combination of several factors. The multilinear model expressed in Eq.

Table 4 Matrix of effects for the R-V-P plan

	R	V	P	Effect RV	Effect VP	Effect RP	$\overline{S^{LIF}}$ (V)
Test 1	(-1)	(-1)	(-1)	(+1)	(+1)	(+1)	2.970
Test 2	(+1)	(-1)	(-1)	(-1)	(+1)	(-1)	5.690
Test 3	(-1)	(+1)	(-1)	(-1)	(-1)	(+1)	2.780
Test 4	(+1)	(+1)	(-1)	(+1)	(-1)	(-1)	5.395
Test 5	(-1)	(-1)	(+1)	(+1)	(-1)	(-1)	6.740
Test 6	(+1)	(-1)	(+1)	(-1)	(-1)	(+1)	13.965
Test 7	(-1)	(+1)	(+1)	(-1)	(+1)	(-1)	6.870
Test 8	(+1)	(+1)	(+1)	(+1)	(+1)	(+1)	13.235
Level (-1)	0.75	2.5	0.1				
Level (+1)	1.4	30	0.65				

(13) does not allow to estimate the importance of every factor *f* or action *A*. To have an homogeneity for the different levels of every factor, the factor values must be dimensionless from a centering relation. The factors f take then the value of the level m, called modality (for instance, (-1) and $(+1)$, instead of $P_{\min}=0.1$ MPa and $P_{\max}=0.65$ MPa). In this case, Eq. (14) becomes:

$$\hat{\alpha}^* = (X^{*t}X^*)^{-1}X^{*t}y \tag{15}$$

Equation (15) can be simplified according to some assumptions on the matrix $(X^{*t}X^*)$, as a diagonal matrix by group for instance. The coefficients for the different factors of modality *m* and relative to an action can be easily calculated from the following equation, in the case of an orthogonal plan, that means a plan with similar levels for the different factors [35]:

$$\hat{\alpha}_m^f = \overline{y_m^f} - \overline{y} \tag{16}$$

with $\hat{\alpha}_m^f$ the estimation of the coefficient linked with the modality *m* of the factor *f*, $\overline{y_m^f}$ the mean value of tests where the factor *f* takes the modality *m*,

$$\overline{y} = \frac{1}{N}\sum_{i=1}^{N} \overline{y_i}$$

The modality suffix *m* of the factor *f* varies between 1 and lev(f), the level number of the factor *f*. The factor suffix *f* varies from 1 to *F*, the factor number in the model. The level number depends on the type of the influence. To estimate a linear influence, two levels are sufficient.

Concerning an interaction of two factors, the coefficient of a level mm′ is expressed by:

$$\hat{\alpha}_{mm'}^{ff'} = \overline{y}_{mm'} - \overline{y} - \hat{\alpha}_m^f - \hat{\alpha}_{m'}^{f'} \tag{17}$$

Moreover, these different coefficients $\hat{\alpha}_m^f$ and $\hat{\alpha}_{mm'}^{ff'}$ are used to validate the importance of every factor or action with a statistical analysis based on a calculation of variances $\sigma^2 = \Sigma_{i=1}^{n}(x_i - \overline{x})^2/n$. The law of Snedecor compares the unknown variances σ_1^2 and σ_2^2 of two normal populations at ν_1 and ν_2 freedom degrees. For instance, for two series of results $x_{11}, x_{12}, \ldots, x_{1n1}$ (mean value $\overline{x_1}$) and $x_{21}, x_{22}, \ldots, x_{2n2}$ (mean value $\overline{x_2}$), the variances σ_1^2 and σ_2^2 are estimated by:

$$\hat{\sigma}_1^2 = \frac{\Sigma_{i=1}^{n_1}(x_{1i} - \overline{x_1})^2}{n_1 - 1}$$
$$\hat{\sigma}_2^2 = \frac{\Sigma_{i=1}^{n_2}(x_{2i} - \overline{x_2})^2}{n_2 - 1} \tag{18}$$

In our case, the variance induced by the action *A* is compared with the residual variance induced by the model *M*. Both variances are expressed by Eqs. (19) and (20), respectively:

$$Var(A) = \frac{C(A)}{l(A)} \tag{19}$$

$$ResVar(M) = \frac{\Sigma_{i=1}^{N}(\varepsilon_i)^2}{N - L} \tag{20}$$

with $C(A)$ the contribution of an action A with a number of levels noted lev(A),

$$C(A) = \frac{N}{lev(A)} \sum_{m=1}^{lev(A)} \hat{\alpha}_m^{f^2} \tag{21}$$

l(A) the number of freedom degree for the action *A*,
N the test number,
L the number of freedom degree for the model. *L* represents the minimum test number to realize and corresponds with the sum of the freedom degrees of the actions.

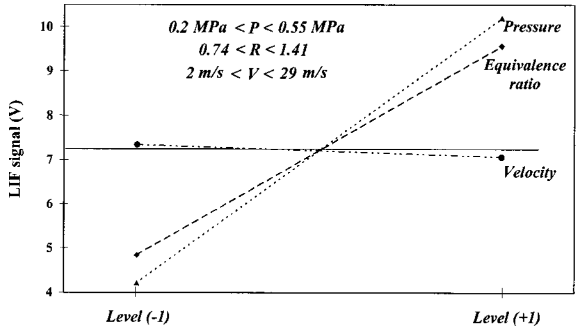

Fig. 8 Influence of the pressure, the equivalence ratio and the flow velocity on the LIF signal

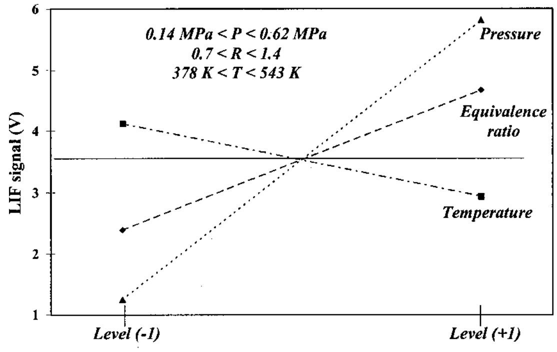

Fig. 9 Influence of the pressure, the equivalence ratio and the temperature on the LIF signal

Table 5 Statistical analysis for the R-V-P plan

Factor	$\hat{\alpha}_m^f$ (Eq. 16) or $\hat{\alpha}_{mm'}^{ff'}$ (Eq. 17)	C(A) Eq. (21)	l(A)	Var(A_j) Eq. (19)	$\hat{F}$ (A_j)= Var(A_j)/Resvar	Conclusion
R	$\hat{\alpha}_{R^-} = -2.366$	89.567	1	89.567	869.58	Significant
	$\hat{\alpha}_{R^+} = 2.366$					
V	$\hat{\alpha}_{V^-} = 0.136$	0.294	1	0.124	2.85	No significant
	$\hat{\alpha}_{V^+} = -0.136$					
P	$\hat{\alpha}_{P^-} = -2.997$	143.712	1	143.712	1395.26	Significant
	$\hat{\alpha}_{P^+} = 2.997$					
RV	$\hat{\alpha}_{R^-V^-} = -0.121$	0.466	1	0.903	4.52	No significant
	$\hat{\alpha}_{R^-V^+} = 0.121$					
	$\hat{\alpha}_{R^+V^-} = 0.121$					
	$\hat{\alpha}_{R^+V^+} = -0.121$					
RP	$\hat{\alpha}_{R^-P^-} = 1.032$	34.081	1	34.081	330.88	Significant
	$\hat{\alpha}_{R^-P^+} = -1.032$					
	$\hat{\alpha}_{R^+P^-} = -1.032$					
	$\hat{\alpha}_{R^+P^+} = 1.032$					
VP	$\hat{\alpha}_{V^-P^-} = -0.014$	0.006	1	0.123	0.06	No significant
	$\hat{\alpha}_{V^-P^+} = 0.014$					
	$\hat{\alpha}_{V^+P^-} = 0.014$					
	$\hat{\alpha}_{V^+P^+} = -0.014$					

To know exactly the importance of every factor, the ratio $\hat{F}(A) = \mathrm{Var}(A)/\mathrm{ResVar}(M)$ is compared with the ratio $F_p = \hat{\sigma}_1^2/\hat{\sigma}_2^2$, where the suffix p can take different values between 0.9 and 0.975, that means a risk between 2.5 percent and 10 percent to make an error by underlining the influence of an action. The ratio F_p is given by the tables of Snedecor with freedom degrees equal to $\mathrm{l}(A)$ and $(N-L)$, for the variance Var(A) and the residual variance ResVar(M), respectively.

In this work, the plans of experiments allow to study p factors, that means 2^p measurements. The matrix X is composed of an alternation between (-1) and $(+1)$ for the column of the first factor, an alternation between (-1) and $(+1)$ from 2 to 2 for the column of the second factor, from 4 to 4 for the column of the third factor. The matrix defined for the equivalence ratio, the flow velocity and the pressure is defined in Table 4 with the mean value of the LIF signal.

The factors have the same number of levels, the effects of the factors R-V-P and R-P-T on the LIF signal can then be plotted (Figs. 8 and 9).

As presented in Fig. 8, the flow velocity has a negligible influence on the LIF signal, whereas the equivalence ratio and the pressure are equivalent effects. Concerning the plan R-P-T (Fig. 9), the flow velocity varies between 2.5 and 30 m/s. The three factors (equivalence ratio, pressure, temperature) have important effects on the LIF signal.

Results of the statistical analysis for the R-P-T and R-V-P plans are summarized in Tables 5 and 6 of the variance analysis, where the significant factors are noted. The exponents $(+)$ and $(-)$ correspond with the levels $(+1)$ and (-1), respectively. The number of tests noted N is equal to 16, the number of freedom degree for the model noted L is equal to 7. Every action has one freedom degree $\mathrm{l}(A)$. For the plans R-V-P and R-P-T, the Snedecor tables give the ratio F_p, with p equal to 0.975, that means a maximum risk of 2.5 percent, with freedom degrees $\mathrm{l}(A)$ and $(N-L)$ equal to 1 and 9, respectively: $F_{0.975}(1,9) = 5.12$. As presented in Table 5, the risk is then lower than 2.5 percent, that the flow velocity from 2.5 to 30 m/s influences the LIF signal. On the other hand, the effects of the equivalence ratio, the pressure and their interac-

Table 6 Statistical analysis for the R-P-T plan

Factor	$\hat{\alpha}_m^f$ (Eq. 16) or $\hat{\alpha}_{mm'}^{ff'}$ (Eq. 17)	C(A) Eq. (21)	l(A)	Var(A$_j$) Eq. (19)	$\hat{F}$ (A$_j$)= Var(A$_j$)/Resvar	Conclusion
R	$\hat{\alpha}_{R^-} = -1.141$	20.821	1	20.821	565.77	Significant
	$\hat{\alpha}_{R^+} = 1.141$					
P	$\hat{\alpha}_{P^-} = -2.281$	83.284	1	83.284	2263.09	Significant
	$\hat{\alpha}_{P^+} = 2.281$					
T	$\hat{\alpha}_{T^-} = 0.594$	5.645	1	5.645	153.40	Significant
	$\hat{\alpha}_{T^+} = -0.594$					
RP	$\hat{\alpha}_{R^-P^-} = 0.826$	21.820	1	21.820	592.91	Significant
	$\hat{\alpha}_{R^-P^+} = -0.826$					
	$\hat{\alpha}_{R^+P^-} = -0.826$					
	$\hat{\alpha}_{R^+P^+} = 0.826$					
RT	$\hat{\alpha}_{R^-T^-} = -0.236$	1.786	1	1.786	48.53	Significant
	$\hat{\alpha}_{R^-T^+} = 0.236$					
	$\hat{\alpha}_{R^+T^-} = 0.236$					
	$\hat{\alpha}_{R^+T^+} = -0.236$					
PT	$\hat{\alpha}_{P^-T^-} = -0.351$	3.942	1	3.942	107.13	Significant
	$\hat{\alpha}_{P^-T^+} = 0.351$					
	$\hat{\alpha}_{P^+T^-} = 0.351$					
	$\hat{\alpha}_{P^+T^+} = -0.351$					

tions of the first order on the LIF signal are significant, for ranges from 0.75 to 1.4 and 0.1 to 0.65 MPa, respectively.

As indicated in Table 6, the equivalence ratio, the pressure, the temperature and their interactions of the first order are significant at 97.5 percent for the following ranges: from 0.7 to 1.4, from 0.14 to 0.62 MPa and from 378 K to 543 K.

II.3 Transfer Function. The transfer function allows to estimate the value of the LIF signal for given experimental conditions. The polynomial models are well adapted; they are not linked to the physical mechanism and are linear against the different coefficients. If the pressure and the temperature are known, the value of the equivalence ratio could be determined from the inversion of this transfer function.

The following quadratic model is studied:

$$f(R,P,T) = \alpha + \alpha_1 R + \alpha_2 P + \alpha_3 T + \alpha_{12} R.P + \alpha_{13} R.T + \alpha_{23} P.T + \alpha_{11} R^2 + \alpha_{22} P^2 + \alpha_{33} T^2 \tag{22}$$

Box and Draper [37] have developed a methodology for the quadratic models. This technique uses a heterogeneous centered plan of experiments, where the factors are five levels (Fig. 10). Ten constants must be determined. The interactions between the different factors are analyzed from this plan. The point at the center of the experimental range is the alone repeated scheme of the plan; the problem of the measurement repeatability is then investigated. The star points, noted (γ) in Fig. 10, represent two tests by factors. Every factor takes then five different levels of the plan.

The value (γ) is chosen from a criterion developed by Box and Draper [37]. The variance of the response defined by the model must be a polynomial function of the distance to the domain center. The value (γ) is then given by:

$$\gamma = N_f^{1/4} \tag{23}$$

with N_f the number of points for the plan.

In our case, the Box and Draper criterion gives $\gamma \approx 1.68$. The levels of the different factors are noted in Table 7.

The coefficients of the transfer function are estimated by identification with the elements given by the following equation:

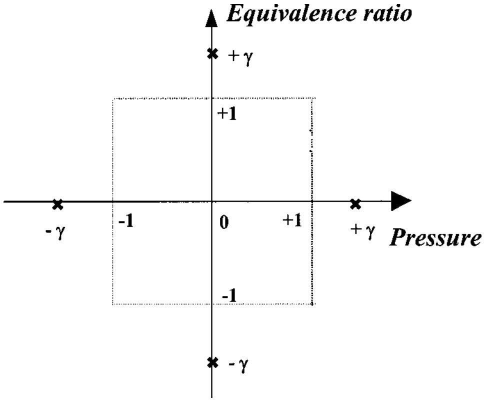

Fig. 10 Example of a heterogeneous centered plan with two factors (equivalence ratio and pressure)

$$\hat{\alpha}=(X^tX)^{-1}X^ty \tag{24}$$

where y is the response vector (15*1) of the LIF signal, X is the matrix of the plan (15*10).

Table 8 presents the estimated coefficients of the model which minimizes the sum of the squared residual differences between the measured responses and the estimated responses.

The mean relative error for the 15 points used in the calculation of the model coefficients for the LIF signal is equal to 2.36 percent. The real phenomenon in the considered experimental range must be correctly explained by the coefficients of the model. The variance analysis applied to the fit allows to check if a dodge to the model exists and if the fit is significant. The residual variance of the model is then compared to the variance of the measurements by a Snedecor test. Concerning the LIF signal, when the quadratic model is applied with 10 experimental points not used in the calculation of the model coefficients, the mean relative error between the calculated LIF signal and the measured one is lower to 3.1 percent. For the points outside the experimental range, the errors are lower to 9 percent.

If the quadratic model is inverted, the equivalence ratio can be expressed from:

$$S^{\mathrm{LIF}}=f(R,P,T) \quad \text{to} \quad R=g(S^{\mathrm{LIF}},P,T) \tag{25}$$

For the test i:

$$S_i^{LIF}=\alpha_{11}R_i^2+(\alpha_1+\alpha_{12}P_i+\alpha_{13}T_i)R_i+(\alpha+\alpha_2P_i+\alpha_3T_i+\alpha_{23}P_iT_i+\alpha_{22}P_i^2+\alpha_{33}T_i^2)$$

noted

$$AR_i^2+BR_i+\mathrm{C}=0 \quad \text{with} \tag{26}$$

$$A=\alpha_{11}; \quad B=(\alpha_1+\alpha_{12}P_i+\alpha_{13}T_i);$$

Table 7 Levels of influent factors for the quadratic model

Level	R	P (MPa)	T (K)
(−1.68)	0.70	0.15	373
(−1)	0.82	0.24	403
(0)	1.00	0.375	448
(+1)	1.18	0.51	493
(+1.68)	1.30	0.60	523

$$C=(\alpha+\alpha_2P_i+\alpha_3T_i+\alpha_{23}P_iT_i+\alpha_{22}P_i^2+\alpha_{33}T_i^2)-S_i^{LIF} \tag{26}$$

After the resolve of the second degree equation $(AR_i^2+BR_i+\mathrm{C}=0)$, the equivalence ratio has for value:

$$R+=\frac{-B+\sqrt{B^2-4AC}}{2A} \tag{27}$$

The roots $R-=(-B-\sqrt{B^2-4AC}/)2A$ obtained from Eq. (26), always higher than 5, are eliminated.

Table 9 reports calculated values of equivalence ratio from values of pressure, temperature, LIF signal for the 15 experimental points used in the calculation of the model. The mean relative error between the calculated equivalence ratio and the measured one by the oxygen sensor with an accuracy of 2 percent is equal to 2.19 percent for the 15 experimental points. Concerning 10 experimental points not used in the calculation of the model, the mean relative error between the calculated and measured equivalence ratio is lower to 2.90 percent for 8 points inside the experimental range, and to 8 percent for two points outside the experimental range.

In conclusion, a quantitative measurement of fuel concentration can be realized from a measurement of LIF signal by inverting the quadratic model expressed in Eq. (22). However, to apply the developed model in an IC engine, the parameters, pressure and temperature, must be known accurately at the measurement point of fluorescence. In an IC engine, the pressure is distributed uniformly at a given time and is easily determined. On the other hand, important gradients of temperature are usually observed. The local and instantaneous temperature is rarely evaluated. In this case, it is necessary to discuss the accuracy of the equivalence ratio determination from the measurement of LIF signal according to the errors in the measurement or estimated values of temperature. To estimate the accuracy of the calculated equivalence ratio, a simplified quadratic model is established, where the contributions RT, PT, P^2, and R^2 are neglected from the variance analysis of the plan:

$$\mathrm{S}^{\mathrm{LIF}}=\mathrm{f(R,P,T)}=\mu+\mu_1\mathrm{R}+\mu_2\mathrm{P}+\mu_3\mathrm{T}+\mu_{12}\mathrm{R.P}+\mu_{33}\mathrm{T}^2 \tag{28}$$

The equivalence ratio is then given as a function of LIF signal, pressure and temperature:

$$R=\frac{S^{LIF}-\mu-\mu_2P-\mu_3T-\mu_{33}T^2}{\mu_1+\mu_{12}P} \tag{29}$$

By considering fixed values of pressure and LIF signal, measured values accurately and easily, the absolute error of equivalence ratio ΔR is calculated for a temperature variation ΔT:

$$R_{T+\Delta T}=R_T+\Delta R$$

with

$$\Delta R=-[\mu_3+\mu_{33}2T]\frac{\Delta T}{\mu_1+\mu_{12}P} \tag{30}$$

The error about the calculated equivalence ratio depends directly on the accuracy of the temperature measurement. For a temperature estimated at 473 K±10 K, a pressure of 0.1 MPa, the equivalence ratio calculated from the transfer function is then $R\pm0.05$.

Table 8 Estimated coefficients for the transfer function

$\hat{\alpha}$	$\hat{\alpha}_1$	$\hat{\alpha}_2$	$\hat{\alpha}_3$	$\hat{\alpha}_{12}$	$\hat{\alpha}_{13}$	$\hat{\alpha}_{23}$	$\hat{\alpha}_{11}$	$\hat{\alpha}_{22}$	$\hat{\alpha}_{33}$
−0.806	1.006	0.1708	0.0033	−1.362	−0.0011	−0.00067	−0.4597	−0.0071	−0.00002

Table 9 Calculation of the equivalence ratio for the 15 points of the plan

Pressure (MPa)	Temperature (K)	S^{LIF} measured (Volts)	$R_{calculated}$	$R_{measured}$	Relative error Er (%)
0.241	400	2.536	0.81	0.83	1.83
0.239	404	3.499	1.13	1.18	4.57
0.511	403	5.519	0.80	0.82	2.08
0.499	402	7.818	1.16	1.19	2.36
0.242	491	2.117	0.85	0.82	3.95
0.238	490	3.128	1.19	1.18	1.23
0.512	491	5.043	0.83	0.82	1.61
0.505	493	7.259	1.18	1.18	0.23
0.378	448	4.680	0.98	0.99	0.70
0.375	444	3.114	0.68	0.69	1.30
0.369	446	6.266	1.34	1.30	2.82
0.152	447	1.654	1.00	1.00	0.26
0.603	449	7.891	1.01	1.00	1.24
0.374	373	5.431	1.06	1.00	5.61
0.384	524	4.023	0.97	1.00	3.05
				$\overline{E_r} =$	2.19

Conclusions

LIF technique was investigated to measure exactly the fuel concentration in a pressurized and heated gas mixture flow. An experimental setup was developed to follow instantaneously the LIF signal for a pressure range of 0.1–0.65 MPa, a temperature range of 360–573 K, a flow velocity range of 2–30 m/s and an equivalence ratio range of 0.7–1.4. The combination of a 2 percent diacetyl volumic fraction as the fluorescence tracer of iso-octane and 355 nm as the excitation wavelength was used in order to minimize the laser beam absorption and to produce strong fluorescence signal. From a parametric study, influent parameters on the LIF signal were determined. The flow velocity is not a preponderant parameter, unlike the equivalence ratio, the ambient pressure, the ambient temperature and their interactions of the first order, which have an important effect on the LIF signal. The technique of plans of experiments was applied to complete the parametric study. Two plans were considered for experimental abilities: the equivalence ratio-flow velocity-pressure plan and the equivalence ratio-pressure-temperature plan. The LIF phenomenon is described by a statistical function from a multilinear regression in the experimental range. For both plans of experiments, the results of the statistical analysis, including the variance and the contribution of actions, the Snedecor tests, are similar to those deduced from the parametric study. The flow velocity has a negligible influence on the LIF signal, whereas the three factors, such as the equivalence ratio, the pressure, the temperature, and their interactions of the first order, have important effects. For instance, the risk is lower than 2.5 percent, that the flow velocity varying between 2.5–30 m/s influences the LIF intensity. From a quadratic model, a transfer function was determined to calculate the value of the LIF intensity for given experimental conditions of pressure, temperature, flow velocity, fuel concentration. By inversion of the quadratic model, the equivalence ratio was calculated, with a mean relative error lower to 2.20 percent. However, the inverted quadratic model can be applied to measure quantitatively the fuel concentration from a measurement of LIF signal when the temperature and the pressure are known accurately. The pressure is a parameter easily determined, even in an IC engine where it is distributed uniformly. Concerning the temperature, the two-line technique based on laser induced fluorescence of a dopant excited with two different wavelengths can be applied for an accurate measurement [38]. From the quasi-simultaneous excitation at two wavelengths, the ratio of the fluorescence signal intensities reflects the local temperature. Moreover, for quantitative measurements of fuel concentration in IC engines, specially engines with stratified load and systems with exhaust gas recirculation, where fuel concentration inhomogeneities are present, the experimental range used in this work for the transfer function application must be increased.

Acknowledgments

William Perrard was supported by a joint grant from the Department of Education.

Nomenclature

A = action of the studied phenomenon (including factors and interactions)
A_{21} = Einstein coefficient for spontaneous emission (fluorescence)
B_{12} = Einstein coefficient for stimulated emission
$C(A)$ = contribution of an action (A)
h_{laser} = laser beam height (mm)
I_υ = spectral intensity of incident laser light ($\text{W}\cdot\text{cm}^{-2}\cdot\text{Hz}^{-1}$)
k_1, k_2 = proportional coefficient
$l(A)$ = number of freedom degree for the action (A)
$\underline{L}$ = number of freedom degree for the model
M = molecular weight ($\text{g}\cdot\text{mol}^{-1}$)
N = test number

N_0^1 = number density of the absorbing species in the ground state (cm^{-3})
P = pressure (MPa)
P_{laser} = laser power (W)
Q_{21} = quenching rate constant
R = equivalence ratio
Resvar(M) = residual variance induced by the model M
S^{LIF} = LIF signal (V)
T = temperature (K)
U_v = spectral density of energy at the frequency v ($\mathrm{J \cdot m^{-3}}$)
V = flow velocity ($\mathrm{m \cdot s^{-1}}$)
Var(A) = variance induced by the action (A)
V_c = collection volume (cm^3)

Greek symbols

ε = detection efficiency of the collection system
Φ = fluorescence flux ($\mathrm{J \cdot cm^{-2}}$)
λ = wavelength (nm)
Ω = solid angle of collection optics (sr)
ϕ_{laser} = laser beam diameter (mm)

References

[1] Zhao, H., and Ladommatos, N., 1998, ''Optical diagnostics for in-cylinder mixture formation measurements in IC engines,'' Prog. Energy Combust. Sci., **24**, pp. 297–336.
[2] Fujikawa, T., Hattori, Y., and Akihama, K., 1997, ''Quantitative 2-D fuel distribution measurements in a SI engine using laser-induced fluorescence with suitable combination of fluorescence tracer and excitation wavelength,'' SAE Paper 972944.
[3] Neij, H., Johansson, B., and Alden, M., 1994, ''Development and demonstration of 2D-LIF for studies of mixture preparation in SI engines,'' Combust. Flame, **99**, pp. 449–457.
[4] Johansson, B., Neij, H., Alden, M., and Juhlin, G., 1995, ''Investigations of the influence of mixture preparation on cyclic variations in a SI-engine using laser induced fluorescence,'' SAE Paper 950108.
[5] Itoh, T., Kakuho, A., Hishinuma, H., Urushiahara, T., Takagi, Y., Horie, K., Asano, M., Ogata, E., and Yamasita, T., 1995, ''Development of a new compound fuel and fluorescent tracer combination for use with laser induced fluorescence,'' SAE Paper 952465.
[6] Urushihara, T., Nakata, T., Kakuhou, A., and Takagi, Y., 1996, ''Effects of swirl and tumble motion on fuel vapor behavior and mixture stratification in lean burn engine,'' JSAE Review, **17**, pp. 239–244.
[7] Hishinuma, H., Urushihara, T., Kakuho, A., and Itoh, T., 1996, ''Development of a technique for quantifying in-cylinder A/F ratio distribution using LIF image processing,'' JSAE Review, **17**, pp. 355–359.
[8] Reboux, J., Puechberty, D., and Dionnet, F., 1994, ''A new approach of planar laser induced fluorescence applied to fuel/air ratio measurement in the compression stroke of an optical S. I. engine,'' SAE Paper 941988.
[9] Reboux, J., Puechberty, D., and Dionnet, F., 1996, ''Study of mixture inhomogeneities and combustion development in a S. I. engine using a new approach of laser induced fluorescence (FARLIF),'' SAE Paper 961205.
[10] Knapp, M., Beushausen, V., Hentschel, W., Manz, P., Grünefeld, G., and Andresen, P., 1997, ''In-cylinder mixture formation analysis with spontaneous raman scattering applied to a mass-production SI engine,'' SAE Paper 970827.
[11] Kim, K. S., Choi, M. S., Lee, C. H., and Kim, W. T., 1997, ''In-cylinder fuel distribution measurements using PLIF in a SI engine,'' SAE Paper 970509.
[12] Krämer, H., Einecke, S., Schulz, C., Sick, V., Nattrass, S. R., and Kitching, J. S., 1998, ''Simultaneous mapping of the distribution of different fuel volatility classes using tracer-LIF and NIR-tomagraphy in an IC engine,'' SAE Paper 982467.
[13] Ghandi, J. B., and Bracco, F. V., 1995, ''Fuel distribution effects on the combustion of a direct-injection stratified-charge engine,'' SAE Paper 950460.
[14] Fujikawa, T., Hattori, Y., Koike, M., Akihama, K., Kobayashi, T., and Matsushita, S., 1999, ''Quantitative 2-D fuel distribution measurements in a direct-injection gasoline engine using laser-induced fluorescence technique,'' JSME Int. J., Ser B, **42**, No. 4, pp. 760–767.
[15] Arnold, A., Buschmann, A., Cousyn, B., Decker, M., Vannobel, F., Sick, V., and Wolfrum, J., 1993, ''Simultaneous imaging of fuel and hydroxyl radicals in an in-line four cylinder SI engine,'' SAE Paper 932696.
[16] Wolff, D., Beushausen, V., Schlüter, H., Andresen, P., Hentschel, W., Manz, P., and Arndt, S., 1994, ''Quantitative 2D-mixture fraction imaging inside an internal combustion engine using aceton-fluorescence,'' International Symposium COMODIA 94, pp. 445–451.
[17] Swindal, J. C., Dragonetti, D. P., Hahn, R. T., Furman, P. A., and Acker, W. P., 1995, ''In-cylinder charge homogeneity during cold-start studied with fluorescent tracers simulating different fuel distillation temperatures,'' SAE Paper 950106.
[18] Meyer, J., Haug, M., Schreiber, M, and Unverzagt, S., 1995, ''Controlling combustion in a spark ignition engine by quantitative fuel distribution,'' SAE Paper 950107.
[19] Berckmüller, M., Tait, N. P., and Greenhalgh, D. A., 1996, ''The time history of the mixture formation process in a lean burn stratified-charge engine,'' SAE Paper 961929.
[20] Berckmüller, M., Tait, N. P., and Greenhalgh, D. A., 1997, ''The influence of local fuel concentration on cyclic variability of a lean burn stratified-charge engine,'' SAE Paper 970826.
[21] Baritaud, T. A., and Heinze, T. A., 1992, ''Gasoline distributions measurements with PLIF in a SI engine,'' SAE Paper 922355.
[22] Deschamps, B., Snyder, R., and Baritaud, T., 1994, ''Effect of flow and gasoline stratification on combustion in a 4-valve SI engine,'' SAE Paper 941993.
[23] Deschamps, B., and Baritaud, T., 1997, ''Visualisation of gasoline and exhaust gases distribution in a 4-valve SI engine; effects of stratification on combustion and pollutants,'' Revue de l'Institut Français du Pétrole, **52**, No. 6, pp. 651–667.
[24] Depussay, E., Mounaïm-Rousselle, C., Burnel, S., Deschamps, B., and Ricordeau, V., 1998, ''Comparative measurements of local iso-octane concentrations by planar laser induced fluorescence and catalytic hot wires probe in SI engine,'' SAE Paper 98FL-567.
[25] Jian-Bang, L., Qi, P., Chang-Sheng, L., and Jie-Rong, S., 1988, ''Principles of flow field diagnostics by laser induced biacetyl phosphorescence,'' Exp. Fluids, **6**, pp. 505–513.
[26] Okabe, H., and Noyes, W. A., Jr., 1957, ''The relative intensities of fluorescence and phosphorescence in biacetyl vapor,'' J. Am. Chem. Soc., **79**, pp. 801–806.
[27] Heicklen, J., 1959, ''The fluorescence and phosphorescence of biacetyl vapor and acetone vapor,'' J. Am. Chem. Soc., **81**, pp. 3863–3866.
[28] Itoh, F., Kyachakoff, G., and Hanson, R. K., 1985, ''Flow visualization in low pressure chambers using laser-induced biacetyl phosphorescence,'' J. Vac. Sci. Technol. B, **3**, No. 6, pp. 1600–1603.
[29] Cruyningen, I., Lozano, A., and Hanson, R. K., 1990, ''Quantitative imaging of concentration by planar laser-induced fluorescence,'' Exp. Fluids, **10**, pp. 41–49.
[30] Lawrenz, W., Köhler, J., Meier, F., Stolz, W., Wirth, R., Bloss, W. H., Maly, R. R., Wagner, E., and Zahn, M., 1992, ''Quantitative 2D LIF measurements of air/fuel ratios during the intake stroke in a transparent SI engine,'' SAE Paper 922320.
[31] Grossmann, F., Monkhouse, P. B., Ridder, M., Sick, V., and Wolfrum, J., 1996, ''Temperature and pressure dependences of the laser-induced fluorescence of gas-phase acetone and 3-pentanone,'' Appl. Phys. B: Lasers and Optics, **62**, pp. 249–253.
[32] Yuen, L. S., Peters, J. E., and Lucht, R. P., 1997, ''Pressure dependence of laser-induced fluorescence from acetone,'' Appl. Opt., **36**, No. 15, pp. 3271–3277.
[33] Bryant, R. A., Donbar, J. M., and Driscoll, J. F., 2000, ''Acetone laser induced fluorescence for low pressure/low temperature flow visualization,'' Exp. Fluids, **28**, pp. 471–476.
[34] Sasayama, T., 1986, ''An advanced computer controlled engine system employing new combustion monitoring sensors,'' SAE Paper 865077.
[35] Sado, G., and Sado, M. C., 1991, *Les plans d'expériences: de l'expérimentation à l'assurance qualité*, Afnor Technique.
[36] Benoist, D., Tourbier, Y., and Germain-Tourbier, S., 1994, *Plans d'expériences: construction et analyze*, Technique & Documentation Lavoisier.
[37] Box, G. E. P., and Draper, N. R., 1987, *Empirical model building and response surfaces*, Wiley, New York.
[38] Einecke, S., Schulz, C., and Sick, V., 2000, ''Measurement of temperature, fuel concentration and equivalence ratio fields using tracer LIF in IC engine combustion,'' Appl. Phys. B: Lasers and Optics, **71**, pp. 717–723.

A Comparison of Data-Reduction Methods for a Seven-Hole Probe

David Sumner
Department of Mechanical Engineering,
University of Saskatchewan,
57 Campus Drive,
Saskatoon, Saskatchewan, S7N 5A9
Canada

Two data-reduction methods were compared for the calibration of a seven-hole conical pressure probe in incompressible flow. The polynomial curve-fit method of Gallington and the direct-interpolation method of Zilliac were applied to the same set of calibration data, for a range of calibration grid spacings. The results showed that the choice of data-reduction method and the choice of calibration grid spacing each have an influence on the measurement uncertainty. At high flow angles, greater than 30 deg, where flow may separate from the leeward side of the probe, the direct-interpolation method was preferable. At low flow angles, less than 30 deg, where flow remains attached about the probe, neither data-reduction method had any advantage. For both methods, a calibration grid with a maximum interval of 10 deg was recommended. The Reynolds-number sensitivity of the probe began at Re=5000, based on probe diameter, and was independent of the data-reduction method or calibration grid spacing. [DOI: 10.1115/1.1455033]

1 Introduction

The seven-hole conical pressure probe is a non-nulling velocity probe used to measure the local time-mean velocity vector in wind-tunnel flows. The probe is sensitive to flow angles up to 80 deg from the probe axis. Calibration of a seven-hole probe requires subjecting the probe to flows of known velocity magnitude and direction. Pressures at the seven ports are measured for each angular position of the probe during the calibration. A calibration data-reduction method is then employed, such as the polynomial curve-fit method of Gallington [1,2] or the direct-interpolation method of Zilliac [3]. In Gallington's method, the calibration data are used to develop a set of response equations. The calibration data are represented as dimensionless pressure coefficients, and a least-squares approach is used to fit the flow properties to third-order polynomial expansions of the pressure coefficients. In Zilliac's method, the calibration data, represented as directional pressure coefficients, are interpolated directly without the need to determine response equations. These two data-reduction methods have been widely adopted for measurements in compressible flows [4,5], vortex flows [6–8], wakes [9], and turbomachinery [10].

Recently, several hybrid data-reduction methods have been developed for the seven-hole probe, by Venkateswara Babu et al. [11], Wenger and Devenport [12], and Johansen et al. [13,14]. The hybrid methods combine various features of the polynomial curve-fit and direct-interpolation methods. A neural network data-reduction method has also been used [15,16]. The motivation for many of these newer methods has been to improve the accuracy of the seven-hole probe.

Because of the number of different data-reduction methods in the literature, it is of interest whether the choice of data-reduction method can influence the measurement uncertainty of the seven-hole probe for a given calibration data set. Most studies have not implemented other data-reduction techniques on the same calibration data set. Therefore, it is not possible to assess if there were other factors, such as a different calibration grid spacing or more accurate pressure transducers, which might also have contributed to an improved accuracy over other studies. For instance, both Venkateswara Babu et al. [11] and Johansen et al. [14] have claimed that their hybrid method is more accurate than a conventional polynomial curve fit. However, these assertions were not substantiated by applying the curve-fit method to their own data set. In the present study, as a step towards clarifying this issue, the measurement uncertainty of Gallington's method and Zilliac's method is compared for the same calibration data set.

Since calibration of a probe can be time-intensive, the influence of the calibration grid density on measurement uncertainty needs to be explored. Authors have rarely reported the calibration grid spacing they adopted. Johansen et al. [14] note that it typically varies from 0.5–5 deg while Venkateswara Babu et al. [11] used 9 deg. Furthermore, the influence of different grid spacings on the measurement uncertainty has not been explored by others, although the success of direct-interpolation methods may be sensitive to the size and density of the calibration data. In the present study, the calibration grid density is varied and its impact on measurement uncertainty is assessed for the methods of Gallington and Zilliac. The sensitivity of the probe to the Reynolds number is also examined.

2 Background

The seven-hole pressure probe originated at the U.S. Air Force Academy [1,2], where there was a need to obtain meaningful velocity information at high flow angles (where a five-hole probe becomes ineffective). The seven-hole probe is conical-shaped, with a cone angle between 30 and 45 deg, and has six outer pressure ports ($n=1-6$) surrounding a central port ($n=7$). Pressure information from the seven holes is combined to compute four pressure coefficients, representing the local pitch angle, θ, yaw angle, ψ, total pressure, P_{total}, and dynamic pressure, q. This information then yields the local velocity vector, $\vec{\mathbf{V}}$; see Fig. 1(*a*).

At low flow angles, flow remains attached over the entire surface of the probe and the central port ($n=7$) reads the highest pressure. Pressure information from all seven holes may be used to determine the flow conditions. At high flow angles, separated flow occurs on the leeward side of the probe and an off-center port ($n=1-6$) will read the highest pressure. Only a subset of the seven pressures is then used to determine the flow conditions, based on the port reading the maximum pressure and those ports immediately adjacent to it. This distinction between low and high angles leads to a sectoring scheme being employed, based on which port ($n=1-7$) reads the highest pressure; see Fig. 1(*b*).

Following an approach similar to that of Zilliac [3], a radial pressure-difference coefficient, C_{Pr}, may be used to represent the local pitch angle, θ, and a tangential pressure-difference coefficient, C_{Pt}, may be used to represent the local yaw angle, ψ. Similar coefficients, C_{Ptotal} and C_q, are used to represent the

---

Contributed by the Fluids Engineering Division for publication in the JOURNAL OF FLUIDS ENGINEERING. Manuscript received by the Fluids Engineering Division May 22, 2000; revised manuscript received November 21, 2001. Associate Editor: J. Bridges.

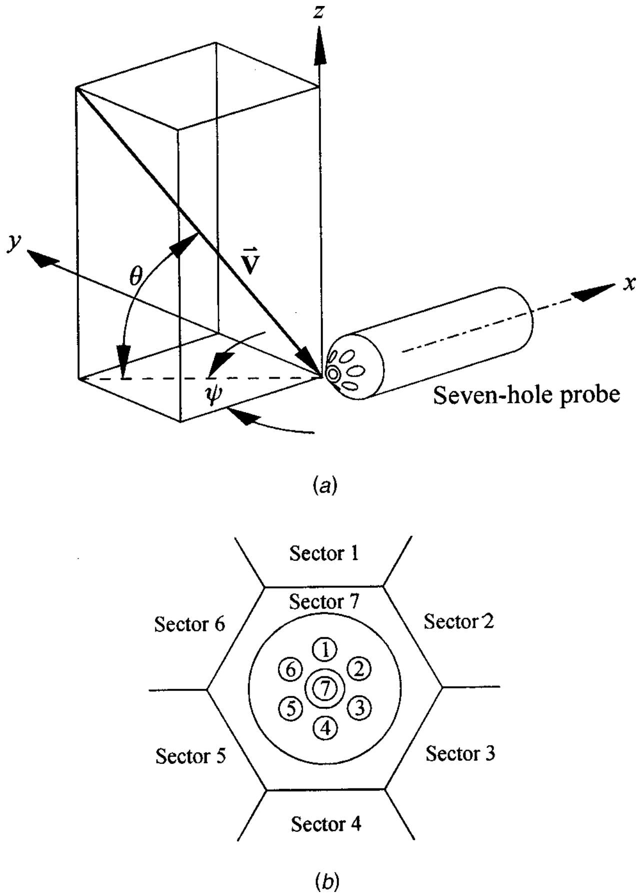

(*a*)

(*b*)

Fig. 1 (*a*) Flow angle nomenclature; (*b*) sectoring scheme, based on hole numbers 1 through 7

local total pressure and dynamic pressure, respectively. These coefficients are defined for low angles (corresponding to sector 7) as follows:

$$C_{Pr,7}=\frac{2(P_4-P_1)+(P_3-P_6)-(P_2-P_5)}{2(P_7-\bar{P}_7)} \tag{1}$$

$$C_{Pt,7}=\frac{(P_3-P_6)+(P_2-P_5)}{\sqrt{3}(P_7-\bar{P}_7)} \tag{2}$$

$$C_{Ptotal,7}=\frac{P_7-P_{total}}{P_7-\bar{P}_7} \tag{3}$$

$$C_{q,7}=\frac{P_7-\bar{P}_7}{q} \tag{4}$$

where

$$\bar{P}_7=\frac{1}{6}\sum_{n=1}^{6} P_n. \tag{5}$$

For high angles, the coefficients are defined for port number (or sector) n, where $n=1$ to 6, as follows:

$$C_{Pr,n}=\frac{P_n-P_7}{P_n-\bar{P}_n} \tag{6}$$

$$C_{Pt,n}=\frac{P_{n-1}-P_{n+1}}{P_n-\bar{P}_n} \tag{7}$$

$$C_{Ptotal,n}=\frac{P_n-P_{total}}{P_n-\bar{P}_n} \tag{8}$$

$$C_{q,n}=\frac{P_n-\bar{P}_n}{q} \tag{9}$$

where

$$\bar{P}_n=\frac{P_{n+1}+P_{n-1}}{2}. \tag{10}$$

The two prevailing calibration data-reduction methods are now briefly described.

2.1 Polynomial Curve-Fit Method. The polynomial curve-fit data-reduction method of Gallington [1,2] is applied separately to each sector's calibration data. Four different response equations must be found for each sector, one for each of the four flow properties $(\theta,\psi,C_{Ptotal},C_q)$. Each flow property is represented by a third-order polynomial expansion of the pressure coefficient data (C_{Pr} and C_{Pt}). Using all of the calibration data within the sector, a least-squares technique is used to find the polynomial coefficients, K_1-K_{10}, for each flow property and sector combination. A total of 280 calibration constants must be found. An example is shown in Eq. (11) for flow property θ and sector 1.

$$\begin{aligned}\theta_1=&K_{1,\theta_1}+K_{2,\theta_1}C_{Pr,1}+K_{3,\theta_1}C_{Pt,1}+K_{4,\theta_1}C_{Pr,1}^2+K_{5,\theta_1}C_{Pt,1}^2\\&+K_{6,\theta_1}C_{Pr,1}C_{Pt,1}+K_{7,\theta_1}C_{Pr,1}^3+K_{8,\theta_1}C_{Pt,1}^3+K_{9,\theta_1}C_{Pr,1}^2C_{Pt,1}\\&+K_{10,\theta_1}C_{Pt,1}^2C_{Pr,1}\end{aligned} \tag{11}$$

2.2 Direct-Interpolation Method. In the direct-interpolation method of Zilliac [3], the calibration data of a given sector $(n=1-7)$ are interpolated directly for each measurement. Because the calibration data within a given sector can be unevenly spaced, the Akima IMSL interpolation scheme [17] is used to interrogate the data and estimate the flow angle and velocity. For each measurement, two interpolations of the calibration data are performed. First, the flow angle coefficient data (C_{Pr} and C_{Pt}) are interpolated to obtain the pitch and yaw angles, θ and ψ, respectively. Second, the flow angle data (θ and ψ) are interpolated to obtain the total pressure and dynamic pressure coefficients, C_{Ptotal} and C_q, respectively.

3 Experiment Setup

Experiments were conducted in a low-speed, closed-return wind tunnel, with a test section of 0.91 m (height) × 1.13 m (width) × 1.96 m (length). The longitudinal freestream turbulence intensity was no greater than 0.6% over the speed range of the experiments ($U=5$ to 30 m/s). The velocity nonuniformity in the central portion of the test section, outside the test section wall boundary layers, was no greater than 0.5%.

A 3.45-mm diameter seven-hole probe was manufactured with a cone angle of 30 deg. The probe was comprised of seven close-packed 1-mm diameter stainless steel tubes fitted into an outer stainless steel sleeve. The probe was mounted in an automated variable-angle calibrator located in the center of the test section. Two stepping motors were used to position the probe in pitch and yaw. The in-situ calibration eliminates uncertainty caused by differences between the test flow conditions and the calibration flow conditions, such as unsteadiness and turbulence levels often encountered when using a calibrator jet (such as for a hot-wire anemometer). In these experiments, the probe Reynolds number ranged from Re=1000 to 6500, based on the probe diameter.

Reference conditions were measured with a Pitot-static probe (United Sensor, 3.2-mm diameter) and Datametrics Barocell absolute and differential pressure transducers. Seven-hole probe pressure measurements were conducted with a Scanivalve pressure multiplexer and a pair of Validyne differential pressure transducers. Data were acquired with a Compaq Deskpro 450 MHz Pentium II microcomputer with a National Instruments AT-MIO-64F-5 data acquisition board. Programs were written in National Instruments LabVIEW software. Pressure signals were typically sampled at 500 Hz for 8–10 seconds, with a 2-second delay time to allow for conditions to reach steady-state and for the probe to be repositioned.

4 Results and Discussion

Probe calibrations were performed at Re=3200 over an angular range of ±72 deg in pitch and yaw. The angular spacing of the calibration grid, which was uniform in the pitch and yaw directions, was varied from 5.6 to 14.4 deg between the calibrations. The separation criteria of Zilliac [3] were applied to the pressure data to eliminate flow angle configurations that could give erroneous results through insufficient meaningful pressure information. This occurs when the flow angle is such that the flow is not attached over four or more ports.

Of interest was the contribution of the data-reduction method to the measurement uncertainty of the seven-hole probe calculated for a range of calibration grid spacings. The measurement uncertainty of each flow property was computed using a standard error approach, which was also adopted by [1,2]. For N measurements evenly distributed over the complete angular range of the probe, the flow properties computed by the data-reduction method are compared with their known (measured) values. For example, the uncertainty in the pitch angle, σ_θ, is given in Eq. (12).

$$\sigma_\theta=\sqrt{\frac{1}{N}\sum_{i=1}^{N}(\theta_{\text{measured},i}-\theta_{\text{computed},i})^2} \qquad (12)$$

For each flow property, one standard error was computed for low flow angles (sector 7) and another was computed for high flow angles (sectors 1 through 6). Approximately 2000 measurements, obtained from the sum of the calibration data, were used to compute the standard errors.

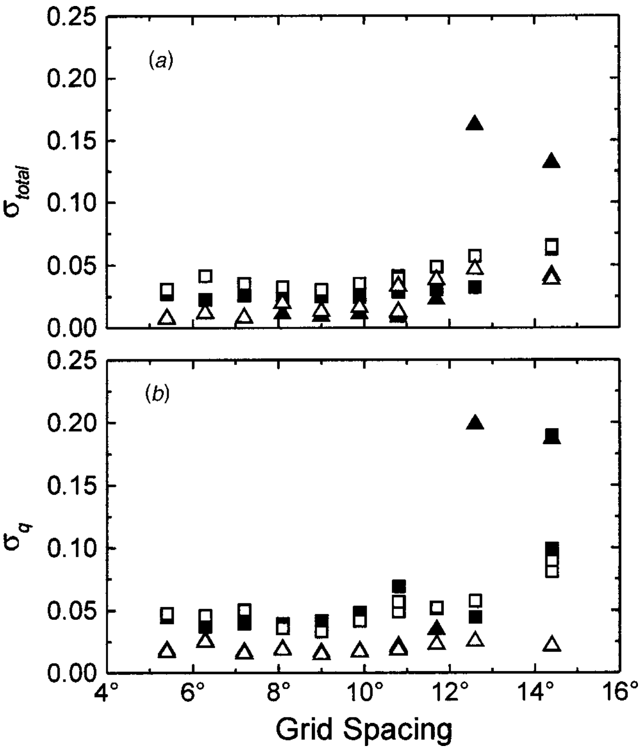

Fig. 3 Measurement uncertainty, Re=3200: (*a*) total pressure; (*b*) dynamic pressure. High flow angles: ■, polynomial curve fit; □, direct interpolation. Low flow angles: ▲, polynomial curve fit; △, direct interpolation.

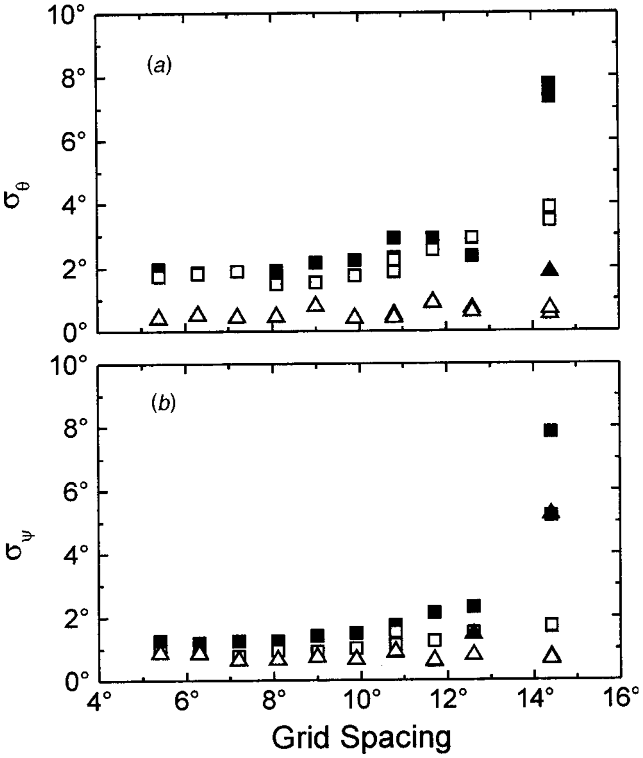

Fig. 2 Measurement uncertainty, Re=3200: (*a*) pitch angle; (*b*) yaw angle. High flow angles: ■, polynomial curve fit; □, direct interpolation. Low flow angles: ▲, polynomial curve fit; △, direct interpolation.

It should be emphasized that the uncertainty results shown represent the precision of the data-reduction method only. The positioning precision of the variable-angle calibrator, of ±0.45 deg, is not incorporated into the results. The precision in the pressure measurements, which was estimated as ±1%, is excluded also. Although the absolute uncertainty levels reported are higher than those of some other studies, it is not these values themselves which are important but rather the comparison between the two data-reduction methods. Nonetheless, the results underscore the need for highly accurate variable-angle calibrators and pressure transducers to minimize any additional sources of measurement uncertainty apart from the data-reduction method. It should be noted that the use of a ±0.5% pressure transducer would greatly improve the overall probe uncertainty.

4.1 Measurement Uncertainty.

The uncertainty in the flow angles, σ_θ and σ_ψ, as a function of the calibration grid spacing, is shown in Fig. 2. For small grid spacings, the two data-reduction methods introduce comparable uncertainty in pitch and yaw for low-angle measurements, of 0.4 and 0.9 deg, respectively. However, the direct-interpolation method was superior for high-angle measurements, with an uncertainty of 1.7 deg in pitch angle and 0.9 deg in yaw angle.

The uncertainty in the local total pressure and dynamic pressure, σ_{total} and σ_q, is shown in Fig. 3. For these measurements, neither data-reduction method had an advantage. For small grid spacings, at low flow angles, the uncertainty was less than 2% for both pressures. At high flow angles, the uncertainty was less than 5% for both pressures. The velocity magnitude could be measured within 1% and 3% for the low and high angle regimes, respectively, for small grid spacings.

These results illustrate that the choice of data-reduction method

Table 1 Measurement uncertainty of the data-reduction method for calibration grid spacings of 5.4 deg and 11.7 deg, Re=3200.

Low flow angles (sector 7)		Pitch Angle	Yaw Angle	Total Pressure	Dynamic Pressure	Velocity Magnitude
5.4°	Polynomial curve fit	0.4°	0.9°	0.8%	1.8%	0.9%
	Direct interpolation	0.4°	0.9°	0.7%	1.7%	0.8%
11.7°	Polynomial curve fit	0.9°	0.6°	2.2%	3.5%	1.7%
	Direct interpolation	0.9°	0.6°	3.8%	2.3%	1.1%

High flow angles (sectors 1 to 6)		Pitch Angle	Yaw Angle	Total Pressure	Dynamic Pressure	Velocity Magnitude
5.4°	Polynomial curve fit	2.0°	1.3°	2.7%	4.4%	2.2%
	Direct interpolation	1.7°	0.9°	3.1%	4.7%	2.4%
11.7°	Polynomial curve fit	2.9°	2.1°	3.1%	5.1%	2.6%
	Direct interpolation	2.5°	1.2°	4.9%	5.2%	2.6%

has an influence on the measurement uncertainty, for the same set of calibration data. In a number of cases, particularly for larger angular spacings, the direct-interpolation method yielded a lower measurement uncertainty. Some results are summarized in Table 1.

The experiments also showed that the uncertainty was mostly independent of the number of calibration grid points, but provided the angular spacing of the calibration grid was less than 10 deg; see Figs. 2 and 3 and Table 1. Both data-reduction methods appear to be influenced in a like manner by the choice of calibration grid density.

4.2 Reynolds Number Sensitivity. Since a calibration is typically performed at a single velocity, whereas measurements are often acquired in flows of spatially varying velocity, the sensitivity of the probe to the Reynolds number was examined. Pitot-static probes and directional pressure probes exhibit a sensitivity at low flow velocities, for $\mathrm{Re}<1000-3000$ [18], so the investigation was focused on flows with velocities lower than the calibration velocity. A calibration was performed with a grid spacing of 9.0 deg at Re=6500, corresponding to $U=30$ m/s. Measurements were then acquired at Reynolds numbers between 1000 ($U=5$ m/s) and 6500 ($U=30$ m/s). At each Reynolds number, 100 measurements were acquired, with the same angular positions for each measurement set. Selected results in Fig. 4 show an increasing measurement uncertainty as the Reynolds number is lowered. These results indicate that the seven-hole probe becomes sensitive to the Reynolds number for Re<5000, and that the sensitivity is independent of the data-reduction method. This result is consistent with [12], who found the seven-hole probe to exhibit Reynolds number effects for Re<8000.

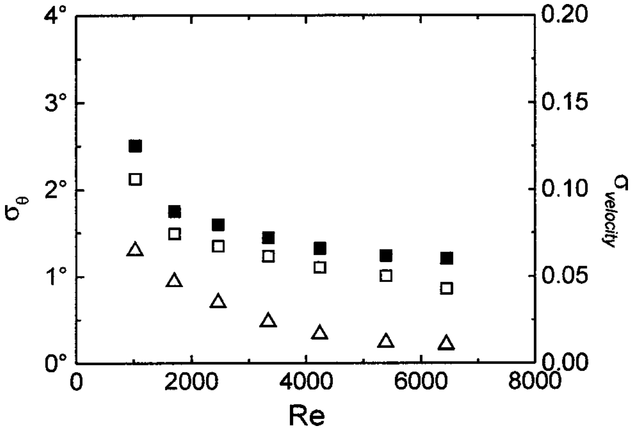

Fig. 4 Reynolds number sensitivity of the seven-hole probe. Calibration at Re=6500 with a 9.0 deg grid spacing. Pitch angle uncertainty (all sectors): ■, polynomial curve fit; □, direct interpolation. Velocity magnitude uncertainty (all sectors): ▲, polynomial curve fit; △, direct interpolation.

Conclusions

Experiments were conducted in a low-speed wind tunnel with a seven-hole conical pressure probe to examine the effectiveness of two calibration data-reduction methods applied to the same set of calibration data. It was demonstrated that the choice of data-reduction method could have an influence on the measurement uncertainty. The direct-interpolation method of Zilliac [3] yielded the lower measurement uncertainty, but only when the flow angle exceeded 30 deg. Otherwise, there was no significant advantage to using the direct-interpolation method over Gallington's [1,2] curve-fit method. Since probe calibration can be a lengthy exercise, the influence of the calibration grid density on the measurement uncertainty was also examined. The experiments showed that the measurement uncertainty of both data-reduction methods is sensitive to the calibration grid spacing, and a maximum calibration grid spacing of 10 deg was recommended. The sensitivity of the probe to the Reynolds number was also studied. The effectiveness of the probe was found to be reduced when Re<5000.

Acknowledgments

The support of the Natural Sciences and Engineering Research Council (NSERC) of Canada is gratefully acknowledged. The assistance of X.-H. Chen, D. Deutscher, J. D. Leuschen, M. D. Richards, and the University of Saskatchewan Engineering Shops, is also appreciated.

Nomenclature

C_{Pr} = radial pressure-difference coefficient
C_{Pt} = tangential pressure-difference coefficient
C_{Ptotal} = local total pressure coefficient
C_q = local dynamic pressure coefficient
K_1-K_{10} = polynomial coefficients
N = number of measurements
P_n = pressure at port n, where $n=1-7$
P_{total} = local total pressure
q = local dynamic pressure
Re = probe Reynolds number, $\mathrm{Re}=Ud/\nu$, where d is the probe diameter, and ν is the kinematic viscosity
U = freestream velocity
$\overline{\mathbf{V}}$ = local velocity vector
x, y, z = coordinate axes
θ = pitch angle
σ = standard error
ψ = yaw angle

Subscripts

n = port number or sector number

References

[1] Gallington, R. W., 1980, "Measurement of very large flow angles with non-nulling seven-hole probe," Aeronautics Digest, USAFA-TR-80-17, pp. 60–88.
[2] Gerner, A. A., Maurer, C. L., and Gallington, R. W., 1984, "Non-nulling seven-hole probes for high-angle flow measurement," Exp. Fluids, **2**, pp. 95–103.
[3] Zilliac, G. G., 1993, "Modelling, calibration, and error analysis of seven-hole pressure probes," Exp. Fluids, **14**, pp. 104–120.
[4] Gerner, A. A., and Maurer, C. L., 1982, "Calibration of seven-hole probes suitable for high angles in subsonic compressible flows," AIAA Paper No. 82-0410.
[5] Pettersson, B., 1987, "Calibration of seven-hole probes within Mach number range 0.50–1.30 in FFA high speed wind tunnel facility," *Proceedings of the*

International Congress on Instrumentation in Aerospace Simulation Facilities, Williamsburg, VA, pp. 156–164.
[6] Payne, F. M., Ng, T. T., and Nelson, R. C., 1989, ''Seven-hole probe measurement of leading edge vortex flows,'' Exp. Fluids, **7**, pp. 1–8.
[7] Chow, J. S., Zilliac, G. G., and Bradshaw, P., 1997, ''Mean and turbulence measurements in the near field of a wingtip vortex,'' AIAA J., **35**, pp. 1561–1567.
[8] Rediniotis, O. K., Klute, S. M., Hoang, N. T., and Telionis, D. P., 1994, ''Dynamic pitch-up of a delta wing,'' AIAA J., **32**, pp. 716–725.
[9] Cogotti, A., 1986, ''Car-wake imaging using a seven-hole probe,'' *Aerodynamics: Recent Developments*, SAE publication SP-656, pp. 1–25.
[10] Yaras, M. I., Sjolander, S. A., and Kind, R. J., 1992, ''Effects of simulated rotation on tip leakage in a planar cascade of turbine blades: Part II-Downstream flow field and blade loading,'' ASME J. Turbomach., **114**, pp. 660–667.
[11] Babu, C. Venkateswara, Govardhan, M., and Sitaram, N., 1998, ''A method of calibration of a seven-hole pressure probe for measuring highly three-dimensional flows,'' Meas. Sci. Technol., **9**, pp. 468–476.
[12] Wenger, C. W., and Devenport, W. J., 1999, ''Seven-hole pressure probe calibration method utilizing look-up error tables,'' AIAA J., **37**, pp. 675–679.
[13] Rediniotis, O. K., Johansen, E. S., Tsao, T., Seifert, A. and Pack, L. G., 1999, ''MEMS-based probes for velocity and pressure measurements in unsteady and turbulent flow fields,'' AIAA Paper 99-0521, Proceedings of the 37th AIAA Aerospace Sciences Meeting, Reno, Jan.
[14] Johansen, E. S., Rediniotis, O. K., and Jones, G., 2001, ''The compressible calibration of miniature multi-hole probes,'' ASME J. Fluids Eng., **123**, pp. 128–138.
[15] Rediniotis, O. K., and Chrysanthakopoulos, G., 1998, ''Application of neural networks and fuzzy logic to the calibration of the seven-hole probe,'' ASME J. Fluids Eng., **120**, pp. 95–120.
[16] Rediniotis, O. K., and Vijayagopal, R., 1999, ''Miniature multihole pressure probes and their neural-network-based calibration,'' AIAA J., **37**, pp. 667–674.
[17] Akima, H., 1978, ''A method of bivariate interpolation and smooth surface fitting for irregularly distributed data points,'' ACM Trans. Math. Softw., **4**, pp. 148–192.
[18] Chue, S. H., 1975, ''Pressure probes for fluid measurement,'' Prog. Aerosp. Sci., **16**, pp. 147–223.

F. B. Freitas Rachid
Professor, Department of Mechanical Engineering
e-mail: rachid@mec.uff.br

J. H. Carneiro de Araujo
Professor, Computer Science
e-mail: jhca@dcc.ic.uff.br

Universidade Federal Fluminense,
Niterói, RJ, 24210-240, Brazil

R. M. Baptista
Senior Petroleum Engineer,
Research and Development Center,
Petrobras-Petróleo Brasileiro S.A.,
Rio de Janeiro, RJ, 21949-900, Brazil
e-mail: renan@cenpes.petrobras.com.br

Predicting Mixing Volumes in Serial Transport in Pipelines

This paper presents a model for predicting the contaminated mixing volume arising in pipeline batch transfers without physical separators. The proposed technique represents an improvement over the existing methods since it takes into account time-dependent flow rates and accurate concentration-varying axial dispersion coefficients. The governing equation of the model forms a nonlinear boundary-value problem that is solved by a finite element method coupled to the Newton's method. A comparison among the theoretical predictions of this method, a field test, and other classical procedures show that the proposed method exhibits the best estimate over the whole range of admissible concentrations investigated. [DOI: 10.1115/1.1459078]

Introduction

The batch transfer of petroleum products in long pipelines is a current practice all over the world. Unless mechanical separators such as scrapers or pigs are employed [1], there will be a certain amount of mixing between products, which is called interface contamination. Since the use of separators requires a somewhat complex operation, it is, in general, avoided, especially when intermediate pump-station manifolds are present.

From the operational viewpoint, the occurrence of contamination implies additional costs associated with shipping the mixture back to refinery for later reprocessing. Thus, the minimization of interface contamination should always be pursued.

During the planning and execution of batch transfers, the interface contamination analysis is carried out in order to establish the best sequence to pump the fluids (to optimize the program of the product sequence aiming to minimize the mixing zones) as well as to control and monitor the spread of the mixing zone, as it travels along the pipe [2].

When the specific weights of the products are similar, the contamination process takes place mainly due to turbulent dispersion of matter and has been currently estimated by a number of models [3–11] of semi-empirical nature. However, the majority of these models are based on several simplifying assumptions that in some cases seems to be inadequate. As a consequence, they do not give satisfactory results as would be expected.

This paper presents a new methodology to evaluate the interface contamination which takes into account the variation of the flow rate during the transfer and an accurate concentration-dependent axial dispersion coefficient. A comparison with experimental data shows that the proposed technique is the most accurate in predicting contaminated mixing volumes, among several other methods used in the literature: Sjenitzer [7], Austin and Palfrey [4], Levenspiel [5], Ovadi and Török [6], Smith-Schulze [8,12], Aunicky [3], and Netchval [11].

Problem Statement

Consider the schematic pipeline installation shown in Fig. 1 which is used to sequentially pump two distinct miscible petroleum products designated as "A" and "B." The pipeline has a constant diameter D and a length L, which is measured from the junction of the pump discharge lines $(x=0)$ until the receiving point at the other pipeline end. By an appropriate valve switching, at time instant $t=0$, the pumping of fluid A is interrupted and, at the same time instant, pumping of fluid B is started, so that fluid B begins to push fluid A along the line. Let $C_\iota(x,t)\in[0,1]$, with $\iota\in\{A,B\}$, be the time-averaged mean concentration of fluid ι within the mixture at the cross-section of the pipeline at an axial coordinate $x\in[0,L]$ and time t. In mathematical form, $C_\iota(x,t)$ is defined as

$$C_\iota(x,t) := \frac{1}{2\Delta t A}\int_A\left[\int_{t-\Delta t}^{t+\Delta t}\hat{C}_\iota(x,r,\theta,\tau)\,d\tau\right]r\,dr\,d\theta \tag{1}$$

in which r and θ stand for the radial and circumferential coordinates, A is the internal cross-sectional area of the pipe and $2\Delta t$ is a suitable time interval sufficiently long to cut out turbulent fluctuations and sufficiently short to capture unsteady changes in the concentration field $\hat{C}_\iota(x,r,\theta,t)$.

Based on the past descriptions, the beginning of the sequential transfer can be described in terms of C_B by,

$$C_B(x=0,t=0)=1 \quad \text{and} \quad C_B(0<x\leqslant L,t=0)=0 \tag{2}$$

or in terms of C_A by,

$$C_A(x=0,t=0)=0 \quad \text{and} \quad C_A(0<x\leqslant L,t=0)=1 \tag{3}$$

since, for all (x,t), the following relationship must hold:

$$C_A+C_B=1. \tag{4}$$

During the passage of products through the pipeline a mixing zone is formed at the boundaries of the two adjacent products (see Fig. 1). Such a zone of contaminated material increases in length as it travels along the line and can be delimited by the interval $[x_f,x_i]\subset[0,L]$, with $x_f=x_f(t)$ and $x_i=x_i(t)$, such that for all $x\in(x_f,x_i)$, $1=C_B(x=x_f,t)>C_B(x,t)>C_B(x=x_i,t)=0$ or $0=C_A(x=x_f,t)<C_A(x,t)<C_A(x=x_i,t)=1$. When the beginning of the mixing zone reaches the pipeline end, that is $x_i(t)=L$, the flow is directed toward the mixture tank. Finally, when the end of the mixture zone reaches the pipeline end $(x_f(t)=L)$, the fluid flow is conducted to the tank containing product B (see Fig. 1). In practice, small degrees of contamination are allowed to take place at the beginning and at the end of the mixing zone, which are expressed in terms of the maximum admissible concentrations C_{BA} and C_{AB}, respectively. Once these values (which are not necessarily equal) have been chosen in such a way that the prod-

---

Contributed by the Fluids Engineering Division for publication in the JOURNAL OF FLUIDS ENGINEERING. Manuscript received by the Fluids Engineering Division November 13, 2000; revised manuscript received November 26, 2001. Associate Editor: L. Mondy.

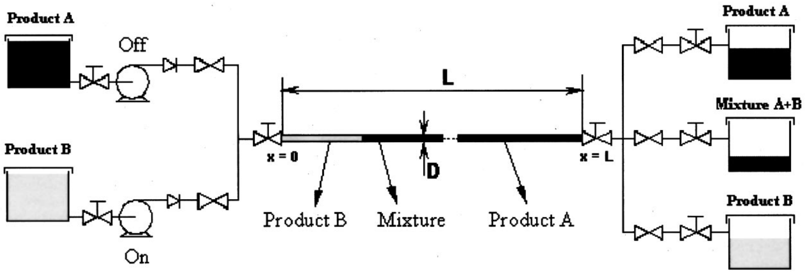

Fig. 1 Schematic representation of a batch transfer installation

ucts technical specifications are not altered, the contaminated volume, which should be stored in the tank for later reprocessing, is defined as:

$$V_c(x=L)=\int_{t_{BA}}^{t_{AB}}\hat{Q}(x=L,t)dt \tag{5}$$

in which $\hat{Q}(x=L,t)$ denotes the volumetric flow rate at the receiving point (that is, the position $x=L$), t_{BA} is the time instant associated to the arrival of the beginning of the contaminated zone with concentration C_{BA} at $x=L$ and t_{AB} is the time instant associated with the arrival of the end of the contaminated zone with concentration C_{AB} at $x=L$. In other words, t_{BA} and t_{AB} are such that $C_B(x=L,t=t_{BA})=C_{BA}$ and $C_A(x=L,t=t_{AB})=C_{AB}$, respectively.

Theoretical Formulation

It has been shown by several investigators [13–15] that, under the assumptions of axisymmetric and incompressible developed isotropic turbulent fluid flow, the intermixing phenomenon of products B and A sequentially transported in a pipeline can be described by the following convection-diffusion equation,

$$\frac{\partial C_\iota}{\partial t}+u\frac{\partial C_\iota}{\partial x}=\frac{\partial}{\partial x}\left[\mathcal{K}\frac{\partial C_\iota}{\partial x}\right] \quad \text{for} \quad \iota\in\{A,B\} \tag{6}$$

in which $u=u(t)$ is the time-averaged bulk velocity,

$$u(t):=\frac{1}{A}\int_A \overline{u}(r,t)rdrd\theta:=\frac{1}{A}\int_A\left[\frac{1}{2\Delta t}\int_{t-\Delta t}^{t+\Delta t}\hat{u}(r,\tau)d\tau\right]rdrd\theta, \tag{7}$$

and $\mathcal{K}=\mathcal{K}(u,C_\iota)$ is the effective axial dispersion coefficient which is given by

$$\mathcal{K}(u,C_\iota)=\nu\,\mathrm{Re}\left[\int_0^1\frac{\left[\int_\xi^1\left(\frac{\overline{u}}{u}-1\right)\xi' d\xi'\right]^2}{2\xi\left\{\frac{\xi f}{16}\left[\left|\frac{\partial}{\partial\xi}\left(\frac{\overline{u}}{u}\right)\right|\right]^{-1}+\left(\frac{1}{Sc}-1\right)\frac{1}{\mathrm{Re}}\right\}}d\xi\right.$$
$$\left.+\int_0^1 2\xi\left\{\frac{\xi f}{16}\left[\left|\frac{\partial}{\partial\xi}\left(\frac{\overline{u}}{u}\right)\right|\right]^{-1}+\left(\frac{1}{Sc}-1\right)\frac{1}{\mathrm{Re}}\right\}d\xi\right] \tag{8}$$

where f is the Darcy-Weisbach friction factor,

$$\xi=\frac{2r}{D},\quad \mathrm{Re}=\mathrm{Re}(u,C_\iota)=\frac{Du}{\nu},\quad Sc=Sc(C_\iota)=\frac{\nu}{\mathcal{D}},$$

$\nu=\nu(C_\iota)$ stands for the kinematic viscosity of the mixture and $\mathcal{D}$ is the molecular diffusivity.

Equation (6) and expression Eq. (8) are obtained by taking the cross-sectional and time average of the momentum equation for the mixture and the mass conservation equations for the products, along with the assumption of long-dispersion times [13,15].

Equation (6) is the basis for a number of models available in the literature used to estimate mixing volumes, which consider as additional simplifying assumptions that $\mathcal{K}$ does not depend on C_ι (the products have similar kinematic viscosities) and that u is constant. However, in some practical cases, these assumptions seem to be inadequate what in turn may endanger the accuracy of the models' predictions.

The dispersion coefficient given by Eq. (8) accounts for the relative motion of the fluid flow with respect to the bulk-average velocity as well as for molecular and eddy diffusion in the axial direction. As reported in some analytical studies [14,16], $\mathcal{K}$, or its nondimensionalized form $K=\mathcal{K}/\nu$, presents a strong dependence not only on the Reynolds number but also on the mean velocity and eddy diffusivity profiles in the turbulent core and pipe wall region. Also, a somewhat less important dependence of K on the Schmidt number is shown to take place at low turbulent Reynolds numbers.

Since Taylor [13] first conceived this approach in 1954, expression Eq. (8) was integrated by several researchers (Tichacek et al. [14], Yablonsky et al. [17], Maron and Galianov [9], Wasan and Dyan [18], Krantz and Wasan [19]) resulting in different correlations of K as function of Re and Sc, i.e., $K=K(\mathrm{Re},\mathrm{Sc})$. These correlations differ mainly due to the mean velocity and eddy diffusivity profiles adopted in evaluating K. The correlation proposed by Krantz and Wasan [19] is the most precise since the mean velocity and eddy diffusivity distributions used to compute K satisfy the equations of motion and boundary conditions in the wall region, providing a smooth and continuous transition to the universal mean velocity profile valid in the turbulent core. Based on these considerations, the Krantz and Wasan's correlation for K will be adopted in this paper. For the sake of simplicity, we consider that K has only the following simpler functional dependence on the Reynolds number of the mixture Re,

$$K=c(\mathrm{Re})^d \tag{9}$$

where c and d are constants. For a fixed Schmidt number, Eq. (9) can be interpreted as being a linearization of the correlation proposed by Krantz and Wasan [19] in a $\log K\times\log\mathrm{Re}$ plot depicted in their paper.

The functional dependence of K on C_ι, which is disregarded in several other models (e.g., Taylor [13], Levenspiel [5], Sjenitzer [7], Aunicky [3], Ovádi and Török [6]), appears when the kinematic viscosity of the mixture is expressed in terms of the viscosities and concentrations of the products in the mixture, such as [20]:

$$\nu^{1/3}=C_A\nu_A^{1/3}+C_B\nu_B^{1/3}. \tag{10}$$

For practical purposes, the parameters c and d of Eq. (9) are determined for a Reynolds number calculated by using the value of u at $t=0$, obtained by Eq. (15) along with the mixture viscosity ν evaluated on the basis of a 50 percent-50 percent blend of A and B through Eq. (10).

One of the effects of considering K as being dependent on C_ι is the asymmetric shape of the concentration distribution profile, as reported by Netchval et al. [11] and pointed out by Austin and

Palfrey [4] and Haisan [21] in field tests. In a more practical sense, Botros [10] has also shown, by using a suitable approximation, that errors up to 20 percent in mixing volumes could be committed when K is assumed not to depend on C_ι.

The success of the models based on Eq. (6) in predicting the intermixing volumes relies heavily on the accuracy of the correlation used for K and on its implicit dependence on C_ι and $u(t)$, through the Reynolds number. Variations in either concentration or the bulk-average fluid velocity can promote changes in the Reynolds number capable to alter substantially the effective axial dispersion coefficient.

The approach considering time dependent fluid velocity and concentration dependent dispersion coefficient was originally proposed by Netchval et al. in 1972 [11]. Nevertheless, Netchval's model has two weak points which severely compromises its application to practical cases. The first is due to the poor correlation used for K, proposed by Yablonski et al. [17]. The second one is related to the approximating analytical solution employed to solve the problem, which is restricted to situations in which the ratio of the products' kinematic viscosities cannot exceed 8.

During a batch transfer, different stretches of the pipeline will be subjected to varying hydraulic conditions inducing, in this way, a slightly time-dependent flow rate. By assuming that the inertia of the liquids is negligible, the specific weights γ_ι, for $\iota \in \{A,B\}$, do not differ significantly from each other, the flow regime remains the same along the whole pipeline, the suction line of the pump is short, minor hydraulic losses can be neglected in the pipe system and, finally, that the mixture process has little effect on the overall balance of linear momentum, this principle can be stated for any time instant as:

$$P_0-\left[\frac{f_B x_m+f_A(L-x_m)}{D}\right]\frac{u^2}{2g}-\Delta z\,\gamma_A-P_L=0 \tag{11}$$

in which

$$\frac{dx_m}{dt}=u. \tag{12}$$

In the above equations $x_m(t)$ stands for the current spatial position of the conventional half-length mixture (that is, the material coordinate in which $C_B(x=x_m(t),t)=C_A(x=x_m(t),t)=0.5$), P_0 and P_L represent, respectively, the pressures at the pump discharge ($x=0$) and at the receiving point ($x=L$), Δz is the topographical level difference between the pipeline positions $x=L$ and $x=0$, g is the gravitational acceleration and f_ι, for $\iota \in \{A,B\}$, is the Darcy-Weisbach friction factor in the stretch of the line occupied by the fluid ι. For the sake of simplicity, the friction factor can be expressed as:

$$f_\iota=\frac{h}{(\mathrm{Re})_\iota^m} \quad \text{with} \quad (\mathrm{Re})_\iota=\frac{uD}{\nu_\iota}, \tag{13}$$

where h and m are constants which depend on the pipe's roughness and ν_ι, for $\iota \in \{A,B\}$, are the kinematic viscosities of the products.

The pump is supposed to be centrifugal and to be operating at constant speed so that its head×flow curve can be expressed as:

$$P_0=(a-bQ^{2-m})\,\gamma_B \tag{14}$$

in which a and b are constants of the pump curve and Q stands for the volumetric flow rate through the pump. If only one pump is employed, then $Q=\pi D^2 u/4$.

Since the pressure at the receiving point is held constant during the transfer, Eqs. (11)–(14) can be combined and solved for x_m, along with the initial condition $x_m(t=0)=0$, to finally obtain the bulk-average velocity as a function of time:

$$u(t)=NL\left[\frac{3-m}{2-m}ANt+B^{3-m/2-m}\right]^{-1/3-m} \tag{15}$$

in which

$$A=\alpha_B-\alpha_A$$

$$B=\alpha_A+b\,\gamma_B$$

$$N=\frac{4}{\pi D^2 L}(a\,\gamma_B-\Delta z\,\gamma_A-P_L)^{1/2-m}$$

$$\alpha_\iota=\frac{h2^{3-2m}\pi^{m-2}\nu_\iota^m\gamma_\iota L}{gD^{5-m}} \quad \text{for} \quad \iota \in \{A,B\}.$$

Since $N>0$ and $m<2$, an analysis of Eq. (15) reveals that the bulk-average velocity can either increase or decrease along the transfer. It will increase (decrease) if $A<0$ ($A>0$), what implies the following inequality in terms of the fluids' properties $\nu_A^m\gamma_A>\nu_B^m\gamma_B$ ($\nu_A^m\gamma_A<\nu_B^m\gamma_B$). As it can be seen in Eq. (15), the larger the difference between the products' kinematic viscosities, the greater the variation of the bulk-average velocity becomes from the beginning to the end of the transfer. Depending on the Reynolds number, such a variation may induce significant changes in K and, consequently, on the mixing volume.

Numerical Solution

The problem described by Eqs. (6), (9), and (15), along with initial conditions given by Eq. (2) or Eq. (3), can be transformed into the following simpler boundary-value problem as shown in Appendix A:

$$\frac{d}{dZ}\left[(1+\lambda_\iota C_\iota)^{-3d}\frac{dC_\iota}{dZ}\right]+2Z\frac{dC_\iota}{dZ}=0 \quad \text{for} \quad \iota \in \{A,B\} \tag{16}$$

with

$$\begin{cases} C_B(Z\to-\infty)=1 \\ C_B(Z\to+\infty)=0 \end{cases} \quad \text{if} \quad \iota=B \tag{17}$$

or

$$\begin{cases} C_A(Z\to-\infty)=0 \\ C_A(Z\to+\infty)=1 \end{cases} \quad \text{if} \quad \iota=A \tag{18}$$

in which

$$\lambda_B=\left(\frac{\nu_B}{\nu_A}\right)^{1/3}-1, \tag{19}$$

$$\lambda_A=\left(\frac{\nu_A}{\nu_B}\right)^{1/3}-1. \tag{20}$$

In the context of this new mathematical formulation, the mixing volume can be readily and accurately evaluated, as shown in Appendix B, once a numerical solution for $C_\iota(Z)$ is obtained. To find an approximating numerical solution of the nonlinear problem described by Eq. (16) with Eq. (17) or Eq. (18), a finite element method coupled with a Newton's scheme is used.

Let β be a real positive number such that the interval $(-\beta,\beta)$ can be taken as adequate approximation of $(-\infty,+\infty)$ in Eq. (16). The Galerkin variational formulation of the problem Eq. (16) with Eq. (17) or Eq. (18) can be stated as: *Find* $C_\iota=C_\iota(Z)\in H^1(-\beta,\beta)$, *such that*

$$\int_{-\beta}^{\beta}[1+\lambda_\iota C_\iota]^{-3d}\frac{dC_\iota}{dZ}\frac{dw}{dZ}dZ-2\int_{-\beta}^{\beta}Z\frac{dC_\iota}{dZ}w\,dZ=0,$$

$$\forall w\in H_0^1(-\beta,\beta) \tag{21}$$

in which $H^1(-\beta,\beta)$ is the classical Sobolev space [22] and $H_0^1(-\beta,\beta)$ is the subspace of $H^1(-\beta,\beta)$ formed by the functions which assume the value zero in $Z=-\beta$ and $Z=\beta$.

Aiming to obtain finite element approximated solutions C_{ι_h} for C_ι, $\iota\in\{A,B\}$, problem Eq. (21) is discretized by using a n dimensional finite element space formed by piecewise linear functions, which is a subspace of $H^1(-\beta,\beta)$. The algebraic nonlinear

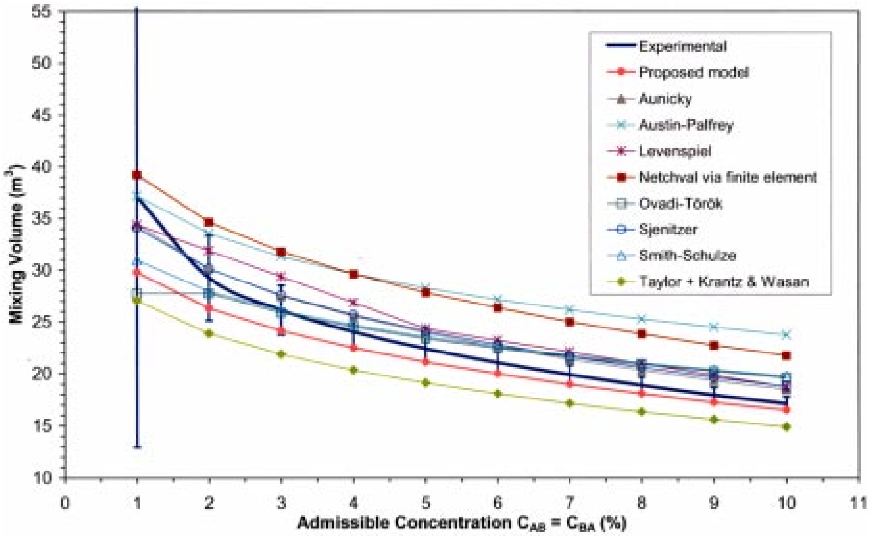

Fig. 2 Predicted and measured mixing volumes versus admissible concentrations at $x = 135.9$ km

system of n equations $\mathbf{F}(\boldsymbol{\chi}_\iota)=\mathbf{0}$ for the n unknowns $\boldsymbol{\chi}_\iota=(\chi_{\iota_1},\cdots,\chi_{\iota_n})$, $\iota\in\{A,B\}$, with $\chi_{\iota_j}=C_{\iota_h}(Z_j)$, being Z_j the nodal points of problem domain, which comes from the discretization process, was solved by the Newton's method.

As an initial approximation of $\boldsymbol{\chi}_\iota^{(0)}$, $\iota\in\{A,B\}$, we have used the analytical approximating solution proposed by Netchval et al. [11]. The convergence criterion used to cease the Newton's iterations is

$$\frac{\|\boldsymbol{\chi}_\iota^{(k+1)}-\boldsymbol{\chi}_\iota^{(k)}\|_\infty}{\|\boldsymbol{\chi}_\iota^{(0)}\|_\infty}\leqslant 1\times 10^{-5} \quad \text{and} \quad \frac{\|\mathbf{F}(\boldsymbol{\chi}_\iota^{(k+1)})\|_\infty}{\|\mathbf{F}(\boldsymbol{\chi}_\iota^{(0)})\|_\infty}\leqslant 1\times 10^{-5} \tag{22}$$

in which $\|\cdot\|_\infty$ is the maximum norm.

Finally, by using this numerical approach, a number of computational tests were carried out in order to establish a value for the parameter β. It was verified that the size of the interval $I=\{Z\in\mathbb{R}:C_{\iota_h}(Z)\in(0,1)\}\subset[-\beta,\beta]$, $\iota\in\{A,B\}$ depends on the value of λ_ι. Specifically, the greater λ_ι is, the larger I becomes. Numerical tests carried out for different practical values of λ_ι have shown that for $\lambda_\iota\leqslant 3$, $\beta=20$ is an adequate threshold. It also should be mentioned that, from the theoretical view-point, if $\lambda_\iota=0$ then, the error committed in approximating C_ι by C_{ι_h}, $\iota\in\{A,B\}$, is, at least, of order h.

Results and Discussion

Aiming to illustrate the performance of the model described in the past sections, a comparison between its predictions and experimental data are next presented, for different values of admissible concentrations $C_{AB}=C_{BA}=1,2,\ldots,9,10$ percent. The experimental data refers to a transfer of gasoline/diesel, being the gasoline the leading fluid ($\gamma_A=734$ kgf/m^3, $\nu_A=0.9$cSt) and the diesel the following product ($\gamma_B=833$ kgf/m^3, $\nu_B=7.6$cSt). The transfer took place in a pipeline 200 km long having a nominal diameter of 25.4 cm (10 inches). The topographical difference level between the receiving point and the pump station is $\Delta z=-895$ m.

The experimental mixing volume was evaluated by continuous monitoring the sonic velocity of the mixture at $x=135.9$ km and at the receiving point, $x=199.9$ km. To do so, a clamp-on transit-time ultrasonic flow meter was used with an acquisition frequency of 0.2 Hz [23,24]. The whole methodology employed to convert the sonic signature of the flowing products into mixing volume as well as its uncertainty analysis are presented in [25]. The volumetric flow rate at the beginning of the transfer was 245 m^3/h and the pressure at the receiving point was $P_L=9.21$ kgf/cm^2. For these conditions, the initial Reynolds number of the mixture (50 percent-50 percent blend) is about 1.3×10^5, rendering the constants $c=0.803$ and $d=-0.136$ in Eq. (9). The parameters a and b of Eq. (14) were determined from the pump curve and are equal to $a=378.8$ m and $b=5099.1$ s$^{1.75}$/m$^{4.25}$. For this pipeline, the following constants $h=0.3164$ and $m=0.25$ associated to the friction factor correlation Eq. (13) were used.

To better characterize the proposed model performance, Figs. 2 and 3 show the contaminated mixing volume as a function of admissible concentrations $C_{AB}=C_{BA}=1,2,\ldots,9,10$ percent for seven traditional methods currently used (Sjenitzer [7], Austin and Palfrey [4], Levenspiel [5], Ovádi and Török [6], Smith-Schulze [8,12], Aunicky [3], Netchval et al. [11]) along with experimental data for $x=135.9$ km and $x=199.9$ km, respectively. Except to Austin and Palfrey [4] and Smith-Schulze [8,12] (which are essentially pure empirical correlations) as well as Netchval et al. [11], the other methods are based on Eq. (6) with different constants values for the dispersion coefficient. Since the original method of Netchval et al. [11] is not capable to deal with kinematic viscosity ratios ν_A/ν_B or ν_B/ν_A greater than 8, the predictions associated with this method-displayed in Figs. 2 and 3-were obtained by using the same finite element technique employed in this paper [26].

As expected, it can be seen in Figs. 2 and 3 that the experimental mixing volume decreases as the admissible concentration increases. Such a trend is also observed for all the seven models, except to the Ovádi and Török [6] which, as the authors say, is valid for $C_{AB}=C_{BA}>2$ percent. Figure 2 reveals that all the methods but the Austin and Palfrey [4] and the Netchval et al. [11] give fairly good predictions of mixing volume at $x=135.9$ km when compared with the experimental data. This same kind of behavior takes place when the mixing volumes are evaluated for $x<135.9$ km. The distinction among the performance of the methods becomes apparent after the batch has traveled the entire pipeline. This assertion is corroborated in Fig. 3, where it can be clearly noted that the proposed method is the only one that still presents the best agreement with experimental data over the whole range of concentration. The proposed model is the unique method whose predictions fits inside the uncertainty bars for any admissible concentration at both spatial positions $x=135.9$ km and $x=199.9$ km.

The greatest discrepancies between the proposed model and the

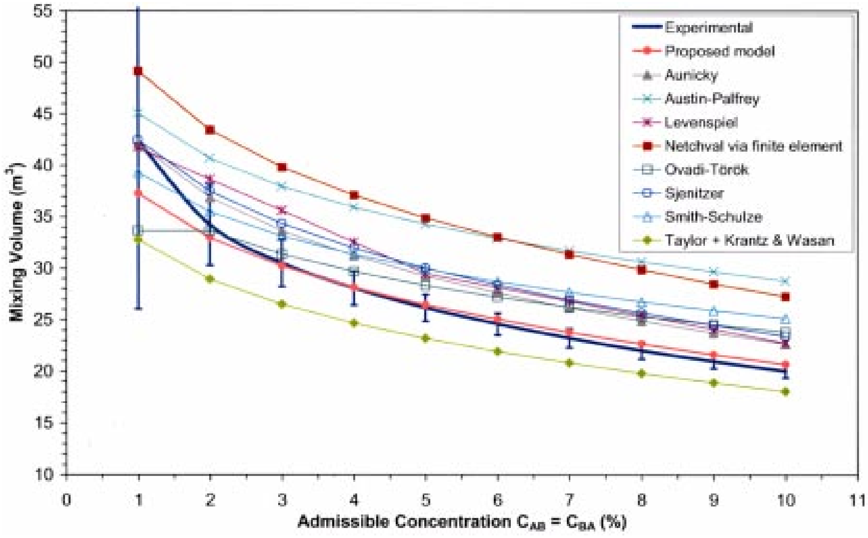

Fig. 3 **Predicted and measured mixing volumes versus admissible concentrations at $x=199.9$ km**

experimental data take place in the range of concentrations $1\% \leqslant C_{AB}=C_{BA} \leqslant 2\%$. However, since the uncertainty associated with the mixing volume varies from ± 16.32 m^3 (for $C_{AB}=C_{BA}=1$ percent) to ± 3.95 m^3 (for $C_{AB}=C_{BA}=2$ percent), as seen in Fig. 3, no comparison among the methods can be effectively done for $C_{AB}=C_{BA}<2$ percent inasmuch as their predictions are within the experimental uncertainty. The practical significance of the proposed method ability in accurately predicting mixing volumes is best highlighted by computing the largest and the smallest relative errors for the best and the worst estimates among the seven methods at $x=199.9$ km. The worst mixing volume estimates are given by the Netchval's method [11], being the relative error in the interval [16.1 percent, 36.5 percent]. For $C_{AB}=C_{BA} \geqslant 2$ percent, the Ovádi and Török [6] method provides the best estimates with relative errors in the range [1.8 percent, 20.6 percent].

To characterize the main feature that renders the proposed model the best performance, it is also depicted in Figs. 2 and 3 the mixing volume predictions obtained by using the Taylor's formulation ($K=$constant) [13], being $K=0.1611$ evaluated by using the Krantz and Wasan [19] correlation for a Reynolds number of 1.3×10^5 (corresponding to an initial flow rate of 245 m^3/h and a mixture kinematic viscosity based on a 50 percent-50 percent blend). As it can be seen in Figs. 2 and 3, the results obtained through this procedure (designated as Taylor+Krantz and Wasan) underestimates the mixing volume for the entire range of admissible concentration analyzed at $x=135.9$ km and at $x=199.9$ km. By comparing the results of Taylor+Krantz and Wasan, Netchval et al., the proposed model and the experimental results, we can conclude that the best estimates of mixing volumes are achieved when both an accurate correlation for K and its functional dependence on the concentration are properly accounted for in the model.

Because of the highly turbulent flow regime, the variation of the bulk-average velocity does not significantly affect the mixing volume in the present case. One can see through Eq. (15) that the fluid velocity at the end of the transfer is approximately 30 percent less than its value at the beginning of the transfer. Such a variation causes the Reynolds number to decrease from 1.5×10^5 to 1.1×10^5, inducing only a small variation in K from 0.161 to 0.170. However, it should be noticed that a 30 percent variation in the flow velocity may induce significant variations in K for Reynolds numbers less than 10^4 [19].

Final Remarks

A model has been proposed in this paper to evaluate mixing volumes in serial transport of petroleum products in pipelines. Its novel features are the incorporation of the flow rate variation with time and the use of a more precise effective dispersion coefficient, which is considered to depend on the concentration. A comparison with experimental data and with other seven traditional methods available in the literature shows that the proposed model is the most accurate over the entire range of admissible concentrations used to compute the mixing volume. It is also shown that the success of the proposed model relies not only on the use of accurate correlations for the dispersion coefficient (in terms of Reynolds and Schmidt numbers) but also on its dependence on the concentration and time-varying bulk-average velocity.

Acknowledgments

The authors kindly acknowledge the financial support provided by CENPES/Petrobras. They also acknowledge the partial financial support provided by the Brazilian Council of Science and Technology (CNPq), the Rio de Janeiro State Research Foundation (FAPERJ) and the Financial Baker of Studies and Projects (FINEP). This work was partially developed in the Laboratory of Theoretical and Applied Mechanics of the Universidade Federal Fluminense (LMTA-UFF).

Nomenclature

a = parameter of the pump curve
A = leading fluid
b = parameter of the pump curve
B = following fluid
c = constant of the correlation between K and Re, Eq. (9)
C_ι = ι-fluid time-averaged mean concentration at the pipeline cross-section, with $\iota \in \{A,B\}$, dimensionless
C_{AB} = maximum admissible concentration at the end of the mixing zone, dimensionless
C_{BA} = maximum admissible concentration at the beginning of the mixing zone, dimensionless
d = constant of the correlation between K and Re, Eq. (9)
D = pipeline diameter, m
f_ι = Darcy-Weisbach friction factor, dimensionless
g = gravitational acceleration, m/s^2

h = constant correlating friction factor and Reynolds' number, Eq. (13)
K = dimensionless effective axial dispersion coefficient, dimensionless
$\mathcal{K}$ = effective axial dispersion coefficient, m^2/s
L = pipeline length, m
m = constant correlating friction factor and Reynolds' number, Eq. (13)
P_0 = pressure at the pump discharge, N/m^2
P_L = pressure at the receiving point, N/m^2
Q = flow rate through the pump, m^3/s
Re = Reynolds' number, dimensionless
u = bulk-average velocity, m/s
V_c = contaminated mixing volume, m^3
x = axial coordinate, m
x_m = instantaneous spatial position of the conventional half-length mixture, *m*
γ_ι = specific weight of fluid ι, with $\iota \in \{A,B\}$, N/m^3
Δz = topographical level difference, m
ν = kinematic viscosity of the mixture, m^2/s
ν_ι = kinematic viscosity of fluid ι, with $\iota \in \{A,B\}$, m^2/s

Appendix A

Boundary-Value Problem. By introducing the following dimensionless parameters for space and time,

$$y=\frac{x}{D}-\tau, \tag{A1}$$

$$\tau=\frac{1}{D}\int_0^t u(t')\,dt', \tag{A2}$$

Eq. (6) can be written in a compact and nondimensionalized form as

$$\frac{\partial C_\iota}{\partial \tau}=\frac{\partial}{\partial y}\left[K\frac{\partial C_\iota}{\partial y}\right] \quad \text{for} \quad \iota \in \{A,B\} \tag{A3}$$

in which $K=\mathcal{K}/\nu$ stands for the dimensionless effective axial dispersion coefficient.

In view of the simple form adopted for K in Eq. (9), it is possible to impose the change of variables in Eq. (A3),

$$Z=\frac{y}{2\sqrt{\eta}} \tag{A4}$$

in which

$$\eta=\int_0^\tau K_J(\tau')\,d\tau' \quad \text{with} \quad K_J=c(\mathrm{Re})_J^d, \quad \text{for} \quad J \in \{A,B\}, \tag{A5}$$

in order to transform the initial-value problem Eq. (6) and Eq. (2) or Eq. (3) into the boundary-value problem Eq. (16) with Eq. (17) or Eq. (18).

Usage of Eq. (16) with $\iota=A$ or $\iota=B$ is carried out depending on the condition: if $\nu_B \geqslant \nu_A$, then $\iota=B$ and $J=A$; if $\nu_A > \nu_B$, then $\iota=A$ and $J=B$.

Appendix B

Mixing Volume Determination. Once the solution $C_B(Z)$ of Eq. (16) with Eq. (17) is determined, Eq. (4) is used to evaluate $C_A(Z)$. Similarly, if $C_A(Z)$ is computed through Eq. (16) with Eq. (18) then $C_B(Z)$ is evaluated by Eq. (4). Whatever the case $\iota=B$ or $\iota=A$ is, the dimensionless time instants $\tau_{BA}=\tau(t_{BA})$ and $\tau_{AB}=\tau(t_{AB})$, associated with the arrival of the beginning and of the end of the mixing volume at a generic position $x=x^\star$, $x^\star \in (0,L]$ can be written from Eq. (A4) as:

$$\tau_{BA}=\frac{x^\star}{D}-2Z_{BA}\sqrt{\eta(\tau_{BA})} \tag{B1}$$

$$\tau_{AB}=\frac{x^\star}{D}-2Z_{AB}\sqrt{\eta(\tau_{AB})} \tag{B2}$$

in which the parameters $Z_{AB}=C_B^{-1}(C_{AB})$ and $Z_{BA}=C_A^{-1}(C_{BA})$ represent the values of Z for which the concentration assumes the pre-set admissible tolerances at the mixture zone extremities. Finally, based on Eq. (B1), Eq. (B2) and using the definition of τ in Eq. (A2), the contaminated mixing volume given by Eq. (5) at $x=x^\star$ can be expressed as

$$V_c(x=x^\star)=2\,\frac{D}{x^\star}\left(Z_{BA}\sqrt{\eta(\tau_{BA})}-Z_{AB}\sqrt{\eta(\tau_{AB})}\right)V_p \tag{B3}$$

in which $V_p=\pi D^2 x^\star/4$ stands for the pipeline volume in the pipeline stretch $[0,x^\star]$.

References

[1] Hara, A., Hayashi, H., and Tsuchiya, M., 1979, "Sphere separation system aids long-haul oil-product transport," Oil & Gas Journal, **22**, pp. 47–51.
[2] Benke, H., and Gravert, W., 1989, "Process analysers for optimisation of reinjection of contaminated product in product pipelines," Oil Gas European Magazine, **1**, pp. 42–44.
[3] Aunicky, Z., 1970, "The longitudinal mixing of liquids flowing successively in pipelines," Can. J. Chem. Eng., **48**, pp. 12–16.
[4] Austin, J. E., and Palfrey, J. R., 1964, "Mixing of miscible but dissimilar liquids in a serial flow in a pipeline," Proc. Inst. Mech. Eng., **178**, Part 1, No. 15, pp. 377–395.
[5] Levenspiel, O., 1958, "How much mixing occurs between batches?," Pipe Line Industry, May, pp. 51–54.
[6] Ovádi, Z., and Török, E., 1977, "Examination of pipeline transport from the viewpoint of goods quality," Köolaj és Földgáz, **10**, No. 4, pp. 121–123. In Hungarian.
[7] Sjenitzer, F., 1958, "How much do products mix in a pipeline?," The Pipeline Engineer, Dec., pp. D31–D34.
[8] Smith, S. S., and Schulze, R. K., 1948, "Interfacial mixing characteristics of products in products pipe line—Part 1," The Petroleum Engineer, **20**, pp. 94–104.
[9] Maron, V. I., and Galianov, A. I., 1970, "Mixture coefficients for liquid flows in pipes," Izsvesta Vischikh Utchebnuikh Zavedenii Neft'i Gaz, **2**, pp. 74–78. In Russian.
[10] Botros, K. K., 1984, "Estimating contamination between batches in products lines," The Oil and Gas Journal, **13**, pp. 112–114.
[11] Netchval, M. V., Tugunov, P. I., and Slesáreva, V. G., 1972, "Mixture formation during the process of sequential pumping of petroleum products of varying viscosities," Neftyanoy Khozyaistvo, **50**, No. 8, pp. 57–59. In Russian.
[12] Smith, S. S., and Schulze, R. K., 1948, "Interfacial mixing characteristics of products in products pipe line - Part 2," The Petroleum Engineer, **20**, pp. 7–12.
[13] Taylor, G. I., 1954, "The dispersion of matter in turbulent flow through a pipe," Proc. R. Soc. London, Ser. A, **223**, pp. 446–468.
[14] Tichacek, L. J., Barkelew, C. H., and Baron, T., 1957, "Axial mixing in pipes," American Institute of Chemical Engineering Journal, **3**, No. 4, pp. 439–442.
[15] Atesmen, K. M., Baldwin, L. V., and Haberstroh, R. D., 1971, "The dispersion of matter in turbulent pipe flows," ASME J. Basic Eng., Dec., pp. 161–477.
[16] Bischoff, K. B., and Levenspiel, O., 1962, "Fluid dispersion-generalization and comparison of mathematical models-II Comparison of models," Chem. Eng. Sci., **17**, pp. 257–264.
[17] Yablonski, V. S., Asaturyan, A. S., and Khizgilov, I. H., 1960, "Turbulent Diffusion in Pipes," Inzh.-Fiz. Zh., **3**, No. 3, pp. 117–122. In Russian.
[18] Wasan, D. T., and Dayan, J., 1970, "The dispersion of solute in turbulent pipe flow of non-Newtonian fluids," Can. J. Chem. Eng. **48**, pp. 129–131.
[19] Krantz, W. B., and Wasan, D. T., 1974, "Axial dispersion in turbulent flow of power-law fluids in straight tubes," Industrial Chemical Fundamentals, **13**, No. 1, pp. 56–61.
[20] Gambill, W. R., 1959, "How to estimate mixtures viscosities," Chem. Eng., **66**, pp. 151–152.
[21] Haisan, Q., 1997, "Contamination due to intermixing in pipelines," Journal of Petrochemical Universities, **10**, No. 2, pp. 68–70. In Chinese.
[22] Adams, R. A., 1968, *Sobolev Spaces*, The Academic Press, New York.
[23] Couto, N. C., 1998, "Products separation in pipeline by using low-density foam pigs (Final Report)," Internal Report Petrobras-Petróleo Brasileiro S. A., CENPES/SUPEP/DIPLOT/SEPROT, Project 02.05.07. In Portuguese.

[24] Freitas Rachid, F. B., Carneiro de Araujo, J. H., Martins-Costa, M. L., and Costa Mattos, H. S., 1999a, ‘‘Development of models and operational procedures aiming to minimize the interfacial volume-Second Report,’’ Internal Report, Project Petrobras-UFF. In Portuguese.

[25] Baptista, R. M., Freitas Rachid, F. B., and Carneiro Araujo, J. H., 2000, ‘‘Mixing volume determination in batch transfers through sonic detectors,’’ *Proceedings of the 8th Brazilian Congress of Thermal Engineering and Sciences*, Paper S22P1, Porto Alegre, October 3–6.

[26] Freitas Rachid, F. B., Carneiro de Araujo, J. H., Martins-Costa, M. L., and Costa Mattos, H. S., 1999b, ‘‘Development of models and operational procedures aiming to minimize the interfacial volume-Third Report,’’ Internal Report, Project Petrobras-UFF. In Portuguese.

Oscillatory Flow in a Physical Model of a Thin Slab Casting Mould With a Bifurcated Submerged Entry Nozzle

Nicholas J. Lawson
Lecturer,
Department of Aerospace, Power and Sensors,
Royal Military College of Science,
Cranfield University,
Shrivenham, Wiltshire. SN6 8LA,
United Kingdom
e-mail: n.j.lawson@rmcs.cranfield.ac.uk

Malcolm R. Davidson
Associate Professor,
Department of Chemical Engineering,
The University of Melbourne,
Parkville, Victoria 3010, Australia
e-mail: m.davidson@unimelb.edu.au

Laser Doppler anemometry (LDA) measurements are presented of the oscillatory flow in a 33% scale water model of thin slab casting mould when the flow enters as two lateral jets through a bifurcated nozzle. The submerged entry nozzle (SEN) and the mould were geometrically scaled to be representative of industrial thin slab casters. Mean and RMS LDA velocity measurements were taken at three selected points in the region surrounding the SEN, at 500 points in the central plane parallel to the broad face of the mould, and at points in selected transverse sections, for casting rates up to 1.53 m/min. Flow visualization was also taken at two selected planes in the mould. The LDA results showed each jet to form an upper and lower recirculation zone with the lower zones adjacent to one another bounded by the jets and the mould walls and the upper zones bounded by the jet, the SEN, the mould walls and the free surface. Both jets were found to have most oscillatory energy at frequencies below 5 Hz with high energy low frequency modes occurring at frequencies below 0.2 Hz. However, no single dominant frequency occurred in the spectrum and flow visualization revealed an apparently chaotic flow pattern in the oscillation. Midpoint jet deflection was restricted to 6–8 mm RMS, and no coherence was observed between jet (and free surface) movements on either side of the mould. The time averaged flow pattern was found to be almost symmetric across the wide face of the mould. It is concluded that both shear layer instability in the impinging jets, and deflection of the jets due to cross-flow at the SEN-mould wall, contribute to the flow oscillation. [DOI: 10.1115/1.1459077]

Introduction

In continuous slab casting of steel [1], liquid metal is injected into a water-cooled bottomless mould using a submerged entry nozzle (SEN). The outer edges of the liquid adjacent to the mould wall freeze to form a shell which increases in thickness as it is continuously withdrawn from the bottom of the mould. The rate of withdrawal, or "casting rate," equals the flow rate of the injected liquid metal. The nozzle is typically bifurcated with two opposed side outlet ports. The two lateral jets exiting the nozzle set up four recirculating cells within the mould as shown in the schematic of the flow in Fig. 1.

The flow system in the mould is complex, involving three-dimensional turbulent liquid flow coupled with heat transfer, solidification, and solute transport. Significant numerical and physical modeling studies of the process have ranged from the consideration of combined models [2,3] to those concentrating specifically on the flow in the nozzle [4] and in the mould [5]. Recent research has considered the effect of increasing the casting rate and using thinner moulds to reduce the cost of subsequent hot rolling [6]. The aim of such procedures is to improve process efficiency [7]. However, they result in increased flow unsteadiness and free surface oscillations of the liquid metal which can reduce product quality [8,9]. Such oscillations can occur when the flow rate through the nozzle is steady (i.e., they can be self-sustaining). Understanding the fluid dynamics in the mould is necessary for the development of improved process design of thin slab casting at increased casting rates.

There have been increasing efforts to model transient fluid flow in the mould both experimentally and numerically. In most cases, the measurement of flow disturbances in water models of the mould [9–12] were based on simple image analysis, free surface measurements, and flow visualization. Broadly, these studies showed that the surface disturbances at increased casting rates are associated with an unstable flow pattern and jet oscillation in the mould. More recently, the authors [13–16] reported laser Doppler anemometry (LDA) and cinematic particle image velocimetry (PIV) measurements of self-sustaining oscillating jet flow in a water model when the SEN consisted of a simple pipe (single downwards jet) rather than a bifurcated arrangement (two lateral jets). They found a single frequency of oscillation which depended on the casting rate and the geometry, obtained detailed pointwise and full field velocity data for a range of parameters, and developed a computational fluid dynamic model which gave close agreement with the experimental data for mean velocity, turbulence, and oscillation frequency.

However, a bifurcated nozzle is more characteristic of industrial practice, and detailed measurements of the fluctuating flow field in the mould are required for that case as a basis for further model development and understanding. Previous flow visualization studies [11,12] have demonstrated flow oscillation and asymmetry in a mould with a bifurcated nozzle; however, significantly greater quantities of data can be provided by LDA which is a nonintrusive velocity measurement technique [17]. Panaras et al. [18] reported some limited LDA measurements in the mould near the nozzle but did not characterize the transient behavior. The aim of the present paper is to investigate the oscillatory flow behavior of the bifurcated jet flow represented in Fig. 1, and to determine the three-dimensional mean and turbulent flow characteristics within the mould.

Contributed by the Fluids Engineering Division for publication in the JOURNAL OF FLUIDS ENGINEERING. Manuscript received by the Fluids Engineering Division April 30, 2001; revised manuscript received November 7, 2001. Associate Editor: K. Zaman.

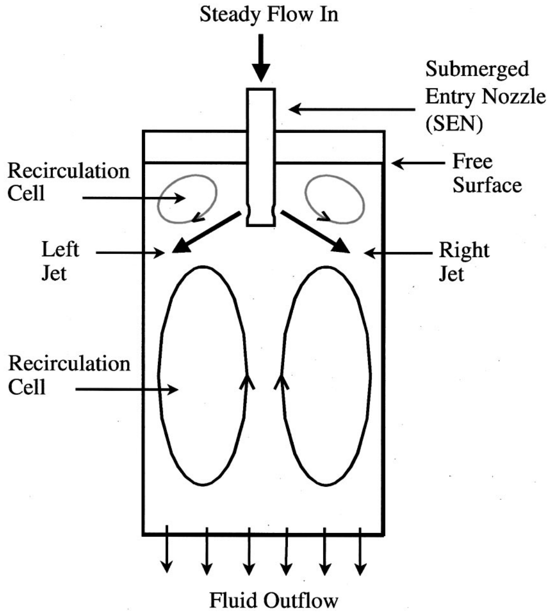

Fig. 1 Schematic of the flow field

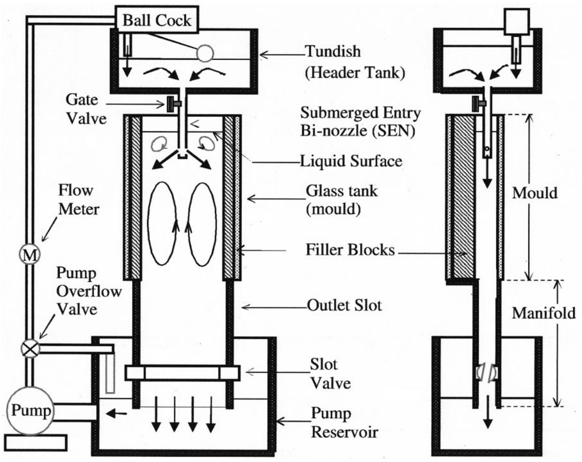

Fig. 2 Schematic of the experimental rig

Experimental Rig

Figure 2 shows the experimental rig consisting of a mould, a tundish, and an outlet manifold. To allow LDA and flow visualization the mould was constructed with glass walls and had maximum dimensions of length $L = 800$ mm, width $W = 500$ mm, and thickness $H = 180$ mm (Fig. 3). These sizes were representative of a 1/3 scale mould geometry as considered by Honeyands [9]. A wide range of mould geometries could also be selected by clamping polystyrene and perspex filler blocks on to the inside of the mould walls. This system permitted a range of mould widths from $80\ \text{mm} < W < 500\ \text{mm}$ and mould thicknesses from between $55\ \text{mm} < H < 180\ \text{mm}$.

To provide a steady mass flow into the mould, a 200 liter tundish (header tank) mounted 500 mm above the free surface, supplied water to the SEN. For all measurements the bifurcated SEN design consisted of a closed ended 38 mm diameter pipe with wall thickness 2.5 mm, having two circular holes at the sides (the nozzle ports) as shown in Fig. 3. The ports are 20 mm in diameter and their centers are located 20 mm above the internal end wall of the pipe. The port angle [19] is zero (i.e., the edges of the nozzle ports are horizontal).

To ensure an even outflow from the bottom of the mould, a manifold was designed with an adjustable slot valve. This was found to be the best solution as other manifold designs would bias the flow to one side of the mould thus affecting jet oscillation [15]. The manifold had dimensions of $300\ \text{mm} \times 500\ \text{mm} \times 100\ \text{mm}$ prior to the valve and a $250\ \text{mm} \times 500\ \text{mm} \times 100\ \text{mm}$ extension slot after the valve. The extension resulted in submergence of the bottom of the manifold into the pump reservoir and this was found to prevent air entrainment into the mould.

The flow circuit through the rig consisted of flow from the tundish to the mould followed by flow into the reservoir and then back to the tundish. This circuit was maintained by a Harland 2 kW centrifugal pump fitted with an overflow into the reservoir to prevent pump stall at low flow rates. The head in the tundish was kept constant using a commercially available Apex ballcock with a 150 mm diameter float and flow through the SEN was controlled by a gate valve placed at the tundish outlet. With this system reliable flow control through the nozzle could be achieved for a range of casting rates of between 0.5 and 1.5 m/min. Here "casting rate" refers to the mean discharge velocity from the manifold.

To monitor the flow rate through the system, a Coles Palmer electronic turbine flow meter, model 05610-40 was fitted between the pump and the tundish. Calibration of the flow meter to convert

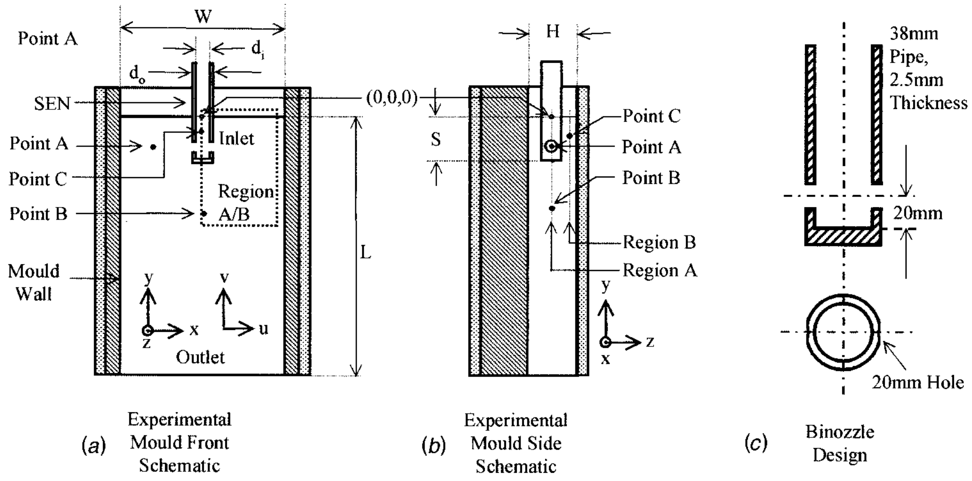

(*a*) Experimental Mould Front Schematic
(*b*) Experimental Mould Side Schematic
(*c*) Binozzle Design

W = Mould Width, L = Mould Length, L*= Dimensionless Length, H = Mould Thickness,
d_o = SEN Outer Diameter, d_i = SEN Inner Diameter, S = SEN Submergence

Fig. 3 Schematic showing experimental parameters

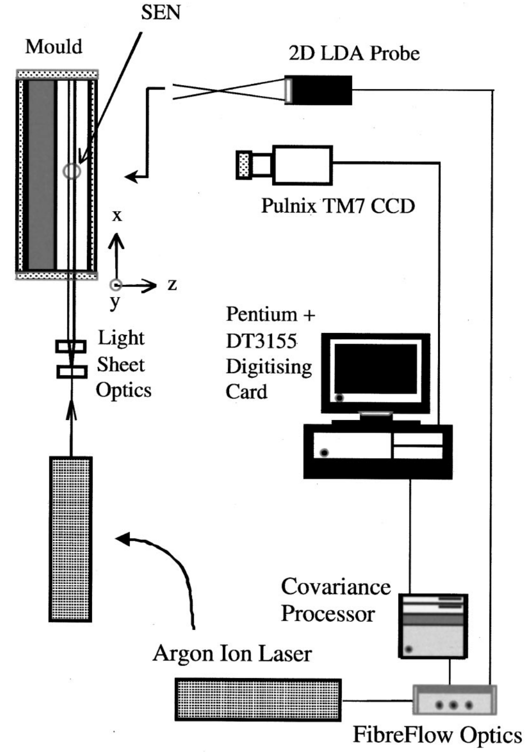

Fig. 4 Schematic of the LDA and flow visualization experimental setup

the flow meter reading into a casting rate was performed by measuring the time taken for the water level in the mould to fall 50 mm for a range of flow meter readings.

Measurement Systems

LDA was primarily used to analyze the fluid flow in the mould. Flow visualization was also used but only to examine large scale transient flow structures around the jet region. These systems are now described in more detail.

LDA System. This consisted of a 2D Dantec FibreFlow system with a 58N40 FVA covariance signal processor and a Coherent 4W Argon Ion laser as illustrated in Fig. 4. A back scatter probe was used with a 250 mm focal length lens and was set up with the green line (514.5 nm) for the horizontal velocity component u and the blue line (488 nm) for the vertical velocity component ν. This provided a measurement probe volume of $0.117\ \mathrm{mm}\times 0.117\ \mathrm{mm}\times 1.544\ \mathrm{mm}$ for the horizontal velocity component and $0.111\ \mathrm{mm}\times 0.111\ \mathrm{mm}\times 1.464\ \mathrm{mm}$ for the vertical velocity component. Seeding was with Fidene silver coated hollow glass spheres with a size range of 10–30 μm and a specific gravity of 1.1. This was expected to provide adequate flow fidelity [20]. Sampling periods were 30–90 s with an average sampling rate of up to 1 kHz. This allowed the raw u-v data to be resampled for spectral analysis as outlined previously [15] in order to examine oscillatory properties of the flow.

Flow Visualization. The flow visualization system was based on the LDA Argon Ion laser with light sheet optics and a commercially available Pulnix CCD camera as shown in Fig. 4. The light sheet optics simply consisted of a 5 mm glass rod mounted in the path of the laser which generated a large angle light sheet with a thickness of around 1.5 mm. Data from the CCD was directly digitized into 768×576 pixel images at up to 12.5 Hz by using a Data Translation DT3155 digitizing board and in-house developed software. Sequences of up to 80 frames were stored to analyze cycles of the flow. The CCD was restricted to recording images from regions A and B about the mould centreline and cross flow region, respectively, as shown in Fig. 3. The digitized frames were subsequently processed into video AVI files for analysis using MS VidEdit software.

Table 1 Measurement conditions (W=500 mm, H=80 mm)

Casting rate R (m/min)	SEN Submergence S (mm)
1.53	120
1.39	120
1.09	120
0.82	120
0.55	120
1.53	100
1.53	80
1.53	60

Flow Measurements

To characterize the flow, LDA measurements in the mould were taken across the central x-y plane and at selected points in other planes through the mould. These measurements were used to obtain the mean flow structure and RMS velocity characteristics in the mould. Measurements were also taken at point A adjacent to the jet ($x=-100$ mm, $y=-10$ mm, $z=0$), at point B below the SEN ($x=0$, $y=-150$ mm, $z=0$) and at point C in the cross flow region between the SEN and the mould wall ($x=0$, $y=-60$ mm, $z=-24$ mm). Points A, B, C are shown in Fig. 3. The position of these three points was based on previous experience from flow measurements of a single oscillatory jet [15]. Spectral analysis of the u-v data at these points was used to provide information on jet and cross-flow oscillation.

The flow visualization was used to link the oscillatory nature of the LDA point measurements at A, B, and C with larger scale jet movements in the mould. For this reason two regions A and B, shown in Fig. 3, were positioned on the mould center-plane on one side of the jet ($x>0$, $z=0$) and in the cross-flow region ($x>0$, $z=-24$ mm) on the same side of the jet.

Measurements were taken for a fixed value of the mould width ($W=500$ mm) and a fixed value of mould thickness ($H=80$ mm). The SEN geometry was also fixed as shown in Fig. 3. Measurements were also taken for a range of casting rates (R) and SEN submergences (S). Table 1 lists the experimental conditions which are variations from a base case casting rate of $R=1.53$ m/min and a submergence of $S=120$ mm. In all cases the SEN was positioned centrally on the vertical line $x=0$, $z=0$. Details of the LDA data and error analysis are given in Lawson and Davidson [15].

Oscillation Characteristics

In the previous study [15,16] the authors considered self-sustaining oscillations of single jet flow from a SEN consisting of a simple vertical pipe, open at the end. A feature of self-sustaining oscillations is the presence of a feedback whereby downstream events can influence the flow from which they originate [21,22]. In the single jet case considered previously, the oscillation relies on the presence of a cross-flow through the gap between the nozzle shaft and the broad face of the mould. This cross-flow provides a feedback loop which links the recirculation cells on each side of the jet and opposes the tendency of the jet to attach to one side wall or the other (Coanda effect) at elevated Reynolds number, thereby setting up a self-sustaining oscillation. The oscillation was roughly sinusoidal in appearance with a single dominant frequency determined from the power spectrum of the time series. The authors concluded that additional feedback between the jet attachment point and the nozzle exit via the individual recirculation cells (as distinct from the cross-flow *between* cells) was not fundamental for flow oscillation in that case.

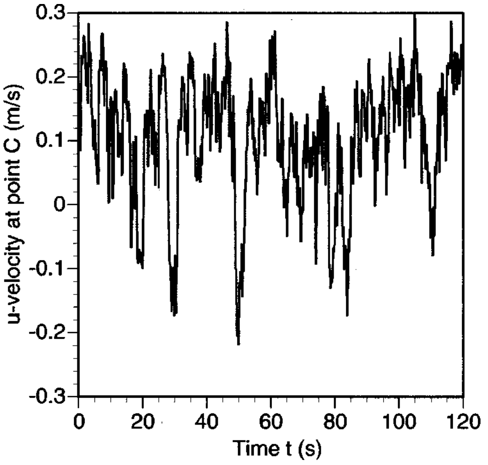

Fig. 5 ***u*** **component time series at point C (casting rate 1.09 m/s, SEN submergence 120 mm)**

For the bifurcated nozzle, the situation is more complicated. As mentioned earlier and shown in Fig. 1, there are now two jets and four recirculation cells. Cross-flow between the top two cells and feedback via individual recirculation cells may both be important in maintaining an oscillation. That the latter feedback loop may be significant in this case is supported by numerical calculations of Brummayer et al. [23] who obtained self-sustained oscillations for a bifurcated nozzle from calculations that assume quarter symmetry of the flow, and hence force cross-flow to be zero. The present authors have also found similar numerical behavior in preliminary three-dimensional simulations [24].

The time series shown in Fig. 5 for the cross-flow velocity at point C does not exhibit the regular cyclic behavior characteristic of the single jet cross-flow oscillation, and is without any obvious pattern. The time series at point A within the top-left recirculation cell is similar. The corresponding power spectra at points A, B, and C (Fig. 6) confirm that the oscillation is not a simple combination of modes. Instead, modes of all frequencies are represented to about 5 Hz. Low frequency modes dominate, especially frequencies less than about 0.2 Hz. For example, at point A the power spectrum exceeds 1×10^{-3} at frequencies 0.008, 0.075, 0.108, 0.117 Hz. Thus although the bulk of the energy is spread over 5 Hz, energetic modes exist with periods as long as 100 s. The oscillation is more energetic in the top recirculation cell (point A) than it is in the cross-flow (point C). The oscillation at point B directly below the nozzle contains much less energy as this point is bypassed by the jets. For the other flow rates given in Table 1, the trends are similar to those in Fig. 6.

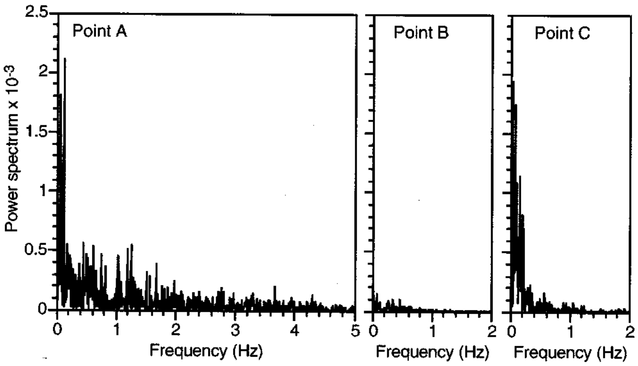

Fig. 6 Power spectrum of horizontal velocity *u* at monitoring points in the cross-flow for a casting rate R=1.09 m/min and SEN submergence S=120 mm

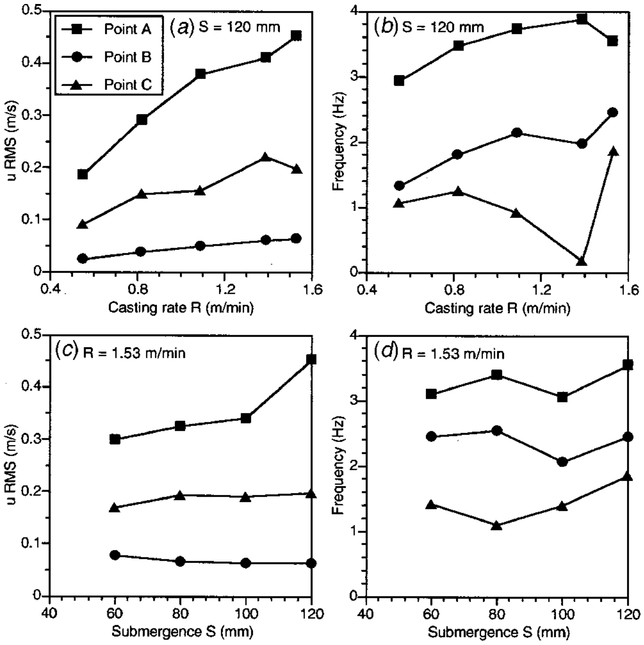

Fig. 7 RMS of the horizontal velocity component (*u*) and the "cut-off" frequency of the oscillation at points A, B, and C versus casting rate and nozzle submergence. The cut-off frequency marks the maximum frequency of modes which together contain 90 percent of the fluctuating (horizontal) kinetic energy.

To explore the dependence of frequency on parameters, such as casting rate and nozzle submergence, a "cut-off" frequency, below which 90% of the fluctuating kinetic energy occurs is considered. The RMS and frequency characteristics for the flow at points A, B, and C, based on the horizontal velocity component, are shown in Fig. 7. These are discussed in the following.

Effect of Casting Rate. At point A, which is adjacent to the jet, the RMS velocity appears to increase linearly with casting rate (Fig. 7(*a*)). Similar trends occur at points B (below the nozzle) and C (cross-flow region). The observation is consistent with cross-flow velocity measurements for single jet flow from a straight-through nozzle considered previously [15] and is associated with the increase in mean velocity of flow from the nozzle generating higher energy levels in the surrounding fluid. A linear relationship is also consistent with a dimensionless flow field (with casting rate as the velocity scale) which is independent of flow rate.

However, the corresponding cut-off frequencies do not scale with casting rate. This is in contrast to the straight-through nozzle case studied previously [15] where frequency increased linearly with casting rate. Furthermore, in the present bifurcated nozzle case, the flow at points A, B, and C shows markedly different frequency behavior with increasing casting rate (Fig. 7(*b*)). For instance, the frequency at point A gradually increases from 3 to 4 Hz before falling at a casting rate of 1.39 m/min. However, at point C there is a decrease in frequency from 1 Hz down to around 0.25 Hz at a casting rate of 1.39 m/min before a sharp increase to 2 Hz. The flow behavior is therefore very dependent on local flow conditions in the mould. The cut-off frequency values at point B are greater than those at point C because the oscillation at point C has relatively more energy concentrated at low frequencies, as shown in Fig. 6.

The small changes in frequency at point A in the region of the jet suggest that the jet is not moving around significantly. Flow visualization confirmed this since, although the jet was seen to move chaotically, no major jet deflection occurred in the point A region. For the straight-through SEN [15,16], jet oscillation is connected with the movement of the recirculation cells surrounding the jet. The lack of significant jet deflection in the present case may be caused by the position of the upper recirculation cell which is bounded by the free surface, the mould wall, the SEN, and the jet itself (see Fig. 1). The recirculation cell formed occupies all of this upper area and thus has no flow volume available for significant movement. This is in contrast to the lower cells formed in the mould below the jet; these have the volume in the manifold to allow displacement or expansion. Therefore it is possible that movement or expansion of the lower recirculation cells in the mould generates the frequency behavior of point B (below the nozzle) which appears to scale more linearly with casting rate.

Point C lies in the cross-flow region connecting the two upper recirculation cells on opposite sides of the SEN. From flow visualization, the cross-flow was found to be highly chaotic like the flow at point A, and was dependent on the position and relative strength of the two upper recirculation cells. Since those recirculation flows act in opposition in the cross-flow region, minor changes in their strength and location can have a marked effect on the cross-flow. The significant frequency minimum with casting rate that occurs at point C is unlike the generally increasing trends at points A and B, and is consistent with such a flow-sensitive balance.

Effect of Nozzle Submergence. From Fig. 7(*c*), the *u*-RMS velocity at point A is seen to increase significantly with submergence (distance between the free surface and the nozzle tip), but changes insignificantly at points B and C. This can be attributed to the position of the jet relative to point A which is fixed at 100 mm below the free surface adjacent to the jet. When the submergence is 60 mm, point A is sufficiently distant from the nozzle ports to experience a reduced effect of the jet. However, at a submergence of 120 mm, the jet centerline is within 20 mm (vertically) of point A and therefore the energy of the fluid, represented by the RMS velocity, increases significantly. In contrast, points B and C appear to be independent of the submergence because they are not near the path of the jet.

The frequency characteristics shown in Fig. 7(*d*) do not exhibit any significant dependence on SEN submergence. This is attributed to the minimal movement of the upper recirculation cell which fills the space bounded by the jet, free surface, the mould wall, and the SEN.

Flow Field Characteristics

Effect of Sampling Period. The finding that energetic modes of oscillation exist with periods of 10-100 s has important implications for the choice of sampling period over which mean and RMS velocities are determined from the time series. If sufficient energy resides in such low frequency modes, then a sampling period between 30 and 90 s, as used here, could be too short, resulting in time averages which are not independent of sampling period. Figure 8 shows the effect of sampling period on the transverse (z) profile of the mean vertical velocity at $y = -145$ mm and $x = \pm 130$ mm. The results show that a sampling period of 30 s is adequate except for positive x and z values. A comparison involving v-RMS gives similar results with the same conclusion.

The local complexity of the flow, however, results in no single appropriate sampling time for the complete flow field. This is because the local time scales of the flow will vary from region to region as has already been demonstrated by frequency analysis of points A, B, and C in the previous section. The time scale of the flow and the sample period have a direct influence on the error in measurement of the mean velocity. If the time taken is too short the error in mean velocity measurement will become significant. For LDA, the error in measurement, *e*, at a point in the fluid has been shown to equal [25]:

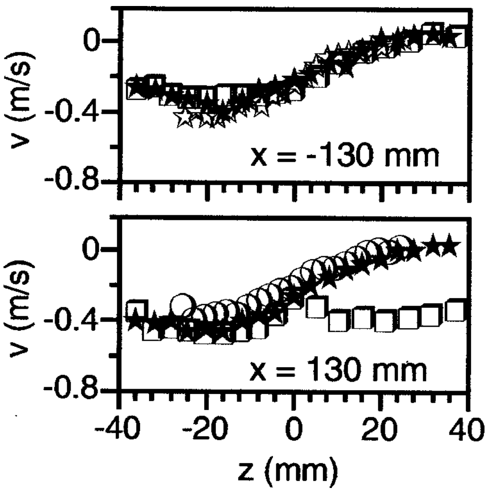

Fig. 8 Comparison of LDA measurements of mean vertical velocity at depth $y = -145$ mm for three different sampling periods (□30 s,★45 s,☆78 s,○90 s) when casting rate R = 1.53 m/min and SEN submergence S = 120 mm

$$e^2 = \frac{2T_u}{T}\left[1 + \frac{1}{2vT_u}\right]\left[\frac{\sigma_u}{\overline{u}}\right]^2 \tag{1}$$

where T_u is the integral time scale, T the sample time, v the sampling rate, $\overline{u}$ the fluid mean velocity, and σ_u the standard deviation of u. Therefore if for example the flow has a time scale of 30 s, the error in measurement will halve if the sample time is increased from 30 s to 120 s. But the error will also be depend on the local flow conditions, i.e., the turbulence level $u_{\rm rms}$. Therefore without a priori information on the shortest and longest time scales in the flow and information on local flow conditions, estimating appropriate sampling periods for this experiment was found to be problematic and resulted in variations in mean velocity plots as illustrated in Fig. 8 Typically, time averaged results presented in the paper were based on sampling periods of between 45–90 s. Therefore for example with a turbulence level of 5%, an integral time scale of 100 s, and a 1 kHz sampling rate, errors in mean velocity measurement of between 7–10% would be expected.

Free Surface and Jet Motion. The characteristics of the free surface and jet oscillations were analyzed using flow visualization images which where taken from the mould at a frame rate of 10 Hz. The frequency characteristics of the free surface oscillations were determined by spectral analysis of the transient free surface height on the mould wall at $x = \pm 250$ mm, and midway between the nozzle and wall at $x = \pm 125$ mm. It was found, as with the LDA data of the flow adjacent to the jet (Fig. 6), that the majority of the energy in the free surface movement is restricted to frequencies below 3 Hz. The dominant frequency at the wall was found to be 0.16 Hz (period 6 s) and that at $x = \pm 125$ mm to be 1.7 Hz (period 0.6 s). Examination of the surface position vs time also shows no obvious coherence between the free surface movement either side of the mould. This result is further reinforced by spectral analysis of the jet centerline position estimated from the images at $x = \pm 125$ mm. As for the free surface motion, the majority of the oscillation energy is contained below 3 Hz with the dominant frequency at 0.16 Hz and no coherence between left and right (jets). Furthermore, the jet oscillation appears to influence the free surface motion. Further observation of the visualization images also shows rapid fluctuations in the jet positions when flow appears to be shed from recirculation zones at the bottom half of the mould. However, despite such fluctuations in jet position, the actual jet movement at its midpoint ($x = \pm 125$ mm) is restricted to 7.77 mm RMS on the left and 6.16 mm RMS on the

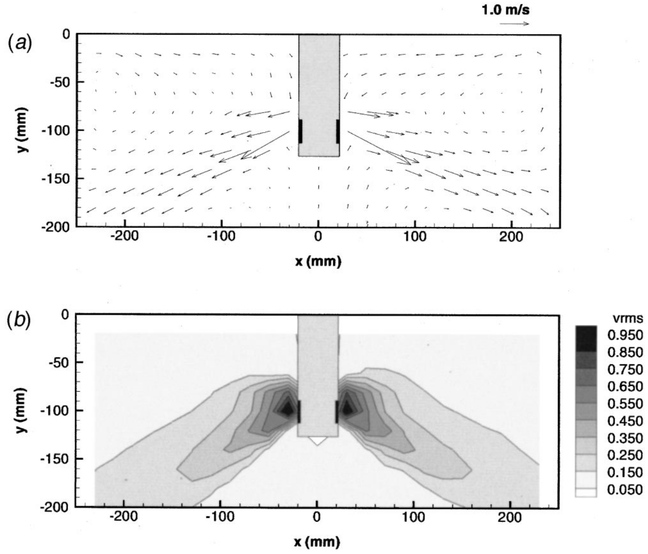

Fig. 9 Plots in the central plane $(z=0)$ of the cross-flow region showing (*a*) mean velocity vectors and (*b*) a contour map of the RMS vertical velocity (m/s) when casting rate R =1.53 m/min and SEN submergence S=120 mm

right. The presence of the recirculation zones above and below the jet and the bounding nature of the wall and the free surface is thought to be responsible for such small movements.

Upper Recirculation. The mean flow in the upper recirculation zone is now discussed. Figure 9 shows the corresponding mean velocity vectors and RMS vertical velocity contours in the central vertical plane $(z=0)$. In contrast to the transient flow behavior described previously, the mean flow field exhibits a high degree of symmetry about the vertical axis. The jets emerge from the lateral ports of the SEN with an estimated angle of 28 degrees to the horizontal. A downwards orientation of the jets, regardless of the port angle (which is zero here), has been reported elsewhere [4]. The two upper recirculation cells driven by the jets are shown. The region directly below the SEN is bypassed by the jets and so is relatively quiescent. The flow there is upwards and forms the top part of the lower recirculation cells. The RMS velocity (Fig. 9(*b*)), which is a function of the turbulence intensity, is found to be greatest within the jets and least where the mean velocity is relatively low, as is expected. Within the jet, the RMS and mean velocities achieve comparable values.

Figure 10 shows horizontal profiles of mean vertical velocity in the plane $z=0$ at different vertical positions in the upper recirculation region, corresponding to the vector plot in Fig. 9(*a*). Depth $y=-20$ mm lies close to the free surface, and the mean vertical velocity there is small and mainly downwards, fed by flow components in the other two directions. The vertical position $y=-100$ mm is in line with the SEN exit, and so the velocity profile at this depth has a maximum negative value near the SEN. Velocities in this profile are mainly downwards, consistent with the vector plot in Fig. 9(*a*). Also consistent is the velocity profile at depth $y=-180$ mm which lies below the nozzle. Those velocities are positive in the central portion and negative near the periphery, corresponding to the top of the two lower recirculation cells.

The mean transverse velocity component (w) is shown in Fig. 11 as a function of coordinate z (perpendicular to the broad face of the mould) in the plane $x=130$ mm for various positions (y) below the free surface in the region of the SEN. Height $y=-20$ mm lies close to the free surface and $y=-145$ mm lies below the tip of the SEN at $y=-120$ mm. Almost all the transverse velocity values are negative, indicating that the jets are directed away from the (front) transparent face of the mould (see the schematic Fig. 3(*b*)). The most negative transverse velocities shown occur for $y=-20$ mm near to the free surface, and those shown nearest to zero occur at $y=-82.5$ which lies just above the SEN port. Furthermore, the transverse velocities at a given height y are surprisingly uniform. These small biases (≈3–5% of the mean exit jet velocity) are thought to be caused by mass flow into the inserts placed at the back of the mould.

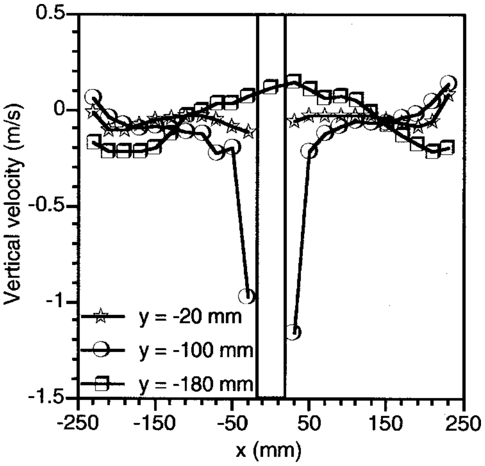

Fig. 10 Mean vertical velocity (v) profile over the width of the cavity in the central plane $(z=0)$ of the cross-flow region at various depths y when casting rate R=1.53 m/min and SEN submergence S=120 mm. The location of the SEN is marked in the center.

The inserts consisted of porous polystyrene blocks sandwiched between perspex sheets. In order to allow for removal of the blocks, a 2 mm gap on either side was necessary, making the block 496 mm where the mould width was 500 mm. The high total pressure from the main jet (≈2500Pa) and the presence of the gap would allow a small flow to pass into the porous insert in the blocks. The gap would also allow additional flow down the side of the mould wall. This small net flow would create a bias away from the opposite side of the mould which was the viewing window for the LDA and flow visualization. Variation of local pressure from the jet can thus result in variation of the flow bias as has been found in the results. This bias also has implications for the jet attachment point as will be discussed in the following.

Figures 12 and 13 show mean horizontal (u) and vertical (v) velocities, respectively, at the same positions (depth) below the free surface as in Fig. 11. The velocities in both Figs. 12 and 13 are also consistent with a jetting flow inclined towards the rear wall of the mould (at negative z). In particular, the horizontal velocity in Fig. 12 becomes increasingly larger outwards in the

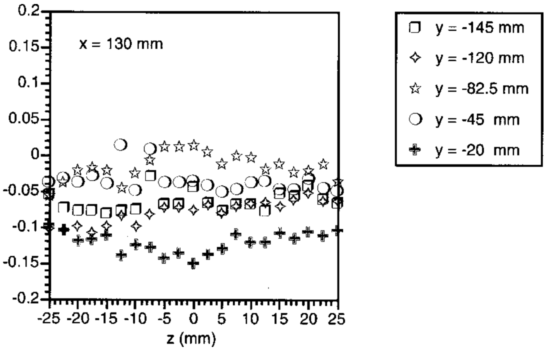

Fig. 11 Out-of-plane mean velocity w versus transverse coordinate z at different depths y when $x=130$ mm for casting rate R=1.53 m/min and SEN submergence S=120 mm

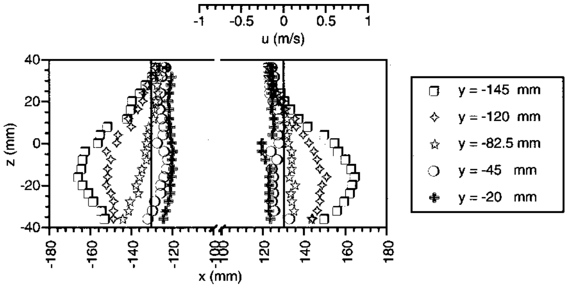

Fig. 12 Mean horizontal velocity *u* as a function of transverse coordinate *z* in horizontal planes at various depths *y* when casting rate R=1.53 m/min and SEN submergence S =120 mm. Results are shown for two values of *x* (+130 mm and −130 mm).

back half of the mould ($z<0$) as the height below the free surface increases from $y=-82.5$ mm near the SEN port to $y=-145$ mm below the SEN. This, in turn, means that the flow is downwards in the back half of the mould, a result confirmed by Fig. 13 which shows the vertical velocity for $z<0$ becoming more negative with increasing depth. Together, Figs. 11–13 describe a mean jetting flow which is downwards, impinging on the rear wall, where it deflects laterally outwards in both horizontal directions.

The components of the mean velocity shown in Figs. 11–13 exhibit considerable symmetry in the x direction. In particular, the u-velocities at equal horizontal distances from $x=0$ take similar values of opposite sign consistent with a mean flow having x-symmetry. Also consistent with this are the vertical velocities in Fig. 12 which take very similar values at $x=\pm 130$ mm.

Full Velocity Field and Lower Recirculation. The vector field of mean velocity, obtained by LDA measurements at 500 points in the central plane $z=0$ over the entire viewing area of the mould, is shown in Fig. 14. The results show the expected pairs of upper and lower recirculation cells. The recirculation below the SEN is oriented such that the flow is upwards in the center and downwards at the side walls. The centers of the lower cells lie between 50–100 mm from the side walls. The aspect ratio of the lower cells is such that the flow there is essentially vertical (up or down).

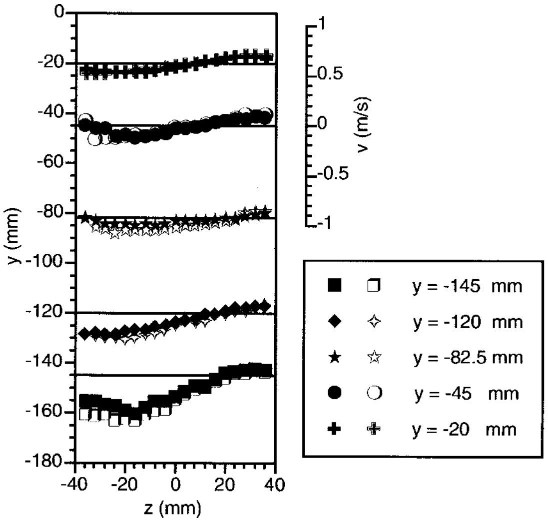

Fig. 13 Mean vertical velocity *v* as a function of transverse coordinate *z* in the vertical *y*-*z* plane (perpendicular to the broad face of the cavity) at *x*=−130 mm (solid symbols) and *x*=+130 mm (open symbols) when casting rate R =1.53 m/min and SEN submergence S=120 mm

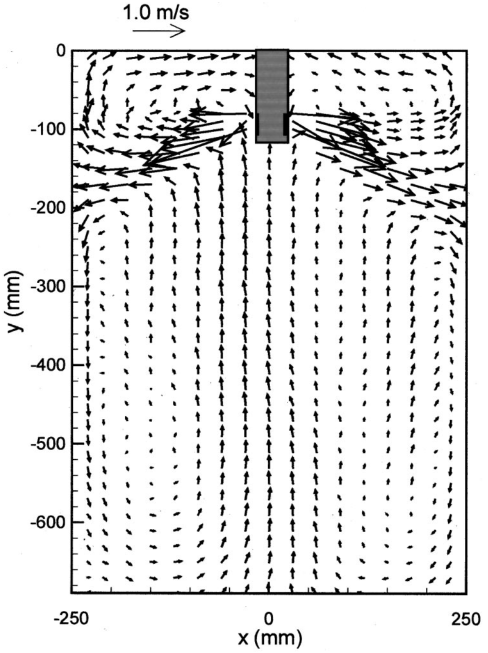

Fig. 14 Full vector field of mean velocity in the central vertical plane *z*=0 when casting rate R=1.53 m/min and SEN submergence S=120 mm

Figure 15 shows the measured mean and RMS vertical velocity profiles at selected heights which lie below the SEN in the central plane $z=0$. These are taken from the data comprising Fig. 14. The curves show the peak velocity down the mould walls to be around 20% of the mean exit jet velocity reversing to 13% up the centerline of the mould at $y=-210$ mm. The velocity down the wall then falls to around 8% of the mean exit jet velocity towards the bottom of the mould at $y=-610$ mm. However, the centerline velocity at this depth is almost unchanged at 8% of the mean exit jet velocity. The highest velocities at the wall would be expected at $y=-210$ mm since this is adjacent to the impingement point of the main jet on the wall. The magnitude of the jet, however, is substantially lower than that of a free jet at 12 diameters which typically has a core velocity of 70% of the mean exit jet velocity. Therefore there is substantially greater viscous dissipation of the jet in this case. This is thought to be caused by the recirculation zones above and below the jet which, from flow visualization, are seen to fluctuate rapidly. Significant viscous dissipation also exists down the mould wall as shown by the high RMS velocities there which range from 170% of the mean velocity near the impingement point ($y=-210$ mm) reducing to 70% at the bottom of the mould ($y=-610$ mm). These large velocity fluctuations are an indication of the chaotic nature of the jet and surrounding recirculation zones.

Discussion

Comparison With Other Water Model Studies. Previous flow visualization [11,12] has observed jet swirl, flow oscillation and asymmetry in cavities having the same thickness (80 mm) and width (500 mm) as in the present experiment, and lengths ranging from 600–2400 mm (Fig. 16). The effective cavity length in this work is 1050 mm which includes the glass viewing section, the manifold prior to the slot valve and the extension slot after the valve. For a related outlet configuration (discharge through the entire mould cross-section, rather than through multiple holes),

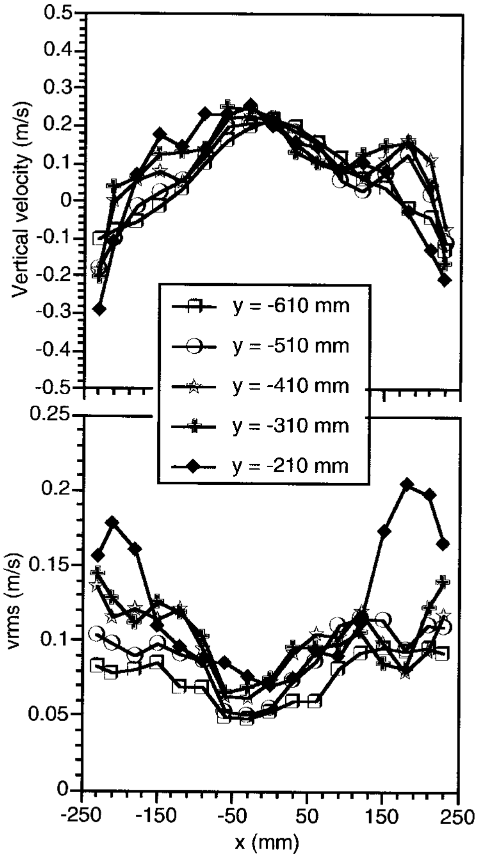

Fig. 15 Mean and RMS vertical velocity profile in the central plane $z=0$ at various depths y in the main body of the cavity below the SEN when casting rate R=1.53 m/min and SEN submergence S=120 mm

Gupta et al. [12] found that the two jets and the flow pattern below the SEN oscillates asymmetrically with a mean frequency of about 0.04 Hz at a casting rate of 1.32 m/min for the mould length considered here. They attributed the jet asymmetry to an observed swirling motion in the jets and its interaction with the wide face of the mould. The frequency found previously [12] lies within the most energetic band (<0.2 Hz) of the frequency spectrum measured in the present work. However, unlike the observation of Gupta et al. [12], the oscillation exhibits no coherent pattern and the jets do not appear to swirl. Nevertheless, the time averaged flow pattern is effectively symmetric across the wide face of the mould (Fig. 14) as was found by Gupta et al. [12].

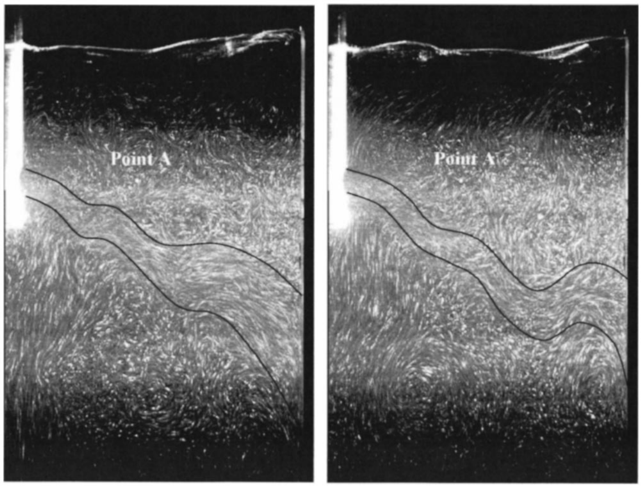

Fig. 16 Flow visualization images of the jet at times 7.8 s apart with the jet outline marked for the base case (casting rate 1.53 m/min, SEN submergence 120 mm)

Previous workers [6,9] conducted water experiments using a multiple hole outlet configuration and found a primary frequency of free surface oscillation of 0.2 Hz in a full scale model (1500 ×60 mm), which corresponds to 0.1 Hz in the present model according to Fig. 16 of Honeyands and Herbertson [6]. This frequency is comparable with the corresponding value of 0.16 Hz found here. Like Gupta et al. [12], Honeyands [9] also found a distinct visual oscillation pattern unlike the present observations which are chaotic in appearance.

Oscillation Mechanism. Previous workers [21,22] have reviewed the main results on self-sustaining oscillations for a wide variety of flows involving impinging or obstructed shear layers. Such flows include the interaction of jets with edges, orifices and surfaces, resonant oscillations in cavities, and confined jet flow. A confined jet is an example of a shear layer bounded by recirculation zones. Such a flow can oscillate due to the hydrodynamic instability of the shear layer (Strouhal number $St \sim O(1)$ based on impingement length), but oscillations of much lower frequency ($St \ll 1$) generated by other mechanisms [22] can also occur. Nathan et al. [26] conclude that the low frequency oscillation is associated with the motion of the jet as a whole and is a quite different phenomenon from that of shear-generated instability within the jet.

The oscillations reported here exhibit modes of both varieties. The shear layer instability generated by jet impingement will occur at frequencies of order 5 Hz which corresponds to $St \geqslant 0.85$ based on an impingement length $L_i = 0.28$ m and $u = 1.6$ m/s. However, the most energetic modes occur at frequencies less than 0.2 Hz (see Fig. 6 and the section "Free Surface and Jet Motion") which corresponds $St \leqslant 0.03$ (the low frequency variety of oscillation). Furthermore, for 0.2 Hz, a Strouhal number based instead on port diameter is 0.002 which is about two orders of magnitude lower than corresponding Strouhal numbers $St \sim O(1)$ of shear-generated structures formed in a jet [26]. This same order of magnitude difference was found by the authors for the low frequency type of oscillation due to single jet flow from a SEN consisting of an open ended pipe [16]. However, a major difference is that the single jet flow oscillates with only one frequency giving a clearly defined flapping motion. In contrast the present bifurcated flow oscillates across a range of frequencies which includes both bulk jet movement and shear layer instability (at the high frequency end), and is without any obvious pattern.

Self-sustaining oscillations require that downstream events can influence the flow upstream. For bifurcated jet flow, two feedback pathways are possible, as was discussed earlier. These are (i) the cross-flow past the SEN which links the two upper recirculation cells and hence the bulk jet movement on either side of the SEN, and (ii) the feedback between the jet attachment point on the cavity wall and the origin of the jet at the SEN port via the individual recirculation cells. In the previous single jet study [16], only feedback pathway (i) was essential to the oscillation (blocking the pathway prevented the oscillation), whereas in the bifurcated jet flow there is evidence for the importance of both feedback pathways (i) and (ii). The single jet study suggests that type (i) feedback is responsible for the low frequency variety of oscillation in the mould which we associate here with the bulk deflection (~6–8 mm RMS) of the bifurcated jet. Type (ii) feedback over the impingement length will drive the higher frequency oscillatory modes because of the instability of the impinging jet (shear layer). These modes manifest as a sinuous motion (standing waves) along the length of the jet occurring at irregular periods with examples shown in Fig. 16 at two selected times.

Conclusion

LDA velocity measurements of flow in the mould from a bifurcated nozzle have been presented which, together with flow visualization, have shown a self-sustaining oscillatory flow which is chaotic in nature without any obvious pattern. The majority of the oscillation energy occurs below a frequency of 5 Hz with dominant low frequency modes occurring at frequencies below 0.2 Hz. RMS velocities adjacent to the jet impingement area are as high as 170% of the local mean velocity. The presence of two jets about the centerline creates four major recirculation zones with the two lower zones bounded by the jets and mould walls and the two upper zones bounded by the jets, the mould walls and the free surface. Two feedback pathways appear to influence the jet oscillation. One pathway is cross-flow through the gap between the SEN and mould wall which leads to a bulk up-down displacement of the jets at an frequency of approximately 0.2 Hz. The second feedback pathway links jet impingement on the mould walls to the jet orifice (SEN port) via the recirculation cells which promotes shear layer instability and generates modes of oscillation at the higher end of the frequency range in the order of 5 Hz.

Acknowledgment

This work was supported by the Australian Research Council using facilities provided by the G. K. Williams Cooperative Research Centre for Extractive Metallurgy, a joint venture between the CSIRO Division of Minerals and the Department of Chemical Engineering at the University of Melbourne. The authors would also like to thank Mr. Tim Berrigan and the workshops of the Department of Chemical Engineering for their help and support during the project.

References

[1] Nilles, P., and Etienne, A., 1991, ''Continuous Casting Today—Status and Prospects,'' Metallurgical Plant. and Technology International, **6**, pp. 56–67.

[2] Seyedein, S. H., and Hasan, M., 1997, ''A Three-Dimensional Simulation of Coupled Turbulent Flow and Macroscopic Solidification Heat Transfer for Continuous Slab Casters,'' Int. J. Heat Mass Transf., **40**, pp. 4405–4423.

[3] Yang, H., Zhao, L., Zhang, X., Deng, K., Li, W., and Gan, Y., 1998, ''Mathematical Simulation on Coupled Flow, Heat, and Solute Transport in Slab Continuous Casting Process,'' Metall. Mater. Trans. B, **29B**, pp. 1345–1356.

[4] Najjar, F. M., Thomas, B. G., and Hershey, D. E., 1995, ''Numerical Study of Steady Turbulent Flow through Bifurcated Nozzles in Continuous Casting,'' Metall. Mater. Trans. B, **26B**, pp. 749–764.

[5] Thomas, B. G., Mika, L. J., and Najjar, F. M., 1990, ''Simulation of Fluid Flow Inside a Continuous Slab-Casting Machine,'' Metall. Mater. Trans. B, **21B**, pp. 387–400.

[6] Honeyands, T. A., and Herbertson, J., 1995, ''Flow Dynamics in Thin Slab Caster Moulds,'' Steel Res., **66**, pp. 287–293.

[7] Samarasekera, I. V., Thomas, B. G., and Brimacombe, J. K., 1997, ''The Frontiers of Continuous Casting,'' *Proceedings of The Julian Szekely Memorial Symposium on Materials Processing*, Cambridge, MA, H. Y. Sohn, J. W. Evans, and D. Apelian, eds. The Minerals Metals and Materials Society, pp. 275–297.

[8] Honeyands, T. A., Lucas, J. and Chambers, J. 1992, ''Preliminary Modelling of Steel Delivery to Thin Slab Caster Moulds,'' 1992 *Steelmaking Conference Proceedings*, Iron and Steel Society, Vol. 75, pp. 451–459, Toronto.

[9] Honeyands, T. A. 1994, ''Flow dynamics in thin slab caster moulds,'' PhD dissertation, University of Newcastle, Australia.

[10] Gupta, D., and Lahiri, A. K., 1994, ''Water Modelling Study of the Surface Disturbances in Continuous Slab Caster,'' Metall. Mater. Trans. B, **25B**, pp. 227–233.

[11] Gupta, D., and Lahiri, A. K., 1996, ''A Water Model Study of the Flow Asymmetry Inside a Continuous Slab Casting Mold,'' Metall. Mater. Trans. B, **27B**, pp. 757–764.

[12] Gupta, D., Chakraborty, S., and Lahiri, A. K., 1997, ''Asymmetry and Oscillation of the Fluid Flow Pattern in a Continuous Casting Mould: A Water Model Study,'' ISIJ Int., **37**(7), pp. 654–658.

[13] Lawson, N. J. and Davidson, M. R. 1988, ''Measurement of Cross-Flow Characteristics from a Transient Water Model of a Thin Slab Casting Mould,'' *IMechE Optical Methods and Data Processing in Heat and Fluid Flow*, Bryanston-Cross et al., eds. pp. 301–310, IMechE, London.

[14] Lawson N. J. and Davidson M. R., 1998, ''The Application of LDA to Characterize Cross-Flow from an Oscillating Jet in a Thin Slab Casting Mould,'' *Proceedings 13th Australasian Fluid Mechanics Conference*, M. C. Thompson, K. Hourigan, eds., Melbourne, Australia, pp. 667–670.

[15] Lawson, N. J., and Davidson, M. R., 1999, ''Cross-Flow Characteristics of an Oscillating Jet in a Thin Slab Casting Mould,'' ASME J. Fluids Eng., **121**, pp. 588–595.

[16] Lawson, N. J., and Davidson, M. R., 2001, ''Self-Sustained Oscillation of a Submerged Jet in a Thin Rectangular Cavity,'' J. Fluids Struct., **15**, pp. 59–81.

[17] Durst, F. Melling, A. and Whitelaw, J. H. 1981, *Principles and Practice of Laser Doppler Anemometry*, Second Edition, Academic Press, London.

[18] Panaras, G. A., Theodorakakos, A., and Bergeles, G., 1998, ''Numerical Investigation of the Free Surface in a Continuous Steel Casting Mold Model,'' Metall. Mater. Trans. B, **29B**, pp. 1117–1126.

[19] Hershey, D. E., Thomas, B., and Najjar, F. M., 1993, ''Turbulent Flow Through Bifurcated Nozzles,'' Int. J. Numer. Methods Fluids, **17**, pp. 23–47.

[20] Dring, R. P., 1982, ''Sizing Criteria for Laser Anemometry Particles,'' ASME J. Fluids Eng., **104**, pp. 15–17.

[21] Rockwell, D., and Naudasher, E., 1979, ''Self-Sustained Oscillations of Impinging Free Shear Layers,'' Annu. Rev. Fluid Mech., **11**, pp. 67–94.

[22] Rockwell, D., 1983, ''Oscillations of Impinging Shear Layers,'' AIAA J., **21**, pp. 645–664.

[23] Brummayer, M., Gittler, P. and Watzinger, J. 1999, ''Stabilization of Unsteady Turbulent Flow in the Mold Region of a Wide Slab Caster by Submerged Entry Nozzle Design Optimization with CFD,'' *Proceedings Second International Conference on CFD in the Minerals and Process Industries*, M. P. Schwarz, M. R. Davidson, A. K. Easton, P. J. Witt and M. L. Sawley, eds., CSIRO, Melbourne, Australia, pp. 217–222.

[24] Chang, C., Davidson, M. R. and Lawson, N. J. 2001, ''CFD Studies on Bifurcated Nozzle Jet Flow in a Water Model of a Thin Slab Casting Mould,'' to be presented at the *6th World Congress of Chemical Engineering*, Melbourne, Australia, 23–27 Sept. 2001.

[25] George, W. K. Beuther, P. D., and Lumely, J. L. 1978, ''Processing of Random Signals,'' *Proceedings of Dynamic Measurements in Unsteady Flows*, S. G. Leslie, F. A. Kovasznay, P. Buchave, L. Fulachier and B. W. Hansen, eds., pp. 757–800.

[26] Nathan, G. J., Hill, S. J., and Luxton, R. E., 1998, ''An Axisymmetric 'Fluidic' Nozzle to Generate Jet Precession,'' J. Fluid Mech., **370**, pp. 347–380.

Journal of
Fluids
Engineering

Technical Briefs

A Rational Method to Choose Optimum Design for Two-Dimensional Contractions

S. Ramaseshan
Scientist, DRDO, CEMILAC, Ministry of Defence,
Bangalore-560037, India

M. A. Ramaswamy
Retired Professor, Indian Institute of Science, Bangalore,
India

1 Introduction

A review was carried out on the studies undertaken to obtain efficient shapes for the contraction designs. It is seen that before the advent of efficient digital computers around 1970, studies in this field Barger et al., Cohen and Ritchie, Johnson, Whitehead et al., Tsien were of analytical nature, i.e., the contraction profiles were obtained for some prescribed velocity distribution. However, after 1970, when the digital computers became widely available, most of the studies, Morel [1], Downie et al. [2] and Borger [3] have been directed at prescribing the contraction profile and computing the flow field. An important observation emerged from the review is that, most of the authors provided only qualitative criteria based on acceptable nonuniformity and avoidance of boundary layer separation to select contraction profile and none of them had determined the optimum profile even within the same family of profiles. It was also seen that no comparison of the performance of the profiles proposed by various authors had been made. Hence the present study was to evolve a rational method for qualitatively assessing the relative performance of various profiles and make the comparisons of the best performances of different family of profiles for two dimensional case. Since the cited references provide all the necessary information in respect of the profiles, the physical characteristics and governing evaluation of these profiles are not repeated here.

2 Criteria for Evaluation of Performance

For computing flow fields inside the contraction, incompressible, inviscid flow equations, in terms of stream function with appropriate boundary conditions were solved by transforming the co-ordinates to get a rectangular computational domain and using a line relaxation method for the discritised difference equations. For details refer to the thesis of Ramaseshan [4]. The norms for evaluate the performance of the contraction profiles are flow nonuniformity at the exit (Morel [1]) and margin of safety for boundary layer separation (MS) using Stratford's criterion [5]. Additionally, in the analysis, a rational criterion to select the best profile within a given family have been evolved. It is that for a chosen value of MS (which is designer's prerogative), the one which gives the least value of the flow nonuniformity at the exit is the best profile. All the performances of 2-D duct during various profile shapes are carried out for a contraction ratio of 4. length 2.0 and Reynolds number of 10^6 (based on entry half width).

2.1 Method to Arrive at the Optimum Performance for One Parameter Family of Contraction Profiles. For one pa-

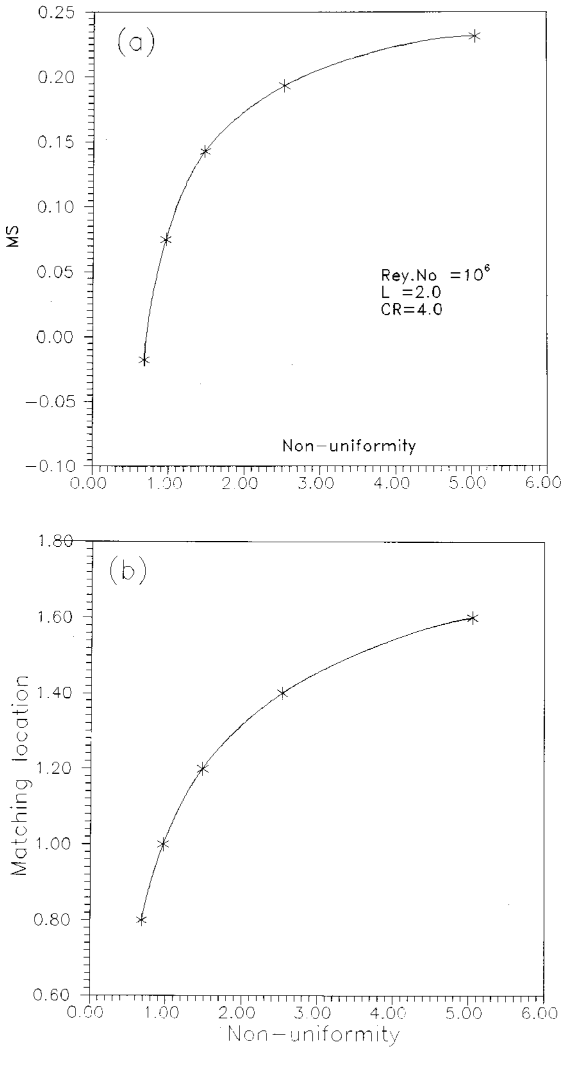

Fig. 1 Design curves for cubic profiles

Contributed by the Fluids Engineering Division of THE AMERICAN SOCIETY OF MECHANICAL ENGINEERS. Manuscript received by the Fluids Engineering Division December 14, 2000; revised manuscript received November 14, 2001. Associate Editor: J. Katz.

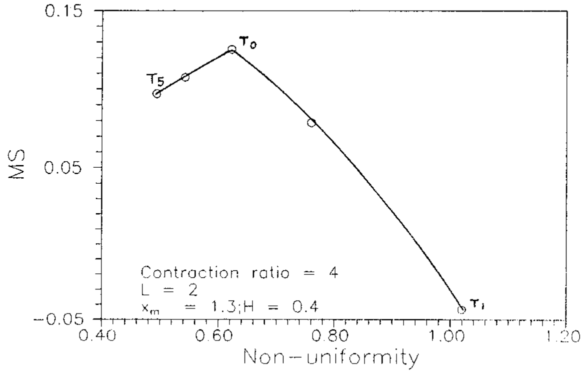

Fig. 2 Performance of Borger's profile for a given H

rameter family of profiles, like cubic profiles, there is only one free parameter, the matching location (x_m). Therefore for each chosen value of the x_m, the MS and non-uniformity can be found and a cross plot of MS versus nonuniformity can be drawn. Such cross plots for cubic profiles are shown in Figs. 1(*a*) and 1(*b*). For a chosen combination of MS and non-uniformity, the value of x_m gets fixed. For these profiles, for the chosen value of MS, corresponding matching location can also be obtained from these figures. Hence these figures can be considered as typical design charts for these family of profiles.

3 General Philosophy to Arrive at the Optimum Performance for Family of Profiles Having More Than One Parameter

To evaluate the performance for such family of profiles having more than one parameter, many combinations of these parameters have to be considered. From these many combinations, the aim is to arrive at those combinations which produce an optimum curve based on the considerations of lowest exit flow nonuniformity for the given MS. The general philosophy of obtaining such an optimum performance curve for three parameter family of profiles (*H*, *T*, and x_m) is given below.

First one has to determine from the equations of profiles, the range of values of *H* and *T* which permit generation of profiles for a given x_m. Then, for that x_m, for a chosen *H*, the performance curve of MS and non-uniformity as *T* is varied has to be obtained. In the same way the performance curves for different *H* have to be got. Then a curve which forms an envelope of these curves (obtained for different x_m) should be obtained. This is the general philosophy to be used for all families of profiles having three free parameters. This is explained in more detail with reference to Borger's profiles. For elliptic profiles, similar method is followed.

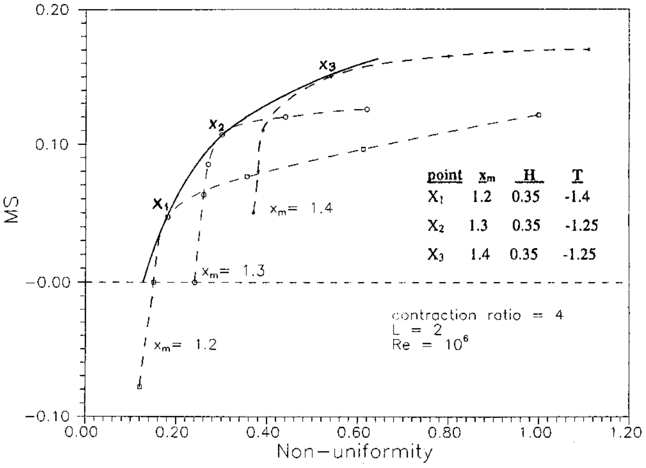

Fig. 3 Optimum performance curve for Borger's profiles

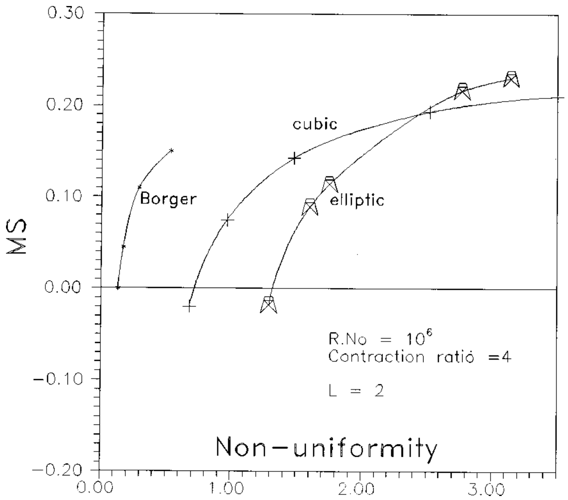

Fig. 4 Comparison of performance for different families of profiles

3.1 Optimum Performance Curve for Three Parameter Family of Profiles. The profile shape is defined as $y=B_1(x+B_4y)^5+B_2(x+B_4y)^3+B_3(x+B_4y)$ [3] where B_1, B_2, B_4, and B_4 are determined by the constraints that, the slope at the inflexion point be equal to the chosen value T and the curve passes through the end coordinates and that the slope and the curvature at the end points of the profile be zero.

The performance for a contraction ratio of 4 and $L=2$ for $x_m=1.3$ and $H=0.4$ is discussed here. The variation of MS and nonuniformity as *T* is varied is shown in Fig. 2. The point where MS is maximum is indicated as To in the figure. Similar performance are obtained for different *H* for the same given x_m. To obtain an envelope of optimum performance for a x_m, the points for every *H* where MS is maximum are joined. Such optimum curves for different x_m are shown in dotted lines for $x_m=1.2$, 1.3 and 1.4 in Fig. 3. To obtain an overall optimum performance curve, an envelope (as shown by bold line) in drawn by joining the points X_1, X_2, and X_3 as shown in Fig. 3. This envelope gives the optimum performance for the family of Borger's profiles for the chosen contraction ration of 4 and length of 2.

4 Comparison of Optimum Performance Curves of Different Families of Profiles

For the chosen parameters, optimum performance curves in terms of MS and nonuniformity is compared in Fig. 4. It is observed that matched cubic profiles is better than matched elliptic profiles. The performance of elliptic profiles is better than cubic profiles in terms of MS only when nonuniformity is more than 2 percent. Borger's profiles offer far better performance than any of the profiles stated earlier. It is to be noted that Borger's work was much earlier than the work by Downie et al. The reason for better performance of Borger's profile could be that, Borger's profile does not contain discontinuities in curvature either at entry, matching location and at the exit (unlike elliptic profiles) and it has more than one free parameter (unlike cubic profiles).

5 Conclusion

For the first time, a rational approach to determine the relative performance of various families of profiles was evolved which permitted obtaining the optimum performance possible from a given family of profiles and also compare the optimum performance of different families of profiles and also permit to choose the optimum design for two dimensional contractions.

References

[1] Morel, T., 1975, "Comprehensive design of axi symmetric wind tunnel contractions," ASME J. Fluids Eng., June, pp. 225–233.
[2] Downie, D. H., Jordinson, R., and Barnes, R. H, 1984, "On the design of three dimensional wind tunnel contraction," Aeronaut. J., Aug./Sept., pp. 287–295.
[3] Borger, G. G., 1976, "The optimization of wind tunnel contractions for the subsonic range," NASA-TT-F-16899.
[4] Ramaseshan, S., 1997, "Optimization and development of superior profiles for two dimensional and axi symmetric contractions," Ph.D thesis, Indian Institute of Science, Bangalore, India.
[5] Stratford, B. S., 1959, "Prediction of separation of the turbulent boundary layer," J. Fluid Mech., **5**, pp. 1–16.

Dimensionless Characteristics of Pumps With Specific Speeds n_q=20...80

W. A. Jędral
Professor

K. J. Karaśkiewicz
Assistant Professor

S. Hamid Ahmad
Postgraduate

Institute of Heat Engineering, Warsaw University
of Technology, Warsaw 00-665, Poland

1 Introduction

When designing a pumping station or other pump installation, pumps of high efficiency and good suction properties are selected. The shape of the flow and the power characteristics of the pump are often important as well. Before specific pumps of a particular producer are selected, a number of analyses should be performed, for which a sufficiently good knowledge of pump characteristics is required. These include the head $H(Q)$, power $P(Q)$, and efficiency $\eta(Q)$ characteristics of the pump, where the only known data are the required nominal parameters Q_n, H_n, often given in several variants. For example, one can consider whether it would be better to apply three pumps of capacity $Q_n'=4000\ \mathrm{m}^3/\mathrm{h}$ each, or instead use four pumps of lower capacity, $Q_n''=3000\ \mathrm{m}^3/\mathrm{h}$ each, taking into account different nominal rotational speeds of these pumps, for instance $n_1=1485$ rpm and $n_2=990$ rpm.

Of course, in practical terms, it is enough to know two of the above mentioned characteristics, as the third one can be determined from the formula

$$P=\frac{\rho g Q H}{\eta} \tag{1}$$

It should be stressed that the presented problem differs from that of estimating the characteristics of a pump being designed, for which all the dimensions have already been settled. Here, we have to estimate the probable characteristics of a hypothetical pump, possibly a not yet existing one, of nominal parameters Q_n, H_n, η_n, needed for the calculations connected with operation of the designed installation, capacity regulation, and so forth.

2 Dimensionless Pump Characteristics, According to the Literature

One can easily evaluate the probable pump characteristics $H(Q)$, $P(Q)$, $\eta(Q)$ if one knows the presumable dimensionless characteristics of it, $h(q), \overline{P}(q), \overline{\eta}(q)$. In the literature, authors have for many years cited the same two sets of collective dimensionless characteristics $h=f_1(q,n_q)$; $\overline{P}=f_2(q,n_q)$; $\overline{\eta}=f_3(q,n_q)$. One of the above sets of characteristics originates from the factory Escher-Wyss [1], the other one—not much newer—is set out in a well-known monograph by Stepanoff [2]. Quite recently, a third set of dimensionless pump characteristics appeared in the handbook published by Sulzer factory [3].

All the above-mentioned characteristics are described as rough ones; there is no information on the kind of research performed, or how many pumps, and of what make, were examined. Moreover, the characteristics differ one from another quite significantly in steepness, which implies differences in the values of parameters $\overline{\eta}, \overline{P}$ and specially h, for the same values of q and n_q. It can be seen in Fig. 1, where some examples of $h(q)$ are shown, based on the quoted sources, for specific speeds $n_q=34.2\ldots109.6$. In this range, the curves by A. J. Stepanoff and Escher-Wyss have a quasi-parabolic shape with apex at the point $q=0$, while the values $h_0=(h)_{q=0}$ are certainly lower than those given by Sulzer. Additionally, according to the first two sources, the characteristics have unstable shape for $n_q \leqslant 40$, while all Sulzer characteristics are stable for $n_q \geqslant 20$. In the range $n_q=20\ldots60$, the shape of the latter ones can be recognized as parabolic, but their apexes lie in the area $q<0$. The characteristics by Escher-Wyss lie even lower than those by A. J. Stepanoff. As can be seen, for the same values of n_q, significant differences in h_0 values may appear, depending on the source of the data.

Differences in shape and steepness between characteristics $h(q)$ of older and newer pumps can be somewhat explained by the fact that, in the period of the last sixty years, the trends in pump construction have changed. Presently, impellers are constructed almost exclusively with blades of spatial curvature, with greater

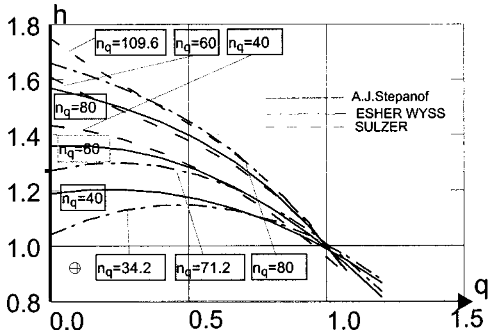

Fig. 1 Examples of flow characteristics $h(q)$ for n_q =34 . . . 110 [1-3]

Table 1 Single-stage, double-suction pumps

q	h	R^2
0	$1.072 + 8.004 \cdot 10^{-3} \cdot n_q$	0.703
0.5	$1.085 + 4.168 \cdot 10^{-3} \cdot n_q$	0.616
1.2	$0.930 - 2.808 \cdot 10^{-3} \cdot n_q$	0.519

q	$\overline{\eta}$	R^2
0.5	$0.811 + 1.247 \cdot 10^{-3} \cdot n_q$	0.224
1.2	$0.963 - 3.592 \cdot 10^{-3} \cdot n_q$	0.058

Contributed by the Fluids Engineering Division of THE AMERICAN SOCIETY OF MECHANICAL ENGINEERS. Manuscript received by the Fluids Engineering Division April 17, 2000; revised manuscript received December 1, 2001. Associate Editor: Y. Tsujimoto.

Table 2 Multi-stage, single-suction pumps

q	h	R^2
0	$1.160 + 2.995\cdot10^{-3}\cdot n_q$	0.040
0.5	$1.224 + 2.059\cdot10^{-3}\cdot n_q$	0.058
1.2	$0.899 - 4.467\cdot10^{-3}\cdot n_q$	0.010

q	$\overline{\eta}$	R^2
0.5	$0.851 + 2.098\cdot10^{-3}\cdot n_q$	0.051
1.2	$1.019 - 2.227\cdot10^{-3}\cdot n_q$	0.365

inlet and outlet angles, and with more compact channels of meridional cross-sections, that is, with lesser shift to front of the impeller's outlet part. Nonetheless, the attempts undertaken by the authors to compare actual characteristics of contemporary pumps of leading producers with the characteristics given by Sulzer, even quite recent ones, confirmed the existing discrepancies.

3 New Proposal for Dimensionless Characteristics

In order to verify and refine the dimensionless pump characteristics, especially the flow characteristic $h=f_1(q,n_q)$, and to improve them to such a degree that they could be considered reliable and appropriate for the applications mentioned in Subsection 1,

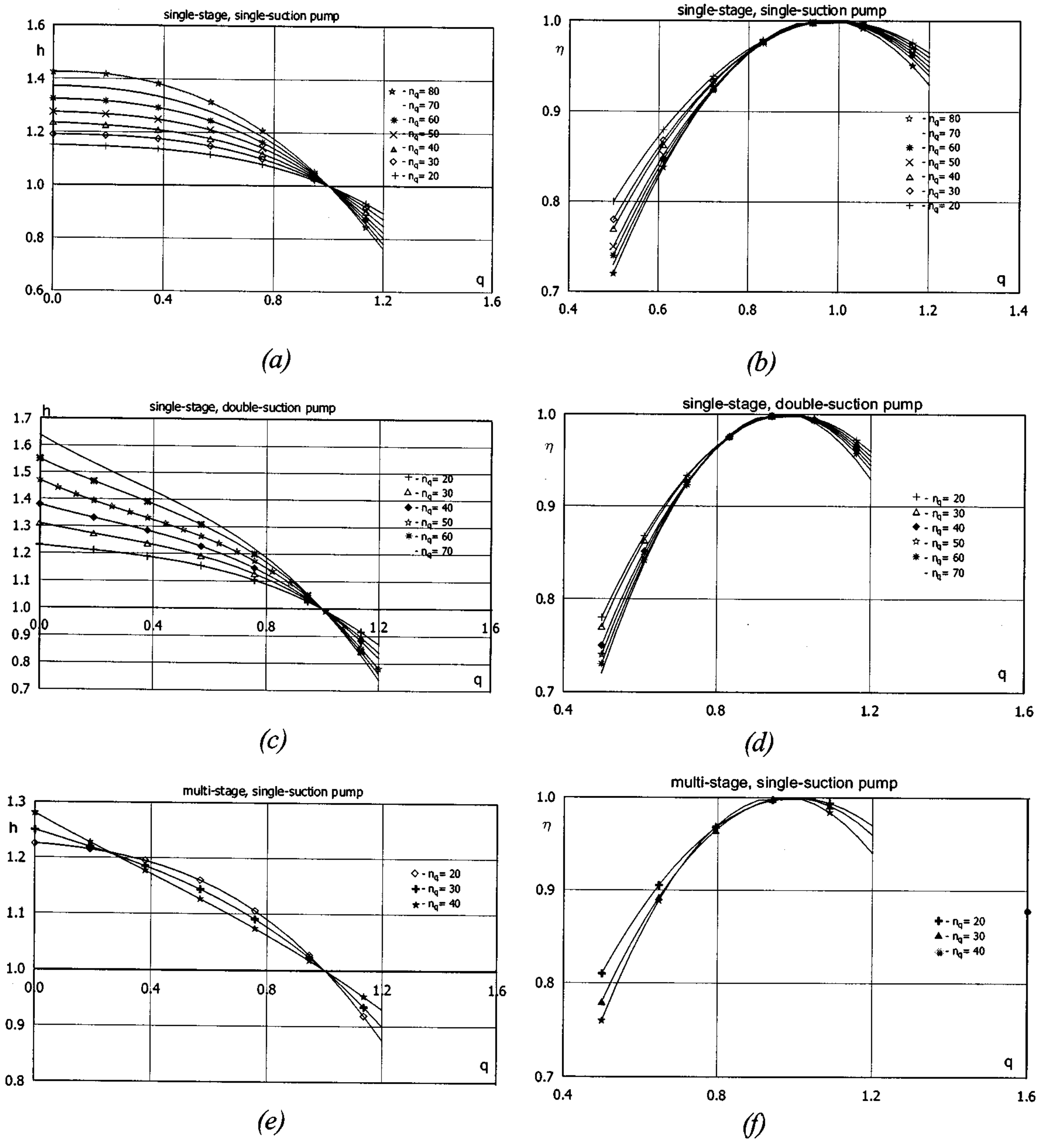

Fig. 2 Dimensionless pump characteristics for $n_q=20\ldots80$

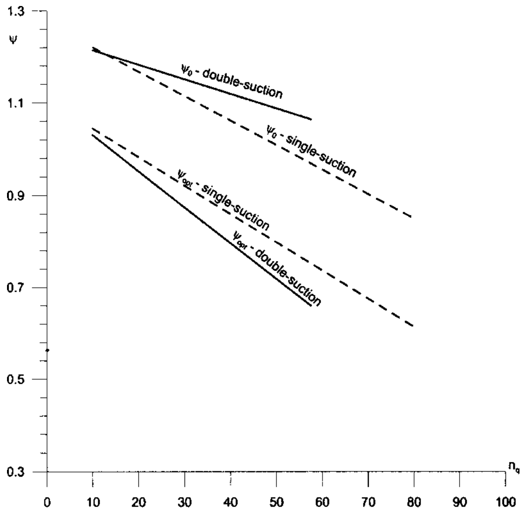

Fig. 3 Pressure numbers for single- and double-suction pumps

the authors based their research on actual characteristics of pumps presently produced, or recently introduced in many countries. The analysis was performed and statistics were developed for the characteristics of over 200 pumps of capacity $Q_{opt}=100\ldots 13000$ m^3/h, and specific speeds $n_q=10\ldots 85$. The pumps were made by manufacturers such as Ahlstrom, Guinard, KSB, Worthington, Warszawska Fabryka Pomp, and many others. All the pump impellers had a number of blades $Z\geqslant 4$.

After initial evaluations, the pumps were divided into three groups:

- single-stage, single-suction pumps,
- single-stage, double-suction pumps,
- multi-stage, single-suction pumps.

The flow characteristic was determined with a sufficient accuracy by setting four (q,h) points: $(0,h_0),(0.5,h_1),(1,1),(1.2,h_2)$. A similar assumption was made concerning the characteristic of efficiency. Based on the dimensional characteristics, optimal parameters for each pump ($Q_{opt}, H_{opt}, \eta_{\max}$) were determined. Then thevalues of h_0, h_1, h_2, the appropriate values of η_1, η_2 and the values of specific speed were determined. The points (h,q) and $(\overline{\eta},q)$, found in such a way, were plotted in the graphs $h\text{-}n_q$, $\overline{\eta}_1\text{-}n_q$, separately for each group of pumps, and are detailed in Fig. 4 and Tables 1 and 2. Using the method of least squares, the equations of lines ensuring the best approximation of the actual data functions were derived. The equations of particular lines, and the respective coefficients of determination R^2 are also shown in Fig. 4 and Tables 1 and 2. The patterns of data distribution in specific sets of characteristics are clearly visible, which explains why the coefficients of determination are in many cases low.

Using the above empirical formulas, the values of parameters h and η for specific speeds $n_q=10\ldots 80$ were calculated, and a cubic parabola through the resulting points (q,h), $(q,\overline{\eta})$ was drawn for specific values of n_q. The pencils of curves $h(q,n_q), \eta(q,n_q)$, obtained in such a way, are presented in Fig. 2 separately for each of the three considered groups of pumps. One can make use of the curves of Fig. 2 directly, estimating the shape of the characteristic for any of the n_q values (within the specified range), for example, $n_q=35$. Alternatively, from the formulas given in the Appendix one can calculate the values of h_0, h_1, h_2, $\overline{\eta}_1$, $\overline{\eta}_2$ for that particular value of n_q, substitute the values $q=0.5$, 1.0 and 1.2 into parabola equations, and, solving two sets of three equations with three unknowns, determine the values of parabola coefficients. The value of $\eta_{\max}$ can be assessed from empirical relations by Anderson [4] or the Hydraulic Institute in New York.

4 The Obtained Dimensionless Characteristics Versus Characteristics Known From Literature: A Comparative Analysis

(a) It is visible in Figs. 2(*a*), (*c*), and (*e*) that the characteristics $h(q)$ of single- and double-suction pumps apparently differ from one another. The respective characteristics of double-suction pumps are much steeper that those of single-suction pumps. The characteristics of multistage pumps take an intermediate position, however, they are closer to single-suction pump characteristics. Because the number of pumps analyzed was large, one could exclude the possibility that any of the characteristics might have a haphazard shape.

Some simplification, especially for the pumps of high specific speeds,[1] can result from the assumption of parabolic shape of the characteristics. However, the differences between the actual and the averaged characteristics of some pumps are most significant for relatively low values of $q=0\ldots 0.35$, assuming the same value of n_q. On the other hand, in analyzing the functioning of pumping stations, one needs curves which refer to a capacity value $q\geqslant 0.5$, and the above mentioned discrepancies are not important in this region, really.

(b) Smaller differences between the three types of pumps appear when one examines the averaged characteristics of efficiency $\overline{\eta}(q)$. However, the curves of single-suction pumps are apparently more flat than those of double-suction pumps. This effect is also depicted by the values of $\overline{\eta}$ higher in single-suction pumps, when the values of q are equal in both cases.

(c) The comparison of pump characteristics derived by the authors, against the respective characteristics known from literature, shows that:

- The characteristics $h(q)$ developed by the factory Escher-Wyss are obviously outdated. This fact seems undeniably due to

— very small values of h, considerably lower than those of actual pumps for low q values (approximately for $q<0.8$),

— inadequate shape of the characteristics, which for $n_q\cong 35$ still remains unstable, an effect never observed in contemporary pumps.

- The Sulzer characteristics of $h(q)$ are approximately consistent with those presented in Fig. 2(*c*) for double-suction pumps. However, for single-suction pumps, and for small q, the values given by Sulzer are overestimated.
- The characteristics $h(q)$ published by A. J. Stepanoff are also, to some extent, already outdated, because of unstable shape that they take for $n_q<40$. However, these characteristics conform well to the characteristics obtained by the authors for single-suction pumps.

(d) An interesting problem is the reason for the difference between the characteristics $h(q)$ in single- and double-suction pumps. The biggest difference appears at the shut-off point. The greater h_0 values for double-suction pumps can be caused by higher H_0 or lower H_{opt}. To check this, pressure numbers $\psi_0(n_q)$, $\psi_{opt}(n_q)$ of double and single-suction pumps were compared, and the results are shown in Fig. 3.

In the whole analyzed n_q area, values of ψ_{opt} are lower for double-suction pumps. This can be explained by one-dimensional flow theory and the Euler-equation:

$$H_{opt}=\frac{1}{g}(u_2c_{u2}-u_1c_{u1}) \tag{2}$$

As the geometric properties of the blades and the shapes of impeller channels in meridional sections are similar in both types of

---

[1] For $n_q\geqslant 50$, actual characteristics $h(q)$ become increasingly steep, and their shape, for $q<0.5$, becomes more and more irregular.

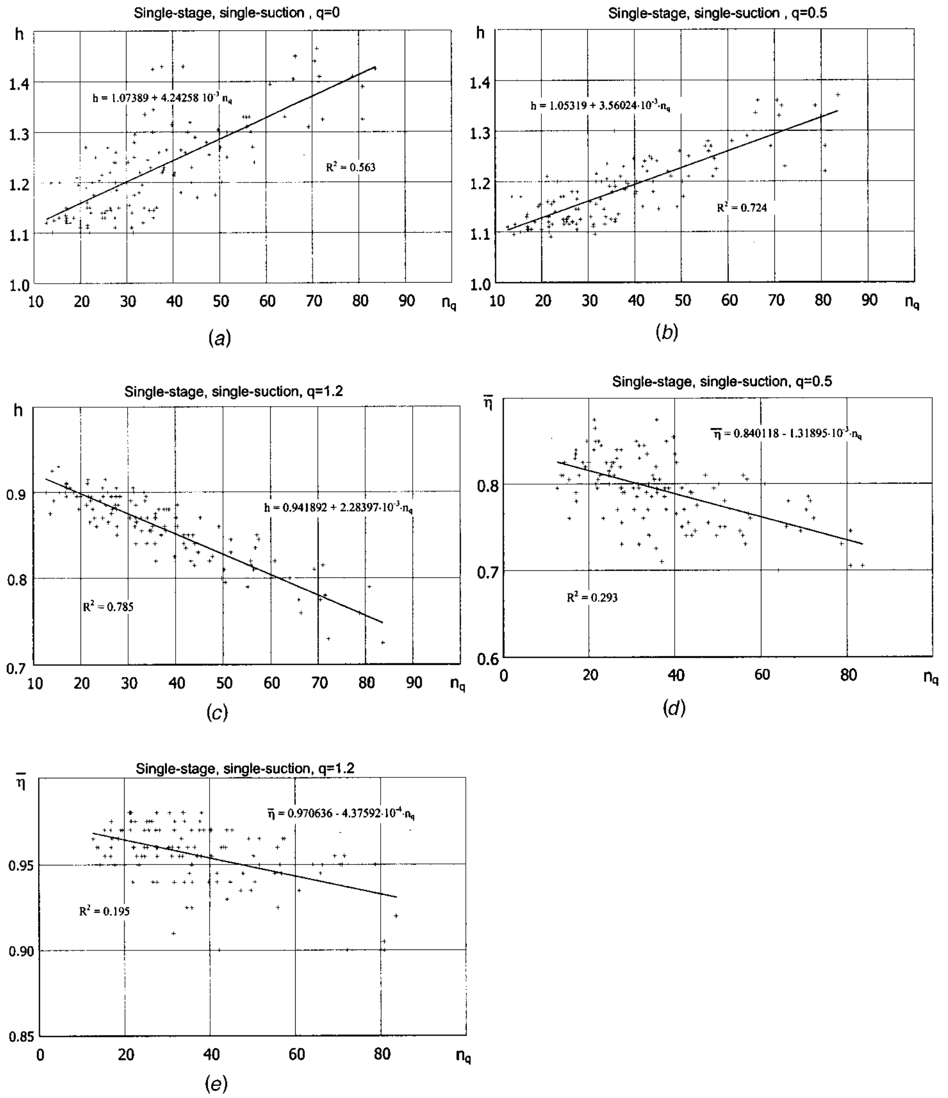

Fig. 4 The approximation lines of the normalized efficiency data for different capacities-single-stage, single-suction pumps

pumps, other explanations might be the different methods of guiding the fluid to the impeller (suction nozzle), or slightly different proportions of dimensions of the volute, for example the ratio b_3/b_2. In single-suction, end-suction type pumps, prerotation can be very small and so the second term in brackets can be neglected (Fig. 4). In double-suction pumps the fluid is guided to the impeller through the volute suction chamber which causes prerotation. The velocity $c_{u1}>0$ and the second term $u_1 \cdot c_{u1}>0$, so ψ_{opt} is lower. The explanation of the difference in pressure numbers ψ_0 is much more convincing. That is because of the complex structure of secondary flows, and reverse flow in the impeller for low flow rates), when one-dimensional theory fails.

5 Conclusion

1 In this paper, the authors have presented new, averaged dimensionless characteristics $h(q,n_q)$ and $\overline{\eta}(q,n_q)$ for single- and double-suction impeller pumps, as well as single- and multi-stage pumps, of specific speeds $n_q = 20 \ldots 80$. The characteristics were developed on the basis of actual characteristics $H(Q)$ and $\eta(Q)$ of over 200 different pumps, produced by factories well-known worldwide.

2 The newly developed characteristics differ from the traditionally used ones—already slightly outdated—published by the firm Escher-Wyss and by A. J. Stepanoff. The differences are particularly visible in the flow characteristics, $h(q,n_q)$.

3 The pencils of characteristics $h(q,n_q)$ of single- and double-suction pumps differ from one another, and this fact is worth a detailed analysis. The differences between efficiency characteristics $\overline{\eta}(q,n_q)$ are less significant.

4 The authors suggest that, in various antecedent calculations carried out before the pump is selected, or in calculations corroborating such a choice, one should use the characteristics presented in this work rather than the previously published ones.

Nomenclature

n_n = nominal (calculated) rotational speed,
Q_{opt} = optimal rate of flow, for $n = n_n$,
H_{opt} = optimal total head of pump, for $n = n_n$,
k = number of streams: $k=1$ or 2 for single- and double-suction pumps, respectively,

i = number of stages; $i=1$ for single-stage, and $i>1$ for multistage pumps.

b_2 = discharge impeller width

b_3 = volute inlet width

u = circumferential impeller velocity

c_u = peripheral component of fluid velocity

$q=\dfrac{Q}{Q_{opt}}, h=\dfrac{H}{H_{opt}},$

$\overline{\eta}=\dfrac{\eta}{\eta_{\max}}, \overline{P}=\dfrac{P}{P_{opt}}$ = dimensionless capacity, head, efficiency, power

$n_q=\dfrac{333\cdot n_n\sqrt{Q_{opt}/k}}{\left(\dfrac{gH_{\text{opt}}}{i}\right)^{3/4}}$ = specific heat

$\psi=\dfrac{gH}{0.5u_2^2}$ = pressure number

$R^2=\dfrac{\Sigma(\hat{Y}_i-Y_i)^2}{\Sigma(\hat{Y}_i-Y_i)^2+\Sigma(\hat{Y}_i-\overline{Y})^2}$ = coefficient of determination

Y_i = actual data values (head or efficiency)

$\hat{Y}_i$ = fit values

$\overline{Y}=\dfrac{1}{n}\Sigma Y_i$ = average of Y_i

References

[1] Escher-Wyss Mitteilungen, 1934, No 3; Information quoted according to: Rittner, C., 1938, Flüssigkeitpumpen, Springer-Verlag, Berlin.

[2] Stepanoff, A. J., 1957, *Centrifugal and Axial Flow Pump*, 2nd Ed., Wiley, New York.

[3] Sulzer, 1992, *Centrifugal Pump Handbook*, Elsevier, London, New York.

[4] Anderson H. H., 1993, *Centrifugal Pumps*, 3rd ed., Elsevier Advanced Technology, Oxford.

A Deterministic Stress Model for Rotor-Stator Interactions in Simulations of Average-Passage Flow

Charles Meneveau and Joseph Katz

Department of Mechanical Engineering,

The Johns Hopkins University, Baltimore, MD 21218

A procedure for modeling deterministic stresses for average-passage simulations of flow in multiple blade-row turbomachines is proposed and tested. This method uses the results of several (two or more) steady Reynolds-averaged Navier-Stokes (RANS) simulations with boundary conditions that are representative of different inflow conditions encountered during the passage of a neighboring blade-row. The deterministic stresses are calculated by averaging the steady results while weighting them with the approximate duration of each inflow condition. This approach incorporates important rotor-stator interactions that are neglected in models based on a swept-wake approximation. The model is tested successfully by computing the deterministic stresses in the stator vane passage of a centrifugal pump, and comparing them with direct measurements using PIV data. Remaining discrepancies between model predictions and experimental data are probably linked to the inability of the turbulence models to account for flow phenomena at each phase, such as mid-vane separation.

[DOI: 10.1115/1.1458580]

Introduction

For multistage turbomachinery simulations, the average-passage technique (Adamczyk [1], Adamczyk et al. [2], Rhie et al. [3], Busby et al. [4]) typically solves the steady, three-dimensional equations (Euler or RANS) separately in each blade-row. Unlike the earlier "mixing plane approach" (e.g., Dawes [5]), in the average-passage method the computational domain of a given row is extended to include the volume occupied by neighboring rows (excluding the blades). The effects of unsteadiness caused by the neighboring rows are accounted for by "deterministic" stresses. The flow-turning effect associated with the blades (pressure difference across a surface) is introduced through steady body-forces. This approach is more rigorous than the mixing plane method since it provides a framework for accounting for the effects of unsteady phenomena on the average-passage flow field. However, important modeling problems associated with unsteady interactions between blade-rows arise. In many current applications a frozen blade wake (obtained from an upstream average-passage simulation) is swept through the field of the following row, and averaged (Adamczyk et al. [2]). Consequently, many unsteady interactions between blade rows are not accounted for. Since the deterministic stresses are typically of similar or higher magnitude than the Reynolds stresses (see Rhie et al. [3]), neglecting these interactions in simulations may lead to significant errors. Sinha et al. [6,7] show, using PIV data, how an unsteady incidence angle resulting from the passage of rotor blades generate cyclic flow separations on the stator blades. The rotor passage also alters the wake of the diffuser vanes and the presence of stator vanes alters the structure of the rotor wake. These phenomena cause high deterministic stresses, which motivate the present development of a model that has the ability to account for such effects. We begin by showing the measured deterministic stresses. Then, the proposed model is introduced and applied to predict the deterministic stresses in the stator blade passage. Finally, the results are compared with the measured distributions.

Experimental Data From Centrifugal Pump

The PIV measurements of Sinha et al. [6,7] were performed in a transparent centrifugal pump with a vaned diffuser that enables simultaneous PIV measurements within the impeller (rotor), the diffuser vane passages and in the volute. Past calibrations (see details in Sinha et al. [6,7]) have shown that the characteristic uncertainty of the instantaneous velocity is about 0.3 pixels, i.e., 0.07 m/s, corresponding to u/U_T of 0.007 at the present magnification. The measurements are performed on the mid-span plane between hub and shroud. The impeller has five backward swept blades with inlet and exit diameters of 8.51 cm and 20.32 cm, respectively. The diffuser has nine blades with inlet and discharge diameters of 24.45 cm and 30.5 cm, respectively. The circular arc vanes have a chord length of 13.44 cm and a span of 1.27 cm. The pump is operating at a design condition of 890 rpm (14.83 Hz).

The phase averaged velocity distributions, $\overline{u_i}(\mathbf{x},t)$, at seven different impeller blade orientations t are obtained by averaging 100 instantaneous velocity distributions at each phase (in 5 phases, only 10 are used in the other two, Sinha et al. [6,7]). Being measured every 10 deg of impeller orientation, they almost complete a blade cycle of 72 deg. The average-passage velocity, $\hat{u}_i^S(\mathbf{x})$, in the stator reference frame is defined as:

$$\hat{u}_i^S(\mathbf{x})=\frac{1}{T_R}\int_0^{T_R}\overline{u_i}(\mathbf{x},t)\,dt$$

Contributed by the Fluids Engineering Division of THE AMERICAN SOCIETY OF MECHANICAL ENGINEERS. Manuscript received by the Fluids Engineering Division November 29, 2000; revised manuscript received November 19, 2001. Associate Editor: E. Graf.

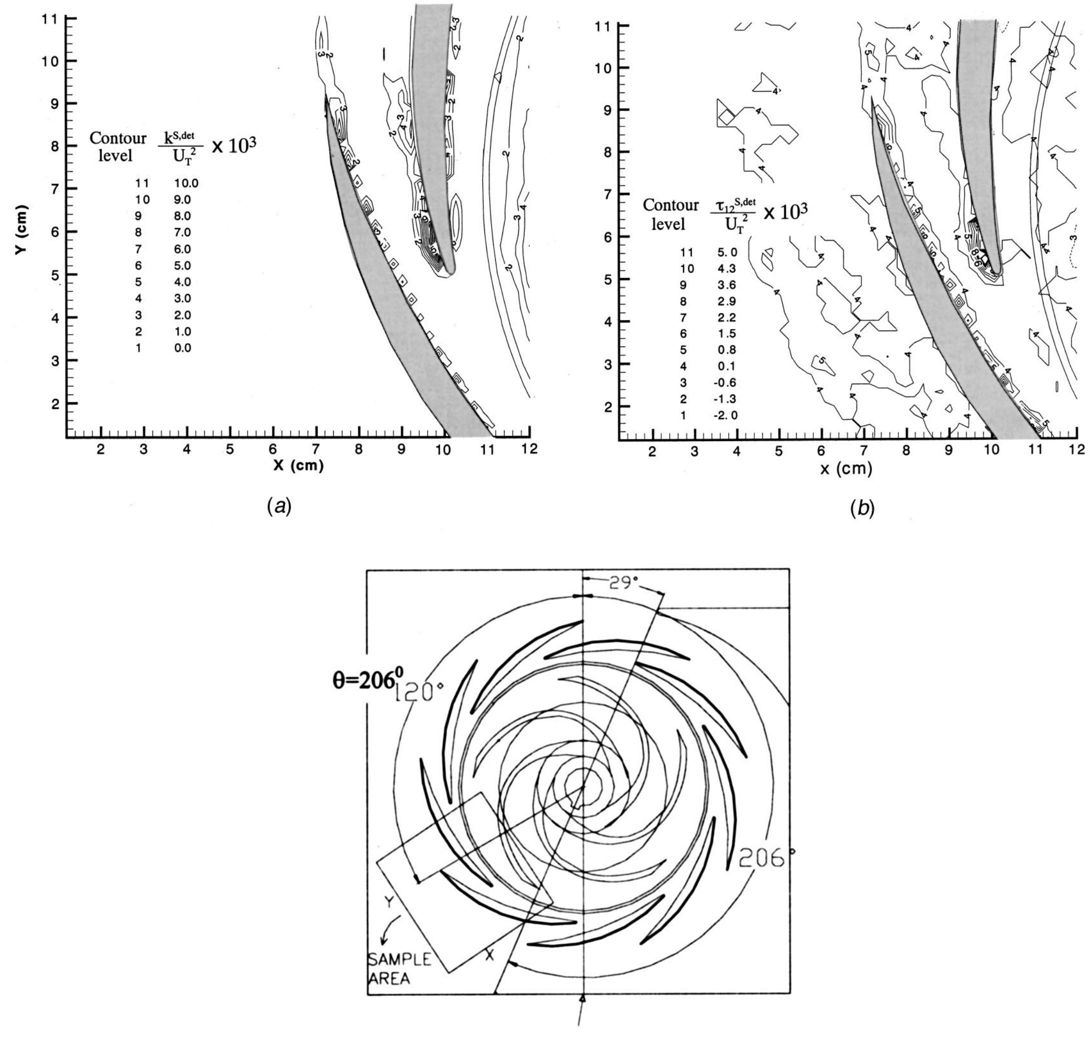

(*a*)

(*b*)

(*c*)

Fig. 1 (*a*) Measured distribution of deterministic kinetic energy and (*b*) measured deterministic shear stress in stator passage, deduced from PIV data in centrifugal pump (Sinha et al. [7]). (*c*) Location of the sample area in the pump.

where T_R is the impeller blade-passage period. For the present data, $\hat{u}_i^S(\mathbf{x})$ is computed by averaging the phase-averaged velocity fields. To avoid patchiness associated with the finite angle difference, additional fields every 2.5 deg are constructed using linear interpolation. The integration is then approximated as a sum over 28 fields. The deterministic stresses are evaluated from the differences between the phase-averaged and average-passage data, according to

$$\tau_{ij}^{S,\det}(\mathbf{x}) = -\frac{1}{T_R}\int_0^{T_R}[\overline{u}_i(\mathbf{x},t)-\hat{u}_i^S(\mathbf{x})][\overline{u}_j(\mathbf{x},t)-\hat{u}_j^S(\mathbf{x})]dt$$

(In Sinha et al. [7] the minus sign is mistakenly omitted in the equation defining $\tau_{ij}^{S,\det}(\mathbf{x})$, but not in the figures.) As an input to the model proposed below, the rotor average-passage velocity, $\hat{u}_i^R(\mathbf{x})$, is also required. Determination of the average-passage velocity and stresses in the rotor frame of reference are performed in the same manner, but this time the process involves rotation of the flow field while fixing the impeller orientation. Details are provided in Sinha et al. [7]. Due to the averaging the uncertainty in the phase-average velocity decreases to $7\times10^{-4}U_T$, and the uncertainty in the averaged-passage velocity is about $3\times10^{-4}U_T$. Accounting for all the contributions, the uncertainty in the deterministic stress is $5\times10^{-5}U_T^2$, i.e., about 5 percent of the characteristic values.

The deterministic kinetic energy, $k^{S,\det}$, in the stator passage is estimated by summing the two normal stresses according to

$$k^{S,\det} = -\frac{1}{2}(\tau_{11}^{S,\det}+\tau_{22}^{S,\det})$$

In Sinha et al. [7], the result is multiplied by 3/2 to account for the missing out-of-plane component. In this paper we assume that the dominant cyclic variations are two-dimensional, and hence the contribution of the out-of-plane velocity component is neglected. The measured distributions of $k^{S,\det}(\mathbf{x})$ and $\tau_{12}^{S,\det}(\mathbf{x})$ are presented in Figs. 1(*a*) and (*b*). As is evident, $k^{S,\det}(\mathbf{x})$ is high within the impeller, at the pressure and suction sides of the diffuser vane and in the wake of the diffuser. It peaks at the leading edge of the vane, where the phase-averaged flow separates intermittently. This separation occurs as the incidence angle at the entrance to the passage increases substantially as this passage faces the pressure side of the impeller blade. This increase is associated with the so-called ''jet-wake'' phenomenon (Dean and Senoo [8]). It consists of a higher radial velocity on the pressure side of the impeller blade and low on the suction side, and conversely, high circumferential velocity on the suction side and low on the pressure side. Another form of phase-dependent flow separation occurs on the same suction (convex) side of the vane, near the point that lines up with the trailing edge of the previous vane. It occurs as the entrance to the passage faces the suction side of the impeller owing to the reduction in total pressure. High values of $k^{S,\det}(\mathbf{x})$ exist also in the wake of the diffuser. Clearly, the highest deterministic stresses in the diffuser are associated with interaction of the nonuniform flow at the exit from the impeller with the boundary layers on the diffuser vanes. These high tangential variations in deterministic stresses cannot be accounted for in the ''swept wake'' model of Adamczyk et al. [2]. Hence, improved models that account for rotor-stator interactions are needed, providing the motivation for the presently proposed deterministic stress model. Furthermore, as discussed in Sinha et al. [7], although in some cases one finds peaks of deterministic and Reynolds stresses at the same location, in general their trends are considerably different. Thus, different modeling approaches must be used. As expected, $k^{S,\det}(\mathbf{x})$ is also very high within the impeller due to internal flow nonuniformities, including the ''jet-wake'' phenomenon and the viscous wake of the blades.

Proposed Model

The present model focuses on cyclic contributions to the deterministic stresses, and neglects the effects of ''passage-to-passage'' variability (Adamczyk et al. [2]). We also assume that the phase-averaged, time-varying outflow from a blade row is reasonably well correlated with sweeping an accurately predicted space-varying average-passage outflow from the same blade row. To illustrate that this assumption is supported by our experimental data, Fig. 2(*a*) shows the measured angle, α, between the velocity at a point P (shown in Fig. 2(*b*) along with a computational grid) and the circumferential direction, as a function of rotor angle, θ. The solid circles in Fig. 2(*a*) show α obtained from the measured phase-averaged velocity fields. The effect of the jet-wake phenomenon is evident: For $\theta < 210$ deg, when point P is located in the pressure side of the impeller blade, the incidence angle is relatively high due to the high radial velocity and low tangential velocity. These phase-averaged results are unknown during average-passage simulations, and therefore cannot be used as input into a model.

However, the nonuniform outflow from the impeller can be modeled based on the average-passage simulations of the flow within the rotor. The solid line in Fig. 2(*a*) is the (measured) angle α formed between the rotor average-passage velocity and the tangential direction, when this steady velocity field is rotated and plotted at the same phase as the phase-averaged data. As is evident, sweeping the rotor average-passage velocity distribution appears to give a reasonable indication of the time-varying inflow angle into the stator. This information would be available during a average-passage simulation and can be used as an input to a model. Indeed, our proposed model is based on using the rotor average-passage field as boundary conditions for separate steady calculations of the flow in the stator.

The model is based on performing two (or more, n) steady RANS calculations of the flow inside the downstream blade-passage, for two (or more) representative phases of the upstream blades. For these simplified calculations, the computational domain only covers the blade-row and does not extend to include upstream and downstream blade-rows, as it does in the full average-passage calculation. Each calculation is identified with the superscript $k(k=1,2,\ldots,n)$. The inlet boundary condition into the domain D_d (subscripts d and u refer to downstream and upstream blade-rows, respectively) is given by the average-passage velocity of the upstream blade-row, $\hat{\mathbf{u}}^{D_u}(\mathbf{x}_{\text{in}})$, at positions $\mathbf{x}_{in}$ that coincide with the inlet boundary of D_d. The velocity field $\hat{\mathbf{u}}^{D_u}(\mathbf{x}_{\text{in}})$ is rotated at various angles with respect to D_d, providing n different inlet conditions along $\mathbf{x}_{\text{in}}$, each denoted below by $\hat{\mathbf{u}}^{D_u-k}(\mathbf{x}_{\text{in}})$. These inlet conditions serve as a model for the inlet conditions of the phase-averaged velocity field. In this regard, the method resembles the mixing plane approach. To each rotor outflow condition, we assign a weight, $w_k(k=1,2,\ldots,n)$, equal to the fraction of time for which that specific condition is assumed to be a representative of the real flow.

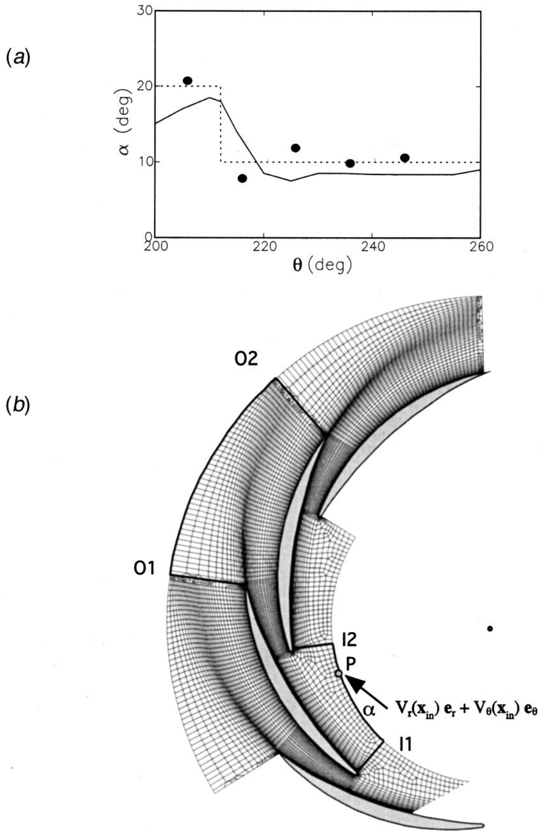

Fig. 2 (*a*) Measured angle between the velocity and the tangential direction, at a point P. P is shown in (*b*). Solid circles: Angle of the phase-averaged velocity as function of rotor phase (orientation). Solid line: angle obtained by sweeping the measured passage-averaged velocity in the rotor frame past point P, as function of angular position of the blade. Dotted line: The bimodal approximation of the variations in the orientation of the velocity used in the present analysis. (*b*) Mesh used in FLUENT™ calculations of flow in the stator domain. The computational domain is marked by the dark contour. Cyclic periodic boundary conditions are used, and two cyclic repetitions are shown for clarity. The inlet of the computational domain is the segment I1-I2 and the outlet is O1-O2.

Each of the n simplified RANS calculations in D_d yields a velocity field $\mathbf{u}^{D_d-k}(\mathbf{x})$, with $\mathbf{x}$ pertaining to D_d. The deterministic stresses are then evaluated as:

$$\tau_{ij}^{D_d,\det}(\mathbf{x}) = -\frac{1}{n}\sum_{k=1}^{n} w_k (u_i^{D_d-k})'(u_j^{D_d-k})',$$

where $(u_i^{D_d-k})'$ is the deviation of the kth velocity field from the mean velocity over all the n simplified simulations,

$$(u_i^{D_d-k})' = u_i^{D_d-k}(\mathbf{x}) - \frac{1}{n}\sum_{k=1}^{n} w_k u_i^{D_d-k}(\mathbf{x}).$$

The practicality of the model relies on our ability to represent the entire cycle by only a few (n) representative inlet conditions, so that only a limited number of steady RANS calcula-

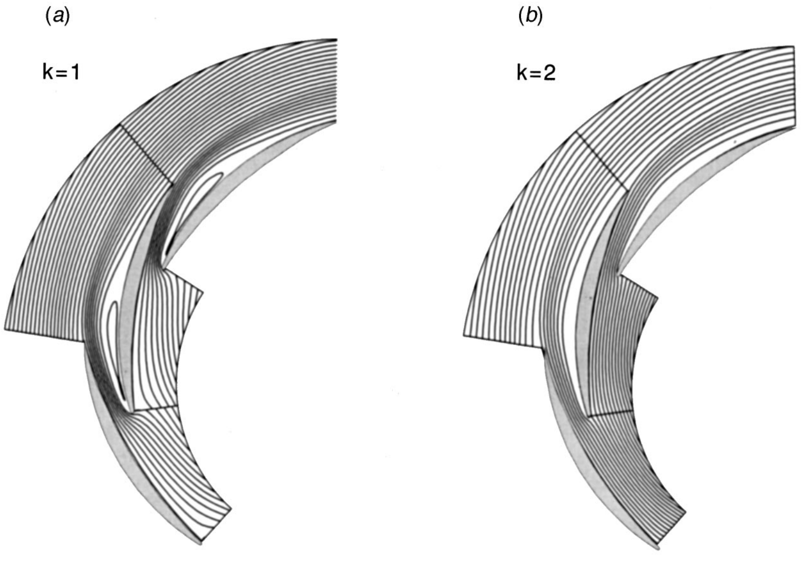

Fig. 3 Streamlines of velocity fields computed for different inlet conditions. (*a*) *k*=1—the high inlet angle of 20 deg case; (*b*) *k*=2—the low inlet angle of 10 deg case. In both cases shown the RNG k-ε model is used. Similar results are obtained using the traditional k-ε model with near-wall corrections. The flow in (*a*) exhibits leading edge separation, while the flow in (*b*) remains attached.

tions are needed. In general these calculations should be performed in 3-D but in the present example, 2-D calculations are sufficient, due to the 2-D nature of the phase-averaged flow in the diffuser.

Application to Centrifugal Pump Data and Discussion

In the present case the upstream blade-row is the rotor, and the downstream blade-row is the stator. From Fig. 2(*a*), it appears that the cycle is reasonably well represented by two different inlet conditions ($n=2$), corresponding (approximately) to a velocity (magnitude) of 2.2 m/s at $\alpha_1=20$ deg, and 4.3 m/s at $\alpha_2=10$ deg. This two-step function is illustrated by the dotted line in Fig. 2(*a*), and both conditions agree with the mean radial velocity at P. Since the $\alpha_1=20$ deg flow angle occurs for about 20 percent of the rotor passage, the assigned weights are $w_1=1/5$ and $w_2=4/5$. To perform the two steady RANS calculation in the stator domain, we use FLUENT™ in a 2-D domain with cyclic periodic boundary conditions. Simulations were done using second-order upwinding, with SIMPLEC velocity-pressure coupling. Both standard k-ε (with wall-function) and RNG, k-ε turbulence models have been used. Since there are no significant differences in the results, only the RNG, k-ε results are shown. Figure 2(*b*) shows the grid, including some periodic repetitions. This geometry reproduces exactly a 2-D section across the stator blade geometry and the mesh has a good resolution of the near-wall and wake regions. The inlet conditions are uniform tangential and radial velocities at the segment $I1$-$I2$. In the $k=1$ simulation, $V_r=0.75$ m/s and $V_\theta=2.07$ m/s, and in the $k=2$ case $V_r=0.75$ m/s and $V_\theta=4.23$ m/s. Outflow boundary conditions are applied at $O1$-$O2$.

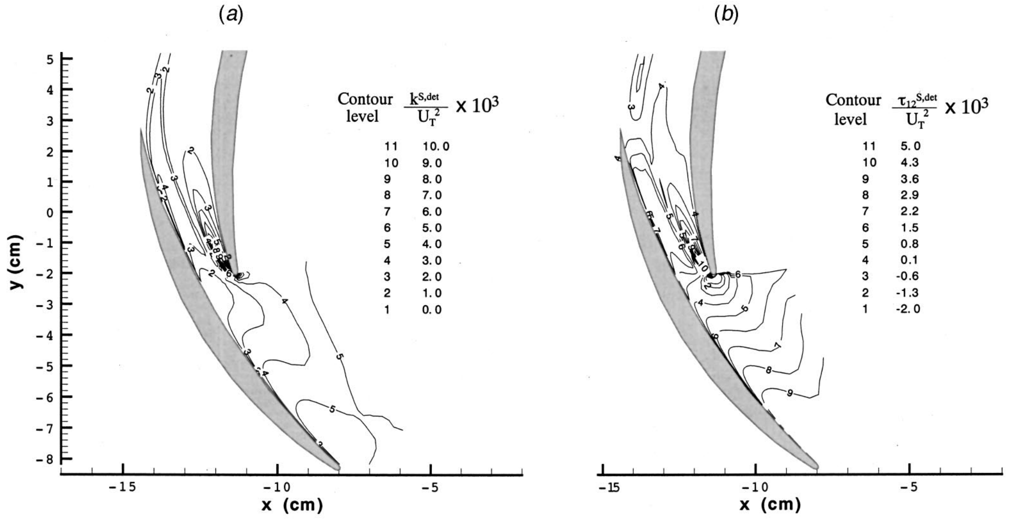

Fig. 4 (*a*) Deterministic kinetic energy $(-\tau_{ii}^{S,\mathrm{det}}/2)$, as calculated from the proposed model. (*b*) Deterministic shear stress $(\tau_{12}^{S,\mathrm{det}})$, as calculated from the proposed model.

The calculated streamline plots are shown in Figs. 3(*a*) and (*b*). For the $k=1$, $\alpha_1=20$ deg case, boundary layer separation occurs at the leading edge of the stator. Tests using two finer grids (reductions of mesh size by factors 0.6 and 0.37) yielded the same shape of the separation bubble, with variations in its length of about 5 percent. Thus, the result is relatively grid independent, at least at the level of accuracy relevant for the present analysis. Conversely, the flow does not separate for the $k=2$, $\alpha_2=10$ deg case (established by detailed examination of the computed results). This ‘‘flip-flopping’’ between attached and separated flow around the leading edge produces strong modeled deterministic kinetic energy there, as shown in Fig. 4(*a*). The model predicts a peak with a maximum value of about $k^{S,\mathrm{det}}=8\times10^{-3}U_T^2$ around the stator leading edge. $U_T=9.47$ m/s is the tip speed of the impeller. Encouragingly, this value is very close to the peak value in the experimental data shown in Fig. 1(*a*). Such a tangentially non-uniform deterministic kinetic energy peak cannot be reproduced at all by a swept-wake model. However, details of the peak region differ: the experimental peak region appears to be more ‘‘attached’’ to the stator blade than the region predicted by the model. Similar conclusions are reached upon comparing the modeled distribution of τ_{12}^{det} (Fig. 4(*b*)) with the measured one (Fig. 1(*b*)). The sign and magnitude of the high stress region near the stator leading edge is well predicted.

The model overpredicts $k^{S,\mathrm{det}}(\mathbf{x})$ and τ_{12}^{det} in the entrance region, where the imposed unsteadiness of the swept inlet is not fully realistic. Discrepancies also remain in the stator wake. When comparing the computed flow-field in the $k=2$ case to the corresponding measured, phase-averaged velocity distributions (Sinha et al. [6]), we find that mid-vane separation occurs on the convex side of the vane, whereas in Fig. 3(*b*) the flow remains attached. This phase-dependent separation causes meandering of the stator wake, whereas in the present calculations the wake does not change significantly between cases $k=1$ and $k=2$. Hence, further work is needed to determine the information needed at the inlet in order to reproduce the mid-vane separation. For example, instead of specifying a constant velocity at the inlet, one can prescribe a profile with a better representation of the average-passage velocity field. It is also possible that the problem lies with the RANS turbulence modeling, which may be insufficient to properly reproduce mid-vane separation. The differences could also be due to the quasi-steady approximation we are using in the RANS simulations, which neglect unsteady effects.

Clearly, while it appears that the presently proposed model reproduces tangential non-uniformities in deterministic stress distributions, that cannot be reproduced by the swept-wake models, further tests in different flow conditions are needed. Also, in this technical brief the proposed model has only been tested in terms of its ability to reproduce measured deterministic stresses. It must still be tested in passage-averaged simulations of pump flow. These continuing efforts are in progress.

Acknowledgments

The pump data base was generated by M. Sinha for his doctoral thesis research. The present work was funded by the Air Force Office of Scientific Research under grant no. F49620-97-1-0110 (Dr. T. Beutner, program director).

References

[1] Adamczyk, J. J., 1985, ‘‘Model Equation For Simulating Flows In Multistage Turbomachinery,’’ *ASME Paper No.*, 85-GT-226.

[2] Adamczyk, J. J., Celestina, M. L., Beach, T. A., and Barnett, M., 1990, ‘‘Simulation Of Three-Dimensional Viscous Flow Within A Multistage Turbine,’’ ASME J. Turbomach., **112**, p. 370.

[3] Rhie, C. M., Gleixner, A. J., Spear, D. A., Fischberg, C. J., and Zacharias, R. M., 1998, ‘‘Development and Application Of A Multistage Navier-Stokes Solver. Part I: Multistage Modeling Using Body Forces and Deterministic Stresses,’’ ASME J. Turbomach., **120**, p. 205.

[4] Busby, J., Sondak, D., Staubach, B., and Davis, R., 2000, ‘‘Deterministic Stress Modeling of a Hot Gas Segregation in a Turbine,’’ ASME J. Turbomach., **122**, p. 62.

[5] Dawes, W. N., 1992, ‘‘Towards improved throughflow capability: the use of three-dimensional viscous flow solvers in a multistage environment,’’ ASME J. Turbomach., **114**, p. 8.

[6] Sinha, M., and Katz, J., 2000, ‘‘Quantitative visualization of the flow in a centrifugal pump with diffuser vanes. Part I: On flow structures and turbulence,’’ ASME J. Fluids Eng., **122**, p. 97.

[7] Sinha, M., Katz, J., and Meneveau, C., 2000, ‘‘Quantitative visualization of the flow in a centrifugal pump with diffuser vanes. Part II: addressing passage-averaged and LES modeling issues in turbomachinery flows,’’ ASME J. Fluids Eng., **122**, p. 108.

[8] Dean, R. C., and Senoo, Y., 1960, ‘‘Rotating Wake in Vaneless Diffusers,’’ ASME J. Basic Eng., **82**, p. 563.

Experimental Investigations of Performance of a Commercial Centrifugal Oil Pump

Wen-Guang Li
Professor
e-mail: Liwg@gsut.edu.cn

Fa-Zhang Su
Senior Engineer

Cong Xiao
Engineer
Hydraulic Machinery Division, Gansu University of Technology, 730050 Lanzhou, The People’s Republic of China

Introduction

Many researchers, such as Daugherty [1], Stepanoff [2], Telow [3], Ippen [4], Itaya and Nishikawa [5], tested the performance of centrifugal oil pumps while the viscosity of the oil was varied.

These typical results provided great insights about the effects of the oil viscosity on the performance of centrifugal oil pumps. These test results were used to obtain important guidelines for selection and design of the pumps which are still in use today. However, these experimental results are based on oil pumps made in the 20s and 50s. In the mean time, both the hydraulic models of the pumps and their constructions have shown significant variations. If the past results are still used to guide the selection and design of the centrifugal oil pumps today, the results calculated will show a greater difference with those in the real situation. The application will be harmful for the technological development of the oil pumps.

On the other hand, some researchers, such as Stoffel [6], Li and Hu [7] used the pumps, which were designed by themselves, to conduct experiments. The application of these results cannot have universal guiding significance.

The centrifugal oil pump of type 65Y60 based on API610 standard is selected in this study. The aim of the study is to explore the relationship of the performance correction factors with the oil viscosity, as well as provide a reference for the design and selection of the pump.

Contributed by the Fluids Engineering Division of THE AMERICAN SOCIETY OF MECHANICAL ENGINEERS. Manuscript received by the Fluids Engineering Division April 21, 2000; revised manuscript received November 26, 2001. Associate Editor: B. Schiavello.

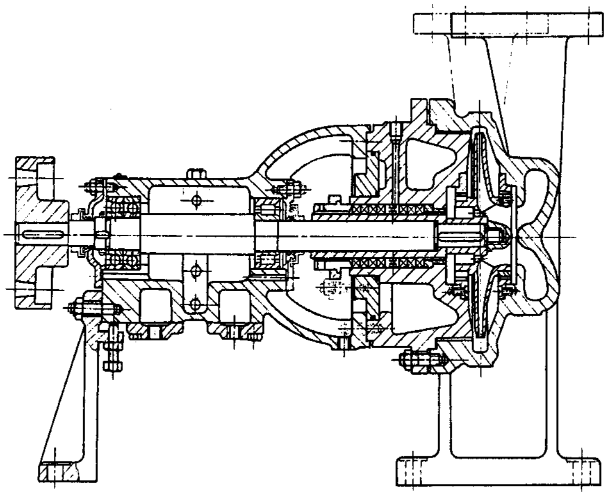

Fig. 1 Test pump cross section

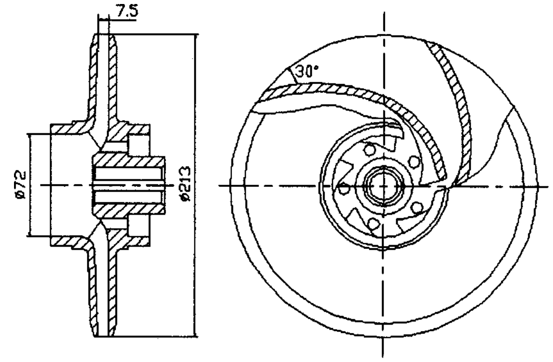

Fig. 2 Test impeller configuration

Apparatus

Test Pump. The test pump is a centrifugal oil pump of type 65Y60 based on API610 standard, which is commonly applied to transport hot oil with temperature less than 350°C. The design parameters of the pump are: flow rate $Q=25\ \mathrm{m^3/h}$, head $H=60$ m, rotating speed $n=2950r/\mathrm{min}$, and specific speed $n_s=n\sqrt{Q}/H^{0.75}=589$ (USGPM). Figure 1 shows the cross section of the pump and Fig. 2 presents the test impeller configuration.

Test Rig. The test rig is composed of a tank, global valve, suction and discharge pipes, turbine flow meter, gate valve, differential pressure sensor and torque detector. The sensor gives the difference of the liquid static pressure between the pump inlet and outlet and the detector indicates the torque input and the shaft speed. The total uncertainties of flow rate, head, input power, and efficiency are 0.707%, 0.205%, 0.515%, and 0.908%, respectively.

Density and Viscosity of the Oil. The test liquids are water and No. 100 mechanical oil, respectively. Both the oil density and the kinematical viscosity are function of the oil temperature. The relationship of the density with the temperature based on the measurement data can be written as

$$\rho=906.653-0.526715T$$

where ρ stands for the density of the oil and its unit is kg/m^3. T is the oil temperature and its unit is centigrade degree.

The relation between the oil viscosity and the temperature is

$$\nu=\frac{1}{1.01198\times10^{-5}T^2-2.222306\times10^{-4}T+2.86581\times10^{-3}}$$

where ν represents the kinematical viscosity and its unit is mm^2/s, that is equal to cSt. The kinematic viscosity values in the performance are: 1(water), 29, 45, 75, 98, 134, 188, and 255 cSt(oil), respectively.

Results

Performance Correction Factors. In order to determine the viscous oil performance when the water performance is known, the flow rate, head, and efficiency correction factors against viscosity are illustrated in Fig. 3. The flow rate, head, and efficiency correction factors K_Q, K_H and K_η are defined as

$$K_Q=\frac{Q_O}{Q_W},\quad K_H=\frac{H_O}{H_W},\quad K_\eta=\frac{\eta_O}{\eta_W}$$

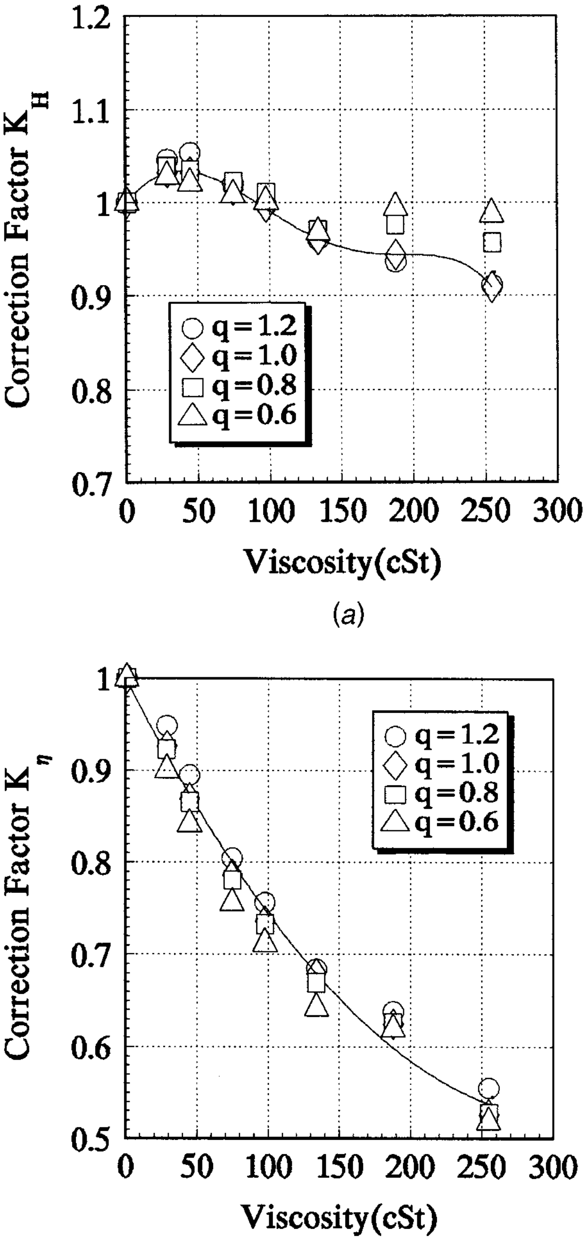

(*a*)

(*b*)

Fig. 3 Performance correction factors, (*a*) Head, (*b*) Efficiency

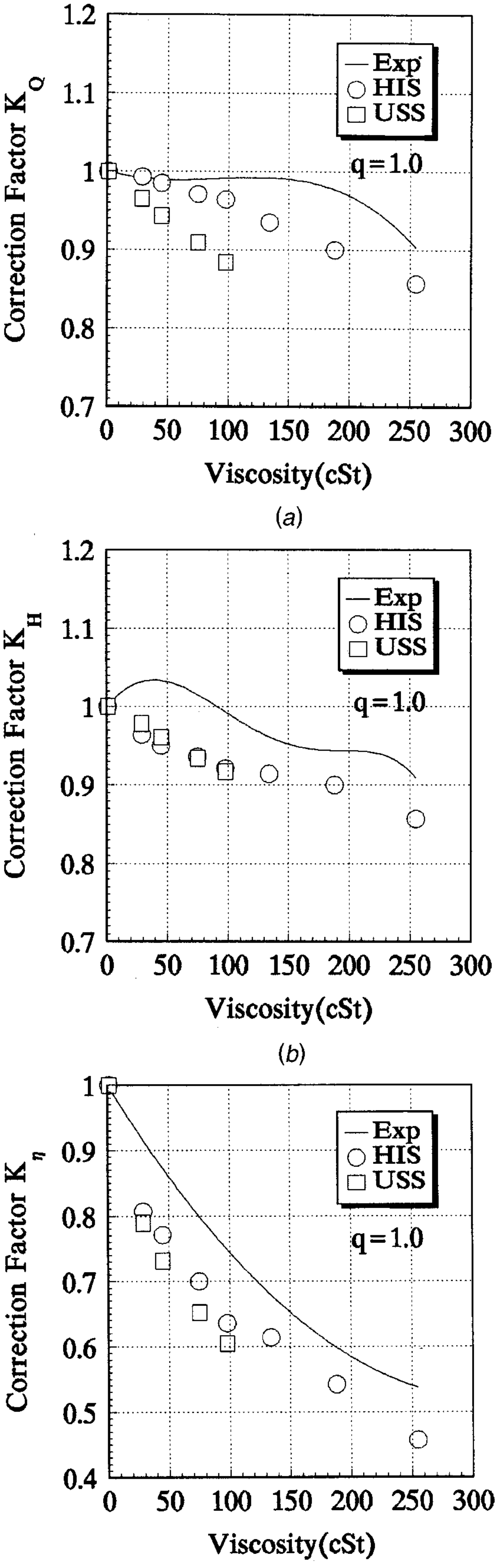

(*a*)

(*b*)

(*c*)

Fig. 4 Comparison of correction factors from author data with published Standards, (*a*) Flow rate, (*b*) Head (*c*) Efficiency

where Q_W, H_W, and η_W stand for the water flow rate, head, and efficiency at the selected point, Q_O, H_O, and η_O stands for the viscous oil flow rate, head and efficiency at the corresponding point. Here q is used to indicate the operation condition while pumping the viscous oil and it is defined as

$$q=\frac{Q_O}{Q_{OBEP}}=\frac{Q_W}{Q_{WBEP}}$$

where Q_{OBEP} represents the viscous oil flow rate at the best efficiency point and Q_{WBEP} denotes the water flow rate at the best efficiency point.

To examine the effects of pump operating condition on the head and efficiency correction factors, the factors corresponding to part-loading points $q=0.6$, 0.8 and over-loading point $q=1.2$ are also shown in the Fig. 3.

While the oil viscosity is less than 100 cSt, the head correction factors are independent from the operating condition. However when the oil viscosity is larger than 100 cSt, the head correction factors strongly depend upon the operating condition. Thus in determining the viscous oil head performance from water known head performance the pump operating condition should be distinguished while pumping high viscosity oil.

The efficiency correction factors depend on the operating condition only by a little. Therefore, in determining the viscous oil efficiency performance from water known efficiency performance the operating condition does not need to be distinguished.

Comparisons With Existing Factors. At present time, there are two sets of curves of the performance correction factors, one set has been proposed by Hydraulic Institute Standards (HIS) in 1994 [8], while the other set was published by the former Soviet Union (USS) in the 50s [9]. Figure 4 illustrates the comparison of presented paper with the two sets of the factors published in the above standards at best efficiency point, i.e., $q=1.0$. Figure 4 shows a large difference between the factors of this paper and those proposed by the former Soviet Union Standard (USS) in 50s. The maximum of the relative error of flow rate, head, and efficiency correction factors is 10%, 10%, and 22%, respectively. The flow rate, head, and efficiency correction factors proposed by Hydraulic Institute Standards (HIS) in 1994 also doesn't agree well with data of this paper, the maximum of the relative error of the flow rate, head, and efficiency correction factors is 8%, 6%, and 15%, respectively.

Conclusions

With regard to the test pump the following conclusions can be drawn:

1 The head correction factors are related to the pump operating conditions. Therefore in determining the performance of liquid with high viscosity from water known performance the head correction factors should be chosen with relation to the pump operating condition.

2 If the correction factors from published standards are used to determine the viscous oil performance such as flow rate, head, and efficiency from water known performance for current centrifugal oil pumps a relative error of 10% or more can occur.

Acknowledgment

This project was financially supported by the Education Department of the former Ministry of Machine-Building Industry and Gansu University of Technology, China. The authors thank Lanzhou Pump Works for providing the centrifugal oil pump and manufacturing the impellers.

References

[1] Daugherty, R. L., 1926, "A Further Investigation of Performance of Centrifugal Pumps When Pumping Oils," *Bulletin 130*, Goulds Pumps, Inc.

[2] Stepanoff, A. J., 1940, ''Pumping Viscous Oils with Centrifugal Pumps,'' Oil & Gas J., **4**, pp. 123–126.

[3] Telow, N., 1942, ''A Survey of Modern Centrifugal Pump Practice for Oilfield and Oil Refinery Services,'' The Institution of Mechanical Engineering, **121**, pp. 21–27.

[4] Ippen, A. T., 1946, ''The Influence of Viscosity on Centrifugal Pump Performance,'' Trans. ASME, **68**, pp. 823–846.

[5] Itaya, S., and Nishikawa, T., 1960, ''Studies on the Volute Pumps Handling Viscous Fluids,'' Bull. JSME, **26**, pp. 202–207.

[6] Stoffel, B., 1980, ''Tests on Centrifugal Pumps for Handling Viscous Liquids,'' Institute of Chemical Engineers, **3**, pp. 153–159.

[7] Li, W. G., and Hu, Z. M., 1997, ''An Experimental Study on Performance of Centrifugal Oil Pumps,'' Fluids Machinery, **25**, pp. 3–7.

[8] American National Standards Institute, 1994, ''American National Standard for Centrifugal Pumps,'' *ANSI/HI1.1-1.5*, p. 71.

[9] Yeshiman, Y. R., 1956, *Pumps* (Chinese edition), Petroleum Industry Press, Beijing, p. 63.